



**UNIVERSITÀ
DEGLI STUDI
DI BRESCIA**

UNIVERSITÀ DEGLI STUDI di BRESCIA

DOTTORATO DI RICERCA IN:

INGEGNERIA MECCANICA E INDUSTRIALE

PROGETTAZIONE MECCANICA E COSTRUZIONE DI MACCHINE (ING-IND/14)

CICLO XXXIII

FATIGUE DAMAGE DUE TO RANDOM LOAD:

NUMERICAL, EXPERIMENTAL ANALYSIS, AND DESIGN AN INNOVATIVE TESTING MACHINE.

DOTTORANDO

Michele CIMA

firma

RELATORE

PROF. LUIGI SOLAZZI

firma

NOTE:

*Cosa è che conferisce valore a una cosa? La **fatica** di poterla raggiungere, la **fatica** impiegata per ottenerla. Nello spazio noi facciamo **fatica** a raggiungere un posto e attraverso questa **fatica** raccogliamo un mare di informazioni e quando questo posto viene raggiunto, [...] ce lo ricordiamo perché è tutta la **fatica** investita che ce lo rende prezioso.*

E nel tempo?

Nel tempo è la stessa cosa. Sarebbe un problema smarrire il senso dell'attesa la velocità repentina di poter ottenere una cosa ci toglie l'attesa. In assenza di attesa il desiderato non ha quel valore che altrimenti avrebbe avuto se lo avessimo dovuto aspettare.

Way Into the Future But Watch Your Step! TEDxLUISS

Paolo Bonolis

*A chi mi ha voluto bene, capito,
non giudicato, dato coraggio, forza e
ha creduto in me . . .*

RINGRAZIAMENTI

Ringrazio il prof. Luigi Solazzi che, con il suo ruolo di tutor è stato guida e supporto per questi tre anni e mezzo di lavoro e di vita.

Ringrazio i Prof. Donzella e Mazzù che mi hanno accolto nel gruppo di costruzioni di machine con spirito propositivo e sono sempre stati disponibili al confronto.

Ringrazio i colleghi dottorandi e in particolare Federico e Andrea con i quali mi sono sentito parte di un gruppo e ho condiviso questo percorso.

Ringrazio l'Ing. Brame e l'azienda GKN WHEELS di Carpenedolo per il supporto.

Ringrazio gli studenti che ho conosciuto con i quali ho collaborato durante questo dottorato. Il loro apporto è stato fondamentale per l'attività.

Ringrazio la mia famiglia per avermi sempre sostenuto, sopportato e avermi dato fiducia sempre, permettendomi di raggiungere anche questo obiettivo.

Infine ringrazio tè papà. Non posso ormai più raccontarti di questa tesi, del dottorato e di nulla. Nel profondo ho un desiderio che però non potrò mai realizzare: poter avere ancora un attimo per ringraziarti di tutto quello che hai cercato di insegnarmi, e tra le tante: del valore del sacrificio e del lavoro. Di certo non potrò essere realizzato ma prometto che cercherò, nella mia pochezza, di renderti orgoglioso e render viva la tua presenza con la mia.

SUMMARY

ITALIAN ABSTRACT	1
PREFACE:.....	2
1. FATIGUE INTRODUCTION.....	1
1.1. Random fatigue.....	1
1.2. Methods not take into account sequence of application of the stresses.....	2
1.2.1. Level crossing.....	2
1.2.2. Peak counting	2
1.3. Methods that take into account the sequence of application of the stresses .	3
1.3.1. Tank method.....	3
1.3.2. Rainflow method.....	4
1.3.3. Palmgren-Miner cumulative damage rule	4
1.4. Outline of fracture mechanics	5
1.5. Strain-life approach.....	6
1.6. Fatigue tests.....	8
1.7. Tests for fatigue characterization of materials.....	9
1.8. Main types of specimen	11
1.9. General information on the test execution procedure.....	12
1.10. Test programs and service simulation	12
1.11. Fatigue test data report	13
1.12. Measurement and analysis of test parameters.....	13
1.13. Laboratory tests for fatigue characterization of the component.....	15
1.14. Loads and actions on the wheel	16
1.15. Rotation bending test.....	20
1.16. Rolling test.....	24

1.17.	Field tests for fatigue characterization of the component	27
1.18.	Finite element analysis for fatigue damage calculation	30
1.19.	Comparison from: laboratory tests, field tests and FEA	32
2.	EXPERIMENTAL TESTS:	36
2.1.	Test on field	36
2.2.	Material	39
2.3.	Tensile tests	39
3.	TESTING PHASE BEFORE ANALYSIS	44
3.1.	Fatigue tests.....	44
3.2.	Input data	47
4.	TIME DOMAIN.....	49
4.1.	Rainflow analysis.....	49
4.2.	Haig's law.....	50
4.3.	Wöhler's curve	51
4.3.1.	How to calculate N_i	53
4.4.	Miner's law	53
4.5.	Hanshin-Rotem correction	53
4.6.	Time domain, results.....	54
5.	STATISTICAL ANALYSIS (an outline).....	54
5.1.	Input signal	54
5.1.1.	Basic parameters.....	55
5.1.2.	Autocorrelation.....	56
5.1.3.	Probability density function (PDF)	57
5.1.3.1.	Independence of contributory causes	58
5.1.3.2.	Interdependent events.....	58

5.1.4.	A common error.....	63
5.1.5.	Choosing a good PDF.....	63
5.1.5.1.	Histogram	64
5.1.5.2.	Probability plots	64
5.2.	Fourier theorem and rearranges	69
5.2.1.	FFT analysis.....	69
5.2.2.	PSD and ASD analysis	70
6.	FATIGUE IN FREQUENCY DOMAIN	74
6.1.	Input signal	75
6.2.	Statistical analysis	75
6.2.1.	Autocorrelation.....	75
6.2.2.	Probability density function (PDF)	79
6.3.	Frequency analysis	84
6.3.1.	FFT applied on load histories.....	84
6.3.2.	PSD applied on load histories	88
6.4.	Fatigue damage estimation	92
6.4.1.	Parameters form PSD.....	92
6.4.2.	Narrow band and broad band processes	93
6.4.3.	Probability density function (PDF)	94
6.4.4.	Fatigue damage.....	95
6.4.5.	Fatigue estimation	96
6.4.5.1.	Narrow Band (NB)	96
6.4.5.2.	Broad Band Approximation	96
6.5.	Fatigue damage calculation.....	97
6.6.	Two new approaches	99

6.6.1.	Ortiz method.....	99
6.6.2.	Dirlik method	99
6.7.	Notes about the use of windows	100
7.	EXP. AND ANALYTICAL STUDY OF FATIGUE, IN t AND f. DOMANI (PAPER).....	101
8.	FREQ. DOMAIN FATIGUE DAMAGE APPLIED TO A VEHICLE WHEEL (PAPER)	127
9.	STUDY OF AN INDUSTRIAL RIM FA APPROACH	156
9.1.	Field tests.....	157
9.1.1.	Test description	157
9.1.2.	Laboratory tests	159
9.1.3.	Laboratory data analysis	160
9.2.	Static study of the rim	165
9.2.1.	Introduction	165
9.2.2.	Inflation tests	166
9.2.2.1.	Experimental data	166
9.2.2.2.	Stress component considered	167
9.2.2.3.	Automotive theory-based analyses	170
9.2.2.3.1.	Introduction to automotive theory-based analyses	170
9.2.2.3.2.	1st analysis: application of p from automotive th	173
9.2.2.3.3.	2nd app. of p from automotive th. with corrective coeff.	177
9.2.2.3.4.	3rd analysis: p from automotive th. for lab. results	180
9.2.2.4.	Tire 3D model approach	184
9.2.2.5.	Empirical approach applied to the inflation problem	187
9.2.3.	Radial load tests.....	207
9.2.3.1.	Rolling tests experimental data	207
9.2.3.2.	Model and analyses applied to the radial load problem	214

10.	Fatigue study of the rim	245
10.1.	Introduction	245
10.1.1.	Analysis instruments and functions	246
10.2.	Study hypotheses	247
10.3.	Fatigue curve of the material	250
10.3.1.	Simulation settings and parameters	252
10.3.2.	Analyses results and comparisons	254
10.4.	Analysis of the load cycle applied to the rim.....	257
10.5.	Simulations results	261
10.6.	Conclusions	264
10.6.1.	Results analysis	264
11.	FEM MODEL FOR PRESSURE PROF. IN IND. RIM (PAPER)	270
12.	CONCLUSIONS.....	296
12.1.	RESERCH ACTIVITY.....	300
	REFERENCES.....	302
13.	APPENDIX 01: TESTING MACHINE.....	305
13.1.	Machine design.....	306
13.1.1.	Gaugh-Stewart platform (exapode table)	307
13.1.2.	Belt unit	308
13.1.3.	Main frame	308
13.1.4.	Press	309
13.1.5.	FE Analysis	310
13.1.6.	Natural freq. analysis	313
13.1.7.	Optimization and check of natural freq.	314
13.2.	Future developments	315

ITALIAN ABSTRACT

In questa tesi viene presentato il lavoro svolto sulla fatica random.

In particolare l'attività di dottorato si è sviluppata con un' iniziale analisi della bibliografia relativa ai metodi di conteggio nel regime del tempo e della frequenza. Definiti gli algoritmi più usati nel dominio della frequenza c'è stata la possibilità, grazie ad acquisizioni sperimentali, di testare questi metodi su un componente reale, ossia una ruota industriale, il tutto tramite la collaborazione con l'azienda *GKN wheels*.

In dettaglio sono state eseguite le prove sperimentali. Estrapolato i dati, tali sono stati utilizzati per applicarle i metodi in frequenza selezionati in bibliografia comparandoli, sulla base del conteggio del danno, con i metodi nel tempo e ottenendo una prima analisi di quali fossero i vantaggi e gli svantaggi, dei singoli metodi. Quest'attività è sfociata in un paper pubblicato sulla rivista *"Engineering failure analysis"* un lavoro intitolato *"Experimental and analytical study of fatigue, in time and frequency domain on an industrial wheel"*.

Durante questa prima fase dell'attività si è poi visto che l'applicazione dei metodi di conteggio in frequenza richiedeva alcune assunzioni legate alla storia di carico del componente; non sempre di facile verifica. Per tale motivo si è deciso di lavorare ulteriormente in questo senso in quanto si è notata una importante differenza tra il valore di danneggiamento calcolato con i metodi in frequenza e quello nel regime del tempo.

Abbiamo quindi lavorato sulle storie di carico per l'analisi delle assunzioni fatte (distribuzione gaussiana, segnale ergodico e segnale a banda stretta) necessarie per l'applicazione dei metodi in frequenza. Si è infine rilevato in bibliografia la possibilità di correggere questi metodi con fattori correttivi. Sono stati applicati tali fattori correttivi ai metodi in frequenza nel caso in studio delle ruote industriali. I risultati non hanno evidenziato una buona sovrapposizione con i metodi nel dominio del tempo che rappresentano, anche in questo caso, il riferimento. Grazie a questa ulteriore analisi sulle assunzioni è stato possibile comprendere maggiormente la logica dei metodi in frequenza e le cautele che sono necessarie quando li si utilizzano in quanto si rischia di tagliare il segnale in zone in cui la sua intensità è elevata.

Per questo lavoro si è in fase di definizione di un paper che è stato riportato nella tesi e deve essere sottomesso per revisione.

L'ultimo *setp* è consistito nell'introduzione del FEM per studiare il comportamento a fatica anche questo caso applicato su un componente reale; si è studiato infatti l'andamento dello stress sul raggio della ruota GKN. Seguendo lo stesso approccio precedente sono stati eseguiti test sperimentali sulla ruota in diverse condizioni di carico del veicolo e di pressione dello pneumatico. Inizialmente acquisiti i dati di stress nella zona di interesse tali sono stati confrontati con quelli calcolabili al FEM. A valle di questa analisi è stato necessario definire una procedura di tuning per calibrare il ns modello. Eseguita la validazione si è poi passati ad utilizzare i dati in uscita dal modello per il calcolo a fatica della zona di interessa.

Questo lavoro si è tradotto in un paper che è in fase di revisione dalla rivista "*Engineering Failure Analysis*"

Come ultima attività è stato studiato un primo concept di macchina di testing per il gruppo pneumatico sospensione. Appurato durante l'esecuzione delle prove sperimentali che tali possono essere molto onerose e richiedere tempi importanti nel caso di applicazioni di fatica, si è pensato ad un concept di macchina che consentisse di impostare e replicare le variabili salienti definite in fase di test, ma in una macchina di laboratorio. Attualmente il primo concept è ancora in fase di sviluppo tramite lavori di tesi e elaborati.

Questa attività è stata presentata alla conferenza MDA 2020 presso l'università di Porto con un poster.

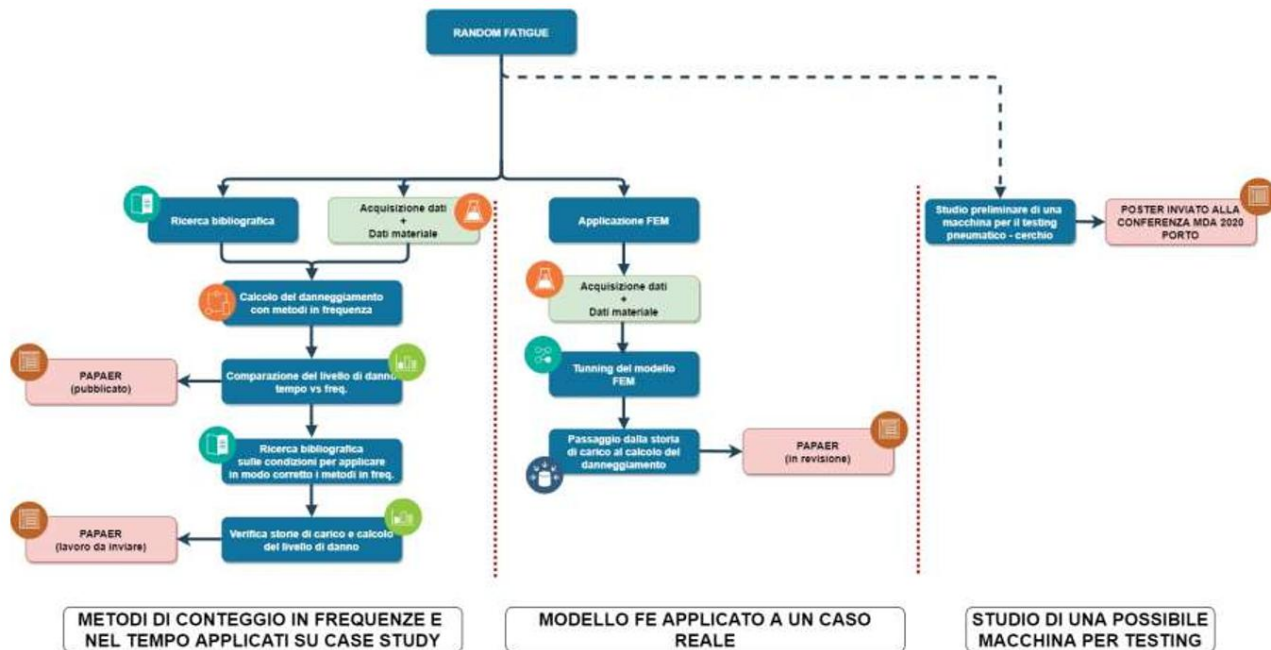
In conclusione si può vedere che l'attività svolta ha spaziato a 360° sulle tematiche della fatica random, sfruttando l'opportunità di poter applicare i concetti sul case study della ruota industriale.

La prima parte del lavoro potrebbe essere proseguita sviluppando una categorizzazione dei metodi in frequenza migliori in funzione: dell'applicazione e in modo indiretto della storia di carico. Oltre a questi due aspetti interessante sarebbe replicare il lavoro per diversi materiali, andando a verificare la sensibilità dei metodi di conteggio usati, rispetto ai parametri materiale e per applicazioni diverse rispetto alle

ruote industriali. In questo modo si potrebbe avere una visione più completa del problema e valutare i metodi in frequenza in modo più dettagliato e su ampio spettro.

Per quanto riguarda la tematica simulazione, interessante potrebbe essere la definizione di modelli FEM che consentano di eseguire test di fatica passando attraverso un *tunning* iniziale e un eventuale calibrazione finale del modello tramite prove sperimentali, sulla falsa riga di quanto abbiamo fatto nella nostra applicazione delle ruote industriali ma per altre applicazioni al fine di definire procedure di lavoro standard che possano agevolare lo sviluppo prodotto.

Infine riguardo alla macchina di prova, sarebbe necessario, una volta ristretto il numero di parametri e variabili impostabili per il test, analizzare l'architettura per facilitarne la programmazione software (ad esempio ad oggi è presente una tavola *exapode* che è molto complessa da movimentare), e renderla poi producibile redigendo la documentazione tecnica necessaria e a seguire un primo prototipo.



PREFACE:

For the last three years, my tutor, students and I have worked together as a team to check what papers and works had already stated about the art in fatigue.

In the industrial field, except for particular applications (aeronautics, military, safety, etc.,) the fatigue problem is usually avoided with the use of a safety factor: by applying a limitless fatigue life it is possible to avoid any analysis. If a fatigue check is instead needed, it is possible to use the Miner Rule.

Therefore, we started by checking the state of the art in term of fatigue methods in frequency domains. After the theory, we tried to apply the most used (but not so common) methods on a real case study.

We were able to perform several tests on the field and to state the deformation on an industrial wheel thanks to the cooperation with the company GKN, which operates worldwide.

After collecting all the data, we applied the methods found in the bibliography and compared the results from time domain methods and frequency domain methods. Therefore, we were able to have a first overview of the problems, advantages and disadvantages of the frequency approach.

From this first research we have developed an article, which was later published.

Though, designers need to be cautious while applying the frequency methods. Some of our assumptions during the first part of the work can lead to a wrong result. Thus, since our research on the industrial wheel gave us pretty different results, we have switched our focus in this case on the assumptions. [Our article based on this research was sent to an international journal and it is still in review.]

We have then decided to study the fatigue problems on the wheel by studding the stress on the radius of the rim. Again, we did some experimental tests on the wheel in different conditions of pressure. We have stated a gap between our data and the FE analysis, which was related to the fatigue. After getting such an unexpected behaviour of the stress on the component, we developed a method which is particularly close to the data acquired on field. Then, we were able to perform the fatigue analysis.

During our research, we have learnt how crucial it is to study problems where the fatigue is involved on the application of wheels. Thanks to our work with the company GKN,

we can also state that a method always requires a validation of the model or a validation of the predictions by field testing.

Therefore, we have thought of a test machine that can reduce the lead time for a validation.

It is only a first draft, but we have already clear in our minds its main characteristics and tasks.

The concept of the machine was presented at MDA 2020 on a web congress.

In conclusion, we need to underline the fact that our work is based on an applied research on nonconventional methods used for a long load history. Our cooperation with GKN and the focus on the industrial wheel led to a second and third research and to a new test approach.

Below, a flow chart with the targets of this work.

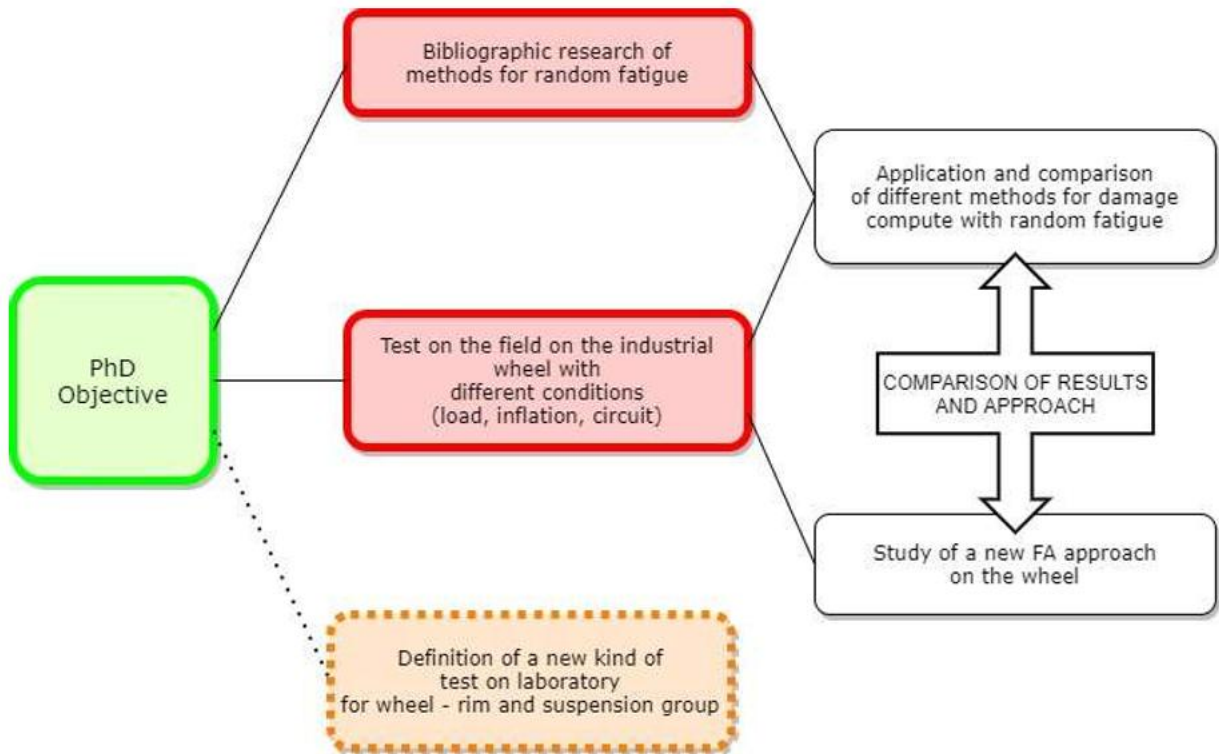


Figure 1 PhD targets

1. FATIGUE INTRODUCTION

1.1. Random fatigue

When the load cycle has a randomly variable stress amplitude over time, it is called random fatigue. A first difficulty of this phenomenon is knowing exactly the trend of the stresses over time. To do this, it is common practice to carry out field tests or laboratory tests, from which the load and deformation cycles are obtained by means of strain gauge measurements. Subsequently the total life of the component is divided between “typical” load spectra, each of which represents a significant and repetitive phase. A further step is to apply counting methods in order to transform the typical load spectrum (Figure 2) into a series of equivalent cycles with constant amplitude (Figure 3). This is done in order to be able to use cumulative damage criteria (usually *Palmgren-Miner*) to calculate the total damage and the fatigue life of the component. [1]

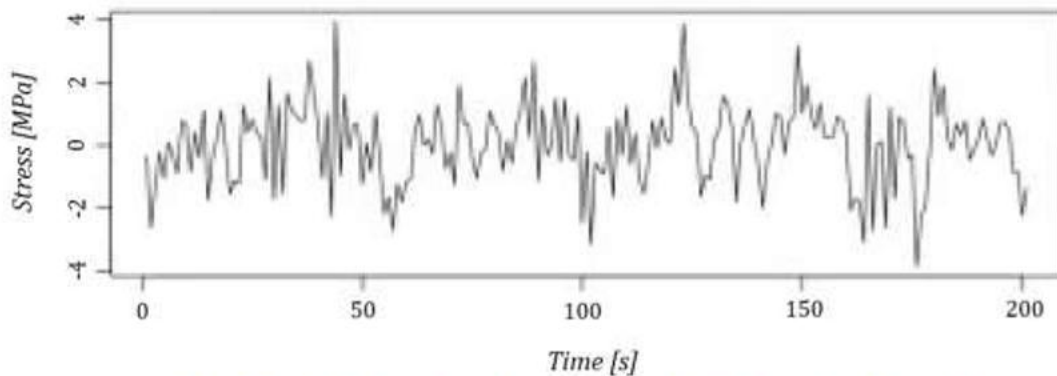


Figure 2 Typical load spectrum of a component subjected to random fatigue. [2]

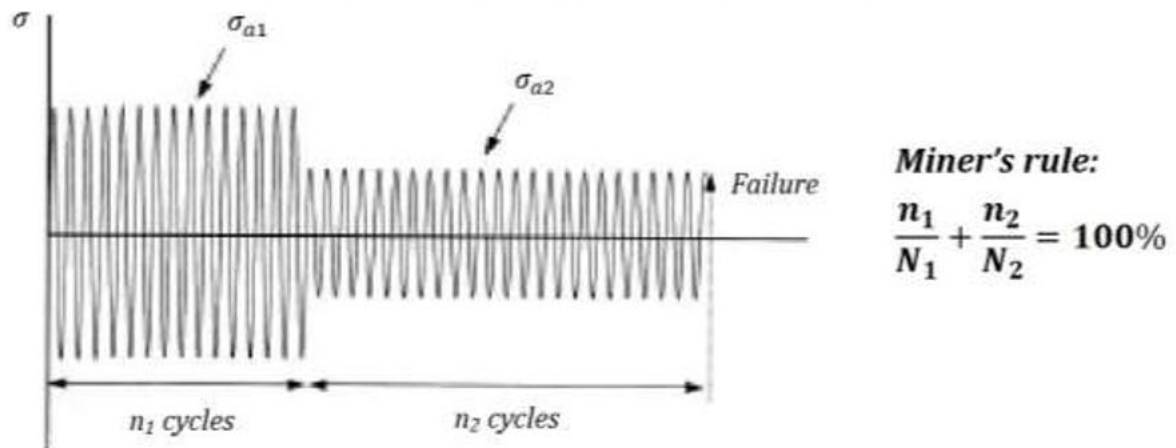


Figure 3 Load spectrum diagram of a component subjected to random fatigue after applying a counting method (left). Miner rule (right). [3]

Counting methods can be divided into two categories: those that take into account the chronology of application of the stresses and those that do not consider it. The former are simpler and faster, while the latter are more complex, but provide a more accurate result. In fact, the succession of cycles of different amplitude determines delay or acceleration in the birth and propagation of the crack. [1]

1.2. Methods not take into account sequence of application of the stresses

1.2.1. Level crossing

Method by which the ordinate axis (stress) is discretized and each time the load history passes through a level, a load cycle with that stress amplitude is counted. [4]

1.2.2. Peak counting

It is a method that consists in detecting the first highest peak and the first lowest valley with respect to a reference value; this pair of points composes the first cycle. Therefore, the second highest peak and the second lowest valley are considered in this way to constitute the second cycle and this procedure continues until all peaks are exhausted (Figure 4). [4]

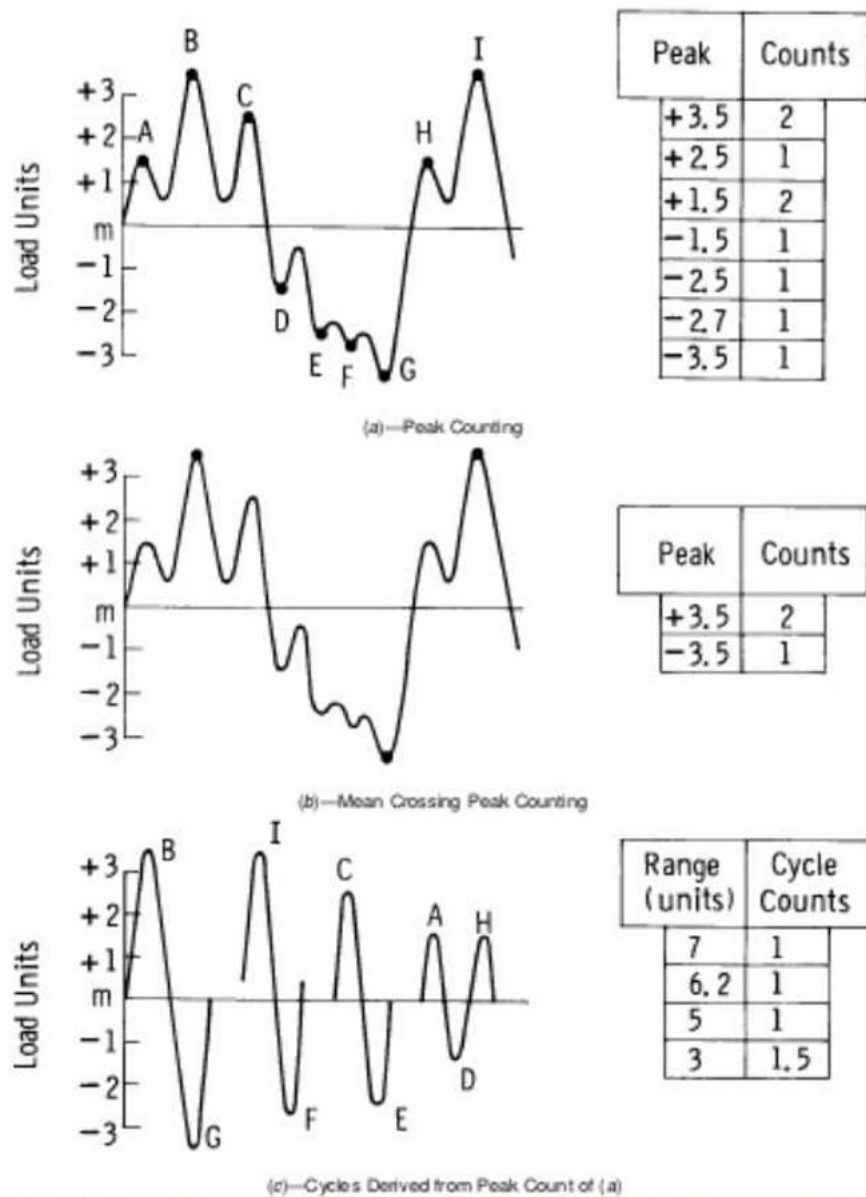


Figure 4 Graphical representation of the application of the peak counting method. [5]

1.3. Methods that take into account the sequence of application of the stresses

1.3.1. Tank method

This method starts from a stress diagram as a function of time and it is assumed to be repeated n -times during the life of the component. Starting from this spectrum, the tank method proceeds as follows:

1. The absolute maximum is identified; the part of the spectrum that precedes it is broken and returned to the end of the cycle, re-joining any discontinuities with a segment;
2. The new spectrum is assumed as a tank full of water, which starts and ends at the same altitude.

Set these conditions, we proceed by imagining to open a tap in the lower valley in order to empty the tank (Figure 5), and we create a cycle that has as its amplitude the difference between the free surface of the water and the height of the minimum considered. The water will remain trapped by other valleys and that will gradually be emptied starting from the lowest remaining valley and considering cycles that have as their stress amplitude always the difference between the free surface of the water and the altitude of the valley considered. Thus, each cycle obtained will then be considered repeated n -times, as assumed for the load history. [1]

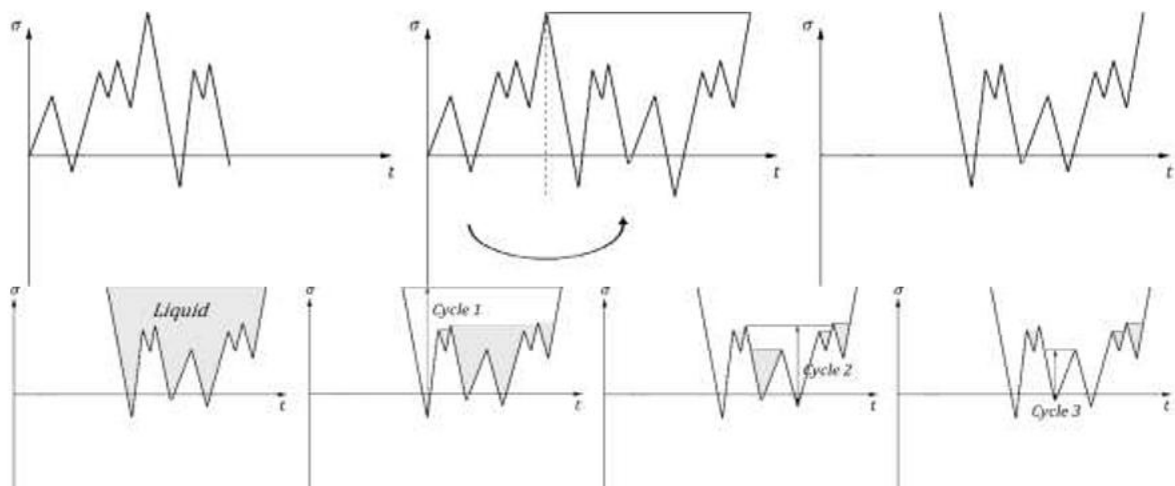


Figure 5 Graphical representation of the first two hypotheses for procedures with the tank method (above) and of the application of the tank method (below). [1]

1.3.2. Rainflow method

The method consists in studying a load history, a portion of which is considered to be repeated n -times. The stress-time diagram must be rotated downwards and then it is assumed that there is rain falling from above, so the different peaks and valleys are like slopes on which the water flows (Figure 6). The origin of the time is positioned in the absolute maximum and then it is considered that the water along the slopes is blocked if:

- encounters a flow of water from a higher slope;
- the water flows reach the altitude of a slope that starts from a higher maximum (or a lower minimum) than the one from which they begin.

Between the start and the end of each cycle, half cycle is considered. [4]

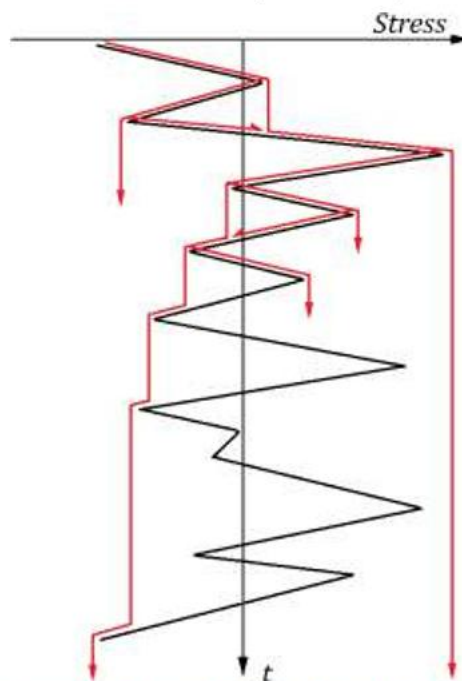


Figure 6 Graphical representation of the application of the Rainflow method. [2]

1.3.3. Palmgren-Miner cumulative damage rule

This criterion assumes that each i^{th} series of cycles, at stress level σ_i , determines a fraction of damage f_i equal to the ratio between the number of cycles n_i carried out at this level and the number of cycles N_i which would determine the failure to the same level [6]:

$$f_i = \frac{n_i}{N_i} \quad 1-1$$

Fatigue failure is obtained when the sum of all the damage components reaches the unit:

$$\sum_i f_i = 1 \quad 1-2$$

Therefore, during the design phase, the total damage value is less than one:

$$\sum_i f_i < 1 \quad 1-3$$

1.4. Outline of fracture mechanics

As shown in the previous paragraphs, the phenomenon of fatigue begins with the formation of micro-cracks in the proximity of defects present inside the material. The fracture then propagates until it reaches a size such as to bring the component to failure. Fracture mechanics studies the growth of the crack at the macroscopic level. The theory starts from the consideration that in the proximity of a defect there is an over-stress zone that can be described by the parameter K_t :

$$K_t = 1 + 2 \sqrt{\frac{a}{\rho}} \quad 1-4$$

Where a is the half-length of the notch and ρ is the radius of the apex. It is possible to note that in the case of a crack the apex is acute and thus the radius ρ becomes infinitesimal bringing the K_t to infinite values. In these conditions the linear-elastic fracture mechanics (*LEFM*) takes over and it considers the stress intensification factor (*K - Stress Intensity Factor*) as a fundamental parameter:

$$K = y \cdot \sigma \cdot \sqrt{\pi \cdot a} \quad 1-5$$

where:

- a is the half-length of the crack;
- σ is the stress that would occur in the crack area if this were not there;
- y is a dimensionless factor that depends on the component geometry.

It is noted that the stress distribution, near the apex of the crack, can be represented by a linear variation of the factor K . In a component subject to cyclical loads there is also the variation of the factor of intensification of the stresses between a minimum value K_{min} and a maximum one K_{max} . The difference between them is:

$$\Delta K = y \cdot \Delta\sigma \cdot \sqrt{\pi \cdot a} \quad 1-6$$

where $\Delta\sigma$ is the stress amplitude to which the structure is subject. The cycle ratio can also be applied to K :

$$R = \frac{\sigma_{min}}{\sigma_{max}} = \frac{K_{min}}{K_{max}} \quad 1-7$$

Experiments can be performed with several specimens stressed with different load amplitudes in order to obtain different ranges of ΔK . Cracks arise in correspondence with the surface or with discontinuities. Taken a defect with semi-length a , the growth of the crack, a function of N , will depend on $\Delta\sigma$ and ΔK . Paris monitored the growth of the crack as a function of K and then represented the results by comparing the growth factor of the crack based on the number of cycles (da/dN) as a function of the stress intensification factor (K).

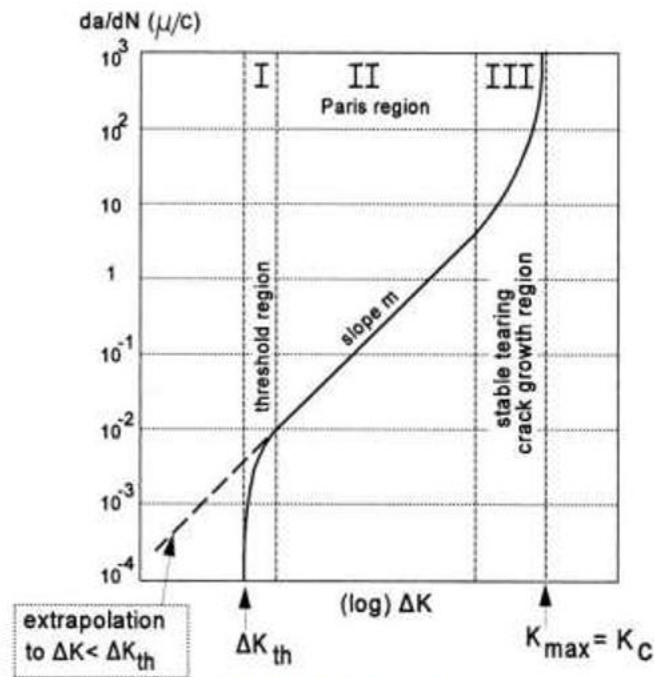


Figure 7 Paris diagram. [3]

From this graph (Figure 7), it is possible to identify three areas:

- the first region (*threshold region*) is identified by a K_{th} value, below which the crack does not propagate, and well described by a curve with slow growth;
- the second region (*Paris region*) shows a linear growth of the crack:

$$\frac{da}{dN} = C \cdot \Delta K^m \quad 1-8$$

- the third region (*stable tearing crack growth region*) shows an unstable growth of the crack up to the failure identified by the achievement of the K_C value.

1.5. Strain-life approach

In the previous sections, a method of studying the fatigue phenomenon linked to the $S-N$ curve was shown, which is called the *stress-life* approach. The latter puts the load at the centre of the analysis of fatigue life and it is mainly used for structures found in the field of

fatigue with high number of cycles (*HCF*). In this paragraph, the *strain-life* approach, which focuses on the deformations that the component undergoes, will be mentioned. This type of fatigue problem analysis focuses on the components that work in the area of the *Wöhler* curve called *low cycle fatigue (LCF)* or also called *oligocyclic fatigue*. In these structures, the stress amplitude is so high that it leads to high levels of plastic deformation. Laboratory tests are carried out on specimens to which a deformation amplitude ($\Delta\varepsilon_a$) is imposed. From the tests, it can be seen that the component has a cyclic behaviour following the variable deformation that leads to the formation of a hysteresis. The latter changes in the first load cycles, as there is a variation in the characteristics of the material, which stabilizes its properties after a certain number of cycles. The results can be hardening (if there is an increase in properties) or softening (if there is a decrease in properties); there is also the eventuality that the material properties remain almost constant. The high stress amplitude causes deformations to enter the plastic field, so the total deformation ($\Delta\varepsilon_t$) is the sum of the elastic ($\Delta\varepsilon_e$) and plastic ($\Delta\varepsilon_p$) component:

$$\varepsilon_t = \varepsilon_e + \varepsilon_p \quad 1-9$$

These can be expressed respectively with *Hooke's law* and *Ramberg-Osgood's law*:

$$\varepsilon_e = \frac{\sigma}{E} \quad 1-10$$

$$\varepsilon_p = \left(\frac{\sigma}{K}\right)^{\frac{1}{n}} \quad 1-11$$

where K and n are parameters related to the properties of the material. When its properties stabilize, a quote is added on the two parameters: K' and n' . By graphing the variation of the deformation components as a function of the number of double logarithmic breaking cycles, a linear variation is obtained for both elastic and plastic deformations (Figure 8).

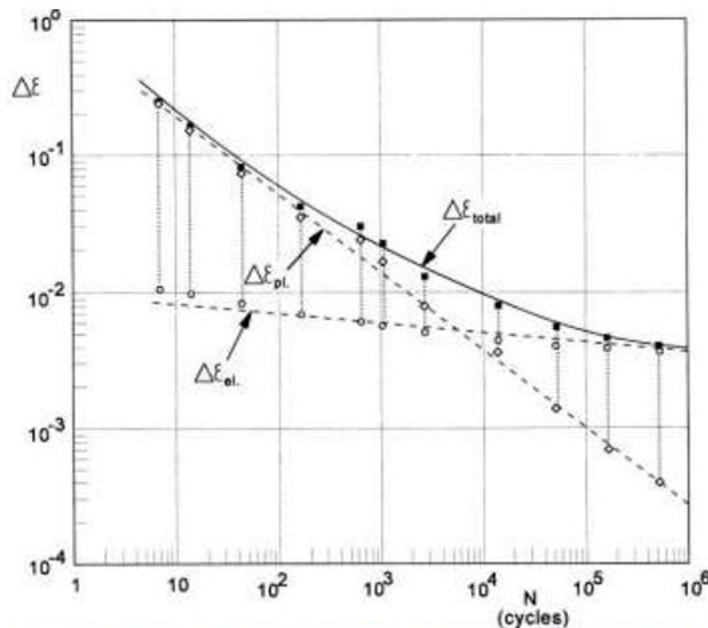


Figure 8 Diagram of the variation of the deformation components. [3]

From the sum of these, it is possible to obtain *Manson-Coffin's law*:

$$\frac{\Delta \varepsilon_t}{2} = \frac{\sigma_f'}{E} \cdot (2N)^b + \varepsilon_f' \cdot (2N)^c \quad 1-12$$

where:

- σ_f' is the fatigue resistance coefficient (defined by the stress intercept for $N=1/2$);
- b is the exponent of the fatigue strength;
- ε_f' is the fatigue ductility coefficient (defined by the deformation intercept for $N=1/2$);
- c is the fatigue ductility coefficient.

Manson-Coffin's law represents the relationship between fatigue life and amplitude of the total deformation used to determine the fatigue life of a component (imposed deformation). The intersection between the straight line of plastic and elastic deformation indicates the approximated boundary between the predominant conditions of oligocyclic fatigue and high cycle fatigue.

1.6. Fatigue tests

In the field of materials characterization and components fatigue analysis, the execution and study of experimental tests becomes fundamental. In fact, it allows to obtain experimental data that can be compared with the results of theoretical and numerical models in order to verify the goodness of the latter, both in the field of material characterization and in the design phase. The purpose of fatigue tests is, first, to determine the fatigue properties of materials, to obtain information on their behaviour under cyclic stress conditions and to be able to detail them to the components in the design phase. Secondly, fatigue tests can be carried out on the components themselves, in order to verify the fatigue behaviour of the specific structure. In general, a fatigue test requires a high experimental and timing effort, which leads to these tests being very expensive. However, the realization of tests is extremely important for the fatigue verification of structural elements, since the empirical results obtained in the field and in the laboratory are assumed more truthful than those of the theoretical analyses. Correct settings and experimental tests are equally fundamental, since a

fatigue test not carefully chosen for the problem in question can give the right answer to the wrong question. Going into more detail, the purposes of fatigue tests can be:

- collecting data on the fatigue properties of the material for the best possible choice of the same during the design phase;
- investigating the effects of different surface finishes and production techniques on the fatigue behaviour of materials and components;
- studying the fatigue strength of structural elements;
- investigating the influence of environmental conditions on the fatigue behaviour of materials and components;
- studying, in the context of fracture mechanics theory, the nucleation and the propagation of cracks, i.e. the defects responsible for fatigue failure of mechanical components;
- elaborating experimental models and verifying theoretical models for predicting fatigue life.

Experimental tests can take place in the field of application of the component, if its characteristics allow it. This allows to take data on the behaviour of the piece in the exact operating conditions for which it was designed and, therefore, to obtain particularly significant information. In parallel with the field tests, the tests can take place in the laboratory activity, within which it is possible to distinguish the mechanical tests between those intended for the characterization of the material and those designed to analyse the fatigue behaviour of specific components. In the laboratory, machineries are used which are designed to generate loads and stress states on the structure considered critical for the fatigue strength of the structural element. The following paragraphs will provide a general description of the laboratory tests for the characterization of the tests, in the field and in the laboratory, intended for the study of the component. In particular, the focus will be put on the examination of the tests that can be performed on the rims for heavy vehicles, object of this thesis. [3]

1.7. Tests for fatigue characterization of materials

Mechanical fatigue characterization tests of materials are performed on specimens of standard geometry. In fact, the standardization of the quality of the material, of the dimensional and shape control and of the surface finish allow a significant reduction in the

variability of the test results. The tests in question are dynamic, carried out using machines capable of producing cyclic axial, torsional or bending stresses (Figure 9).



Figure 9 Machines for the mechanical characterization tests of the material. [7]

The legislation prescribes, for each type of test, the geometric characteristics and surface finish that the specimen must report and the conditions in which the test must be carried out. The purpose of these tests is to determine the fatigue limit of the material, i.e. the maximum cyclic stress which can be applied so that the working life of the specimen, and therefore of the material, is infinite. As mentioned, however, the fatigue limit of the material varies considerably depending on the type of action applied to the specimen and, for this, there are different fatigue limits (axial, torsional and flexural), which can be identified with different types of mechanical tests. Among them, the most common is the rotating bending fatigue test, in which the specimen is rotated around its axis and, at the same time, a load is applied perpendicular to it. The test is performed in order to generate a deflection, which, in a reference system integral with the specimen, turns continuously around the specimen axis. In this way, the generic point inside the specimen will be subjected to a symmetrical alternating stress with a sinusoidal trend, continuously passing from a traction state to a compression state. A similar test is used to determine the bending fatigue limit (σ_{FA_f}) of the material by applying, during different test sessions with separate specimens, gradually decreasing loads and counting for what number of cycles the failure occurs. The axial fatigue limit (σ_{FA_a}) can be obtained by means of tensile testing machines, which are capable of developing a cyclic displacement of the mobile cross member. Finally, dedicated machines are used for cyclic torsion test in which the torsional fatigue limit (σ_{FA_t}) is identified.

1.8. Main types of specimen

In the context of the various cyclic dynamic tests, different types of specimens can be used in order to study the behaviour of the material in presence of strong geometric discontinuities. Therefore, it is possible to distinguish:

- *Specimens without notch*: these are specimens with sufficiently regular geometry and surface, according to standards imposed by regulations. In practice, minimal discontinuities are inevitable and the notch coefficient K_t cannot be considered perfectly unitary. The irregularities of the specimen determine areas where the resistant section is lower, as well as the defects of the material can give rise to nucleation and propagation of the crack. However, the notch effects can be significantly reduced by adding chamfers and through the appropriate dimensional control. The tests carried out with specimens of this type cannot give information about the sensitivity to notching of the material, but they can give useful results to characterize their fatigue behaviour in relation of the surface finish [7]
- *Notched specimens*: these types of specimens are characterized by geometric discontinuities such as to allow the onset of the notch effect inside a portion of the specimen itself (Figure 10). The fatigue properties given by the supplier are usually limited, for this kind of specimens, to the fatigue limit (σ_{FA}) of the material only, without information on the type and geometry of the specimen used to determine it. Often a preliminary activity consists in carrying out tests to derive the $S-N$ curve in the conditions of average zero stress and minimum zero stress. However, the purpose of the tests involving carved specimens is to estimate the notch sensitivity of the material studied, in order to generalize the result and to be able to use it during the design phase of the mechanical components. [3] In particular, in the field of fracture mechanics, cyclic stress tests with carved specimens are carried out to indirectly measure the intensification coefficient of the critical stress (K_{IC}) of the tested material, i.e. the intensification coefficient beyond which the crack propagation occurs. This

is done by monitoring the crack propagation as the number of cycles performed advances: this parameter allows calculating the K_I coefficient. [8]



Figure 10 Notched specimen for fracture characterization of the material. On the specimen are clearly visible the crack occurred during the test and the measurements performed. [9]

1.9. General information on the test execution procedure

Testing procedures are highly standardized in various aspects. In modern machines standardized jaws that ensure a simple installation of the specimen guarantee an accurate clamping. One aspect to pay particular attention to is the alignment of the load application axis and the specimen axis, a condition that can be monitored by strain gauges. Furthermore, any phenomenon of wear by rubbing between the clamps and the specimen must be avoided: it is often used to interpose between the two waxed paper and thin sheet. Finally, it is good to make sure that the compression stress induced by tightening in the end area of the specimen is not such as to influence the stress state of the useful section. Generally, this condition is averted by means of a “*dog bone*” design, which offers a greater resistant section in the clamping area. This problem is of considerably less impact in tests with notched specimens, since the state of stress present in the notch area is considerably greater than the one present in the clamping area.

1.10. Test programs and service simulation

In order to have larger and therefore statistically significant sets of results, fatigue tests are generally organized and performed in programs which consist in a given number of tests. Within these programs, the number of specimens used in the tests and the conditions under which they were carried out are documented, so that the machine parameters and the characteristics of the specimens are known and can enrich the test data. In modern machines,

load histories can be generated by computers, which are also responsible for the feedback control of the load applied during the test. Load histories are generally taken from regulations containing standard load conditions; of course, this is valid for tests intended to characterize the material, while tests for the study of the fatigue behaviour of the component should recreate load cycles as similar as possible to those the ones the structure may encounter in operation. In the latter case, the stress cycles can be sampled in service directly on the field and then returned to the laboratory.

1.11. Fatigue test data report

In order for the results of a test to be as complete and meaningful as possible, the evaluation of the data obtained should include the description of the following characteristics:

- Material: chemical composition, heat treatment, microstructure and mechanical properties must be reported;
- Specimens: dimensions, production technique and surface finish must be indicated;
- Experimental details: characteristics of the test machine, tightening methods, stress levels, number of specimens, frequency of tests and environmental conditions, as well as any description of techniques and special procedures used.

1.12. Measurement and analysis of test parameters

The cyclic dynamic tests for the study of fatigue materials, as already mentioned, are very varied in many aspects: from the type of load applied to the characteristics of the specimen, passing through the methods of carrying out the test up to the cycle history. The data measurement and analysis techniques differ according to the parameters of interest that must be monitored during the test and subsequently analysed. There is an entire branch of fracture mechanics specialized in the study of nucleation and propagation of the crack, which is the defect responsible for fatigue failure of mechanical components. Various models have been developed within this theory, many of which consider the propagation of the crack as the determining parameter for the advancement of the phenomenon of fatigue. Thus, the dimension of the crack is continuously monitored as the test proceeds. In the past, the crack

size measurement techniques were rather coarse and discreetly carried out. At regular intervals of the number of elapsed cycles, the position of the apex of the crack and therefore the length of the crack was measured visually, with the help of suitable measuring instruments. The poor reliability of such a measurement technique was accompanied by very short preparation times. Observations improved with the introduction of binocular microscopes with small magnifications (15x) and graduated lines to locate the apex of the crack. Nowadays, there are techniques of the residual resistant section based on the electrical resistance that the specimen opposes to the passage of an electric current. Knowing the voltage at the end of the specimen, the current flowing inside it is the lower the greater the resistance of the conductor, i.e. the lower the residual section not yet affected by the advance of the crack. In this way, it is possible to continuously monitor the progress of the defect for each single cycle and with good precision. Other methodologies allow estimating the area of the residual section by correlating the load applied to the specimen and the relative displacement between the two edges of the notch through mechanical relations. Such automation techniques for measuring the growth of the crack improve the quality of the data and allow to check during the test the trend of the variation of the intensification coefficient of the forces (ΔK) imposed by the machine as the cycles proceed. Visual defect measurement techniques persist based on modern optical technologies: some solutions provide that a photo of the specimen is taken at each cycle in order to have a visual documentation of the evolution of the crack as the test proceed. Other tests are conceived for the calculation of the stress intensification coefficient (K_I) not starting from the measurement of the crack size (a), but through an indirect measurement of the stress itself: strain gauges are applied near the apex of the notch and from the measured strain values it is possible to obtain the stress values and, therefore, the K_I coefficient.

A correct measurement of the parameters of interest must be accompanied by an equally important operation, that is a careful fractographic analysis of the fracture surface of the specimen, if the test is designed to bring the specimen to failure. Fractographic analysis consists of visual inspection both with naked eye and by means of optical magnification tools aimed at determining the number of nucleated cracks and the nucleation zone of the same, which can be superficial and sub-superficial (Figure 11).

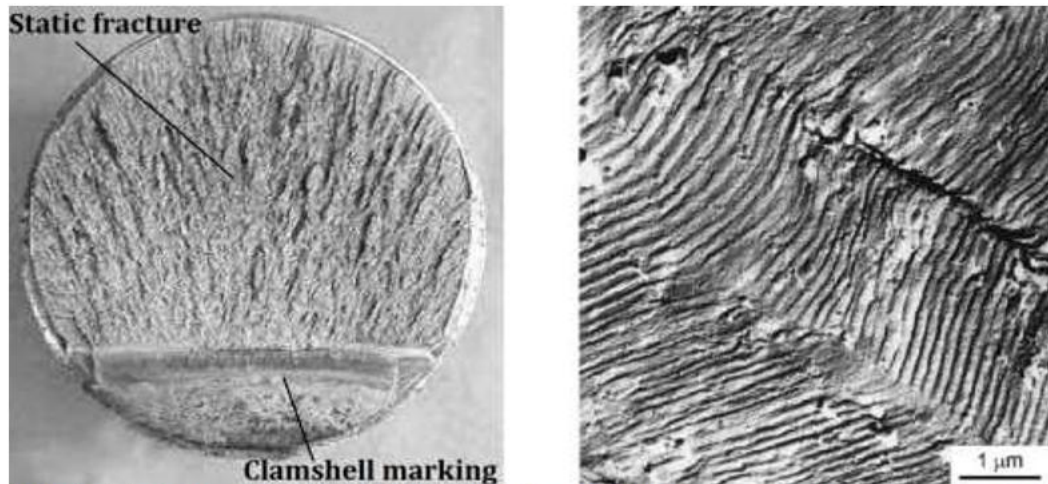


Figure 11 On the left, the fracture surface of a specimen subject to fatigue bending test; the crack propagation area and the static fracture area are clearly visible. On the right, the detail of the clamshell markings in the crack propagation area. [10,11]

The analysis is also useful to establish whether the fracture started from the most critical area, the shape of the crack front and the size of the fracture at the time of failure. This latter information is crucial in defining the sensitivity of the material to fatigue cracks. The shape of the advancing fronts of the crack can be observed through special procedures. A constructive method consists in interrupting the fatigue test and statically breaking the specimen. The fracture surface will reveal the size and shape reached by the crack at the established cycle. A second technique instead provides the application of periodically variable loads. The load with greater amplitude will give rise to larger and distinguishable bands on the fracture surface. Knowing the cycle number during which it has been applied, it becomes possible to plot the progress of the crack as the cycles proceed. Alternatively, it is possible to perform a traditional fatigue test and analyse the fracture surface with scanning electron microscope, which allows, in addition to counting the streaks, an analysis of the nucleation zone and of the region of first propagation of the crack.

1.13. Laboratory tests for fatigue characterization of the component

As mentioned in the previous paragraphs, the mechanical fatigue characterization tests carried out in the laboratory can be aimed at determining the fatigue behaviour of a material or of a specific component. The first type of test is fundamental in order to make choices in the design phase, taking into consideration the properties of the materials tested and the cyclical stresses that the component service imposes.

The second type of test allows, at the end of the design, to verify the behaviour of the mechanical piece under cyclic loading conditions generated in the laboratory and which must tend to recreate as much as possible the operating condition of the component, in terms of load history and environmental conditions. In order for this to happen, it is necessary to have a good knowledge of the internal actions to which the structural element may be subjected during the exercise. With regard to the component studied in this thesis, the internal actions that arise in service are manifold. In the following paragraphs, we want to give a description of the actions to which the rim can be subjected and, subsequently, the laboratory tests that can be carried out to determine the influence of the internal actions on the fatigue life of the component will be described.

1.14. Loads and actions on the wheel

The wheel can be schematically described as the assembly of two main components: the tire and the rim. The first is characterized by a composite structure, consisting of a carcass of intertwined steel fibres, which gives resistance and stiffness in the direction of extension, and a highly deformable rubber matrix, capable of ensuring excellent adhesion of the wheel to the ground. Furthermore, the pressurized air contained in the internal chamber confers stiffness to the tire. Such a system allows combining good stiffness and excellent deformability to the tire, so that the dynamic vehicle performances can be obtained without the ground roughness being perceived in the passenger compartment. In fact, it is only in the presence of adequate inflation pressure that the tire is able to transfer the loads for which the wheel has been designed to the rim. The transmission of these actions takes place in the tire-rim interface area. It is good to specify that the pressurized air contained in the tire contribute only to the tire's stiffener. Therefore, the forces generated by the internal pressure are self-balanced and only contribute indirectly to the actions that take place between the tire and the rim. The actions transmitted by the tire to the rim are in turn generated by the contact forces between the ground and the tire. Therefore, a good knowledge of the overall behaviour of the tire is of great importance in the study of the loads that can be transmitted to the rim in operation. [12]

It is good to define a reference system like the one shown in the Figure 12, in order to describe the forces that can be applied to the wheel in service.

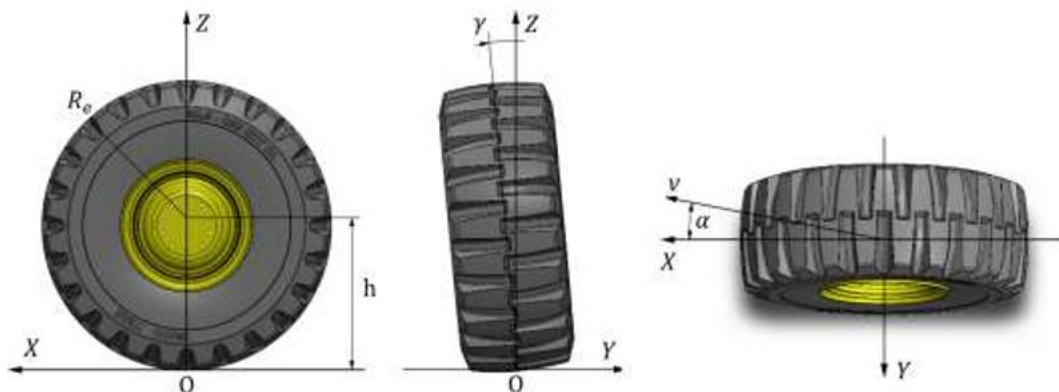


Figure 12 The reference system applied to the wheel.

The origin lies on the road surface at the centre of the wheel footprint, i.e. at the point of intersection among the road surface, the middle longitudinal plane of the rim and the vertical plane containing the wheel rotation axis. The x -axis is defined as the direction of advancement of the wheel projected on the road surface; the y -axis coincides with the rotation axis of the wheel also projected on the road surface, while the z -axis is orthogonal to the ground. It is good to specify that this reference system does not vary with the variation of the angle γ , i.e. the camber angle. The actions transmitted from the ground to the wheel can be described schematically as a force \vec{F} , which in general does not pass through the chosen origin O of the reference system. The offset of the application point of this resulting force with respect to O shows that a transport moment \vec{M} is also applied to the wheel. In this way, the actions exchanged from the ground to the wheel are completely integrated using the vectors relating to a resulting force and a moment of transport, both applied at the origin (Figure 13):

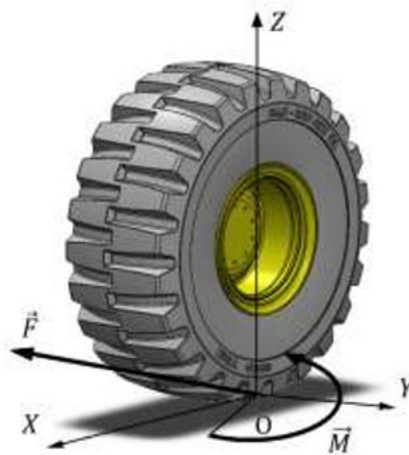


Figure 13 The resultant force and momentum applied to the wheel in the origin of the reference system.

$$\vec{F} = (F_x\vec{x}, F_y\vec{y}, F_z\vec{z}) \quad 1-13$$

$$\vec{M} = (M_x\vec{x}, M_y\vec{y}, M_z\vec{z}) \quad 1-14$$

It is possible to identify a distinction between the components that act in the road plane and those that have a place in the vertical plane. The first are the tangential actions due to the adhesion between wheel and ground and are F_x , F_y and M_z , called *longitudinal force*, *lateral force* and *moment of self-alignment* or *drift*. The second are given by the pressure distribution and are F_z , M_x and M_y , called the *vertical force*, the *overturning moment* and the *rolling resistance moment* (Figure 14).

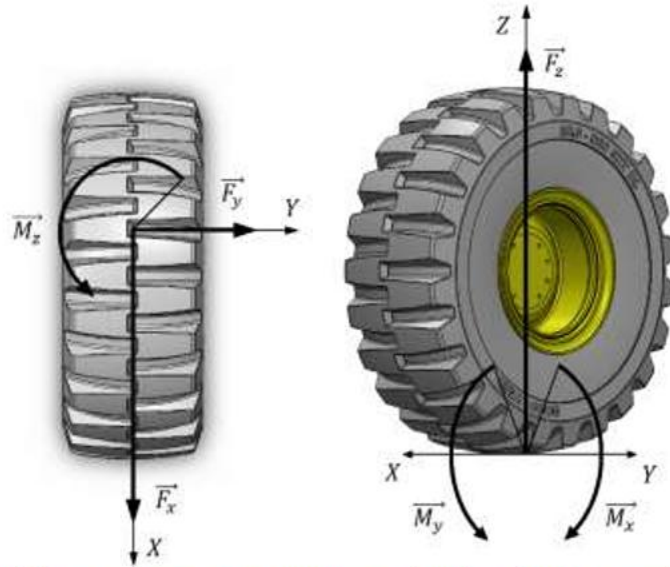


Figure 14 Force and momentum components along the reference system's axes.

Finally, the angle α reported in Figure 12 called *slip angle*, i.e. the angle between the x -axis and the direction of the vehicle speed (\vec{V}), is identified. The extent of the forces and moments described varies, of course, depending on the characteristics of the vehicle and the dynamic conditions in which it operates. Therefore, accelerations, braking, steering and load of the bucket determine continuous load transfers that are variations of the values of the components of the forces and moments during the service of the vehicle. In particular, it is possible to define new components according to the forces on which they depend:

- Component F_x is the longitudinal friction force between the ground and the wheel;
- Component F_B is the longitudinal force generated during acceleration or deceleration;
- Component F_Y is the lateral force generated by the centrifugal force of the vehicle when cornering;
- Component F_z is the vertical constraint reaction of the soil on the wheel.

Moreover, it is possible to give an overview of the conditions of use of the vehicle in which there are significant variations in the components of the mentioned forces. It should be specified that the longitudinal friction force (F_x) in a wheel in the rolling phase is of modest entity compared to the other components in the field, while it becomes relevant if the wheel is dragged during the braking phase.

In general, two important load transfer conditions can be identified: the longitudinal load transfer and the lateral load transfer.

- The longitudinal load transfer occurs during the vehicle acceleration due to inertial effects. In case of running at a constant speed, the two axles of the machine will weigh the so-called static loads, which depend on the position of the centre of gravity alone. During acceleration, the inertial effects of the vehicle body will tend to largely shift the weight on the rear axle and vice versa in the event of braking. Therefore, the F_B component is not only influenced by the inertial forces opposed by the vehicle body while accelerating, but also by the transfer of load suffered by the wheel and therefore the fraction of traction for which that wheel is responsible. Similarly, the vertical constraint reaction (F_z) is also closely related to the longitudinal load transfers.
- The lateral load transfer occurs during the steering phase, during which the inertial forces oppose the change in direction of speed and are therefore transverse to the vehicle body. Similarly, to what happens for the longitudinal load transfer, the effect of this inertial phenomenon is the overloading of the wheels placed outside the curve with respect to those inside the curve. This causes component F_Y to be determined not only by the centrifugal force of the vehicle, but also by the lateral load transfer.

In addition to the longitudinal and lateral inertial effects, it is essential to consider that for the earth moving vehicles, for which the component under examination is intended, the position of the centre of gravity is not constant during service, but varies considerably depending on the front load, as well as the total load applied to the four wheels. Therefore, in industrial vehicles, the value of the components of forces and moments is variable and the stress to which the wheel rims are subjected is not only cyclical, but also strongly variable in terms of amplitude of the stress. [12]

After this premise, it is possible to clarify the relationship between the forces applied to the wheel and the actions inside the rim. In particular, the effects of longitudinal and lateral dynamic phenomena are again distinguished.

Component F_z is the only force present even in the quiet condition of the vehicle. It is influenced by both longitudinal and lateral load transfer phenomena and it is, therefore, determined by adding the forces due to the load transfer to the weight that would weigh on the wheel under static conditions. This component is responsible for a compression action of the lower part of the rim between the axle of the rim and the tire. This action, being the component in continuous rotation, is cyclical. The F_x and F_B components are responsible for a torque that has the axis of the wheel as its axis of application and, therefore, have flexural effects in the x direction of the rim. Finally, force F_Y arises when the vehicle is traveling through a curve and both centrifugal force and lateral load transfers influence it. This has the effect of generating a bending action on the wheel, with a torque that has the x -axis as its application axis. All the actions described are cyclical, given the rotation of the rim during operation. From the description of the main operating conditions in which the wheel may be found, it is evident that the experimental tests necessary to study its behaviour in situations similar to those of service are substantially two. A test, called *rolling test*, which recreates the functioning of the wheel in conditions of advancement at constant speed or during acceleration or deceleration, in order to study the effects of the actions induced by F_z , F_x and F_B . A second test, called *rotating bending test*, which instead recreates the state of stress generated by the lateral dynamic phenomena and, therefore, gives information about the effects of the component F_Y on the structure. These tests will be described in more detail in the following paragraphs.

1.15. Rotation bending test

As mentioned in the previous paragraph, the rotating bending test (Figure 15) is a mechanical laboratory test on the structure, having the task of determining the effect of the component F_Y of the cyclic load that weighs on the wheel on the fatigue behaviour of the rim. Even load F_z can generate a bending moment on the wheel which axis is parallel to the x axis. This occurs if the offset, i.e. the horizontal component of the distance between the centre of the tire contact area on the ground and the point where the perforated disc is secured to the axle shaft, is not null. Therefore, the rotating bending test has the task of evaluating the effect of both the lateral loads deriving from changes in the direction of the vehicle and of the vertical load, which has non-zero offsets.

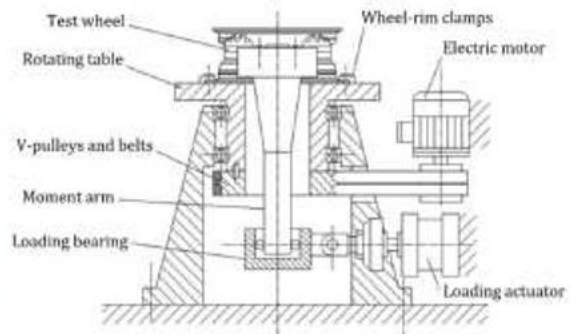


Figure 15 Machine for the rotating bending tests on rims. [13,14]

In fact, both types of load cause bending moments with a direction belonging to the longitudinal plane of the wheel (i.e. the x - z plane). In the rotating bending test, the cyclic bending moment is generated by a rotating eccentric mass connected via a rotating joint to an attachment plate mounted on the rim disc. The rotation of the eccentric mass generates a centrifugal force, which is brought back from the joint to the disc of the rim in the form of a rotating bending moment, if observed by a reference system integral with the circle. In particular, the bending moment is equal to the value of the centrifugal force generated by the rotation of the eccentric mass for the joint arm, i.e. the distance between the eccentric mass and the rim disc. The wheel is secured to the table of the testing machine by clamping the rim. Alternatively, the cyclic bending action on the shaft can be generated by a loading actuator integral with the chassis of the machine.

The wheels selected for the test must be taken from the standard production cycle, in order to be representative of the mechanical characteristics of the entire lot; this means that they must also have undergone the latest processes, including cataphoresis. They are secured to the plate with non-lubricated bolts and with the tightening torque provided by the laboratory regulations for testing. It is also advisable that the contact surfaces are free of excess dirt and paint and that they do not present unexpected deformations. Screws and nuts can be replaced or retightened during the test, while the rim must not be used for more than one test.

The rotating bending test involves the application of the rotating bending moment through the mechanical system quickly outlined above. This allows inducing a state of cyclic stress inside the circle, which must be detected and measured using the appropriate tools. For this purpose, strain gauges are applied in the areas of interest of the component in the

directions in which the measurement of the deformations is required. The signal from the transducers is received by the acquisition system, which amplifies it before sending it to the computer, which can finally store and process the data. The execution of the test also includes a preliminary setting of the test parameters via computer. Among them, there are the intensity of the cyclic bending moment, the moment constant, the number of cycles and the test stop intervals for the inspection of the component.

The purposes of the rotating bending test and the results that can be extracted from it can be manifold. The main objective is undoubtedly estimating the fatigue life of the component by monitoring the onset of cracks as the test proceeds. Secondly, the test can prove useful for the development of a model that relates the external loads to the stresses in the instrumented points of the structure. Therefore, by carrying out various tests with gradually increasing intensities of the bending moment (using wheels not tested yet for each test) and measuring the strains incurred, it is possible to create an experimental model that allows to predict the extent of the stresses in function of the load applied. Stresses are measured indirectly from the deformations measured by strain gauges using the linear elastic relation of the material.

The classic application of the rotating bending test involves the following procedure:

- The machine is started and the wheel subjected to rotating bending.
- The machine is stopped at regular cycle intervals, the wheel is inspected to identify any cracks that have formed and to tighten the plate bolts if necessary. If conditions permit it, the machine can be restarted and the test can continue.
- The test ends if:
 - the set number of cycles is reached;
 - cracks are visible;
 - obvious breaks in the rim occur, in which case the machine stops automatically.
- If the test has reached the set number of cycles, the rim is subjected to inspection using penetrating liquids. The test is considered passed if no crack triggers are detected. If cracks are identified following the check or if the test stopped earlier, the test is considered not to have passed.

In order to reduce the test times, the load conditions applied in the test can be more severe than those of normal use in service. Moreover, this allows to obtain higher safety coefficients. The bending moment acting on the wheel calculated in the operating conditions can be expressed as:

$$M = K_1 \cdot K_2 \cdot F_z \cdot (\mu \cdot R + S) \quad 1-15$$

where:

- K_1 is a dimensionless parameter which depends on the type of stress applied to the wheel;
- K_2 is a dimensionless parameter which depends on the duration of the test;
- F_z is the load capacity of the wheel;
- μ is the friction coefficient between tire and ground;
- R is the dynamic radius of the tire used;
- S is the wheel offset.

The bending moment generated during the rotating bending test can instead be approximated as:

$$M = K_1 \cdot K_2 \cdot F_z \cdot (\mu \cdot R + S) \quad 1-16$$

$$M = F_c \cdot h \quad 1-17$$

where:

- F_c is the centrifugal force developed by the eccentric mass, a function of the rotation speed of the system;
- h is the arm of the centrifugal force, i.e. the distance between the rotating eccentric mass and the coupling area between the rim disc and the plate.

Once these relationships are known, it is possible to establish what the machine parameters are to be set in order to generate, in the test phase, a bending moment equal to that of the operating conditions in the field, which in turn can be found knowing the parameters of the first equation.

1.16. Rolling test

The rolling test is a mechanical characterization test of the wheel capable of reproducing the forward condition in the longitudinal direction. The load on the wheel can be modified according to requirements so that load transfers as well as inertial effects typical of various situations in the exercise of the component can be reproduced and simulated, such as advancing at constant speed, acceleration and braking.



Figure 16 Example of a wheel during a rolling test. [15]

Rolling test machines are generally equipped with several stations, some of which are capable of simultaneously generating longitudinal and lateral loads on the wheel, in order to reproduce as faithfully as possible, the typical conditions of use present when traveling a curve or a not perfectly horizontal ground in the lateral direction.

The rolling test machine can be schematically represented in the following way: the wheel to be tested, including rim and tire, is secured to an arm, with respect to which it can rotate freely around its axis. Hydraulic actuators, to which the arm is secured, are capable of generating the load needed for the test. The constraining reaction is developed by a roller against which the wheel lays. The roller is driven by an electric motor, which develops the power necessary to bring it into rotation. The wheel is in turn rotated by the roller by friction. The generic machine designed for this type of test can also allow the variation of the camber angle. In addition to the longitudinal load generated by the friction force exerted by the roller on the wheel and the vertical load produced by the hydraulic drive, some machines also allow to generate a lateral load through a secondary drive.

The tests that can be carried out with this type of machine are various and can be distinguished between static and dynamic tests:

- In the first, the behaviour of the component under static stress conditions is meant to be tested. Based on this principle, the practicable strategies for measuring the deformation state of the circle are two, depending on which parameter is considered as variable. A first approach may consist in keeping the wheel stationary and varying the load applied. Therefore, the component is not put into rotation, but only the hydraulic cylinders responsible for generating the vertical load are operated. By instrumenting the wheel with strain gauges in the areas of interest, it is possible to measure the deformation in these points as the load applied varies. The load must be made to vary in a range of values that includes the load weighing under static conditions (stationary vehicle), but also conditions that simulate load transfers the vehicle can generate during its use, whether they are lateral or longitudinal. Vice versa, the second strategy can be used when defining a deformation field for an entire portion of the wheel in response to a constant external applied load is the aim of the test. In this case, the test consists in rotating the roller at extremely low speeds, blocking it before an excessive number of wheel rotations is carried out to avoid damage to the measuring instrumentation. In this way, the output data from the strain gauges will provide how the state of deformation and stress varies for a given point of the rim during a complete rotation of the wheel. It is good to specify that for this kind of tests it is not necessary to bring the component into a failure condition, since relevant information is already contained in the deformation response to the external load. It is also possible to carry out various tests by varying from time-to-time other parameters of interest such as the tire inflation pressure, in order to estimate the rim's response to changes in operating conditions. Generally, the most critical operating configuration for the structural strength of the wheel is the low inflation pressure. In this situation, the high degree of deformation of the tire not only subjects the fibres of the carcass to very high stresses, but also produces a state of contact

between tire and rim that is not desired and therefore possibly dangerous stresses can occur. A second parameter on which it may be interesting to intervene to study the system response is the camber angle, i.e. the angle of inclination in the vertical lateral plane of the load applied with respect to the wheel. This kind of tests can be particularly useful for the development of empirical relations that can predict the peak of stress that is generated within the rim as a function of the parameters of use, as well as to study the entity of the safety factor of the component depending on the conditions of use.

- The second large type of test which can be performed using the rolling test machine is the dynamic test. In this kind of experiments, the wheel is simultaneously subjected to the action of the load of the hydraulic drive and of the motorized roller, in order to be rotated in dynamic conditions similar to those of operation. The main purpose of a dynamic characterization test is to study the fatigue behaviour of the component. Due to the high number of rotations of the wheel, the strain gauges cannot be connected to a fixed acquisition system by wire, as they would be damaged after a few rotations. Thus, the data acquisition system must be inserted directly inside the rim or connected to the strain gauges by wireless systems. For these tests, strain measurements similar to the ones described above are performed. The main difference is that the strain measurements refer to a high number of cycles. Changes in the stress field due to variation of the load settings can therefore be appreciated. Another approach to the dynamic test consists in monitoring the cracks nucleation and propagation. For this kind of experiments, the tests are usually divided into intervals of cycles. At the end of each of the groups of cycles, the wheel is inspected through non-destructive tests, such as penetrating liquids, to highlight the possible occurrence of cracks or to measure their advancement. Therefore, the test consists of various steps at the end of which the condition of the component is monitored. Similarly, to what happens for cyclic rotating bending tests, the test is generally carried out with increased loads to reduce the number of cycles necessary to complete the test, which can

be considered completed in the case of the onset of cracks, in the case of sudden failures or if it reaches the expected number of cycles without damage. Only in the latter case, the circle passes the test. The test in question has a dynamic nature as the rotating bending test. Therefore, it shares with the latter a good part of the preliminary procedures and criteria for carrying out the test, such as the selection of the wheel, its preparation, the criteria behind the setting of the load cycle and those that determine the end of the test.

1.17. Field tests for fatigue characterization of the component

As part of the fatigue characterization of a component, it is essential that experimental laboratory tests are accompanied by field tests.



Figure 17 Example of an earth-moving vehicle during a field test.

These have the twofold task of providing additional sets of results useful for deepening the models developed on the laboratory data and checking the correct setting of the same. Only the test of the component in service can confirm, in fact, the good approximation of the operating conditions carried out in the laboratory. The data output from a mechanical fatigue characterization test carried out in the field are mainly the load spectrum acting on the component, which provides information on the history of stress as a function of time. The most significant points of the stress spectrum graph are the maximum and minimum stress values. However, the detection of the load spectrum on the field must necessarily be preceded by a series of preliminary assessments on aspects such as how the load changes over time and the use of the component in service. It is also good to evaluate if some cycles can be neglected in the fatigue study, to check the influence of both the frequency and the speed of the load application on the fatigue strength, to estimate how long periods of rest and operation in

overload can weigh. These preliminary considerations must be followed by the definition of a procedure for carrying out the measurements and for processing the load spectrum. The strategy for the acquisition and processing of data must also be based on the nature of the expected solicitation. In fact, the types of cyclical loads that can weigh on a component can be divided into:

- deterministic loads;
- stochastic loads.

The former are loads that can be defined as specific events that can be foreseen in intensity and, known the functioning of the structure, also on a time scale. Usually, this type of load occurs from the standard use of the component, a condition in which the application of theoretical and experimental models developed for predicting loads and stresses is possible. If the use of the structure in service is not the one foreseen in the design phase, the nature of the loads can become stochastic, i.e. highly variable from a statistical point of view. In other words, this operating condition does not allow to predict the intensity of a given quantity in a given instant of time. Therefore, the description of a load condition can only be based on a statistical approach, and, therefore, on the study of sequences of random loads over time. It is good to specify that the two types of load can be applied simultaneously, so it may be difficult to combine the study to carry out assessments on fatigue life. Therefore, the problem still remains the way in which the load spectrum must be obtained in order to have a significant evaluation of the behaviour of the structure with varying stress. Then, it is necessary to proceed considering all the possible scenarios of use of a component and the possible fractures it can suffer. From this point of view, the execution of field tests allows to simulate the conditions of service in much more faithful, flexible and variable way than the tests carried out in the laboratory allow. In other words, it is possible to recreate the operating conditions that are expected to occur, by measuring the quantities of interest and thus obtaining specific results for the given method of use. Detailing the procedure described in the study of a rim for earth-moving vehicles similar to the one considered in this discussion, several tests must be carried out in order to study the state of stress of the rim in the various possible conditions of use. Each test is aimed at collecting data on the deformation state of the component in a precise operating condition.

For example, the tests in question can be the following:

- Constant speed vehicle in motion on a circular trajectory with loaded blade and predetermined number of revolutions.
- *Bump test*: the vehicle travels at a fixed speed with loaded shovel on a path with obstacles and bumps placed at regular distances.
- *V test*: the vehicle goes through a series of cycles on a predefined path, carrying out loading and unloading operations of the blade with earthy material.
- Vehicle moving on an oval path, unloaded and lowered blade at high speed; the test is concluded after the completing a given number of laps. The same test can be carried out with loaded shovel.
- Stationary vehicle and loaded shovel; a predetermined number of turns are performed.

The tests that involve testing the vehicle in full straight are also called normal driving style tests, while those that include driving in curves are called hard driving style. It is clear that the different types of load history provide different stress spectra and distinct critic points. The loads used in this kind of tests must be determined based on the manufacturer's needs. The load cycles generally tested are those with maximum and minimum load, in order to have an estimate of the response of the structure in the widest range of conditions possible. It should be remarked that, even with the help of field tests, fatigue design can be particularly difficult, since a variation in the design aimed at reducing the cyclical stress generated by a given load may not bring benefits towards the action of the other loads applied. In addition, fatigue failures reveal that not all the relevant loads acting on a component are always known, so it is difficult to predict all the stresses present. After following a first qualitative approach to the examination of the expected applied loads, a quantitative evaluation follows which consists of instrumenting the component using strain gauges to obtain the deformation state of the points considered during the test. In the specific case, the component studied in this thesis, i.e. the rim of the wheel of the earth-moving vehicle, is in continuous rotation during operation, so that a normal instrumentation with strain gauges connected by wire to the acquisition system would be unusable. In order to measure the deformations of the wheel and

more generally of the components that have to perform a high number of rotations during service, infrared signal transmission systems are therefore necessary. The signal from the strain gauge is amplified and transmitted to the system of acquisition connected to the computer by the infrared transmitter mounted on the wheel, so that the measurement system and the acquisition system remain physically free. In order to have a data campaign as significant as possible, it is good to place a considerable number of strain gauges on various areas of the structure. This choice is useful also to compensate for any malfunctions as well as to have a set of statistically more valid results, to obtain the greatest number of data in portions adjacent to those relevant for the study or to identify any symmetries in the stress distribution. The areas where the strain gauges are applied are generally chosen through previous finite element simulations or based on experience of breakage or of onset of cracks and fractures in the component operation. The next step is to apply counting methods and models for calculating fatigue damage. The experimental data processing is entrusted to special software capable of counting the cycles and of applying models for calculating the damage to the component and the fatigue life of the structure, i.e. the number of cycles it can withstand if subjected to a combination of the detected load spectra.

1.18. Finite element analysis for fatigue damage calculation

In the finite element method, it is assumed that the component is divided into structural elements (finite elements) interconnected by points (nodes) on which external loads and forces exchanged by adjacent elements are applied. The set of these elements is called *mesh*. With this approach, the problem can be solved numerically; in fact, it is possible to write a constitutive equation for each element:

$$\mathbf{F} = \mathbf{K} \cdot \boldsymbol{\delta} \quad 1-18$$

Where \mathbf{F} is the nodal force vector, \mathbf{K} is the stiffness matrix (function of the element and of the characteristics of the material), $\boldsymbol{\delta}$ is the vector of the nodal displacements. The solution is obtained by the conditions of compatibility of the movements and by the equations of equilibrium. The latter contain the nodal displacement as unknown. In this method, a system of differential equations is obtained, which is reduced to a system of algebraic equations.

The latter is built starting from the equation of equilibrium and, for the i^{th} node, we have:

$$\mathbf{R}_i = \sum \mathbf{K}_i \cdot \delta_i \quad 1-19$$

where \mathbf{R}_i is the vector of the external loads applied to the i^{th} node and the sum must be extended to the elements that converge in the i node. For the structure, we get:

$$\mathbf{K} \cdot \delta = \mathbf{R} \quad 1-20$$

where \mathbf{K} is the stiffness matrix of the structure, whose components k_{ij} , called coefficients of influence, represent the entity of the nodal force (f_i) when a unit displacement is imposed and all the other components of the displacement vector (δ_i) are null. The vector δ is the vector of the structure's nodal displacements and is the unknown term of the problem, while \mathbf{R} is the vector of the structure's load. Once the boundary conditions are imposed, the system can be solved. Therefore, the finite element method is a representation of a continuous system with equivalent discrete elements, from which a system solvable with incremental iterative numerical methods is obtained. The reliability of the solution depends on the level of discretization (mesh density) and on the approximations introduced on constraints and loads (boundary conditions). By solving the system, the displacements of all points within the single element are obtained through form functions:

$$\mathbf{u} = \mathbf{N} \cdot \delta^e \quad 1-21$$

Where \mathbf{u} is the vector of displacements, \mathbf{N} is the matrix of form functions and δ^e is the vector of nodal displacements. The form functions depend on the element considered and they are usually polynomial functions.

Once the displacements are known, the congruence equations in the elastic field and in the hypothesis of small displacements are solved:

$$\boldsymbol{\varepsilon} = \mathbf{L} \cdot \mathbf{u} \quad 1-22$$

The deformation field is therefore obtained. Later, it is possible to resolve the constitutive laws deriving from the theory of elasticity:

$$\boldsymbol{\sigma} = \mathbf{D} \cdot \boldsymbol{\varepsilon} \quad 1-23$$

from which the state of stress is obtained in the structure [16].

In order to carry out the structural analysis of a wheel through a finite element model (*FEM*), it is necessary to use software that are usually composed of three parts: pre-processor, solver and post-processor. The data necessary for subsequent analysis are set in the pre-processor. The following are defined: the geometry of the model, the data relating to the material and the subdivision into finite elements (mesh). Then, loads and constraints are introduced and the file necessary for the analysis with the solver are created. The solver varies according to the type of analysis (linear, non-linear...) that that is meant to be performed on the model introduced in the pre-processing. At the end of the analysis, the data necessary for the interpretation of the model are acquired through a graphical interface in the post-processing phase. The use of symmetry properties makes the analysis faster. In fact, the halving of the number of nodes allows reducing the analysis time even by 1/6 and the file size also by 1/3. Introducing excessive approximations in the mesh, in the constraints or in the loads can lead to considerable variations and inaccuracies in the results. A modelling close to real conditions and a structure with a more dense discretization in elements allows to obtain data close to the real situation. In the case of complex models, such as that of a wheel for earth-moving machines, often not all the loads acting is assessed at the same time, but portions of the rim are studied and the only the higher stresses are considered in order not to weigh the calculation too much. With this method, results can be obtained quickly and the portions subject to the greatest stress can be identified immediately. At the *GKN Company*, *Ansys* is used as *FEA* (Finite Element Analysis) software. *Ansys* allows to introduce load spectra detected in laboratory or field tests into the program in order to approximate the components of the stress and to get the most accurate results possible.

1.19. Comparison from: laboratory tests, field tests and FEA

As shown in the previous paragraphs, different approaches can be used to study the fatigue life of a wheel for earth-moving vehicles:

- Laboratory tests: these can be performed on specimens, on portions of the structure under examination or on the entire component. Using the entire structure can be advantageous to reproduce as closely as possible constraints and loads in order to obtain results similar to the real situation. In any case, specific test machines are required. These usually reproduce only a particular

load (bending, rolling...) and constraint condition. They may require prolonged times, but it is also possible to reduce the temporal extension of the test by increasing the frequency of solicitation. Furthermore, the load history can be reproduced with extreme precision, thanks also to computerized controls. The data is collected using strain gauges positioned in the area of interest for the study, which is limited to a portion of the component even if the entire structure is subjected to the test. Therefore, considerable expertise is required in the application of strain gauges, as well as adequate reading of the results. In fact, from the strain gauge data it is possible to evaluate symmetries and malfunctions of the strain gauges in order to consider only the significant results. Once the interest graphs (variation of deformation as a function of time) have been obtained, it is possible to re-elaborate everything and obtain stress graphs, estimate the fatigue life and the damage to the component through software (for example: *nCode Glyphworks*).

- Field tests: these tests require the use of the component in a path that simulates the real operating conditions. Tests are often carried out under different load conditions in order to highlight the influence on the wheel stress state. Precision in the positioning of strain gauges is required, in addition to the need for an acquisition unit to be affixed directly to the structure or connected via infrared. The time for this type of test can be long depending on how variable the stress condition over time is considered. As for laboratory tests, the data obtained are then studied through software from which it is possible to obtain an estimate of the fatigue life of the component and its damage.
- Finite element simulations: this type of test requires specific software. Within the latter, data are entered concerning the geometry of the component, the material (usually provided by the supplier), the mesh and the boundary conditions. The simulation on the component introduces a certain degree of approximation, which may be due to mesh, constraints and loads. To optimize the results, the discretization of the material has a higher density in the critical areas. Problems can occur due to the complexity of constraints and loads that are often simplified; this allows speeding up the calculation times but leads to less precise final data.

The main characteristics of each test listed in the following table are summarized in the following table.

<i>Type of test</i>	<i>Loading condition</i>	<i>Constraint condition</i>	<i>Instrumentation- data acquisition</i>	<i>Any approximations</i>	<i>Test duration</i>
Test in the laboratory	Specific load defined by the type of test machine. Set via PC, usually reproduction of loads obtained from field tests.	Reproduction of localized constraints based on the type of test to be performed.	Strain gauges in the area of interest, connected to the data acquisition unit of the test machine. Difficulty applying strain gauges.	Load condition limited to the action to be studied. Geometry, in some cases only a portion of the component is tested.	Tests with long times to try to break the component in order to estimate the fatigue life and to study the type of fracture.
Field test	Loads represent the standard condition of use. The circuit test does not include special uses.	The conditions for binding the operating component are maintained.	Strain gauges in the area of interest with acquisition unit on the wheel to then manipulate the results via software.	Test duration limited to a few load applications cycles. Test in a circuit, special applications are not considered	Short tests, which allow obtaining a load history that reflects the cyclical repetition of the conditions to which the structure is subjected.
Finite element simulation	Approximate loading conditions, limited to loads of interest to the study area. Value and trend of loads often from standard data or from field tests.	Approximate constraint conditions, which reproduce the real conditions as faithfully as possible.	Discretization of the component into elements. Solution through algebraic equations on each element.	Constraint on constraints and loads. Often reduced geometry, based on symmetry properties. Distribution and mesh density.	Short tests, also based on the degree of approximation (the higher the lower duration) and the power of the calculator.

Table 1 Comparison between the different kind of test to study the fatigue behaviour of the wheel.

Each approach shown has limitations. From the comparison, it can be seen how the constraint conditions of the wheel are fully respected in the field test. In this type of test, it can be difficult to obtain easy to read and error free results; this happens due to the difficulty of applying the strain gauges. Because the test ends before the component breaks, only a portion of the load history is available, even if it refers to the most demanding condition. In laboratory tests, load conditions detected in operation can be reproduced on the component. The advantage of these tests is that the component failure can be tested and thus the fracture surface can be analysed. For these tests as well, the difficulty of arranging the strain gauges is noted. Finally, the simulation with finite elements allows carrying out rapid tests, but at the price of approximating the component in different aspects (load, constraint, mesh). It can often be useful to combine all these methods to compare the results and define the most indicative data of the structure's fatigue life. In particular, it is possible to develop a finite element model to which the standard load conditions of the wheel can be applied. In a first approximation, the areas with greater stress are detected. This step does not take place if there are numerous breakages in operation, which show an area particularly subject to heavy load. Then the study can continue with a field test on the instrumented wheel. The data obtained are then used to derive the fatigue life and damage suffered by the component. These results can be compared with any laboratory tests, where the structure is brought to failure. Finally, by comparing these results, a final comparison with a finite element simulation can be added, using the load spectrum obtained from the tests already carried out, and thus highlighting the correct reading of the strain gauges, the presence of any anomalies, load symmetries and particularly critical areas in conditions of heavy load. (Figure 18)

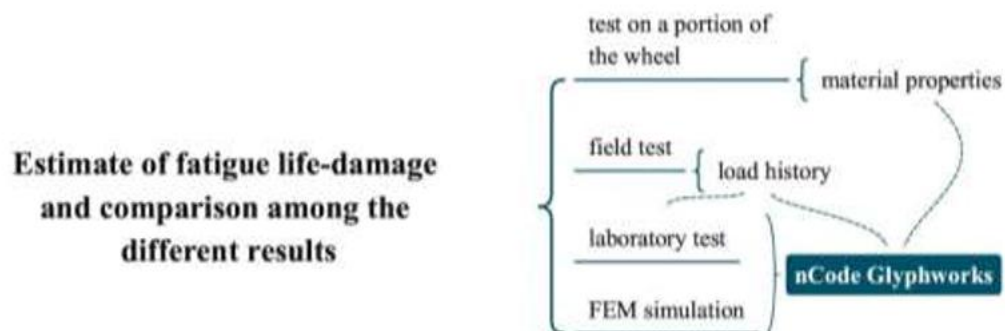


Figure 18 Diagram of the operations carried out to study the fatigue behaviour of a component.

2. EXPERIMENTAL TESTS:

2.1. Test on field

The studied component is a wheel of a material transfer vehicle produced by GKN WHEELS.

The data which will be used to verify the wheel against fatigue failure have been collected using strain gauges placed close to one of the holes (necessary to connect the wheel to the hub). This position is critical because of the stress concentration which is described by notch factor k_t .

Tests in different track conditions have been performed in order to simulate and characterize the life of the component. In this work data coming from gauges 4 and 6 will be discussed. The first step is to place the strain gauges on the wheel. Figures from 3.1 to 3.7 show the position of the gauges and the tested vehicle.

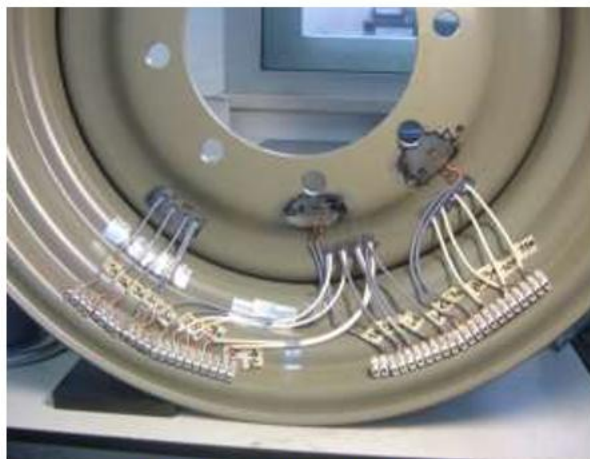


Figure 19 Instrumented wheel



Figure 20 Gauges position (1)

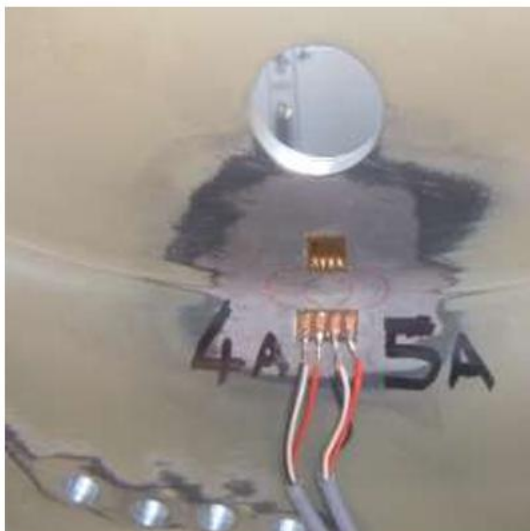


Figure 21 Gauges position (2)



Figure 22 Gauges position (3)

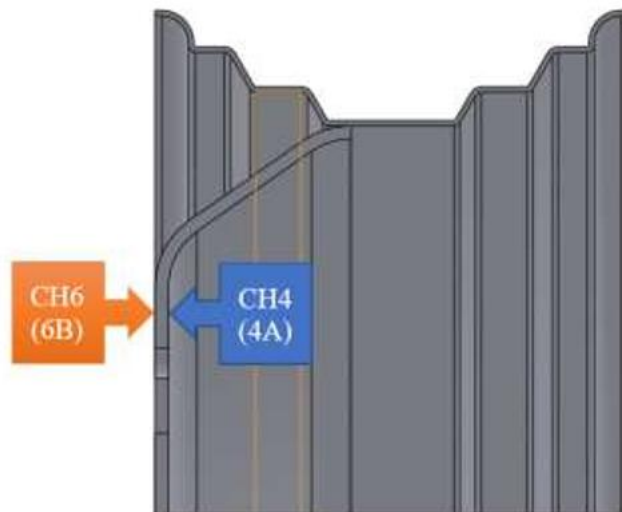


Figure 23 Position of the studied gauges



Figure 24 Vehicle configuration

Loading histories are obtained from tests performed in the following track condition:

ON ROAD CONDITION: the vehicle makes some laps in an oval asphalt track



Figure 25 On road test phase

OAD PLACEMENT: the vehicle charge and discharge materials;



Figure 26 Load placement test phase

LOADER: the vehicle charge and discharge heavy materials; it is similar to the previous condition but it is a particular case more dangerous than the Load one;



Figure 27 Loader test phase

OFFROAD: the vehicle makes off road laps



Figure 28 Ofroad test phase

2.2. Material

The wheel is cold formed starting from plates in steel grade S355MC EN 10149-2. In order to characterize the material behaviour tensile and fatigue tests have been performed in collaboration with GKN.

2.3. Tensile tests

Three important parameters, which can be obtained from a tensile test, are needed for computing the fatigue analysis. Ultimate tensile strength, yielding strength and Young's modulus are the first parameters required. A simple tensile test is capable of giving these parameters as results. Six specimens are obtained from an unused portion of plate of the same material of the wheel.

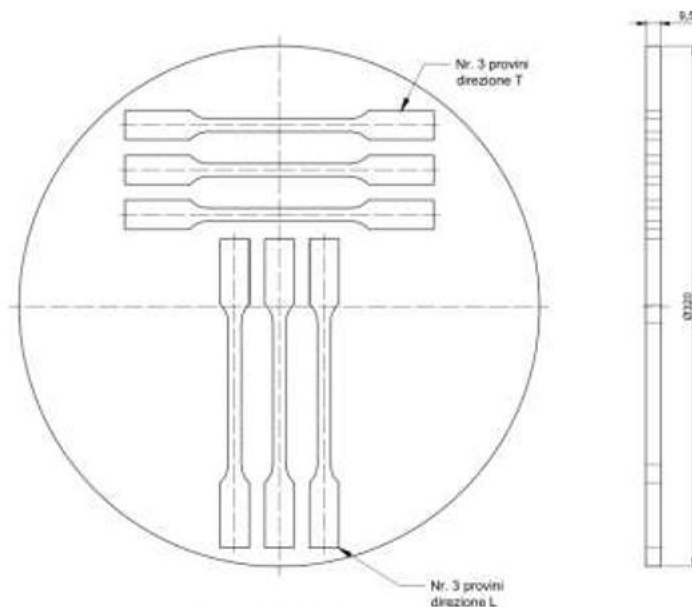


Figure 29 Position of specimens

The specimens are cut in longitudinal (L) and transversal (T) direction. L and T directions are determined from the orientation of the fiber. In fact, the studied wheel is built starting from metal plates. The production process of a plate causes a preferential orientation of the crystalline grain, which produces an anisotropic plate. It is important to know the plate behavior in every direction; it would be a mistake to consider only the properties along the fibers preferential direction.

Figure 29 reports also the dimension of the plate which has a diameter of 320mm and a thickness of 9.5mm.

Specimen dimensions are obtained from standard EN 10002-1; moreover, the specimens thickness is the same of the plate in order to preserve any residual stresses coming from the production process. Figure 30 reports the specimens dimension.

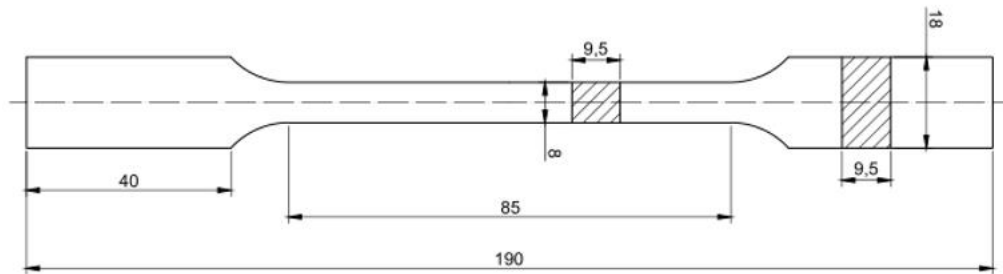


Figure 30 Specimens dimension



Figure 31 Tensile test



Figure 32 - Tensile test (3) - broken specimens

Looking at the broken specimens, it could be seen that the longitudinal specimens have a breaking surface more ductile than the transversal ones. However, it is a very little difference: even the transversal specimens have a ductile behaviour. Specimens $\sigma - \epsilon$ plot are collected in Figure 33 from Figure 38.

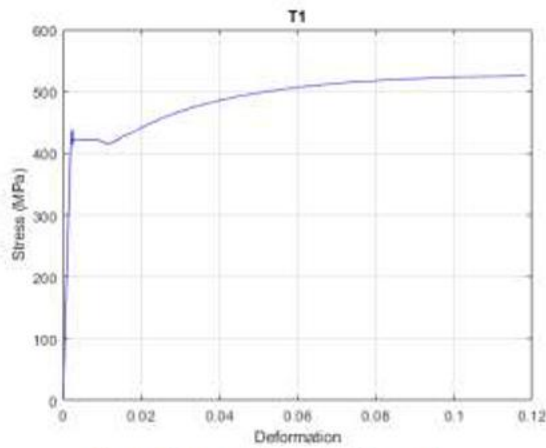


Figure 33 $\sigma - \epsilon$ plot for specimen T1

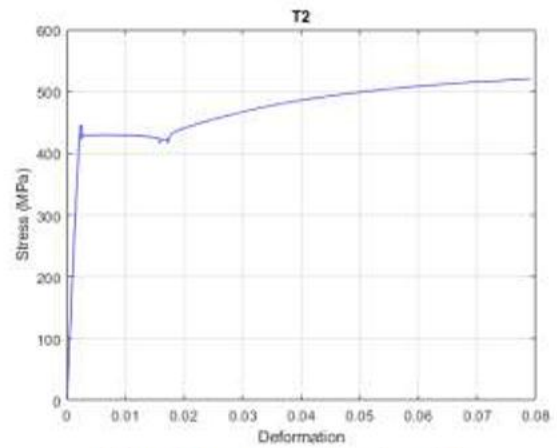


Figure 34 $\sigma - \epsilon$ plot for specimen T2

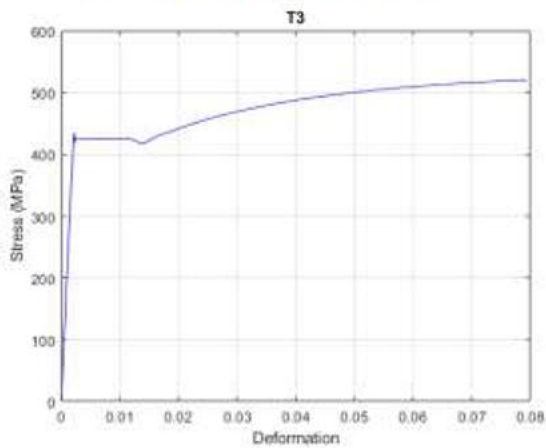


Figure 35 $\sigma - \epsilon$ plot for specimen T3

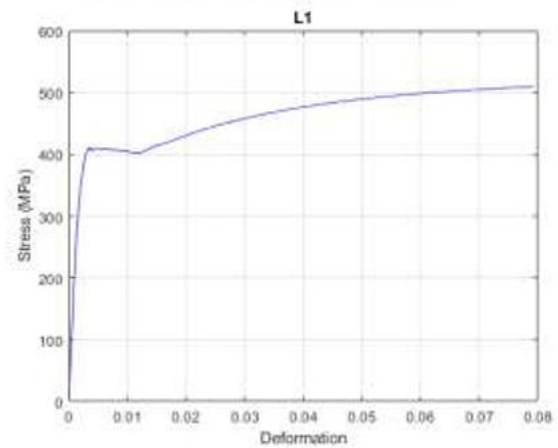


Figure 36 $\sigma - \epsilon$ plot for specimen L1

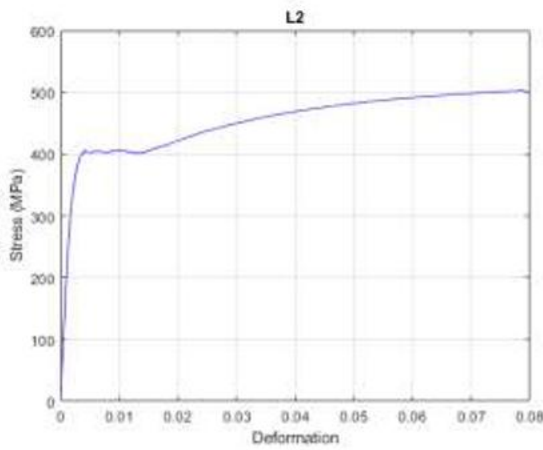


Figure 37 $\sigma - \epsilon$ plot for specimen L2

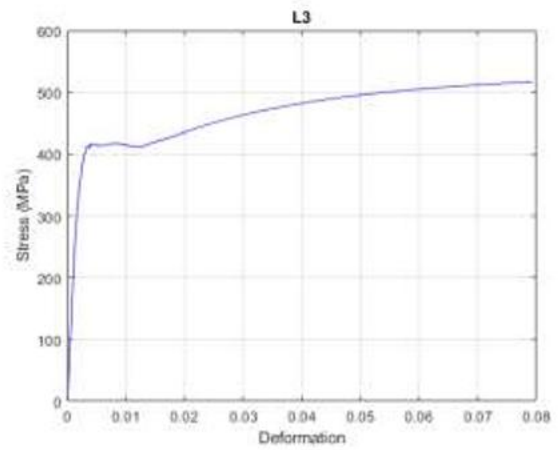


Figure 38 $\sigma - \epsilon$ plot for specimen L3

Thanks to standard EN 10002-1 we can obtain the material properties:

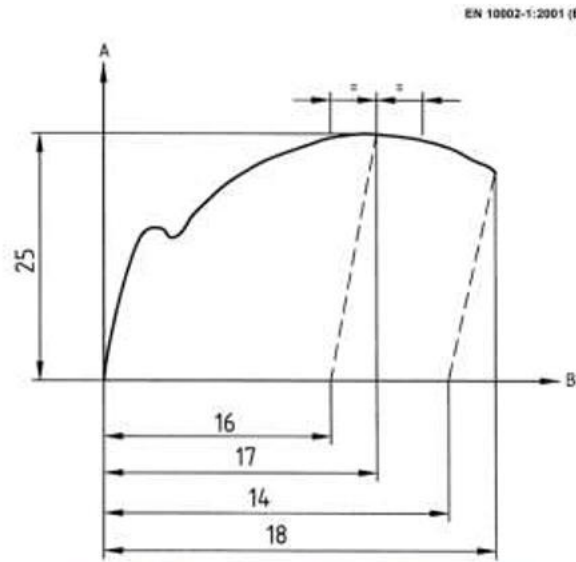


Figure 39 Ultimate tensile strength (value n°25)

EN 10002-1:2001 (E)

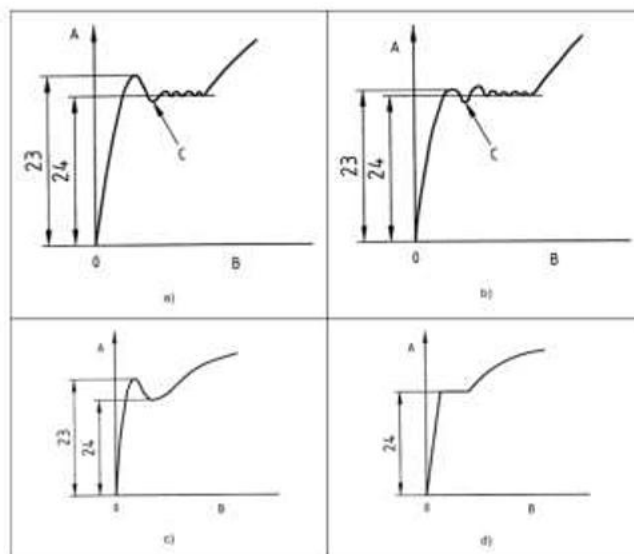


Figure 40 Upper (23) and lower (24) yield strength

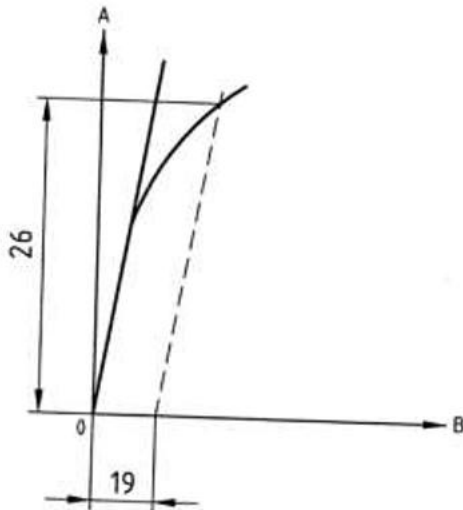


Figure 41 $\sigma - \epsilon$ plot for specimen L3

In the $\sigma - \epsilon$ plots is possible to see that the material has a yielding point. Standard EN

100025-1 clearly reports that “for the specified yield strength in the table on mechanical properties of EN 10025-2 to EN 10025-6 the upper yield strength shall be determined”. The tensile tests results are collected in the following table:

	σ_{UTS} [MPa]	σ_{yH} [MPa]	E [MPa]
T1	525.7	438.2	214640
T2	520.3	446.1	209342
T3	520.5	434.4	214317
L1	509.8	411.4	206988
L2	503.3	406.1	209800
L3	517.0	408.5	214938

Table 2

Now, it is necessary to choose the reference value of f_{iUTS} , f_{iy} and E. The values chosen are the mean of the results collected in the previous table:

- $\sigma_{UTS} = 515$ MPa (standard deviation = 8 MPa);
- $\sigma_{yH} = 425$ MPa (standard deviation = 15 MPa);
- $E = 211\ 000$ MPa (standard deviation = 3000 MPa).

The tensile properties needed for the fatigue analysis are known.

3. TESTING PHASE BEFORE ANALYSIS

3.1. Fatigue tests

Proper fatigue tests are now necessary for the complete characterization of the material behaviour. Fatigue parameters are, in fact, necessary for the analysis. In particular, a fatigue limit and the equation of Wöhler's curve are fundamental. Fatigue tests were done in the past years in GKN: instrumented wheels were tested on a rotating bending machine (see Figure 42) which imposed an alternated symmetrical bending moment on the wheel for a pre-set number of cycles.



Figure 42 Rotating bending machine

With a strain gauges placed close to a hole (see Figure 43) it was possible to measure the deformation imposed by the machine. A wide campaign of test on wheels was carried out and it has confirmed that the starting point of cracks is in proximity of the hole (see Figure 44) which connects the wheel to the hub, as it was expected.



Figure 43 Gauge position



Figure 44 Crack position

After all the test, the experimental Wöhler curve shown in Figure 45 was obtained. In this section it is used the elastic modulus obtained from the tensile test described in 2.3.

Wohler curve

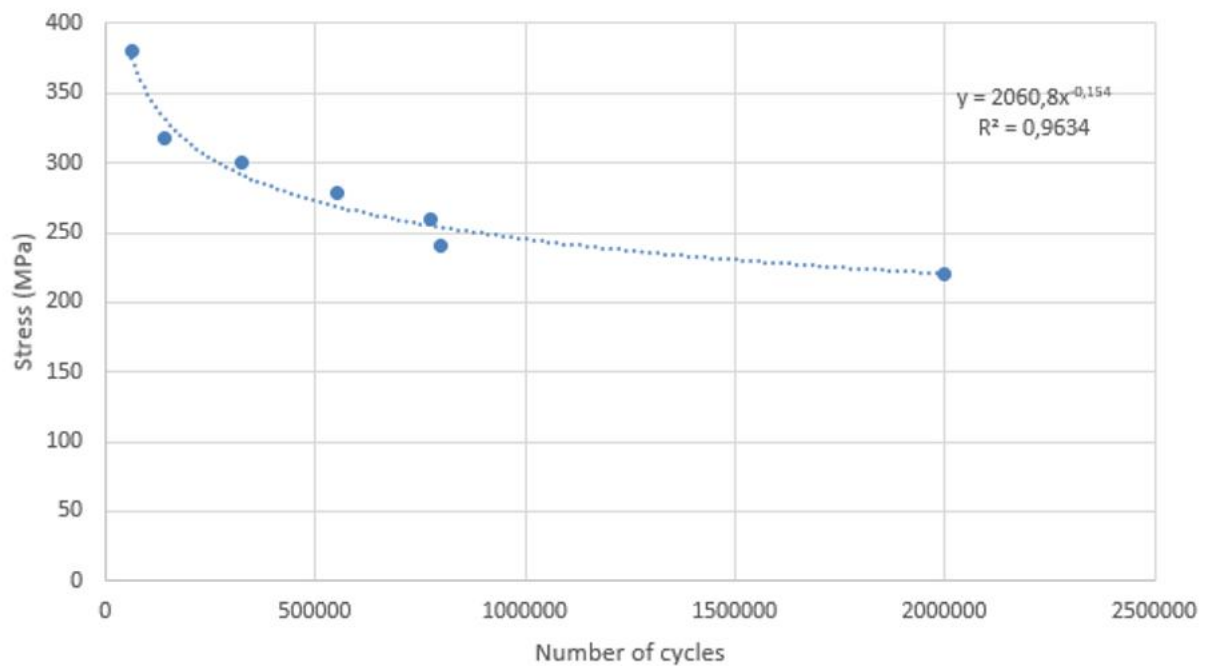


Figure 45 Wöhler's curve

The value of R_2 , which is very close to 1 (0.9634) shows that the equation chosen to represent the fatigue behaviour fits properly to all the experimental data. Therefore, the following equation can be used for the Wöhler's curve.

$$\sigma_a = 2060.8N^{-0.154} \quad 3-24$$

Where σ_a is the amplitude of an alternated symmetrical cycle and N is the number of cycles which has the 50% of probability of breaking the wheel. In bi-logarithmic field, Wöhler's curve equation can be written as:

$$\log \sigma_a = m_w \log N + q_w \quad 3-25$$

Where:

- $q_w = \log_{10} 2060.8$;
- $m_w = -0.154$.

Standard EN 13001-3 gives the number of cycles of infinite life beginning (N_{os}) and the value of infinite life (N_f) as shown in following table:

N_{os}	$10E4$	Cycles
N_f	$510E6$	Cycles

Table 3

The last experimental point has been obtained at $2 \cdot 10^6$ cycles, not so far from the $5 \cdot 10^6$ prescribed in the standard. This means that the experimental Wöhler's curve is capable of describing also the behaviour of the material for a high number of cycles. The fatigue strength of the material is then obtained from equation 3-24 which gives a value of:

$$\sigma_f = 190 \text{ MPa} \quad 3-26$$

In this paper it will be studied the finite life fatigue; a simplified representation of the Wöhler plot can be used. The first part of the plot (low cycles fatigue) is not considered in this work, so a horizontal line with the value of $\log(\sigma_f)$ will represent this part. The Wöhler's curve has been obtained before as the fatigue strength.

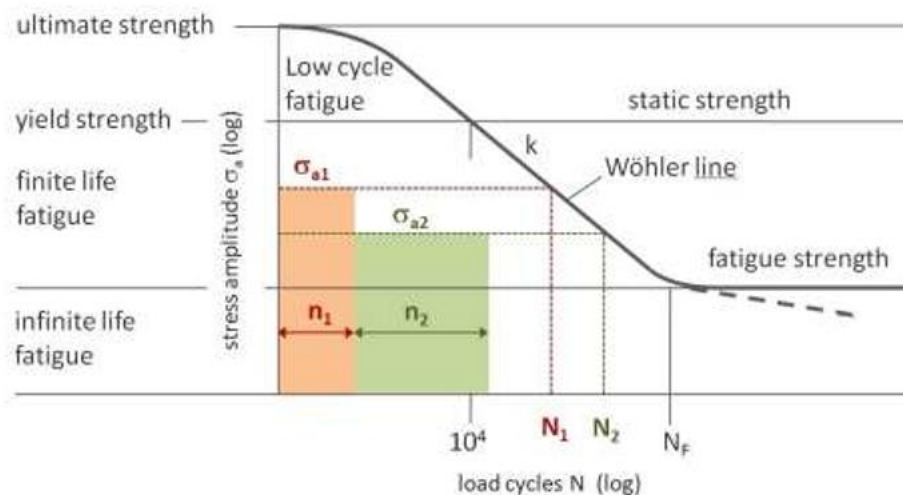


Figure 46 Wöhler plot description

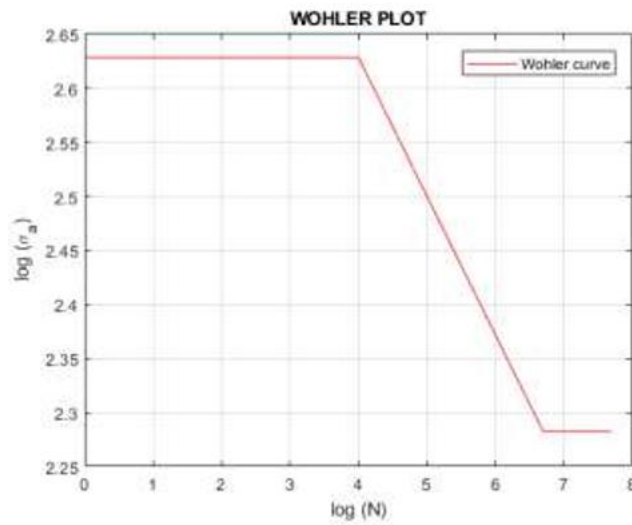


Figure 47 Final Wöhler's curve

In the following table all the material parameters which will be used from fatigue analysis are shown:

σ_{UTS}	515	MPa
σ_y	425	MPa
E	211000	MPa
N_{Os}	10E4	Cycles
N_f	5 10E6	Cycles
m_w	-0.154	
q_w	3.314036	
σ_f	190	MPa

Table 4 Material parameters

3.2. Input data

We have available the strain for ch 4 and ch 6 and under the hypothesis of elastic-linear strain and uni-axial stress state, load histories can be calculated with Hooke's law:

$$\sigma = E \cdot \varepsilon \quad 3-27$$

where E is Young's module. The hypothesis of linear-elastic yield is correct because the maximum value of stress is lower than the yield strength in all the load histories ($\sigma_y=425$ MPa).

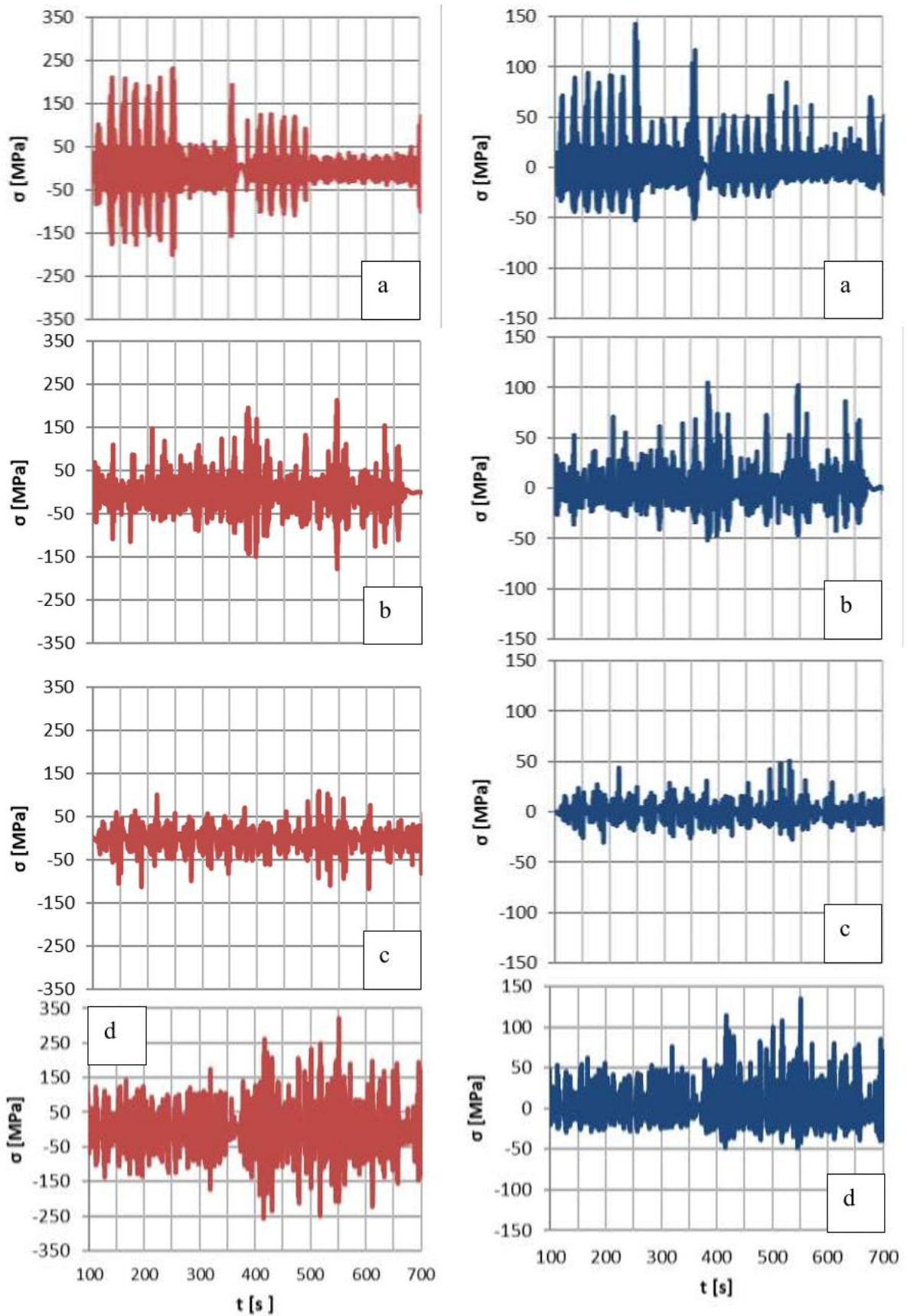


Figure 48 Stress values for CH4 (red) and CH6 (blue) a) on-road, b) load placement, c) loader d) off-road.

4. TIME DOMAIN

In this chapter it will be shown how to manage random fatigue in time domain. First, signals reported in 3.2 will be analysed with Rainflow method which produce equivalent fatigue cycles. After that, with the help of Haigh law, all the equivalent fatigue cycles will be transformed in alternated symmetrical cycles at the same danger level of original ones. Then, it is possible to calculate the fraction of damage using Miner's rule. The reason why in this work only Rainflow and Miner's law are used is that these methods are the most effective, known and used in time domain. The purpose of this research is to find an equivalent method in frequency domain. In this chapter the calculation procedure will be explained step by step. Then, the results of all the gauges will be collected in a table.

4.1. Rainflow analysis

To start this analysis, it is necessary to handle the input signal (sec. 3.2). Rainflow method allows to transform a random signal in equivalent cycles with mean value (σ_m) and range (σ_r) generally different from zero. Another output is how many times a cycle repeats itself (n_i). This step is fundamental because working on package of smaller cycles is the only way to use Miner's law. Figure 49 shows the input signal and the output of the Rainflow analysis.

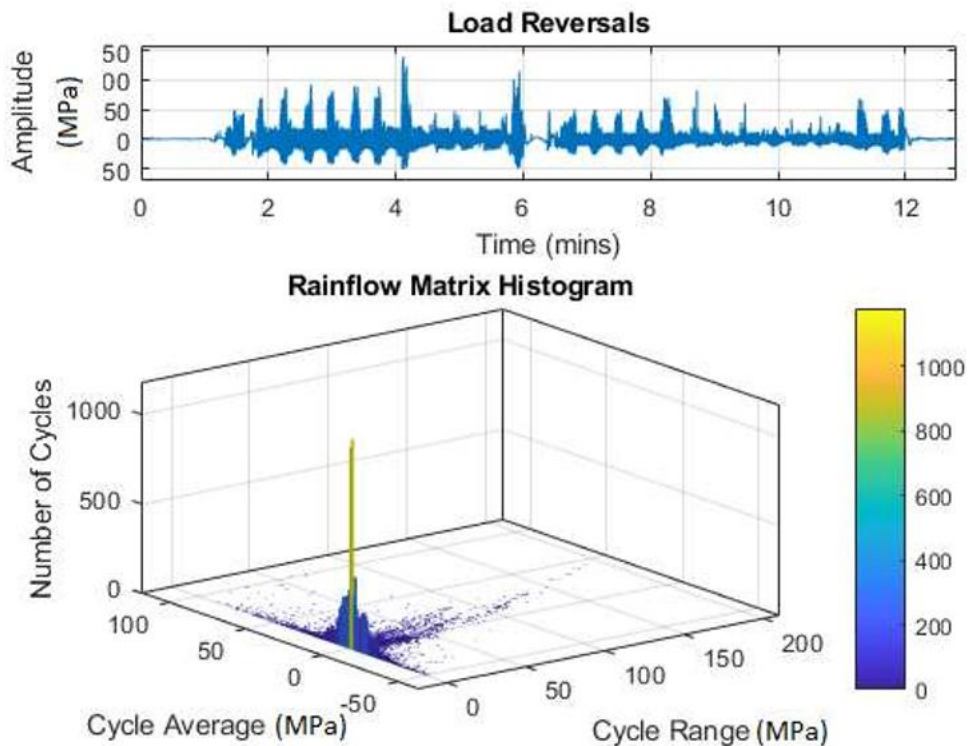


Figure 49 Rainflow gauge 4: on road test

4.2. Haig's law

The second step is to transform the cycles that come from rainflow analysis with the Haigh's diagram (Figure 50). The purpose of this step is to modify the initial cycles in new ones with $\sigma_m = 0$. In the next section the reason of this transformation will be explained.

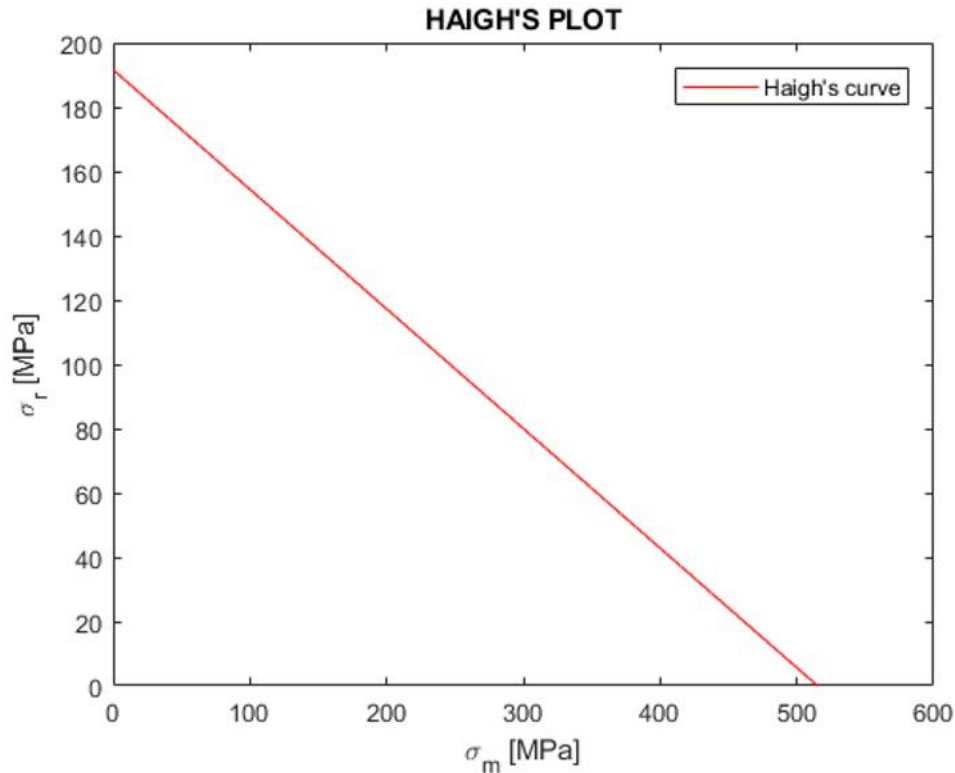


Figure 50: Haigh's diagram

The equation of Haigh's curve (the red line in Figure 50) is:

$$\begin{cases} \sigma_r = \sigma_f & \text{if } \sigma_m \leq 0 \\ \sigma_r = \sigma_f - \frac{\sigma_f}{\sigma_{UTS}} \sigma_m & \text{if } \sigma_m \geq 0 \end{cases} \quad 4-28$$

For those cycles that have negative mean value ($\sigma_{mi} < 0$) the transformation is easy. Negative mean value is not critical for fatigue life as it inhibits the crack's progress. To stay on the safe side, the new cycle has the same alternated component of the original one.

On the other hand, for those cycles that have positive mean value, the transformation is more complicated. Looking at the portion of Haigh's diagram with $\sigma_m > 0$ (Figure 51), it can be considered that all the points on Haigh's curve (the red line) have the same level of danger.

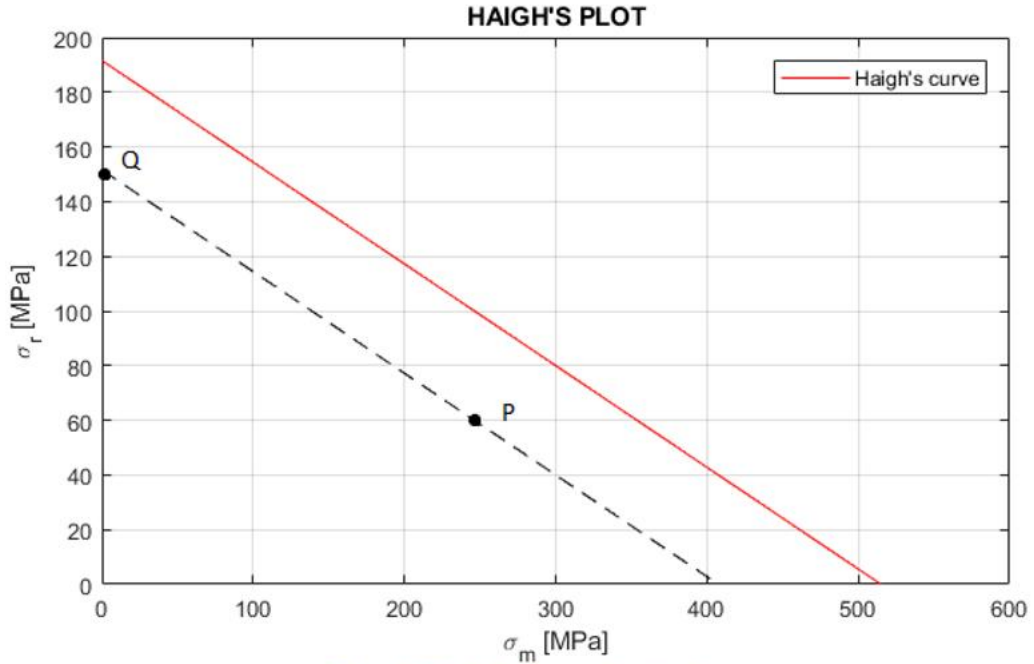


Figure 51: Haigh's diagram (positive)

The slope of Haigh's curve can be calculated in this way:

$$m_H = -\frac{\sigma_f}{\sigma_{UTS}} \quad 4-29$$

It is important to notice that this slope has a negative value. Now, each cycle i correspond to a point $P = (\sigma_{mi}; \sigma_{ri})$ in Haigh's diagram. The purpose of this step is to find the equivalent point Q (i.e. a cycle with the same "level of danger" of P but with mean value equals to 0). With the algebraic procedure shown below and in Figure 51 it is possible to find Q .

$$\begin{cases} y = mx + q \\ \sigma_{Pr} = m_H \sigma_{Pm} + \sigma_{Qr} \\ \sigma_{Qr} = \sigma_{Pr} - m_H \sigma_{Pm} \end{cases} \quad 4-30$$

This procedure must be done for every cycle. To sum up, any cycle can be re-arranged in an alternated symmetrical one (σ_{ei}) thanks to this equation:

$$\begin{cases} \sigma_{ei} = \sigma_{ir} & \text{if } \sigma_{mi} \leq 0 \\ \sigma_{ei} = \sigma_{ir} - m_H \sigma_{mi} & \text{if } \sigma_{mi} > 0 \end{cases} \quad 4-31$$

4.3. Wöhler's curve

Now that each cycle has been transformed in an alternated symmetrical one (described with only one parameter σ_{ei}), Wöhler's curve can be used to define the number of cycles to failure (N_i) of an alternated symmetrical cycle (σ_{ei}). Wöhler's curve was obtained in 3.1. However, a few changes will be done to process all the data as explained in the following section.

$$\begin{cases} \log(\sigma_a) = \log(\sigma_y) & \text{if } \log(N) \leq \log(N_{OS}) \\ \log(\sigma_a) = m_w \log(N) + q_w & \text{if } \log(N_{OS}) \leq \log(N) \leq \log(N_f) \\ \log(\sigma_a) = m_{w1} \log(N) + q_{w1} & \text{if } \log(N) \geq \log(N_f) \end{cases} \quad 4-32$$

Where m_w and q_w have been determined in chapter 2. The values of m_{w1} and q_{w1} are calculated following the standard UNI 130001. An extract is shown in Figure 52.

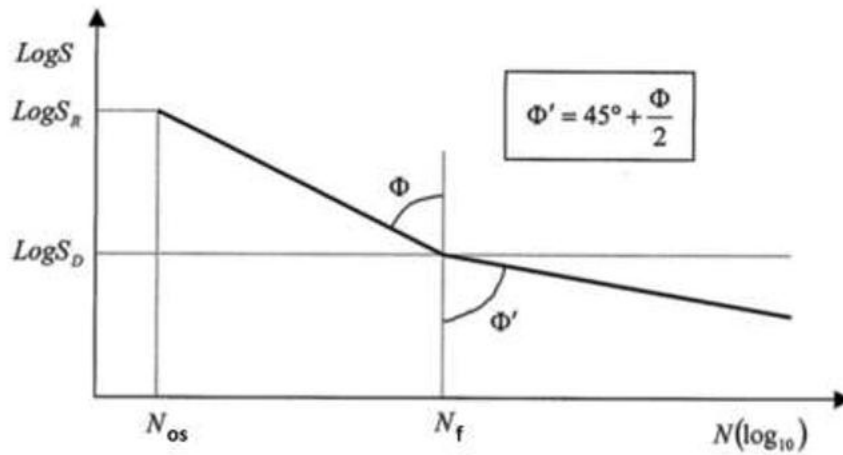


Figure 52 UNI 130001

m_{w1} can be obtained from Φ' , while q_{w1} is calculated with this formula:

$$q_{w1} = \log(\sigma_f) - m_{w1} \log(N_f) \quad 4-33$$

Using the parameters presented in chapter 2, Wöhler's curve can be plotted (Figure 53) and used to calculate the fatigue damage.

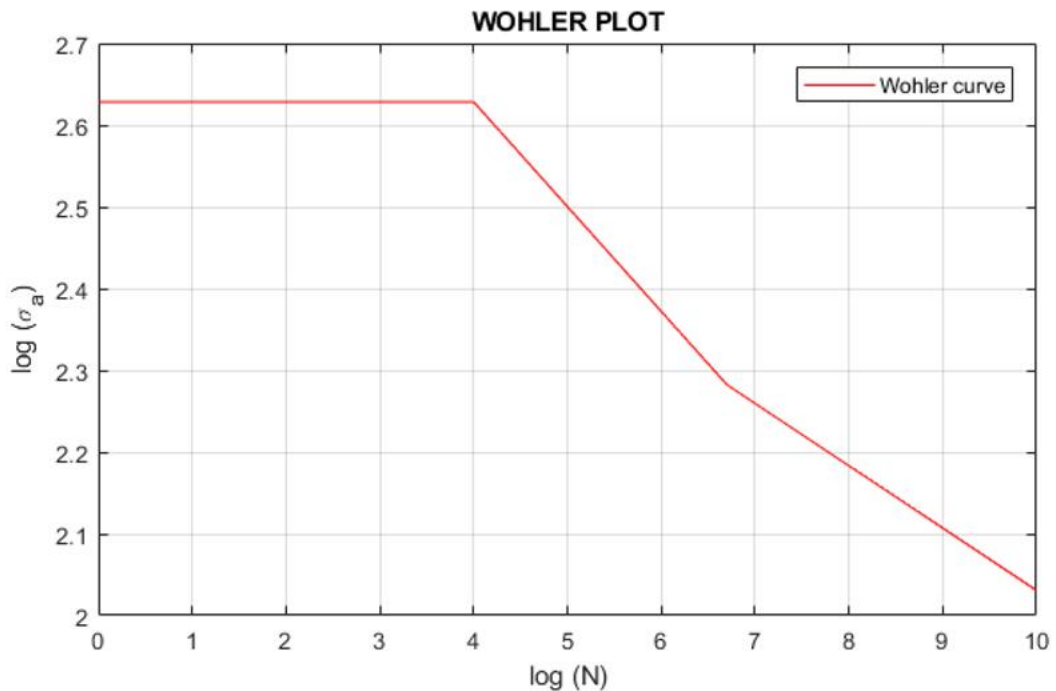


Figure 53: Wöhler's curve

The Wöhler's curve is not drawn by the two typical horizontal sectors for LCF and infinite life (Figure 47) because it does not seem compatible to this problem. In the studied cases the effect produced by stress cycles with amplitude smaller than fatigue limit cannot be neglected. It has been proved through tests with high number of cycles that, in case of variable amplitude stresses (random fatigue), the life calculated neglecting the effect of stress cycles lower than fatigue limit is evaluated in excess.

4.3.1. How to calculate Ni

The number of cycles to failure (Ni) is calculated with this algorithm:

1. Using equation 4–32, σ_a is replaced by σ_{ei} . The only unknown term is $\log(N)$. With a simple math passage Ni can be calculated with equation 4–34 replacing m and q with the correct value coming from Wöhler's curve.

$$\log(N_i) = \frac{\log(\sigma_a) - q}{m} \quad 4-34$$

2. By the repetition of point 1, each equivalent component has now its number of cycles to failure.

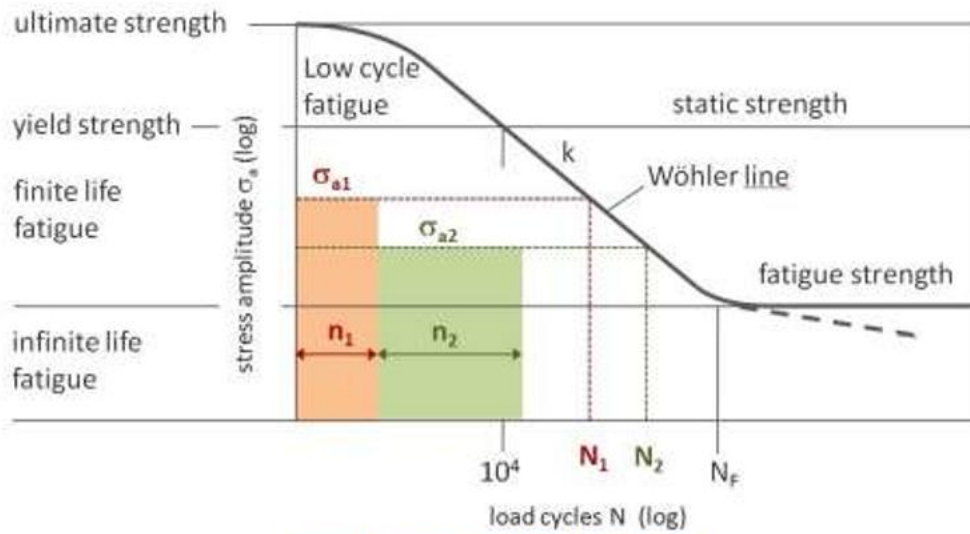


Figure 54: Wöhler curve and how to use it

Figure 54 shows the graphical method used to calculate Ni. Using $\log(\sigma_{ei})$ as an input value, Wöhler's curve returns the value of $\log(N_i)$.

4.4. Miner's law

It is now possible to calculate the damage fraction with Miner's law.

$$D_m = \sum_{i=1}^n d_i = \sum_{i=1}^n \frac{n_i}{N_i} \leq 1 \quad 4-35$$

In fact, Ni has been calculated in 4.3.1 and ni comes from rainflow analysis. It is possible now to calculate the number of cycles to failure of the entire random sequence:

$$N_{bm} = \frac{1}{D_m} \quad 4-36$$

4.5. Hanshin-Rotem correction

Now that the damage percentage is known, it is possible to modify this result with the Hanshin-Rotem correction using the following equation:

$$D_{hr} = \sum_{i=1}^n \left(\frac{n_i}{N_i} \right)^{\frac{1-s_i+1}{1-s_i}} = \sum_{i=1}^n d_i^{\frac{1-s_i+1}{1-s_i}} \leq 1 \quad 4-37$$

It can be noticed that the term d_i is the same in Miner's law. Even in this case, the next step is to calculate the number of cycles to failure of the entire random sequence:

$$N_{bhr} = \frac{1}{D_{hr}} \quad 4-38$$

4.6. Time domain, results

Using the material data coming from paragraph 2, damage ratio and cycles to failure are collected in table 4.1:

	MINER			
	GAUGE 4		GAUGE 6	
	N	D [%]	N	D [%]
Onroad	1.1275E+06	8.8695E-07	2.4429E+03	4.0936E-04
Loadplacement	1.5920E+07	6.2813E-08	1.4434E+04	6.9282E-05
Loader	2.8105E+10	3.5581E-11	2.3208E+05	4.3089E-06
Oroad	5.4739E+05	1.8268E-06	1.6172E+05	6.1834E-06
	HANSHIN-ROTEM			
	GAUGE 4		GAUGE 6	
	N	D [%]	N	D [%]
Onroad	2.5059E+06	3.9906E-07	1.3950E+03	7.1686E-04
Loadplacement	2.8616E+07	3.4946E-08	4.2904E+03	2.3308E-04
Loader	6.1910E+10	1.6153E-11	4.3431E+06	2.3025E-07
Oroad	1.0527E+06	9.4990E-07	1.9249E+05	5.1951E-06

Table 4.1: Time domain results

5. STATISTICAL ANALYSIS (AN OUTLINE)

This chapter shows how to analyse a signal in order to obtain data useful in further fatigue analysis. Things will be made simple and easy to understand, a sinusoidal signal will be used as example. Then, in chapter 6, a real fatigue signal will be analysed with the same method presented below.

5.1. Input signal

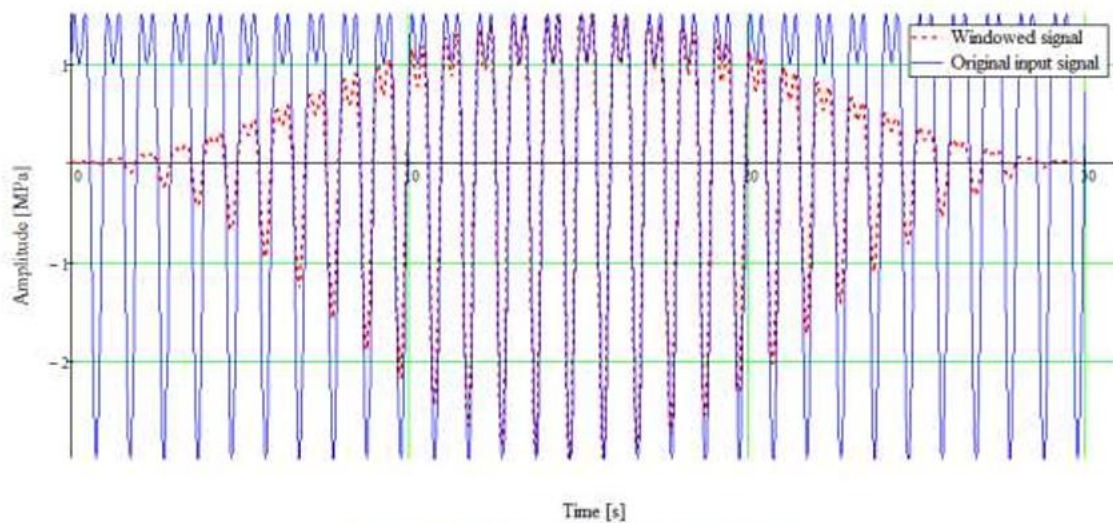


Figure 55: Input signal and windowed signal

As reported in Figure 55, a sinusoidal signal is sampled. In this preliminary analysis, no window will be applied; otherwise, later it will be discussed what kind of window can be the best choice for the input signal.

The signal observed is known ex ante (see equation 5–39), so it is possible to test the analysis process and its results.

$$y(t) = 2 \cdot \sin(2\pi \cdot t) + \cos(4\pi \cdot t) \quad 5-39$$

Signal has been sampled for $t_c = 29:98s$ with a sampling frequency of $f_c = 50$ Hz. Thus, the sampling period is $T_c = \frac{1}{f_c} = 0.02s$ and the number of points sampled is $N_c = f_c \times t_c = 1499$.

According to Nyquist-Shannon sampling theorem, if the N_{HF} harmonic frequency has to be seen without aliasing at least $N_{cMin} = 2 \times N_{HF} + 1$ points has to be sampled. In this case $N_{cMin} = N_c$, N_{HF} becomes equal to $N_{HF} = (1499-1)/2 = 749$ and therefore, the harmonic frequencies until the 749th can be seen without aliasing.

Aliasing is avoided also because the maximum frequency in signal is $f_{maxS} = 4$ Hz and the $f_c > 2f_{maxS}$, that is the equivalent form of the Nyquist-Shannon theorem.

5.1.1. Basic parameters

First of all it is useful to calculate the basic statistical parameters. The points sampled have a mean value of $\mu_{Si} = -4:786 \cdot 10E-4$, a variance of $\sigma^2 = 2:5$ and a standard deviation of $\sigma = 1:581$. Mean value, standard deviation and variance are defined as follows:

- Mean value (μ). For a vector whose elements are y_k , the arithmetic mean value is defined as $\mu = \frac{\sum_{k=1}^n y_k}{n}$. It represents the value that is less distant from all the othervalue. If y_k represents a finite population, the population mean value is equal to the arithmetic mean value. The sample mean value may differ from population mean value, especially for small samples. Otherwise, the law of large numbers states that the larger is the size of the sample, the closer the sample mean value will be to the population mean one;
- Standard deviation (σ): In statistics, it is a measure used to quantify the amount of dispersion of a set of values. A low standard deviation indicates that data tend to be close to the mean value (also called the expected value). A high standard deviation points out that the data are spread out over a wider range of values;
- Variance (σ^2). It measures how far a set of numbers are spread out from their average value. The variance is the square of the standard deviation and can also be calculated as the second central moment of a distribution.

5.1.2. Autocorrelation

When dealing with random signals, it is reasonable to ask whether the particular signal being analysed is truly representative of every possible signal in every possible interval of observation time. Luckily it exists a propriety, called autocorrelation, that provides a measure of the regularity (or, better, ergodicity) of the process. In addition, the delay introduced using this method, allow to discover periodicity in signal.

While the probability density (PDF, which it will be calculated further on) contains the information related to the variations of the amplitude of the process, the autocorrelation contains information related to the variations on time axis. Furthermore, it is very useful to know that the spectral density of a signal is the Fourier transform of the autocorrelation function.

When a signal is ergodic (i.e., it is not time-invariant respect to itself), autocorrelation provides values close to zero or negative. It is similar to destructive interference, in which the negative parts of the curve are erased with positive ones, so the correlation function has smaller values. The maximum correlation value is an index of how much the signals are in phase.

Assume to have a sampled signal $S(t)$; if τ is the delaying parameter, the autocorrelation formula can be written as:

$$R_{xx} = \sum_{t_0=0}^{t_{max}} [S(t) \cdot S(t + \tau)] \quad 5-40$$

Observing the formula, it can be noticed that the autocorrelation function is simply the correlation between the signal $S(t)$ translated and the signal $S(t)$ itself; the variable t is free and is not saturated in the operation of integration. In other words, equation 5-40 represents an infinity of sums, one for every possible value of $t \in [t_0; t_{max}]$ and τ .

The autocorrelation function is limited and measures the similarity of a signal with its copy translated of τ . As it can reasonably be noted, the maximum is obtained by a translation with $\tau= 0$. For energy signals, which have a limited domain, the domain of the two copies overlaps less and the function tends to zero if translation is increased.

For power signals, if no periodic or constant components are present, while increasing translation similarity tends to decrease, and therefore the autocorrelation function tends towards to zero.

This is not true for periodic signals. It is easy to verify that the autocorrelation is itself periodic, with the same period. Even in the case of a constant signal, autocorrelation is a constant.

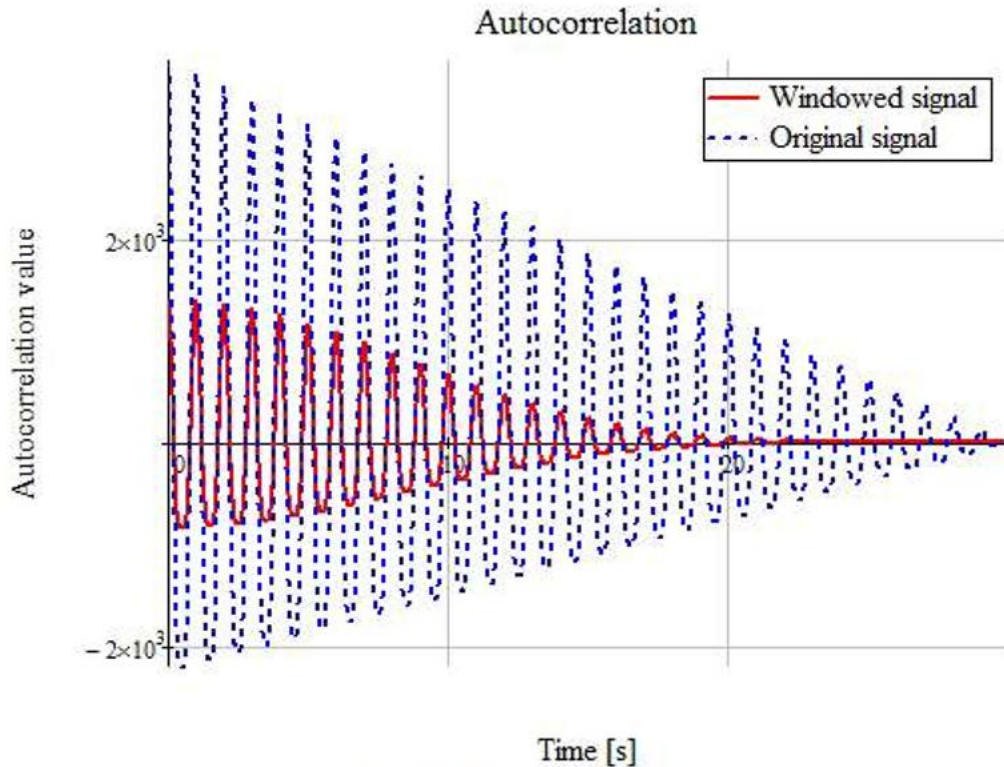


Figure 56: Autocorrelation signal

The results of autocorrelation are useful to obtain the power spectral density function(PSD). In fact, Wiener-Khinchin's theorem ensures that the power spectral density of a signal coincides with the Fourier transform of the autocorrelation function of the signal itself.

5.1.3. Probability density function (PDF)

The study of fatigue in frequency domain is, above all, a statistical analysis. Using as input the load history of the component (stress vs time), statistical parameters are deduced in order to characterize the same load history, but in the frequency domain.

In addition to the classic parameters (mean, variance and standard deviation) it is useful to extend the analysis on samples to obtain the probability density function (PDF).

This function associates a probability for each stress value (σ) reported on the abscissas. The result is a continuous curve, of total area equal to 1 and representing the range of values that the magnitude of interest can - most likely - assume.

5.1.3.1. Independence of contributory causes

The same physical phenomenon can be analysed from several points of view. The simplest way is to detect how many times that phenomenon occurs, regardless of what has generated it. A more detailed point of view, on the other hand, requires to analyse the different causes that may have risen the observed phenomenon. In the first case, the analysis is rather simple. If a phenomenon (for example the occurrence of a given σ value) can take X different values, each of these values can be treated as a discrete random variable.

Simplistically, if the occurrence of an event is unrelated to the occurrence of others, the probability of measuring the X value is equal to $\frac{100}{X}\%$. The analogy with a dice roll is obvious: only 6 values can be obtained and each value has a probability of $\frac{100}{6}\% = 16.6\%$.

5.1.3.2. Interdependent events

Instead, most physical phenomena need a more accurate analysis.

First of all, it is necessary to underline that it is highly unlikely that a phenomenon depends only on one parameter. For example, if the statistical measurement of the temperature in a room is needed, it would be a too great approximation to consider that the temperature depends only on the value set on the thermostat. Actually, the effect of irradiation, the thermal conductivity of the walls, any open window and the temperature outside the house should be considered. All these parameters, which have their own intrinsic and statistical variability, combine themselves in a stochastic way and provide the final room temperature.

Therefore, it is clear the need of a method that can describe a phenomenon including the statistical variability of the parameters. This method - or better - this probability function, is the normalized Gaussian distribution and the mathematical work on which it is based is the central limit theorem.

In order not to bundle this already complex chapter, the key points of this statistical analysis are reported below. Let n be the number of contributory causes that affect an event and assume that np is the number of measurements done.

- If X is distributed as a random binomial variable with a very large n (to give an idea of how large, it can be said that it should be $n \geq 30$), and approximately $np \geq 10$, then the binomial can be approximated with a normal Gaussian PDF with expected value equal to np ;

- If X is distributed as a random Poissonian variable with a very large λ parameter ($\lambda > 10$), then the Poissonian can be approximated with a Normal with expected value and variance equal to λ : $N(\lambda; \lambda)$.

Figure 57 and Figure 58 how the PDF change in function of n .

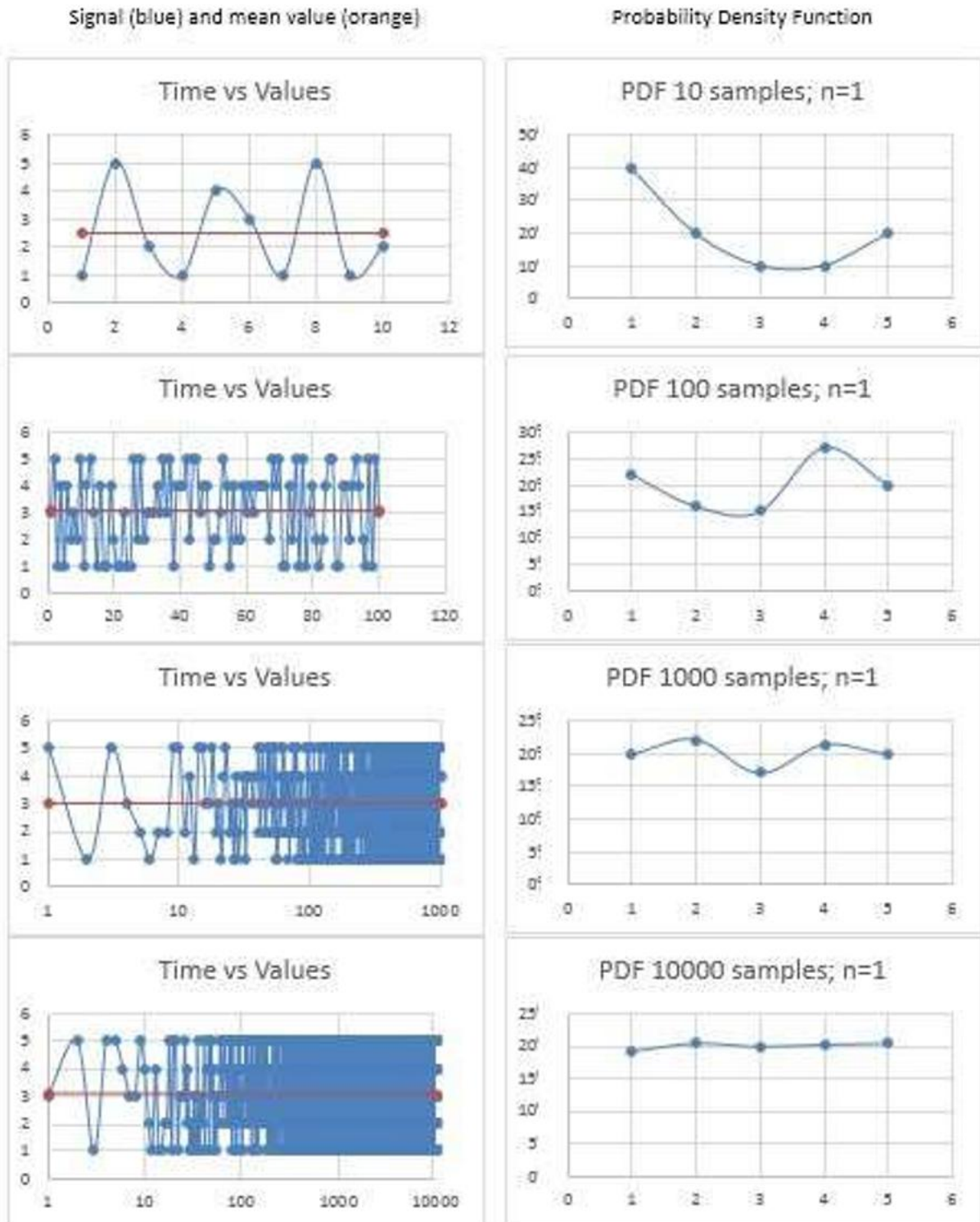


Figure 57: Changes in PDF curve when $n = 1$ and the number of point analysed increases

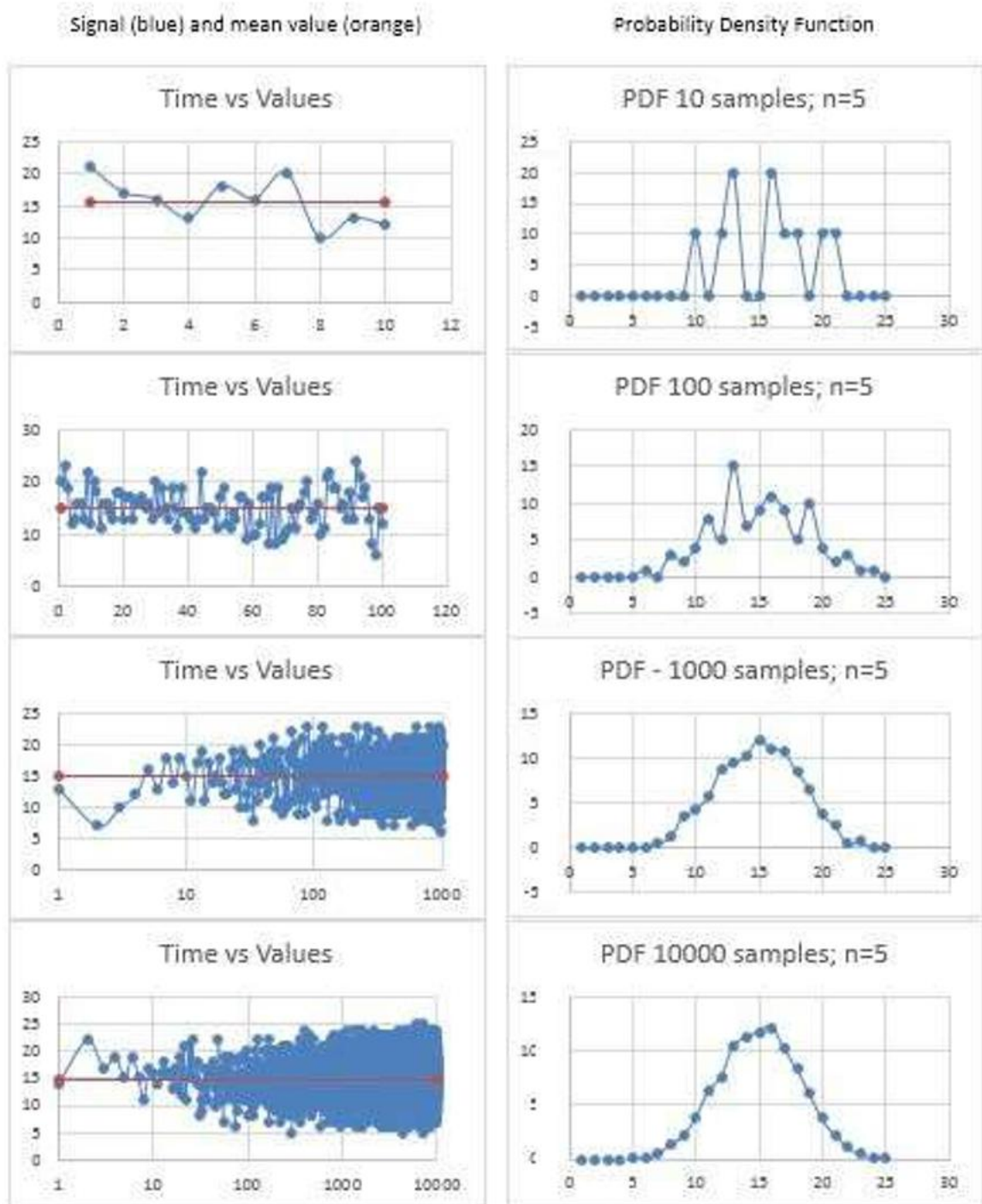


Figure 58: Changes in PDF curve when $n = 5$ and the number of point analysed increases

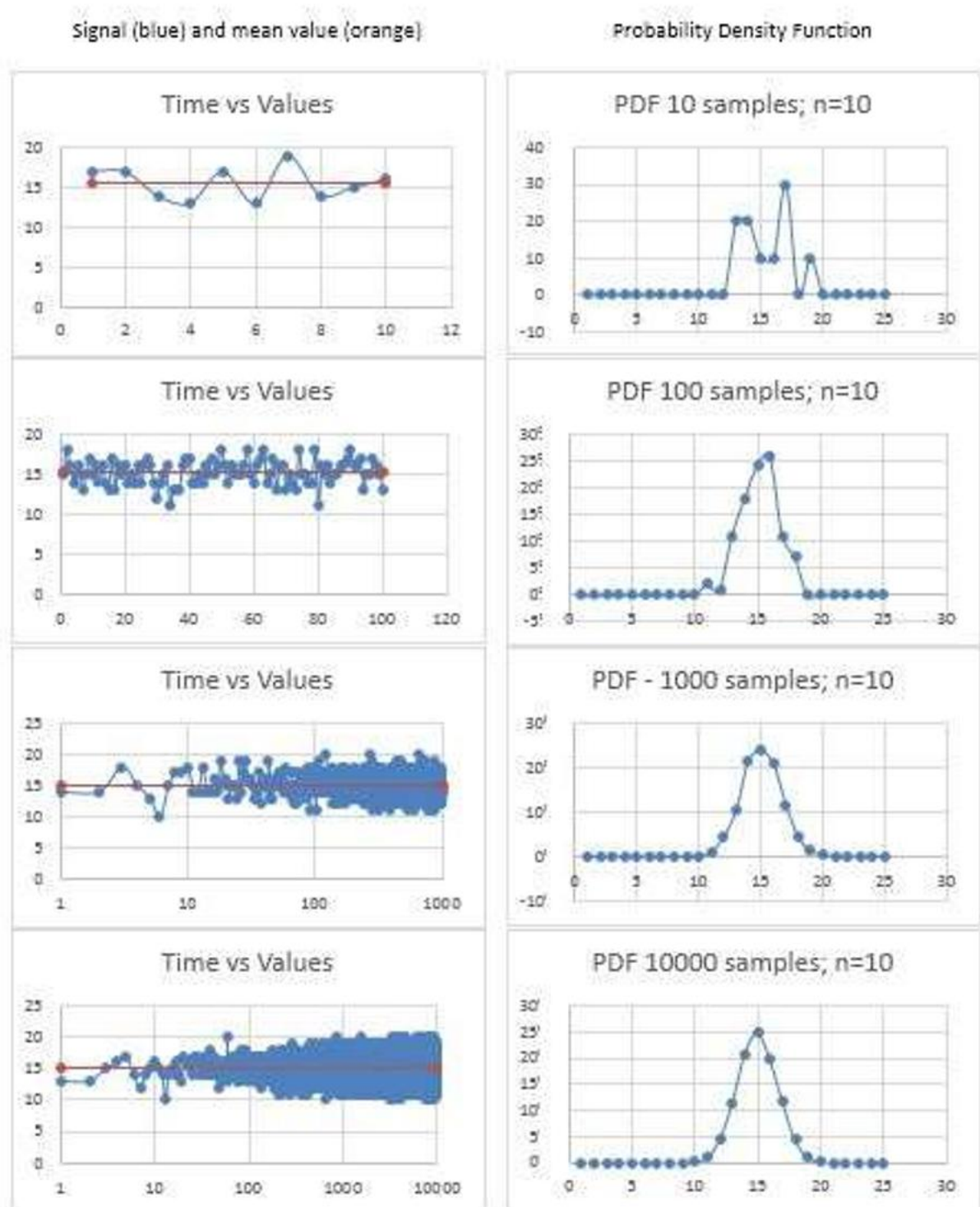


Figure 59: Changes in PDF curve when $n = 10$ and the number of point analysed

Therefore, it remains to understand if the variable X (in this work $X = \text{stress}$) is a binomial variable.

First of all, a choice is made considering the main application _eld of each discrete probability functions: Poisson's one is called "law of rare events", while the binomial one is called "law of multiple independent events".

Since the stress value is an event that occurs randomly in each cycle, it will be first verified if the data can be approximated with a binomial coefficient distribution.

In probability theory, the law of large numbers (LLN) is a theorem that describes the result of performing the same experiment a large number of times. According to the law, the average of the results obtained from a large number of trials should be close to the expected value, and will tend to become closer as more trials are performed. The LLN is important because it guarantees stable long-term results for the averages of random events. In this situation the LLN theorem has a strong relevance as it introduces stability in the normal distribution. It has been supposed that the input random data may be viewed as a normal distribution, but in order to build this distribution mean and variance are needed. Otherwise, someone could object that for a random distribution the mean value is - indeed - random and it changes for every measurement. This is true, but if a large number of data are processed, the LLN theorem guarantees that the mean value deduced is not too far from the real mathematical mean. An evidence of this theorem is given in Figure 60.

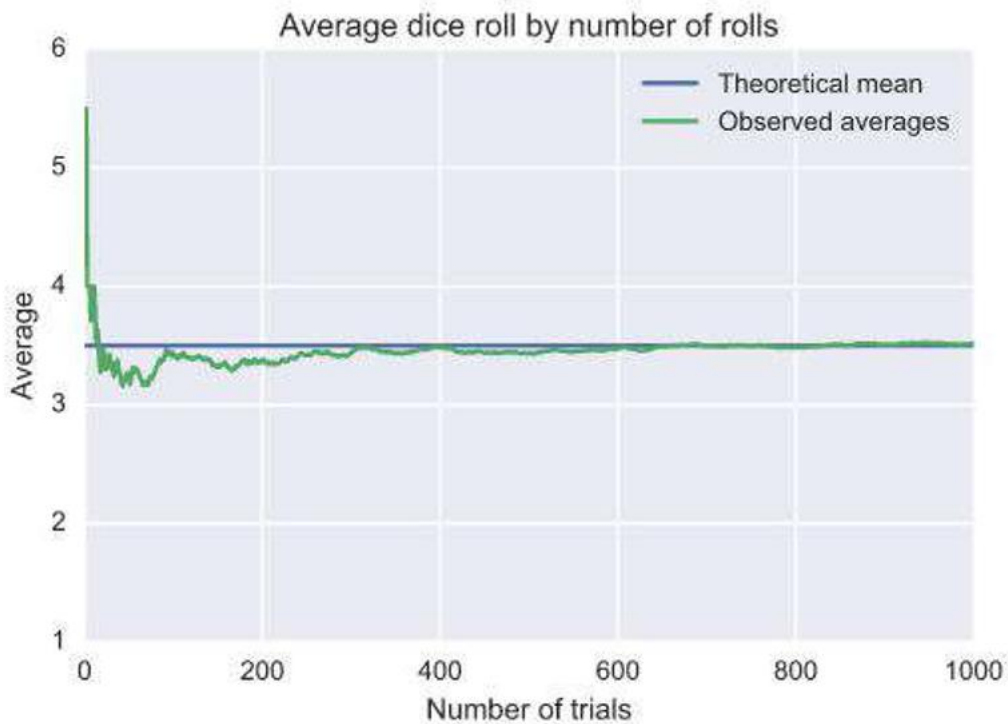


Figure 60: Mean value in roll dice

5.1.4. A common error

Sometimes a continuous phenomenon is treated as a discrete one only because the measuring instrument has a discrete output. Let's try to explain with an example. Assume to have two different events:

1. A dice roll, that can assume only 6 values in the sampling space $\Phi_1 = [1; 2; 3; 4; 5; 6]$;
2. A balance, that can measure the weight of a jug, so $\Phi_2 [1; 6]$, with a resolution of 1kg.

Obviously, a dice can show only one of Φ_1 values, so it has always a discrete output, randomly chosen in Φ_1 . In the second case, the jug might have a weight of 1:2, but considering the balance resolution, only a natural number between 1 and 6 will be shown. So, the second event is continuous, but the measuring instrument makes it discrete. Even if the measure is discrete, the right way to approach the second case is to use a continuous approach. Therefore, the statistic output should preferably be a curve that points out how much possibility a value has to be between x and y .

In other words: the discrete measurement given by the balance should be used to understand which is the suitable PDF distribution. Do the events have the same chance of happening? A linear PDF will be chosen. Are the events the result of at least 30 independent events? A normal Gaussian PDF can be a good choice. Is there an event that is extremely unusual and rare? Probably a Poisson's PDF will fit to this random event.

The example just made explain the reason that allow the use of a PDF for the analysed dataset: even if the gauges measure a discrete output, the strains and the stresses are continuous phenomena, like the weight of the jug. Therefore, the right way to handle.

5.1.5. Choosing a good PDF

Until now, it has been supposed to have a Gaussian-standard dataset. Is this a good hypothesis? A way to verify the goodness of the approximation is using the descriptive statistics. Computing particular statistical parameters, it can be estimated the degree of adherence of a certain hypothesis (i.e. the Gaussian one) towards the problem under examination.

5.1.5.1. Histogram

A histogram is a plot that consists of columns, whose heights are linked to the number of repetitions of a particular event. Chosen the casual variable on which the statistic will be made (in this case, the stress range σ), the maximum and the minimum σ are searched. A histogram plots will be made following these steps:

1. the significant decimal place (a) for approximating the casual variable is chosen by the user
2. maximum and minimum values must be approximated to the same decimal place of n (for example, if maximum value σ_{max} is 3.4736 and $a=0.1$ then $\sigma_{max}; a = 3:5$; if $a = 0:01$ then $\sigma_{max}; a = 3:47$);
3. the number of bars (b) in the histogram is calculated as $b = (\sigma_{max}; a - \sigma_{min}; a)/a$;
4. the values of the casual variable are divided into classes. Assuming that $n \in [1; b - 1]$, the lowest value of each class is $a \cdot n$, the centre-value is $a(n+0.5)$ and the highest value is $a(n + 0.5)$;
5. For each class it has to be counted how many times an event is found in the dataset and what is the probability of finding that event. Then, a rectangle with an area proportional to the probability has to be built and plotted.

Example: Assume to have these 10 values: $\sigma = [1; 2; 3; 2; 2; 3; 1; 5; 3; 3]$, that can be rewritten as shown in table 5.1:

VALUE	REPETITIONS
1	2
2	3
3	4
4	0
5	1

Table 5.1: Value used in histogram's example

Now a histogram plot with four classes will be created. First of all, classes have to be set and an easy statistical analysis on classes has to be done as shown in table 5.2.

LOWEST VALUE	CENTRE VALUE	HIGHEST VALUE	REPETITIONS	PROBABILITY
0	0.625	1.25	2	20%
1.25	1.875	2.5	3	30%
2.5	3.125	3.75	4	40%
3.75	4.375	5	1	10%

Table 5.2: Classes and statistic,1

5.1.5.2. Probability plots

Using the probability column, the area of each histogram column can be found. The basis of each histogram column is the difference between the highest value and the lowest value. Therefore, the height can be found as $Area/Basis$ (see table 5.3). Finally, the plot can be created (see Figure 61).

It is useful to add to the plot the following curves:

- the red one which connects the centre points of each histogram rectangle, representing also a good PDF for the studied phenomenon;
- the green curve which is the PDF obtained if the phenomenon is supposed to be Gaussian.

AREA	BASIS	HEIGHT
0.2	1.25	0.16
0.3	1.25	0.24
0.4	1.25	0.32
0.1	1.25	0.08

Table 5.3: Classes and statistic, 2

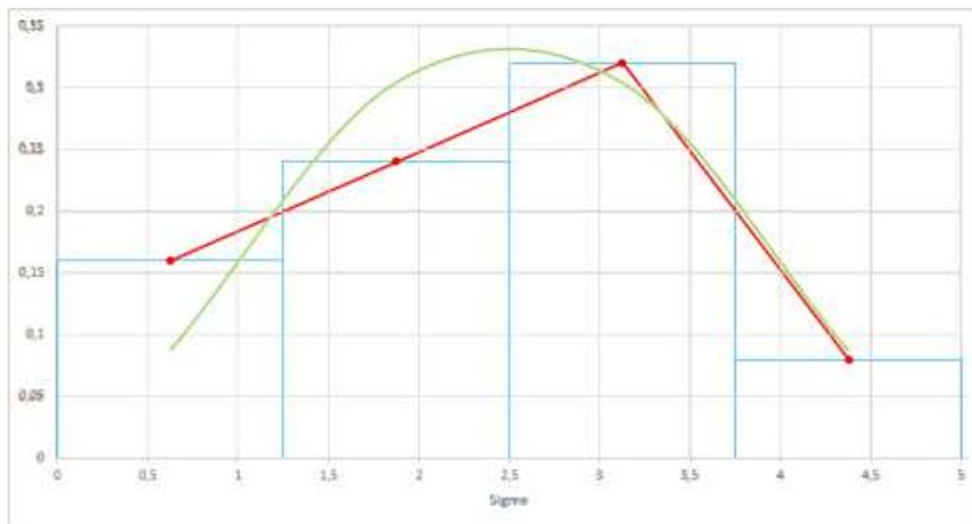


Figure 61: Histogram and Gaussian using the data in histogram's example

Sometimes more powerful tools are used in order to show if data are truly distributed as a Standard Normal distribution. First of all, mean value and standard deviation are calculated; then using Excel (or Mathcad, or Matlab, ...) spreadsheet a table may be created as follows:

- the first column includes the data examined;
- the second column shows the probability to find the data in the first column if they are distributed as a Gaussian distribution;
- the third column includes the real probability to find the data in first column;
- the fourth column includes the cumulate probability of the second column;
- the fifth column includes the cumulate probability of the third column.

Now two plots can be created:

- The real probability and the Gaussian probability versus the data examined (i.e. Second column vs. first plus third column vs. first column);
- The real cumulative probability and the cumulative Gaussian probability versus the data examined (i.e. fourth column vs. first plus fifth column vs. first column);

Now a control chart (called graph of Normal probability) will be generated. An interesting propriety of a Gaussian dataset is that to generate a straight line if it is plotted in this particular way:

- On abscissas the data examined (in this case, the stress value σ);
- On Y axis, the z value that respect the equation $\Phi(z) = F_x(\sigma)$, where $F_x(\sigma)$ is the cumulative Gaussian probability and $\Phi(z)$ is the Gaussian normalized distribution.

If data are truly Gaussian, they lay onto a straight line characterized by an angular coefficient $m = \frac{1}{\text{std deviation}}$ and $q = \frac{\text{mean}}{\text{std deviation}}$, thus $t(\sigma) = m \sigma + q$ is the straight line searched.

Lastly, if data seems to be not so different form the Gaussian straight line, a regression line can be estimated, whose m and q will be the new mean and standard deviation of a new (and more adherent) Gaussian curve. (Obviously it will be: std deviation $1/m$ and mean q/m).

Now some plots will be shown: they have been calculated from the non-windowed phenomenon in Figure 55. First, histogram plot will be shown (Figure 62), then a check between Gaussian PDF and the real one will be made (Figure 63). After that, the cumulative probability function will be calculated (Figure 64). Lastly, the normal probability plot will show if the hypothesis of Gaussian distribution is a good hypothesis (Figure 65).

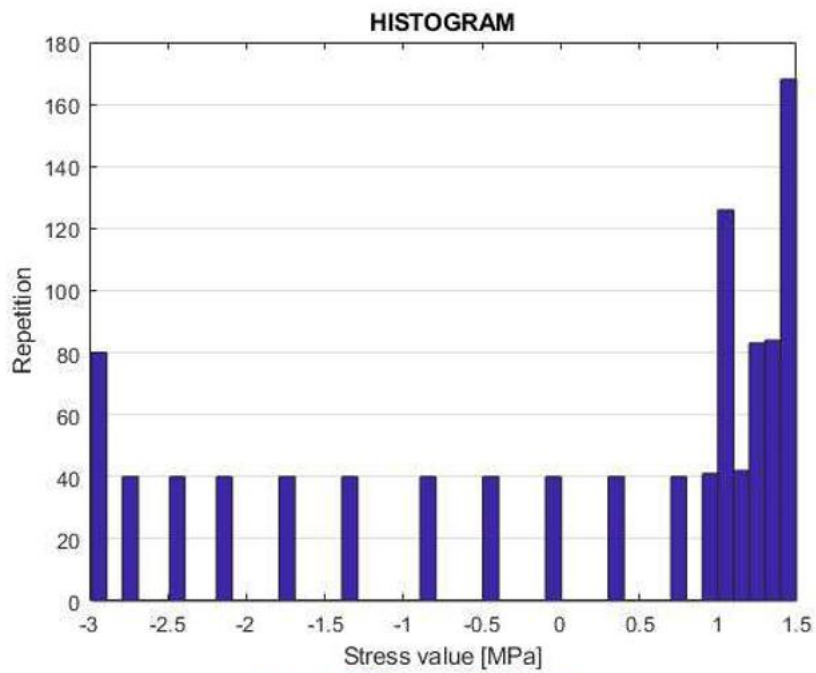


Figure 62: Histogram; basis = 0:1

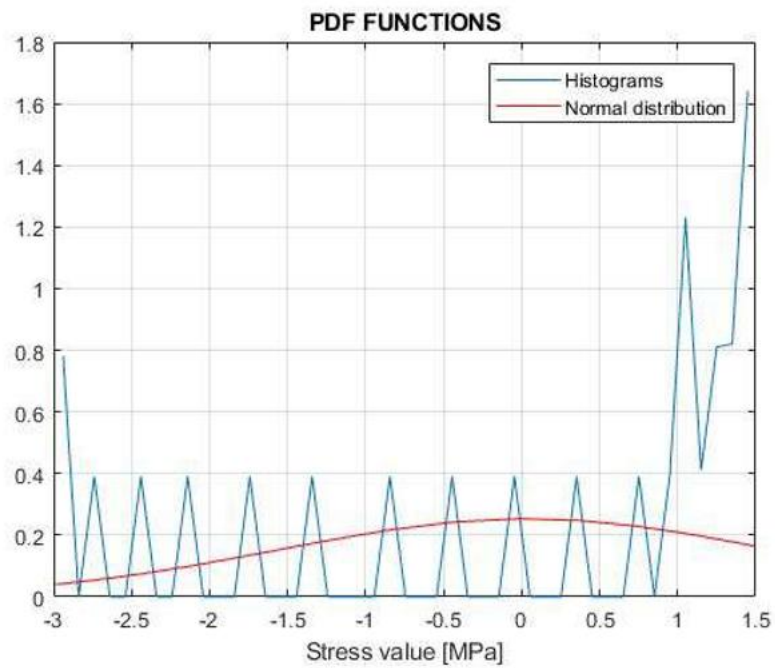


Figure 63: Gauss PDF and a line that connect the centre point of every histogram's rectangle

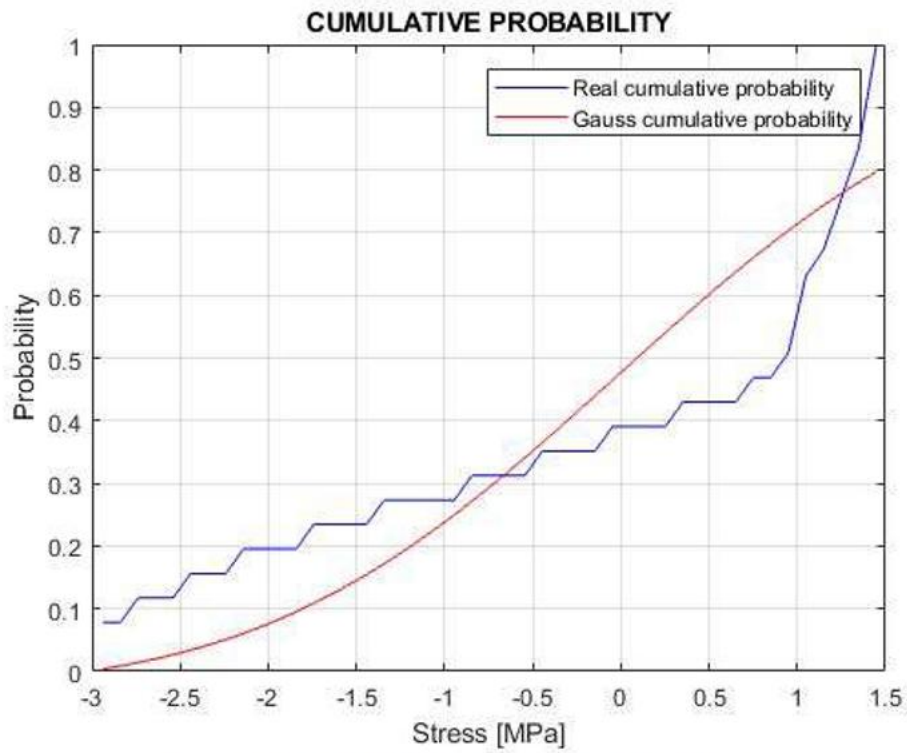


Figure 64: Gaussian cumulative probability and the real one

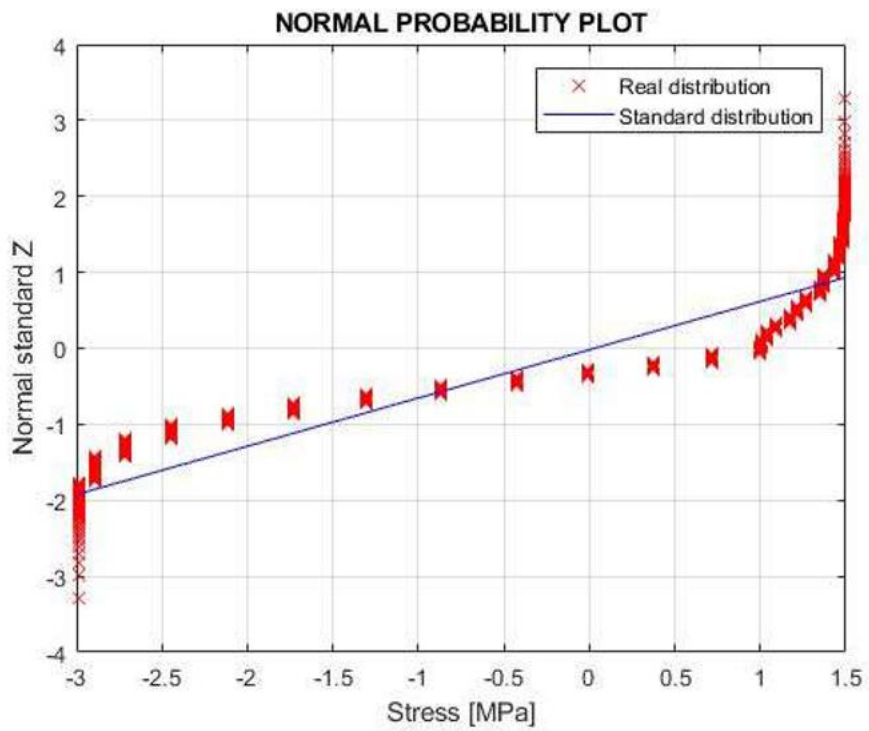


Figure 65 : Normal probability plot

Figure 65 is the demonstration of the non-Gaussian nature of the data reported in Figure 55.

5.2. Fourier theorem and rearranges

Once the input signal has been statistically analysed, the real frequency domain analysis can start.

5.2.1. FFT analysis

If all the previous statistical conditions are respected, frequency analysis should give good results.

Let's start with the Fourier theorem: the original Amplitude-Time signal will be now converted in a Magnitude-Frequency one. As shown in Figure 66 and Figure 67, even if the window allows to have better results when a random signal is elaborated, it is not the best solution every time. Especially when the input signal does not have many asynchronous frequencies or if it does not have many peaks, a windowed-Fourier-transformed signal produces a big error. The reason of this incorrect result can be found in a lack of energy that the window drains from the proper original signal. In this case, using an Hanning's window, the 50% of the original energy is lost resulting in a reduction of a factor 2 in the FFT peak. The worst effect is made on FFT phase diagram, where the sine and the cosine wave are significantly distorted from their original phasing.

Lastly, a proof of correctness in FFT calculus is obtained by the reverse-transformed signal, that gives back the original input (Figure 68).

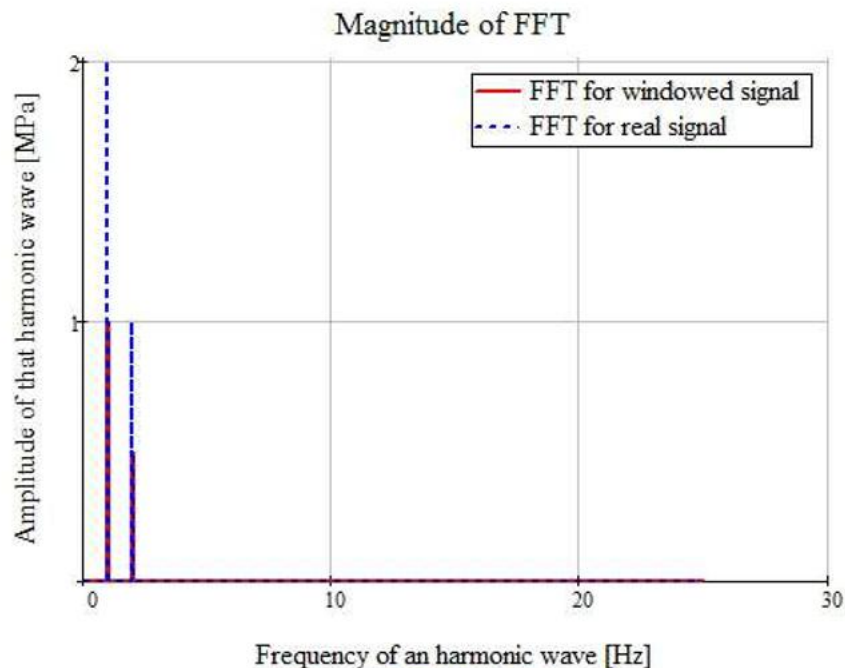


Figure 66: FFT – Magnitude

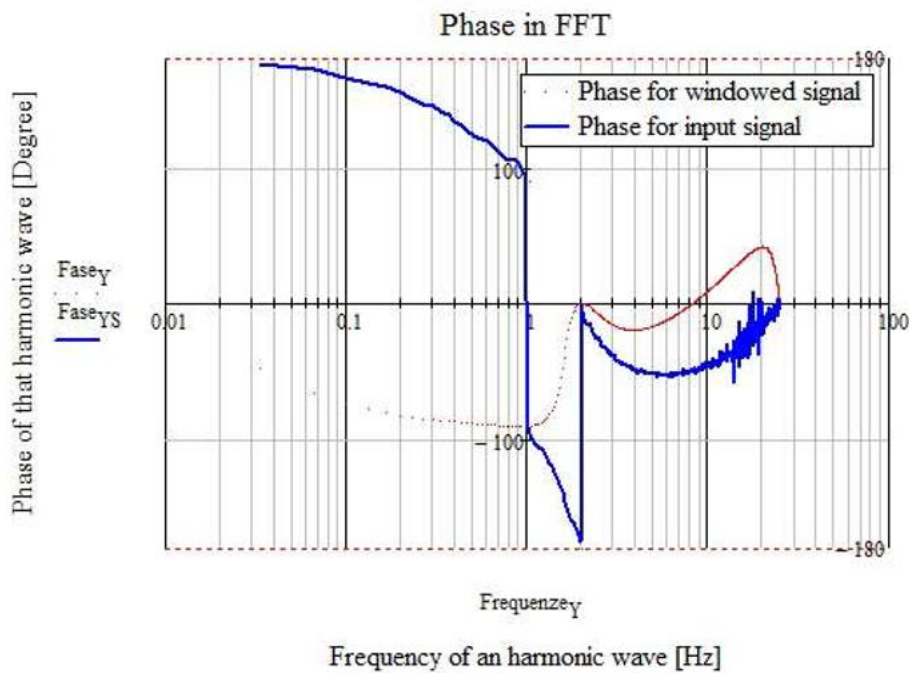


Figure 67: FFT – Phase

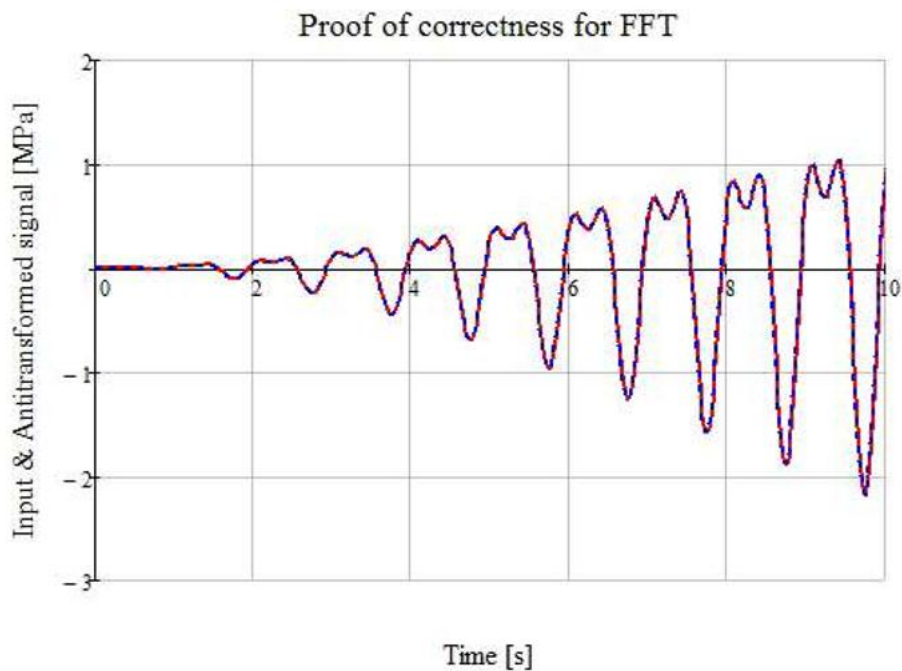


Figure 68: FFT - proof of correctness

5.2.2. PSD and ASD analysis

Reasons of the PSD use. The characterization of a random vibration usually occurs through the spectral power density curve (PSD, Power Spectral Density). The PSD is defined as the average quadratic response of a random variable, in which an ideal narrowband filter is applied.

The result is divided by the bandwidth of the filter, to tend the latter to zero. The term power is rather generic and it can refer to acceleration, speed, displacement, deformation, force, and so on. In the case of a random load description, the PSD is generally referred to the input value of the strain gauge (Volt or microstrain).

The PSD of a signal describes the distribution of power between the frequencies that make up that signal. Through Fourier analysis, every signal, even a continuous one, can be decomposed into a discrete number of frequencies; the statistical processing of that signal represents its spectrum. When the energy of a signal is concentrated in a finite time interval, the spectral energy density of that signal can be calculated; the results will then be better if the input signal is discrete (as in our case, where it is provided for a finite number of points).

There are many ways of calculating the density of energy, but the most recognised is the PSD (power spectral density) method, which works particularly well on signals that span a wide time lapse.

In addition, the PSD spectrum of a physical process often contains essential information on the nature of the vibratory phenomenon under examination. For example, the tone and the timbre of a musical instrument are immediately determined by a spectral analysis; also, the colour of a light source is determined by the electric field spectrum of the electromagnetic wave.

In many cases, time domain is not specifically used in practice, and for a good reason.

In time domain, information transmitted by physical systems are easily readable, but in frequency domain the same signals show their constitutive nature and are more easily intelligible.

A deeper point of view. Any signal that can be represented as a time-varying amplitude has a corresponding frequency spectrum. When these signals are displayed in form of a frequency spectrum, some aspects of the received signals or of the underlying processes that produce them are revealed. In some cases, frequency spectrum may include a distinct peak corresponding to a sine wave component, and there may be peaks corresponding to harmonics of a fundamental peak, indicating a periodic signal which is not simply sinusoidal.

The power spectral density of a signal describes the power stored in the signal as a function of frequency, or, better, per unit of frequency. Spectral power density is commonly

expressed in watts per hertz (W/Hz). In addition, the area under the curve is related to the actual signal strength over the whole frequency or to a specified bandwidth.

When a signal is only defined in terms of voltage, for example, there is not a unique power associated with the declared amplitude. In this case, "power" is simply calculated in terms of the square of the signal, as this would always be proportional to the actual power delivered by that signal in a given impedance.

The power spectral density of a signal describes the power stored in the signal as a function of frequency, or, better, per unit of frequency. Spectral power density is commonly expressed in watts per hertz (W/Hz). In addition, the area under the curve is related to the actual signal strength over the whole frequency or to a specified bandwidth. When a signal is only defined in terms of voltage, for example, there is not a unique power associated with the declared amplitude. In this case, "power" is simply calculated in terms of the square of the signal, as this would always be proportional to the actual power delivered by that signal in a given impedance.

So, units of v^2/Hz for the PSD and v/Hz for the ESD (energy spectral density) are used even if no "power" or "energy" is specified effectively. Sometimes the spectral amplitude density (ASD), which is the square root of the PSD, is encountered; the ASD of a voltage signal has units of $v/\sqrt{\text{Hz}}$. This is useful when the shape of the spectrum is rather constant, since the variations in the ASD will therefore be proportional to the variations in the voltage level of the signal itself.

Anyway, it is mathematically preferred to use the PSD because only in this case the area under the curve is significant in terms of actual power over the whole frequency or on a specified bandwidth.

A useful knowledge. The PSD calculus can be difficult, but if a good statistical analysis is made before the frequency analysis, things can be made in an easier way.

In fact, using a theorem that here will not be demonstrated the PSD can be obtained by:

$$PSD = 2 \cdot FFT(R_{XX}) \quad 5-41$$

where the 2 is used because the FFT algorithm of a 2n-length vector produces a n-length output with the half of the input energy.

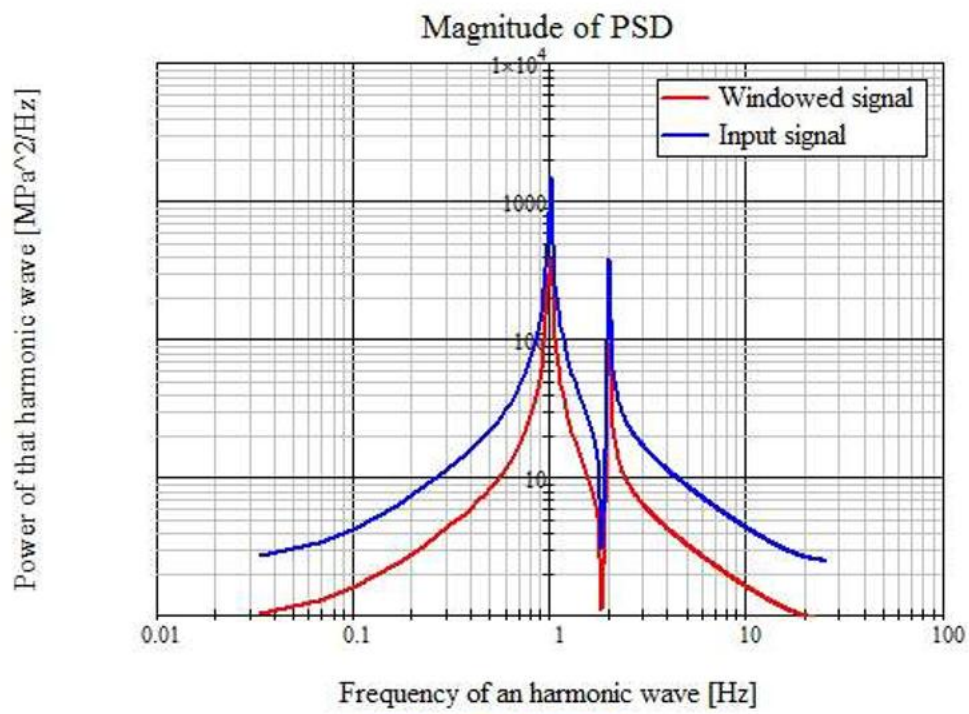


Figure 69: PSD – Magnitude

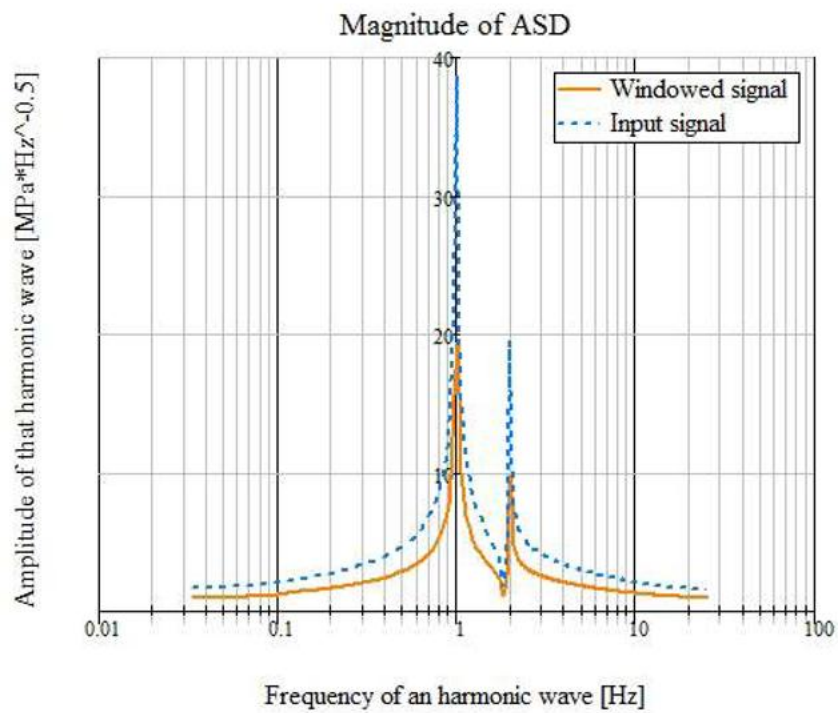


Figure 70: ASD - Magnitude

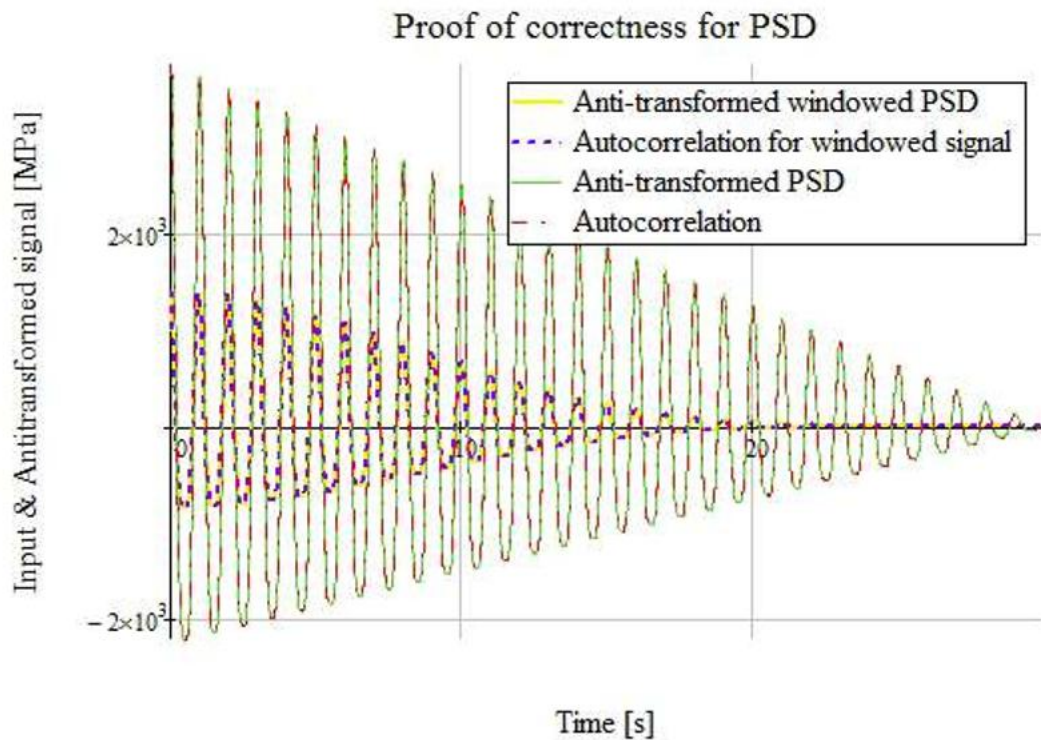


Figure 71: PSD - Proof of correctness

As previously shown in Figure 69, Figure 70, Figure 71, the graphs obtained by the PSD process give a good approximation of the process. In this case, having a singular and known harmonic wave, the PSD calculus might have been omitted, but in real cases, the PSD analysis significantly decreases errors on estimation about the most energetic wave in the wavelet processed.

Furthermore, it is important notice the difference between the original signal and the Hanning-windowed one. It has been already pointed out that for a singular and synchronous-sampled harmonic wave no window is needed, so this is a good circumstance to observe the potentially dangerous effects of a bad window. In the ASD plot the windowed signal and the one not windowed are scaled by a factor of 2: this is due to the chosen Hanning window, that cut half of the energy stored in the wave. the PSD plot has an even worst situation. The squares made to transform the energy of the ASD into the powers of the PSD has amplified errors by a factor of 4.

6. FATIGUE IN FREQUENCY DOMAIN

In this chapter it will be shown how to manage random fatigue in frequency domain. All the theoretical information is collected in this chapter. Then, these methods are applied to the signals reported in paragraph 3.2.

6.1. Input signal

As reported in paragraph 3.2, real load histories are sampled signals. In this preliminary analysis, no windows will be applied; otherwise, later, it will be discussed what kind of window could be the appropriate choice for signals and if a window is really necessary. It is important to remember that every sampled signal could be analysed in frequency domain, but the number of harmonics that could be studied must respect the Nyquist-Shannon theorem.

6.2. Statistical analysis

6.2.1. Autocorrelation

In figures from Figure 72 to Figure 79, it will be shown the autocorrelation function for every load history. Notice that autocorrelation functions decrease to zero and there is no periodical component. this is the proof of ergodicity.

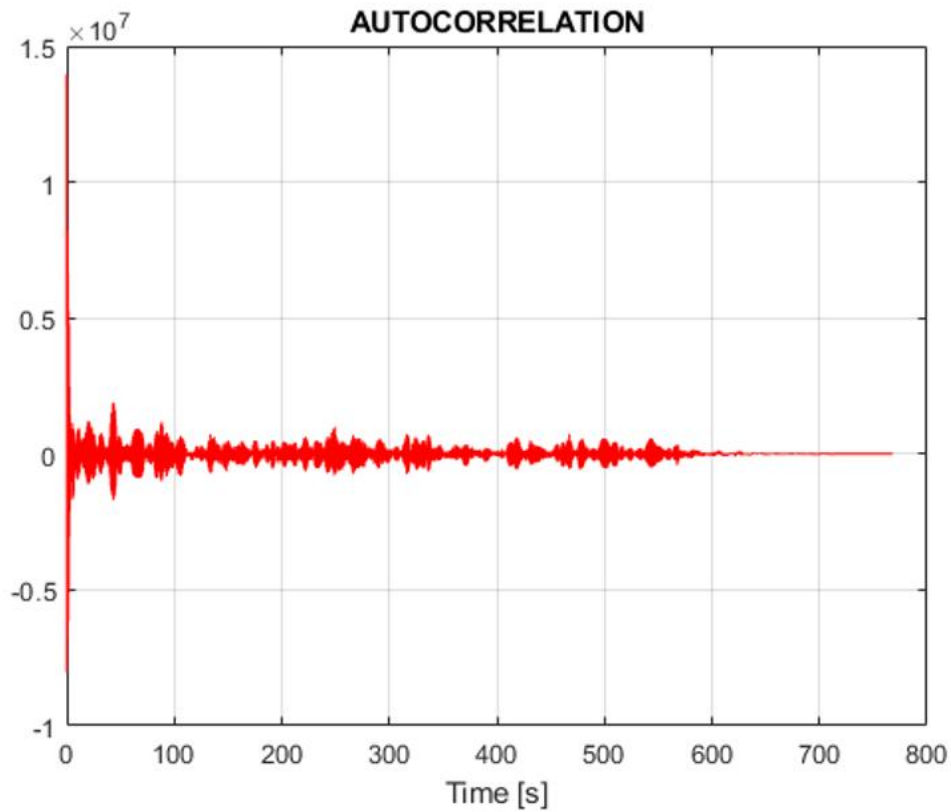


Figure 72: Gauge 4, On road: autocorrelation

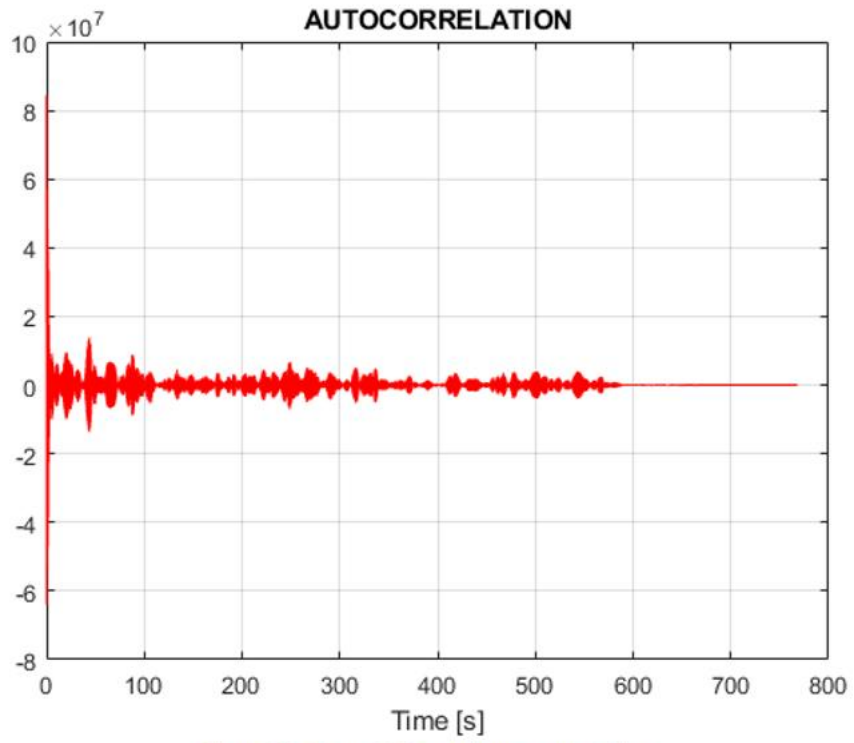


Figure 73: Gauge 6, On road: autocorrelation

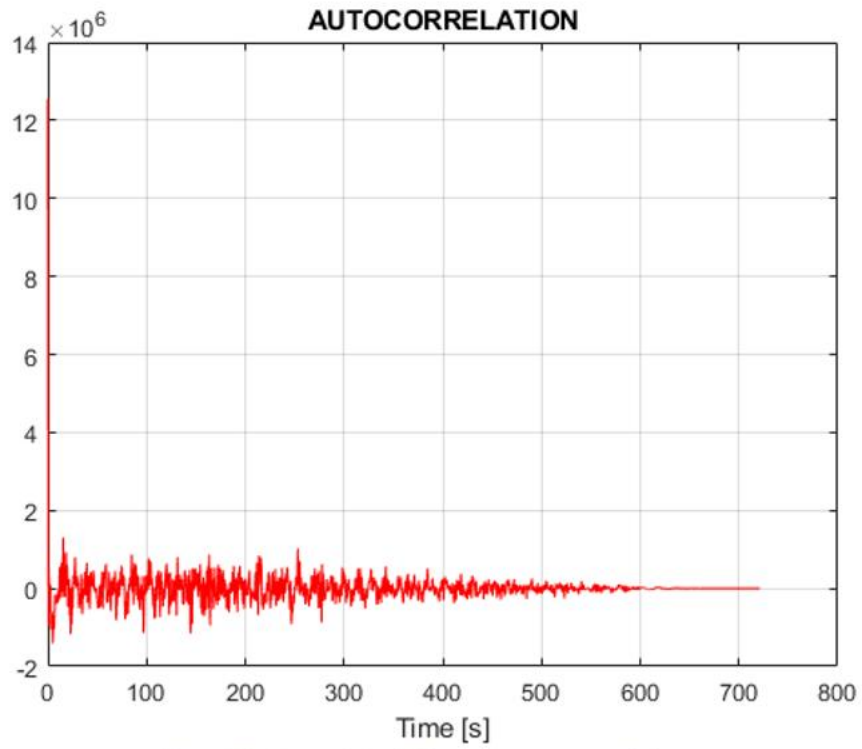


Figure 74: Gauge 4, Load Placement: autocorrelation

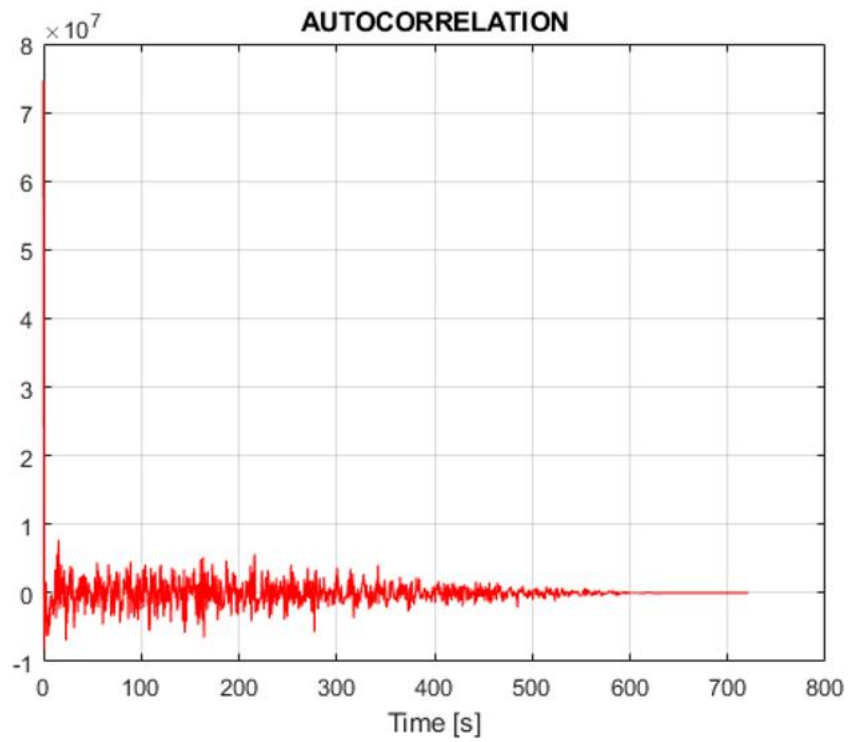


Figure 75: Gauge 6, Load Placement: autocorrelation

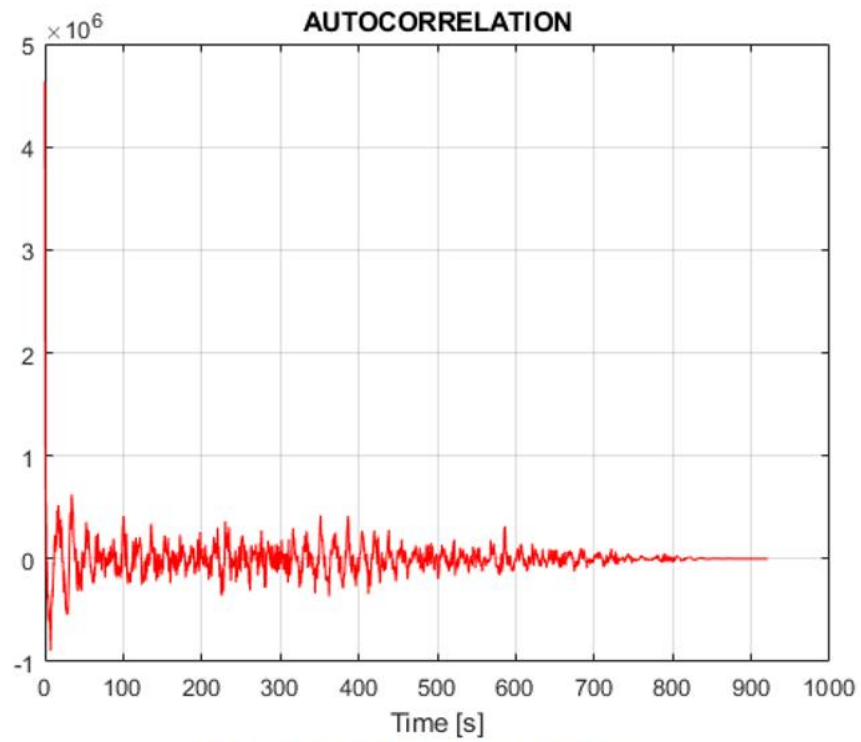


Figure 76: Gauge 4, Loader: autocorrelation

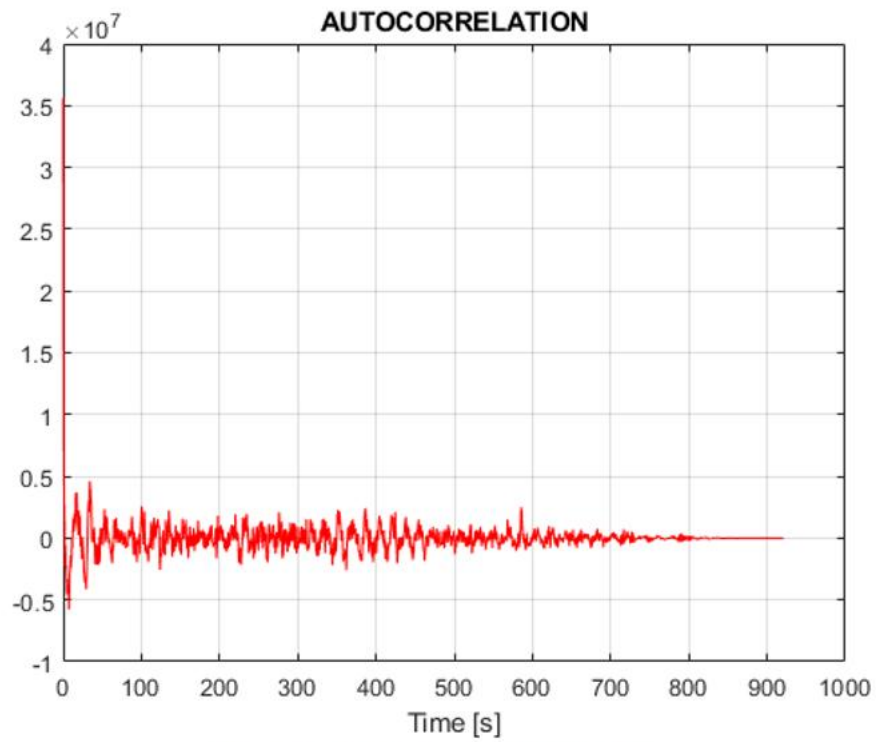


Figure 77: Gauge 6, Loader: autocorrelation

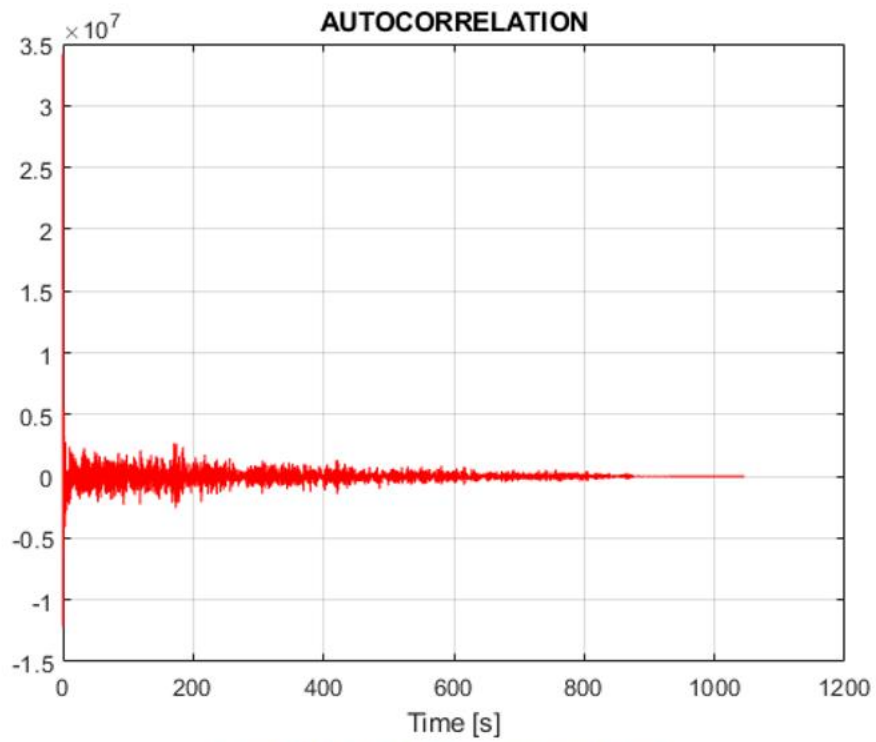


Figure 78: Gauge 4, Offroad: autocorrelation

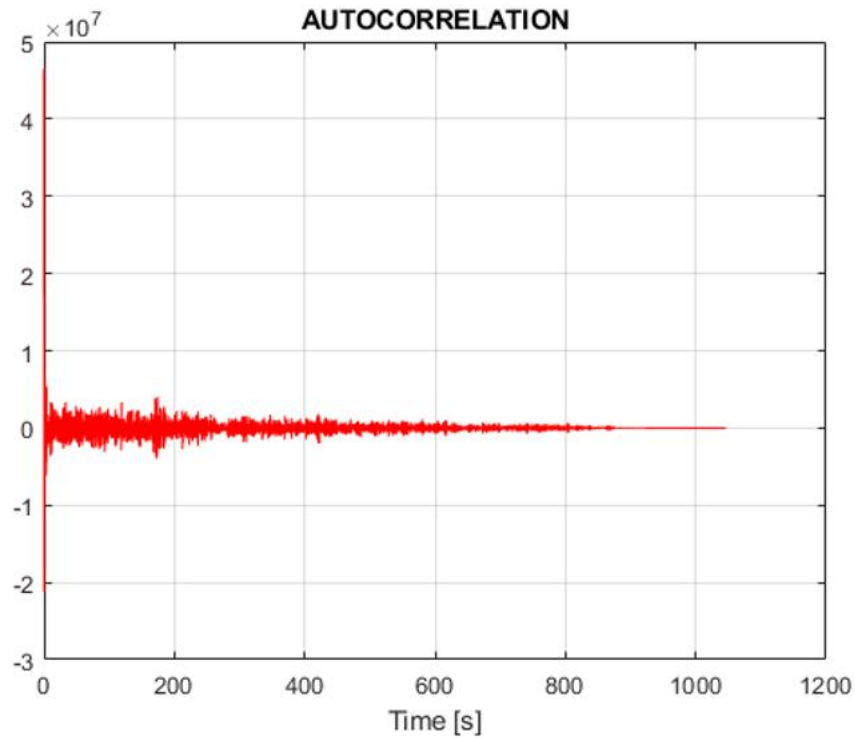


Figure 79: Gauge 6, Offroad: autocorrelation

6.2.2. Probability density function (PDF)

With the algorithm presented in paragraph 5.1.5, it could be possible to calculate the PDF for each load history but, for now, it is not necessary. In fact, it will be now supposed to have signals that can be statistically analysed as Gaussians. Therefore, a bell normalized curve will be built using mean value and variance obtained from every load history.

	GAUGE 4		GAUGE 6	
	μ [MPa]	σ [MPa]	μ [MPa]	σ [MPa]
Onroad	6.69E-04	13.4825	2.19E-04	33.1509
Loadplacement	1.00E-04	13.1914	-8.56E-04	32.1884
Loader	-4.57E-04	7.095	-0.0011	19.667
Onroad	1.50E-04	18.0843	1.94E-04	21.0751

Table 5 Statistical parameters

Gaussian PDFs are shown in figures from Figure 80Figure 87.

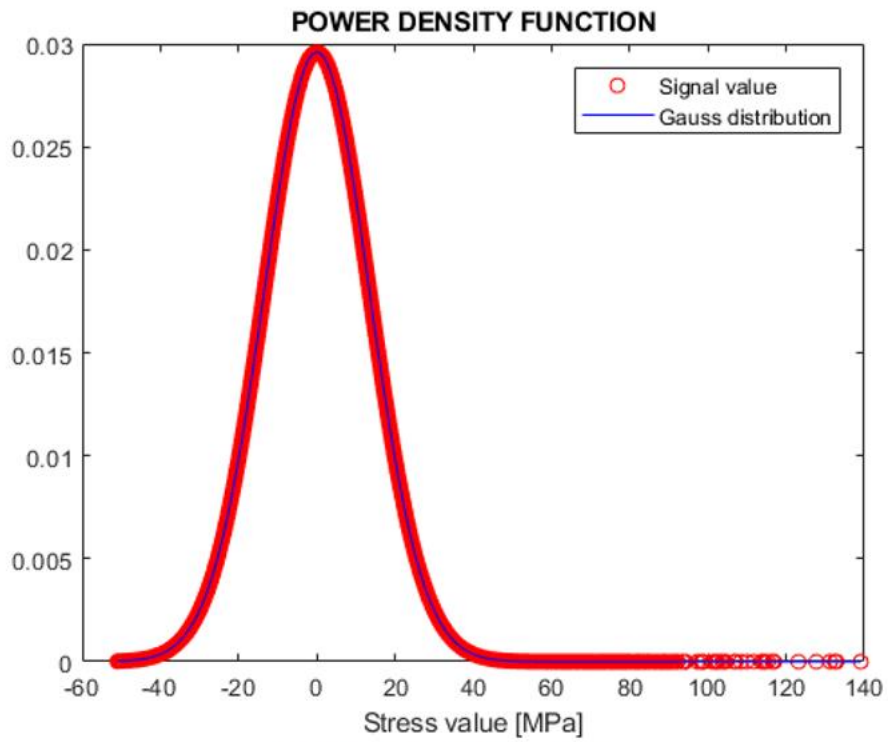


Figure 80: Gauge 4, On road: PDF

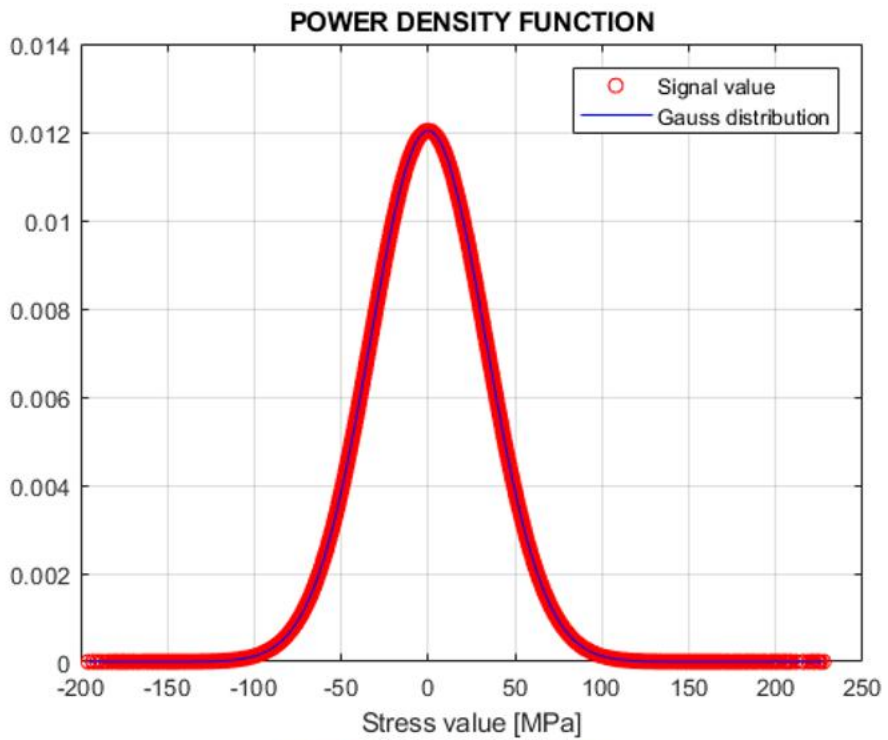


Figure 81: Gauge 6, On road: PDF

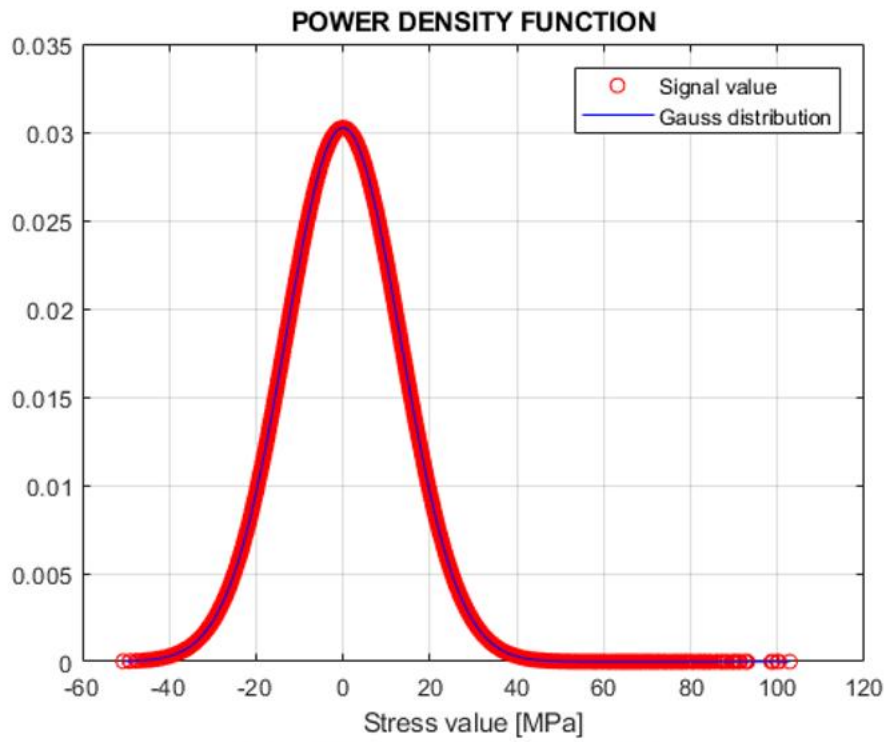


Figure 82: Gauge 4, Load Placement: PDF

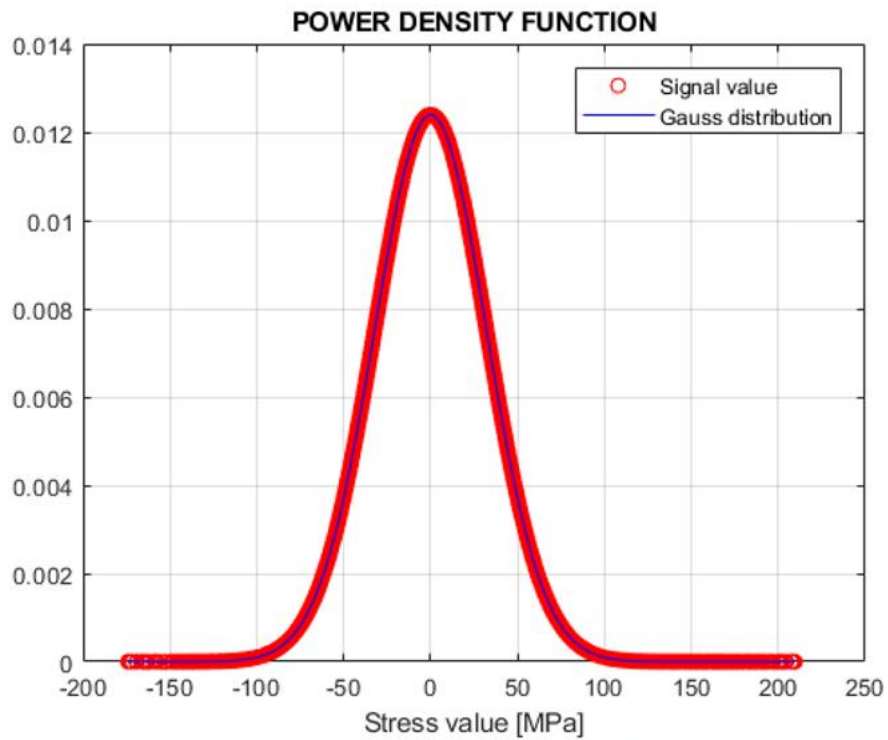


Figure 83: Gauge 6, Load Placement: PDF

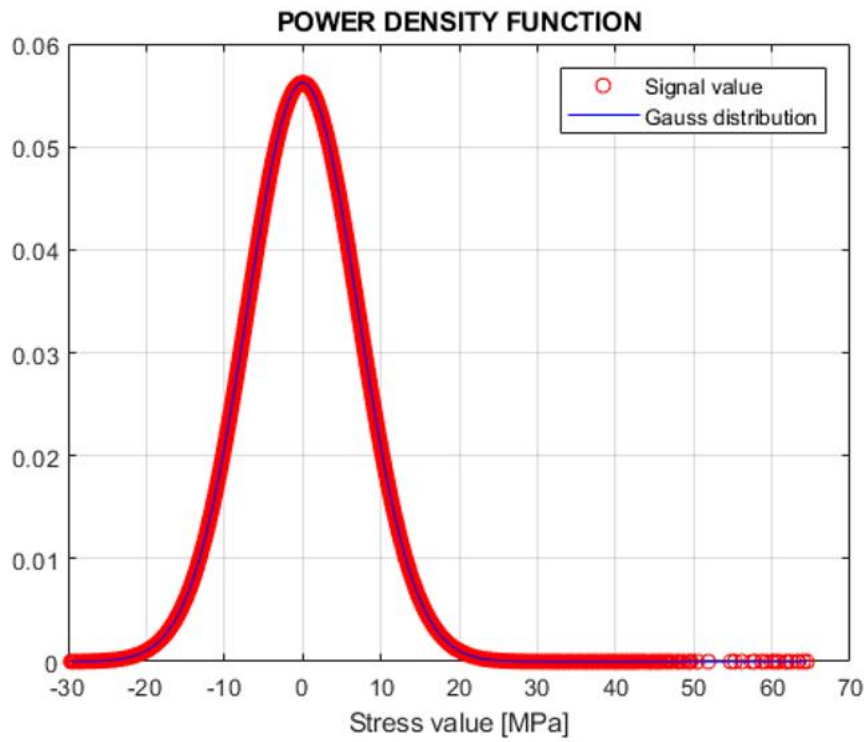


Figure 84: Gauge 4, Loader: PDF

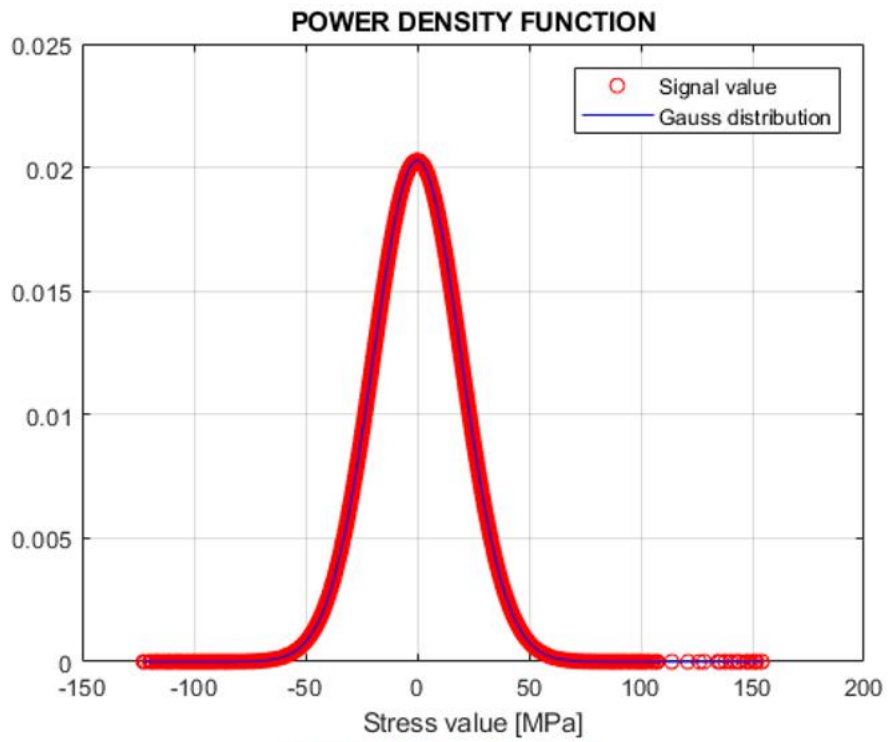


Figure 85: Gauge 6, Loader: PDF

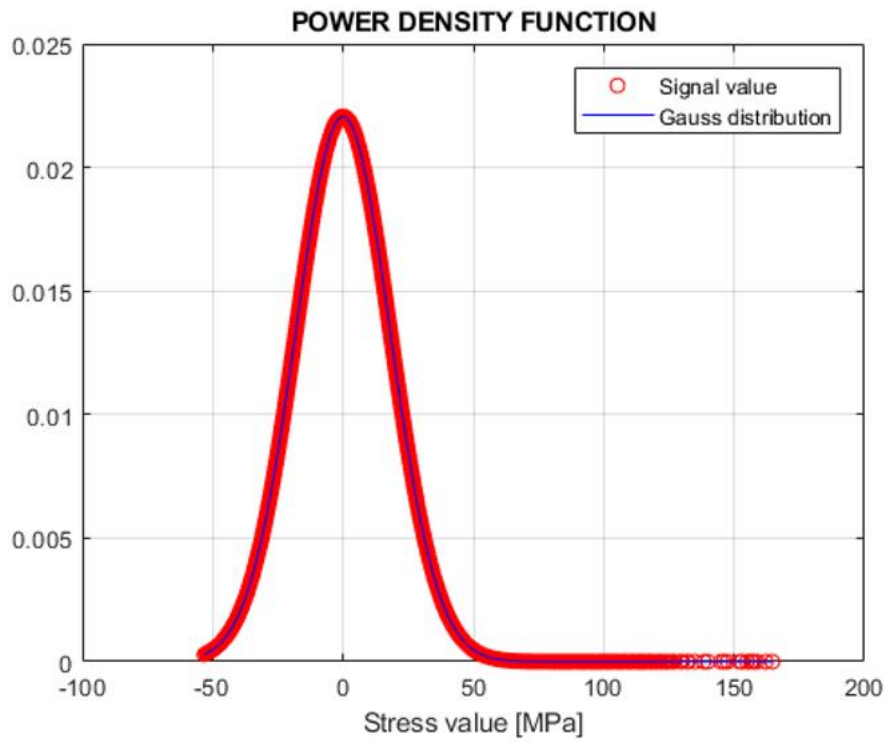


Figure 86: Gauge 4, Offroad: PDF

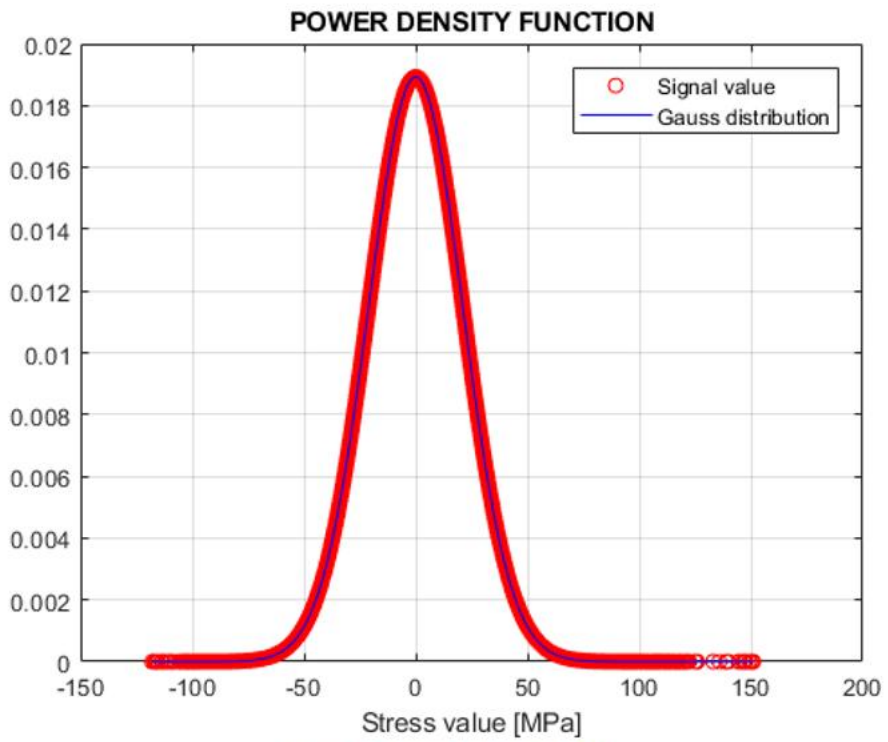


Figure 87: Gauge 6, Offroad: PDF

Assuming that every PDF is a Gaussian one is a strong imposition. However, the most recent frequency criteria suggest to process load history as a Gaussian one and then a corrective coefficient must be calculated.

6.3. Frequency analysis

Once that input signals have been statistically studied, frequency domain analysis can start.

6.3.1. FFT applied on load histories

Let's begin with the Fourier theorem: original time-amplitude signals are now converted in a frequency-amplitude one. Figures from Figure 88 to Figure 95 show the results of Fourier's theorem on data collected by the strain gauges applied as shown in paragraph 2:

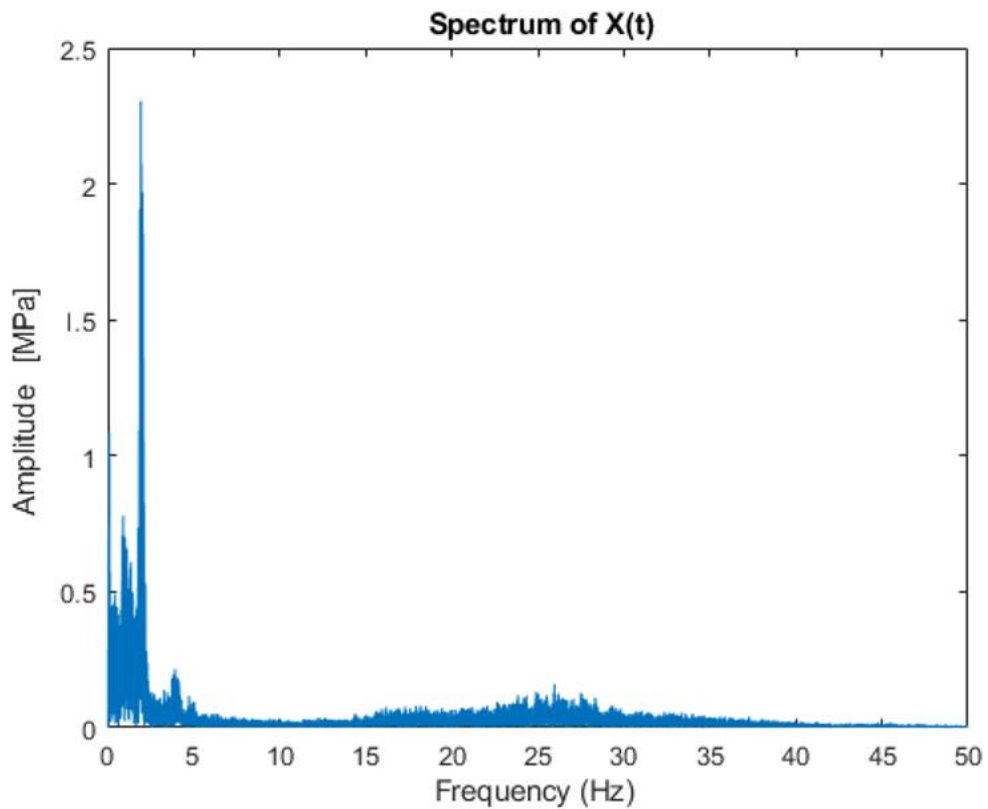


Figure 88: Gauge 4, On road: FFT

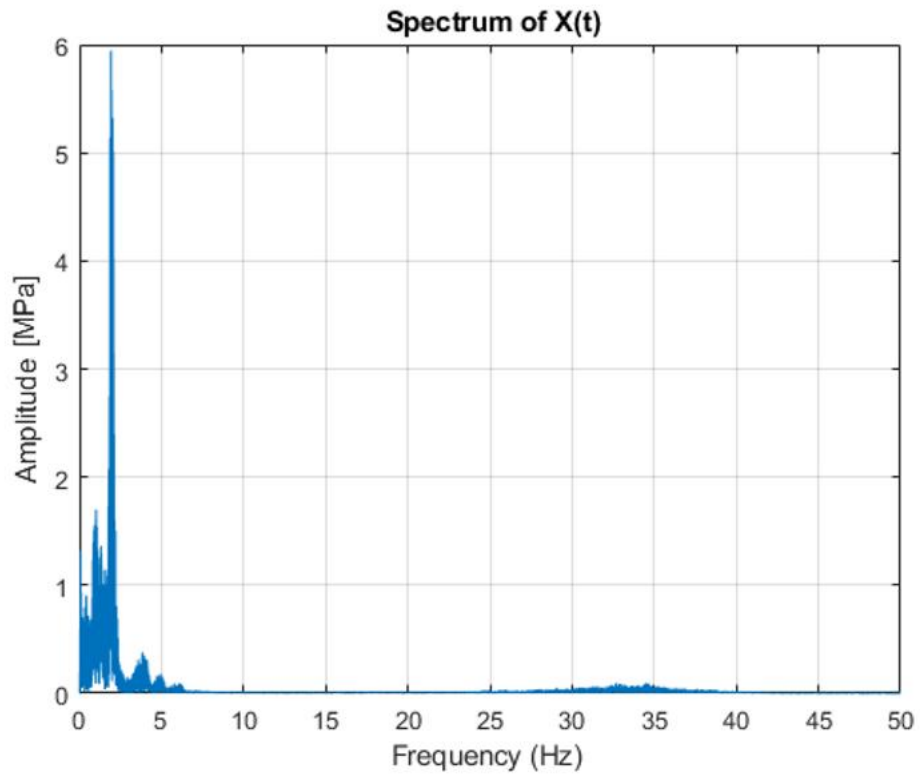


Figure 89: Gauge 6, On road: FFT

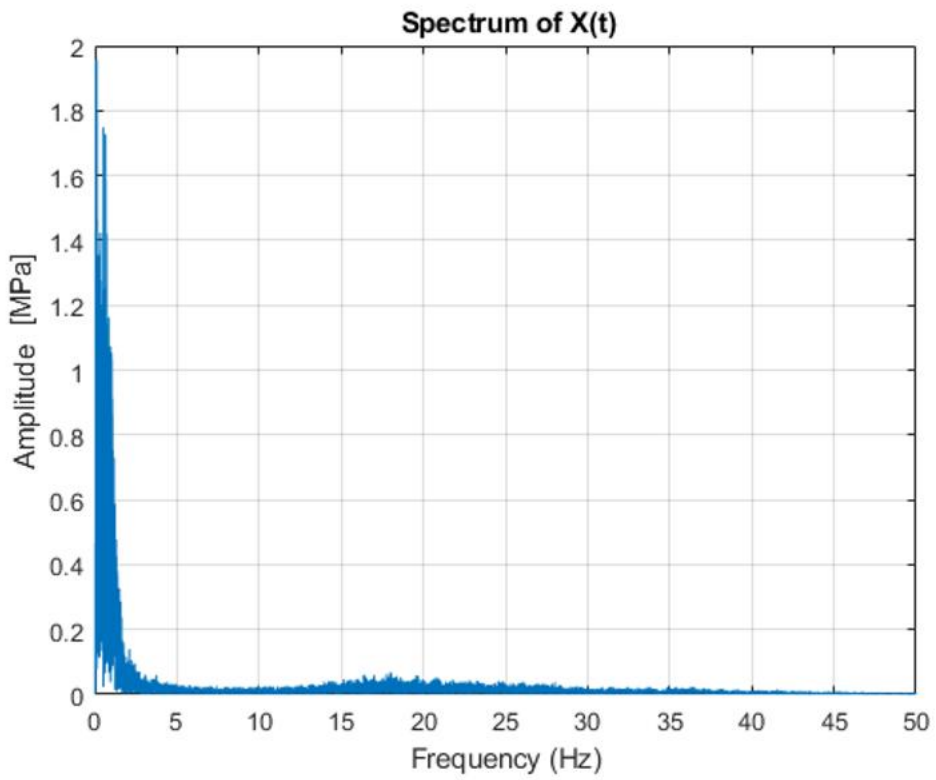


Figure 90: Gauge 4, Load Placement: FFT

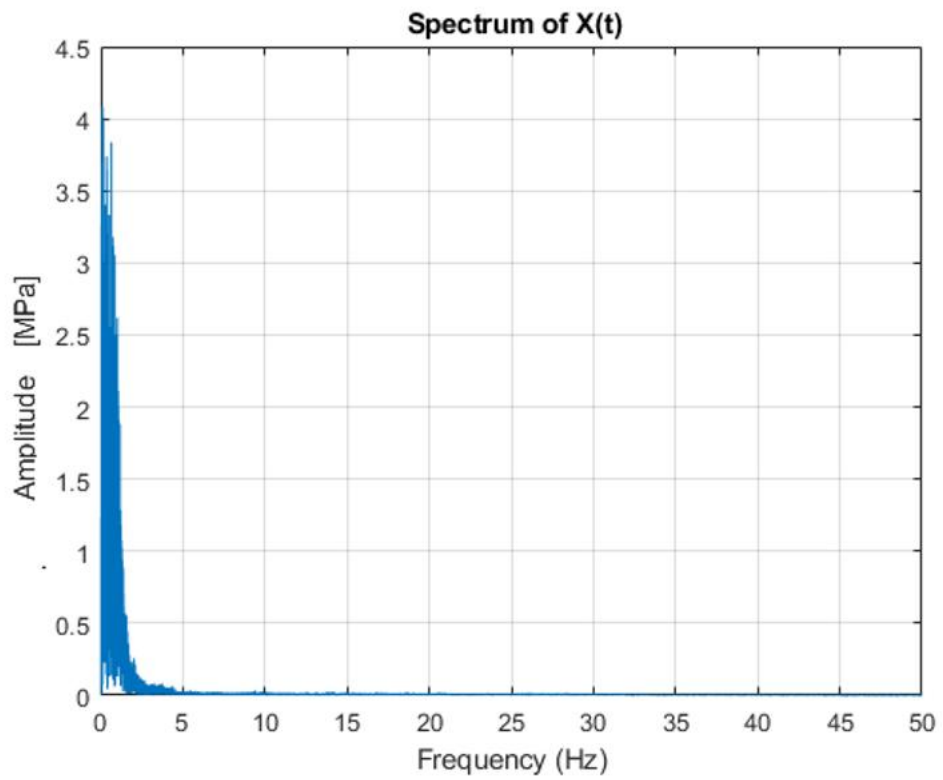


Figure 91: Gauge 6, Load Placement: FFT

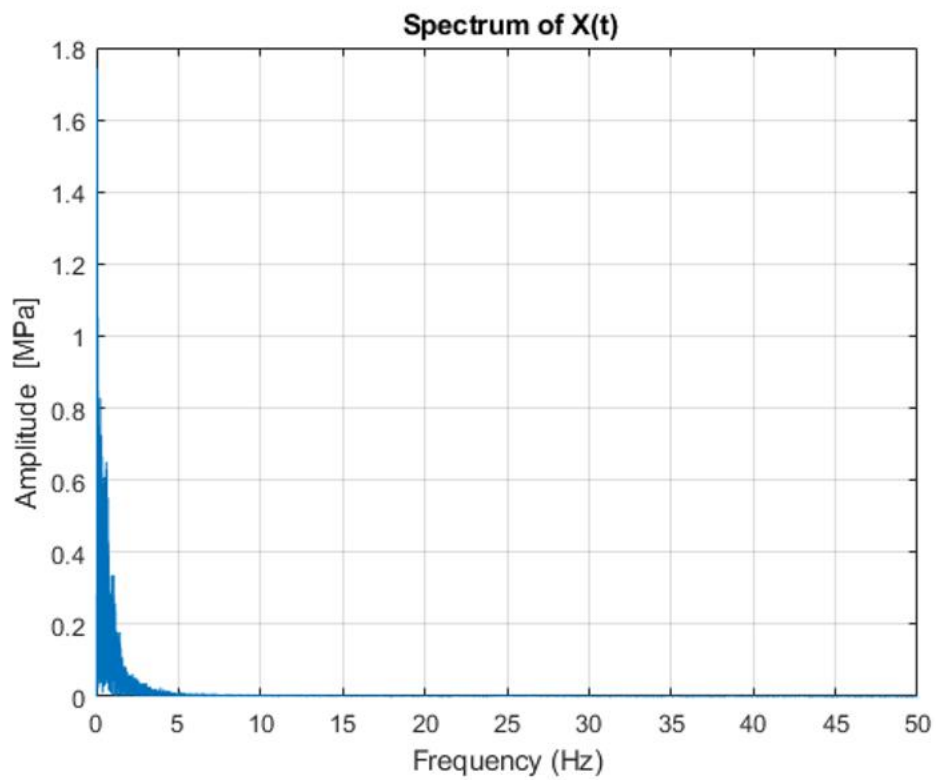


Figure 92: Gauge 4, Loader: FFT

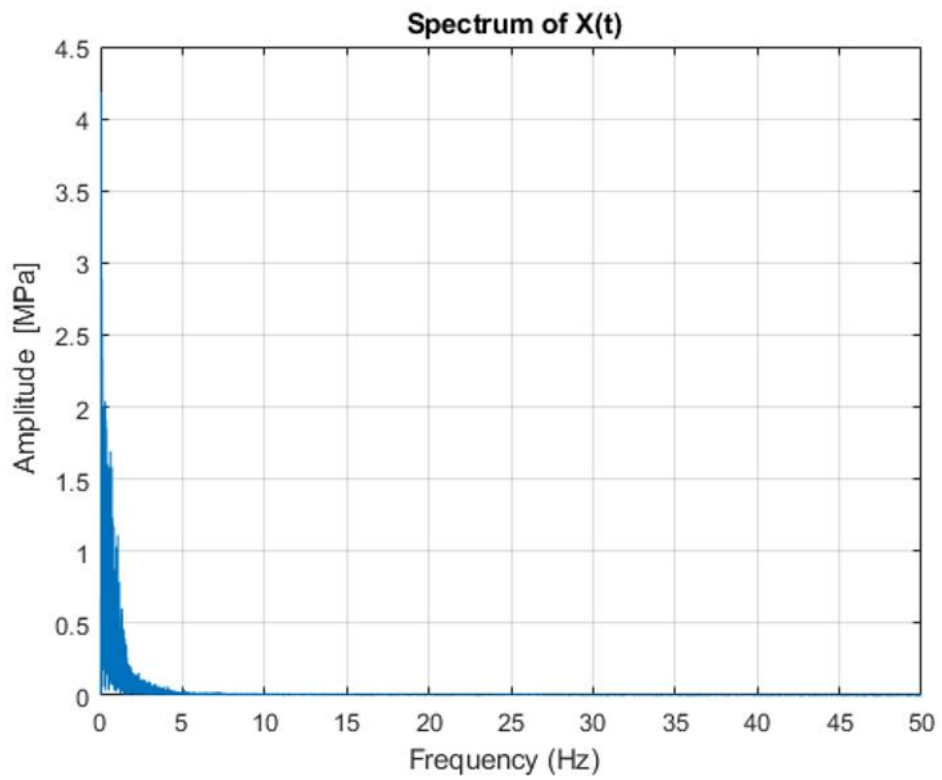


Figure 93: Gauge 6, Loader: FFT

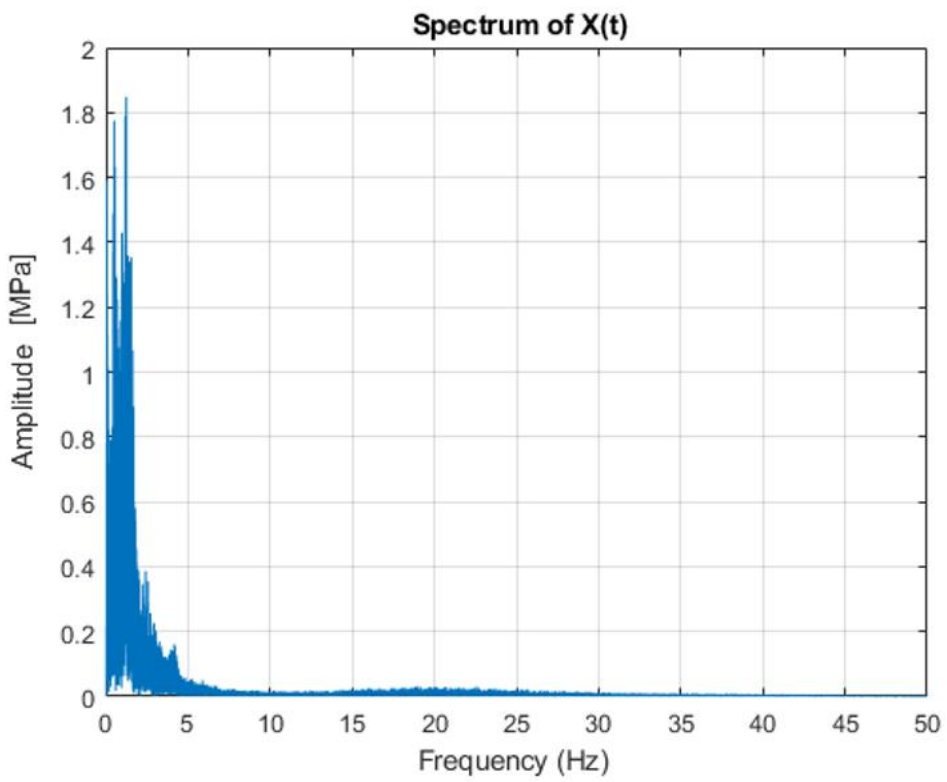


Figure 94: Gauge 4, Offroad: FFT

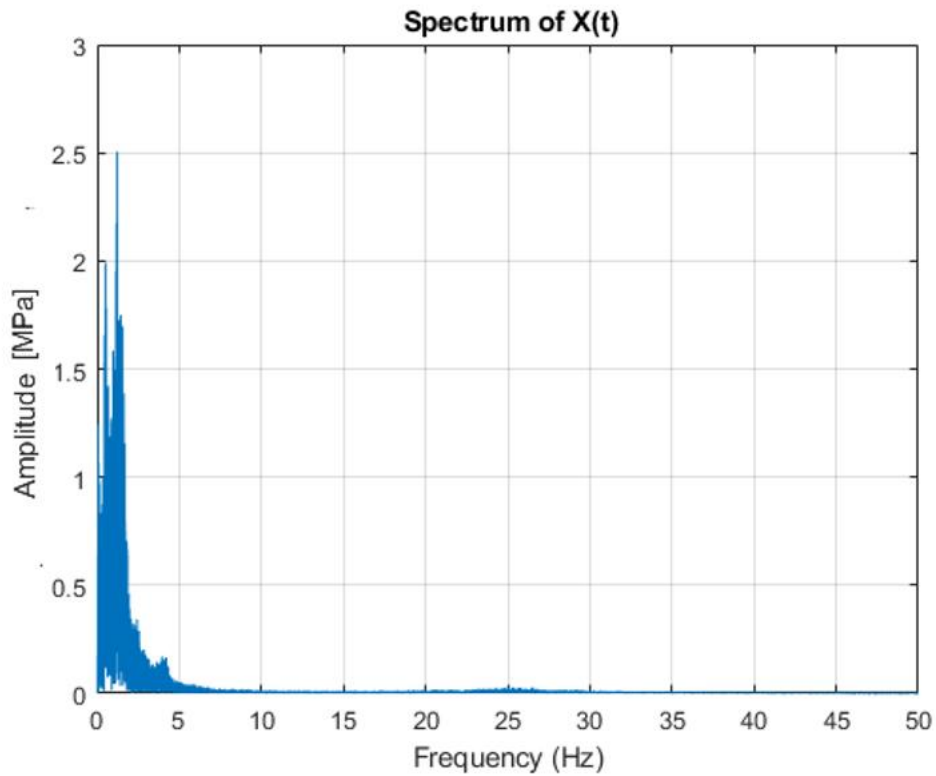


Figure 95: Gauge 6, Off-road: FFT

6.3.2. PSD applied on load histories

It is time now to calculate the PSD functions. This passage is fundamental to understand the power of harmonics that compose the signal. Moreover, the PSD is the starting point in the determination of spectral moments.

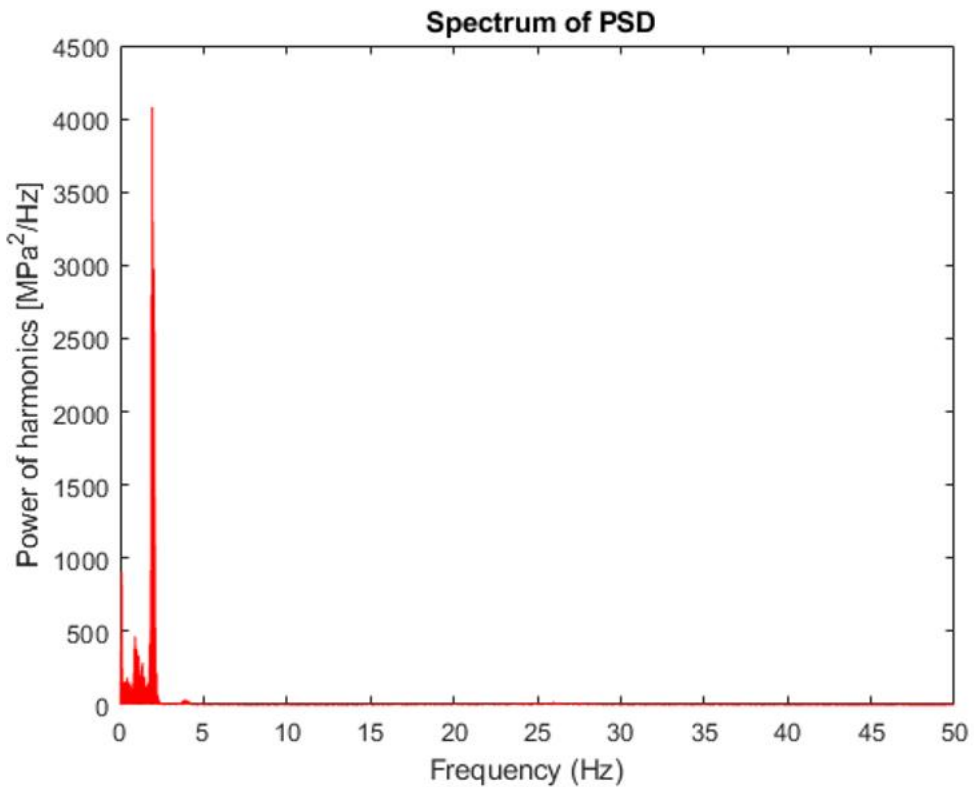


Figure 96: Gauge 4, On road: PSD

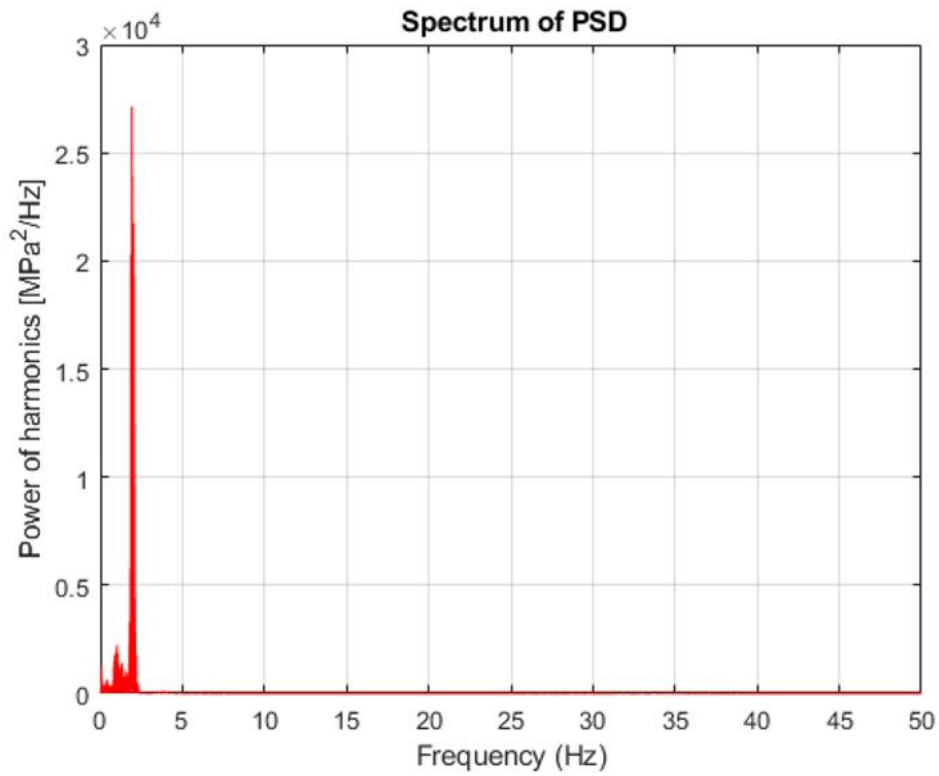


Figure 97: Gauge 4, On road: PSD

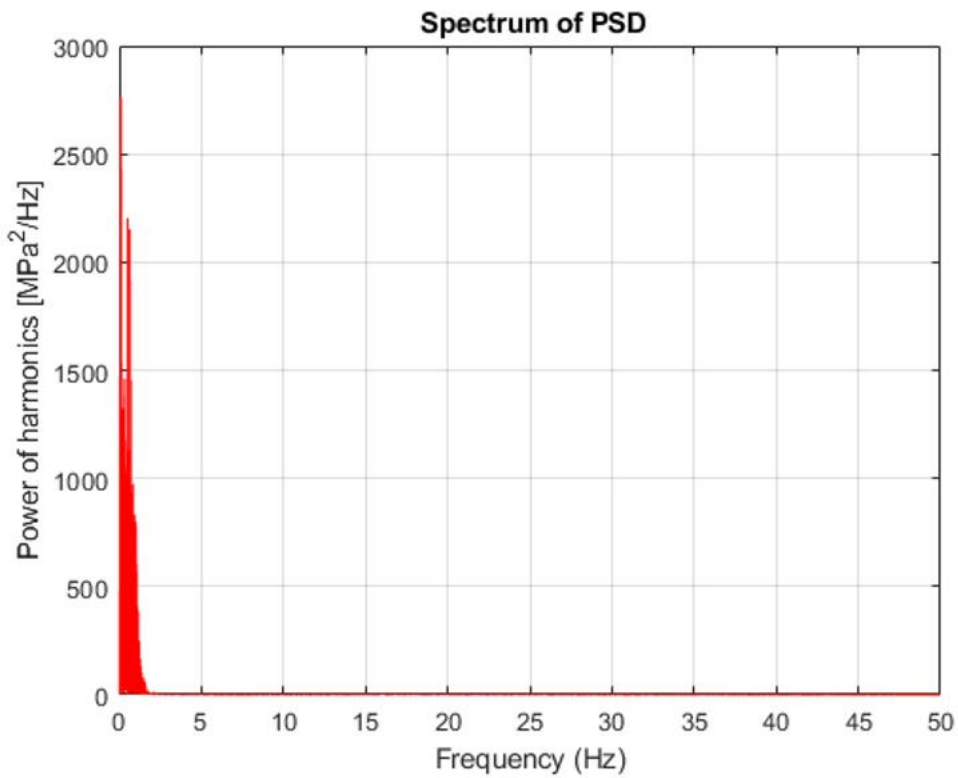


Figure 98: Gauge 4, Load Placement: PSD

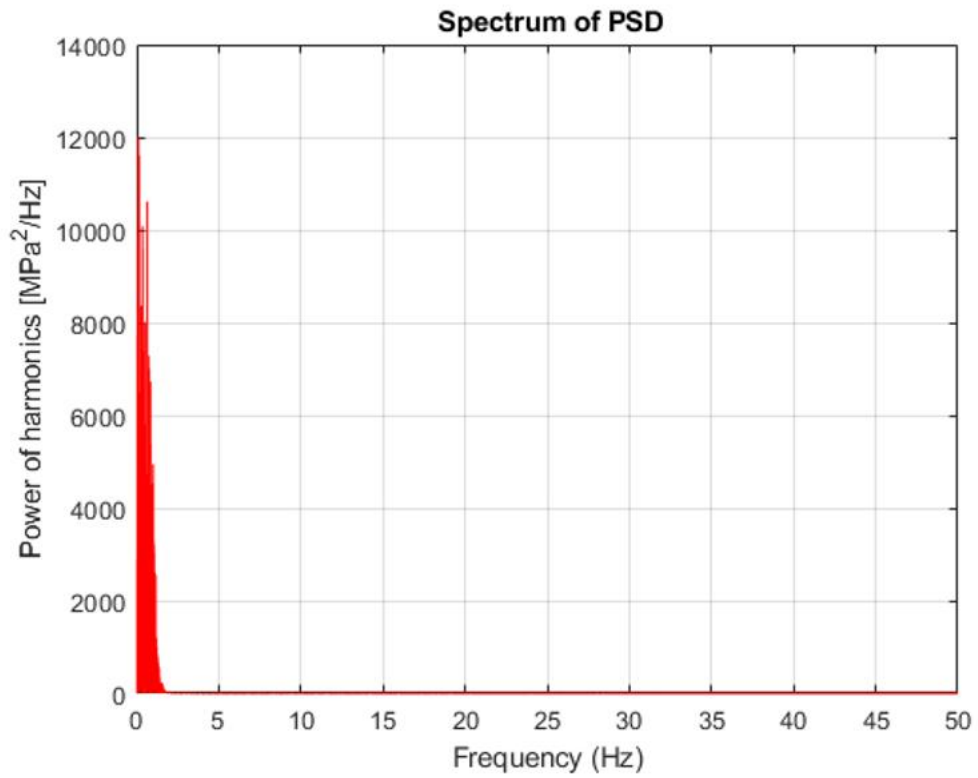


Figure 99: Gauge 6, Load Placement: PSD

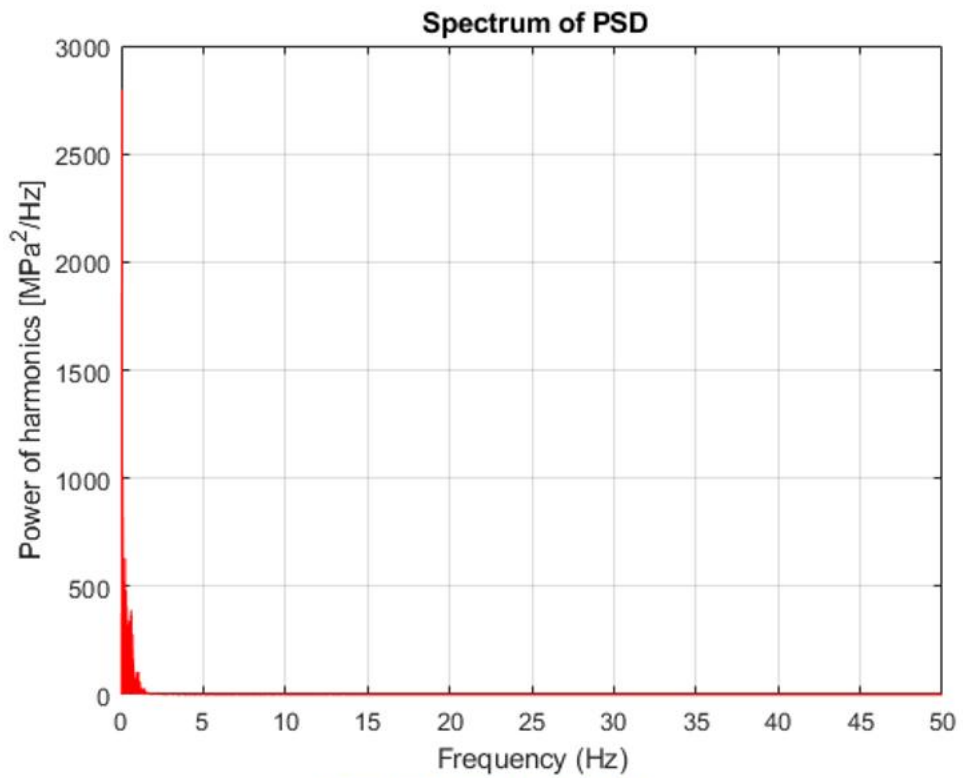


Figure 100: Gauge 4, Loader: PSD

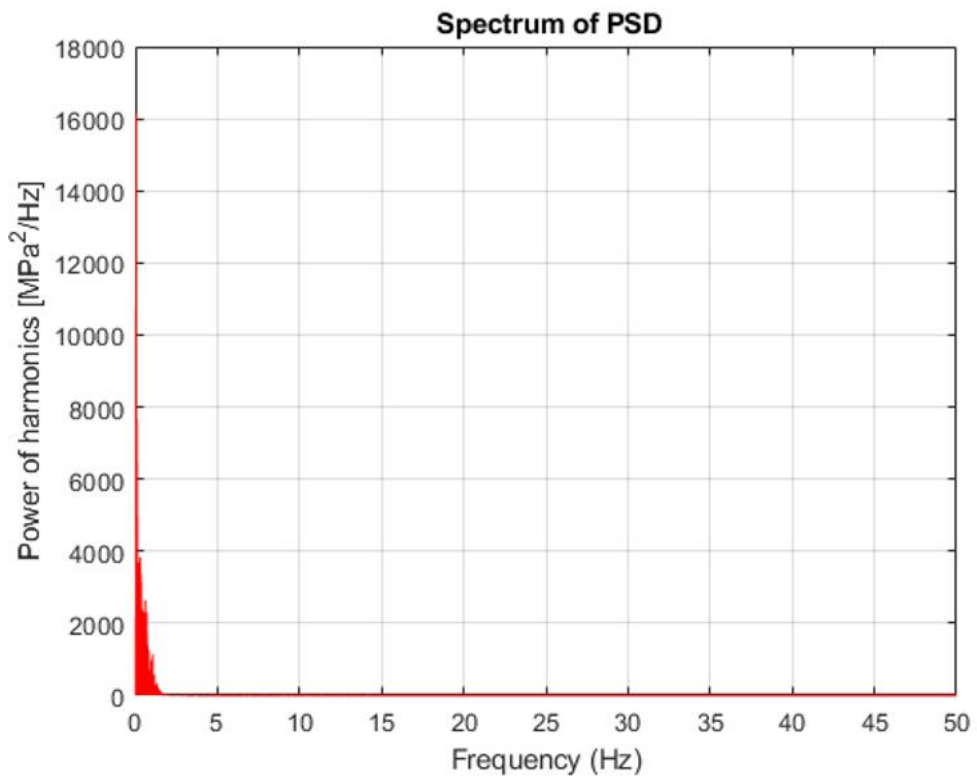


Figure 101: Gauge 6, Loader: PSD

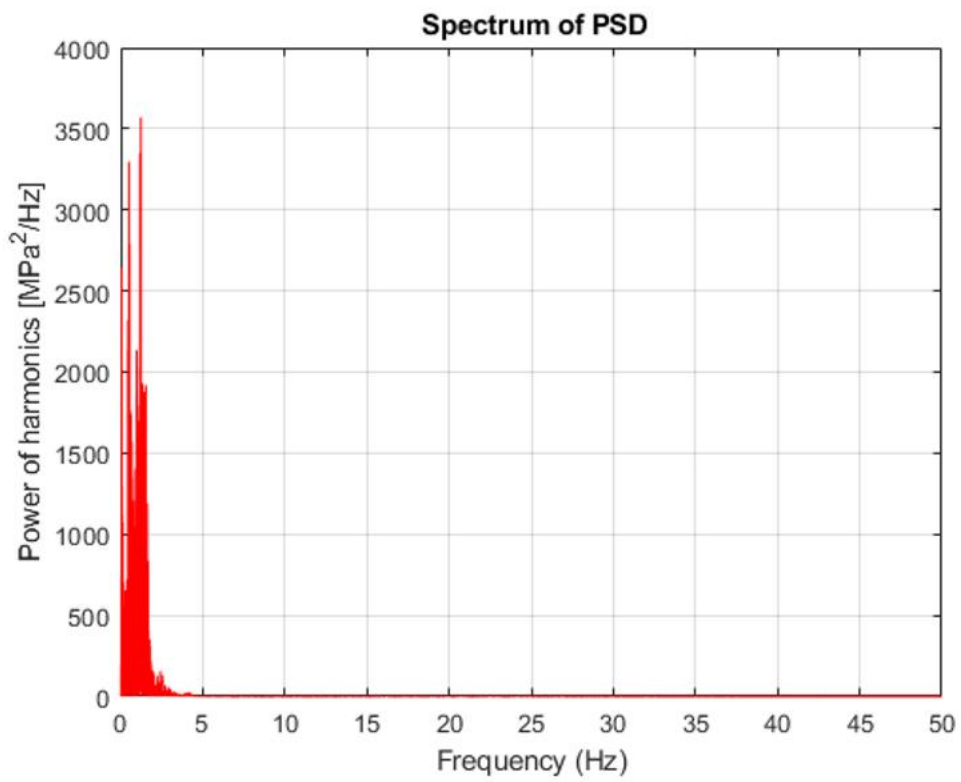


Figure 102: Gauge 4, O_road: PSD

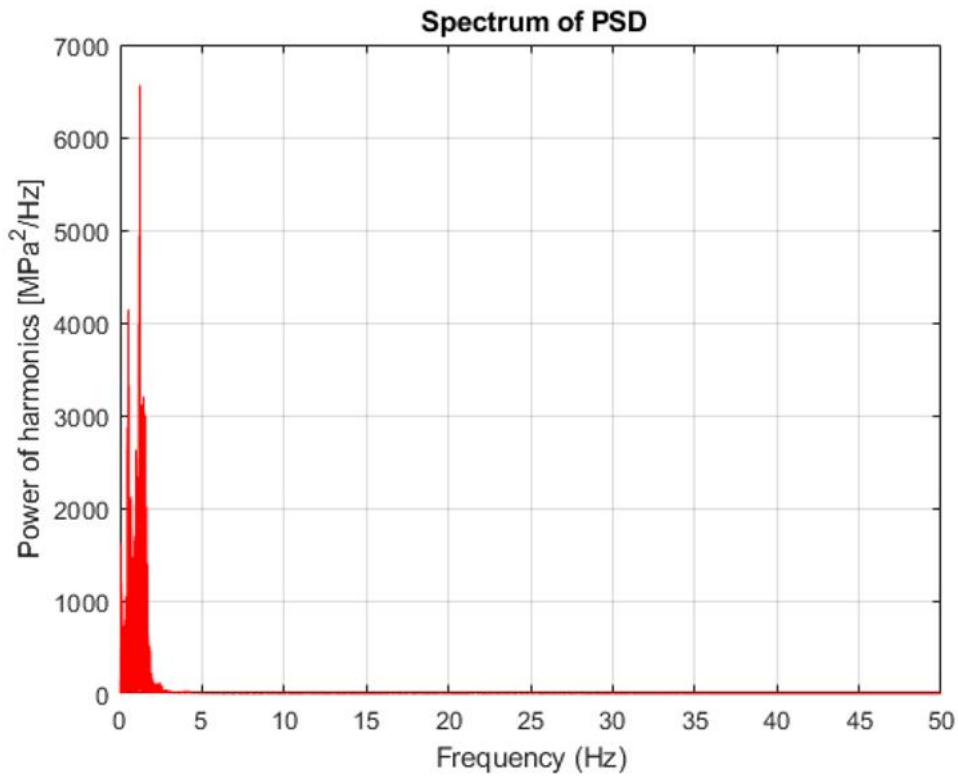


Figure 103: Gauge 6, Offroad: PSD

6.4. Fatigue damage estimation

In this section useful knowledge about ergodic, stochastic and stationary processes will be introduced. Then, damage criteria will be discussed.

6.4.1. Parameters form PSD

In paragraph 5.1.4 it has been discussed why in this work a continuous approach must be chosen: even if the signal is sampled with a discrete number of point, the events that are here modelled are a continuous phenomenon.

Let's consider a stress on a structural element; furthermore, assume that stress can be described by a stochastic, stationary and ergodic process $X(t)$ with zero as mean value.

Additionally, statistical proprieties of $X(t)$ are deduced using only one sufficiently long measurement; that is possible due to the ergodicity of the signal.

In frequency domain, a stochastic process is described by power spectral density (PSD or S_{XX}), defined as the Fourier transform of the autocorrelation function:

$$S_{xx}(\omega) = \frac{1}{2\pi} \int_{-\infty}^{\infty} R_{XX}(\tau) \cdot e^{-i\omega\tau} \cdot d\tau \quad 6-42$$

where ω represents pulsation and:

$$R_{XX} = \lim_{T \rightarrow \infty} \int_0^T X(t) \cdot X(t + \tau) dt \quad 6-43$$

T is the period of signal and t is the time in which signal is observed. Lastly, using Lutes function spectral moments can be calculated as follow:

$$\lambda_m = \int_{-\infty}^{\infty} |\omega|^m \cdot S_{XX}(\omega) d\omega \quad 6-44$$

where m represents the order of that spectral moment. Spectral moments are related to the nature of the signal with this relation:

$$\begin{cases} \lambda_0 = \sigma_X^2 \\ \lambda_2 = \sigma_{\dot{X}}^2 \\ \lambda_4 = \sigma_{\ddot{X}}^2 \end{cases} \quad 6-45$$

In this case, the number of crossing mean value represents also the zero crossing in time unit because it has been supposed $\mu_X = 0$. According to Lutes works, E_0 represents how many times the mean value is crossed in one-time unit and with a positive slope. It can be calculated as follow:

$$E_0 = \frac{1}{2\pi} \sqrt{\frac{\lambda_2}{\lambda_0}} \quad 6-46$$

In a similar way, it is possible to estimate how many maximum values are found in a period of time:

$$E_P = \frac{1}{2\pi} \sqrt{\frac{\lambda_4}{\lambda_2}} \quad 6-47$$

A lot of attention should be paid to the fact that in this paragraph it has been supposed to have an ergodic, continuous, stationary stochastic signal with 0 as mean value. Even if there are a lot of processes that can be described in that way (wind, sea, traffic, ...), there are some that doesn't satisfy that hypothesis.

6.4.2. Narrow band and broad band processes

Sometimes it is necessary to estimate if a process is a narrow band or broad band one.

Shape and geometrical features of PSD function can be used to solve this problem. First of all, a geometrical propriety has to be calculated:

$$\alpha_m = \frac{\lambda_m}{\sqrt{\lambda_0 \cdot \lambda_{2m}}} \quad 6-48$$

Here $m \geq 0$, but the most common value for m is 1 and 2, thus:

$$\begin{aligned} \alpha_1 &= \frac{\lambda_1}{\sqrt{\lambda_0 \cdot \lambda_2}} \\ \alpha_2 &= \frac{\lambda_2}{\sqrt{\lambda_0 \cdot \lambda_4}} \end{aligned} \quad 6-49$$

α_m are non-dimensional numbers, $0 \leq \alpha_m \leq 1$ and $\alpha_m \geq \alpha_{m+1}$. These parameters are useful to show if a process is a narrow band one, because in this case it will be really close to 1. Instead, it will be close to 0 if the process is a broad band one.

6.4.3. Probability density function (PDF)

Once λ and α parameters have been calculated, it can be generated a Gaussian PDF for maximum values in a time unit ($p_p(X)$). Here it will be used Rice's function:

$$p_p(X) = \frac{\sqrt{1 - \alpha_2^2}}{\sqrt{2\pi}\sigma_X} \cdot e^{-\frac{X^2}{2\sigma_X^2(1 - \alpha_2^2)}} + \frac{\alpha_2 X}{\sigma_X^2} \cdot e^{-\frac{X^2}{2\sigma_X^2}} \cdot \phi\left(\frac{\alpha_2 X}{\sigma_X \cdot \sqrt{1 - \alpha_2^2}}\right) \quad 6-50$$

where $\phi(x)$ is the normal standard probability density function that, for a generic stochastic Gaussian process $x(t)$, can be written as:

$$\phi(x) = \frac{2}{\pi} \int_{-\infty}^x e^{-t^2} dt \quad 6-51$$

The cumulative probability to find a maximum in a period of time is given by the following equation:

$$Pp(X) = \phi\left(\frac{X}{\sigma_X \cdot \sqrt{1 - \alpha_2^2}}\right) - \alpha_2 e^{-\frac{X^2}{2\sigma_X^2}} \cdot \phi\left(\frac{\alpha_2 X}{\sigma_X \cdot \sqrt{1 - \alpha_2^2}}\right) \quad 6-52$$

A plot of $p_p(X)$ is shown in Figure 104.

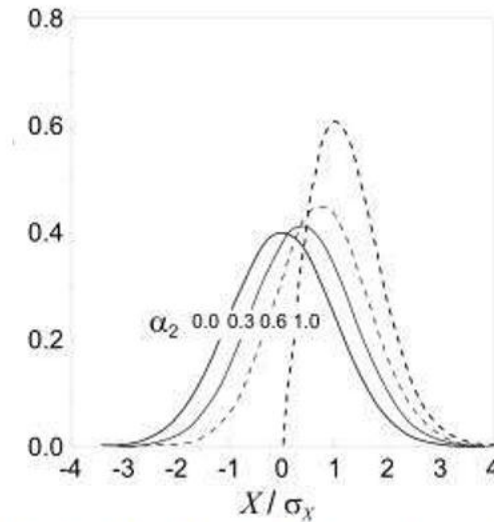


Figure 104: Probability density function about relative maximum $p_p(X)$ when α_2 increases.

For minimum values, it has to be noticed the symmetry between max and min, so $p_v(X) = p_p(-X)$ and:

$$Pv(X) = \phi\left(\frac{X}{\sigma_X \cdot \sqrt{1 - \alpha_2^2}}\right) + \alpha e^{-\frac{X^2}{2\sigma_X^2}} \left[1 - \phi\left(\frac{\alpha_2 X}{\sigma_X \cdot \sqrt{1 - \alpha_2^2}}\right)\right] \quad 6-53$$

According to Lutes' works, for a narrow band process where $\alpha_1 \approx \alpha_2 \approx 1$ the PDF and the cumulative probability are equal to a Rayleigh density function onto a generic stochastic Gaussian process $x(t)$:

$$r(x) = \frac{x}{\sigma_X^2} \cdot e^{-\frac{X^2}{2\sigma_X^2}} \quad 6-54$$

$$R(x) = 1 - e^{-\frac{X^2}{2\sigma_X^2}} \quad 6-55$$

where $x \in \mathbb{R}^+$. Finally, with references to Figure 104, it is important to notice that a narrow band process has only positive maximum values, while a broad band process can have positive and negative maximum values.

6.4.4. Fatigue damage

If the load history has a variable amplitude, it is mandatory to define a method in order to count the right number of cycles. This method, or criterion, has to group and order maximum and minimum value in the history load, creating a sort of new history load describable with packages of cycles. Every package shall include cycles with has the same amplitude s and the same mean value m . If u is the number of relative maximum and v that of the minimum, these two relations can be written as follows:

$$s = \frac{u - v}{2} \quad 6-56$$

$$m = \frac{u + v}{2} \quad 6-57$$

The main problem on estimate the fatigue strength is to define an appropriate PDF function for the $X(t)$ process. In fact, a correct value in fatigue resistance is strictly linked to the PDF chosen.

A good PDF is the combined PDF $h(u; v)$, whose cumulative probability is:

$$H(u, v) = \int_{-\infty}^u \int_{-\infty}^v h(x, y) dx dy \quad 6-58$$

$H(u; v)$ is the probability to have a cycle with a relative max lower than u and a min lower than v . Through a variable change the PDF can be written as a function of s and m :

$$p_{a,m}(s, m) = 2h(m + s, m - s) \quad 6-59$$

In this case the PDF of the cycle amplitude is given by the marginal probability of the power spectrum density (marginal PDF of PSD):

$$p_a(s) = \int_{-\infty}^{+\infty} p_{a,m}(s, m) dm \quad 6-60$$

Once the marginal PSD ($p_a(s)$) is known, the damaging can be calculated invoking Palmgren-Miner's law:

$$E[D] = v_a \cdot C^{-1} \int_0^{\infty} s^k \cdot p_a(s) ds \quad 6-61$$

where $E[D]$ is the probabilistic damage, v_a is the number of cycles in the time unit, k and C are Wöhler's parameters for a S-N curve when the stress is symmetric and alternated (thus, $S \cdot N^k = C$).

The $p_a(s)$ function (i.e. the marginal PDF of PSD) depends on the method used to count cycles in the original history load. Commonly, four different methods could be found in scientific literature:

- Peak Counting (PC);
- Level Crossing Counting (LCC);
- Range Counting (RC);
- Rainflow Counting (RFC).

Rainflow Counting is nowadays the best way to summarize a complex history load. With references to Dowling's works, the previous equation 6–61 can be transformed as follow:

$$E[D_{RFC}] = v_a \cdot C^{-1} \int_0^{\infty} s^k \cdot p_{RFC}(s) ds \quad 6-62$$

6.4.5. Fatigue estimation

Below some spectral verification laws will be presented. Their use is common when fatigue resistance has to be proved for metallic structural components.

6.4.5.1. Narrow Band (NB)

If the process is Narrow-Band-type (i.e $\alpha_1 \approx \alpha_2 \approx 1$) the $p_p(s)$ is Rayleigh like:

$$p_p(s) = \frac{s}{\sigma_s^2} \cdot e^{-\frac{s^2}{2\sigma_s^2}} \quad 6-63$$

$$P_p(s) = 1 - e^{-\frac{s^2}{2\sigma_s^2}} \quad 6-64$$

In this kind of process, the damage is:

$$E[D_{NB}] = E_0 \cdot C^{-1} \cdot (\sqrt{2\lambda_0}) \cdot k \Gamma\left(1 + \frac{k}{2}\right) \quad 6-65$$

where $\Gamma(\cdot)$ is the Euler gamma function: $\Gamma(1 + n) = n!$

If a Broad Band signal is treated as a Narrow Band signal with the NB method, the damage calculated will be equal to a NB signal with variance of λ_0 . NB method usually give a bigger damage if compared to RFC method. Even if this is an error that is in favour of security, it is important to know that the damage calculated is overestimated.

6.4.5.2. Broad Band Approximation

Some authors have proposed to change the NB formula using coefficient that could made the damage more linked to real phenomena, even if the process is a broad band one. the most famous one is the Wrishing-Light method:

$$E[D_{RFC}^{WL}] = \rho_{WL} E[D_{NB}] \quad 6-66$$

ρ_{WL} is the Wrishing-Light coefficient, and it depends only on spectral moments λ_0 , λ_2 and λ_4 by α_2 parameter.

$$\rho_{WL} = a(k) + [1 - a(k)] \cdot (1 - \varepsilon)^{b(k)}$$

$$\varepsilon = \sqrt{1 - \alpha_2^2}$$

6-67

$$a(k) = 0.926 - 0.033 \cdot k$$

$$b(k) = 1.587 \cdot k - 2.323$$

where k is determined from S - N curve: $S^k N = C$.

A good approximation Notice that for a Narrow Band process $\alpha_2 = 1$, so $\varepsilon = 0$ and $\rho_{WL} = 1$, as it was expected if a narrow band phenomenon were treated with NB method.

6.5. Fatigue damage calculation

First of all, spectral moments have to be calculated. Equation 6-44 can be used.

The moment calculation is a common exercise in the probability theory. The spectral moment method has the advantage that the analysis requires only the first-order and the second-order moment calculations of the energy spectra and that the method does not require the knowledge on the power-law behaviour (spectral index) or even a shape of the spectrum.

Basically, the zeroth moment is the area under any spectral curve. The first moment gives a weight to higher frequencies and it is like a centre of gravity/mean value. The second moment gives information about the variance of a frequency if compared to the centre of gravity value. Lastly, the third and the fourth moments give information on skewness (i.e. the asymmetry of the process) and on kurtosis (i.e. how much the process is far from a Gaussian process) of the process.

Moments can be normalized if they are divided by the zeroth moment: if a moment is normalized it is usually written as m_n , otherwise as λ_n .

In this process:

- λ_0 is the zeroth spectral moment;
- λ_1 is the first spectral moment;
- λ_2 is the second spectral moment;
- λ_3 is the third spectral moment;
- λ_4 is the fourth spectral moment.

Using those parameters three useful quantities can be estimated:

- $E_0 = \frac{1}{2\pi} \sqrt{\frac{\lambda_2}{\lambda_0}}$ is the probabilistic number of zero crossing in a period of time;
- $E_p = \frac{1}{2\pi} \sqrt{\frac{\lambda_4}{\lambda_2}}$ is the probabilistic number of peak value in the time unit;
- $IF = \frac{E_0}{E_p}$ is the irregularity factor, that shows how much the process is not regular in the time unit.

	IF	
	GAUGE 4	GAUGE 6
Onroad	0.2296	0.1096
Loadplacement	0.0996	0.0521
Loader	0.0411	0.0426
Onroad	0.0883	0.0925

Table 6 Irregularity factors

One of the hypotheses in Narrow-Band method is that to have an IF approximately next to 1. IFs are really far from a unit value (as shown in Table 7, but a Narrow Band calculation will still be made.

Let's remember some useful material data which comes from Basquin's law:

- $C=4.0657 \cdot 10^{21}$;
- $k=6.4935$.

Both terms comes from the linear part of the Wöhler's diagram ($S^k N = C$).

According to equation 6–65, that is the one for the Narrow Band damage, it is possible to calculate the damage.

	NARROW BAND			
	GAUGE 4		GAUGE 6	
	N	D [%]	N	D [%]
Onroad	2.55E+11	3.92E-12	1.84E+09	5.43E-10
Loadplacement	6.78E+11	1.48E-12	7.39E+09	1.35E-10
Loader	1.40E+14	7.16E-15	1.88E+11	5.42E-12
Onroad	1.43E+11	6.97E-12	5.99E+10	1.67E-11

Table 7 NB results

Remembering this is a too safe way to estimate a non-Narrow band damage, let's correct this value using Wrishing-Light coefficient, that is equal to:

$$\rho_{WL} = a(k) + [1 - a(k)] \cdot (1 - \varepsilon)^{b(k)}$$

6–68

	WRISHING-LIGHT			
	GAUGE 4		GAUGE 6	
	N	D [%]	N	D [%]
Onroad	3.42E+11	2.93E-12	2.23E+09	4.48E-10
Loadplacement	8.10E+11	1.23E-12	8.21E+09	1.22E-10
Loader	1.52E+14	6.57E-15	2.01E+11	4.96E-12
Onroad	1.69E+11	5.92E-12	7.09E+10	1.41E-11

Table 8 WL results

6.6. Two new approaches

6.6.1. Ortiz method

Like Wrishing-Light method, Ortiz studied a coefficient that could correct NB results.

First of all, he considered Wöhler's parameters (S NK = C) and he defined h = 2 k. Then it must be calculated:

$$\zeta_0 = \sqrt{\frac{\lambda_2 \cdot \lambda_h}{\lambda_0 \cdot \lambda_{h+1}}} \quad 6-69$$

That is the coefficient used to correct NB damage. Thus, $D_0 = \zeta_0 D_{NB}$:

	WRISHING-LIGHT			
	GAUGE 4		GAUGE 6	
	N	D [%]	N	D [%]
Onroad	3.76E+11	2.66E-12	2.41E+09	4.15E-10
Loadplacement	1.22E+12	8.16E-13	1.01E+10	9.88E-11
Loader	2.20E+14	4.56E-15	2.84E+11	3.52E-12
Onroad	2.01E+11	4.99E-12	7.72E+10	1.29E-11

Table 9 WL results

6.6.2. Dirlik method

In 1985 Dirlik tried to build a new approach to fatigue frequency analysis. He succeeded in approximating the pRFC(s) (i.e. the PSD of the amplitude of the considered cycles) using an exponential PDF and two Rayleigh PDF. His method is explained with the formulas:

$$\rho_{RFC}^{DK}(s) = \frac{1}{\sqrt{\lambda_0}} \left[\frac{D_1}{Q} \cdot e^{-\frac{z}{Q}} + \frac{D_2 Z}{R^2} e^{-\frac{z^2}{2R^2}} + D_3 Z \cdot e^{-\frac{z^2}{2}} \right] \quad 6-70$$

$$Z = \frac{s}{\sqrt{\lambda_0}} \quad 6-71$$

$$x_m = \frac{\lambda_1}{\lambda_0} \sqrt{\frac{\lambda_2}{\lambda_4}} \quad 6-72$$

$$D_1 = \frac{2 \cdot (x_m - \alpha_2^2)}{1 + \alpha_2^2} \quad 6-73$$

$$D_2 = \frac{1 - \alpha_2^2 - D_1 + D_1^2}{1 - R} \quad 6-74$$

$$D_3 = 1 - D_1 - D_2 \quad 6-75$$

$$R = \frac{\alpha_2 - x_m - D_1^2}{1 - \alpha_2 - D_1 + D_1^2} \quad 6-76$$

$$Q = \frac{1.25 \cdot (\alpha_2^2 - D_3 - D_2 \cdot R)}{D_1} \quad 6-77$$

This model gives a $p_{RFC}(s)$ that depends on four spectral moments; in fact, and it is a difference with Wrishing-Light method, now σ_1 comes into formulas too. Invoking equation 6.36, that it has already been used to obtain damages from $p_{RFC}(s)$, Dirlik damage can be estimated (see equation 6–79).

$$E[D_{RFC}] = v_a \cdot C^{-1} \cdot \int_0^{\infty} s^k \cdot p_{RFC}(s) ds \quad 6-78$$

$$E[D_{RFC}^{DK}] = \frac{v_p}{C} \cdot \lambda_0^{k/2} \cdot \left[D_1 \cdot Q^k \cdot \Gamma(1+k) + (\sqrt{2})^k \cdot \Gamma\left(1 + \frac{k}{2}\right) \cdot (D_2 |R|^k + D_3) \right] \quad 6-79$$

Many studies show that Dirlik method is the best one to calculate fatigue damage. However, even if Dirlik method is the best one, it only works for Gaussian-defined processes.

	DIRLIK			
	GAUGE 4		GAUGE 6	
	N	D [%]	N	D [%]
Onroad	1.08E+21	9.27E-22	1.06E+21	9.39E-22
Loadplacement	9.75E+20	1.03E-21	1.62E+21	6.19E-22
Loader	1.09E+21	9.15E-22	1.31E+21	7.65E-22
Onroad	1.29E+21	7.75E-22	1.38E+21	7.25E-22

Table 10 Dirlik results

6.7. Notes about the use of windows

Several times during this work windows have been named; furthermore, it has been given a deep explanation about their usefulness and the dangers that may derive from an imprudent use. Now is the time to analyse the real signal to see if the effects of a window are really so advantageous or not. First of all, it has to be checked if there is a high quantity of asynchronous harmonics. Recalling that an asynchronous harmonic generates a dispersion of energy around the peak of the FFT and also remembering that the faster the sampling, the less the asynchronous harmonics have effect, it can be deduced that the effect of asynchronous part of the signal can reasonably be neglected.

However, windows can be used in those cases where it is not possible to process all the loading history. This danger is also avoided, since although Excel and Mathcad fail, Matlab is sufficiently performing to handle all the data collected with the strain gauge. [17,18]

7. EXP. AND ANALYTICAL STUDY OF FATIGUE, IN T AND F. DOMANI (PAPER)

EXPERIMENTAL AND ANALYTICAL STUDY OF RANDOM FATIGUE, IN TIME AND
FREQUENCIES DOMAIN, ON AN INDUSTRIAL WHEEL

M. CIMA, L.SOLAZZI (*)

(*)Brescia University (Università degli Studi di Brescia), Department of Industrial and Mechanical Engineering, via Branze 38, 25123 Brescia, Italy.

ABSTRACT

Industrial wheels are components subject to fatigue under a high number of stress cycles, depending on the type of vehicle they are installed to.

The reliability of these components is strictly dependent on the accuracy of the fatigue validation method adopted.

A common practice in the industry is to test loads under constant amplitude in laboratory through fatigue and test parameters according to the standards used in the industry.

The object of this research is to compare the results in terms of damage and the number of failure cycles, adopting both the time domain and frequency domain approach on a real industrial component.

Different theories were developed and applied to the real case of study of an industrial wheel, under specific load cases. Eventually, we applied different criteria to the numerical analysis.

The added value of this study is the application of the fatigue criteria on a real industrial component, in order to check the reliability of the criteria.

Eventually, we determined that the results show that, for these specific experimental load conditions, frequency-domain methods are a bit more conservative than time-domain methods.

KEYWORDS: random fatigue, industrial wheel, stress cycle, material characterization, stress acquisition, damage counting, experimental analysis, fatigue life assessment.

NOMENCLATURE:

S'_f : real stress at break for Manson – Coffin law [MPa];
 $S_{a,d}$ is the alternate component of the stress [MPa];
 ε'_f (E'_f): real strain at break for Manson – Coffin law;
 μ : Mean of the data distribution;
 a_s : factor for ζ_w function of the slope of Wöhler curve;
 b : is the slope of the regression line of the elastic component for Manson – Coffin law;
 b_s : factor for ζ_w function of the slope of Wohler curve;
 c : is the slope of the regression line of the plastic component for Manson – Coffin law;
CH: channel;
D: fatigue damage [Hz];
 D_{Dirlik} : damage computed with Dirlik Method;
 D_{NB} : damage computed with Narrow Band Method;
 D_{Ortiz} : damage computed with Ortiz Method;
 D_{WB} : damage computed with Wide Band Method;
E(0): number of zero crossing of load history computed in freq. domain;
E(P): number of peaks of load history computed in freq. domain;
E[0]: total number of zero crossing;
E[P]: total number of peaks;
 f : frequency;
FEA: finite element analysis;
FEM: finite element method;
 f_i : probability to find a cycle with amplitude of σ_a ;
 f_{sa} : probability density function of stress amplitude;
IF(λ): ratio from number of zero crossing & number of peaks;
K: experimental parameter for Ramberg – Osgood law [MPa]
 k : is the index that counts the cycles of load history;
 K_f : fatigue concentration factor;
 m : slope of Wöhler curve;
 M_i : spectra moments;
 m_n : spectra momentum computed on n order (M_n);
 n : experimental parameter for Ramberg – Osgood law [MPa];
 N_{E1} : number of cycles after failure;
 n_i : number of cycles at a certain amplitude;
PDF: probability density function;
PSD: power spectral density;
S(f): is the value of the PSD at the frequency f [Hz];
sps: sample per second;
UTS: ultimate tensile strength;
 Γ : gamma function;
 ζ : corrective factor for wide band method;
 ζ_o : corrective factor for Ortiz method;
 ζ_w : corrective factor for Wirsching-Light method;
 η_D : ratio from damage computed and reference damage;
 η_{N1} : ratio from number of cycles at break computed and reference numbers of cycles.
 λ : irregularity factor;
 σ : Variance;
 t : time lapse τ ;

1 INTRODUCTION

Wheels are a critical component in industrial vehicles, as far as safety is concerned. The load conditions they are subject to differ depending on the use of the vehicle. [1]

Some variables to take into consideration are the speed, the maximum load acting on the wheel and the route (curves, straights, jolts, etc.) While examining wheels for industrial vehicles, some variables need to be taken into consideration, as they are induced by the operating modes of the use of the vehicle (e.g. in the wheel loader.) [2, 3].

A new and progressive trend is to build lighter machines (by using non-conventional materials like composite materials) not only for the wheel [5, 6] but for the whole machine (e.g. trucks [7, 8], earthmoving machines [9] or working platforms [10, 11].)

The aim of this trend is to improve the performance of the wheels, from an economic and technical points of view.

Consequently, the standard tests used in the classic industry may not be able to completely cover the variability of the load conditions to which the wheel itself is subject during its useful life.

In fact, wheels for agricultural, construction or material-handling vehicles normally carry heavy loads, which might be distributed in an uneven way, and operate on an uneven ground. Each wheel revolution can be identified as a complete stress cycle: indeed each wheel is subject to many millions of stress cycles during its lifetime.

However, the size of the wheel can differ from 8" (203 mm) to 54" (1'371 mm) in diameter and from 3" to 36" in width with a nominal wheel load between 4'000 N and 250'000 N.

Rims and discs are manufactured from hot rolled steel, in particular structural steels like S235, S275 or S355 (UNI EN 10025) or high strength steel HSLA (UNI EN 10268, UNI EN 10149, etc.) and then cold formed and welded together. Hot rolled profiles are instead used for multi-piece wheels.

Wheels can be subject to several load conditions. In this research, we analysed four different load cases, as a representation of the entire life of a wheel.

To make sure that the wheel can endure these loading conditions (e.g., adequate safety factor) we need to apply a design validation method, able to verify the fatigue resistance in the rim and disc area.

The most common approach in the industry of industrial wheel is to use numerical analysis, tests on the field and fatigue tests in laboratory as validation methods for the design of a wheel. It is possible to apply two different methods to define the parameter for specific wheels [12, 13]:

- through empirical load calculations registered on the field under different working conditions;
- by analysing test results of wheels being used in the field for years and using these results to set a minimum test life expectation.

Therefore, it is fundamental for fatigue tests in laboratory to be directly linked to the stress history on the field. In this way, it would be possible to minimize the ones without a fully adequate fatigue life on the field or wheels over conservative in their design, with higher costs and lower dynamic efficiency for the vehicle.

An experimental approach becomes increasingly important in order to achieve a more reliable component and to optimize a series of experimental tests that provide the real use conditions of the vehicle. [14]

With no doubts, this approach helps the designer; without it, it would not be possible to improve the properties of the material used. For example, we could use the shot peening, but the real load conditions acting on the wheel are not clear.

In addition, on some machines (e.g. container-handling machines,) the loads per wheel are so high that it could become extremely difficult to perform an accelerated fatigue test in laboratory due to the limitation of the test equipment.

For this reason, a new design and validation approach was developed, based on the flow chart reported in Figure 1.

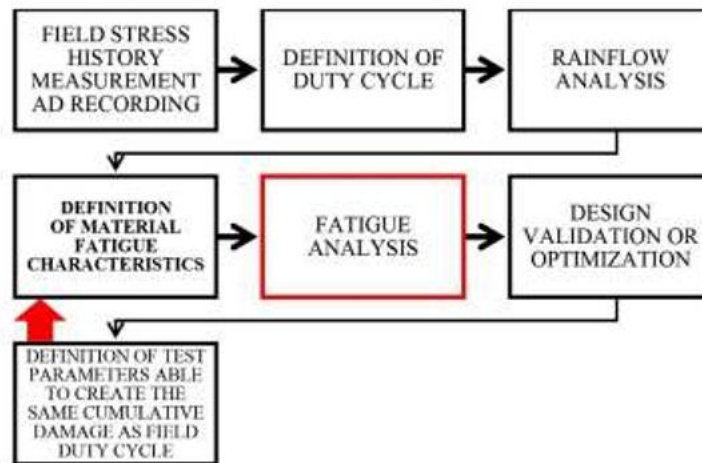


Figure 1 Flow chart of the process of designing a wheel.

The object of this publication is the fatigue analysis; we have both considered the experimental data applied and compared them with different fatigue damage theories in time domain and frequency domain.

Our aim is to obtain an instrument for designers to choose the best theory while designing industrial wheels. This would be a means to increase the reliability of the wheel itself.

In addition, we would like to extend this study and thus its results in a general application in the random fatigue field.

2 WHEEL GEOMETRY AND LOAD CONDITIONS

Figure 2 shows the main size of the wheel studied; this kind of wheels are commonly used for telescopic lifters.

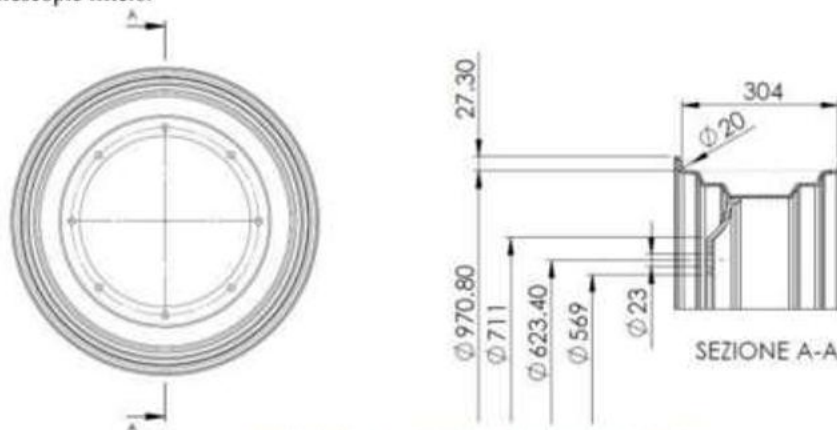


Figure 2 Main measurements of the wheel studied [mm]

The wheel is composed of three different elements made of structural steel S355 UNI 10025 (Figure 3) and placed on a loader or excavator. Figure 4 shows the loader (Manitou MT 1840) used for the experimental tests.

The main parameters of this machine are: weight unladen: 116'300 N; rated load on forks: 40'000 N; weight on front axle (unladen): 54'800 N; weight on front axle (rated load on forks): 129'300 N; tyres used: Michelin POWER CL 440/80 – 24" 168 A8 and tyre pressure used for the test: 4,5 bar.

The main parameters of this machine are: weight unladen about 115'000 N; rated load on forks: 40'000 N; weight on front axle (unladen) about 55'000 N; weight on front axle (rated load on forks) about 130'000 N; tyres used: Michelin POWER CL 440/80 – 24" 168 A8 and tyre pressure used for the test: 4,5 bar.



Figure 3 Main measures [mm] of the wheel (sectioned view):
1) Rim base 2) Ring



Figure 4 Loader used for the experimental test.

For this research, we chose four different load cases. Together with the manufacturer of the machine, we defined a test sequence in order to simulate all the different load cases foreseen for this specific machine.

We chose four load cases, for they represent the life cycle of the wheel. Moreover, the load history comes directly from the know-how of the manufacturer and his internal standards.

In particular, the load cases analysed are:

1. Movement on paved road (**On-road case.**) The loader moves on a paved and straight road in a specific oval circuit, with test-instrumented wheels placed on the inner and outer radius. The test was performed with the machine unladen.
2. Loading and unloading (**Load placement case.**) The loader was subject to a 20'000 N load placed on the fork at different heights.
3. Heavy load and unloading (**Loader case.**) The load condition is the same as the previous case but 4 tons were placed on the fork.
4. Movement on a dirty road (**Off-road case:**) In this condition the truck moves on a dirty street (with bumps), with curves and slaloms, with 15'000 N placed on the fork.

It is important to note that each test was repeated three times. The results are useful both for the damage and for the PSD.

3 MEASURING INSTRUMENTS

The first step in the design and validation process of a wheel for a specific application is the identification of the significant areas where fatigue failure could happen.

This identification comes both from the experience of previous fatigue failures in lab tests or on the field and by means of the Finite Element Analysis (with linear and nonlinear schematization of material and bolts connection.)

The FEM model is realized by brick elements at quadratic order. More details from the report of the software are: number of nodes=303'643, number of elements= 153'669, number of DOF= 903'369. The size mesh adopted was chosen after different repetitions, in order to obtain a converging solution not dependent on the dimension. In particular, we can report the maximum stress in the hole, which measures 23mm, (as shown in the figure below;) the length of one side of the element is 1 mm. The bolt is the beam element, with an axial force of 190 kN that equals a closing torque of 650 kN (using a torque wrench.) The position of the strain gauges is slightly offset from the edge of the hole. The numerical values in that zone are not particularly affected by the bolt schematization because of the presence of a very rigid flange to which the bolts are fixed.

The analysis was carried on assuming linear features of the material. The following image shows the results of a FEM analysis performed on the wheel; the analysis shows in details that the stress in the configuration with a vertical force equal to 50'000 N and a tyre pressure equal to 0.45 MPa. This group of forces acts as the ordinary use of the component.

Once the significant areas have been identified, strain gauges are applied on each wheel. Figure 5a shows the main results of FEM analyses. Figure 5b shows the strain gauges applied to the wheel in a number of 20 (Figure 6.) The centre of the grid is almost 25 mm far from the centre of the hole. The diameter of the washer is ca. 45 mm.

Both uniaxial and biaxial strain gauges were used for the rim; the grid size is 3 mm and the resistance is 350 Ω . Strain gauges signals were acquired at 1'000 sps in order to get all fundamental technical information and relevant data. The transition from strain and strain gauges is made by the equation of continuum mechanics. This allows, for example, to define the main stress (with strain rosette). This translation was possible to make thanks to the Poisson Coefficient and the Young Modules of the material. The values are reported in Table 2.

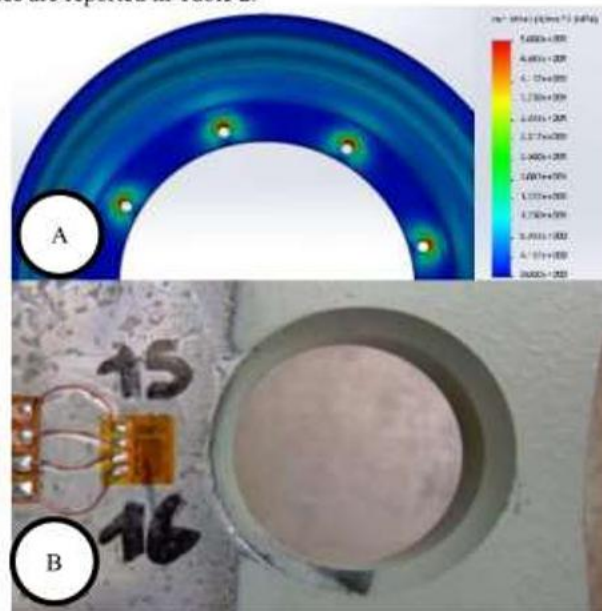


Figure 5 Finite Element Analysis A) and detail of a strain gauge B)

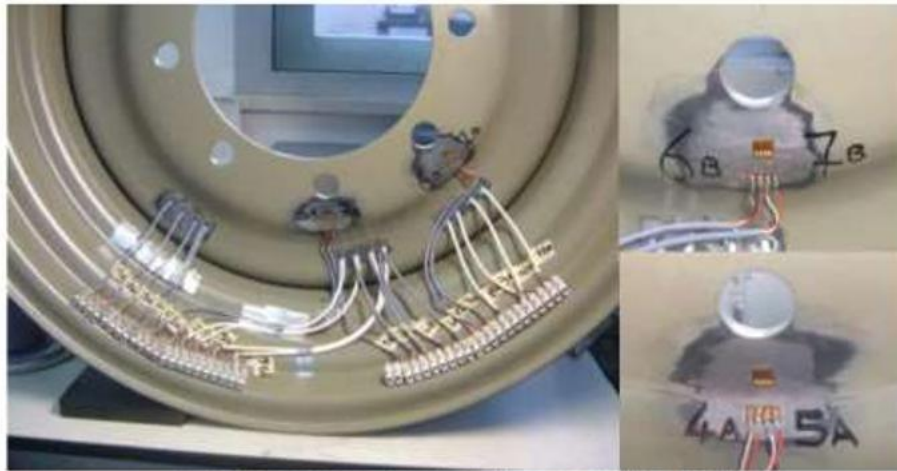


Figure 6 Experimental configuration (strain gauges placed near the hole)

The wheel is placed on the vehicle and a data logger is connected to the wheel to allow the direct recording of data without the need of telemetry or cables going into a cabin. Then, each load case can be measured by recording the strain gauge values for the significant areas of the wheel. Figure 7 shows an example of “on the field” measurement and data which are recorded. In particular, it is possible to observe the data logger placed on the wheel, which records strain gauge data during manoeuvres.

The main aim of this work is to report the values acquired by the uniaxial strain gauges positioned near the hole (Figure 6.) It is exactly in this zone that the strain gauges show the maximum value.



Figure 7 Position of a DAQ system on MANITOU TELEHANDLER

4 DATA ANALYSIS IN THE TIME DOMAIN

The recorded strain gauges data were used to build a full mission profile according to the full duty cycle of a wheel (which contemplates the different load cases and their percentage of duration vs. the full life of the wheel.) Some signals show a drift in the raw state. In order for this “drift” to be removed, we applied a low pass filter named “Butterworth” to the whole signal, with a cut-off frequency equal to 100 Hz.

Moreover, in order for the filter not to compromise the information inside the signal, we compared the moving average of the range, which does not change: in this way, the filter does not cut the peak. No significant noise shall be reported (regarding the amplitude of the stress.)

Several methods are used to compute the stress spectrum [15, 16, 17] with the Rainflow Method being the most used. [18, 19] The stress spectrum can be developed for each of the area of interest in the wheel and for each of the wheels to analyse (sometimes different design solutions are tested on the same machine.) Figure 9 shows a trend stress in the rim for container handlers on the four different

load conditions. Through Figure 9 it is possible to understand that in the CH4 position the stress values are higher than the values in the CH6 position; the third load condition (i.e. heavy load condition) shows the maximum stress values.

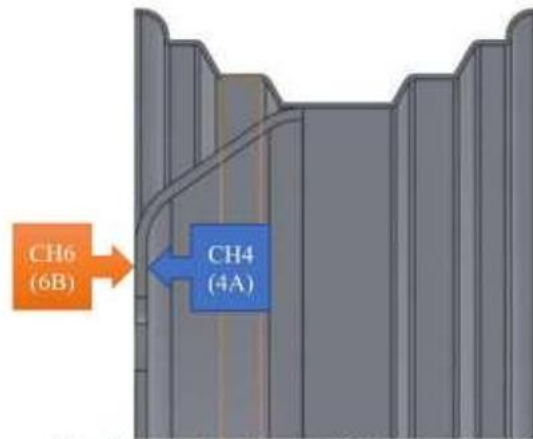


Figure 8 Location of strain gauge for CH 6 (outer rim) and CH 4 (inner rim)

By the same acquisition of the data, it is possible to understand which loading condition is more dangerous for the component.

The fatigue life was evaluated by using as input the data from the strain gauges, the characteristics of fatigue material and the Young Modulus, a Rainflow calculation of strain cycles (Figure 9) and a cumulative damage calculation based on Miner Equation, which can be found using a software specifically developed.

The damage follow equation (that is not linear) can be calculated according to several methods (i.e. considering such an exponential law.) [20, 21, 22, 23, 24]

However, the application of these formulations requires a high number of tests; a linear approach was instead used during this stage.

After identifying the cumulative damage through the duration of the strain history acquired, it is easy to obtain a life estimation for the different areas of the wheel.

This formulation in the time domain is the most used, as it is reliable in terms of damage. Otherwise, more calculations should be done.

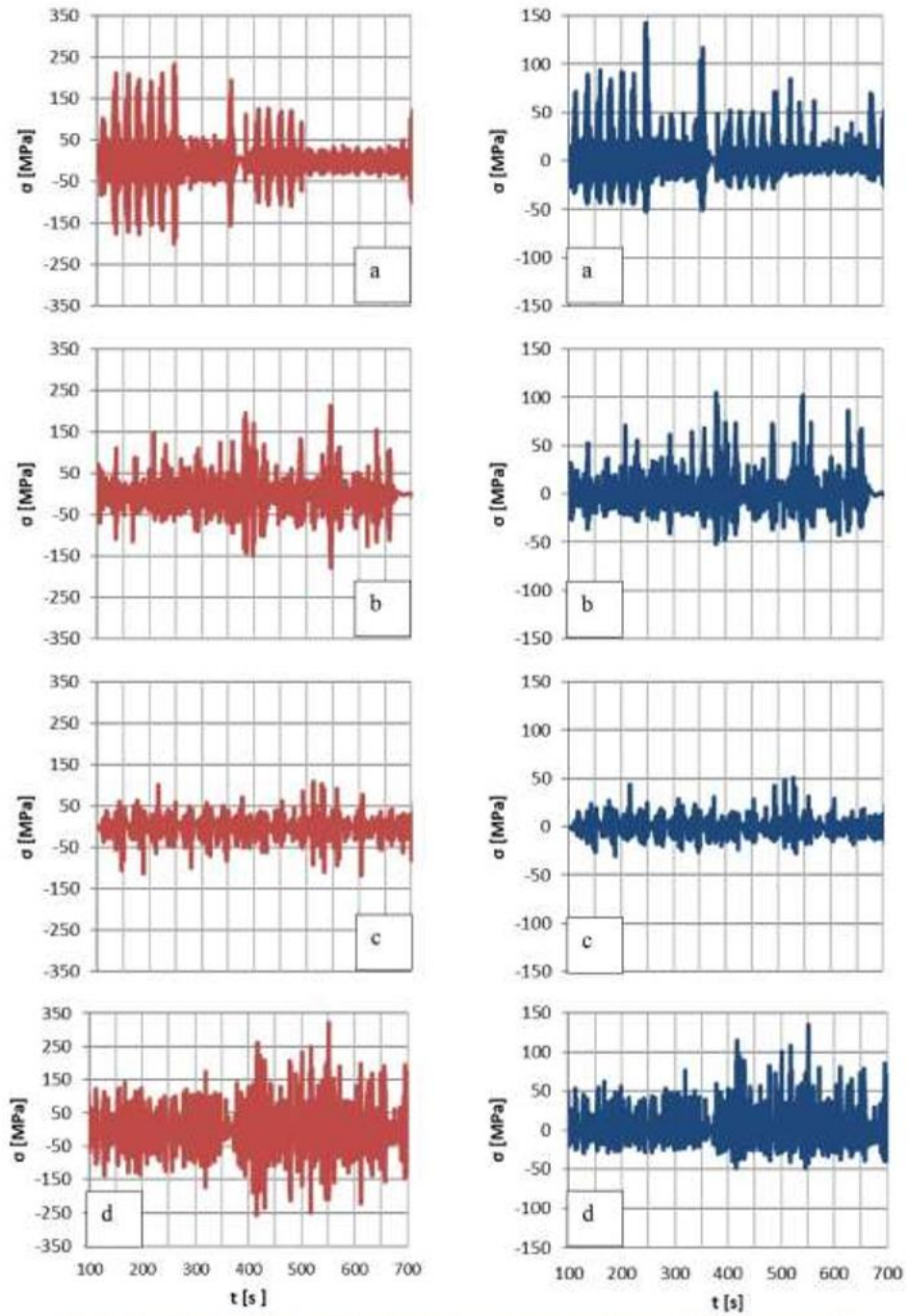


Figure 9 Stress values for CH4 (red) and CH6 (blue) a) on-road, b) load placement, c) loader d) off-road.

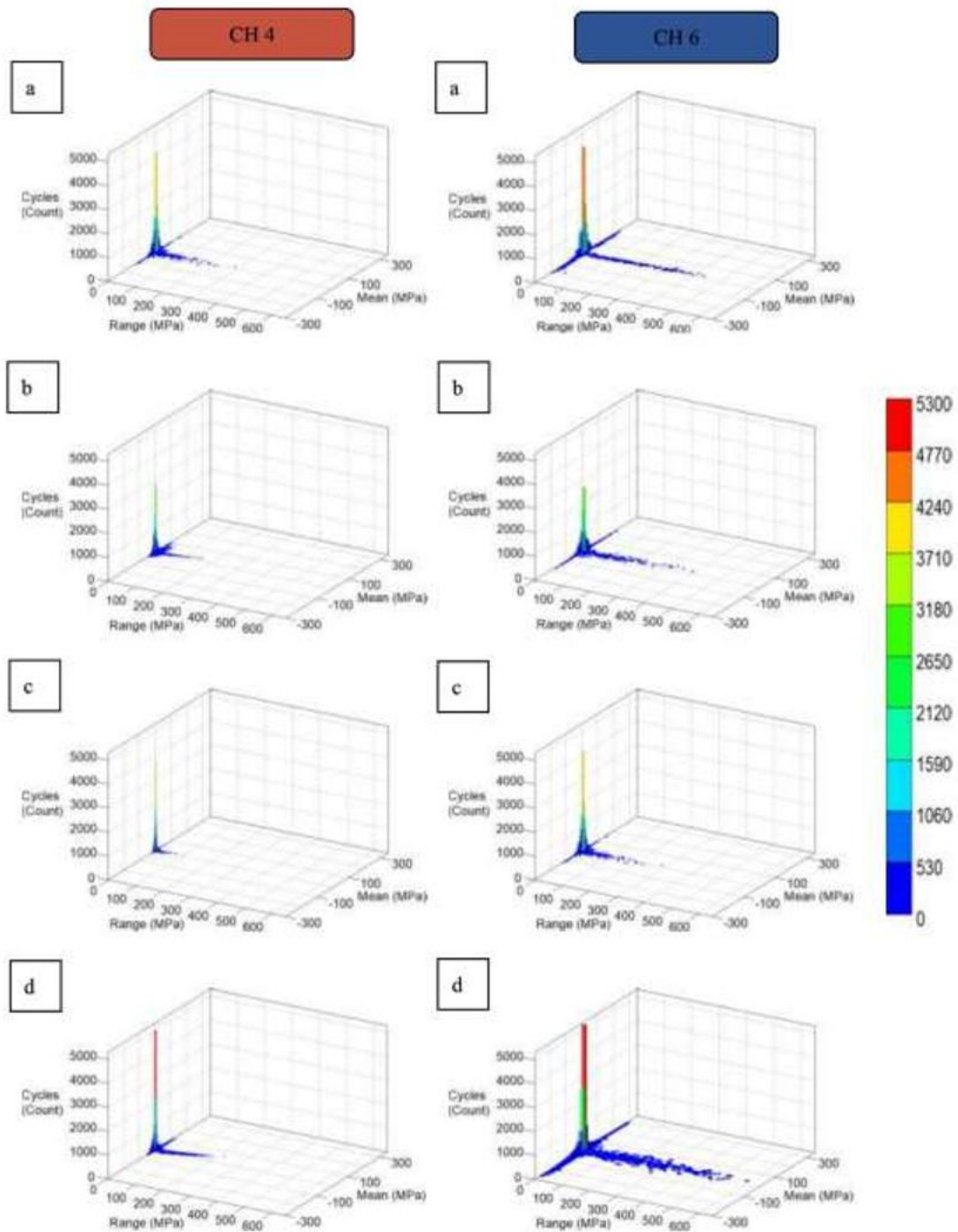


Figure 10 Rainflow for CH4 and CH6; for different load case: a) on-road, b) load placement, c) loader d) off-road.

4.1 DATA ANALYSIS IN THE TIME DOMAIN

In order to compare the fatigue damage value in the time and frequency domain approach, we need to assume that [25, 26]:

- The load history needs to follow the Gaussian distribution;
- The process is stationary (i.e. the load history is not time dependant);
- The process is ergodic (i.e. a part of the load history has the same characteristics (mean, variance, etc.) compared to the whole data acquired.

Thanks to the previous points it is possible to migrate from time domain to frequency domain with the PSD (Power Spectral Density).

We can check if the first hypothesis is solid by checking the PDF (Probability Density Function). Figure 11 shows the PDF function for CH4 and CH6 for the "on-road" load case, while table 1 reports the values of the two parameters that characterize the Gaussian function. [27, 28]

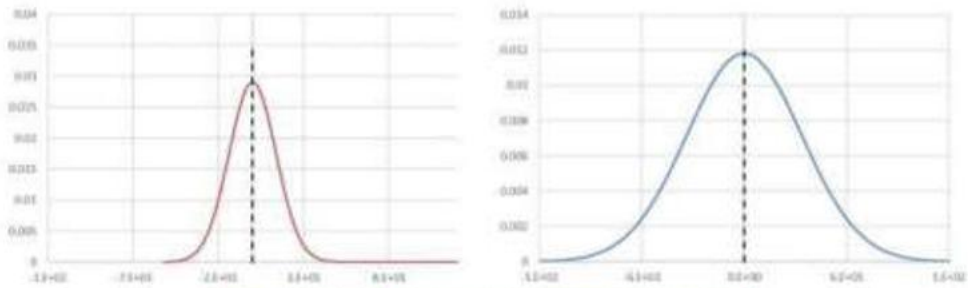


Figure 11 Probability Density Function for CH 4 (red) and CH 6 (blue)

Table 1 Parameters for Gaussian function computed from PDF function

LOAD CASE	CHANNEL	μ [MPa]	σ [I]
ON-ROAD	CH 4	7.059E-04	13.73
	CH 6	2.235E-04	33.8
LOAD PLACEMENT	CH 4	1.022E-04	13.44
	CH 6	-8.725E-04	32.80
LOADER	CH4	-4.655E-04	7.23
	CH6	-1.163E-03	20.04
OFF-ROAD	CH4	1.533E-04	18.43
	CH6	4.931E-04	53.70

Looking at the table, it is clear that the signal has a very close-to-zero average and that the highest variability is for channel 6 in the off-road condition.

After this step we can apply the PSD. We used the LABVIEW software, which can process a signal. Figure 12 shows the PSD for all load cases. The white signal is for CH4 and the red one for CH6.

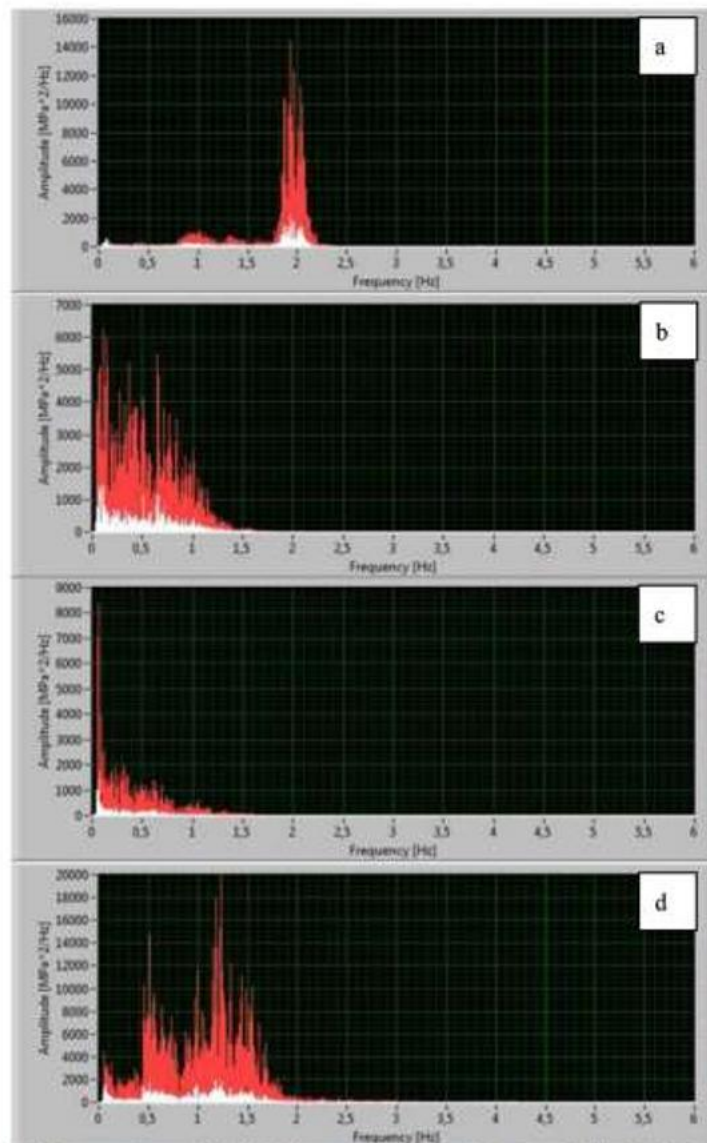


Figure 12 PSD for all load caves a) on-road, b) load placement, c) loader, and d) off-road; white signal for CH4, red for CH 6.

Looking at the figure above, we can underline the fact that the PSD function (computed with the periodogram method) differs according to the different load conditions. The two channels show a quite different trend and the magnitude is very different: CH6 shows the highest magnitude.

While looking at the on-road load condition, we can observe a peak on 2 sps: the peak of the energy is concentrated between 1.7 sps and 2.3 sps. For the load placement condition, the energy is concentrated between 0 sps and 1 sps and then it decreases to 0 at 1.5 sps. For the loader condition, there is a peak between 0.2÷0.3 sps and then a quite uniform distribution until 1 sps. For the last load condition (off-road,) we registered the highest peak of the four, with several peaks from 0.5 to 1.3 sps, where the energy is distributed.

5 MATERIAL FATIGUE PARAMETERS

Wheels and, in particular, rims are made of steel S355 UNI 10025. The main parameters, acquired from the literature, are reported in table 2. [29, 30, 31, 32]

Table 2 Main parameters for the material

ELASTIC PARAMETERS	S_r	117	
	b	-0.055	
PLASTIC PARAMETERS	E_r	1.220	
	C	-0.672	
CYCLIC PARAMETERS	K'	888	
	n'	0.082	
UTS		536	[MPa]
YOUNG MODULUS		215000	[MPa]
SURFACE FINISH		Hot Rolled	
SURFACE TREATMENT		Cold rolled	
CERTAINTY OF SURVIVAL		50%	

6. TIME DOMAIN ANALYSES

The fatigue analysis in the time domain is the common approach to estimate the fatigue life of a component. Figure 11 shows a schematic block diagram, which was used for our analysis. This approach is based on the stress history (Figure 9), Rainflow analysis (Figure 10) and material parameters (Table 2). In order to estimate the damage values for the two channels and the different load conditions, it is possible to adopt different criteria such as: Smith-Watson-Topper, Morrow and Morrow modified. [17, 33, 34] The damage value and thus the estimation of the fatigue life of components (i.e. number of failure cycles (N_f)) was developed by Smith – Watson – Topper, with this model being born for automotive components made of steel [35] (such as the wheel, object of this research.)

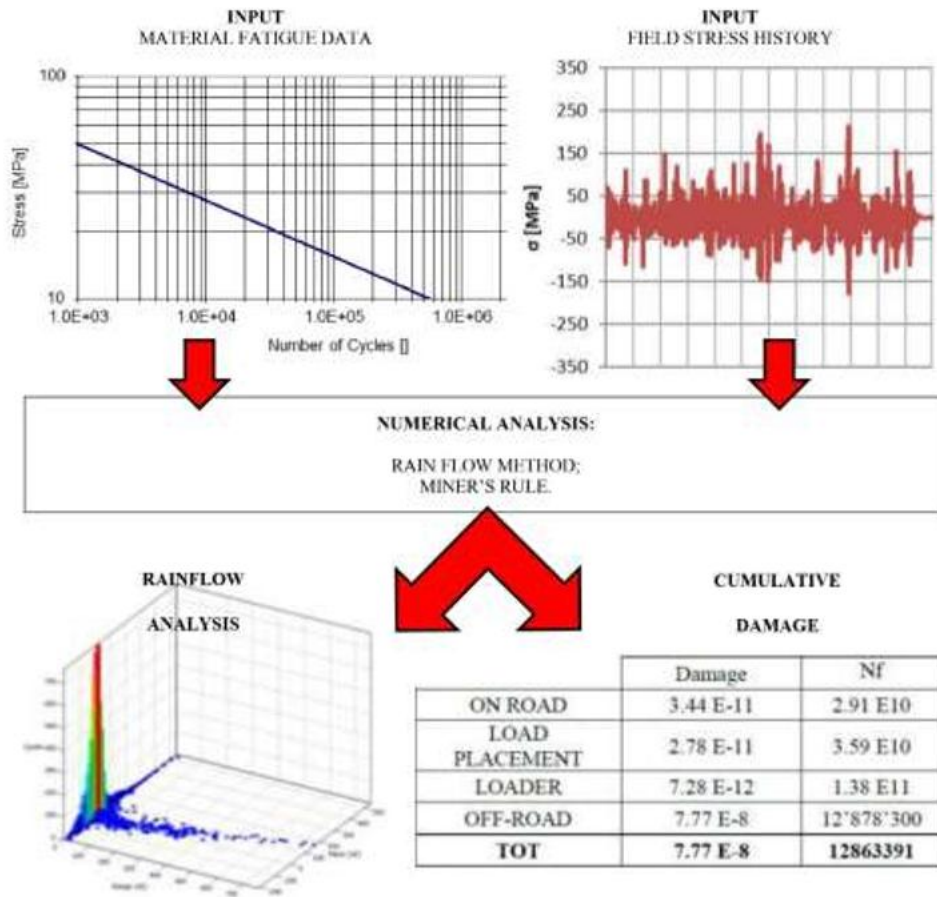


Figure 13 Block diagram for fatigue analysis in the time domain.

Table 3 shows the damage values and number of failure cycles for all load conditions and for each channel. This table also shows the total values of these variables, assuming that the entire life cycle of wheels is given by the sum of each load conditions.

Table 3 Damage values and number of cycles failure (time domain)

	CH4		CH6	
	DAMAGE	Nf	DAMAGE	Nf
ON-ROAD	3.44 E-11	2.91 E10	2.50 E-5	40'032
LOAD PLACEMENT	2.78 E-11	3.59 E10	4.44 E-6	225'479
LOADER	7.28 E-12	1.38 E11	1.51 E-7	6'631'299
OFF-ROAD	7.77 E-8	12'878'300	1.56 E-4	6'410
TOT	7.77 E-8	12863391	1.86 E-4	5'390

8. FREQUENCIES ANALYSIS

There are several techniques for the estimation of the damage value in the science of fatigue life. [17, 33, 36, 37, 38, 39]

For all these approaches, we need to introduce three different parameters (looking at figure 13):

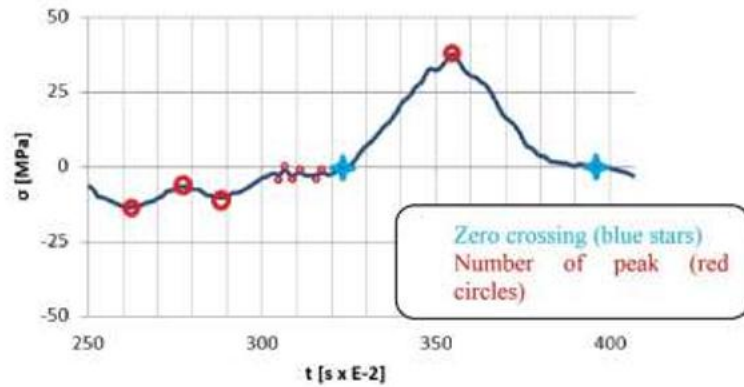


Figure 14 Example of load history with peak and zero crossing

We start by computing the zero-crossing ratio:

$$IF(\lambda) = \frac{\text{number of zero crossing}}{\text{number of peak}} \quad (1)$$

First of all, it is necessary to compute the moments of the PSD [40], which is the integral (2)

$$m_n = \int_0^{\infty} f^n \cdot S(f) df \quad (2)$$

Where $S(f)$ is the value of the PSD at the frequency f [Hz] and n is the order of the spectra momentum being computed.

From this momentum it is possible to compute the parameters described in (3) (for zero crossing) and (4) (for peaks counting):

$$E[0] = \sqrt{\frac{m_2}{m_0}} \quad (3)$$

$$E[P] = \sqrt{\frac{m_4}{m_2}} \quad (4)$$

With these parameters, it is possible to describe the load history in the frequency domain. In the table below are the spectra moments values of the PSD function for the different load conditions, as well as the channels analysed (table 4.) Through these parameters it is possible to estimate the fatigue damage in the frequency field by using different techniques.

Table 4 Moment values for the PSD function

LOAD CASE	CHANNEL	M ₀	M ₁	M ₂	M ₄
ON-ROAD	CH4	188.74	553.88	7'266.62	5.31 E06
	CH6	1'141.06	2'110.40	7'114.89	3.70 E06
LOAD PLACEMENT	CH4	180.67	147.54	1'312.20	960'043
	CH6	1'075.76	577.12	611.66	128'358
LOADER	CH4	52.26	21.57	28.08	8'952.80
	CH6	401.60	173.76	220.05	66'595
OFF-ROAD	CH4	339.38	364.97	968.34	34'1924
	CH6	2'888.78	3'170.40	6'511.75	1.69 E06

8.1 – NARROW BAND TECHNIQUE

This method was developed by Bendat [41, 42] around 1960. This technique is useful only for narrow band signals with an irregularity factor of 1 or near 1.

In this analysis we consider a linear stress strain relation and a linear cumulative damage law. As known, the Palmgren - Miner's laws for damage evaluation is (5):

$$D = \sum_{i=1}^k \frac{n_i}{N_{f,i}} \quad (5)$$

Where n_i is the number of the cycle on a certain amplitude and means value, $N_{f,i}$ is the number of the cycle that gives the back down at a certain amplitude and means value. k is the index of the cycle on the load history.

As the Basquin Law:

$$S_{a,i} = S'_f (2N_{f,i})^b \rightarrow N_{f,i} = \frac{1}{2} \left(\frac{S_{a,i}}{S'_f} \right)^{1/b} \quad (6)$$

Where:

- S'_f is the fatigue resistance coefficient [MPa];
- $S_{a,i}$ is the alternate component of the stress [MPa];
- b is the fatigue exponent.

If we define the following parameters:

$$m = -\frac{1}{b} \text{ \& } A = 0.5(S'_f)^m \rightarrow N_{f,i} = AS_{a,i}^{-m} \quad (7)$$

The number of the cycles observed in the load history is:

$$\sum_{i=1}^k n_i \quad (8)$$

The chance to find a cycle of a S_a amplitude is computed as described in the (9)(Probability density function of the S_a)

$$f_i = \frac{n_i}{\sum_{i=1}^k n_i}$$

As for (9) we specify $\sum_{i=1}^k n_i$, we substitute it in (5) and we obtain: (9)

$$D = \sum_{i=1}^k \frac{n_i}{N_{f,i}} = \sum_{i=1}^k \frac{f_i \cdot \sum_{i=1}^k n_i}{N_{f,i}} \quad (10)$$

If we use the $N_{f,i}$ from the (7), we obtain:

$$D = \sum_{i=1}^k \frac{f_i \cdot \sum_{i=1}^k n_i}{N_{f,i}} = \frac{\sum_{i=1}^k n_i}{A} \sum_{i=1}^k f_i \cdot S_{a,i}^m \quad (11)$$

We can define the total number of the cycles in the following way:

$$E(S_a^m) = \sum_{i=1}^k f_i \cdot S_{a,i}^m \quad (12)$$

We can also observe that the total number of cycles can be seen as the number of the zero-crossing multiplied for the time T of the whole load history:

$$\sum_{i=1}^k n_i = E[0]T \quad (13)$$

If we assume that the S_a is continuous, we can assert that:

$$E(S_a^m) = \int_0^{\infty} S_a^m f_{sa}(s_a) ds_a \quad (14)$$

In case of a stationary event or of Narrow Band, it is possible to prove that the strain amplitude follows the Rayleigh distribution, so:

$$E(S_a^m) = (\sqrt{2}\sigma_s)^m \Gamma\left(\frac{m}{2} + 1\right) \quad (15)$$

And in the end, we can find the equation that estimates the level of damage:

$$D(T) = \frac{E[0]T}{A} (\sqrt{2}M_0)^k \Gamma\left(\frac{k}{2} + 1\right) \quad (16)$$

In the execution of this elaboration, it was developed a spread sheet with Mathcad software for each load case.

The damage values for different load cases and channels are reported in Table 5.

Table 5 Damage values and number of cycle failures in the frequency domain (Narrow Band Method)

	CH4		CH6	
	DAMAGE	Nf	DAMAGE	Nf
ON-ROAD	3.50 E-9	2.90 E8	1.26 E-5	80*321
LOAD PLACEMENT	1.12 E-9	8.96 E8	2.62 E-6	38*1213
LOADER	7.58 E-15	1.32 E12	2.27 E-3	1.10 E7
OFF-ROAD	2.51 E-8	3.98 E7	1.11 E-3	900
TOT	2.90 E-8	2.90 E8	1.13 E-3	1.13 E3

8.2 – WIDE BAND TECHNIQUE

New techniques for the calculation of fatigue damage have been recently developed, to increase the accuracy of Narrow Band Techniques. [34, 43, 44]

As reported in the previous chapter, the Narrow Band Approach provides a result of the damage, that is one order higher than the result from the time approach.

Here we are going to analyse two methods of the Wide Band Technique: the Wirsching-Light Method and the Ortiz Method.

These new techniques are based on a corrective factor, obtained from experimental tests and applied to the damage calculated through the Narrow Band Method (D_{NB}). In particular, the damage on the Wide Band Approach comes from this transformation:

$$D_{WB} = \zeta \cdot D_{NB} \quad (17)$$

8.2.1 – WIRSCHING – LIGHT METHOD

The factor ζ is calculated here by a series of simulations of the Monte Carlo Method as follows (18). [34, 43, 45]

$$\zeta_W = a_s + [1 - a_s](1 - \lambda)^{b_s} \quad (18)$$

Where:

$$\begin{aligned} a_s &= 0.926 - 0.033m \\ b_s &= 1.587m - 2.323 \end{aligned} \quad (19)$$

Where m is the slope of the Wöhler curve and λ is the irregularity factor (see (1)).

Table 6 Damage values and number of cycle failures - frequency domain - Wirsching – Light method

	CH4		CH6	
	DAMAGE	Nf	DAMAGE	Nf
ON-ROAD	2.50 E-9	1.02 E8	8.85 E-6	112'991
LOAD PLACEMENT	8.67 E-10	1.15 E9	1.99 E-6	503'778
LOADER	4.49 E-13	2.23 E12	1.35 E-8	7.13 E7
OFF-ROAD	1.31 E-8	7.621 E7	5.80 E-4	1725
TOT	1.72 E-8	5.82 E7	6.67 E-4	1'498

8.2.2 – ORTIZ METHOD

This approach is similar to the Wirsching – Light Method, as we still calculate a coefficient. This coefficient takes into account the distribution of the energy on several frequencies rather than only on one frequency [34].

The Ortiz corrective factor is:

$$\zeta_O = \sqrt{\frac{M_2 M_k}{M_0 M_{k+2}}} \text{ with } k = \frac{2}{m} \quad (20)$$

Where m is the slope of the Wöhler curve.

$$D_{Ortiz} = \zeta_O \cdot D_{NB} \quad (21)$$

Table 7 Damage values and number of cycle failures frequency domain Ortiz method

	CH4		CH6	
	DAMAGE	Nf	DAMAGE	Nf
ON-ROAD	4.51 E-9	2.21 E8	1.16 E-4	8'636
LOAD PLACEMENT	1 E-8	1 E8	5.32 E-5	18'807
LOADER	1.39 E-11	7.18 E10	4.42 E-7	2'261'192
OFF-ROAD	2.06 E-3	1'861'118	9.29 E-3	108
TOT	2.24 E-7	1.18 E6	9.16 E-3	108

8.5 – DIRLIK METHOD

As previously shown, the aim of the above mentioned methods is to migrate from time domain to frequency domain. The first attempt through Narrow Band techniques is very rough, because it overestimates the damage one order more than time domain (which is our reference,) in case of a large band signal.

For this reason, we need more reliable and accurate techniques. The previous methods (Wirsching – Light and Ortiz) are a first approach to the problem but their use is limited.

The technique of Dirlik [46], developed around 1985, defines a closed formula of the probability of the stress amplitude f_{sa} tested on a wide band signal. It is based on a wide series of Monte Carlo simulations on amplitude stress.

The Dirlik model for a time period τ is:

$$D_{WB,Dirlik} = \frac{E[P]\tau}{A} \int_0^{\infty} S_a^m f_{sa}(s_a) ds_a \quad (22)$$

$$f_{sa} = \frac{D_1}{2\sqrt{M_0}Q} e^{-\frac{Z}{Q}S_a} + \frac{D_2 \cdot Z}{2\sqrt{M_0} \cdot R^2} e^{-\frac{Z^2}{2R^2}S_a^2} + \frac{D_3 \cdot Z}{2\sqrt{M_0}} e^{-\frac{Z^2}{2}S_a^2} \quad (23)$$

f_{sa} is the Probability Density Function of the stress amplitude. Starting from a defined amplitude with this formula, it is probable to find a cycle with that amplitude in the load history.

$$\begin{aligned} Z &= \frac{1}{2\sqrt{M_0}} & \gamma &= \frac{M_2}{\sqrt{M_0 \cdot M_4}} & X_m &= \frac{M_1}{M_0} \sqrt{\frac{M_2}{M_4}} \\ D_1 &= \frac{2(X_m - \gamma^2)}{1 + \gamma^2} & R &= \frac{\gamma - X_m - D_1^2}{1 - \gamma - D_1 + D_1^2} & D_2 &= \frac{1 - \gamma - D_1 + D_1^2}{1 - R} \\ D_3 &= 1 - D_1 - D_2 & Q &= \frac{1.25(\gamma - D_3 - D_2R)}{D_1} \end{aligned} \quad (24)$$

These different parameters carry the information of the load history and are based on the spectral momentum extracted from PSD.

Table 8 Damage values and number of cycle failures frequency domain Dirlik method

	CH4		CH6	
	DAMAGE	Nf	DAMAGE	Nf
ON-ROAD	1.96 E-8	5.10 E7	5.26 E-5	19'003
LOAD PLACEMENT	4.49 E-9	2.23 E8	1.18 E-5	85'031
LOADER	9.82 E-12	1.02 E11	1.10 E-7	9.07 E6
OFF-ROAD	1.27 E-7	7.86 E6	5.88 E-4	1'702
TOT	1.51 E-7	6.6 E6	6.52 E-4	1533

9 COMPARISON OF THE FATIGUE LIFE

Table 9 shows a comparison between the results of fatigue analysis both with different approaches and different theories. This comparison considers both damage values and the number of failure cycles for each theory and channel. A safety coefficient for the damage and for a number of failure cycles was also set. In order to compare the results, we assumed that the load on the wheel is the result of the sum of the four load conditions previously described. We assume that, on the lifetime of the wheel, there is one time between each load condition (on-road, load placement, loader, and off-road). The safety factor allows us to know how many times this sequence of loads can be repeated. We can thus understand how many times we can repeat the load conditions to reach the break. In the following table, we can find a comparison between time and frequency approach.

$$\eta_{D,i} = \frac{DAMAGE (time domain)}{DAMAGE (frequency domain theory)_i} \quad (25)$$

$$\eta_{Nf,i} = \frac{CYCLE AT BREAK (time domain)}{CYCLE AT BREAK (frequency domain theory)_i} \quad (26)$$

Table 9 Comparison of results of fatigue analysis according to different approaches and theories.

CHANNEL	TIME	NARROW-BAND		WIRSCHING LIGHT		ORTIZ		DIRLIK	
	D	D	η_D	D	η_D	D	η_D	D	η_D
CH 4	7.8E-8	2.9E-8	2.7	1.7E-8	4.57	2.2E-7	3.5E-1	1.5E-7	5.1E-1
CH 6	1.9E-4	1.1E-3	1.7E-1	6.7E-4	2.7E-1	9.2E-3	2E-2	6.5E-4	2.9E-1
	Nf	Nf	η_{Nf}	Nf	η_{Nf}	Nf	η_{Nf}	Nf	η_{Nf}
CH 4	1.3E7	3.4E7	2.7	5.9E7	0.2	4.5E6	2.8	6.7E6	1.9
CH 6	5.4E3	9.1E2	5.9	1.5E3	3.6	1.1E2	5	1.5E3	3.5

From Table 9, it is possible to share some observations.

The best situation is to be found in CH 4, on the Wirsching-Light Method (as it gives 4.5 times the number of cycles at break, computed with the method in the time domain). The worst situation is depicted by the Dirlik Method, where the cycles at break are about 2 times ($1/5.1E-1$) than our reference (time domain.) The best situation for CH 6 is to be found in the time domain (5380 cycles at break,) while the worst is registered with the Narrow Band Method, with 909 cycles at break, (about 6 times less, which means that the safety factor is 6.)

All these methods are applicable, and the Power Density Function shows that all of them follow a normal distribution of Gauss. Nevertheless, as we can see in the Power Spectral Density graphics, there is a different distribution of frequency deriving from the different purpose of the vehicle. Therefore, some of these methods are applicable for a specific type of PSD (e.g. Narrow Band Method) and not for the others with a large band signal. This is the reason why our reference is always the damage computed in the time domain.

In detail:

- **NARROW BAND:** This approach can be applied only if the PSD is concentrated around a small number of frequency (from which the name Narrow Band). In our load history the PSD are very wide and spread on the frequency spectrum.
- **WIRSCHING-LIGHT:** This approach is an improvement to the Narrow Band Approach. It uses an experimental coefficient defined from Wirsching and Light, that corrects the results of the Narrow Band Approach.
- **ORTIZ:** This method is very similar to the WIRSCHING-LIGHT except for the correlation from the estimated damage through the Narrow Band Method and a corrective factor;
- **DIRLIK:** The results are similar to the Wirsching-Light Method. We can register a factor of about 3 deriving from the damage both in the frequency and time domain.

The first theory applied, the Narrow Band Method is the easiest and fastest in terms of calculation. However, the results are very far from our reference in the time domain. To understand if this method is solid, we need to check it on a Narrow Band signal.

Looking at the Wide Band techniques, the Ortiz Method gives the worst results in our load history, because it is too conservative.

The two last methods (Wirsching-Light and Dirlik) show similar results, which are also similar to the ones in the time domain. Therefore, they are the most suitable for our analysis. Moreover, in this case, the results underestimate the damage, even if the order is the same as the one computed in the time domain.

We can also consider the approach of relative error; in fact, we can observe η_D from table 9 (first two rows) the minimum is with Ortiz method for each channel (see red values). Starting from this the relative error for the methods are presented in the following table:

Table 10 Relative error based on Ortiz method

CHANNEL	NARROW-BAND	WIRSCHING LIGHT	DIRLIK
CH4	6,59E+02	1,19E+03	3,18E+01
CH6	7,36E+02	1,27E+03	9,29E+01

From this point of view is clear that the three theories show safety factor very different than the one computed with Ortiz method and in particular we can see that the Wirsching Light have a relative error bigger of three orders of magnitude on η_D computed with Ortiz.

After this analysis based on relative error, we can say that compared to Ortiz method we can make a scale where starting from the more accurate we have Dirlik, Wirsching light and finally Narrow Band method.

Also, with this analysis we can confirm that for define the best method we have to go deep the frequency analysis because as we observed the relative error is big compared to η_D of Ortiz.

CONCLUSION

In this work, we analysed a wheel (with its own geometry, material, etc.) under different experimental load conditions.

We decided to use the data provided by an industrial wheel manufacturer to make a comparison among different methods from the literature, and check their results in terms of fatigue life.

Moreover, with the fatigue parameters of the material (given by the manufacturer.) we were able to compute the damage and estimate the cycle numbers from two different approaches (time domain and frequency domain.)

In general, the results show that frequency methods are more conservative than what can be found in the theory and in the time domain. These theories provide comparable values both in terms of damage and safety factor.

We found out that frequency methods can be used only if the PSD is stable, which is not our case, as seen from our data. Thus, frequency methods cannot find here their application.

These results are of fundamental importance in the fatigue design process of a component, in order to increase its reliability (especially with regard to the structural elements that are very important for the safety of the vehicle, e.g. wheels.) This study can be applied to the other structural components as well.

In the end, we can assert that this experimental approach is an added value to the different papers from the literature, full of theories in the time and frequency domain. We applied these theories to a real component to find out if and how they are valid or not for the research.

The research is still in progress as for the following points:

- First of all, we want to try more experimental tests (in laboratory, on a uniaxial test machine) on the material and components, in order to estimate which theory provides the best experimental results.
- We want to study the specific load conditions to apply to a particular bench test (rotary bending machine (Figure 145).) in order to simulate the real load history, directly on the field.
- Last but not least, we want to go deep into the assumptions of frequency domain, and check how these assumptions can affect the final results.

This work will be likely developed in a further article.



Figure 15 Rotary bending machine

BIBLIOGRAPHY:

- 1 J. Balkwill, Weight Transfer and Wheel Loads, in: *Perform. Veh. Dyn.*, 2018. <https://doi.org/10.1016/b978-0-12-812693-6.00003-1>.
- 2 M. Peeters, V. Kloster, T. Fedde, L. Frerichs, Integrated wheel load measurement for tractors, *Landtechnik*. (2018). <https://doi.org/10.15150/lt.2018.3188>. Muhlmeier, M. (1995). Evaluation of wheel load fluctuations. *Int. J. of Vehicle Design*. 16. 397 - 411. 10.1504/IJVD.1995.061945.
- 3 L. Solazzi, Wheel rims for industrial vehicles: Comparative experimental analyses, *Int. J. Heavy Veh. Syst.* 18 (2011) 214–225. <https://doi.org/10.1504/IJHVS.2011.040503>.
- 4 A. T.L., Anderson T. L., *Fracture Mechanics - Fundamentals and Applications*, 3rd ed, 2004, 1998. <https://doi.org/10.1007/978-1-4612-1740-4>.
- 5 W. Xiaoyin, L. Xiandong, S. Yingchun, W. Xiaofei, L. Wanghao, P. Yue, Lightweight design of automotive wheel made of long glass fiber reinforced thermoplastic, *Proc. Inst. Mech. Eng. Part C J. Mech. Eng. Sci.* (2016). <https://doi.org/10.1177/0954406215583081>.
- 6 A. Wilczynski, M. Bartczak, K. Siczek, P. Kubiak, Carbon fibre reinforced wheel for fuel ultra-efficient vehicle, *Mech. Mech. Eng.* (2018).
- 7 L. Solazzi, Applied research for weight reduction of an industrial trailer, *FME Trans.* (2012).
- 8 M. Collotta, L. Solazzi, New design concept of a tank made of plastic material for firefighting vehicle, *Int. J. Automot. Mech. Eng.* (2017). https://doi.org/10.15282/ijame.14.4.2017.2.0363_old.
- 9 L. Solazzi, A. Assi, F. Ceresoli, Excavator arms: Numerical, experimental and new concept design, *Compos. Struct.* 217 (2019) 60–74. <https://doi.org/10.1016/j.compstruct.2019.02.096>.
- 10 L. Solazzi, R. Scalmana, New design concept for a lifting platform made of composite material, *Appl. Compos. Mater.* (2013). <https://doi.org/10.1007/s10443-012-9287-2>.
- 11 L. Solazzi, Experimental and analytical study on elevating working platform, in: *Procedia Eng.*, 2017. <https://doi.org/10.1016/j.proeng.2017.09.364>.
- 12 C.Y. Loi, H.Y. Choy, Modelling and Fatigue Analysis of Automobile Wheel Rim, in: *2019 5th Int. Conf. Control. Autom. Robot. ICCAR 2019*, 2019. <https://doi.org/10.1109/ICCAR.2019.8813410>.
- 13 X. Jiang, R. Lyu, Y. Fukushima, M. Otake, D.Y. Ju, Lightweight design and analysis of automobile wheel based on bending and radial loads, in: *IOP Conf. Ser. Mater. Sci. Eng.*, 2018. <https://doi.org/10.1088/1757-899X/372/1/012048>.

-
- 14 D. Roylance, Introduction to Fracture Mechanics, Department of Materials Science and Engineering Massachusetts Institute of Technology Cambridge, MA 02139 (June 14, 2001);
 - 15 Peter J. Massarelli, Thomas T. Baber, Fatigue reliability of steel highway bridge details, Virginia Transportation Research Council (A Cooperative Organization Sponsored Jointly by the Virginia Department of Transportation and the University of Virginia) In operation with the U.S. Department of Transportation Federal Highway Administration Charlottesville, Virginia (August 2001) VTRC 02-R4;
 - 16 A. Halfpenny, A Practical Introduction to Fatigue, Sheff. UK Co. Publ. NCode Int. Ltd. (2005).
 - 17 C. Braccesi, F. Cianetti, L. Tomassini, Random fatigue. A new frequency domain criterion for the damage evaluation of mechanical components, *Int. J. Fatigue*. (2015). <https://doi.org/10.1016/j.ijfatigue.2014.07.005>.
 - 18 S.D. Downing, D.F. Socie, Simple rainflow counting algorithms, *Int. J. Fatigue*. (1982). [https://doi.org/10.1016/0142-1123\(82\)90018-4](https://doi.org/10.1016/0142-1123(82)90018-4).
 - 19 L.L. Schluter, H.J. Sutherland, User's Guide For LIFE2's Rainflow Counting Algorithm, Sandia Rep. (1991).
 - 20 V. Shinde, J. Jha, A. Tewari, S. Miashra, Modified rainflow counting algorithm for fatigue life calculation, *Lect. Notes Mech. Eng.* (2018). https://doi.org/10.1007/978-981-10-6002-1_30.
 - 21 Y.L. Lee, J. Pan, R. Hathaway, M. Barkey, *Fatigue testing and analysis*, 2005. <https://doi.org/10.1016/B978-0-7506-7719-6.X5000-3>.
 - 22 D.G. Shang, W.X. Yao, A nonlinear damage cumulative model for uniaxial fatigue, *Int. J. Fatigue*. (1999). [https://doi.org/10.1016/S0142-1123\(98\)00069-3](https://doi.org/10.1016/S0142-1123(98)00069-3).
 - 23 K.A. Sweitzer, N.W.M. Bishop, V.L. Genberg, Efficient computation of spectral moments for determination of random response statistics, in: *Proc. 2004 Int. Conf. Noise Vib. Eng. ISMA*, 2004.
 - 24 J.L. Chaboche, P.M. Lesne, A non-linear continuous fatigue damage model, *Fatigue Fract. Eng. Mater. Struct.* (1988). <https://doi.org/10.1111/j.1460-2695.1988.tb01216.x>.
 - 25 A. Halfpenny, Frequency domain approach for fatigue life estimation from finite element analysis, *Key Eng. Mater.* (1999).
 - 26 D. Benasciutti, R. Tovo, Frequency-based analysis of random fatigue loads: Models, hypotheses, reality, *Materwiss. Werksttech.* (2018). <https://doi.org/10.1002/mawe.201700190>.

-
- 40 A. V Oppenheim, G.C. Verghese, Alan V. Oppenheim and George C. Verghese, *CI. Notes* 6.011 *Introd. to Commun. Control Signal Process.* - Massachusetts Inst. Technol. (2010).
 - 41 Pierre Darry Versaillot *Effects of cyclic loading on the mechanical properties of steel* Universitatea Politehnica Timisoara, Romania (2015-2017);
 - 42 Zhang, F. & Zhou, L. & Jiang, J. & Wang, K.. (2016). Random vibration fatigue accelerated test design based on frequency domain methods. 36. 659-664. 10.16450/j.cnki.issn.1004-6801.2016.04.008;
 - 43 I. Rychlik, On the "narrow-band" approximation for expected fatigue damage, *Probabilistic Eng. Mech.* (1993). [https://doi.org/10.1016/0266-8920\(93\)90024-P](https://doi.org/10.1016/0266-8920(93)90024-P).
 - 44 F.F. Curiel, R.R. Ambriz, M.A. Garcia, M.C. Ramirez, S. Garcia, Smith Watson and Topper Model in the Determination of the Fatigue Life of an Automotive Steel, in: *Proc. 17th Int. Conf. New Trends Fatigue Fract.*, Springer International Publishing, 2018: pp. 197–207. https://doi.org/10.1007/978-3-319-70365-7_23.
 - 45 J. Wijker, Random vibrations in spacecraft structures design, *Solid Mech. Its Appl.* 165 (2009) 1–530, https://doi.org/10.1007/978-90-481-2728-3_1.
 - 46 Dirlik T., "Application of computers in fatigue analysis", PhD thesis, University of Warwick, 1985;

ACKNOWLEDGEMENTS:

The authors of this work are willing to thank Eng. Bramè Giampietro of the company GKN Wheels for the information provided for the development of this research.

8. FREQ. DOMAIN FATIGUE DAMAGE APPLIED TO A VEHICLE WHEEL (PAPER)

EXPERIMENTAL AND ANALYTICAL STUDY OF RANDOM FATIGUE, IN FREQUENCIES DOMAIN, ON AN INDUSTRIAL WHEEL

L. SOLAZZI ⁽¹⁾, M. CIMA^(*)

⁽¹⁾Brescia University (Università degli Studi di Brescia), Department of Industrial and Mechanical Engineering, via Branze 38, 25123 Brescia, Italy.

ABSTRACT

This article shows how to process random fatigue in an industrial context and how to perform the same calculation on other components. Data coming from strain gauge placed on an industrial vehicle's wheel are analysed first in time domain. It is shown how to manage random cycles and how to rearrange them for the fatigue analysis. Then an equivalent damage is calculated. An alternative way is to carry out the analysis in frequency domain. This solution makes possible the use of simpler, less expensive and faster methods. However, a lot of attention must be paid in frequency analysis. There are strong hypotheses which must be verified before the analysis. This article will show strengths and weaknesses of an analysis in time and frequency domain. Four innovative methods (Narrow Band, Wrishing-Light, Oritz, Dirlik) coming from literature will be applied on a real sample and it will be shown how to improve, interpret and correct the result obtained.

KEYWORDS: random fatigue; time domain; frequencies domain; spectral methods; non-Gaussian PDF.

^(*) Corresponding author. E-mail michele.cima@unibs.it Department of Industrial and Mechanical Engineering, via Branze 38, 25123 Brescia, Italy.

NOMENCLATURE:

Symbols:

α : geometrical features of PSD function;
 ε : Deformation
 Γ : Euler gamma function
 λ : spectral moment
 λ_{NG} : Damage's corrective coefficient for non Gaussian process
 μ : Mean value
 ρ : Corrective coefficient
 σ : Normal stress value
 σ^2 : Variance
 σ_f : Fatigue limit
 σ_{std} : Stress standard deviation
 σ_{UTS} : Ultimate tensile strength
 σ_y : Yield stress
 τ : Delaying parameter
 $a(k)$: Wirsching-Light parameter
 $b(k)$: Wirsching-Light parameter
 C : Basquin parameter
 d : Fatigue damage
 D_x : Total fatigue damage calculated with the x criteria
 E : Young's modulus
 $E[D_x]$: Probabilistic damage calculated with the x counting method
 f : Frequency
FFT: Fast Fourier transform
IF: Irregularity factor
 k : Basquin parameter
 k_0 : Kurtosis
 m : Slope
 N : Number of cycles that break off the component
 n : Number of cycles with the same properties
 N_f : Number of cycles of infinite life
 N_{OS} : Number of cycles of start HCF
 P_p : Cumulative probability function
 p_p : Probability density function
PSD: Power spectral density function
 q : y-intercept
 R_{xx} : Autocorrelation function
 s : Stress (frequency domain)
 $S(t)$: Sampled signal
 s_k : Skewness
 s_r : Hanshin-Rotem coefficient

T: Period
t: Time
 v_0 : Probabilistic number of zero crossing in a period of time
 v_p : Probabilistic number of peak values in the time unit

Subscripts

a: Amplitude
DK: Dirlik
e: Value of an equivalent cycle with 0 mean
H: Haigh parameter
i: Value of the *i*th cycle
LLC: Level crossing counting method
m: Mean value
max: Maximum value
min: Minimum value
O: Ortiz
PC: Peak counting method
RC: Range counting method
RFC: Rainflow counting method
s: Sampling
W: Wöhler parameter
WL: Wrishing-Light

1 INTRODUCTION

The structural components of a motor vehicle such as the driving wheels, are subject to cyclical stresses that depend randomly on the nature of the terrain on which the vehicle will move. Therefore, a fatigue analysis is necessary to verify the resistance of the component throughout its useful life. The most precise method to validate the mechanical resistance to fatigue is the analysis in time domain: Miner's law [1] or Hansim and Rotem [2] have been widely confirmed by both theoretical studies and experimental tests. However, when dealing with random fatigue, it is necessary to transform the load history into a series of stress packets. Numerous counting methods have been proposed to achieve this purpose, but nowadays the only one with a proved effectiveness is the Rainflow, which is long, slow and, as far as concerned in industrial context, expensive method. Moreover, Rainflow algorithm requires a different software that is necessary to buy if the load history has to be analysed. An alternative approach is the study of fatigue in frequency domain. In the last years, academic world has shown great interest in this field because it seems to be the solution to the problems which are related to counting methods.

This article will illustrate the principal laws of damage in frequency domain which work with the load spectra. These methods (such as Dirlik [3] and Narrow Band methods [4,5]) eliminate the pre-analysis in which the load history is rearranged and starts directly calculating the damage that each harmonic of the load spectrum causes on the material.

Time and cost savings are considerable; even the software needed are cheaper and more common. Classic methods need calculation program like Matlab or similar, while these new methods are implemented in Excel spreadsheet.

One could wonder why such a fast and cheap method is not massively used in today's industrial reality. Frequency damage methods must satisfy the Gaussian, ergodic and narrow-band load spectrum hypotheses; obviously not all the processes fall into this case and, unfortunately, there is still no adequate mathematics treatment to deal with deviations from the aforementioned hypotheses. The scientific literature provides corrective coefficients that can be calculated to correct the deviation of a spectrum from a standard case. This article will demonstrate that, after having illustrated and applied the theory of frequency analysis, not even the coefficients can guarantee an adequate correction or, at least, comparable to the results provided by the treatment in the time domain.

These theories (time vs frequency) have been applied to a load history obtained by a test on a industrial vehicle's wheel. More experimental test campaigns are in place to look for a link between the calculated coefficients and the actual damage on the components. The purpose of this research is to find an equivalent method in frequency domain which gives results similar to the more reliable time domain methods.

Figure 1 reports a diagram which highlights the most important steps necessary to perform random fatigue analysis in time and frequency domain.[6,7]

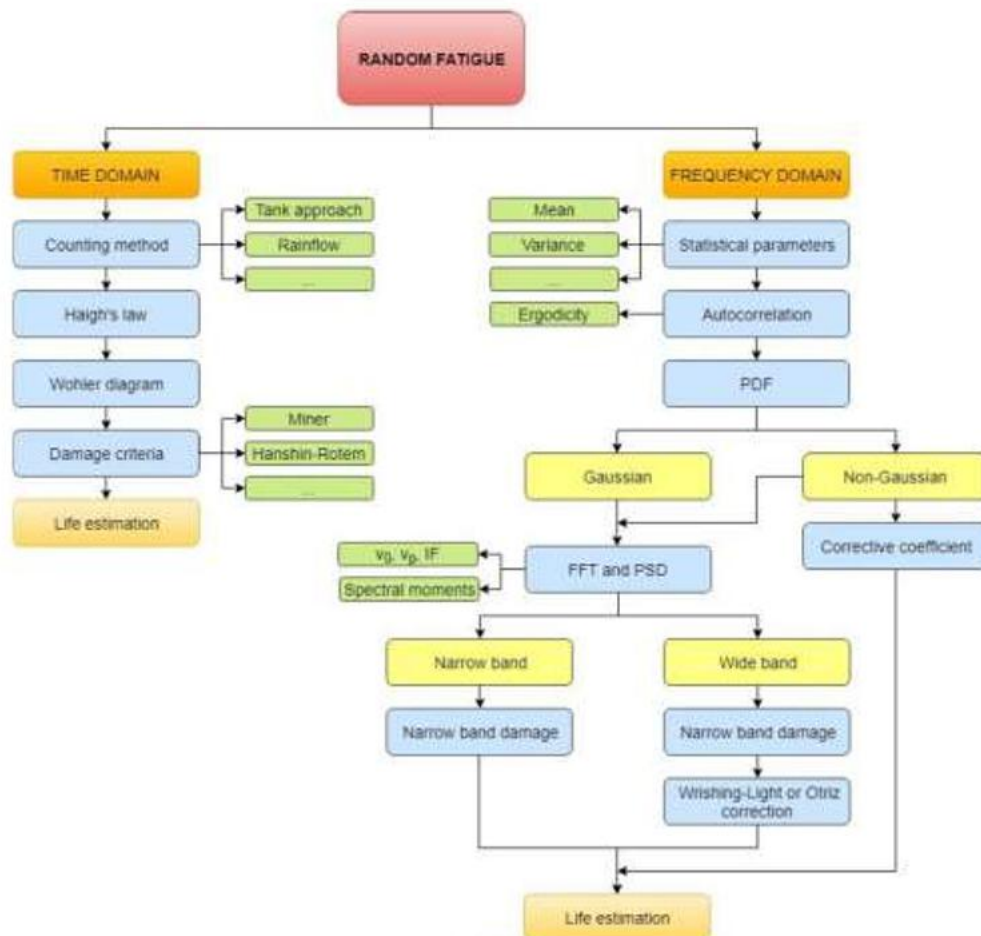


Figure 1

The goal of this article is the fatigue study of a rim for earthmoving vehicles. In particular, we want to identify the distribution of loads acting on the fixed flange (Figure 2) see due to rolling, starting from results obtained from laboratory tests. After having highlighted the best distribution of pressures, we proceed with numerous finite element analyses from which it is possible to evaluate the influence of different parameters, such as: the vertical load, the inflation pressure and the type of tire. What is now exposed is one of the most critical points of fatigue analysis in time domain. Faced with a random stress history, in which peaks and valleys follow each other without any order, it is necessary to obtain packages of cycles between the latter uniform in amplitude σ_a and average load σ_m . The result of this sort is the input required by the methods used for time analysis of fatigue, although a drastic choice is required to obtain this result. Methods like peak counting or level crossing are very fast, but the risk of making rough approximations is high. In contrast, counting algorithms such as the tank method or the famous Rainflow counting are excellent mathematical models to represent the physical phenomenon of random loads in an orderly manner. The price to pay is the high expenditure of time and resources. It must be remembered that fatigue is a slow phenomenon

and it requires many hours of experimental observation, the difficulty of systematically using such precise methods can easily be understood.

Increasingly efficient Rainflow algorithms and other algorithms have been developed over the years [8,9], but they are still too slow to cope with the enormous amounts of data that come from experimental tests.

2 FATIGUE ANALYSIS

Once the load history has been settled with a counting method, clusters are obtained with equal mean and amplitude. Clusters are the starting point for the methods which provide an estimate of fatigue damage.

Two different methods can be chosen.[10,11]

If laws of linear damage are used, fatigue damage will be calculated assuming that the moment in which a given load condition has occurred is indifferent: in this case the Palmgren-Miner law 1 will be used.

$$D = \sum_{i=1}^n d_i = \sum_{i=1}^n \frac{n_i}{N_i} \leq 1 \quad (1)$$

So, in this case, D is supposed to have a linear growth. According to this method, a structure is broken when D equals to 1. More wisely and more safely, it is a common habit to reduce the maximum value of D under one, in order to prevent structures, break off caused by unexpected dangerous situations. [12–14]

On the other hand, non-linear damage laws, though more complex, take into account material reinforcement mechanisms in the early stages of damage. Obviously, they provide a more accurate estimate of the damage. The Hansim-Rotem [15,16] law is a simple and effective law to take the reinforcement into account.

Assuming that fatigue damage represented by the S - N curve added in a logarithmic ratio, Hanshin and Rotem modified fatigue damaging expressions with the (2):

$$D = \sum_{i=1}^n d_i = \sum_{i=1}^n \left(\frac{n_i}{N_i} \right)^{\frac{1-s_{i+1}}{1-s_i}} \leq 1 \quad (2)$$

Where $\frac{1-s_{i+1}}{1-s_i}$ depends on the static strength of the material $s_i = \sigma_i / \sigma_{UTS}$.

More complex laws derive from the theories of Mark and Starkey, Henry or Gatts, but their complexity, especially regarding the determination of material parameters, does not make them suitable to be a quick method to validate frequency results.

This kind of methods are the most recent ones. They could be a faster way to analyze a random fatigue history and they can give extra information about the signal (like what is the most powerful wave that constitute a signal). A lot of attention should be pay when these methods are used, some strong hypothesis are needed.

Analyze a signal in frequency domain requires some statistical steps before the calculation of the damage [17]. In the next section these passages will be described and shown in a proper way. To sum up, frequency domain analysis follows the steps presented in Figure 1.

3 STUDIED COMPONENT

The studied element is a wheel of a material transfer vehicle produced by GKN in Carpenedolo, Italy. Strain gauges are placed all over the wheel, two of them close to a hole (which is necessary to connect wheel and hub). In fact it is a critical place because of the stress concentration (this phenomenon is described by notch factor). Loading histories are obtained from some tests performed in different conditions of tracks to simulate the life cycle of this component. This article will analyze the most common load history: on road condition.[18]

The figures show the tested wheel (Figure 2) and the position of the strain gauges (Figure 3).[19]



Figure 2 Wheel with strain gauge

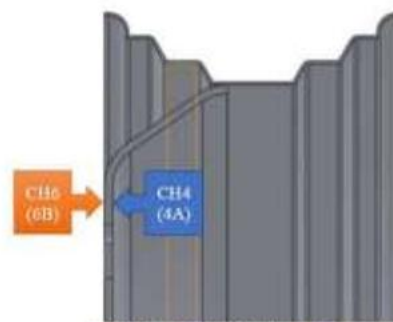


Figure 3 Wheel with strain gauge

The data coming from gauge 4 and on road condition will be studied in this work.

The wheel is built of S355 steel, static proprieties are given in standard EN 10025-3 (N) and in standard EN 10025-4 (M). Instead, fatigue parameters are given in standard EN 13001-3-1:2012 + A1:2013:

- Yield stress: $\sigma_y = 355$ MPa;
- Ultimate tensile strength: $\sigma_{UTS} = 450$ MPa;
- Elastic modulus: $E = 215$ GPa;
- Value of high cycle fatigue beginning: $N_{00} = 104$ cycles;
- Infinity life value: $N_f = 5 \times 10^6$ Cycles.

In safety condition, the fatigue limit (σ_f) is approximated with the formula (3) [20–23]

$$\sigma_f = 0.3 \cdot \sigma_{UTS} \quad (3)$$

For S355 steel, the value of fatigue limit is $\sigma_f = 135$ MPa. This precautionary value is taken to execute an analysis in safety condition, as the σ_{UTS} value. The analysis is done with low values because the wheel is a S355 steel bent and welded. [24,25]

4 LOAD CONDITION

To simulate the wheel's work conditions, a test on a oval paved track has been done by GKN. The industrial vehicle has been loaded and it has done some laps on this truck. Data acquisition lasted for about ten minutes with a sampling frequency of 100 Hz.

Under the hypothesis of elastic-linear strain and uni-axial stress state, load history can be calculated with Hooke's law:

$$\sigma = E \cdot \varepsilon \quad (4)$$

where E is Young's module. The hypothesis of linear-elastic field is correct because the maximum value of stress is $\sigma_{MAX} = 141.7 \text{ MPa}$, which is minor than the material's yield strength ($\sigma_y = 355 \text{ MPa}$). [26]

In Figure 4 is shown the load history of the wheel. [27,28]

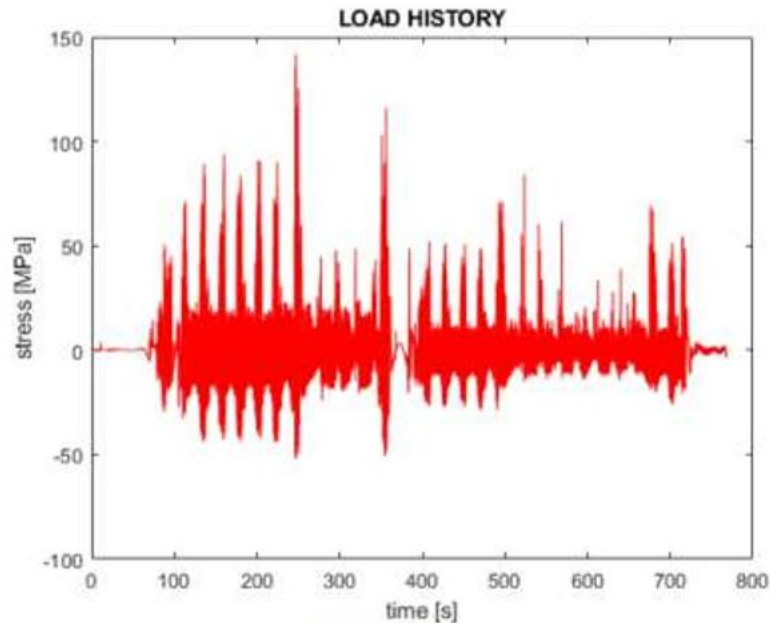


Figure 4 On road test, stress

5 Time domain analysis

How to manage random fatigue in time domain will be shown in this section. First, the signal reported in Figure 4 will be analysed with Rainflow method which produces equivalent fatigue cycles. After that, with the help of Haigh law, all the equivalent fatigue cycles will be transformed in alternated symmetrical cycles at the same danger level of original ones. Then it is possible to calculate the fraction of damage thanks to Miner's rule. The reason why only Rainflow and Miner's law are used in this work is that these methods are the most effective, known and used in time domain. [29,30]

Rainflow analysis

To start this analysis, it is necessary to handle the input signal (Figure 4). Rainflow method allows to transform a random signal in equivalent cycles with mean value (σ_m) and range (σ_a) generally different from zero. Another output is how many times a cycle repeats itself (n_i). This step is fundamental, because working on package of smaller cycles is the only way to use the Miner's law. The Figure 5 shows the input signal and the output of the Rainflow analysis. [31]

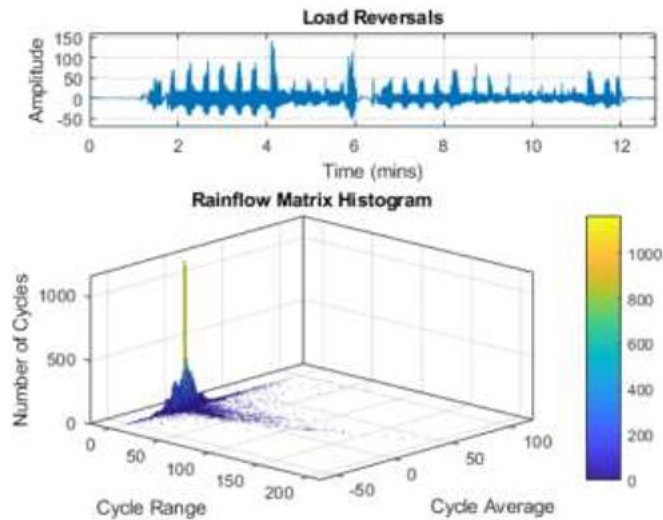


Figure 5 Rainflow input and output

Haigh's law

The next step is to transform the cycles that comes from Rainflow analysis with the Haigh's diagram. The purpose of this step is to modify the initial cycles in new ones with $\sigma_{im} = 0$. In the next subsection the reason of this transformation will be explained.

The equation of Haigh curve is:

$$\begin{cases} \sigma_{ia} = \sigma_f & \text{if } \sigma_{im} \leq 0 \\ \sigma_{ia} = \sigma_f - \frac{\sigma_f}{\sigma_{URS}} \cdot \sigma_{im} & \text{if } \sigma_{im} > 0 \end{cases} \quad (5)$$

For those cycles that have negative mean value ($\sigma_{im} < 0$) the transformation is easy. In fact, negative mean value is a good thing for fatigue life because it inhibits the crack's progress. In safety condition, the new cycle has the same alternated component of the original one.

On the other hand, for those cycles that have positive mean value, the transformation is more complicated. Looking at the positive part of the Haigh diagram, it can be considered that all the points on the Haigh curve (the red line) have the same level of danger.

The slope of Haigh curve can be calculated in this way:

$$m_H = -\frac{\sigma_f}{\sigma_{URS}} \quad (6)$$

Now, every cycle i can be located in High diagram as a point $P = (\sigma_{im}; \sigma_{ia})$. The purpose of this step is to find the equivalent point Q . With some algebraic passage it is possible to find Q .

$$\begin{cases} \sigma_{Pa} = m_H \cdot \sigma_{Pm} + \sigma_{Qa} & \text{if } \sigma_{im} \leq 0 \\ \sigma_{Qa} = \sigma_{Pa} - m_H \cdot \sigma_{im} & \text{if } \sigma_{im} > 0 \end{cases} \quad (7)$$

Now, this passage must be done for every cycle.

To sum up, any cycle can be re-arranged in an alternated symmetrical one (σ_{ie}) thanks to this equation:

$$\begin{cases} \sigma_{ie} = \sigma_{ia} & \text{if } \sigma_{im} \leq 0 \\ \sigma_{ie} = \sigma_{ia} - m_H \cdot \sigma_{im} & \text{if } \sigma_{im} > 0 \end{cases} \quad (8)$$

Now that every cycle has been transformed in an alternated symmetrical one (described with only one parameter σ_e), the Wöhler curve can be used to define the number of cycles to failure (N_i) of a constant reversal stress (σ_e).

The Wöhler curve (Figure 6) can be approximated with four parameters of the considered material. These four parameters are σ_{UTS} , σ_f , N_{OS} and N_f . In bi-logarithmic field, Wöhler curve can be written with the (9) formula:

$$\begin{cases} \log(\sigma_a) = \log(\sigma_{UTS}) \\ \text{if } \log(N) \leq \log(N_{OS}) \\ \log(\sigma_a) = m_w \cdot \log(\sigma_{UTS}) + q_w \\ \text{if } \log(N_{OS}) < \log(N) \leq \log(N_f) \end{cases} \quad (9)$$

Where:

$$\begin{cases} m_w = \frac{\log(\sigma_f/\sigma_{UTS})}{\log(N_f/N_{OS})} \\ q_w = \log(\sigma_f) - m_w \log(N_f) \end{cases} \quad (10)$$

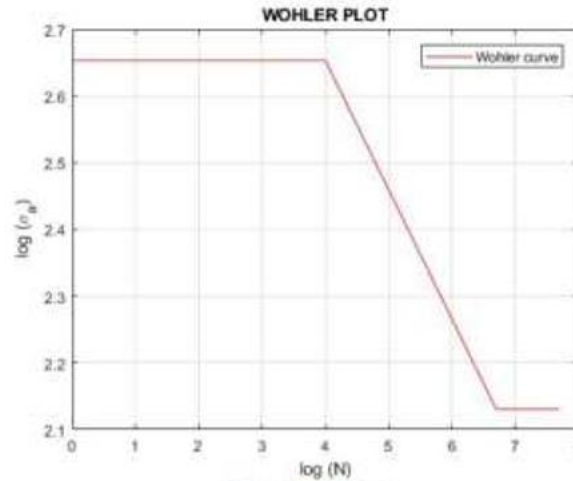


Figure 6 Wöhler curve

It is important to underline that this curve is not the real one of the materials, but it is an approximation made by using the suggestions coming from standard EN 10025-3 (N) and standard EN 13001-3-1:2012 + A1:2013 that give the value of N_f and N_{OS} . Moreover, all the stress values that are minor than the fatigue limit are neglected. Notice that these results (even in frequency domain) could be far from reality, but time domain and frequency domain must give similar results because of the Wöhler curve that is used in each method is the same.[32]

Now that the Wöhler curve is known, it is possible to calculate the damage caused by every equivalent cycle (d_i). In fact, Rainflow method has given as output the number of repetition (n_i) of each cycle which has been transformed in an alternate symmetrical one (σ_e). The number of cycles with σ_e that break off the component can be calculated with the (11) formula, that comes from the linear part of the Wöhler diagram:

$$\log(N_i) = \frac{\log(\sigma_a) - q_w}{m} \quad (11)$$

Using Miner's law, it is possible to calculate the total fatigue damage (D) caused by the entire load history:

$$D_m = \sum_{i=1}^n d_i = \sum_{i=1}^n \frac{n_i}{N_i} \leq 1 \quad (12)$$

Let's now calculate the number of cycles to failure of the entire random sequence:

$$N = \frac{1}{D} \quad (13)$$

Damage ratio and cycles to failure are:

- $D = 1.0545 \cdot 10^{-5}$;
- $N = 94,835$ cycles.

Input Signal

As reported in Figure 4, the load history is sampled. In this preliminary analysis, no window will be applied; otherwise, later, it will be discussed what kind of window will be the best choice for the signal and in case a window is really necessary.

The signal has been sampled for $t_s = 767.99$ seconds with a sampling frequency of $f_s = 100$ Hz. Thus, the sampling period is $T_s = 1/f_s = 0.01$ seconds.

The number of points sampled is $N_s = f_s \cdot t_s = 76799$; invoking the Nyquist-Shannon sampling theorem $N_{s,min} = 2 N_{HF} + 1$. If the N_{HF} harmonic frequency has to be seen without aliasing, at least $N_{s,min}$ points has to be sampled.

In this case $N_{s,min} = 76799$, so $N_{HF} = (76799 - 1)/2 = 38399$. It means that harmonic frequencies until 38399^{th} can be seen without aliasing.

Basic parameters

- **Mean value** (μ). For a vector whose elements are y_k , arithmetic mean is defined as $\mu = \frac{\sum_{k=1}^n y_k}{n}$. It represents the value which is less distant from all the other values. If y_k represents a finite population, the population mean is equal to the arithmetic mean.
- **Standard deviation** (σ_{std}). In statistics, it is a measure used to quantify the amount of variation or dispersion of data-set values. A low standard deviation indicates that data tend to be close to the mean value (also called the expected value). While, an high standard deviation points out that data are spread out over a wider range of values.
- **Variance** (σ^2). It measures how far a set of numbers are spread out from their average value. The variance is the square of the standard deviation and can also be calculated as the second central moment of a distribution.

The points sampled have a mean value of $\mu = 7.93 \cdot 10^{-4}$ MPa, a variance of $\sigma^2 = 188.7373$ MPa² and a standard deviation of $\sigma = 13.73817$ MPa. [33,34]

LLN theorem

The law of large numbers (LLN [35]) is an assumption that describes the result of performing the same experiment a large number of times. According to the law, the average of the results obtained from a large number of trials should be close to the expected value, and it will tend to become closer as more trials are performed. The LLN is important because it guarantees stable long-term results for the averages of some random events. In this situation the LLN theorem has a strong relevance as it introduces stability in normal distribution.

Autocorrelation

When dealing with random signals, it is reasonable to ask whether the particular signal being analysed is truly representative of every possible signal in every possible interval of observation time. Luckily a propriety exists and it is called autocorrelation, that provides a measure of the regularity (or, better, ergodicity) of the process. In addition, the delay introduced using this method allows to discover periodicity in signal.

While the probability density (PDF, which it will be calculated further on) contains the information related to the variations of the amplitude of the process, the autocorrelation contains information related to the variations on the time axis. Furthermore, it is very useful to know that the spectral density of a signal is the Fourier transform of the autocorrelation function.

When a signal is ergodic (i.e., it is not time-invariant respect to itself), autocorrelation provides values close to zero or negative. It is very similar to destructive interference, in which the negative parts of the curve are now erased with positive, so the correlation function has smaller values. The maximum correlation value is an index of how much the signals are in phase.

Assume to have a sampled signal $S(t)$; if τ is the delaying parameter, the autocorrelation formula can be written as (14):

$$R_{xx} = \sum_{t_0=0}^{t_{max}} [S(t) \cdot S(t + \tau)] \quad (14)$$

Observing the summation formula, it can be noticed that the autocorrelation function is simply the correlation between the signal $S(t)$ translated of $t + \tau$ and the signal $S(t)$ itself, the variable t is free and is not saturated in the operation of integration

In other words, not only a summation has been written, but also an infinity of sums, the one for every possible value of $t \in [t_0; t_{max}]$ and τ .

The autocorrelation function is limited and it measures the similarity of a signal with a copy of the translated signal of τ . The maximum is obtained by a translation with $\tau = 0$.

For power signals, if no periodic or constant components are present, with increasing translation similarity autocorrelation tends to decrease, and therefore the autocorrelation function tends towards zero.

This is not true for periodic signals. It is easy to verify that the autocorrelation is itself periodic, with the same period. Even in the case of a constant signal, autocorrelation is a constant and it does not tend to zero.

Using the non-windowed input signal in Figure 4, the autocorrelation function gives as output the curve in Figure 7. Notice that the autocorrelation function decreases to zero: this is the proof of signal's ergodicity: with a delay of few seconds, peak and valley in the signal are random enough to erasing each other's.

The results obtained by calculating autocorrelation are useful to obtain PSD (power spectral density). In fact, the Wiener-Khinchin theorem ensures that the power spectral density of a signal coincides with the Fourier transform of the autocorrelation function of the signal itself.

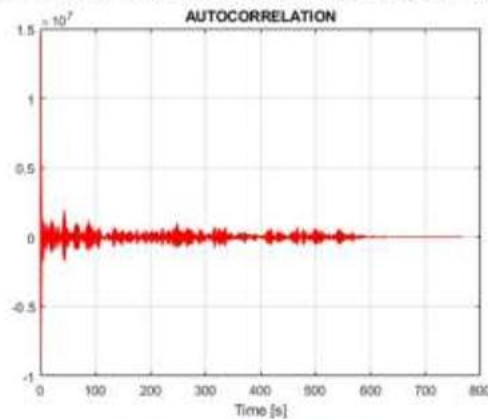


Figure 7 Autocorrelation function

Probability density function (PDF)

In addition to the classic parameters (μ , σ^2 and σ_{std}) it is useful to extend the analysis in order to obtain the probability density function (PDF). This function associates a probability for each stress (σ) value reported on the abscissas. The result is a continuous curve, of total area equal to 1 and represents the range of values that the magnitude of interest can - most likely - assume.

The same physical phenomenon can be analysed from several points of view. The simplest way is to detect how many times that phenomenon occurs, regardless of what has generated it. A more detailed point of view requires analysing the different causes that may have given rise to the observed phenomenon. In the first case, the analysis is rather simple. If a phenomenon (for example the occurrence of a given σ value) can take X different values, each of these values can be treated as a discrete random variable. Simplistically, if the occurrence of an event is unrelated to the occurrence of others, the probability of measuring the X value is equal to $100/X$ %.

Instead, most physical phenomena need a more accurate analysis. First of all it is necessary to underline that it is highly unlikely that a phenomenon depends only on a parameter. For example, if the statistical measurement of the fatigue damage of a wheel is needed, it would be too great an approximation to state that it depends only on the length of the road which was driven. Actually, the effect of notch factor, the thermal effects on materials, any stone or hole on the road should be considered. All these parameters, which have their own intrinsic and statistical variability, combine themselves in a stochastic way and provide the final damage.

Though, it is clear the need of a method that can describe a phenomenon including the statistical variability of the parameters. This method - or better - this probability function, is the normalized Gaussian distribution and the mathematical work on which is based on the central limit theorem.

Let n be the number of contributory causes that affect an event and assume that np is the number of measurements done.

- If X is distributed as a random binomial variable with a very large n (to give an idea of how large, it can be said that it should be $n \geq 30$), and approximately $np \geq 10$, then the binomial can be approximated with a Normal Gaussian PDF with expected value equal to np.
- If X is distributed as a random Poissonian variable with the very large λ parameter (orientatively $\lambda > 10$), then the Poissonian can be approximated with a Normal with expected value and variance equal to λ : $N(\lambda; \lambda)$.

Therefore, it remains to understand if the variable X, which in the case described in this paper is X = stress, is a binomial variable.

It has been supposed that the input random data may be viewed as a normal distribution, but in order to build this distribution mean and variance are needed. Otherwise, someone could object that for a random distribution the mean value is - indeed - random and it changes for every measurement. This is true, but if a large number of data are processed, the LLN theorem guarantees that the mean value deduced isn't too far from the real mathematical mean.

It will now be supposed to have a signal that can be statistically analysed as a Gaussian one.

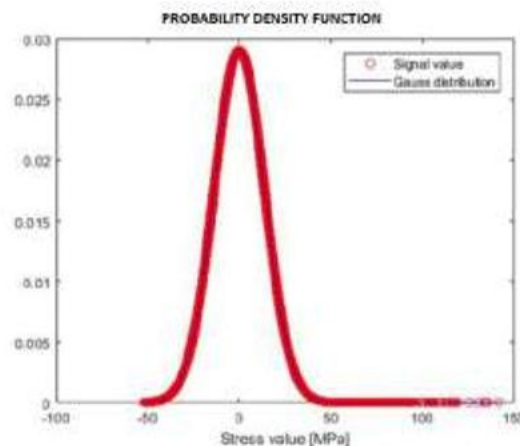


Figure 8 PDF for a supposed Gaussian-distributed signal

Therefore, a bell-normalized-curve will be built using mean value and variance of stresses previously measured. The result is shown in Figure 8.[36,37]

FFT and windows

If all the previous statistical conditions are respected, frequency analysis should give good results. Let's start with the Fourier theorem: the original Amplitude-Time signal will now be converted in a Magnitude- Frequency one (Figure 9). Notice that even if windows allow to have better results when a random signal is elaborated, this solution isn't every time the best one. Especially when the input signal hasn't so much asynchronous frequencies or if its queue has not so many peaks, a windowed-Fourier-transformed signal produces a big error. The reason of this incorrect result can be found in a lack of energy that the window drains from the proper original signal. As example, using an Hanning's window [38], the 50% of the original energy is lost: that results in a reduction by a factor 2 in the FFT peak. A worst effect is made on FFT's phase diagram, where waves are significantly distorted from their original phasing.

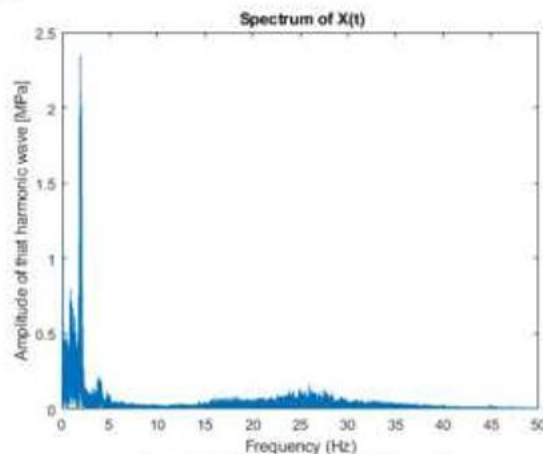


Figure 9 FFT of the input signal (Figure 4)

Power spectrum density (PSD)

The characterization of a random vibration usually occurs through the spectral power density curve (PSD, Power Spectral Density).

The PSD is defined as the average quadratic response of a random variable, to which an ideal narrowband filter is applied. The result is divided by the bandwidth of the filter, to tend the latter to zero. The term power is rather generic and it can refer to acceleration, speed, displacement, deformation, force, and so on. In the case of a random load description, the PSD is generally referred to the input value of the strain gauge (Volt or microstrain).

The PSD of a signal describes the distribution of the power between the frequencies that make up that signal. Through Fourier analysis, every signal, even continuous, can be decomposed into a discrete number of frequencies. The statistical processing of that signal represents its spectrum. When the energy of a signal is concentrated in a finite time interval, the spectral energy density of that signal can be calculated. The results will then be better if the input signal is discrete, as in case studied, where it is provided for a finite number of points.

There are many ways of calculating the energy density of energy, but the most well established is the PSD (power spectral density) method, which works particularly well on signals that span a wide time span. In addition, if autocorrelation has been calculated, Wiener-Khinchin theorem can be invoked in order to transform autocorrelation into PSD [39,40].

In addition, the PSD spectrum of a physical process often contains essential information on the nature of the vibratory phenomenon under examination.

Any signal that can be represented as a time-varying amplitude has a corresponding frequency spectrum. When these signals are displayed in the form of a frequency spectrum, some aspects of the received signals or of the underlying processes which produce them are revealed. In some cases the frequency spectrum may include a distinct peak corresponding to a sine wave component, and there may be peaks corresponding to the harmonics of a fundamental peak, indicating a periodic signal which is not simply sinusoidal.

The power spectral density (PSD) of the signal describes the power stored in the signal as a function of frequency, or, better, per unit of frequency. Spectral power density is commonly expressed in watts per hertz (W/Hz). In addition, the area under the curve is related to the actual signal strength over the whole frequency or to a specified bandwidth.

When a signal is only defined in terms of voltage, for example, there is not an unique power associated with the declared amplitude. In this case, "power" is simply calculated in terms of the square of the signal, as power would always be proportional to the actual power delivered by that signal in a given impedance.

Units of V^2/Hz for the PSD and V/Hz for the ESD (energy spectral density) are used even if no "power" or "energy" is specified effective. Sometimes the spectral amplitude density (ASD), which is the square root of the PSD, is encountered; the ASD of a voltage signal has units of V/\sqrt{Hz} . This is useful when the shape of the spectrum is rather constant, since the variations in the ASD will therefore be proportional to the variations in the voltage level of the signal itself.

Anyway, it is mathematically preferred to use the PSD because only in this case the area under the curve is significant in terms of actual power over the whole frequency or on a specified bandwidth. The results of this analysis can be seen in Figure 10.

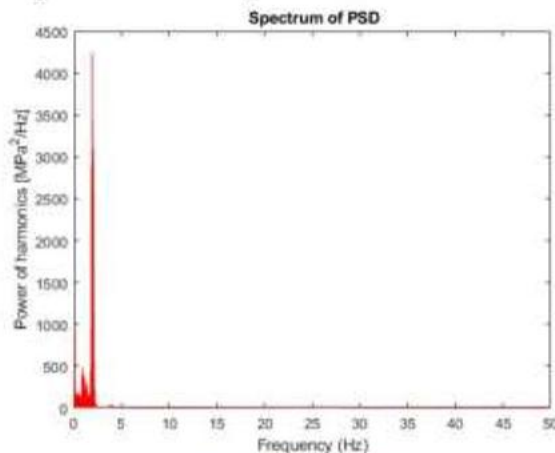


Figure 10 PSD – magnitude

The PSD calculus can be difficult, but if a good statistical analysis is made before the frequency analysis things can be done in an easier way. In fact the PSD can be obtained by $PSD = 2 \text{ FFT}(R_{xx})$ where the 2 is used because the FFT algorithm of a $2n$ -length vector produces a n -length output with the half of the input energy.

For the fatigue estimation let's consider stresses on a structural element; furthermore, let's assume that stresses can be described as a stochastic, stationary and ergodic process $X(t)$ with a mean value of zero. Additionally, statistical propriety of $X(t)$ is deduced using only one sufficiently long measurement $X(t)$: which is possible due to the ergodicity of the signal.

In frequency domain, a stochastic process is described by power spectral density (PSD), defined as the Fourier transform of the autocorrelation function, R_{XX} [41,42]

$$S_{XX}(\omega) = \frac{1}{2\pi} \int_{-\infty}^{\infty} R_{XX}(\tau) \cdot e^{-i\omega\tau} \cdot d\tau \quad (15)$$

where ω represents the pulsation and:

$$R_{XX} = \lim_{T \rightarrow \infty} \int_0^T X(t) \cdot X(t + \tau) dt \quad (16)$$

where T is the period of signal and t is the time in which signal is observed.

Lastly, using Lutes's function spectral moments can be calculated as follow:

$$\lambda_m = \int_{-\infty}^{\infty} |\omega|^m \cdot S_{XX}(\omega) d\omega \quad (17)$$

where $m \in \mathbb{N}$ represents the order of that spectral moment.

If σ_x is the variance of $X(t)$, $\sigma_{\dot{X}}$ is the variance of $\dot{X}(t)$ and $\sigma_{\ddot{X}}$ is the variance of $\ddot{X}(t)$, it could be written that:

$$\begin{cases} \lambda_0 = \sigma_x^2 \\ \lambda_2 = \sigma_{\dot{X}}^2 \\ \lambda_4 = \sigma_{\ddot{X}}^2 \end{cases} \quad (18)$$

Number of crossing of mean value represents also the zero crossing in time unit, because in this case it has been supposed $\mu_x = 0$.

Accordingly, to Lutes's works [43,44], v_0 (that represents how many time the mean value is crossed in one time unit and with a positive slope) can be calculated as follow:

$$v_0 = \frac{1}{2\pi} \sqrt{\frac{\lambda_2}{\lambda_0}} \quad (19)$$

In a similar way it is possible to estimate how many maximum values are found in a period of time:

$$v_p = \frac{1}{2\pi} \sqrt{\frac{\lambda_4}{\lambda_2}} \quad (20)$$

In this paragraph the process is supposed to be ergodic, continuous, stationary stochastic with 0 as mean value. Even if there are a lot of processes that can be described in the same way (wind, sea wave, traffic, ...), there are some that doesn't satisfy that hypothesis.[27]

6 Narrow band and broad band processes

Sometimes it is necessary to estimate if a process is a narrow band or broad band one. As known, a narrow band process identifies a situation in which spectrum is concentrated around a few frequencies; otherwise, a broad band one identifies a spectrum with a large amount of frequencies involved. In few words: NB processes are signal that in time domain are made up of few harmonic waves; BB processes, the opposite. [45]

Shape and geometrical features of PSD function can be used to solve this problem. First of all, a geometrical propriety has to be calculated:

$$\alpha_n = \frac{\lambda_n}{\sqrt{\lambda_0 \cdot \lambda_{2n}}} \quad (21)$$

Here $m \in \mathbb{Q}$, but the most common value for n are 1 and 2, thus:

$$\begin{aligned} \alpha_1 &= \frac{\lambda_1}{\sqrt{\lambda_0 \cdot \lambda_2}} \\ \alpha_2 &= \frac{\lambda_2}{\sqrt{\lambda_0 \cdot \lambda_4}} \end{aligned} \quad (22)$$

α are non-dimensional numbers, $0 \leq \alpha_n < 1$ and $\alpha_n \geq \alpha_{n+1}$ (see Figure 11).

These parameters are useful to show if a process is a narrow band one, because in that case the two parameters will be really close to 1. Instead, they will be close to 0 if the process is a broad band one.

Once λ and α parameters have been calculated, a Gaussian PDF for maximum values in a time unit ($p_p(X)$) can be generated. Here Rice's function (1945) will be used:

$$Pp(X) = \phi\left(\frac{X}{\sigma_X \cdot \sqrt{1 - \alpha_2^2}}\right) - \alpha_2 e^{-\frac{X^2}{2\sigma_X^2}} \cdot \phi\left(\frac{\alpha_2 X}{\sigma_X \cdot \sqrt{1 - \alpha_2^2}}\right) \quad (23)$$

where $\phi(\cdot)$ is the normal standard probability density function, that for a generic stochastic Gaussian process $x(t)$ can be written as

$$\phi(x) = \frac{1}{\sigma} \int_{-\infty}^x e^{-t^2} dt \quad (24)$$

Lastly, the cumulative probability to find a maximum in a period of time is given by:

$$Pp(X) = \Phi\left(\frac{X}{\sigma_X \cdot \sqrt{1 - \alpha_2^2}}\right) + \left[-\alpha_2 e^{-\frac{X^2}{2\sigma_X^2}} \cdot \Phi\left(\frac{\alpha_2 X}{\sigma_X \cdot \sqrt{1 - \alpha_2^2}}\right)\right] \quad (25)$$

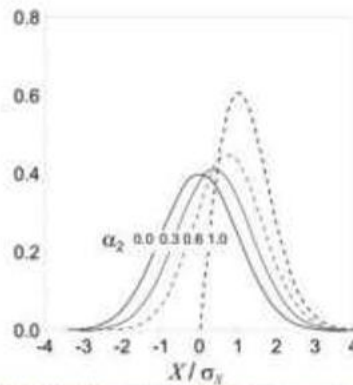


Figure 11 Probability density function about relative maximum $p_p(X)$ when α_i increases

For minimum values, the symmetry between max and min has to be considered, so $p_v(X) = p_p(-X)$ and:

$$Pv(X) = \phi\left(\frac{X}{\sigma_X \cdot \sqrt{1 - \alpha_2^2}}\right) + \alpha_2 e^{-\frac{X^2}{2\sigma_X^2}} \left[1 - \Phi\left(\frac{\alpha_2 X}{\sigma_X \cdot \sqrt{1 - \alpha_2^2}}\right)\right] \quad (26)$$

Accordingly, to Lutes' works, for a narrow band process where $\alpha_1 \approx \alpha_2 \approx 1$ the PDF and the cumulative probability are equal to a Rayleigh density function onto a generic stochastic Gaussian $x(t)$ process:

$$r(x) = \frac{x}{\sigma_x^2} \cdot e^{-\frac{x^2}{2\sigma_x^2}} \quad (27)$$

$$R(x) = 1 - e^{-\frac{x^2}{2\sigma_x^2}} \quad (28)$$

where $x \in \mathbb{R}^+$, $r(x)$ is the Rayleigh probability and $R(x)$ is the cumulative probability density function. Lastly, with references to Figure 11, it has to be noticed that a narrow band process has only positive maximum values, while a broad band could have positive and negative maximum values.

Fatigue damage

If the history load has a variable amplitude, it is mandatory to define a method in order to count the right number of cycles. This method, or criterion, has to group and order maximum and minimum value in the history load, creating a sort of new history load describable with packages of cycles. Especially, every group of cycles has the same amplitude s and the same mean value m . If u is the number of relative maximum and v that of the minimum, these two relations can be written:

$$s = \frac{u - v}{2} \quad (29)$$

$$m = \frac{u + v}{2} \quad (30)$$

The main problem with estimation of the fatigue strength is to define an appropriate PDF function for the $X(t)$ process.

In fact, a correct value in fatigue resistance is strictly linked to the PDF chosen.

A good PDF is the combined PDF $h(u, v)$, whose cumulative probability is:

$$H(u, v) = \int_{-\infty}^u \int_{-\infty}^v h(x, y) dx dy \quad (31)$$

which expresses the probability to have a cycle with a relative max minor of u and a min minor of v . Changing variables it is possible to obtain the PDF as a function of s and m :

$$p_{a,m}(s, m) = 2h(m + s, m - s) \quad (32)$$

In that case the PDF of the cycle amplitude is given by the marginal probability of the power spectrum density (marginal PDF of PSD):

$$p_a(s) = \int_{-\infty}^{+\infty} p_{a,m}(s, m) dm \quad (33)$$

Once the marginal PSD ($p_a(s)$) is known, the damaging can be calculated invoking Palmgren-Miner's law:

$$E[D] = v_a \cdot C^{-1} \int_0^{\infty} s^k \cdot p_a(s) ds \quad (34)$$

where $E[D]$ is the probabilistic damage, v_a is the number of cycles in the time unit, k and C are Wöhler's parameters for a S-N curve when the stress is symmetric and alternated (thus, $S N^k = C$). The $p_a(s)$ function (i.e. the marginal PDF of PSD) depends on the method used to count cycles in the original history load. Commonly, four different methods could be found in scientific literature:

- Peak Counting (PC)
- Level Crossing Counting (LCC)
- Range Counting (RC)
- Rainflow Counting (RFC)

Anyway, Rainflow Counting is nowadays the better way to summarize a complex history load, so, with references to Dowling works, the previous (34) can be transformed as follow:

$$E[D_{RFC}] = v_a \cdot C^{-1} \int_0^{\infty} s^k \cdot p_{RFC}(s) ds \quad (35)$$

Some spectral verification laws are presented. Their use is common when fatigue resistance has to be proved for metallic structural components.

7 Narrow Band (NB)

If process is Narrow-Band-type (i.e. $\alpha_1 = \alpha_2 = 1$) the $pp(s)$ is Rayleigh like:

$$p_p(s) = \frac{s}{\sigma_s^2} \cdot e^{-\frac{s^2}{2\sigma_s^2}} \quad (36)$$

$$P_p(s) = 1 - e^{-\frac{s^2}{2\sigma_f^2}} \quad (37)$$

In this kind of process the damage is:

$$E[D_{NB}] = \nu_0 \cdot C^{-1} \cdot (\sqrt{2\lambda_0}) \cdot \Gamma\left(1 + \frac{k}{2}\right) \quad (38)$$

where $\Gamma(\cdot)$ is the Euler gamma function: $\Gamma(1 + n) = n!$

If a Broad Band signal would be treated as a Narrow Band signal with the NB method, the damage calculated will be equal to a NB signal with variance of λ_0 . The NB method usually give a bigger damage if compared to RFC method; even if this is an error that is in favour of security, it is important to know that the damage calculated is not a proper damage.

Some authors have proposed to change the NB formula using coefficients that could make the damage more linked to real phenomena. The most famous one is the Wrishing-Light method:

$$E[D_{RFC}^{WL}] = \rho_{WL} E[D_{NB}] \quad (39)$$

Where ρ_{WL} is the Wrishing-Light coefficient, and it depends only on spectral moments λ_0 , λ_2 and λ_4 by α_2 parameter.

$$\rho_{WL} = a(k) + [1 - a(k)] \cdot (1 - \varepsilon)^{b(k)}$$

$$\varepsilon = \sqrt{1 - \alpha_2^2}$$

$$a(k) = 0.926 - 0.033 \cdot k$$

$$b(k) = 1.587 \cdot k - 2.323 \quad (40)$$

where k is determined from S N curve: $S^2 N = C$.

Notice that for a Narrow Band process $\alpha_2 = 1$, so $\varepsilon = 0$ and $\rho_{WL} = 1$, as expected if narrow band phenomenon were treated with NB method.

8 Fatigue damage calculation

First of all, spectral moments have to be calculated. (17) can be used.

The spectral moment method has advantages. The analysis needs only the first-order and the second-order moment calculations of the energy spectra and the method does not require the knowledge of the power-law behavior (spectral index) or even a shape of the spectrum.

Basically the zeroth moment is the area under any spectral curve. The first moment gives a weight to higher frequencies and it is like a center of gravity/mean value. The second moment gives information about the variance of a frequency if compared to the center of gravity value. Lastly, the third and the fourth moments give information on skewness (i.e. the asymmetry of the process) and on kurtosis (i.e. how much the process is far from a Gaussian process) of the process.

Moments can be normalized if they are divided by the zeroth moment. If a moment is normalized it is usually written as m_n , otherwise as λ_n .

In this process;

- $\lambda_0 = 377.4722$ is the zeroth spectral moment;
- $\lambda_1 = 1107.7$ is the first spectral moment;
- $\lambda_2 = 14533$ is the third spectral moment;
- $\lambda_3 = 3.695 \cdot 10^5$ is the third spectral moment;
- $\lambda_4 = 1.0615 \cdot 10^7$ is the fourth spectral moment;

Using those parameters three useful quantities can be estimated:

$$\bullet \nu_0 = \frac{1}{2\pi} \sqrt{\frac{\lambda_2}{\lambda_0}} = 0.9875 \text{ is the probabilistic number of zero crossing in a period of time;}$$

$$\bullet \nu_p = \frac{1}{2\pi} \sqrt{\frac{\lambda_4}{\lambda_2}} = 4.3014 \text{ is the probabilistic number of peak values in the time unit.}$$

•Lastly, $IF = \frac{v_0}{v_p} = 0.2296$ is the irregularity factor, that shows how much the process is not regular in the time unit.

One of the hypotheses in Narrow-Band method is to have an IF approximately next to 1. In the studied case, IF is really far from a unit value, but a Narrow Band calculation will still be made. Obviously, useless and not-realistic results could be expected.

Accordingly, to (38) which is the one for the Narrow Band damage $E[D_{NB}] = 1.9394 \cdot 10^{-10}$ and assuming 1 as a rupture limit, with NB life calculation $5.1563 \cdot 10^9$ cycles should be done to reach the rupture limit.

Remembering this is far too safe way to estimate a non-Narrow band damage so let's correct this value using Wrishing-Light coefficient, ρ_{WL} , that is equal to 0.8085, so the Wrishing-Light damage is $1.5680 \cdot 10^{-10}$ that gives $6.3774 \cdot 10^9$ cycles until rupture.

9 Oritz method

Like Wrishing-Light method, Ortiz [20] studied a coefficient that could correct NB results. First of all, he considered

Wöhler's parameters ($S N^k = C$) and he defined $h = 2 k$. Then we calculate:

$$\rho_0 = \sqrt{\frac{\lambda_2 \cdot \lambda_h}{\lambda_0 \cdot \lambda_{h+1}}} = 0.6190 \quad (41)$$

which is the coefficient used to correct Narrow-Band damage. Thus, $D_{Ortiz} = \rho_{WL} D_{NB} = 1:2005 \cdot 10^{-10}$ which gives $8.33 \cdot 10^9$ cycles until rupture.

10 Dirlik method

In 1985 Dirlik [3] tried to build a new approach to fatigue frequency analysis. He succeeded in approximating the $\rho_{RFC}(s)$ (i.e. the PSD of the amplitude of the considered cycles) using an exponential PDF and two Rayleigh PDF. His results are stored from (42) to (52) formulas:

$$\rho_{RFC}^{DK}(s) = \frac{1}{\sqrt{\lambda_0}} [\phi + \psi + \chi] \quad (42)$$

$$\phi = \frac{D_1}{Q} \cdot e^{-\frac{Z}{Q}} \quad (43)$$

$$\psi = \frac{D_2 Z}{R^2} e^{-\frac{Z^2}{2R^2}} \quad (44)$$

$$\chi = \frac{D_3 Z}{S} \cdot e^{-\frac{Z^2}{2}} \quad (45)$$

$$Z = \frac{s}{\sqrt{\lambda_0}} \quad (46)$$

$$x_m = \frac{\lambda_1}{\lambda_0} \sqrt{\frac{\lambda_2}{\lambda_4}} \quad (47)$$

$$D_1 = \frac{2 \cdot (x_m - \alpha_2^2)}{1 + \alpha_2^2} \quad (48)$$

$$D_2 = \frac{1 - \alpha_2^2 - D_1 + D_1^2}{1 - R} \quad (49)$$

$$D_3 = 1 - D_1 - D_2 \quad (50)$$

$$R = \frac{\alpha_2 - x_m - D_1^2}{1 - \alpha_2 - D_1 + D_1^2} \quad (51)$$

$$Q = \frac{1.25 \cdot (\alpha_2^2 - D_3 - D_2 \cdot R)}{D_1} \quad (52)$$

This model gives a $p_{RFC}(s)$ which depends on four spectral moments; in fact, and it is different from Whirling-Light method; now λ_1 comes into the previous formulas too. Invoking (53), that it has already been used to obtain damages from $p_{RFC}(s)$, Dirlik damage can be estimated (see (54)).

$$E[D_{RFC}] = v_a \cdot C^{-1} \cdot \int_0^{\infty} s^k \cdot p_{RFC}(s) ds \quad (53)$$

$$E[D_{RFC}^{DK}] = \frac{v_p}{C} \cdot \lambda_0^{k/2} \cdot \left[D_1 \cdot Q^k \cdot \Gamma(1+k) + (\sqrt{2})^k \cdot \Gamma\left(1 + \frac{k}{2}\right) \cdot (D_2 |R|^k + D_3) \right] \quad (54)$$

Many studies show that Dirlik method is the best to calculate fatigue damage.

Accordingly to Dirlik, damage is $7.3305 \cdot 10^{-18}$ on a maximum amount of 1.

Thus, 1.3642 1017 cycles can be made.

Notice that even if Dirlik method is the best one, it only works for Gaussian-defined processes.

We can show now a table (see Figure 12) with a resume the damage computed for each method:

	TIME DOMAIN			FREQUENCY DOMAIN		
	Miner	Hanshin Rotem	Narrow Band	Whirling-Light	Ortiz	Dirlik
Dmg. [%]	$1.054 \cdot 10^{-3}$	$6.323 \cdot 10^{-6}$	$1.939 \cdot 10^{-10}$	$1.568 \cdot 10^{-20}$	$1.200 \cdot 10^{-10}$	$7.330 \cdot 10^{-18}$
Cycles [N]	94'835	158'149	$5.1563 \cdot 10^9$	$6.3774 \cdot 10^9$	$8.33 \cdot 10^9$	$1.3642 \cdot 10^{17}$

Figure 12 Resume of results

Obviously, something must have gone wrong in frequency domain as the table 1 shows a difference of five orders of magnitude (even thirteen for Dirlik). This discrepancy cannot be caused by the software used (Matlab is the most reliable). Even the algorithms and material data used are correct. Books quoted in bibliography contains the mathematical demonstration of methods used and implemented in this paper.

11 EFFECT OF THE ASSUMPTIONS:

Until now, the process has been supposed to have a Gaussian-standard data-set. Is this a good hypothesis? A good way to verify the goodness of the approximation is to use the descriptive statistics. By computation of particular statistical parameters, the degree of adherence of a certain hypothesis (i.e. the Gaussian one) towards the problem under examination can be estimated.

A histogram is a plot that consists of columns, whose height is linked to the number of repetitions of a particular event. Chosen the casual variable on which the statistic will be made (in our case, the stress's range σ), the maximum and the minimum σ are searched. Then an approximation is chosen as $app = \sigma_{max} - \sigma_{min} / number$, where the denominator is decided by the user on basis of the user's own preferences.

The second step is to create classes: they will be in a number of numbers, in a wide of app , with a starting value of $app \cdot n$ (where $n \in [1; number - 1]$), with a center-value of $app \cdot (n + 0.5)$ (where $n \in [1; number - 1]$) and with an ending value of $app \cdot (n + 1)$, where $n \in [1; number - 1]$.

For each class it is necessary to count how many times an event is found in the data-set and what is the probability of finding that event. Lastly, a rectangle with an area proportional to the probability has to be built and plotted.

Sometimes a more powerful tool is used in order to show if data are truly distributed as a Standard Normal distribution. First of all, mean value and standard deviation are calculated from the data; then, using a software like Excel (or Mathcad, or Matlab, ...) we can calculate:

- First column: the data examined;

- Second column: how much is the probability to find the data in the first column if the data is distributed as a Gaussian distribution;
- Third column: the real probability to find the data in first column;
- Fourth column: the cumulate probability of the second column;
- Fifth column: the cumulate probability of the second column;

Now two plots may be created:

- The real probability and the Gaussian probability versus the data examined (i.e. Second column vs. first column plus third column vs. first column);
- The real cumulative probability and the cumulative Gaussian probability versus the data examined (i.e. Fourth column vs. first column plus fifth column vs. first column);

Now a control chart (called graph of Normal probability) can be generated. An interesting propriety of a Gaussian dataset is that a straight line can be generated if it is plotted in a particular way:

- On abscissas the data examined (in this case, the stress value σ);
- On Y axis, the z value that respect the equation $\Phi(z) = Fx(\sigma)$, where $Fx(\sigma)$ is the cumulative Gaussian probability and $\Phi(z)$ is the Gaussian normalized distribution.

If data are truly Gaussian, they lay onto a straight line characterized by an angular coefficient $m = 1/\sigma_{std}$ and a $q = \mu/\sigma_{std}$, thus $t(\sigma) = m \cdot \sigma + q$ is the straight line searched.

Lastly, if data seems to be not so different form the Gaussian straight line, a regression line can be estimated, whose m and q will be the new mean and standard deviation of a new (and more adherent) Gaussian curve. (Obviously it will be: $\sigma_{std} = 1/m$ and $\mu = q/m$).

Once the input signal has been statistically analysed, the real frequency domain analysis can start.

In statistics, a Q-Q² plot is a probability plot, which is a graphical method to compare two probability distributions by plotting their quantiles against each other.

First, the set of intervals for the quantiles is chosen. A point (x, y) on the plot corresponds to one of the quantiles of the second distribution (y-coordinate) plotted against the same quantile of the first distribution (x-coordinate). Thus, the line is a parametric curve with the parameter which is the number of the interval for the quantile.

The main step in constructing a Q-Q plot is calculating or estimating the quantiles to be plotted. If one or both of the axes in a Q-Q plot is based on a theoretical distribution with a continuous cumulative distribution function (CDF), all quantiles are uniquely defined and can be obtained by inverting the CDF. If a theoretical probability distribution with a discontinuous CDF is one of the two distributions being compared and some of the quantiles may not be define an interpolated quantile may be plotted. If the Q-Q plot is based on data, there are multiple quantile estimators in use. Rules for forming Q-Q plots when quantiles must be estimated or interpolated are called plotting positions. A simple case is where one has two data sets of the same size. In that case, to make the Q-Q plot, one orders each set in increasing order, then pairs them off and plots the corresponding values. A more complicated construction is the case where two data sets of different sizes are being compared. To construct the Q-Q plot in this case, it is necessary to use an interpolated quantile estimate so that quantiles corresponding to the same underlying probability can be constructed.

- If the two distributions being compared are similar, the points in the Q-Q plot will approximately lie on the line $y = x$.
- If the distributions are linearly related, the points in the Q-Q plot will approximately lie on a line, but not necessarily on the line $y = x$.

A Q-Q plot is used to compare the shapes of distributions, providing a graphical view of how properties such as location, scale, and skewness are similar or different in the two distributions. Q-Q plots can be used to compare collections of data, or theoretical distributions.

Q-Q plots are commonly used to compare a data set to a theoretical model, because they can provide an assessment of "goodness of fit" that is graphical, rather than reducing to a numerical summary.

As shown in Figure 13, data provided are not Gaussian. Furthermore, the less a value is, the more it is near to Gaussian line: this means that these values that causes fatigue damage are the biggest, and here they are all under the Gaussian (so, they will be neglected). Another discrepancy in using a Normal distribution can be seen if the PDF plot is zoomed in the high stress zone (Figure 14). In fact, the normal distribution is almost 0 over 50MPa, but the real PDF function is above the Gauss one. This mean that stress with value over then 50MPa are neglected, but they are the most dangerous!

Blue line in Figure 13 only depends on mean and variance of Gaussian. In facts, its parameters are calculated as:

$$m = \frac{1}{\sigma}$$

$$q = -m \cdot \mu = -\frac{\mu}{\sigma} \quad (55)$$

Someone could try to approximate the real distribution using a linear regression. If this way is followed, the result will be a new straight line (the black one in the graph) with an m and a q that will be linked to mean and variance of a new Gaussian curve. Lastly, this new Gaussian can be built as $N(-q/m, 1/m)$. Results are provided in Figure 14 and they show that even in this case, the Gaussian curve isn't a good choice for the given data-set.

To prove this point, the probability of finding a stress value between 50 and 150 MPa will be calculated. Using the normal distribution this probability is $1.36 \cdot 10^{-4}$, instead with the real PDF this probability is 0.011. The difference in this probability is the cause of the huge difference between the orders of magnitude in the results presented in table 1: neglecting all those stress value cause the big underestimation of the damage.

As presented in the previous section, the normal distribution is the most important cause of the failure of frequency analysis.

For every criteria used in this section will be described what has influenced the results.

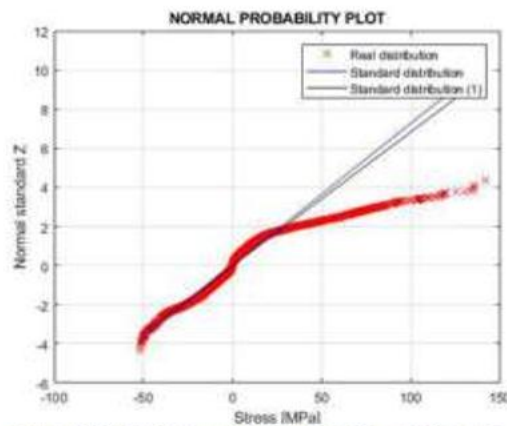


Figure 13 Q-Q plot for the input data-set and its regression curve

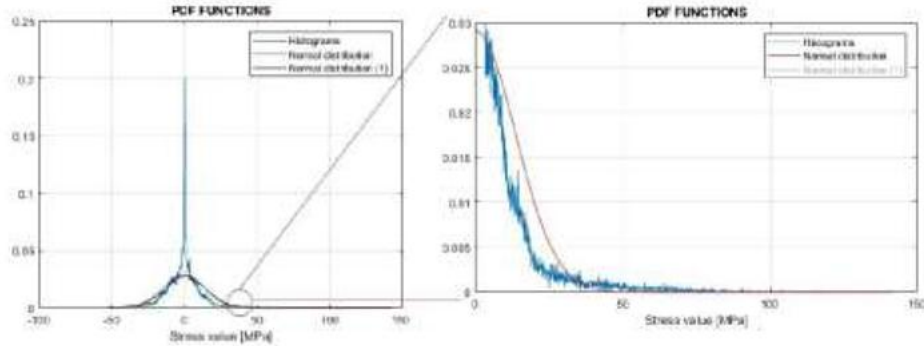


Figure 14 Gaussian approximation vs real process (2)

Narrow Band, Wriehing-Light and Ortiz are incorrect because of the two hypotheses of Normal distribution and $IF \approx 1$. In fact, as it can be seen in the previous section, stress distribution is not a normal one. Moreover, the irregularity factor is 0.2 which has made the Narrow Band criterion incorrect. However, approximating to 1 the IF is a “safety mistake” because the damage obtained is bigger than the real one. Wriehing-Light and Ortiz use the Narrow Band damage as a starting point to find the damage, so even these two criteria are incorrect.

Dirlik criteria could be used only if the distribution is a normal one. Moreover, Dirlik method neglects the effect of the mean stress. Furthermore, in this algorithm the PDF function can be found in an exponential equation, so the errors propagation is exponential (in fact, as it can be seen in table 1, there is a difference of thirteen orders of magnitude). This is a good method to use only under particular circumstances. It cannot be used in general analysis of damage.

In case of non-Gaussian loading stories, it is possible to identify three macro-areas that eliminate the normality of probability distribution:

- an external non-Gaussian excitation;
- a non-Gaussian response of the structure;
- a non-linear and Gaussian conduct of the material considered.

The study of these phenomena is particularly important because, as it has been previously shown in this work, if a non-Gaussian load history is treated in a Gaussian way, the calculated damage results much less than the one which would be generated in reality. In order to eliminate this too conservative estimate, it is useful to define the parameters of kurtosis and skewness, which can be obtained from the spectral moments of 3rd and 4th order by (17).

Among the major researchers of non-Gaussian random fatigue, Braccesi’s work is particularly important, as it calculates a coefficient to be multiplied to Gaussian damage to make it non-Gaussian. Let k_u be the kurtosis and s_k be the skewness.

First of all, if $\begin{cases} k_u = 3 \\ s_k = 0 \end{cases}$ the process is Gaussian. Otherwise, let $k\sigma$ be the inverse negative slope of Basquin equation. Then a coefficient named λ_{nG} can be written in a closed form as follow:

$$\lambda_{nG} = e^{\frac{\sqrt{k\sigma^2}}{\pi} \left(\frac{k_u - 3}{5} - \frac{s_k^2}{4} \right)} \quad (56)$$

Thus, if D_G is the calculated Gaussian damage and D_{nG} is the non Gaussian one,

$$D_{nG} = \lambda_{nG} \cdot D_G \quad (57)$$

For the process considered in this article, $k_u = 11:03$ and $s_k = 1:42$, so $\lambda_{nG} = 60:93$.

If a Narrow band process is supposed, the NB damage would be $1:9394 \cdot 10^{-10}$. Otherwise, the process is not a narrow band one, so Ortiz correction should be applied; a $1:2005 \cdot 10^{-10}$ damage will be expected. Lastly, the process is not Gaussian, so the real damage would become $7:3147 \cdot 10^{-10}$. The latter is a better result (because it is closer to the exact time-domain result), but lot of researches should be already done on this problem because the correction is too inaccurate.

12 CONCLUSION

In the last years, the study of random fatigue has been developed in a more efficient and precise way, also thanks to the power of computers. Random fatigue processes in frequency domain are faster and easier to study than time domain, because no counting methods are needed. In fact, in frequency domain, these methods are already included in formulas used to calculate the damage (38 for example, which contain in itself the Rainflow counting method). However, frequency domain methods have some strong hypothesis to verify.

Implementing this method could be an advantage for industries as additional software are not needed to process data. Implementing a Rainflow algorithm for time domain methods in Excel is very hard, instead a frequency analysis can be done with the same software because the calculation of FFT is the only complex mathematical operation required for this type of studies.

For example, to develop all the algorithm necessary to calculate the damage in time and frequency domain, Matlab has been used. This software requires more time to compute the time algorithm than the frequency one (about more than 4 times). Moreover, if a frequency algorithm is used, Matlab becomes useless because even Excel is capable of doing all the operations required.

On the other hand, a lot of attention is required in frequency analysis. A lot of restrictive hypothesis are made with this method. There are lots of random solicitations that have zero mean value and a Gaussian PDF (like wind, vibrations, etc...) but not all of mechanical components can be studied with this formulation. A wheel is a very common components and, in this work, the most common load history ("on road" situation) has been processed. This article is proof that a common load history (like the on road one) does not respect the hypothesis of Gaussianity. For this reason, corrective coefficients attested in scientific bibliography have been applied.

This paper proves that the coefficients presented in Bibliography ([1]) are a strong correction (about 60.93 times more) but this is not enough. Using a Gaussian distribution for a PDF when the real distribution is a leptokurtic

one is not a safe approximation. It has been proved that cutting all the high values of stress with a Gaussian distribution produces a very low damage. Even if the λ_{eG} is usually a good improvement for the results, in this situation it is not able to correct the data.

13 FUTURE DEVELOPMENTS

This article is the proof that a lot of experimentation and theoretical research must be done. The following steps are planned in order to give a more complete solution of fatigue analysis in frequency domain.

1. To improve the theory, the acquisition of more load histories is necessary. This article is only a starting point that is used to apply some methods coming from the literature to a real component. In this application has been proved a behaviour that doesn't fit with the expected data. This different behaviour has been explained and the solution is to improve the corrective coefficient. A good way to do so is to program a test matrix on different components under some different real history loads. It will be helpful to understand how to correct the current formulas.

2. For giving results close to reality mechanical tests on the wheel are needed. A better characterization will be obtained with a tensile test on the component. In fact, even if the wheel is made in S355, its proprieties are different from a generic S355 specimen. This happens because the material is bent and welded. Yielding value, ultimate tensile strength and elastic modulus are necessary for the analysis. Even a Wöhler curve is needed to obtain all the values that belong to the calculation of the damage.

3. After the wheel's characterization, it is necessary to execute the analysis in time and frequency domain for all the load histories. Seeing the difference between the two types of analysis is indispensable to study the effect of the non-Gaussianity contribute; after that, a better approximation of the coefficient $\ln G$ could be obtained experimentally.

4. At last, a verification of goodness of the models (time and frequency) is planned. It is strongly suggested to apply the same load histories to the wheel obtaining the real damage with on field measurement.

BIBLIOGRAPHY:

- [1] A. Carpinteri, A. Spagnoli, S. Vantadori, A review of multiaxial fatigue criteria for random variable amplitude loads, *Fatigue Fract. Eng. Mater. Struct.* (2017). <https://doi.org/10.1111/ffe.12619>.
- [2] Y.L. Lee, J. Pan, R. Hathaway, M. Barkey, *Fatigue testing and analysis*, 2005. <https://doi.org/10.1016/B978-0-7506-7719-6.X5000-3>.
- [3] T. Dirlik, *Application of computers in fatigue analysis* University of Warwick, University of Warwick, 1985.
- [4] M. Cima, L. Solazzi, Experimental and analytical study of random fatigue, in time and frequencies domain, on an industrial wheel, *Eng. Fail. Anal.* (2020). <https://doi.org/10.1016/j.engfailanal.2020.105029>.
- [5] S. Cima, M.; Rosa, *Analisi comparativa dei diversi metodi per lo studio della fatica random*, Università degli studi di Brescia, 2009.
- [6] C. Ronchei, *Sviluppo e applicazione di nuovi criteri per la verifica a fatica multiassiale di componenti strutturali in leghe di acciaio e alluminio*, Università degli studi di Parma, 2016.
- [7] A. Zehnder, J. Carroll, K. Hazeli, R. Berke, G. Pataky, M. Cavalli, A. Beese, S. Xia, *Fracture, Fatigue, Failure and Damage Evolution, Volume 8: Proceedings of the 2016 Annual Conference on Experimental and Applied Mechanics*, 2017. <https://doi.org/10.1007/978-3-319-42195-7>.
- [8] L.L. Schluter, H.J. Sutherland, *User's Guide For LIFE2's Rainflow Counting Algorithm*, Sandia Rep. (1991).
- [9] S.D. Downing, D.F. Socie, Simple rainflow counting algorithms, *Int. J. Fatigue.* (1982). [https://doi.org/10.1016/0142-1123\(82\)90018-4](https://doi.org/10.1016/0142-1123(82)90018-4).
- [10] Jack A. Collins, *Failure of Materials in Mechanical Design: Analysis, Prediction, Prevention*, 2nd Edition, 1993.
- [11] S.B. Clay, P.M. Knuth, Experimental results of quasi-static testing for calibration and validation of composite progressive damage analysis methods, *J. Compos. Mater.* (2017). <https://doi.org/10.1177/0021998316658539>.
- [12] L. Solazzi, Experimental and analytical study on elevating working platform, in: *Procedia Eng.*, 2017. <https://doi.org/10.1016/j.proeng.2017.09.364>.
- [13] L. Solazzi, N. Zmic, Design of a high capacity derrick crane considering the effects induced by load application and release, *J. Appl. Eng. Sci.* (2017). <https://doi.org/10.5937/jaes15-11930>.
- [14] Donzella G., Evaluation of the residual stress state in pressed discs by hole drilling method, (2011).
- [15] Z. Hashin, A. Rotem, A cumulative damage theory of fatigue failure, *Mater. Sci. Eng.* 34 (1978) 147–160. [https://doi.org/10.1016/0025-5416\(78\)90045-9](https://doi.org/10.1016/0025-5416(78)90045-9).
- [16] Z. Hashin, A. Rotem, A Fatigue Failure Criterion for Fiber Reinforced Materials, *J. Compos. Mater. - J. Compos. MATER.* 7 (1973) 448–464. <https://doi.org/10.1177/002199837300700404>.
- [17] M. Lancini, I. Bodini, D. Vetturi, S. Pasinetti, A. Mazzù, L. Solazzi, C. Petrogalli, M. Faccoli, Using vibration measurements to detect high wear rates in rolling contact fatigue tests, *Acta IMEKO.* (2015). https://doi.org/10.21014/acta_imeko.v4i4.237.
- [18] L. Solazzi, Wheel rims for industrial vehicles: Comparative experimental analyses, *Int. J. Heavy Veh. Syst.* 18 (2011) 214–225. <https://doi.org/10.1504/IJHVS.2011.040503>.
- [19] M. Decker, G. Savaidis, Measurement and analysis of wheel loads for design and fatigue evaluation of vehicle chassis components, *Fatigue Fract. Eng. Mater. Struct.* (2002). <https://doi.org/10.1046/j.1460-2695.2002.00593.x>.
- [20] S.B. P. Davoli, L. Vergani, S. Beretta, M. Guagliano, *Costruzione di Macchine 1*, McGraw-Hill Education, 2007.

- [21] A. M.E. De Paulis, *Costruzione di macchine. Criteri di base e applicazioni principali*, 2012.
- [22] A.M.P. De Jesus, R. Matos, B.F.C. Fontoura, C. Rebelo, L. Simões Da Silva, M. Veljkovic, A comparison of the fatigue behavior between S355 and S690 steel grades, *J. Constr. Steel Res.* (2012). <https://doi.org/10.1016/j.jcsr.2012.07.021>.
- [23] M. Matsuichi, T. Endo, *Fatigue of Metals Subjected to Varying Stress*, Proc. Kyushu Branch Japan Soc. Mech. Eng. 102 (1968).
- [24] International Scientific-technical Conference on Innovative Engineering Technologies, Equipment and Materials 2016 ({ISTC}-{IETEM}-2016), {IOP} Conf. Ser. Mater. Sci. Eng. 240 (2017) 11001. <https://doi.org/10.1088/1757-899x/240/1/011001>.
- [25] I. Versaillot, P. D.; Stratan, A. & Both, Effects of cyclic loading on the mechanical proprieties of steel, *Universitatea Politehnica Timisoara*, 2017.
- [26] N.R. Gates, *Fatigue Behavior under Multiaxial Stress States Including Notch Effects and Variable Amplitude Loading*, The University of Toledo, 2016.
- [27] C. Braccesi, F. Cianetti, L. Tomassini, Random fatigue. A new frequency domain criterion for the damage evaluation of mechanical components, *Int. J. Fatigue.* (2015). <https://doi.org/10.1016/j.ijfatigue.2014.07.005>.
- [28] J. Wijker, Random vibrations in spacecraft structures design, *Solid Mech. Its Appl.* (2009). https://doi.org/10.1007/978-90-481-2728-3_1.
- [29] L. Solazzi, C. Petrogalli, M. Lancini, Vibration based diagnostics on rolling contact fatigue test bench, in: *Procedia Eng.*, 2011. <https://doi.org/10.1016/j.proeng.2011.04.571>.
- [30] L. Solazzi, C. Petrogalli, M. Lancini, Rolling contact fatigue damage detected by correlation between experimental and numerical analyses, *SDHM Struct. Durab. Heal. Monit.* (2012). <https://doi.org/10.32604/sdhm.2012.008.329>.
- [31] ASTM, ASTM E1049 - Standard Practices for Cycle Counting in Fatigue Analysis, n.d.
- [32] R. Ulewicz, P. Szataniak, F. Novy, Fatigue properties of wear resistant martensitic steel, *Met. 2014 - 23rd Int. Conf. Metall. Mater. Conf. Proc.* (2014) 784–789.
- [33] F. Hlawatsch, F. Auger, *Time-Frequency Analysis*, Wiley, 2013. <https://www.wiley.com/en-it/Time+Frequency+Analysis-p-9781118623831>.
- [34] M. Mršnik, J. Slavič, M. Boltežar, Frequency-domain methods for a vibration-fatigue-life estimation - Application to real data, *Int. J. Fatigue.* (2013). <https://doi.org/10.1016/j.ijfatigue.2012.07.005>.
- [35] A. Preumont, *Random Vibration and Spectral Analysis/Vibrations aléatoires et analyse spectral*, 1994. <https://doi.org/10.1007/978-94-017-2840-9>.
- [36] A. Niesłony, E. Macha, *Spectral Method in Multiaxial Random Fatigue*, 2007. <https://doi.org/10.1007/978-3-540-73823-7>.
- [37] M. Laddomada, *Elaborazione numerica dei segnali*, 2007.
- [38] M. Butta, *L'elaborazione Numerica Dei Segnali Spiegata Ai Miei Nonni*, CreateSpace Independent Publishing Platform, 2016.
- [39] T. Irvine, *Estimating Fatigue Damage from Stress Power Spectral Density Functions*, (2014).
- [40] S.J. Orfanidis, *Optimum Signal Processing*, 2007.
- [41] P. Masani, Wiener's contributions to generalized harmonic analysis, prediction theory and filter theory, *Bull. Amer. Math. Soc.* 72 (1966) 73–125. <https://projecteuclid.org:443/euclid.bams/1183527586>.
- [42] V. Ricci, *Fitting distribution with R*, (2005).
- [43] L. Lutes, S. Sarkani, *Stochastic analysis of structural and mechanical vibrations*, in: 1996.
- [44] L. Lutes, M. Corazao, S. Hu, J. Zimmerman, Stochastic Fatigue Damage Accumulation, *J. Struct. Eng.* 110 (1984) 2585–2601. [https://doi.org/10.1061/\(ASCE\)0733-9445\(1984\)110:11\(2585\)](https://doi.org/10.1061/(ASCE)0733-9445(1984)110:11(2585)).
- [45] I. Rychlik, On the 'narrow-band' approximation for expected fatigue damage, *Probabilistic Eng. Mech.* (1993). [https://doi.org/10.1016/0266-8920\(93\)90024-P](https://doi.org/10.1016/0266-8920(93)90024-P).

ACKNOWLEDGEMENTS:

The authors of this work are willing to thank Eng. Bramè Giampietro of the company GKN Wheels for the information provided for the development of this research, Eng. Marco Bosio, and Eng. Federico Lio for the important activity done on this topic.

9. STUDY OF AN INDUSTRIAL RIM FA APPROACH

The present part of the work aims to study the fatigue life of a wheel rim for earth-moving vehicles through numerical finite element analyses. The study stems from the need of the *GKN Wheels* company to deepen the analysis of some breaks occurred along the radius of the fixed flange of the rim under study, named with the code 32519065. This rim's design has undergone a reduction in thickness from *11 mm* to *9 mm* in 2015. The thickest product was distributed in *105.000* pieces from 2012 to 2017 without showing any type of failure; the new product was initially sold in *68.000* units from 2012 and 2014 without presenting any problems. From 2015 the first fractures were found, which were equal to *58* until 2017 on a total volume of *23.500* rims supplied between 2015 and 2017. The study starts from the desire to be able to discover the influence of different parameters on the fatigue life of the rim. In particular, the following factors can be distinguished: tire inflation pressure, radial load and type of tire. In reality, other aspects could also be considered such as: the operating temperature, the variation in inflation pressure with the temperature and many others that are left to any future developments. Inflation pressure and radial load are redistributed on the flanges with different pressure conditions on the rim surface. The study started with the analysis of results obtained in static laboratory tests carried out on wheel rolling test machines. From these, a model of redistribution of the loads on the fixed flange, the critical area where the breaks were detected, was developed. This study was done first with just the inflation test, then also adding a radial load, considering two different types of tire: radial and bias. In particular, different load conditions have been studied in the finite element model in order to reproduce the results obtained in the laboratory as faithfully as possible. From the static results it was possible to proceed with the fatigue study. This saw a first part related to the choice of material and the fatigue curve and a second part related to the fatigue simulations performed with *SolidWorks Simulation*. At the end, there is a comparison between the different load conditions considered. The final comparison made it possible to give a first estimate of how much each factor affects the analysis results and how much the model developed from the data obtained in the laboratory can be used to have information on the fatigue life of the wheel rim. The principles described for the past works are used also in this one. Some recall will be presented in the following chapters.

9.1. Field tests

9.1.1. Test description

The field tests were held in China, in the “LiuGong Test Area”, and a wheel loader called “Liugong Wheel Loader GL850H” was used as a vehicle. A “Armour 23.5-25 16 PR L-3” tire with a diagonal configuration (*bias*) and an inflation pressure of 3,2 bar was mounted on the rim.

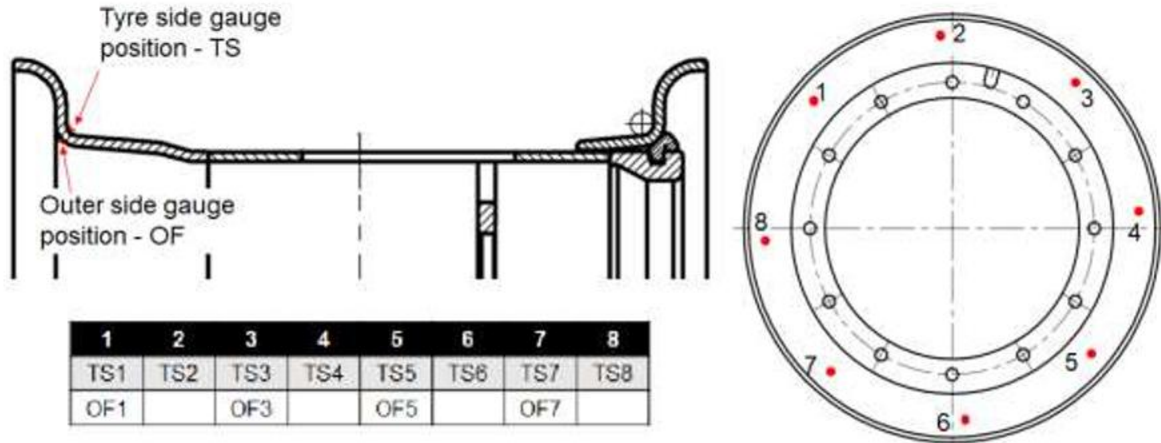


Figure 105 Strain gauge position on the rim during field tests.

The front-right rim has been instrumented with strain gauges of the type “HBM uniaxial grid 350Ω”, which are uniaxial strain gauges with resistance of 350 Ω. These were placed near the removable flange in symmetrical positions, as shown in Figure 105. In total, the strain gauges positioned were 8 on the external side (pneumatic side) and 4 on the internal side of the wheel. These were then connected to a data acquisition unit of the “Edaq lite 4 channels” type. The field test is composed by different tests (Table 11):

<i>Test</i>	<i>Description</i>	<i>Load type</i>	<i>Note</i>
1	Rehandling	Stones	
2	Circular motion without load	None	Slow movement with variation of the radius of curvature (small-medium)
3	Circular motion with load	5 tons standard load	20 km/h speed, medium radius of curvature
4	Figure of 8	5 tons standard load	
5	External circuit with braking at the first corner	5 tons standard load	
6	Off-road	5 tons standard load	
7	Figure of 8	5 tons standard load	Changed the connection of strain gauges, added an external strain gauge
8	Oval off-road	5 tons standard load	
9	Circular motion with stones	Stones	
10	Figure of 8 with stones	Stones	
11	Deflation from 3,2 bar	None	

Table 11 Descriptive table of field tests.

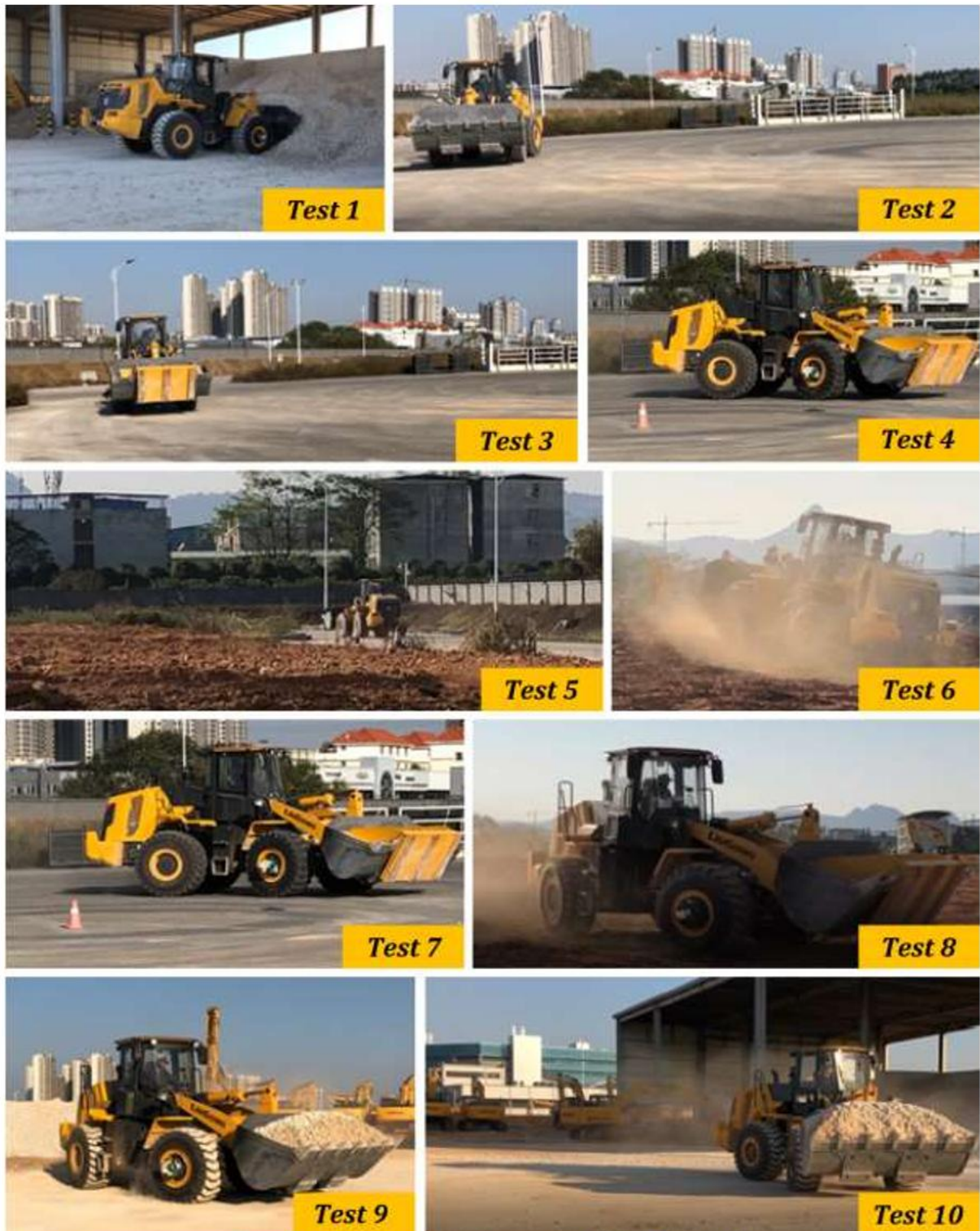


Figure 106 Images relating to the tests described in Figure 3.3.2

It can be seen from the table (Figure 106) how the types of tests are different in order to ensure that data on operations in different load conditions can be collected and the multiple conditions of use that can be found in reality are exhausted.

The strain gauges used in the various tests are reported in the table (Table 12):

<i>Test</i>	<i>Description</i>	<i>Ch1</i>	<i>Ch2</i>	<i>Ch3</i>	<i>Ch4</i>
1	REHANDLING	TS3	TS5	TS2	TS7
2	CIRCULAR MOTION WITHOUT LOAD – different radii of curvature	TS3	TS5	TS2	TS6
3	CIRCULAR MOTION WITH LOAD – 5 ton – 20 km/h – medium curve radius	TS3	TS5	TS2	TS6
4	FIGURE OF 8 LADEN – 5 ton – 20 km/h	TS3	TS5	TS2	TS6
5	EXTERNAL CIRCUIT WITH BRAKING AT THE FIRST CURVE LADEN	TS3	TS5	TS2	TS6
6	OFF-ROAD LADEN	TS3	TS5	TS2	TS6
7	FIGURE OF 8 LADEN - with an OF strain gauge (on the inside of the wheel)	TS3	TS5	TS2	OF5
8	OVAL OFF-ROAD LADEN	TS3	TS5	TS2	OF5
9	CIRCULAR MOTION WITH STONES	TS3	TS5	TS2	OF5
10	FIGURE OF 8 WITH STONES	TS3	TS5	TS2	OF5
11	DEFLATION FROM 3,2 bar	TS3	TS5	TS2	OF5

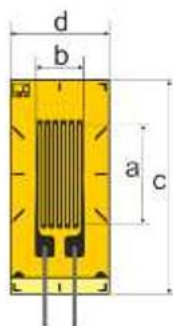
Table 12 Strain gauge channel table for each field test.

There are two different positions of the strain gauges: TS (*Tyre Side*), i.e. external position of the wheel (on the tire side), e OF (*Outside of Flange*), i.e. internal position of the wheel. The channels remain almost unchanged, with the exception of the fourth channel. In fact, in the first test there is a breakdown of TF7, which is replaced by TF6. The latter is replaced starting from test 7 with an OF strain gauge, in order to have information on the inside of the wheel.

9.1.2. Laboratory tests

The laboratory tests were carried out in the *Woodridge* (United States) laboratory by GKN technicians. In this structure, the wheel has been subjected to rolling test with radial load.

The rim has undergone several tests with the use of both radial and bias tires. In order to detect the stresses on the flange, strain gauges of the *HBM LY11-3/350* model were applied (Figure 107):



Characteristic	Quantity
Temperature range [°C]	From -200 to 200
Temperature range (self-compensation) [°C]	From -10 to 120
Grid length a [mm]	3
Grid width b [mm]	1,6
Stand length c [mm]	4,5
Stand width d [mm]	4,5
Measuring grid material	Constantan
Grate support material	Polyamide

Figure 107 HBM LY11-3/350 strain gauge and table of its technical characteristics

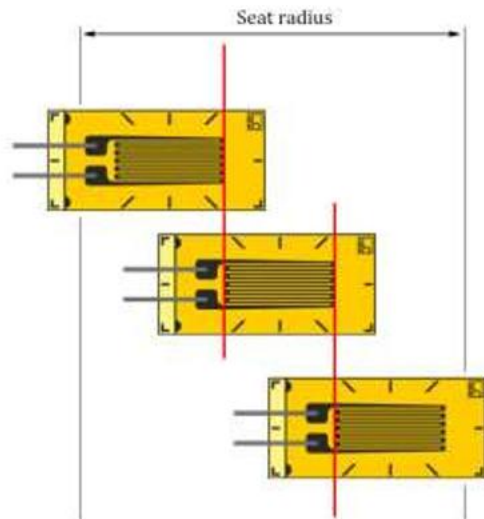


Figure 108 Representation of the methodology for arranging the strain gauges on the radius of the flange being studied.

These were placed on the radius of the flange, which is the most stressed area. In particular, the positioning was carried out starting from the centre of the beam (F2, F5, D2, D4) and then the adjacent strain gauges were placed as a continuation based on the size of the grid (Figure 108).

At the end, the following configuration is obtained (Figure 109) where the strain gauges indicated with *F* refer to the fixed flange and those with *D* to the detachable flange. The test sequence was the following for each type of tire:

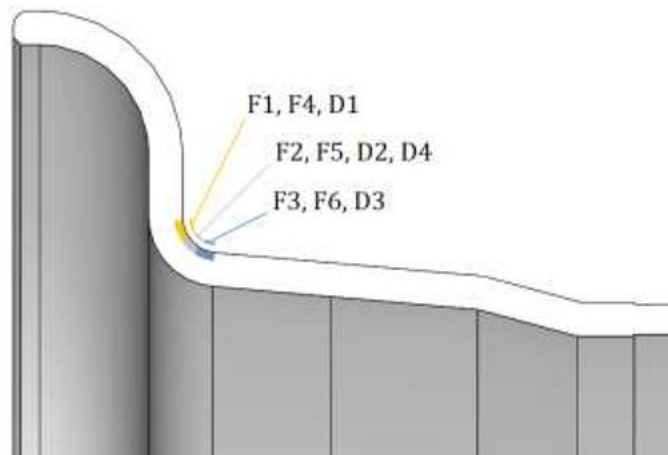


Figure 109 Qualitative representation of the positions of the strain gauges along the radius of the flange.

- application of the strain gauges as shown in Figure 108 on the seat radius surface both on the removable flange side and on the fixed flange one;
- strain gauges connection to the SOMAT E-DAQ Lite acquisition unit;
- strain gauges reset;

- inflation of the tire with detection of deformation measurements given by the strain gauges;
- application of stepped loads and detection of strain gauge data;
- deflation of the tire and verification of zero setting of the strain gauges.

This procedure was repeated for four pressure values: *2 bar*, *4 bar*, *6 bar* and *8 bar*, in order to detect a possible connection between the breakages that occurred during operation and the tire inflation pressure. The technicians started from the highest-pressure value and applied five different radial loads, respectively of *5.000 kg*, *7.500 kg*, *10.000 kg*, *12.500 kg* and *15.100 kg*, up to the test with *2 bar* where the test was concluded with a maximum applied load of *12.500 kg*.

9.1.3. Laboratory data analysis

The tests were carried out following the procedure indicated in the previous paragraph, even if the strain gauges data in positions F1 and F2 were lost due to malfunctions of the same during the test. The remaining data were grouped into graphs for the comparison and variation of the loads by dividing the results according to the type of tire: radial (Figure 110; Figure 111) or bias (Figure 112; Figure 113):

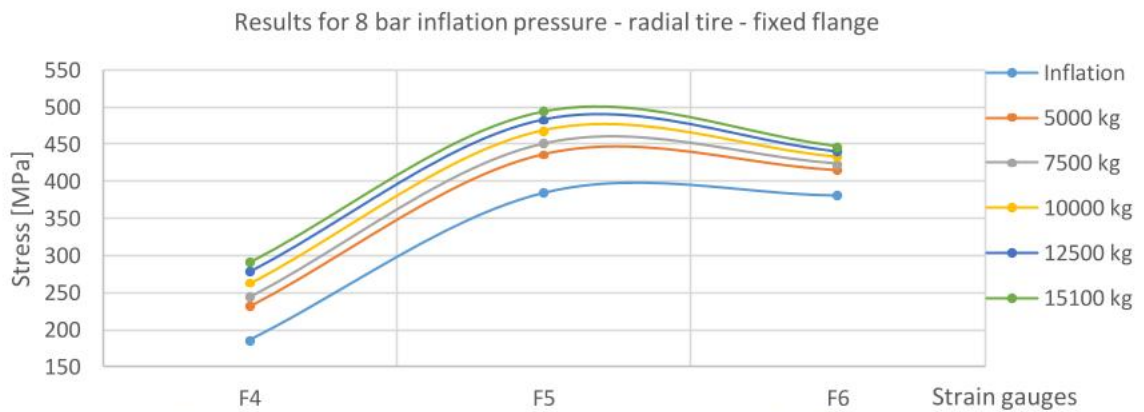
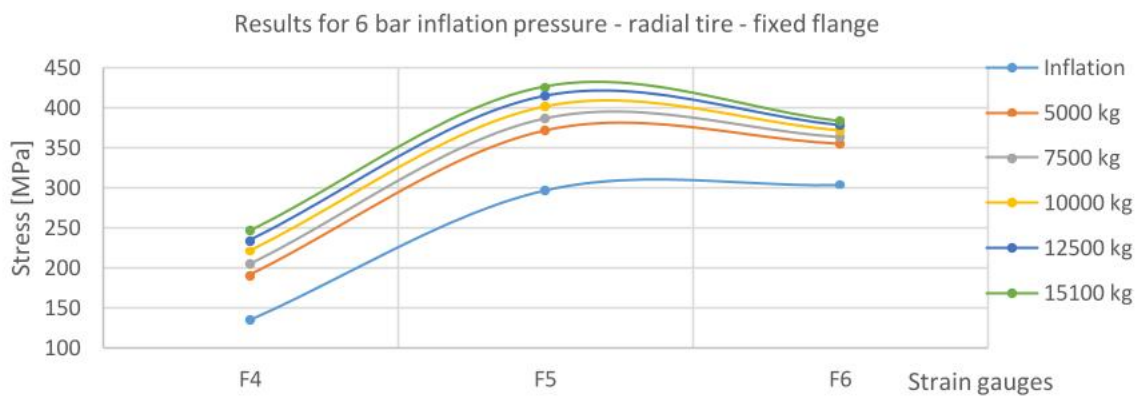
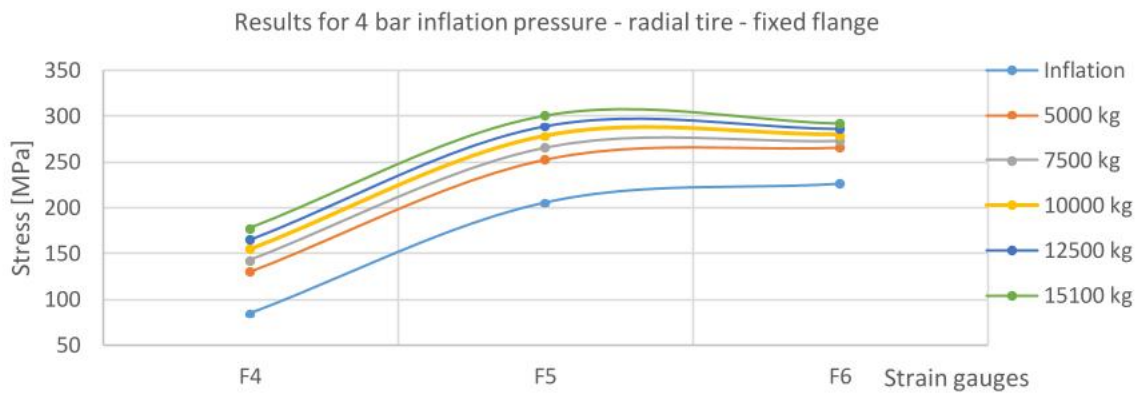
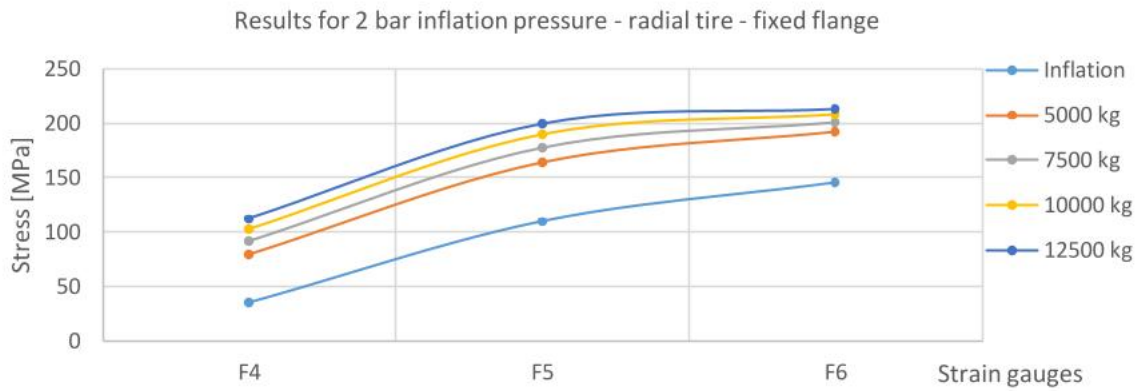


Figure 110 Graphs of the maximum values detected by the strain gauges on the fixed flange when using the radial tire

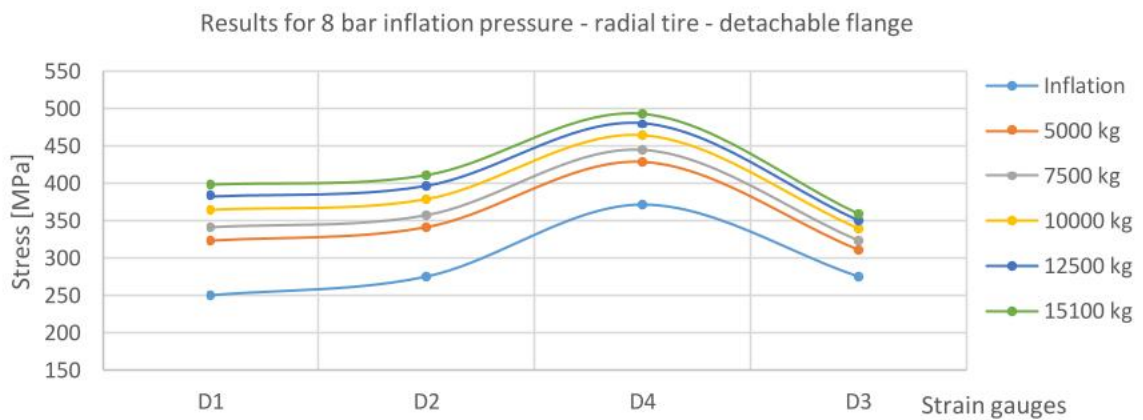
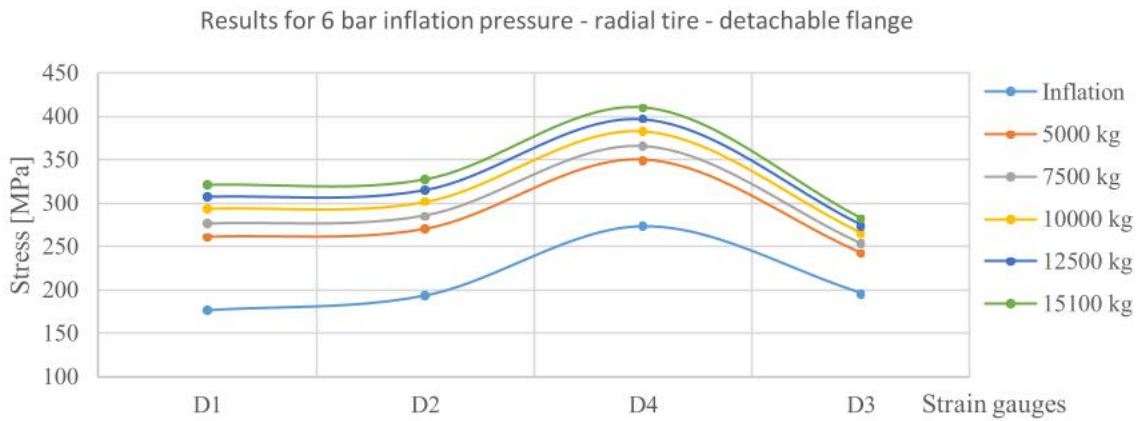
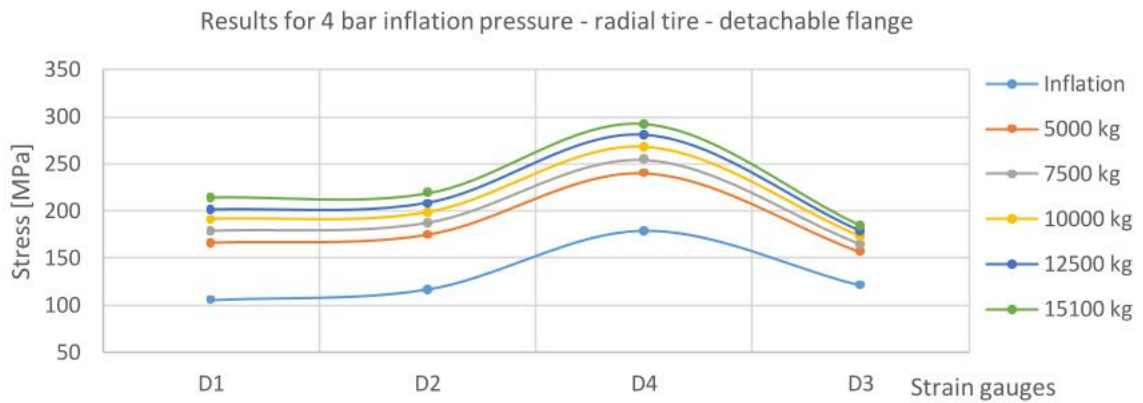
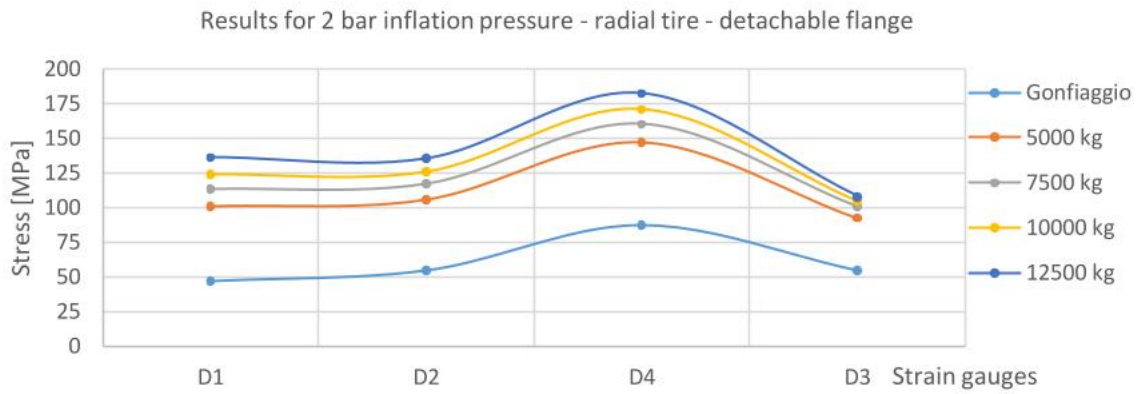


Figure 111 Graphs of the max values detected by the strain gauges on the removable flange when using the radial tire.

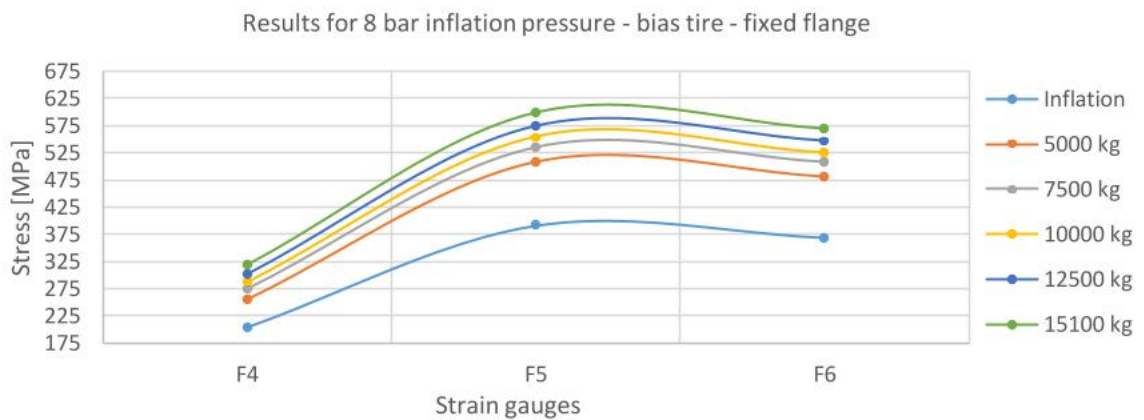
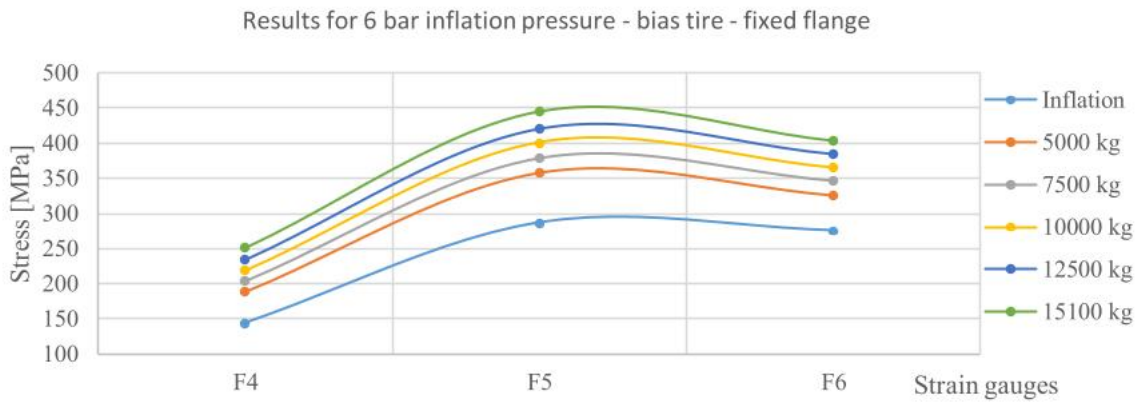
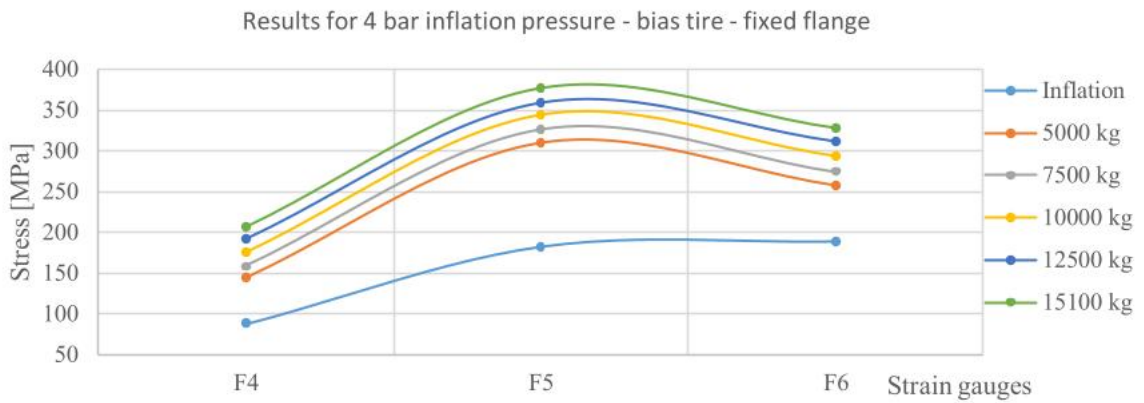
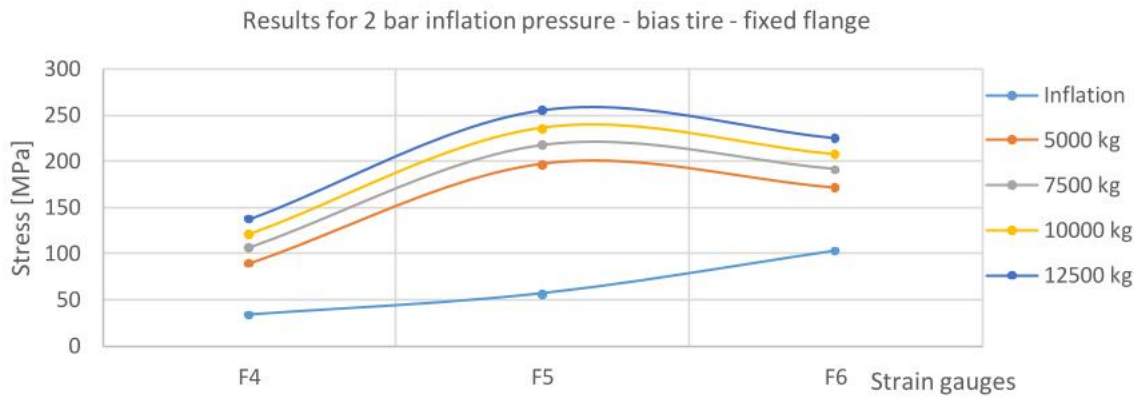


Figure 112 Graphs of the maximum values detected by the strain gauges on the fixed flange when using the bias tire.

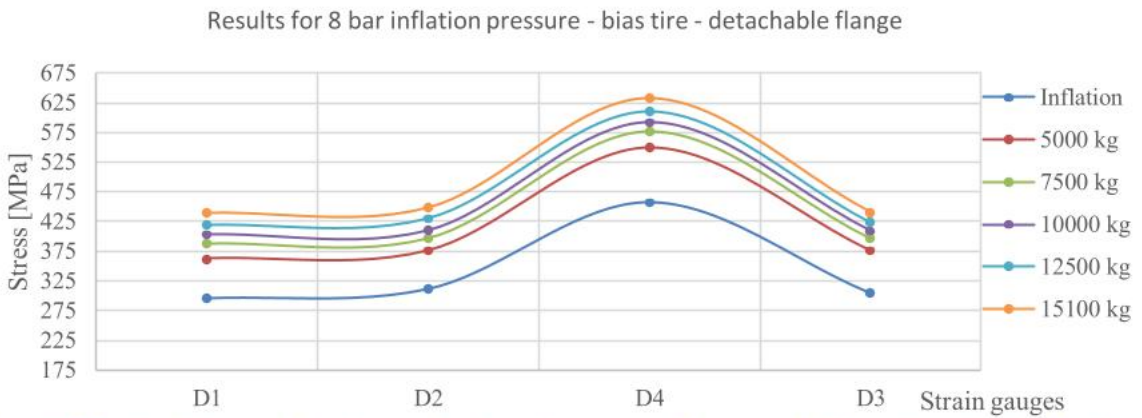
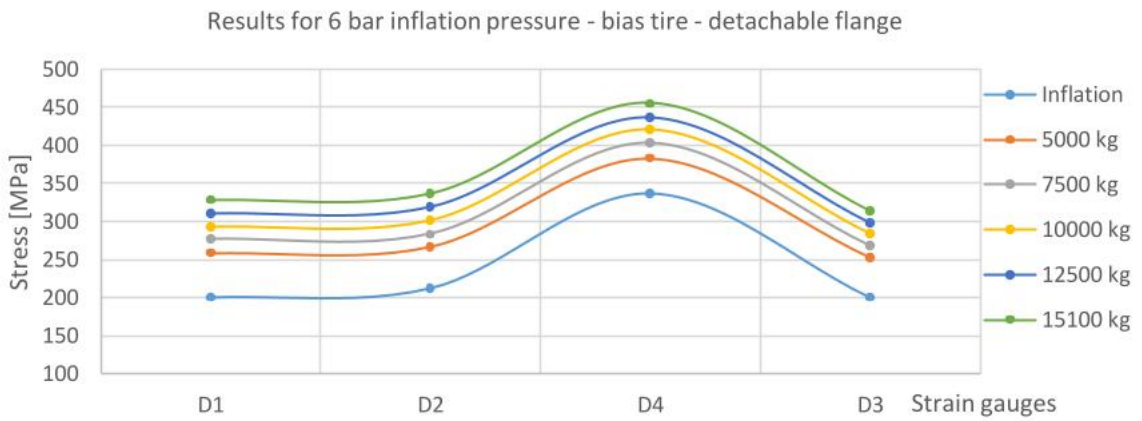
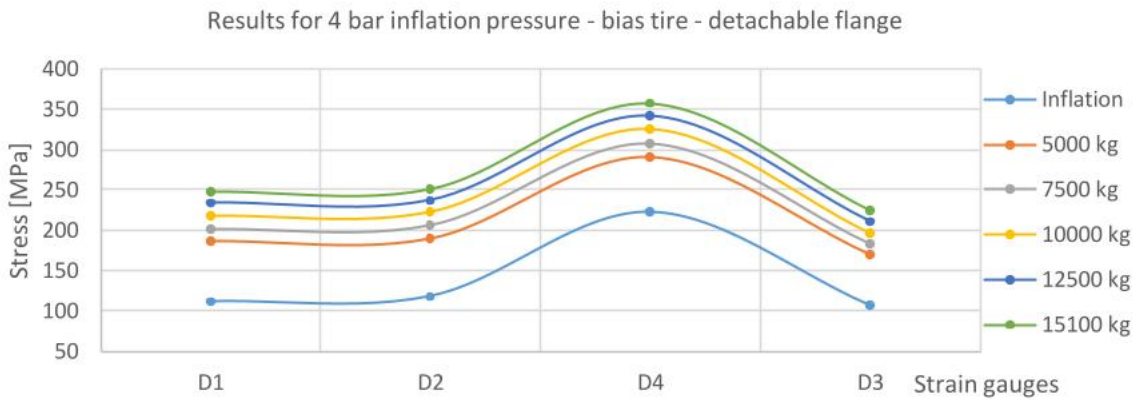


Figure 113 Graphs of the max values detected by the strain gauges on the removable flange when using the bias tire.

The linear decrease does not entail an equal trend in stress, as evidenced by the fact that the spacing between the curves of the graphs does not remain constant. The same behaviour is observed by keeping the inflation pressure constant and by changing the radial load, especially with heavy weights. Furthermore, from the comparison between the uses of a radial and a bias tire, it is possible to notice how the stresses of the strain gauges *F5* and *F6* are greater in the radial case than in the inflation tests. By keeping the pressure constant and increasing the radial load, it is possible to identify how the bias tire transfers a greater load to the flange, in particular to the fixed component. The latter is of particular importance, as it is the area where the breakages were found in operation. With reference to the fixed flange, it is noted that the radial tire stresses the position *F6*, while the bias stresses the position *F5*, demonstrating a different distribution of loads due to the configuration of the tire mounted on the rim.

9.2. Static study of the rim

9.2.1. Introduction

In this chapter, the static study carried out on the rim will be presented; the analysis focuses on the fixed flange, since it is the most critical part of the component. In fact, the highest stress as well as the failures of the component have been recorded in the seat radius area next to the fixed flange, as explained in *Chapter 9.1*. For this reason, even if the strain gauges used during the tests in Woodridge were placed on both the flanges of the rim, only the fixed flange data were analysed. The analysis was done with the *SolidWorks Simulation* function. As previously stated, the *SolidWorks Fatigue Analysis* functions work by processing the results of a static analysis, so the main aim of the static study was actually to reproduce within the simulation space stress distributions the most similar to the experimental ones so they could be processed in the fatigue simulations. From literature, the confirmation that many FE softwares, such as ANSYS, need a static stress distribution in order to perform fatigue analyses was found [19]. Moreover, regardless of the type analysis meant to perform, static simulations are always executed on the tire model as a preliminary evaluation of the load capacity of the component as well as the mesh refinement needed [20]. However, this study also allowed us to deepen our knowledge of the forces exchanged between tire and rim flange. In this chapter, the experimental data, the rim 3D model, the constraint and load conditions will be described. Every FE test performed has been compared to the experimental results in order to improve the finite elements model and to obtain the most accurate fatigue analysis possible. Following the results of experimental tests, the FE simulations have been divided into inflation simulations and both inflation and radial load simulations. In the first set of tests, the contact pressure on the flange due to inflation only has been evaluated, while both the effects of inflation and radial load on the pressure distribution have been studied in the second set of tests.

9.2.2. Inflation tests

9.2.2.1. Experimental data

In this section, the results of the experimental inflation tests are presented. They were needed to develop and verify the models of interaction between tire and rim; they have already been discussed (Table 12):

INFLATION EXPERIMENTAL DATA

201_Radial_Tire_Inflation_Run1										
Inflation P	STRESS [MPa]									
	F1	F2	F3	F4	F5	F6	D1	D2	D3	D4
2 bar	Lost	Lost	37,3	36,0	109,8	145,7	47,0	54,7	54,2	87,4
4 bar	Lost	Lost	107,0	84,5	205,5	225,9	105,7	116,9	121,4	178,6
6 bar	Lost	Lost	178,6	135,1	296,5	304,0	177,1	193,3	196,0	274,0
8 bar	Lost	Lost	250,2	185,9	384,6	381,2	250,6	275,3	274,8	371,7

104_Bias_Tire_Inflation_Run4_ReCal_Repair										
Inflation P	STRESS [MPa]									
	F1	F2	F3	F4	F5	F6	D1	D2	D3	D4
2 bar	Lost	55,5	32,6	33,9	56,6	103,4	32,9	33,1	11,3	96,6
4 bar	Lost	150,3	120,9	88,1	181,7	188,3	111,9	118,3	106,9	223,2
6 bar	Lost	245,5	211,9	144,4	286,7	275,3	200,3	211,5	200,8	337,2
8 bar	Lost	347,3	310,0	202,9	391,0	367,5	296,6	311,4	304,9	456,5

Table 12 Experimental results from Woodridge laboratory tests.

As shown in the tables, F1 and F2 strain gauges data were lost during the test of the radial tire, so these two sets have been excluded from the analysis of the bias tire as well. The inflation pressure was increased linearly in the different tests; as can be noticed in Figure 114, the seat radius stress increases linearly as well, even though with different slopes depending on the seat radius areas.

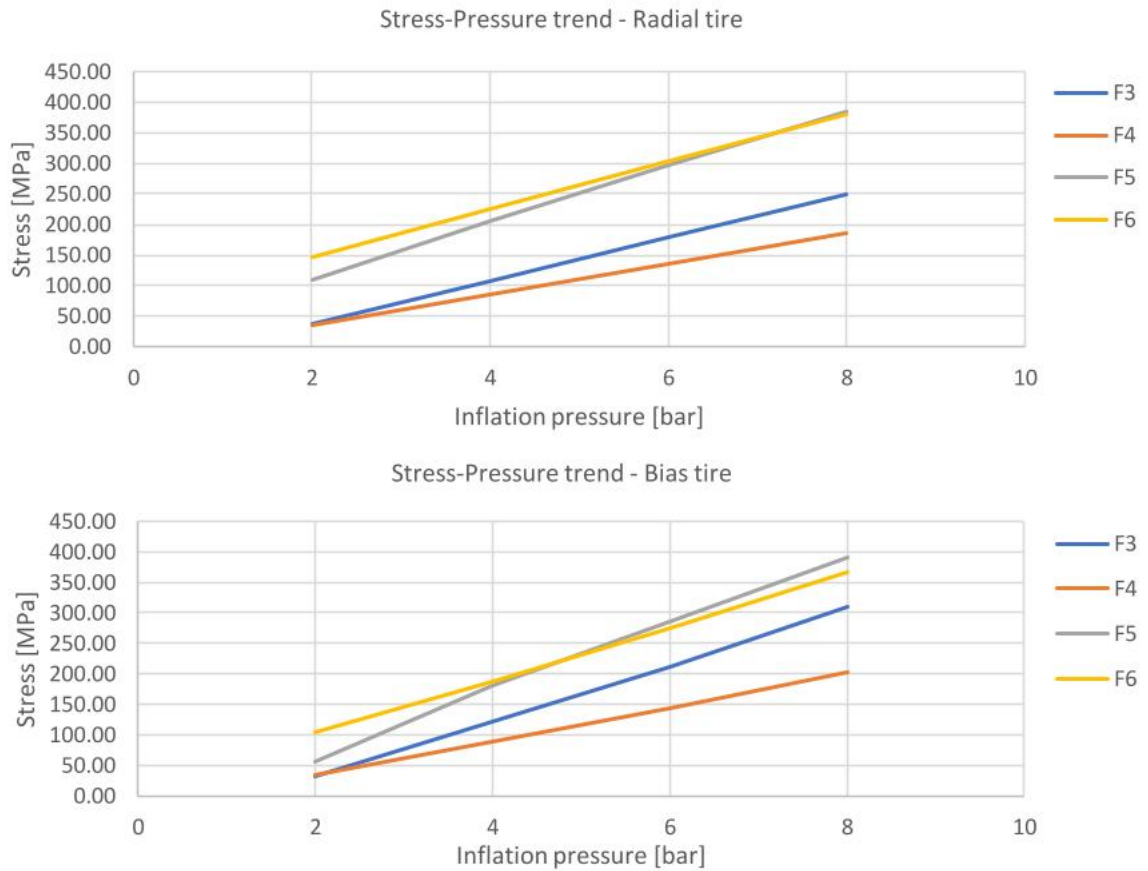


Figure 114 Stress – pressure trend from the experimental results. As visible, the increase of the radius stress is linear for all the areas studied. The stress pressure ratio, however, changes depending on the radius area.

9.2.2.2. Stress component considered

The strain gauges used during the tests are uniaxial gauges, so the stress measured is uniaxial as well. In particular, the component of the stress measured by the gauges is parallel to the surface of the rim and contained into the y-z plan as shown in Figure 115:

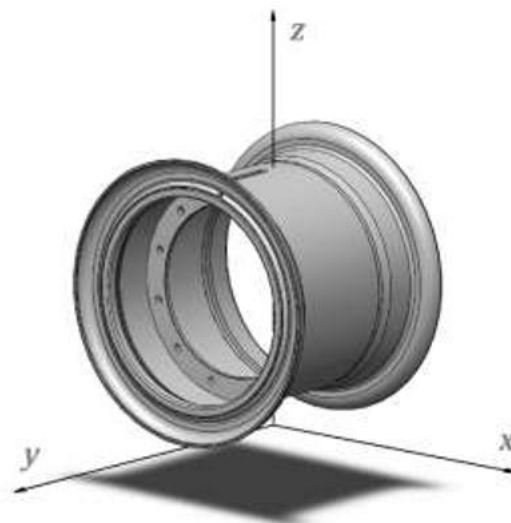


Figure 115 Reference system applied to the rim 3D model

SolidWorks Simulation does not allow extrapolating the values of the stress resulted from an analysis along a generic direction, but it gives the results of the stress parallel to the fixed reference system only and a few other stress definitions such as Von Mises stress and maximum main stress called P1. As a result, it was not possible to extrapolate from the analysis the stress parallel to the surface; it had to be used instead a different definition of stress as an approximation. In order to choose the best stress definition to approximate the surface parallel stress, a specific study on the fixed flange with the following settings and properties was carried out (Figure 116):

MATERIAL					
Property	Value	UM			
Elastic module (E)	200.000	MPa			
Poisson coeff. (ν)	0,29	MPa			

MESH		
Nodes number	78.909	
Elements number	38.923	

CONDITION	TYPE	APPLICATION AREA	VALUE	UDM
Constraint	Fixed	Drilled disc for axle shaft coupling	/	/
Load	Pressure	External rim surface (tire side), bead seat included	0,2	MPa
Load*	Pressure*	Radial surface of both the fixed and detachable flanges	4,96	MPa
Load	Pressure	Seat radius of both fixed and detachable flanges	0,2	MPa

DATA FOR THE CALCULUS OF *			
Tire	Radius	806	mm
Rim	Flange radius	326,21	mm
Rim	Flange height	16,79	mm
Pressure	Inflation	2,00	bar

Figure 116 Simulation parameters applied in the FE model for the comparison among the different definitions of stress.

The mesh has been thickened in the flange area in order to get more reliable results (Figure 117):

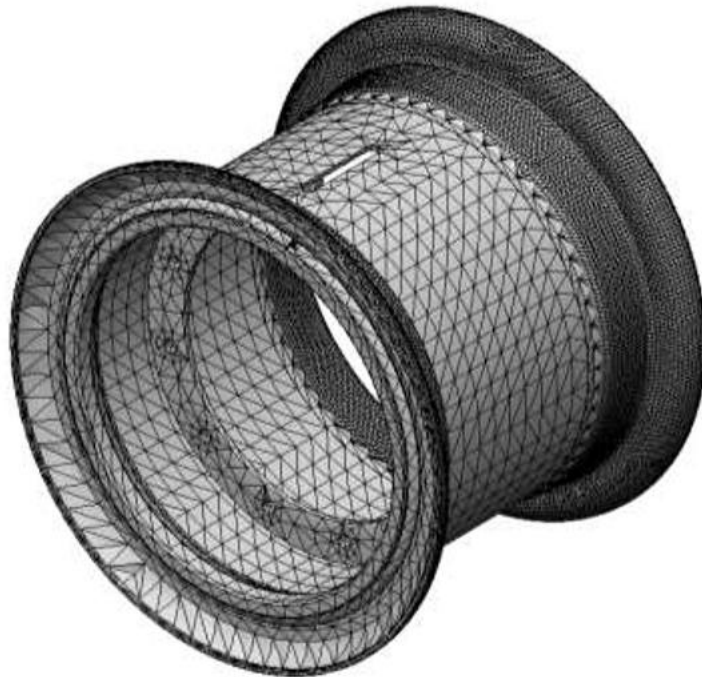


Figure 117 Mesh used for the study on the stress definition comparison.

A linear reference system centred at the end of the flange has been set (Figure 118):

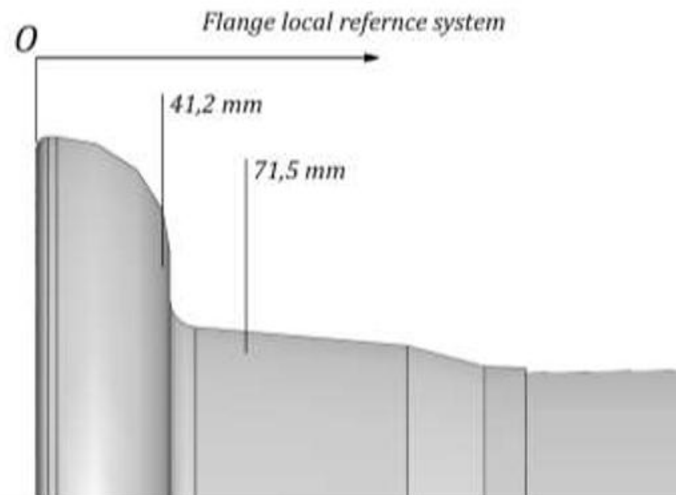


Figure 118 Linear reference system centred on the edge of the flange. The extremes of the study domain are also shown.

The analysis with the setting shown above has been carried out; the results obtained by defining the stress with Von Mises, with the main stress P1 and with the uniaxial stress have been compared in order to evaluate the best approximation. For the latter case, the study has been more complex, as the uniaxial stress parallel to the component surface cannot be automatically obtained from the software.

In fact, the *SolidWorks Simulation* function only allows extrapolating stresses parallel to geometrical objects like axes. For this reason, separation lines had to be created on the flange as a reference to build local axes parallel to the rim surface. The local axes have been used to obtain the uniaxial stress in each area of the discretized flange. The results comparison is shown in Figure 119:

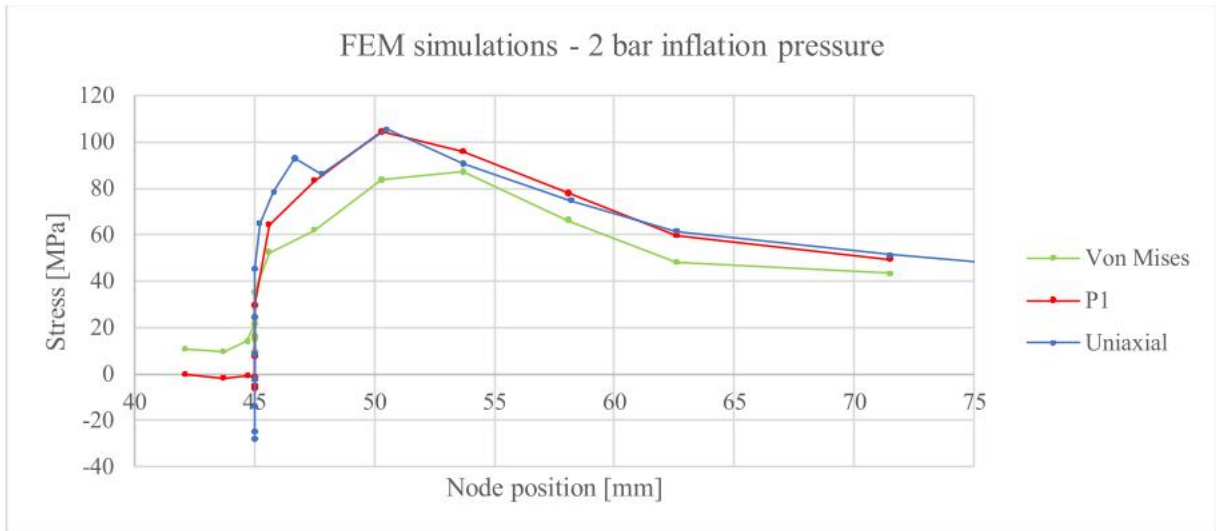


Figure 119 Comparison of the results from the FEA simulation of the 2 bar inflation configuration obtained considering different stress definitions on the nodes of the fixed flange.

It can be noticed that the P1 main stress gives a good approximation of the uniaxial results, especially with regard to the most critical area that is the seat radius area. Following these assessments, it has been decided to use P1 main stress to approximate the uniaxial stress of the flange area in the following simulations as well.

9.2.2.3. Automotive theory-based analyses

9.2.2.3.1. Introduction to automotive theory-based analyses

In this paragraph, the first analyses carried out to evaluate the forces exchanged between tire and rim are presented. These analyses are based on the automotive theory formulas. Following these relations, the axial load applied to the flange by the tire can be estimated as follows:

$$P_f = \frac{W_p}{2 \cdot 2 \cdot \pi \cdot r_f \cdot h_f} = (a^2 - r_f^2) \frac{P_0}{4 r_f \cdot h_f} \quad [N/m^2] \quad 9-80$$

Where a is the tire radius, r_f is the average radius of the circular crown identified by the vertical wall of the flange and h_f is the height of the vertical wall of the flange. From a wider point of view, both the rim flange and the bead seat should be loaded to perform a more complete analysis. According to the literature and to comparisons between numerical computing and experimental campaigns, the ratio of the flange load to the bead seat one is

considered to vary depending on the contact conditions at the tire-rim interface. This is influenced by the type of tire, the inflation pressure, the reinforcement of the composite materials and by the design of the rim [21]. However, in this model, a simplification has been applied and the load on the bead seat has been neglected.

The rim parameters have been extrapolated by the rim design, while the tire radius has been supposed following catalogues of tire manufacturers (Table 13):

OBJECT	GEOMETRY	VALUE	UM
Tire	Radius a	806	mm
Rim	Radius r_f	326,21	mm
Rim	Height h_f	16,79	mm
Pressure	Inflation pressure P_0	2 – 4 – 6 – 8	bar

Table 13 Tire and rim dimensional parameters used in the simulations.

The mesh has been thickened in the fixed flange area both inside and outside the rim in order to obtain more accurate results.

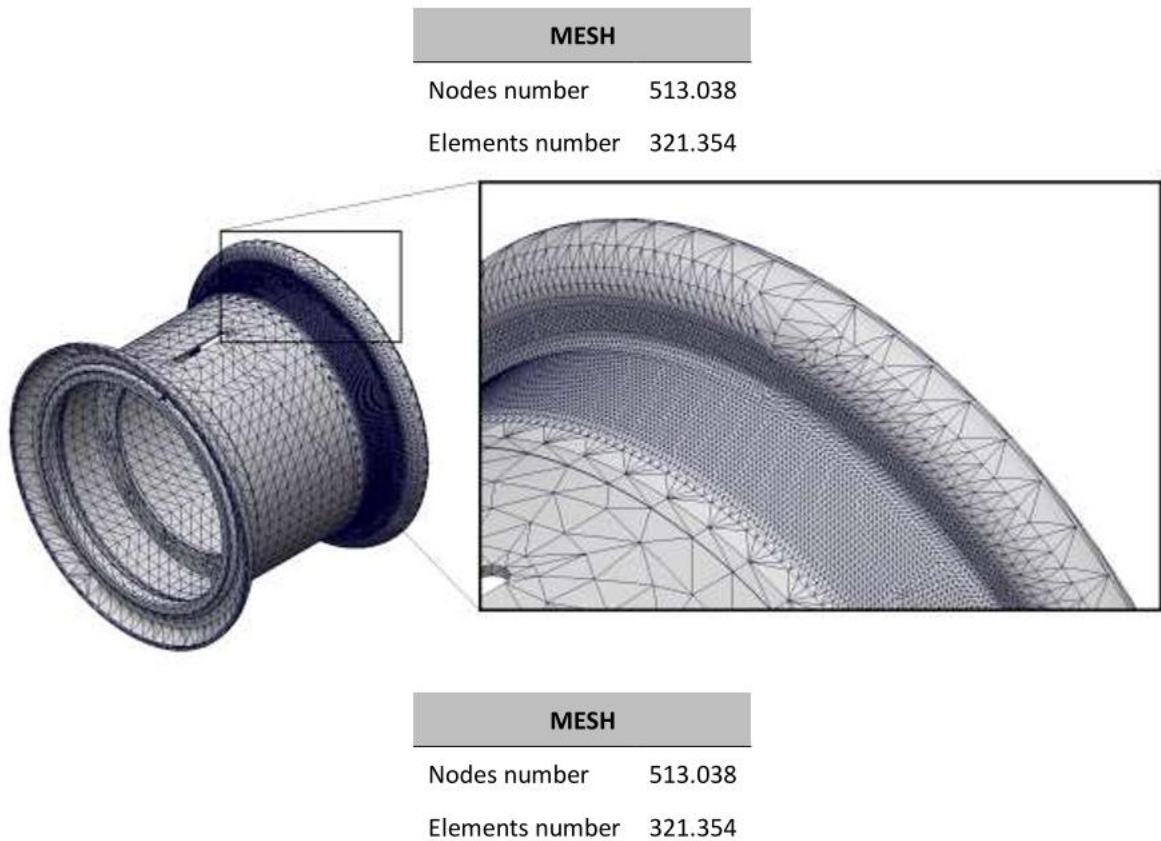


Figure 120 Mesh applied to the rim 3D model in the FE simulations (above) and mesh parameters (below). The minimum dimension of the nodes, equal to about 3,7 mm, is applied in the critical seat area.

Load conditions are different for each analysis and will be described case by case, except for the pressure on the lateral cylindrical surface of the rim, which is equal to the inflation pressure (Figure 121).



Figure 121 Pressure applied in the simulations on the lateral surfaces of the rim. The pressure is set equal to the inflation pressure.

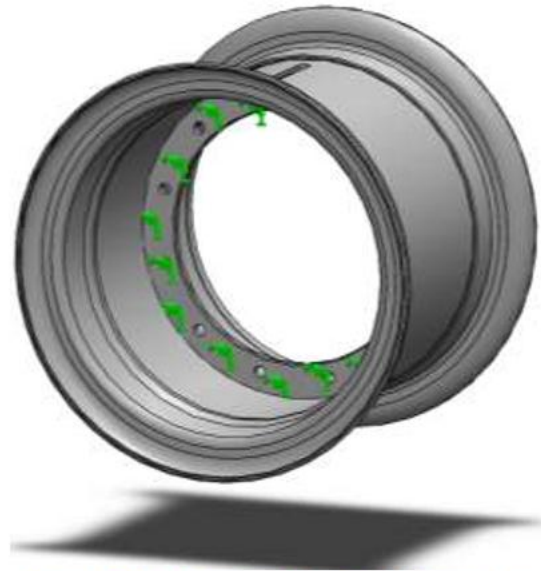


Figure 122 Fixed constraint applied to the coupling surface between rim and axle shaft.

In each numerical simulation, a fixed constraint has been applied on the drilled disc surface, in order to reproduce the coupling with the vehicle's axle shaft (Figure 122). For these analyses as well, a reference system centred in the end of the flange was designed.

Particular attention was paid to the area identified by the following axial dimensions (Figure 123):

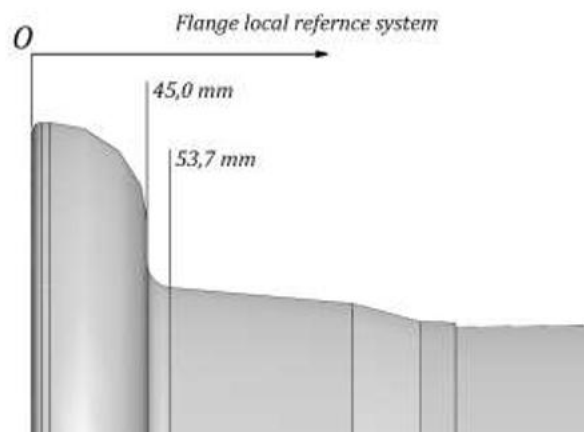


Figure 123 Dimensions corresponding to beginning and end of the seat radius, following the reference systems defined in Figure 118

The strain gauges position in the reference system shown above have been assumed as follows (Table 14):

STRAIN GAUGES POSITION			
ZF4 [mm]	ZF5 [mm]	ZF6 [mm]	ZF3 [mm]
45,00	46,29	49,42	53,67
46,29	49,42	53,67	56,67

Table 14 Axial dimensions corresponding to the positions of the strain gauges following the reference system shown in Figure 118

9.2.2.3.2. 1st analysis: application of p from automotive th

In the following analyses, load conditions are obtained directly from the theory introduced previously. In this way, as the inflation pressure varies, the following pressures applied to the vertical walls of the flange are obtained (Figure 124):

RADIAL TIRE	
Inflation pressure [bar]	Pressure on the flange [MPa]
2	4,96
4	9,92
6	14,88
8	19,84

Figure 124 Pressures (above) applied on the vertical surface of the fixed flange (below). This distribution refers to the supposed load configuration produced by a radial tire on the rim flange.

It can be noted that the load condition varies linearly with the inflation pressure. The results of the analysis, which will be shown later, are quite close to the experimental measurements from the radial tire, so the load configuration predicted by the automotive theory has been considered valid without need for any corrective coefficient. For the bias tire, on the other hand, a coefficient k was needed to get a good match between numerical results and experimental data. The different design of the bias tire causes, in fact, a different stress distribution on the flange as well, so the k coefficient can be considered as an evaluation of the effect of the design of the tire on the stress curve. The k coefficient can be obtained from the comparison of the experimental data and can be defined as:

$$k = \frac{\sigma_{F6_radial}}{\sigma_{F6_bias}} = \frac{226}{188} = 1.202 \quad 9-81$$

Where σ_{F6_radial} is the stress detected at 4 bar by the strain gauge F6 on the radial tire, while σ_{F6_bias} is stress measured at 4 bar by the same strain gauge on the bias tire. A reference pressure value of 4 bar was chosen since it is close to the inflation pressure recommended in the tire data sheet, equal to 3,2 bar.

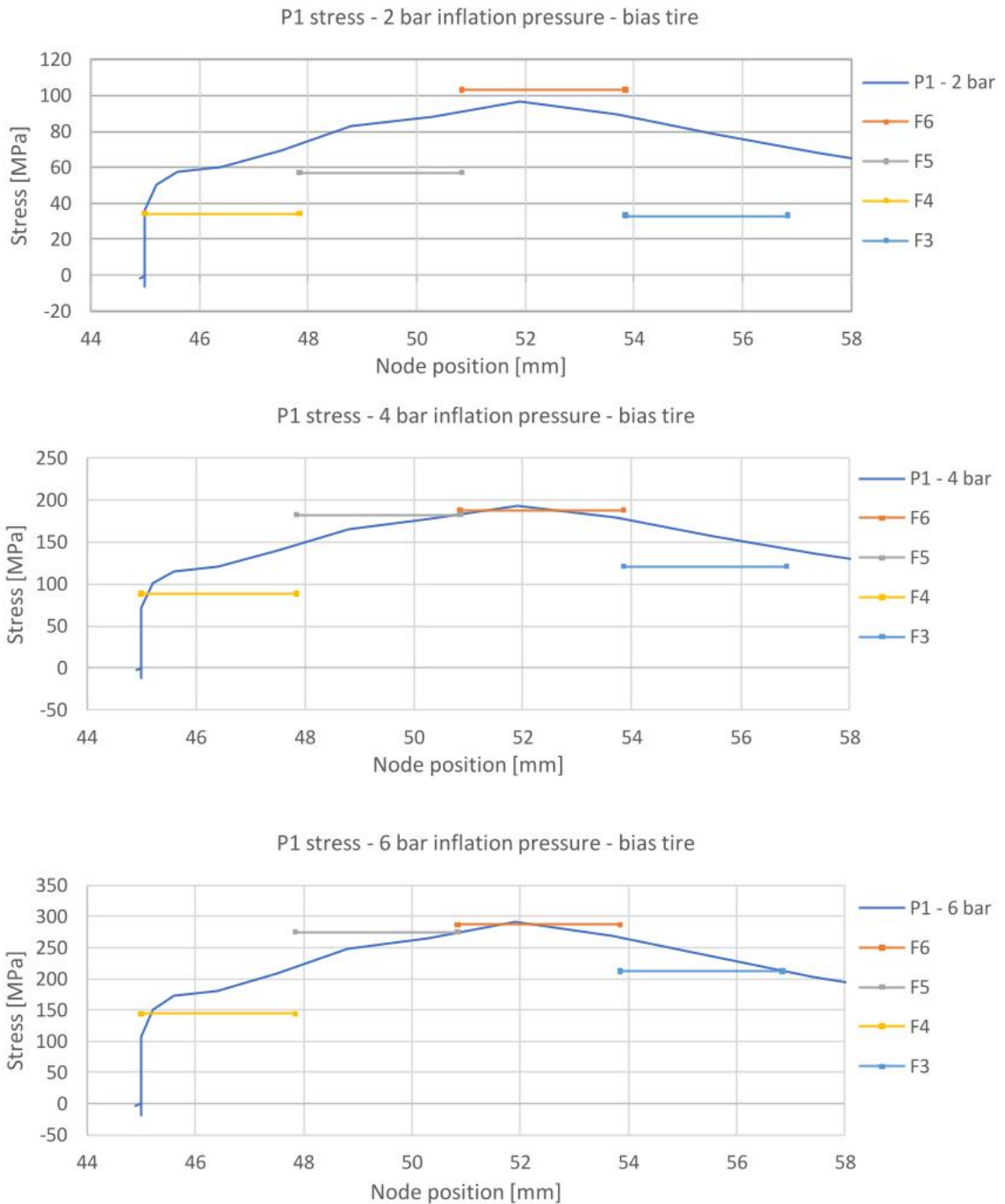
As stated above, the k coefficient considers the different type of tire used in the test; by applying this coefficient, the following load conditions are obtained for the bias tire (Figure 125):

BIAS TIRE	
Inflation pressure [bar]	Pressure on the flange [MPa]
2	4,13
4	8,25
6	12,38
8	16,51

Figure 125 Pressures applied in the simulations on the vertical surface of the rim flange for the load condition of the bias tire.

The graphs below compare the results of the numerical simulation of the load pressure reported above and the experimental data from the laboratory tests for each combination of tire design and inflation pressure. As visible, the experimental values are not matched to a single coordinate, but rather to an interval which consider both the actual dimensions of the strain gauges and any possible inaccuracy due to manual application on the rim.

The comparison of the results for the bias tire is reported below (Figure 126):



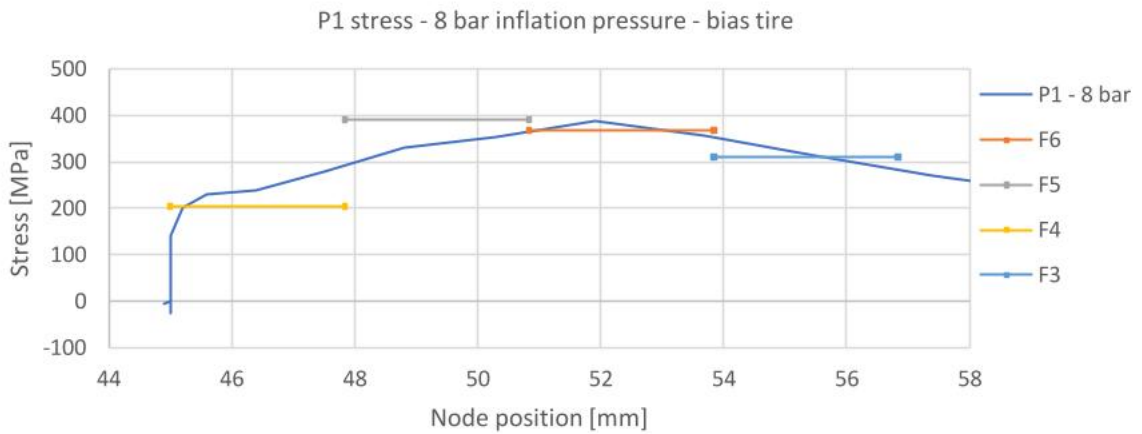
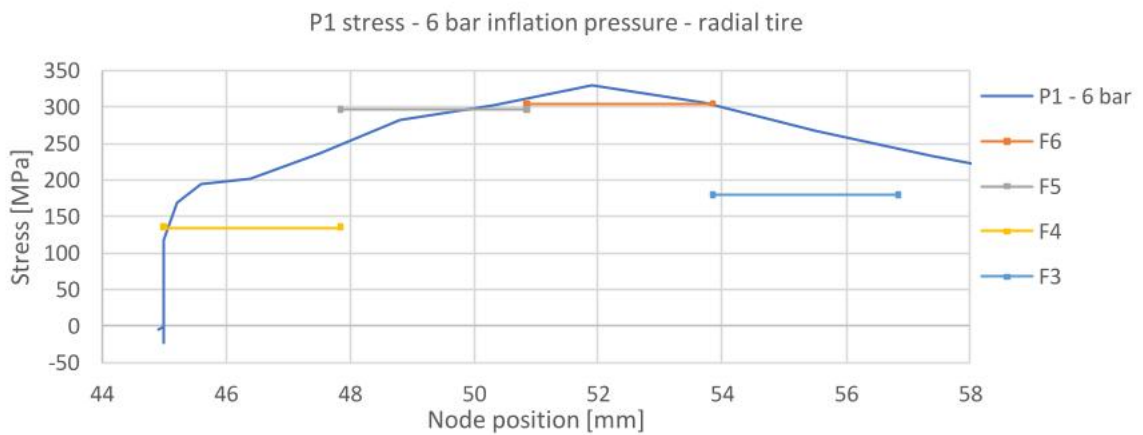
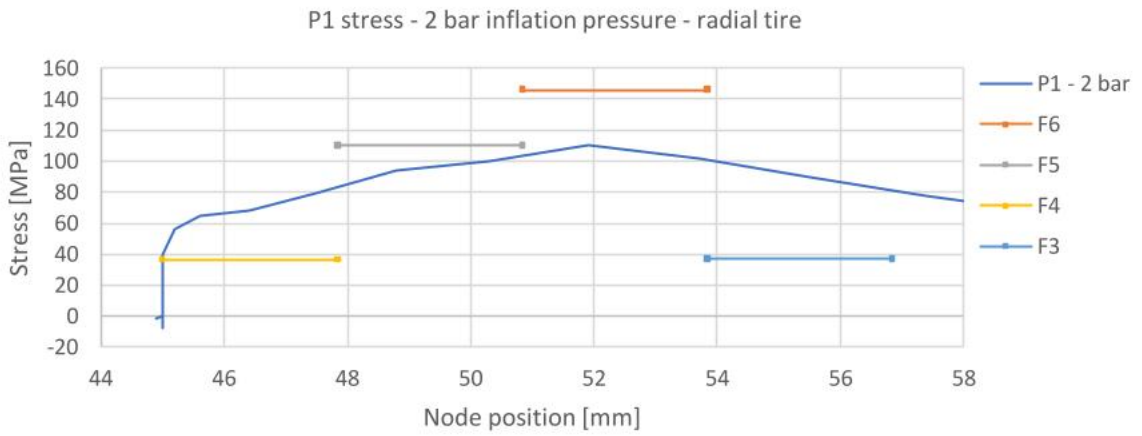


Figure 126 Comparison between the numerical results from FE simulations and experimental results for the bias tire.

The comparison for the radial tire is shown below (Figure 127):



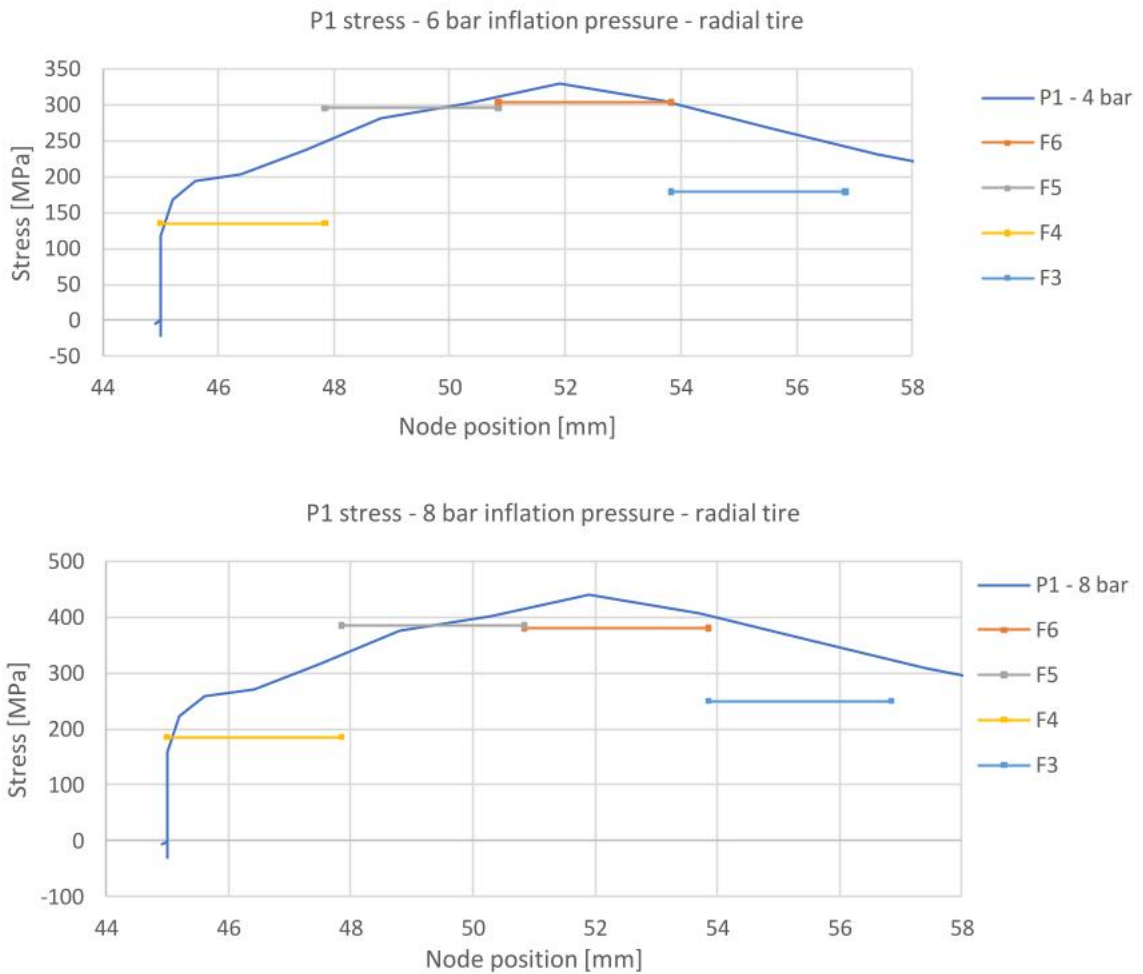


Figure 127 Comparison between the numerical results: FE simulations and experimental results for the radial tire.

It can be noticed that the model studied interprets the experimental stress trend quite well. Above all, the bias configuration curves intersect the value reported by the strain gauges in several points. The strain gauge best simulated is F4, which always intersects the curve in one point. However, the match between the numerical curve and the experimental results cannot be considered sufficient overall. The 2 bar configuration experimental result is highly underestimated by the numerical model in both the radial and the bias case, especially for the F6 gauge; in the radial configuration, for both 6 and 8 bar inflation pressure, the numerical model overestimates the experimental data and the highest error concerns F6 gauge once again. In many cases F5 strain gauge does not intersect the curve, reporting a different stress distribution with less slope along the radius. Finally, F3 strain gauge was probably placed slightly farther from the radius area during the tests, since the numerical model systematically and greatly overestimates it, especially in the radial configuration.

9.2.2.3.3. 2nd app. of p from automotive th. with corrective coeff.

The purpose of the following analysis is to focus on the F6 strain gauge and adjust the automotive theory model on it, since it is the gauge which returns the greatest stress values. In order to obtain more accurate peak values in the simulations, corrective coefficients (f) have been introduced. These have been obtained from each one of the experimental tests, since the strain gauge values show a non-linear increase of the stress. The pressure applied on the vertical wall of the rim flange was calculated referring to the inflation pressure of 4 bar following the formula already introduced (9–81).

Then three corrective coefficients for the remaining inflation pressures have been calculated:

$$\begin{aligned}
 f_{2_bias} &= \frac{\sigma_{F6_bias_2bar}}{\sigma_{F6_bias_4bar}} = \frac{103}{188} = 0,55 \\
 f_{6_bias} &= \frac{\sigma_{F6_bias_6bar}}{\sigma_{F6_bias_4bar}} = \frac{275}{188} = 1,46 \\
 f_{8_bias} &= \frac{\sigma_{F6_bias_8bar}}{\sigma_{F6_bias_4bar}} = \frac{368}{188} = 1,96
 \end{aligned}
 \tag{9-82}$$

The same coefficients have been obtained for the radial configuration:

$$\begin{aligned}
 f_{2_radial} &= \frac{\sigma_{F6_radial_2bar}}{\sigma_{F6_radial_4bar}} = \frac{146}{226} = 0,65 \\
 f_{6_radial} &= \frac{\sigma_{F6_radial_6bar}}{\sigma_{F6_radial_4bar}} = \frac{304}{226} = 1,35 \\
 f_{8_radial} &= \frac{\sigma_{F6_radial_8bar}}{\sigma_{F6_radial_4bar}} = \frac{381}{226} = 1,69
 \end{aligned}
 \tag{9-83}$$

Therefore, the load conditions for the radial tire were obtained starting from the 4 bar configuration through (9–81); then the other load configurations were calculated by applying the coefficients reported above (9–83). The results are shown below (Table 15).

RADIAL TIRE	
Inflation pressure [bar]	Pressure on the flange [MPa]
2	6,45
4	9,92
6	13,39
8	16,76

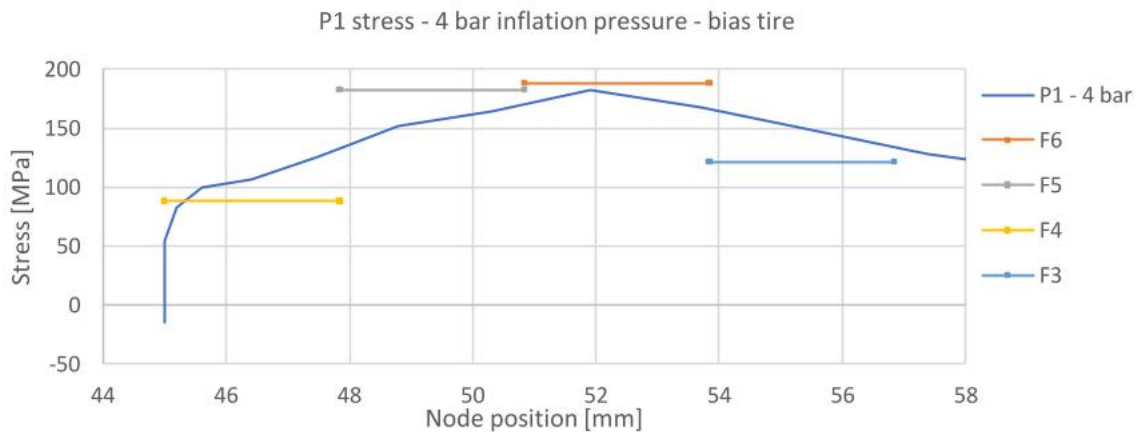
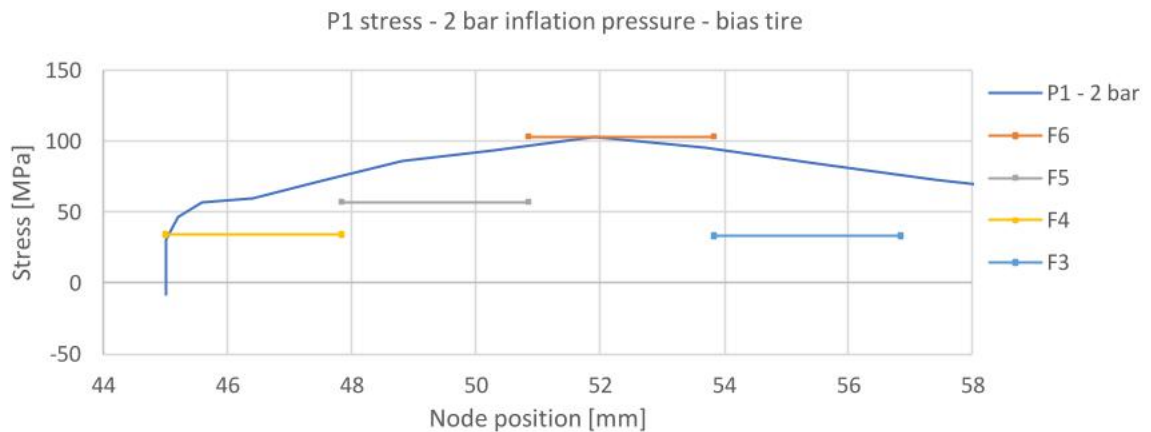
Table 15 Table reporting the pressures applied on the vertical wall of the flange for a radial tire after correction with the f coefficients (9–83).

For the bias tire, the 4 bar load condition has been obtained from the radial one through the k coefficient (9–81), while the other pressures have been found by applying the f parameters for the bias configuration (9–82) (Figure 128):

BIAS TIRE	
Inflation pressure [bar]	Pressure on the flange [MPa]
2	4,54
4	8,25
6	12,05
8	16,17

Figure 128 Table reporting the pressures applied on the vertical wall of the flange for a bias tire after correction with the f coefficients (9–82).

By applying the load conditions described in the tables above, a curve of the main stress P1 has been obtained. The comparison of the results for the bias configuration follows below (Figure 129):



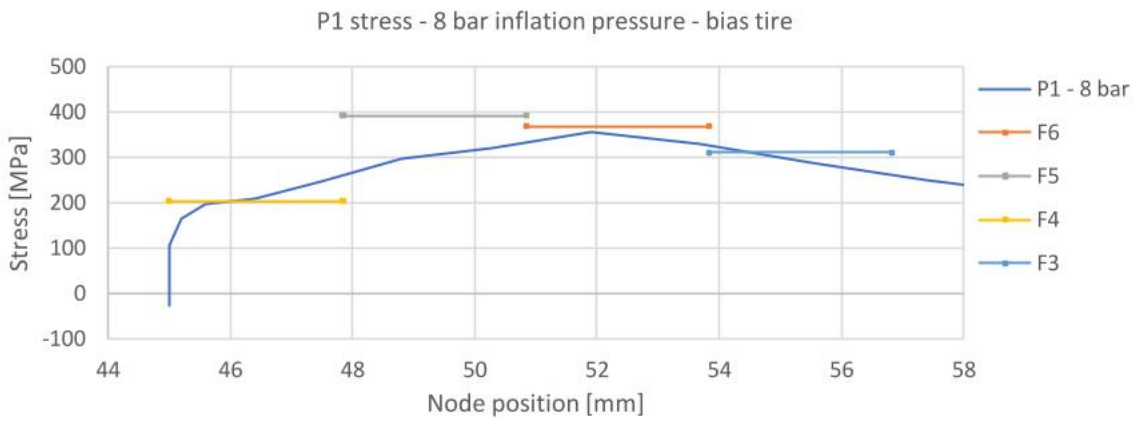
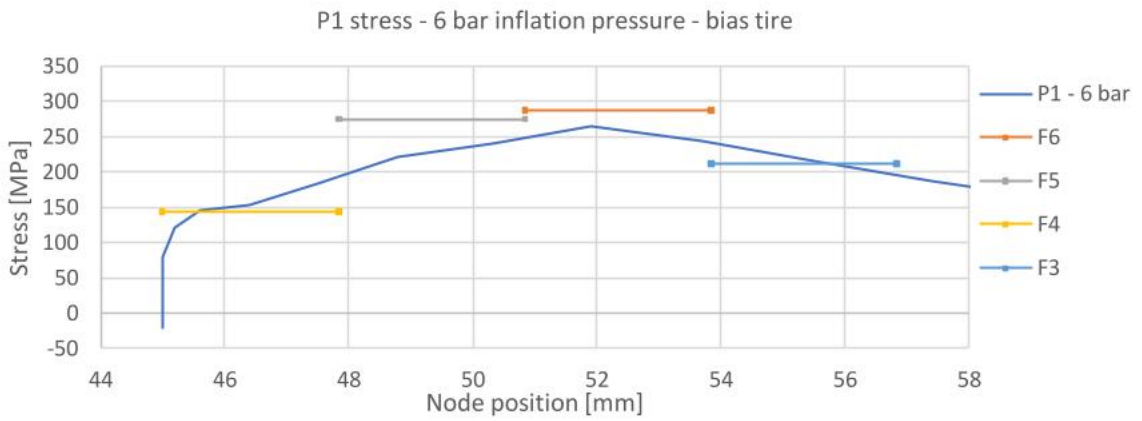
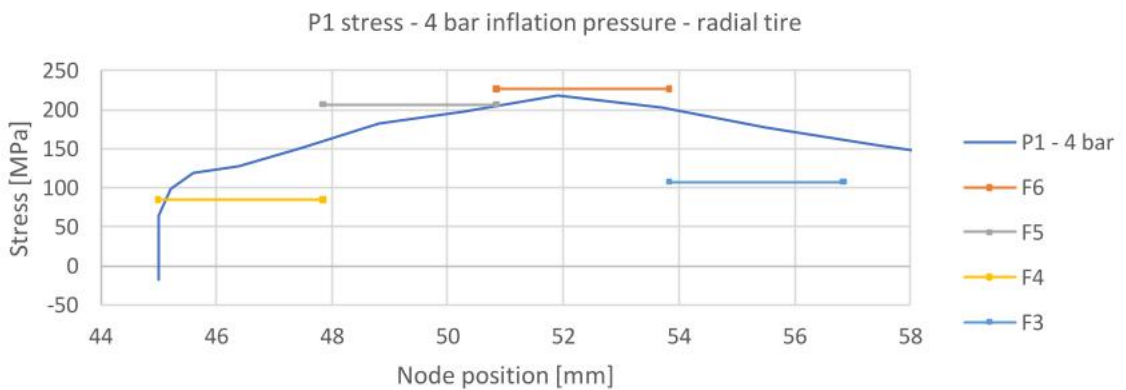
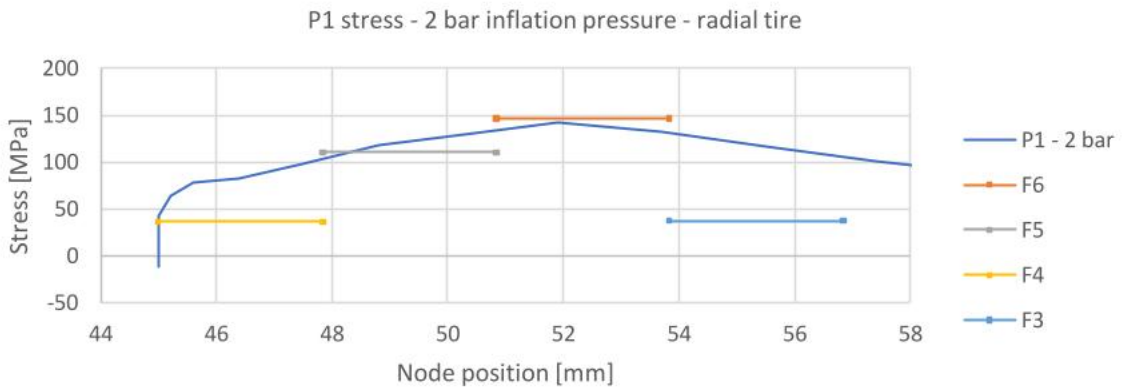


Figure 129 Comparison between the num results from FE sim of the adjusted model and exp results for the bias tire. The results for the radial tire are compared below (Figure 130):



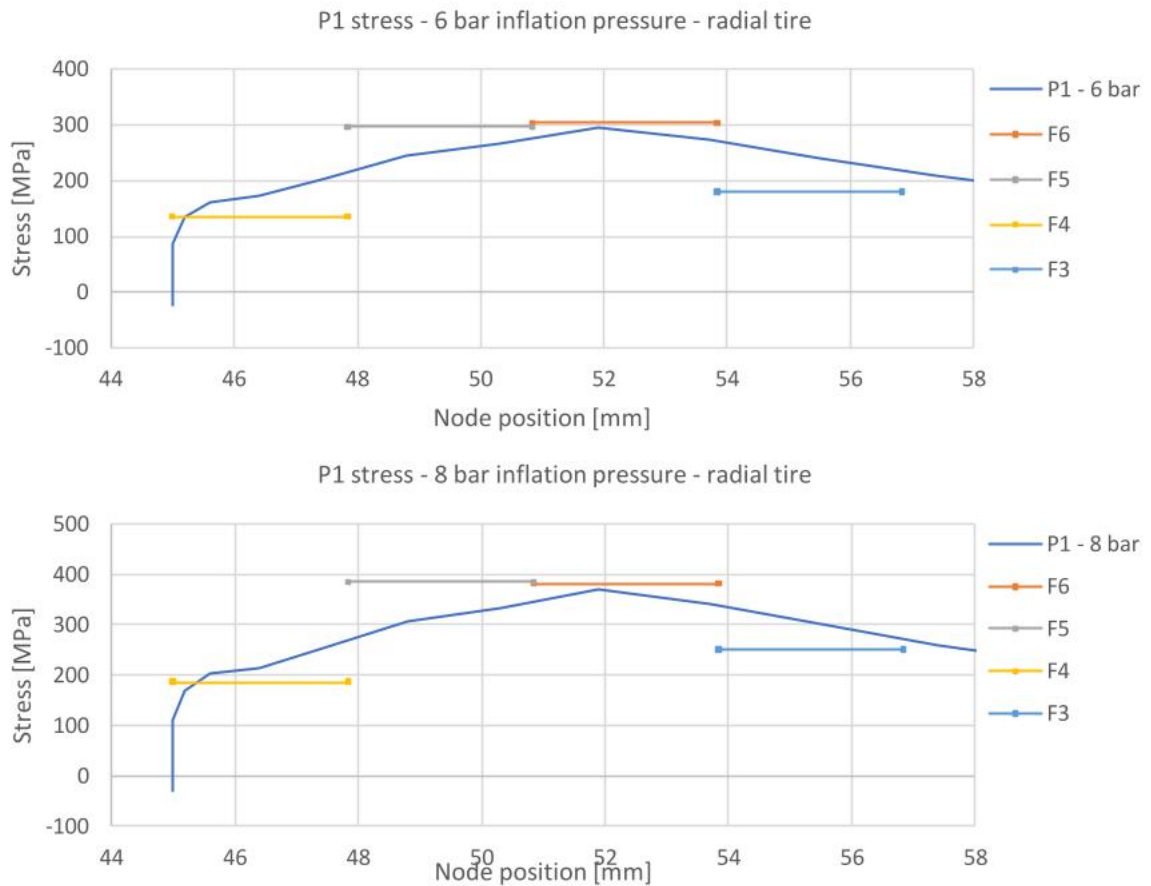


Figure 130 Comparison between the numerical results from FE simulations of the adjusted model and experimental results for the radial tire.

The adjustment of the model seems to have reduced the differences between the numerical curve peak and the F6 strain gauge experimental values. However, there are still large gaps for F3 and F5 strain gauges, which probably derive either from inaccuracy in the hypothesis of the strain gauges positioning or from an error in the load conditions that lead to a wrong stress distribution in the fillet radius area.

9.2.2.3.4. 3rd analysis: p from automotive th. for lab. results

The following analysis has been carried out to obtain the same stress peak values from the numerical simulations and the experimental measurements; thus, once again, the F6 strain gauge has been used as a reference to calibrate the model. We started considering the pressure applied on the flange obtained from the 4-bar inflation pressure configuration in the second analysis, in which the evaluated peak is equal to 218,7 MPa. A maximum stress of 226 MPa has been measured in the laboratory tests by F6 strain gauge (instead Table 1); therefore, a proportion has been applied so that the numerical peak result and the F6 strain gauge measurement could match.

Then, f coefficient (9–82; 9–83) and k coefficient (9–81) has been applied, allowing us to obtain all the load conditions for both radial and bias tire (Figure 131):

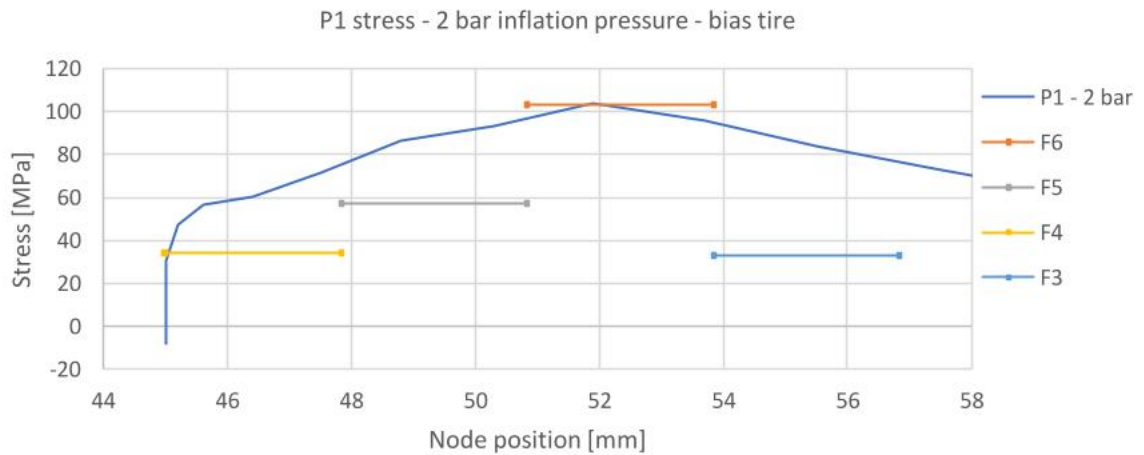
BIAS TIRE	
Inflation pressure [bar]	Pressure on the flange [MPa]
2	4,63
4	8,42
6	12,29
8	16,50

RADIAL PRESSURE	
Inflation pressure [bar]	Pressure on the flange [MPa]
2	6,57
4	10,11
6	13,65
8	17,09

Figure 131 Tables reporting the pressures applied on the flange for a bias tire (above) and a radial tire (below) after correction through proportion and f coefficient and k coefficient.

By applying the load configurations described in the tables above, a curve of the main stress P1 is obtained from the simulations and it is compared with the stress detected by the strain gauges (Figure 132; Figure 133).

The comparison of the results for the bias tire are shown below (Figure 132):



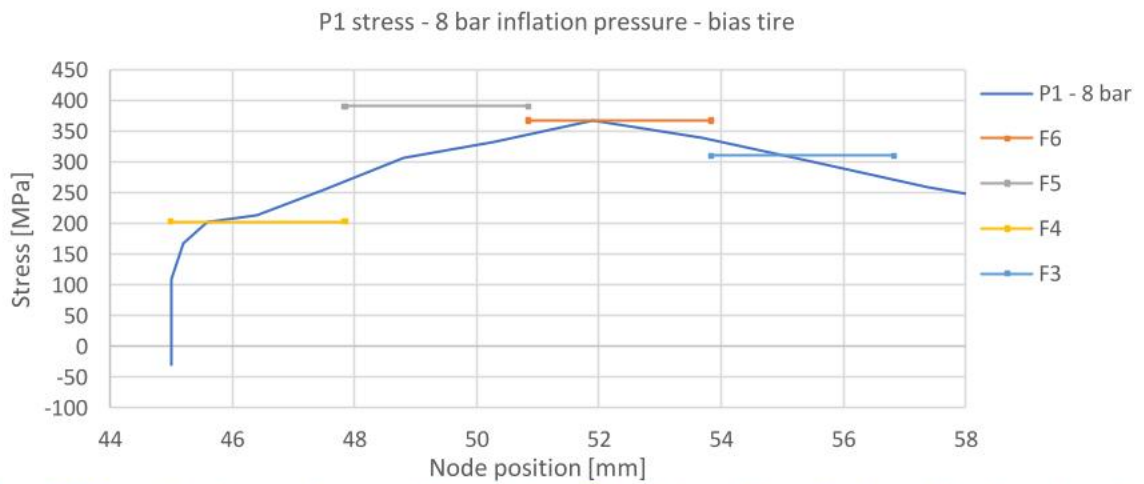
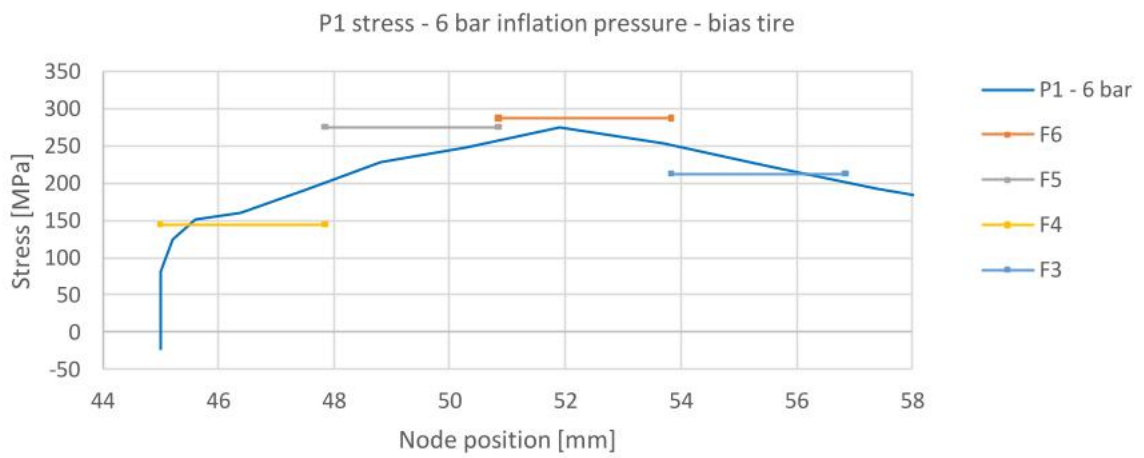
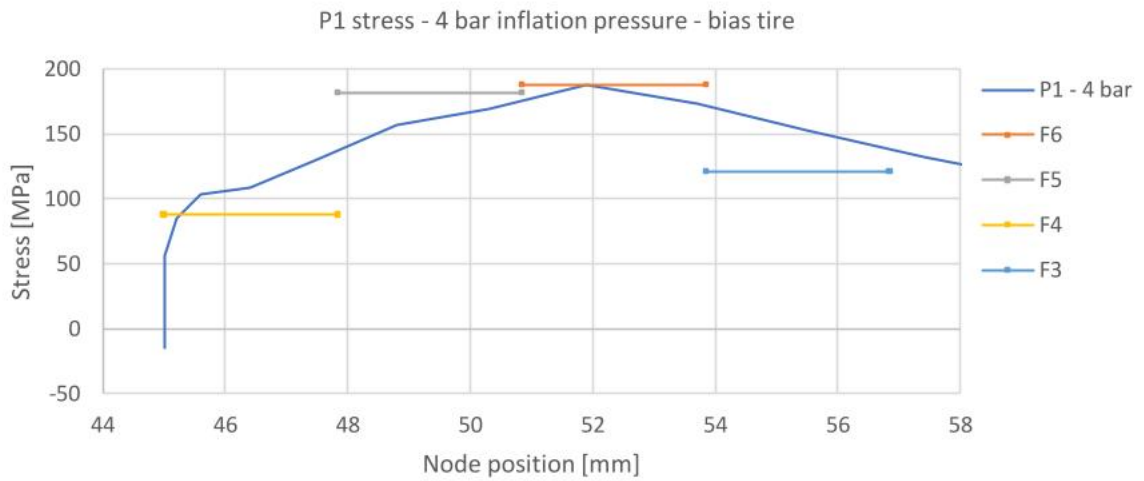


Figure 132 Comparison between the numerical results from FE simulations of the adjusted model and experimental results for the radial tire. F6 results are used as reference.

The comparison of the results for the radial tire are presented as well (Figure 133):

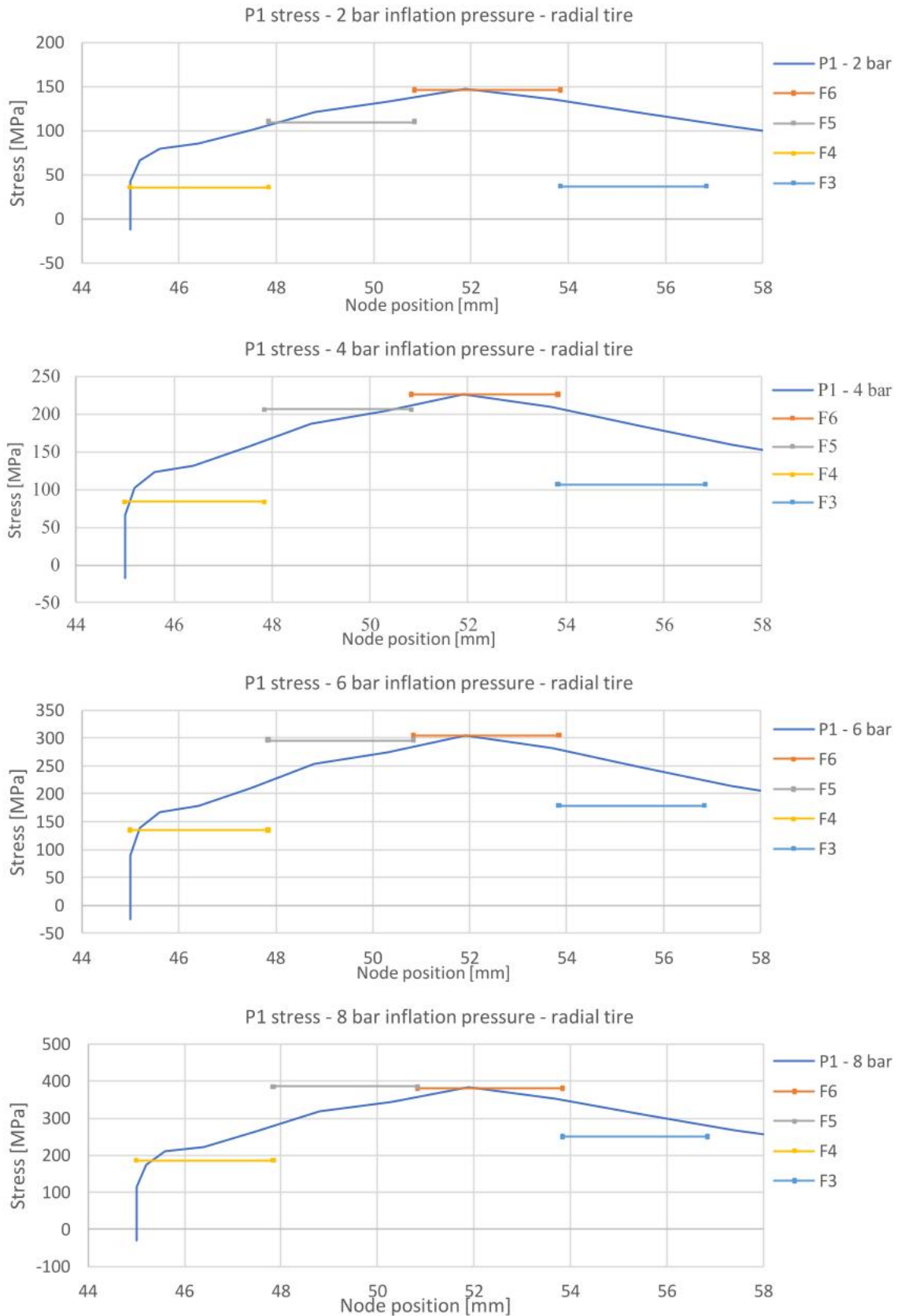


Figure 133 Comparison between the numerical results from FE simulations of the adjusted model and experimental results for the radial tire. F6 results are used as reference.

Even if the introduction of the corrective coefficient improved the match between the numerical curve peak and the F6 strain gauge measurements, the automotive theory-based model still maintains many limits, since it cannot precisely predict the stress trend in the seat radius from experimental tests and thus the match for the remaining strain gauge with the numerical results is rarely obtained.

These analyses clearly showed that the contact pressure problem in the flange area between tire and rim is much more complex and cannot be approximated with a uniform contact pressure as suggested by the automotive theory. Therefore, other modelling options have been studied to improve our knowledge of the tire-rim contact phenomenon.

9.2.2.4. Tire 3D model approach

In this chapter, the second study approach attempted to understand the mechanical interaction between tire and rim is exposed. As the automotive theory formulas could not give a good prediction of the stress distribution in the critical area, a more complex modelling approach has been considered. In fact, it was decided to create a 3D model of the tire used in the experimental tests, on which FE simulations could be performed. The advantage of this approach was that, if the tire was accurately modelled, ground-tire interaction loads could be directly applied on the tire tread. Then, the FE simulation of the tire would have given as a result the load exchanged with the rim; the rim itself could have been simulated in a second analysis with the loads previously found in order to obtain the stress distribution in the seat radius area. The finite elements analysis applied to tire models has become an increasingly common practice, thanks to the improved computing capabilities of the new systems. However, even nowadays, tire structure modelling and analysis represent a challenging operation as non-linearity occurs in the material properties as well as in the contact boundary conditions. Moreover, the tread pattern, the complex and composite internal tire design and their influence on the load distribution must be considered. The great non-linear mechanical behaviour of the tire is proved by many studies: one of the most relevant aspects is the non-linear vertical stiffness, for which that with the increase of the radial vertical load applied, the tire vertical deflection increases non-linearly [22]. Nevertheless, where it is possible, the FE analysis allows the improvement of the tire design and reduces prototyping costs. Static analyses of tire models are generally meant to provide results on stress states induced by inflation and radial loads, as well as loads parallel to the pavement.

Stresses in the bead wires, influence of the tire geometry, effect of the inflation pressure and the radial load can be estimated. Moreover, FE analysis can give important information about the contact pressure distribution on the tire-rim interface, which is the main purpose of the current study [20,23]. For this reason, an approximated 3D model of the tire was designed in Solidworks. The model created is shown below (Figure 134):



Figure 134 3D model of the tire to evaluate the loads exchanged between tire and rim.

As it can be seen in the picture above, all the main structural components of the tire have been included: bead wire, carcass, plies and rubber, which has been distinguished between tread rubber and sidewall rubber. In fact, an accurate modelling of the tire can be performed only if all its structural elements, which have different functions and are made of different materials, are considered. Unfortunately, no information about the design of the tire nor about the structural properties of its component and related materials could be collected. For this reason, the 3D model was just an approximated recreation of the supposed design of the actual tire used in the experimental tests. Hence, since no information about the internal design of the plies and the carcass could be found, the bead wires, carcass and plies design could only be guessed from the literature. The tread was simplified by modelling the circumferential grooves only, which is a common practice for 3D tire models [20]. The lack of data, moreover, was not limited to the geometry, but regarded the materials as well. This was a great limit for the development of the FE tire model, as the structural properties of the tire components are essential in order to perform an accurate simulation.

From the literature, it has been found that a great variety of materials and many elastic behaviours must be included in the tire study:

- Nylon, which constitutes the wires of the body plies and should be modelled as an elastic isotropic material.
- Steel, modellable as an elastic isotropic material, it is employed for different parts within the tire, that are the bead wires and the steel plies contained into the belt. The bead wires should be modelled as a bunch of smaller steel wires. The belt steel plies provide resistance to the tread. They are composed of several parallel steel wires and are often placed with different orientation according to the ply.
- Rubber: as the great majority of the rest of the vulcanized elastomers, it is usually modelled as a hyper-elastic isotropic material, since linear elastic models are unable to describe the material stress-strain isotropic and non-linearly elastic characteristic. The stress-strain characteristic of a hyper-elastic material can be derived from a strain energy density function. The Mooney-Rivlin model, which is one of the most accurate approaches to study the rubber mechanical behaviour, is based on this assumption. In this model, two of the Cauchy invariants are linked to the strain energy density function:

$$W = C_{01} \cdot (I_2 - 3) + C_{10} \cdot (I_1 - 3) + D_1 \cdot (J - 1)^2 \quad 9-84$$

Where W is the strain density function, C_{01} and C_{10} are empirically determined constants which describe the deformation response of the material and D_1 is a constant associated to the material volumetric response. I_1 and I_2 are the first two invariants of the deformation tensor while J is the determinant of the deformation gradient. The Mooney-Rivlin equation, thus, contains several material coefficients that should be derived experimentally. As the rubber properties for the tread and the sidewall are different, the Mooney-Rivlin coefficients should be differentiated as well [24].

All the materials component reported above require elastic coefficients for the associated materials, especially the rubber, for which many constants are needed. All the coefficients should be known in order to correctly define the mechanical behaviour of the tire.

However, the Mooney-Rivlin constants for the rubber of the test tire were not available. Besides, neither an empirical fitting of the coefficients could be done, as dedicated experimental tests could not be performed. Even if the material properties were found, no information about the carcass design nor the plies displacement were available, so the modelling would have been much approximated [20,24]. Moreover, the composite structure and the highly non-isotropic behaviour of the materials could not have been accurately simulated through the functions of the software, since *Solidworks Simulation* only allows setting orthotropic properties along the orthogonal global axes. Dedicated rebar elements for the reinforcement of the composite materials could not be available. Lastly, the highly non-linear and non-isotropic mechanical properties of the composite structure of the tire made would have been extremely complex to set up in the study.

For all this reason, it was soon realized that FE tire modelling could not have been a reasonable study approach for both the time and the resources it would have requested. Manufacturer suggested trying different approaches, since the simulation of the whole tire needed too many unknown parameters and it would hardly have returned consistent results with the experimental tests. It is important to remember, in fact, that an accurate fatigue evaluation of the rim needed a faithful reproduction of the experimental stress state in the static simulation. According to literature and scientific papers, predictions reported from some researchers are not accurately consistent with the experimental results due to oversimplification needed in FE models. These approximations often regard the tread pattern, the anisotropy of the ply and carcass cords, the tire-rim contact conditions [20,23]. From literature, it has been confirmed that simplification of the tire model does not induce significant changes in the load-deflection curves nor in the footprints, but causes significant variations in the tire stiffness [20]. For this reason, it was decided to continue the study of the tire-rim contact phenomenon through a different approach, as described in the following paragraphs.

9.2.2.5. Empirical approach applied to the inflation problem

As stated before, the study approach first applied to the problem of the tire-rim contact could not give consistent results. An accurate description of the tire stiffness in all its components is, in fact, so complex as to make the development of a model very prohibitive. It was realized that the phenomenon of the interaction is so complicated it cannot be studied through a usual modelling approach, if not spending great resources and time.

Thus, it was understood that a completely different resolution approach had to be used. In fact, it was decided to apply a reverse study method, so all the analytical and numerical based models was put aside and it was decided to use the data from inflation tests as an experimental starting point on which an empirical model could be developed, instead of using them as comparison terms. This empirical model should then have allowed us to reproduce the stress distribution detected experimentally.

As starting hypothesis, it was supposed that the distribution of the loads exchanged between the tire and the rim could not be limited to the flange vertical surface, but to a wider area instead, including the upper part of the flange and the bead seat area. Secondly, it was assumed that the contact pressure could not be uniform and that it could vary instead along the surface in the y - z plane (Figure 115). Following these assumptions, it was decided to divide the flange area into many circular areas shown in Figure 135, so that different load conditions could be applied to different zones of the flange, even though without continuity. Given the axial symmetry of the component and the load condition (at least for the inflation problem), the division was necessary only in the axial direction.

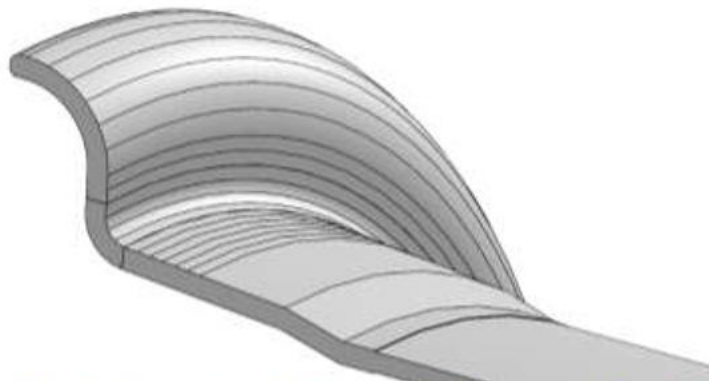


Figure 135 Division applied to the inner surface of the flange and of the seat area of the rim 3D model.

The areas have been identified as follows (Figure 136):

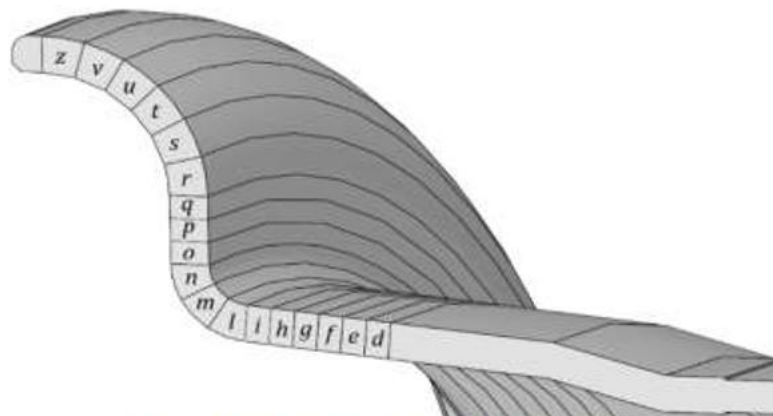
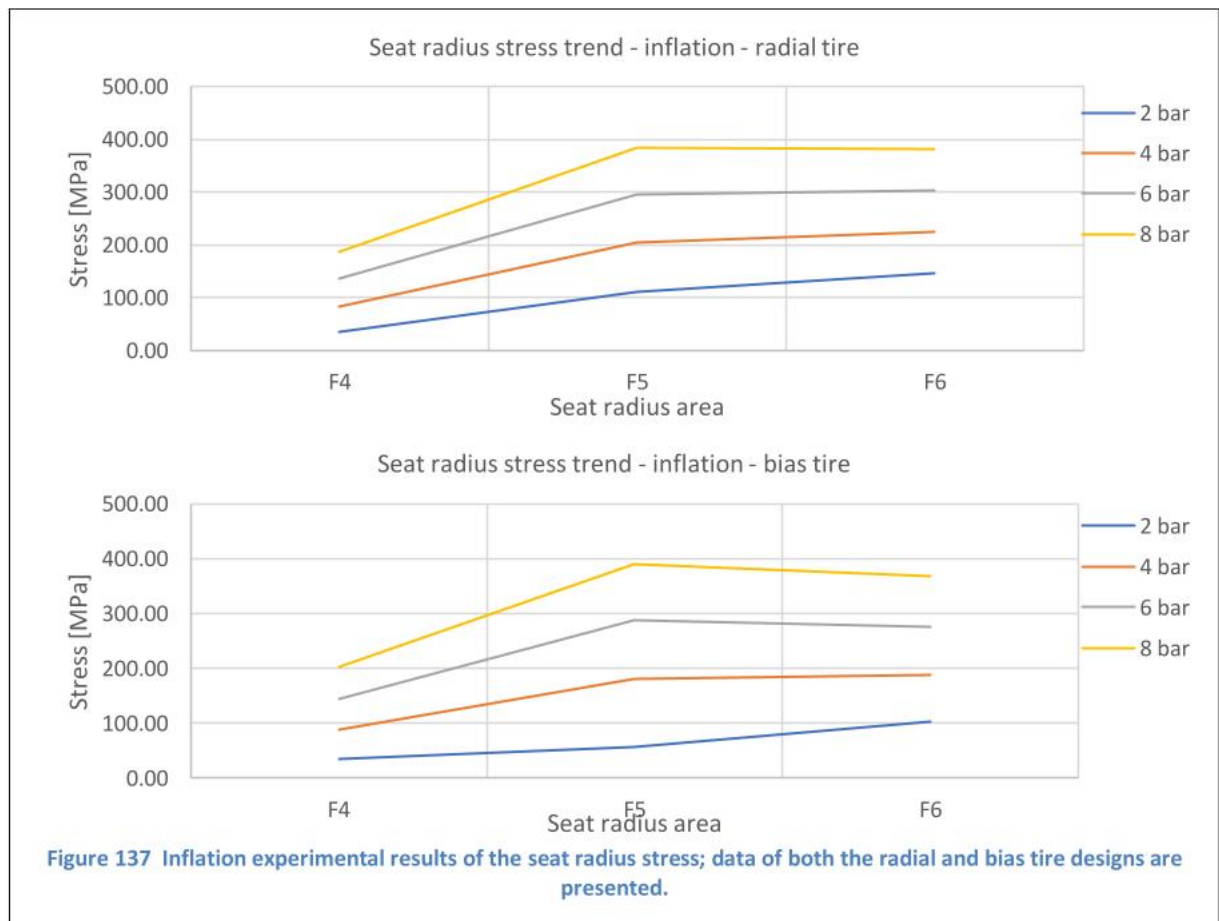


Figure 136 Designation of the subdivision areas.

As shown above, the inner seat radius area has been divided into three zones, which approximately correspond to the strain gauges positions, as previously described. Each one of the three areas is 4,5 mm long alongside the surface, while the strain gauge length is equal to 3 mm. From the Woodridge laboratory experience report, it was known that the F5 strain gauge was manually placed in the centre of the seat radius; F4 and F6 strain gauges were placed next to F5, so where a gauge ended, the adjacent one began. Therefore, it would have been more accurate to create division lines in the seat radius area that would reproduce a similar location. However, it was presumed that, since the application of the strain gauges was manual and therefore associated with a certain error, the gap between the two lengths of 3 mm and 4,5 mm could take into account any possible positioning inaccuracy.

Moreover, attention must be paid to the stress compared from laboratory tests and numerical simulations. Since the strain gauge measurement is an average of the material strain occurring under its application surface, it was supposed that the mean values extrapolated on the corresponding area in the simulation could be effectively compared with the experimental result. Therefore, in each subsequent simulation performed, the average stress value from the FE analysis was compared with the experimental one.

Before going on with the model description, it is necessary to briefly present and analyse the experimental results of the inflation tests, which are shown below. The graphs report the measurements of the stress for each strain gauge considered and they are linked by a series of line segments, so that an approximated trend can be visualized (Figure 137).



As can be seen, as the inflation pressure increases, the amplification of the stress is not the only effect that follows. Instead, the trend of the stress in the seat radius changes as well. For some inflation conditions, the stress curve is strictly monotone and the stress peak is therefore reached in F6; for other inflation conditions the maximum stress value correspond to the F5 measurement. After some tests, it was realized that the reason of the curve shape change could be the variation of the loaded zones of the rim flange. In other words, an increase of the inflation pressure could produce a variation of the deformed configuration of the tire and, thus, of the flange area mainly loaded as well.

The problem which resulted therefrom was understanding how the load distribution on the flange could affect both the intensity and the shape of the stress curve. Hence, the discretization of the flange area of the 3D model previously shown (Figure 135) was thought and introduced; in fact, it was realized that a deeper understanding of the phenomenon could be reached only by studying the influence of each flange's loaded area on the stress distribution. Therefore, the first set of simulations of this model was performed: as many analyses as the discretization areas were carried out, from zone z to zone l . In each of these simulations, just one of the division areas was loaded with an arbitrary pressure normal to the rim surface, so that the influence of the loaded area on the shape of the stress curve could be evaluated. It must be specified that a similar study could give information about the curve shape only and not about the stress intensity itself, since the load pressure value was completely arbitrary. Moreover, it is necessary to point out that the entire rim study was supposed to be based on the elastic linear field hypothesis. Only thanks to this, the principle of superposition of the effects could be applied; this principle was necessary in order to consider the stress distribution in the seat radius as a linear combination of the effects induced by each discretized load.

Before presenting the results of this study, it must be described the optimization of both the 3D model and the mesh operated for this set of simulations and all the analyses that will be described in the following chapters as well. Firstly, a quarter of rim 3D model has been introduced (Figure 138):

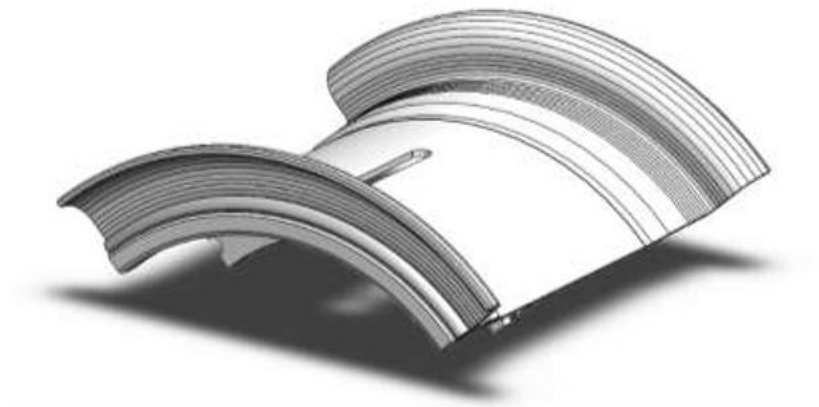


Figure 138 90° 3D simplified model of the rim.

The introduction of the 90° 3D model simplification was considered fully acceptable, since in both the inflation and the radial load problems it had no significant impact on the value of the results. The inflation problem is, in fact, axial-symmetrical, so any portion of the rim would be sufficient to study the stress distribution. Regarding the radial load problem, even though it is not axial-symmetrical, the circumferential stress distribution does not affect in any way the fatigue evaluation for which the static simulations are carried out. Finally, the axial-symmetry of the rim itself allows considering just a portion of the component without affecting the analysis results. Naturally, some constraint expedients have been consequently adopted: a sliding constraint have been applied on the sectioned surfaces, in order to reproduce the axial-symmetry of the rim (Figure 139):

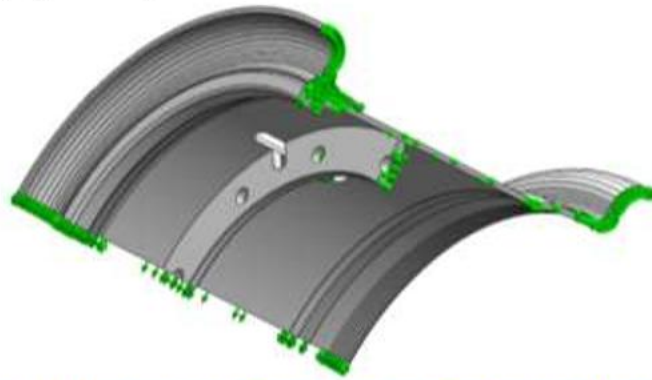
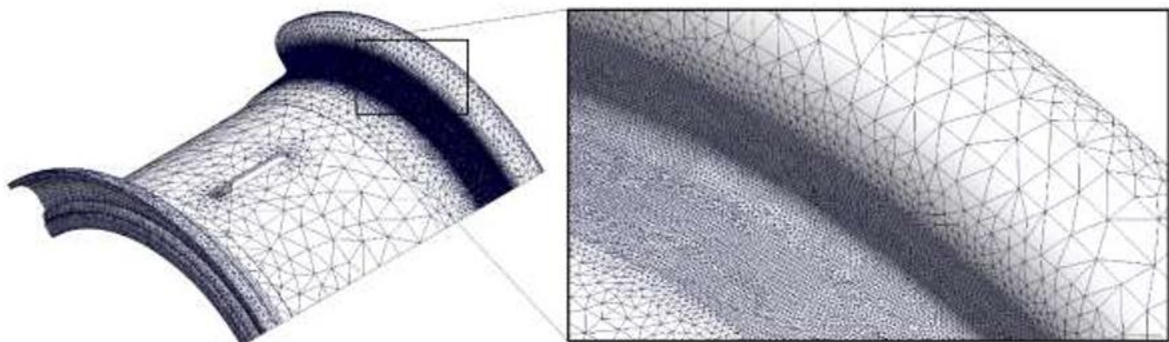


Figure 139 Sliding constraints applied to the sectioned surfaces of the model.

A fixed constraint was applied as well on the coupling area between rim and axle shaft as done in the previous simulations and shown in Figure 122.

The mesh applied for these analyses and for all the following studies as well was set to be particularly subtle in the critical area only. The general mesh had elements with dimensions going from 5 mm to 40 mm, while the thickened mesh elements applied to the flange area was 1,5 mm long. The mesh is shown below:



MESH	
Nodes number	1.453.924
Elements number	1.009.933

Figure 140 Mesh applied to the rim model for the static and fatigue analyses.

A maximum 1,5 mm dimension for the mesh elements was chosen for many reasons. First, it was noticed this thicker mesh provided more accurate results compared to coarser meshes; for instance, a gap of several MPa was recorded in the seat radius stress using a mesh of 3 mm elements compared to the 1,5 mm mesh. It was later noticed that small differences in the stress field could give greatly variable fatigue life results in the FE analyses. Moreover, since the length of the strain gauges was 4,5 mm, 1,5 mm long elements choice allowed us to match the area corresponding to a single gauge to at least 3 finite elements. Therefore, the area corresponding to a single strain gauge could be modelled more accurately and the stress extrapolated from the simulations would have been the average of many elements, giving us more precise samples.

As described before, the purpose of this first set of analyses was to evaluate the influence of each of the loaded flange areas on the stress curve shape in the seat radius. Therefore, as many simulations as the discretized zones have been carried out; in each one, just one of the areas shown in Figure 136 has been loaded. An example is shown below (Figure 141):

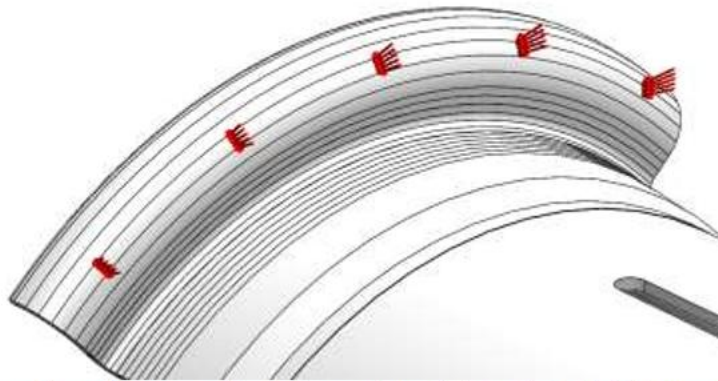


Figure 141 Load conditions of one of the many simulations performed to evaluate the influence of the loaded area on the radius stress distribution.

As stated, normal pressures have alternatively been applied; the normal pressure has been calculated so that the resulting axial force applied on the flange was always the same. It must be specified that this condition has been set just to evaluate how a similar axial force applied in different flange areas could affect the magnitude of the radius stress, but the main aim of this set of simulations remained estimating the influence of the loaded area on the stress curve shape. Since the simulations performed were linear, the value of the normal pressure applied could not affect the stress curve shape.

The parameters and the results of the simulations are reported below (Table 16):

ZONE	AXIAL FORCE F_A [N]	AREA [mm ²]	PRESSURE AXIAL COMPONENT P_A [MPa]	PRESSURE NORMAL COMPONENT P_N [MPa]
h	10.000	2.778	3,60	41,30
i	10.000	2.782	3,59	41,24
l	10.000	2.342	4,27	13,01
m	10.000	2.360	4,24	5,75
n	10.000	2.390	4,18	4,32
o	10.000	2.895	3,45	3,45
p	10.000	2.942	3,40	3,40
q	10.000	2.991	3,34	3,34
r	10.000	5.437	1,84	1,86
s	10.000	5.587	1,79	1,94
t	10.000	5.720	1,75	2,20
u	10.000	5.830	1,72	2,82
v	10.000	5.907	1,69	4,42
z	10.000	5.947	1,68	12,88

Table 16 Load parameters and normal pressure applied in the simulations.

The results of the simulations are presented as well (Table 17):

AREA	STRESS [MPa]		
	F4	F5	F6
l	-0,05	-0,59	-4,17
m	-0,04	-3,26	-0,18
n	-2,46	4,47	8,67
o	3,96	12,31	15,19
p	9,34	17,11	19,72
q	14,68	22,82	23,96
r	20,10	28,08	28,48
s	25,80	33,74	33,53
t	32,09	39,98	39,06
u	40,79	48,59	46,68
v	57,81	65,45	61,58
z	135,40	142,20	129,50

Table 17 Stress results from the simulations for each area loaded.

A graphic representation of these results is proposed (Figure 142):

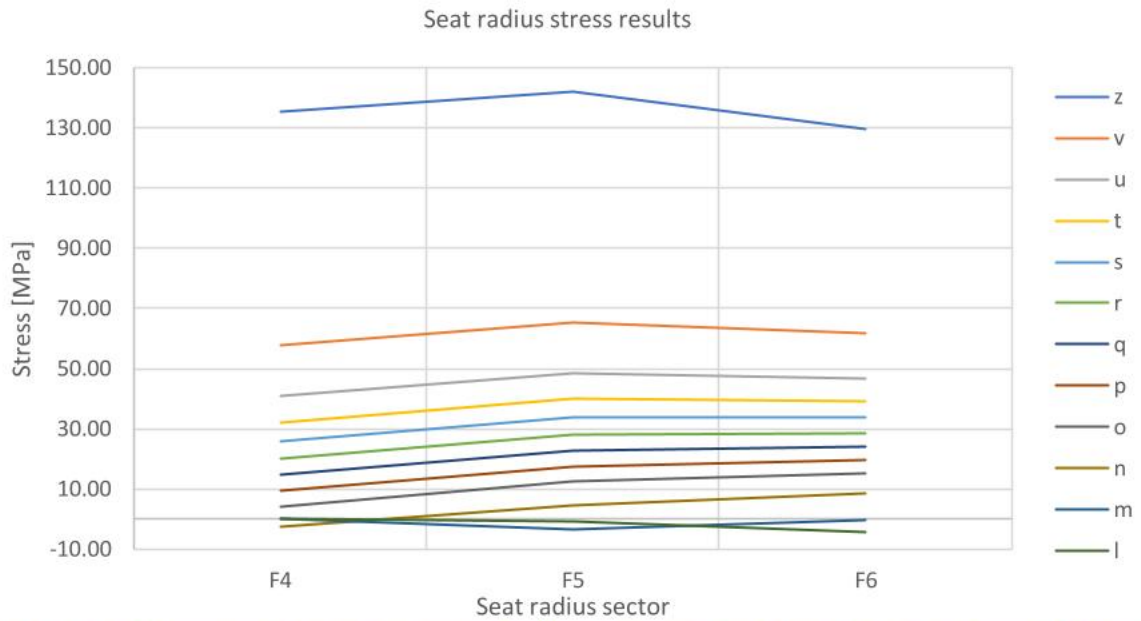


Figure 142 Graphic representation of the simulations results. The stress values obtained in the three areas of the seat radius are reported for each flange zone loaded. The different trends of the stress in the radius are visible.

As stated before, the most relevant result which was intended to derive from this set of simulations was the trend of the stress distribution in the seat radius area. This could be numerically evaluated regardless of the magnitude of the curve by normalizing the F4 and F6 stress values with respect to F5, which has been considered as reference. The result of the normalization is shown below (Figure 143):

AREA	STRESS [MPa]		
	F4	F5	F6
l	0,08	1,00	7,04
m	0,01	1,00	0,05
n	-0,55	1,00	1,94
o	0,32	1,00	1,23
p	0,55	1,00	1,15
q	0,64	1,00	1,05
r	0,72	1,00	1,01
s	0,76	1,00	0,99
t	0,80	1,00	0,98
u	0,84	1,00	0,96
v	0,88	1,00	0,94
z	0,95	1,00	0,91

Figure 143 Stress ratio between F4, F5 and F6. The simulations results have been normalized with respect to F5.

A graphic representation of the stress ratios of three of the most significant load configurations and the graphic representation of the stress distribution given by the software are presented (Figure 144; Figure 145; Figure 146; Figure 147):

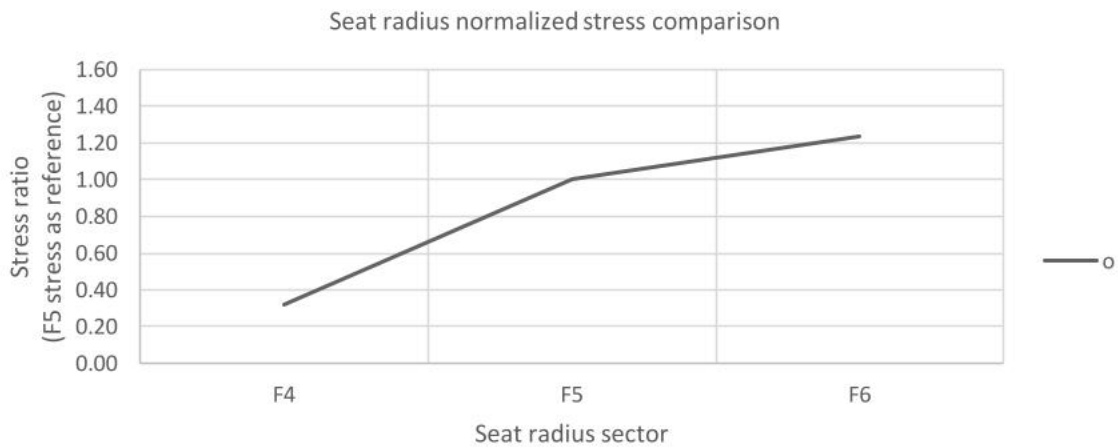
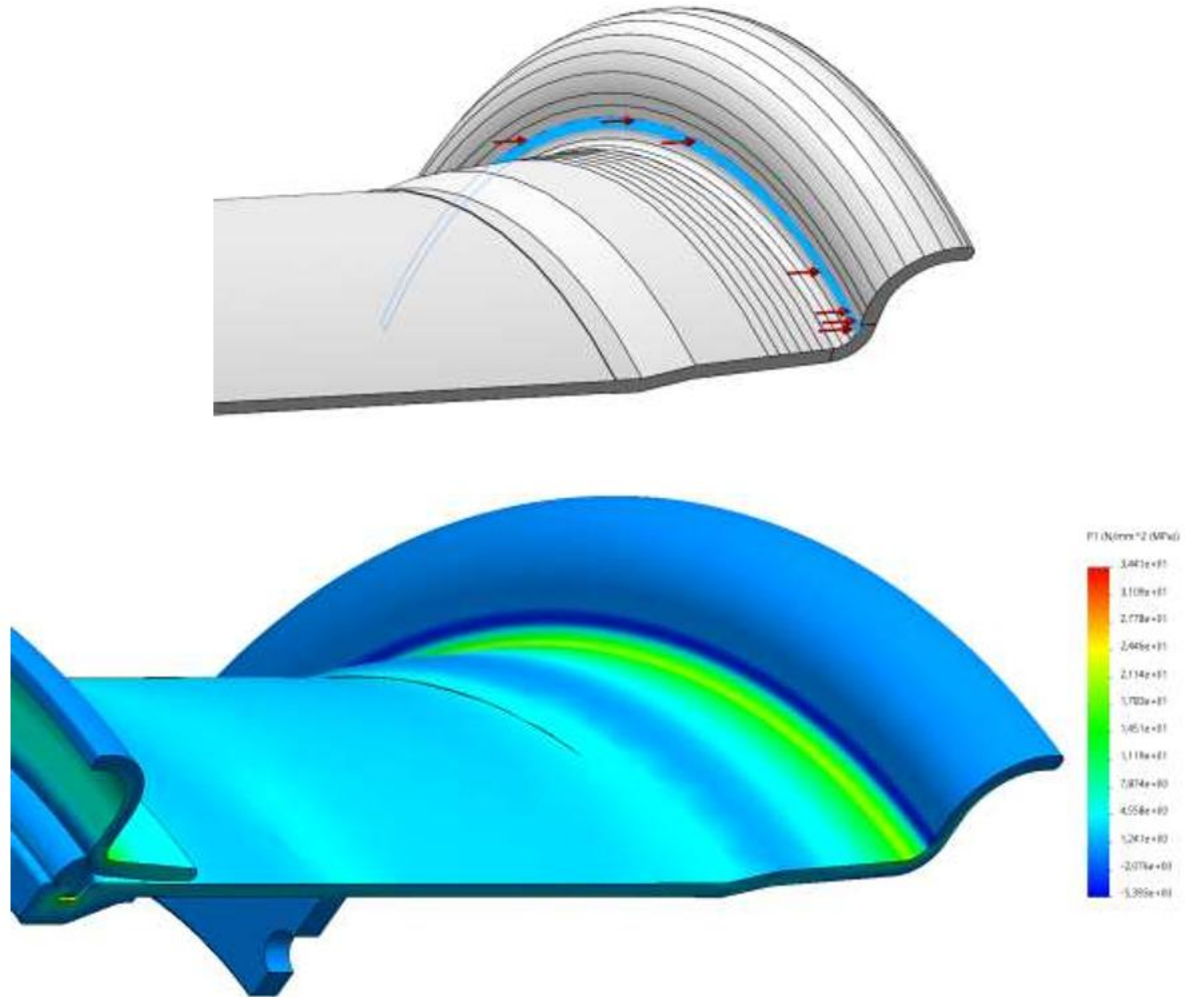


Figure 144 Seat radius stress trend obtained by loading the “o” area with a normal pressure.

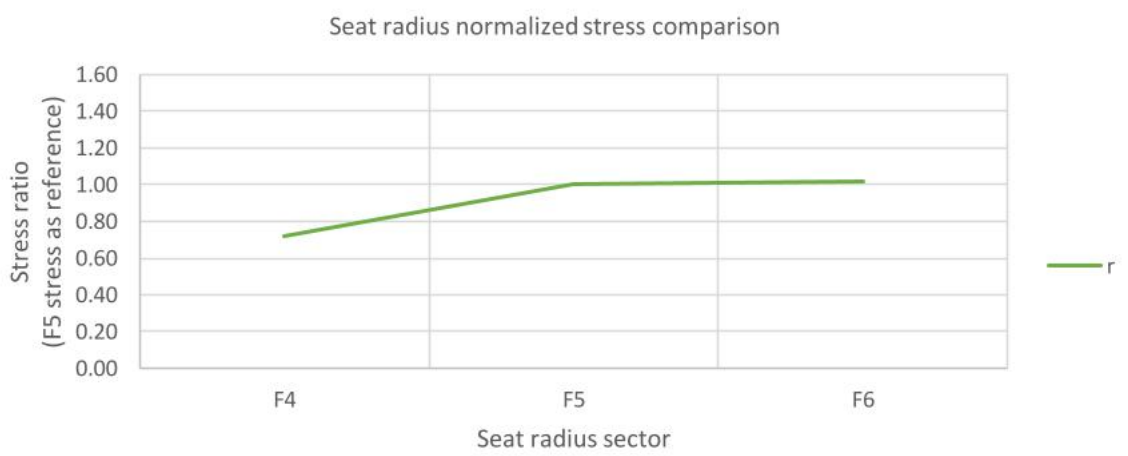
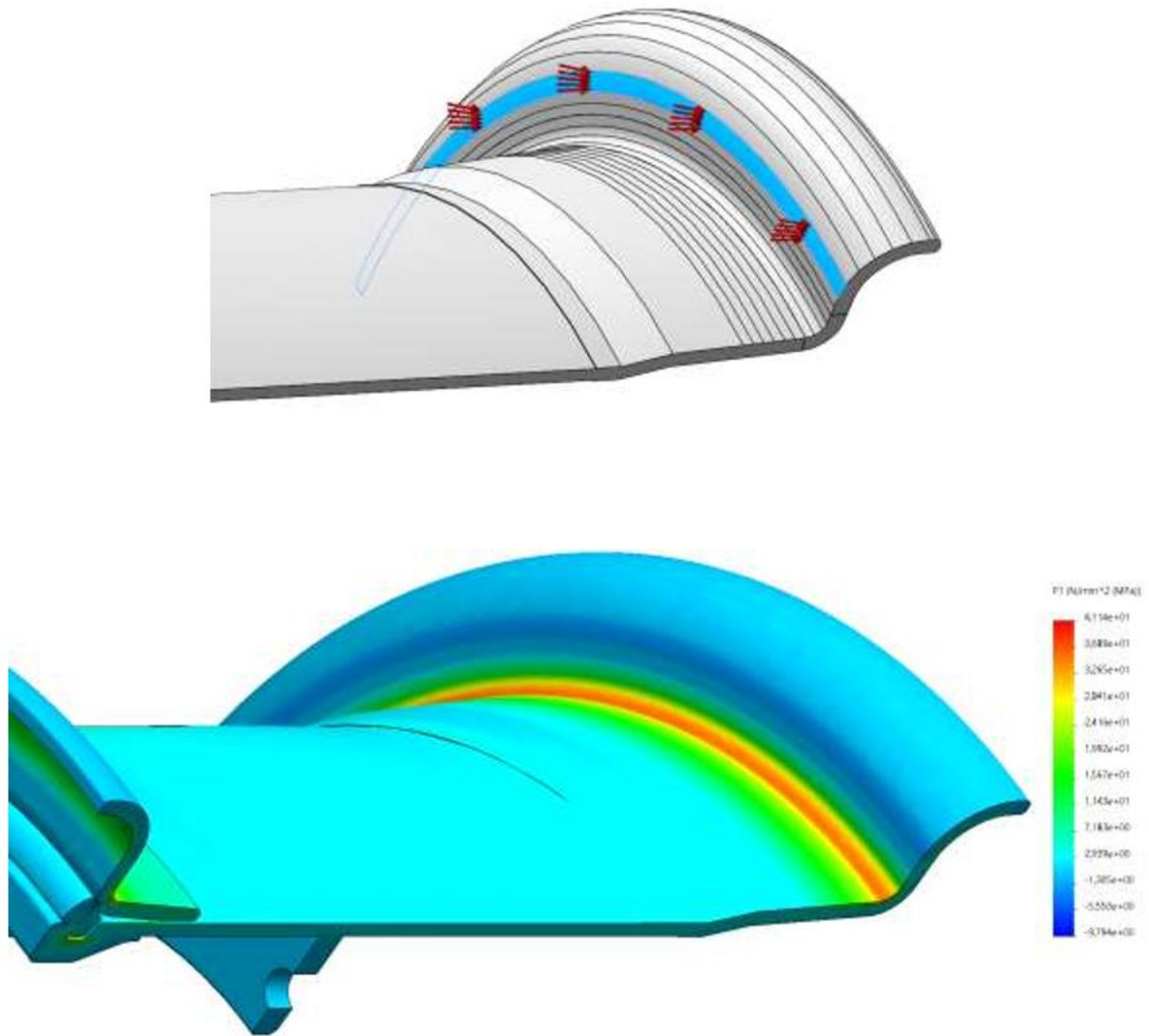


Figure 145 Seat radius stress trend obtained by loading the "r" area with a normal pressure.

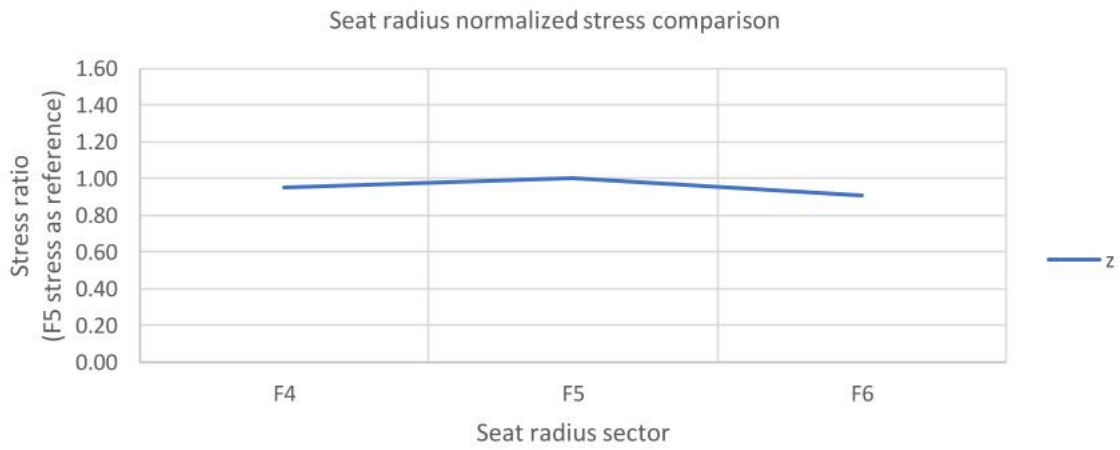
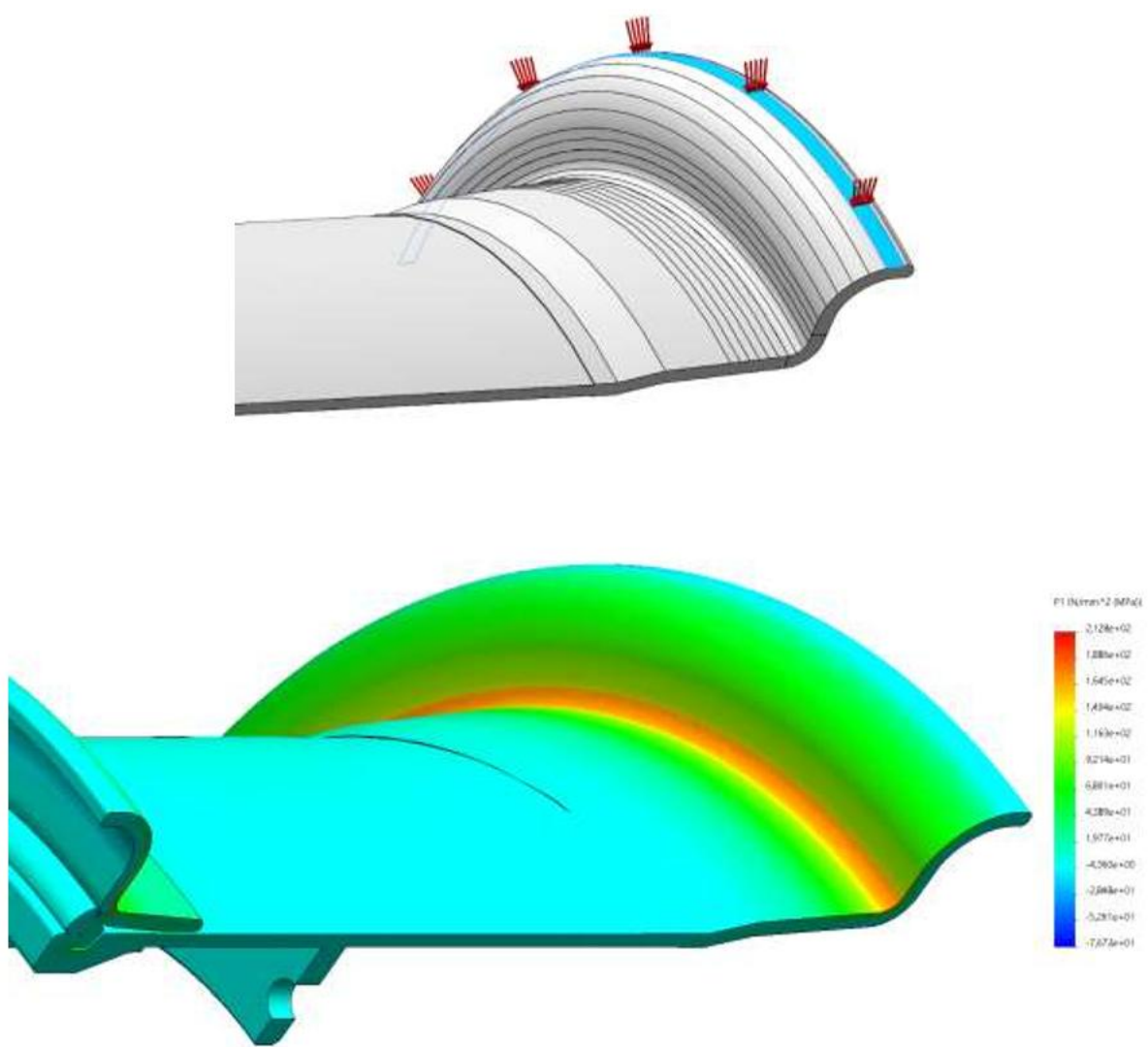


Figure 146 Seat radius stress trend obtained by loading the "z" area with a normal pressure.

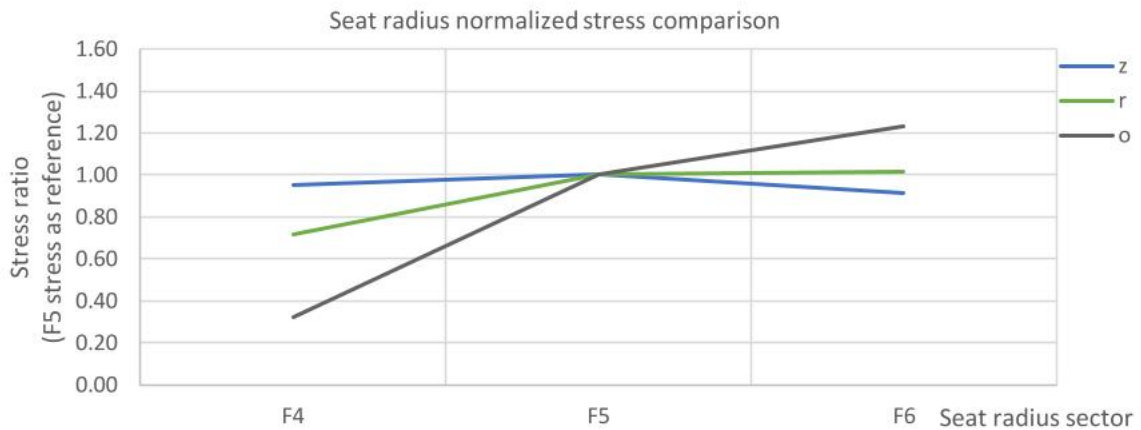


Figure 147 Comparison of three simulation results. “o”, “r” and “z” load config return different stress curve shapes.

As it can be noticed, normal loads applied to different areas of the flange cause significantly different stress trend in the seat radius, clearly visible also from the simulation images. In particular, pressure applied on the lower part of the flange on the vertical wall produces a monotone increasing curve and the maximum stress is located in the F6 area. On the other hand, if the upper area of the flange is loaded, the curve is not monotone and the maximum stress is placed in F5. All the intermediate load configurations produce a stress trend included between these two extremes. This study turned out to be extremely useful in the following simulations, since it allowed foreseeing which areas should have been loaded to reproduce the stress distribution of the seat radius from the experimental results. Therefore, this set of analysis saved a lot of time when pressure configurations had to be hypothesized in the next simulations, since it gave a good reference to rely on. If a monotone stress curve resulted from the experimental data, it could be supposed that the lower vertical part of the flange had to be loaded; vice versa, if a maximum in F5 was observed, it was reasonable to suppose that the pressure had to be applied in the upper area of the flange. Thanks to the study exposed above, the inflation problem could be faced more easily. In the next paragraphs, the approach used to suppose the contact pressure distribution will be exposed.

The inflation problem was interpreted through a linear combination of the single load pressures exposed above. Since no information about how the tire and rim exchange forces between each other were available, only a few hypotheses were assumed. First, it has been supposed that the contact pressure had to be roughly continuous and, thus, large irregularities in the pressure distribution could not be admitted. In second instance, it has been assumed that the pressure trend had to present a peak approximately in the middle of the application area.

A significant assumption has also been applied: in fact, some areas of the flange surface had not to be necessarily loaded. This was clearly an approximation, since a pressure should have been applied wherever tire and rim got in touch. However, this approach helped us to understand how loads on wider areas could affect the stress in the seat radius. This approximation has been removed in the following studies on the radial load, in which a more complex contact model has been developed. As stated before, loads on different areas of the flange cause different stress curve shape; this criterion was the main one applied in order to make the experimental curve shape and the numerical one overlap. In other words, the first aim of the study was to reproduce the trend of the radius stress curve: at this point, obtaining the right magnitude of the stress was not essential. Thus, the approach adopted was the one following described. It was assumed that the total axial force acting on the flange was equal to the one predicted by the automotive theory (9–85):

$$F_a = (a^2 - r_m^2) \cdot P_0 \quad [N/m^2] \quad 9-85$$

Where a is the tire radius, supposed equal to 750 mm, r_m is the radius of the “m” area in the middle of the seat radius, which can be reasonably considered as the lower extreme of the axial forces exchanged; r_m is equal to 318,3 mm. P_0 is the inflation pressure. The next step was to allocate to each flange area a fraction of axial load, so that the sum of all the loads could return the total axial force predicted by the automotive theory. From there, normal pressures were derived and applied to the model in the simulations. The allocation coefficients c_i , have been changed many times in many attempts to reproduce the experimental stress curve shape. Several contact pressures were supposed and simulated, until a distribution that could reproduce the experimental stress trend could be find. However, pressure distributions that gave a good interpretation of the stress curve shape could not predict the magnitude of the radius stress as well. Thus, once a good numerical curve trend was found, a corrective k coefficient was multiplied to all the contact pressure identified before in order to adjust the magnitude of the stress.

The k coefficient was set to match the highest stress (F5 or F6 depending on the inflation conditions). Hereafter the pressure distribution found by following this study approach are presented; the stress results are shown as well (Figure 148; Figure 149; Figure 150; Figure 151; Figure 152; Figure 153; Figure 154; Figure 155):

4 bar - radial – inflation							
MODEL PARAMETERS			APPLIED LOADS				
INFLATION PRESSURE		ALLOCATION COEFFICIENTS		F [N]		P _N [MPa]	
P ₀ [MPa]	0,4	c _l	0,00	F _l	0	P _{nl}	0,00
		c _m	0,00	F _m	0	P _{nm}	0,00
AXIAL LOAD - AUTOMOTIVE THEORY		c _n	0,10	F _n	11175	P _{nn}	4,02
F _a [N]	144892	c _o	0,30	F _o	33525	P _{no}	9,65
		c _p	0,25	F _p	27937	P _{np}	7,91
AXIAL LOAD - SIMULATION		c _q	0,15	F _q	16762	P _{nq}	4,67
F _a ' [N]	111749	c _r	0,15	F _r	16762	P _{nr}	2,59
		c _s	0,05	F _s	5587	P _{ns}	0,90
CORRECTIVE COEFFICIENT		c _t	0,00	F _t	0	P _{nt}	0,00
k	0,77	c _u	0,00	F _u	0	P _{nu}	0,00
		c _v	0,00	F _v	0	P _{nv}	0,00
		c _z	0,00	F _z	0	P _{nz}	0,00

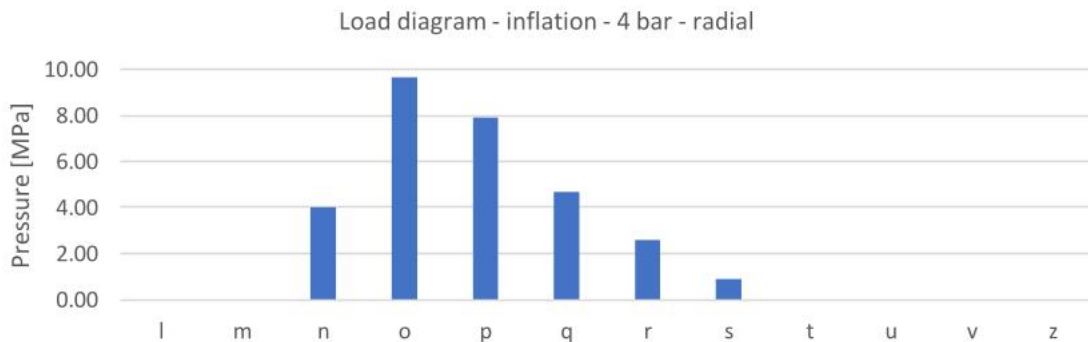


Figure 148 Loading parameters (above) and contact pressure diagram (below) applied in the simulation of the 4 bar inflation on a radial tire.

STRESS RESULTS COMPARISON [MPa]

AREA	EXPERIMENTAL	NUMERICAL
F4	135,12	210,90
F5	296,46	297,00
F6	304,00	303,70

STRESS RATIOS COMPARISON [/]

AREAS	EXPERIMENTAL	NUMERICAL
F4/F5	0,456	0,710
F5/F5	1,000	1,000
F6/F5	1,025	1,023

Stress comparison - inflation - 4 bar - radial

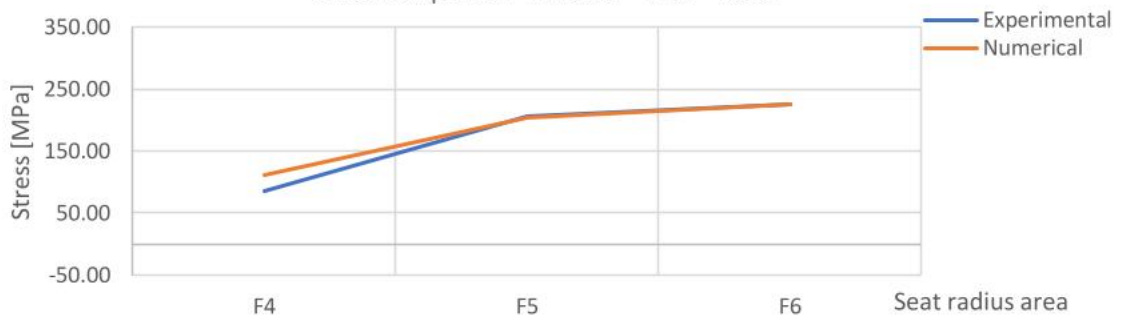


Figure 149 Results comparison of the 4 bar simulation on a radial tire.

4 bar - bias - inflation							
MODEL PARAMETERS			APPLIED LOADS				
INFLATION PRESSURE		ALLOCATION COEFFICIENTS		F [N]		P _n [MPa]	
P ₀ [MPa]	0,4	c _l	0,00	F _l	0	P _{nl}	0,00
AXIAL LOAD - AUTOMOTIVE THEORY		c _m	0,00	F _m	0	P _{nm}	0,00
F _a [N]	144892	c _n	0,00	F _n	0	P _{nn}	0,00
AXIAL LOAD - SIMULATION		c _o	0,10	F _o	7126	P _{no}	2,05
F _a ' [N]	71265	c _p	0,15	F _p	10690	P _{np}	3,03
CORRECTIVE COEFFICIENT		c _q	0,22	F _q	15678	P _{nq}	4,37
k	0,49	c _r	0,32	F _r	22805	P _{nr}	3,53
		c _s	0,16	F _s	11402	P _{ns}	1,84
		c _t	0,05	F _t	3563	P _{nt}	0,65
		c _u	0,00	F _u	0	P _{nu}	0,00
		c _v	0,00	F _v	0	P _{nv}	0,00
		c _z	0,00	F _z	0	P _{nz}	0,00

Load diagram - inflation - 4 bar - bias

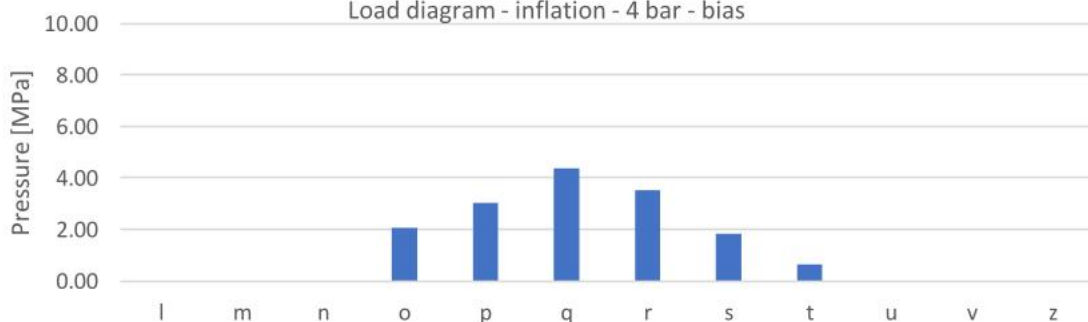


Figure 150 Loading parameters (above) and contact p diagram (below) applied in sim. of 4 bar inflation on a bias tire.

STRESS RESULTS COMPARISON [MPa]

AREA	EXPERIMENTAL	NUMERICAL
F4	88,08	126,60
F5	181,69	183,10
F6	188,27	189,00

STRESS RATIOS COMPARISON [/]

AREAS	EXPERIMENTAL	NUMERICAL
F4/F5	0,485	0,691
F5/F5	1,000	1,000
F6/F5	1,036	1,032

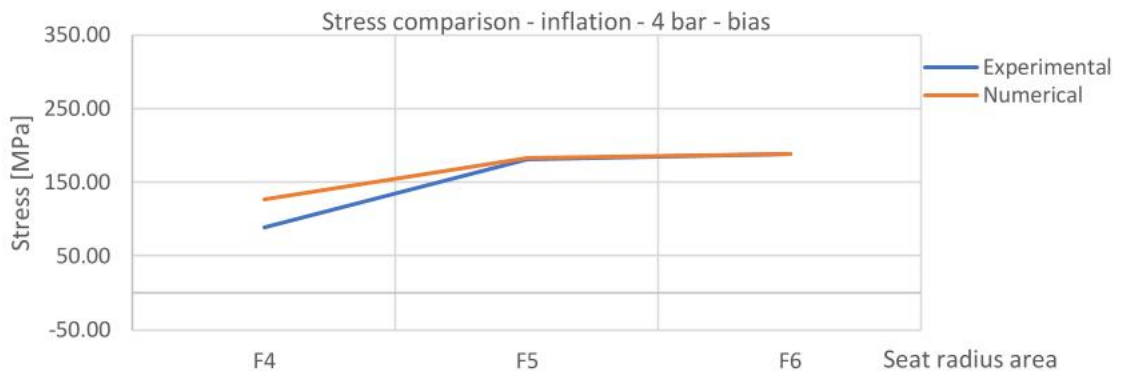


Figure 151 Results comparison of the 4 bar simulation on a radial tire.

6 bar - radial - inflation							
MODEL PARAMETERS			APPLIED LOADS				
INFLATION PRESSURE		ALLOCATION COEFFICIENTS		F [N]		P _n [MPa]	
P ₀ [MPa]	0,6	c _l	0,00	F _l	0	P _{nl}	0,00
AXIAL LOAD - AUTOMOTIVE THEORY		c _m	0,00	F _m	0	P _{nm}	0,00
F _a [N]	217337	c _n	0,00	F _n	0	P _{nn}	0,00
AXIAL LOAD - SIMULATION		c _o	0,05	F _o	5456	P _{no}	1,57
F _a ' [N]	109118	c _p	0,13	F _p	14185	P _{np}	4,02
CORRECTIVE COEFFICIENT		c _q	0,21	F _q	22915	P _{nq}	6,39
k	0,50	c _r	0,34	F _r	37100	P _{nr}	5,74
		c _s	0,20	F _s	21824	P _{ns}	3,52
		c _t	0,07	F _t	7638	P _{nt}	1,40
		c _u	0,00	F _u	0	P _{nu}	0,00
		c _v	0,00	F _v	0	P _{nv}	0,00
		c _z	0,00	F _z	0	P _{nz}	0,00

Load diagram - inflation - 6 bar - radial

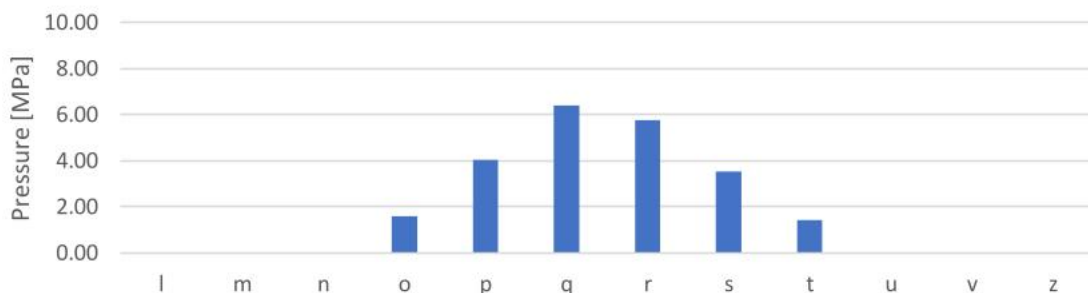


Figure 152 Loading param (above) and contact p diagram (below) applied in the sim 6 bar inflation on a radial tire.

STRESS RESULTS COMPARISON [MPa]

AREA	EXPERIMENTAL	NUMERICAL
F4	135,12	210,90
F5	296,46	297,00
F6	304,00	303,70

STRESS RATIOS COMPARISON [/]

AREAS	EXPERIMENTAL	NUMERICAL
F4/F5	0,456	0,710
F5/F5	1,000	1,000
F6/F5	1,025	1,023

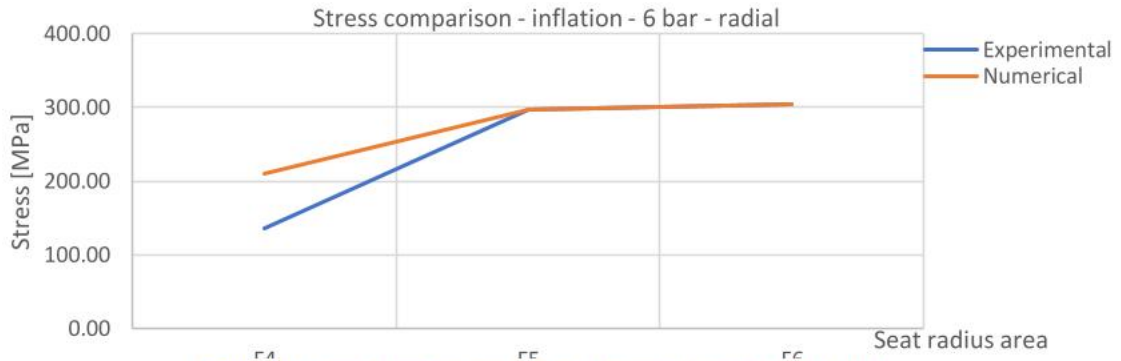


Figure 153 Results comparison of the 6 bar simulation on a radial tire.

6 bar - bias - inflation			
MODEL PARAMETERS		APPLIED LOADS	
INFLATION PRESSURE		F [N]	
P ₀ [MPa]	0,6	F _l	0
AXIAL LOAD - AUTOMOTIVE THEORY		F _m	0
		F _n	0
F _a [N]	217337	F _o	0
AXIAL LOAD - SIMULATION		F _p	0
		F _q	0
F _a ' [N]	58557	F _r	4099
CORRECTIVE COEFFICIENT		F _s	11711
		F _t	14639
k	0,27	F _u	16396
ALLOCATION COEFFICIENTS		F _v	9369
		F _z	2342
		P _{nl}	0,00
		P _{nm}	0,00
c _l	0,00	P _{nn}	0,00
c _m	0,00	P _{no}	0,00
c _n	0,00	P _{np}	0,00
c _o	0,00	P _{nq}	0,00
c _p	0,00	P _{nr}	0,63
c _q	0,00	P _{ns}	1,89
c _r	0,07	P _{nt}	2,69
c _s	0,20	P _{nu}	3,85
c _t	0,25	P _{nv}	3,45
c _u	0,28	P _{nz}	2,51
c _v	0,16		
c _z	0,04		

Load diagram - inflation - 6 bar - bias

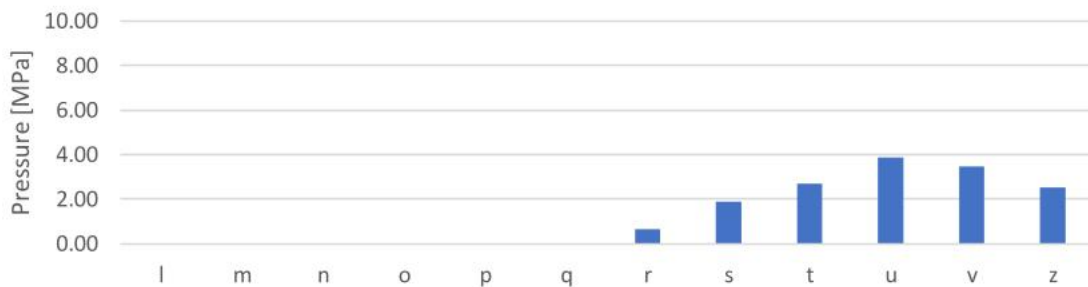


Figure 154 Loading param (above) and contact p diagram (below) applied in the sim 6 bar inflation on a bias tire.

STRESS RESULTS COMPARISON [MPa]

AREA	EXPERIMENTAL	NUMERICAL
F4	144,38	245,00
F5	286,67	288,10
F6	275,33	275,50

STRESS RATIOS COMPARISON [/]

AREAS	EXPERIMENTAL	NUMERICAL
F4/F5	0,504	0,850
F5/F5	1,000	1,000
F6/F5	0,960	0,956

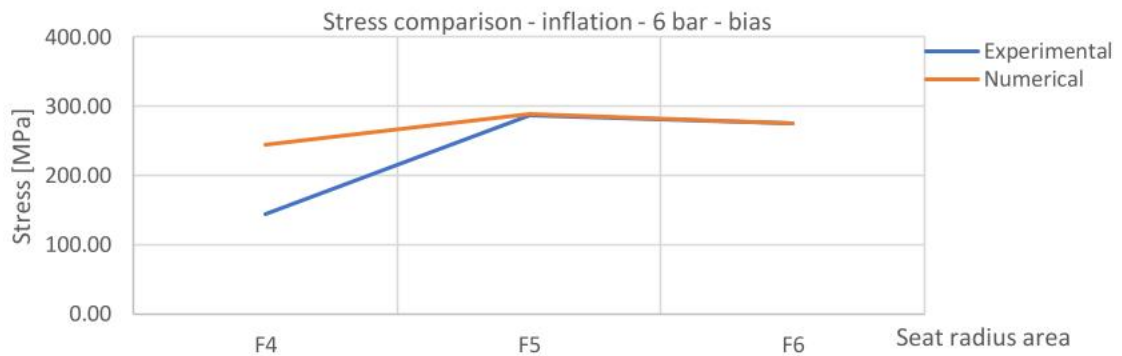


Figure 155 Results comparison of the 6 bar simulation on a bias tire.

An exemplificative illustration of the graphic results of the FE simulations is proposed as well (Figure 156):

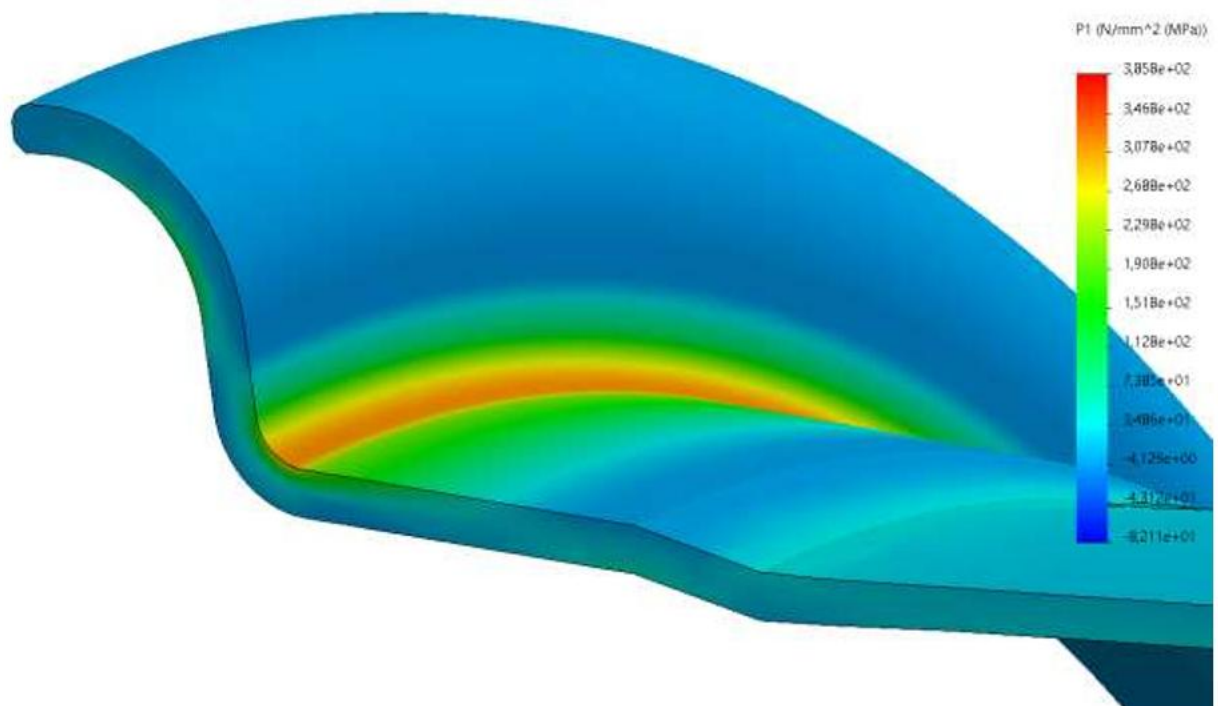


Figure 156 Graphic representation of the main stress field returned by the FE static simulation for the 6 bar – 15.100 – radial tire configuration.

As can be noticed, a good regularity was reached in the load diagrams supposed: in all the inflation configurations, in fact, both the loading hypotheses and conditions exposed before were respected. As described previously, the best matching between the stress ratios in the seat radius areas was searched firstly; from the stress ratios results it is clear that a good overlapping between experimental and numerical values was obtained for the F6/F5 ratio in all the inflation studies. The F4/F5 experimental ratio, instead, could not be interpreted numerically in any way: F4 values, in fact, systematically overestimate the F4 laboratory results. This could be due either to the limits and approximations of the model developed or to inaccuracies of the strain gauges application during the tests. In any case, such model limit was considered acceptable, since F4 stress is the lowest of the three stress samples and, thus, cannot be considered responsible of static nor fatigue failures of the rim. In fact, this inaccuracy of the model remained even in furthermore accurate model versions, which was applied in the radial load study. However, since F4 stress has a relatively low relevance in both the static and the fatigue resistance verifications, this model flaw was considered negligible.

A quick analysis of the simulation results compared to the contact pressure diagrams reveals a few evaluations of both the tire design and the inflation pressure influence on the way of interaction between tire itself and rim. Of course, these statements can be considered significant only if the accuracy and hypothesis of the model used to study the contact phenomenon prove to be enough accurate. The first association that can be done is between the tire design and the main loading area on the flange. As visible from the diagrams, in fact, it is reasonable to presume that bias tires tend to load upper areas of the flange compared to radial tires. In fact, even if the dependency of the load applied to the rim flange and bead seat areas under loading still remains a challenging and not completely understood problem, from literature and experimental evidence it emerges that the tire design highly affects the stress state of the bead seat [25]. Moreover, the pressures that is necessary to apply in order to reproduce the experimental data seem to be lower for the bias tires. With equal tire design, it seems that higher inflation pressures produce higher contact in the upper area of the flange. This can be ascribed to the way the tire deforms under the action of the internal inflation pressure: it is plausible that, the higher the inflation pressure, the higher the tire is pushed on the hook of the flange.

In the following pictures, a qualitative representation of the mainly loaded areas of the flange depending on the inflation conditions is presented. It is good to remember that these load distributions derive from a model which is quite approximated and then represent only an interpretation of the possible contact solution between the tire and the rim (Figure 157; Figure 158; Figure 159; Figure 160).

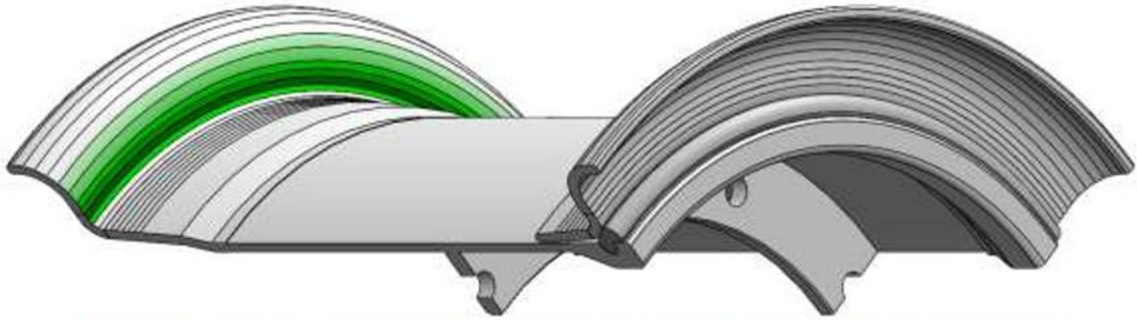


Figure 157 Qualitative supposed load distribution for the 4 bar inflation configuration on a radial tire.

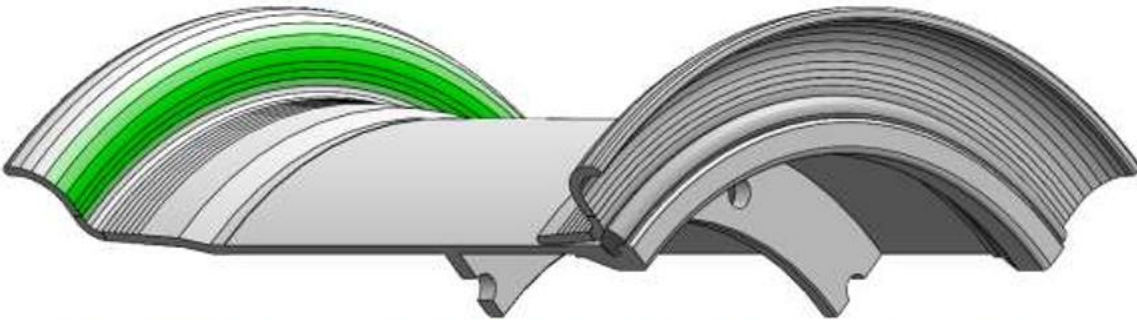


Figure 158 Qualitative supposed load distribution for the 4 bar inflation configuration on a bias tire.

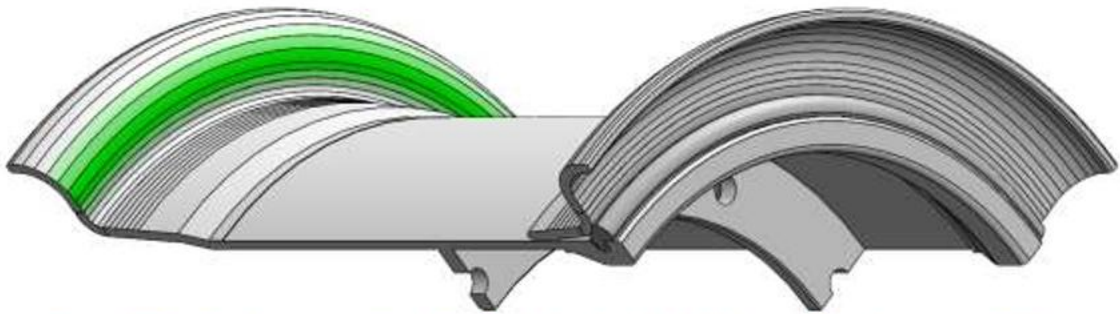


Figure 159 Qualitative supposed load distribution for the 6 bar inflation configuration on a radial tire.

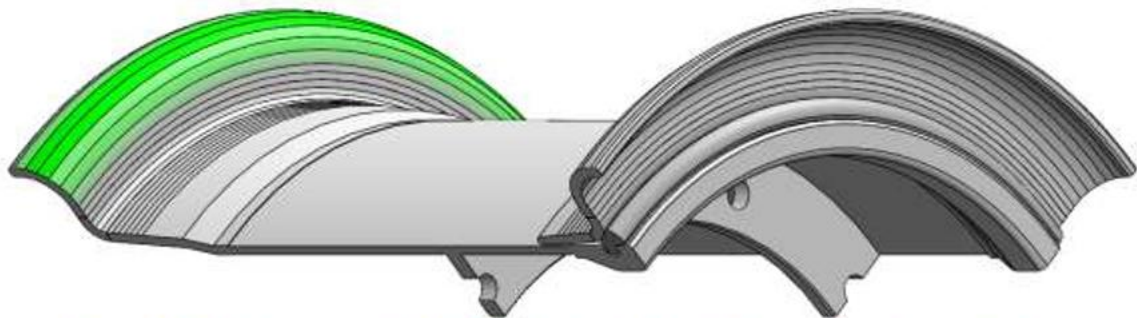


Figure 160 Qualitative supposed load distribution for the 6 bar inflation configuration on a bias tire.

From the images above, it is clear, following the model developed for the inflation study, that the higher the inflation pressure, the upper the flange zone which is loaded. Moreover, bias design tends to reduce the contact pressure onto the flange compared to the radial one; furthermore, with equal inflation pressure, the bias design seems to mainly apply the load on a upper area of the flange compared to the radial tire.

Even if the model applied at inflation problem is quite rough and has a few limits, it revealed to be very helpful to understand the behaviour of different tire design and the influence of the inflation pressure on the contact area on the flange. With these results, the inflation study can be considered accomplished. More detailed and accurate models, which will be exposed in the next paragraph, have been developed for the radial load problem.

The need to improve the model used for the inflation study went hand in hand with the will to better understand the rim-tire contact phenomenon and therefore perform FE simulations as close as possible to the real interaction.

9.2.3. Radial load tests

After obtaining the results exposed in the previous paragraph for the inflations simulations, the radial load problem was faced. In this section, the experimental data from rolling laboratory tests will be analysed and a more complex empirical model will be applied in order to understand and reproduce the contact phenomenon in the FE simulations. The radial load problem has a higher relevance compared to the inflation problem, since on the static results of the analyses of the radial load the fatigue simulations will be based. Therefore, a more complex model for this study has been considered appropriate. In the next paragraphs, experimental data and numerical simulations will be presented.

9.2.3.1. Rolling tests experimental data

In this paragraph, the experimental data from Woodridge laboratory rolling tests are presented. The rolling tests performed are eight: for both the radial and the bias tires, four inflation pressures have been tested (2, 4, 6 and 8 bar). For every inflation value, five increasing radial loads have been applied: 5000 kg, 7500 kg, 10000 kg, 12500 kg and 15100 kg. For safety reasons, the 15100 kg load has not been applied on the 2 bar inflated tires. The tables with the maximum stress values measured are reported below (Table 18):

ROLLING TESTS EXPERIMENTAL DATA

2011_Radial_Tire_2bar_5k_7.5k_10k_12.5k_Loading

Radial Load	Stress [MPa]									
	F1	F2	F3	F4	F5	F6	D1	D2	D3	D4
5,000 kg	Lost	Lost	80,4	79,9	164,3	192,6	100,4	105,6	92,5	147,0
7,500 kg	Lost	Lost	88,6	92,0	177,5	200,9	113,4	117,4	100,8	160,2
10,000 kg	Lost	Lost	95,8	103,0	190,1	208,0	124,3	126,2	104,9	171,0
12,500 kg	Lost	Lost	101,4	112,4	199,9	213,8	136,1	135,6	108,1	182,3

1011_Bias_Tire_2bar_5k_7.5k_10k_12.5k_Loading

Radial Load	Stress [MPa]									
	F1	F2	F3	F4	F5	F6	D1	D2	D3	D4
5,000 kg	Lost	Lost	85,5	89,5	196,9	171,9	102,7	103,6	77,3	179,3
7,500 kg	Lost	Lost	103,7	106,5	217,3	191,2	118,1	118,9	92,4	198,3
10,000 kg	Lost	Lost	119,7	121,1	235,7	207,7	132,2	132,7	107,1	215,3
12,500 kg	Lost	Lost	137,3	137,4	255,4	225,4	147,5	148,2	121,8	232,3

2021_Radial_Tire_4bar_5k_7.5k_10k_12.5k_15.1k_Loading

Radial Load	Stress [MPa]									
	F1	F2	F3	F4	F5	F6	D1	D2	D3	D4
5,000 kg	Lost	Lost	146,0	130,1	253,0	265,3	166,4	174,9	156,7	240,2
7,500 kg	Lost	Lost	153,2	142,6	265,8	272,8	178,7	186,8	165,2	254,5
10,000 kg	Lost	Lost	159,8	154,7	278,0	279,6	190,8	198,0	172,8	268,5
12,500 kg	Lost	Lost	165,3	165,2	288,3	285,5	201,9	207,9	178,8	280,4
15,100 kg	Lost	Lost	171,6	177,4	301,0	292,1	214,6	219,1	184,4	291,7

1021_Bias_Tire_4bar_5k_7.5k_10k_12.5k_15.1k_Loading

Radial Load	Stress [MPa]									
	F1	F2	F3	F4	F5	F6	D1	D2	D3	D4
5,000 kg	Lost	Lost	180,7	145,3	309,7	257,5	187,1	190,5	170,0	291,6
7,500 kg	Lost	Lost	196,9	158,8	326,1	274,5	201,8	206,2	183,1	307,9
10,000 kg	Lost	Lost	214,3	175,5	343,9	293,7	218,3	222,7	197,0	325,3
12,500 kg	Lost	Lost	230,6	191,9	359,1	311,7	233,9	237,7	211,4	342,3
15,100 kg	Lost	Lost	247,0	207,0	377,0	328,3	248,4	252,0	225,2	357,6

2031_Radial_Tire_6bar_5k_7.5k_10k_12.5k_15.1k_Loading

Radial Load	Stress [MPa]									
	F1	F2	F3	F4	F5	F6	D1	D2	D3	D4
5,000 kg	Lost	Lost	231,1	191,0	372,3	355,3	260,6	270,0	242,0	349,6
7,500 kg	Lost	Lost	240,2	205,0	386,4	363,6	276,3	285,0	253,1	365,6
10,000 kg	Lost	Lost	249,7	221,5	402,4	372,0	294,0	301,8	265,4	383,3
12,500 kg	Lost	Lost	256,5	234,3	414,8	378,3	307,9	314,8	274,3	397,2
15,100 kg	Lost	Lost	262,7	246,6	426,4	383,6	321,6	327,4	282,5	410,1

1031_Bias_Tire_6bar_5k_7.5k_10k_12.5k_15.1k_Loading

Radial Load	Stress [MPa]									
	F1	F2	F3	F4	F5	F6	D1	D2	D3	D4
5,000 kg	Lost	Lost	259,7	188,4	358,1	325,5	258,6	267,1	253,1	383,2
7,500 kg	Lost	Lost	280,7	204,4	379,5	346,8	277,2	283,3	269,1	402,8
10,000 kg	Lost	Lost	299,5	218,8	400,8	366,0	293,5	301,5	283,7	420,6
12,500 kg	Lost	Lost	316,6	234,8	421,4	384,6	310,9	319,1	297,8	437,5

15,100 kg	Lost	Lost	334,9	251,7	444,8	403,7	328,5	336,2	313,3	455,4
-----------	------	------	-------	-------	-------	-------	-------	-------	-------	-------

2041_Radial_Tire_8bar_5k_7.5k_10k_12.5k_15.1k_Loading

Radial Load	Stress [MPa]									
	F1	F2	F3	F4	F5	F6	D1	D2	D3	D4
5,000 kg	Lost	Lost	283,1	231,8	436,1	415,2	323,8	340,5	310,5	428,0
7,500 kg	Lost	Lost	291,7	244,7	450,4	423,2	341,5	357,6	322,8	444,7
10,000 kg	Lost	Lost	302,3	263,0	468,4	433,2	364,4	379,0	338,6	464,0
12,500 kg	Lost	Lost	310,9	278,1	482,8	440,9	382,9	396,1	350,1	479,6
15,100 kg	Lost	Lost	317,4	290,7	494,3	446,7	399,0	410,4	358,7	493,2

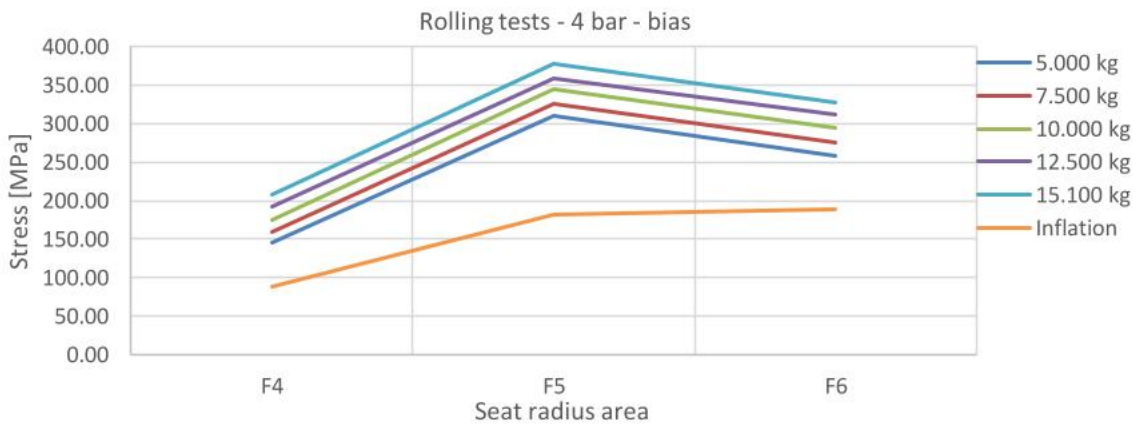
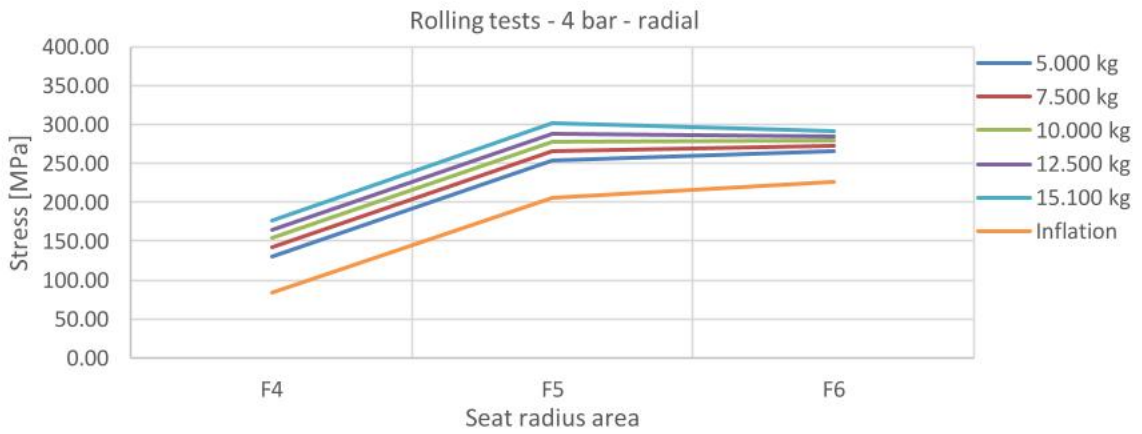
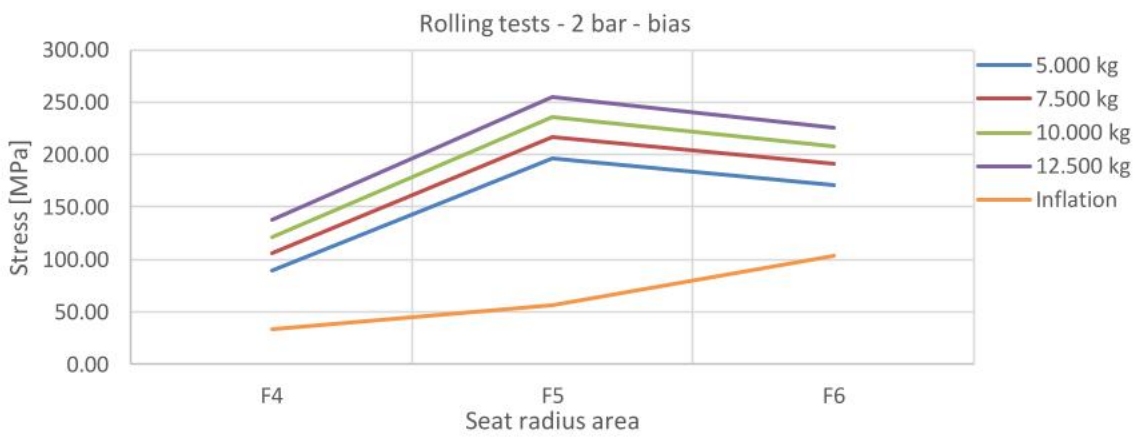
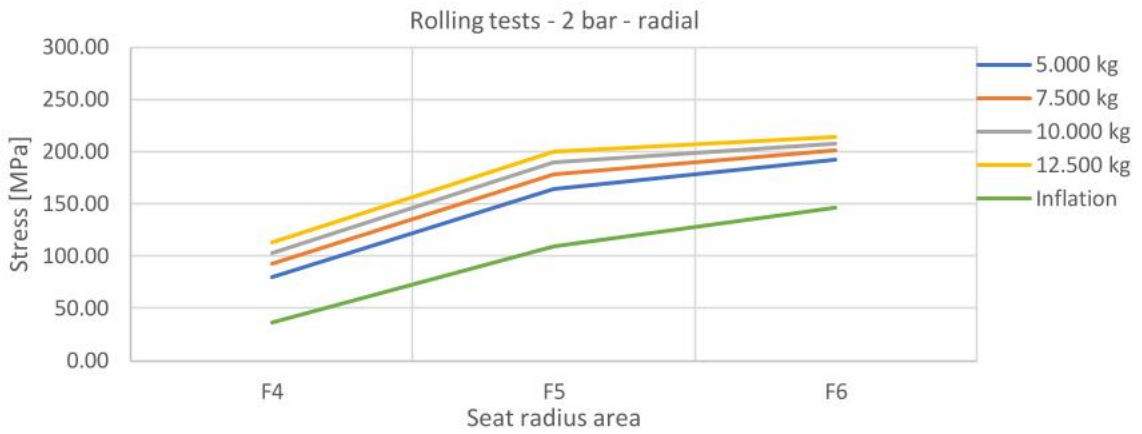
1041_Bias_Tire_8bar_5k_7.5k_10k_12.5k_15.1k_Loading

Radial Load	Stress [MPa]									
	F1	F2	F3	F4	F5	F6	D1	D2	D3	D4
5,000 kg	Lost	Lost	442,1	255,0	508,6	480,2	362,3	375,7	375,9	549,3
7,500 kg	Lost	Lost	470,6	275,1	535,5	508,3	387,8	397,5	397,4	576,7
10,000 kg	Lost	Lost	487,7	287,6	553,5	526,2	402,8	410,4	409,9	592,0
12,500 kg	Lost	Lost	507,9	301,8	574,6	546,5	419,8	429,5	424,0	611,2
15,100 kg	Lost	Lost	529,6	318,8	598,9	568,9	439,2	449,1	441,0	632,2

Table 18 Maximum stress results from Woodridge rolling tests.

As stated before, the stress reported are the maximum recorded during the rolling tests. Therefore, reproducing in the FE simulations this stress values meant to study the most critical load condition the tires faced during the rolling tests. Once again, only F4, F5 and F6 data have been considered; in fact, F1 and F2 gauges measurement was lost during the tests, while F3 data had no consistency with the other results. Finally, D data refer to the detachable flange, which is not object of our study.

A quick comparison of the data allows observing that, as expected, the higher the inflation pressure and the radial load, the higher the stress in seat radius area. A deeper analysis is possible only representing graphically the results (Figure 161):



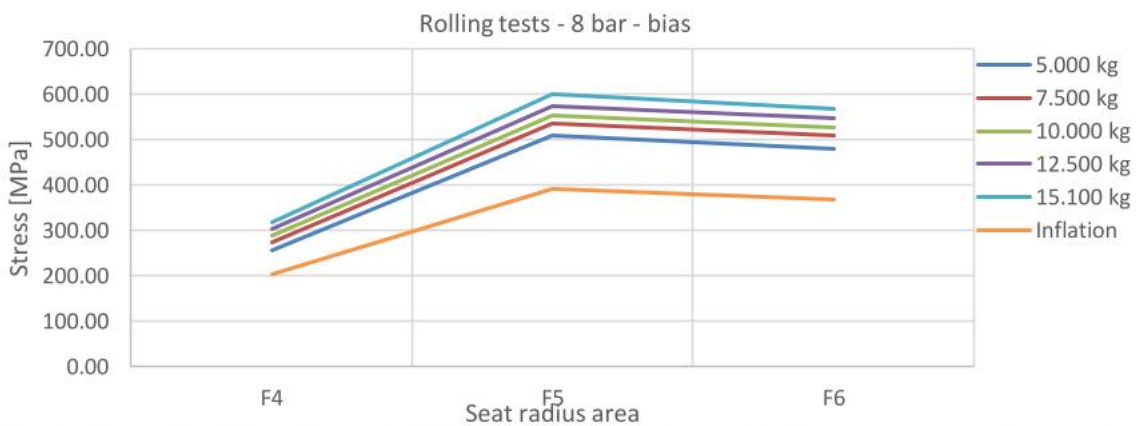
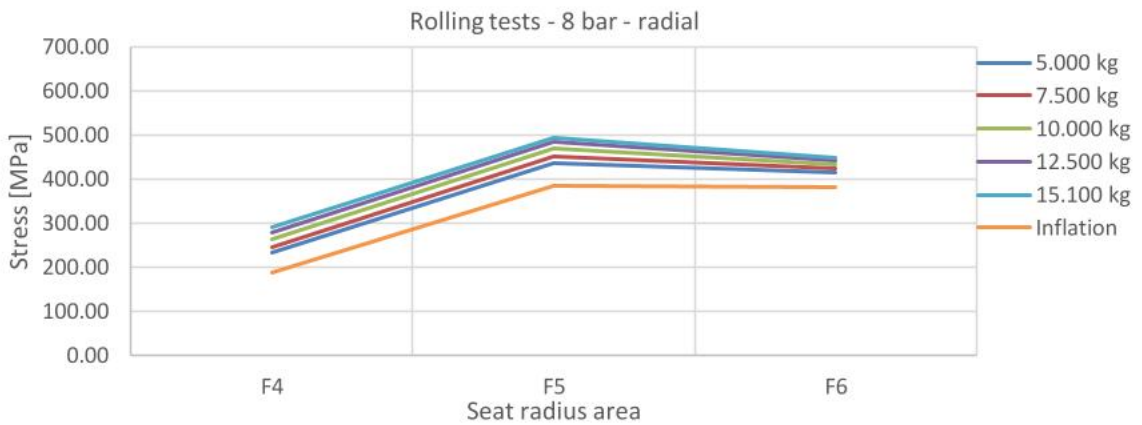
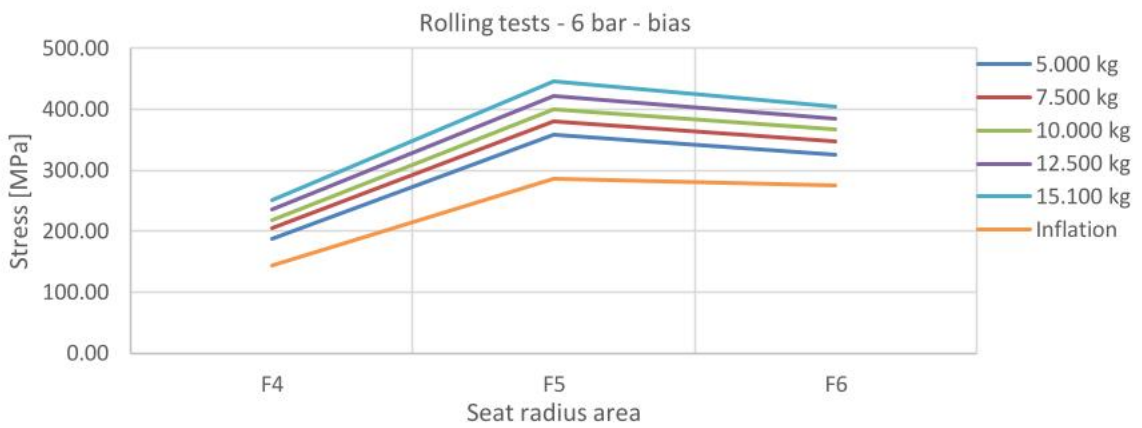
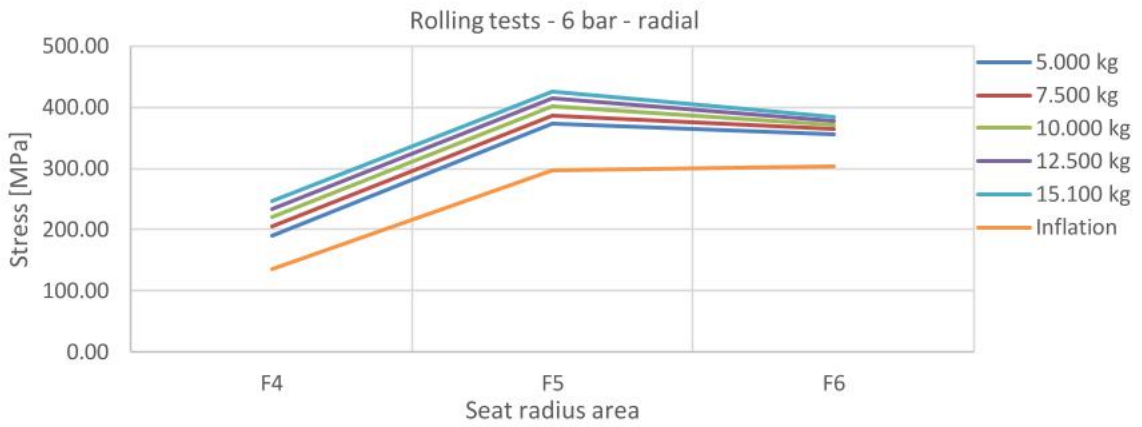
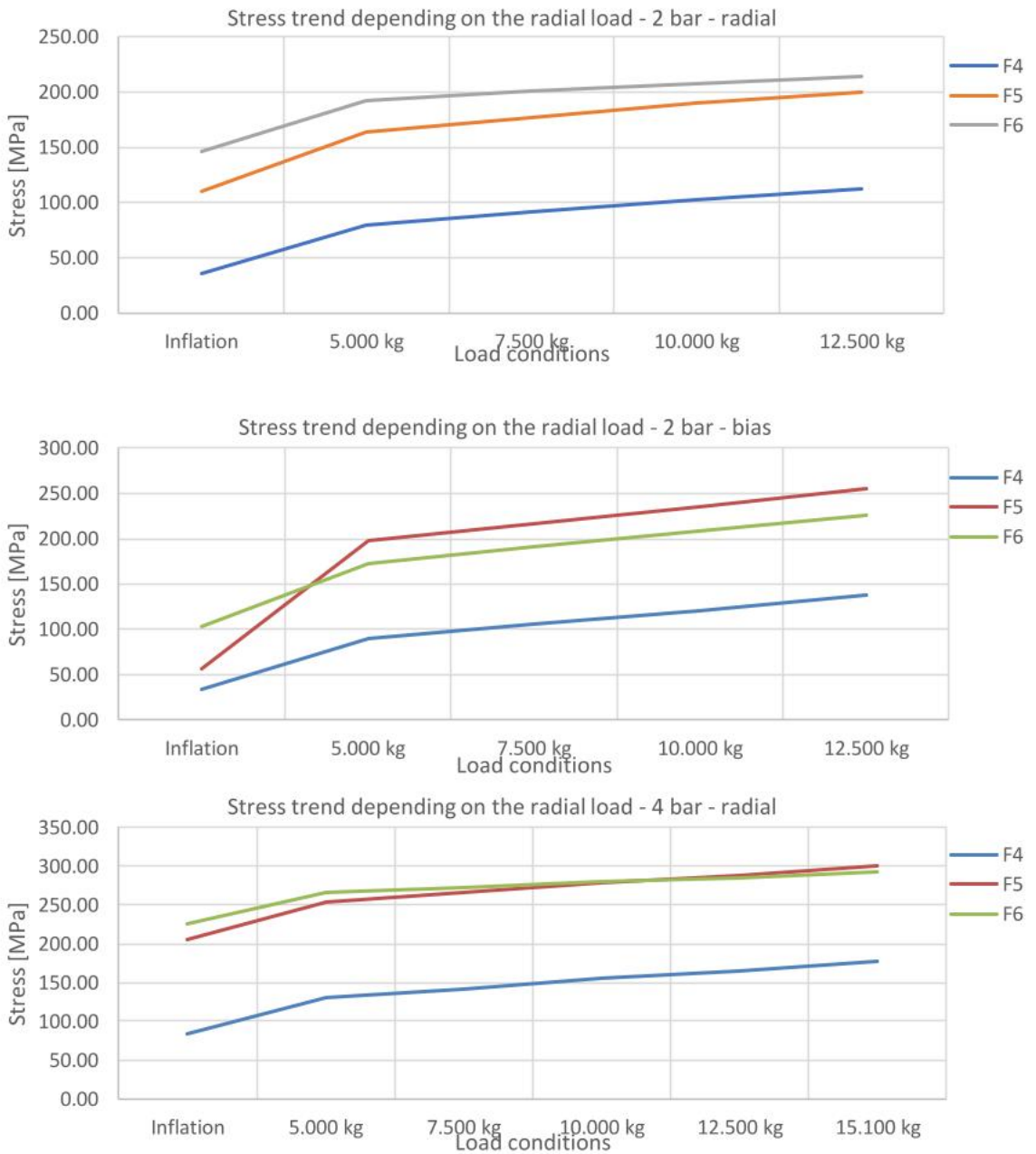


Figure 161 Graphical representation of the maximum stress recorded during the rolling tests on the seat radius surface.

This graphic representation offers a few further information. First, it can be noticed that in many load configurations, the stress curve produced by the radial load cannot be considered simply as a translation of the inflation curve; in other words, the stress is not just amplified, but the stress curve shape is changed as well. In view of what was observed in the previous paragraph about stress trends and load areas, this means that applying and increasing a radial load on the wheel does not only intensify the contact pressure values, but also produces variation in the deformed configuration of the wheel and, thus, in the flange areas mainly loaded. This is clearly visible in the 2 and 4 bar graphs. It was thus excluded the possibility to use the inflation study as starting point on which add up the radial load effects. Ultimately, the radial load study had to be analysed as a case of its own, since the deformation of the tire cannot be considered in any way linear and, therefore, the effects of several loads cannot be summed up. The non-linearity of the tire excludes, in other words, the chance to apply any principle of superposition of effects. By plotting the same data on a different abscissa axis, this phenomenon can be further understood (Figure 162):



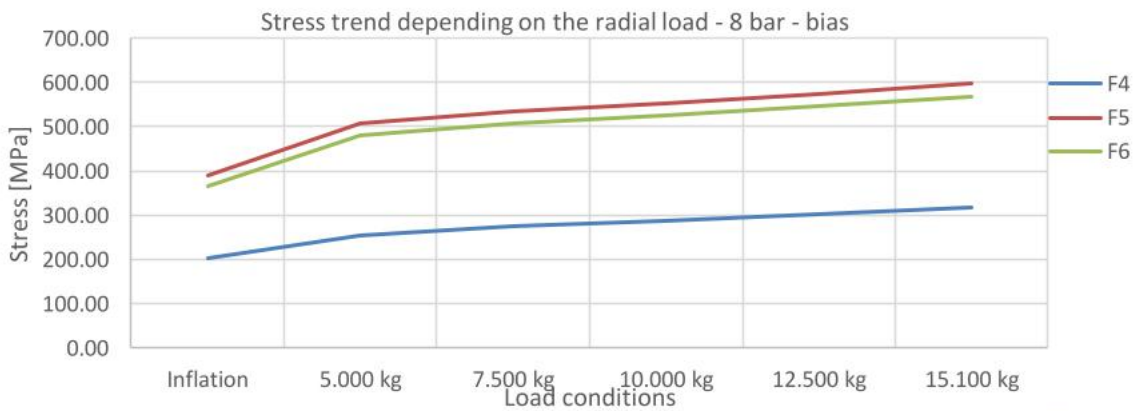
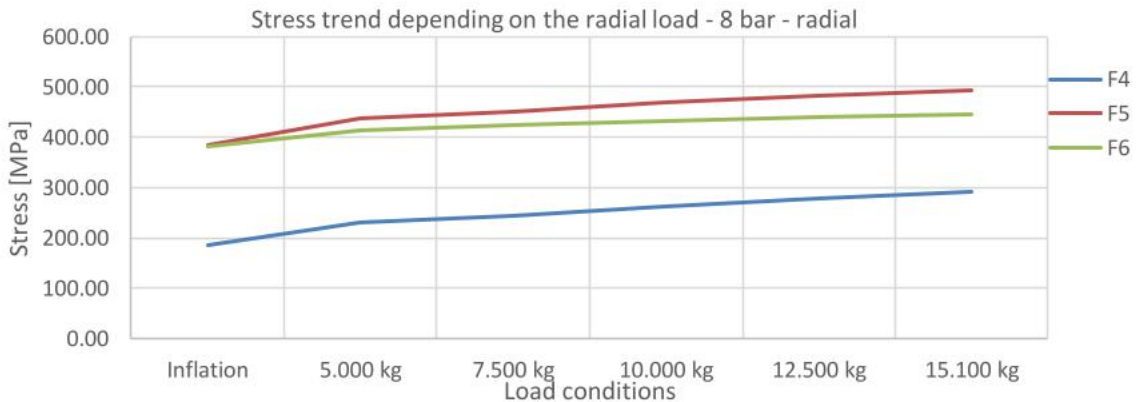
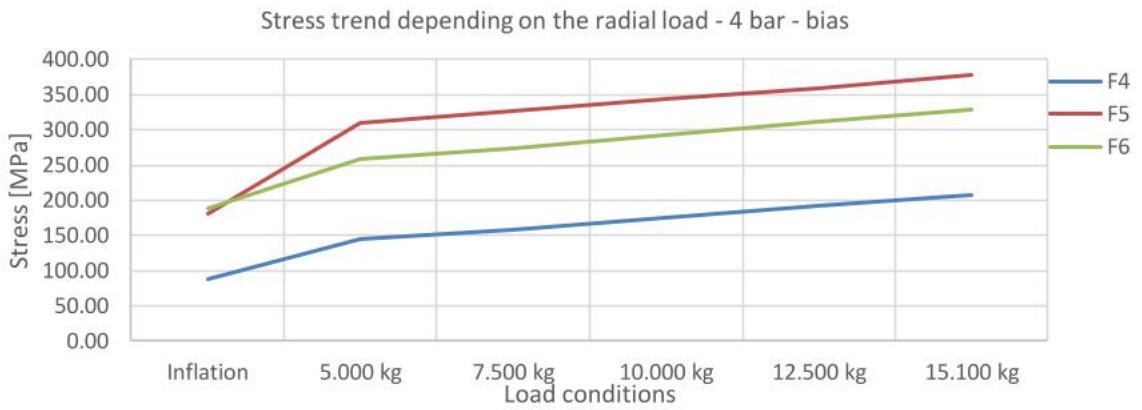


Figure 162 Measured stress trend depending on the load conditions; all the combination of tire design, inflation pressure and radial load are presented.

As shown in the graphs above, the stress increases quite linearly with the radial load applied to the tire, but curves of different areas of the seat radius have different slopes. This confirms what stated before about the contact zone varying with the intensity of the radial load. As described before, this phenomenon did not allow a study based on the decomposition of the whole problem into an inflation problem and a radial problem, because their effect could not be summed up together. Thus, an empirical model similar to the one applied to the inflation study has been used.

9.2.3.2. Model and analyses applied to the radial load problem

As stated before, an empirical reverse model was applied to the radial problem as well. The principle behind it was still to reproduce the experimental results by applying a pressure distribution on the flange. For this study, however, a more complex and accurate model for the contact pressure between rim and tire was developed. The need to improve the model applied to the inflation problem came from some limits of the previous approach. First, in the model applied to the inflation problem, some of the flange areas lacked of contact pressure; in the model developed for the radial load instead, this approximation was removed and it was supposed that every surface of the flange in touch with the tire had to be loaded with a normal pressure. Secondly, a more systematic and valid procedure to suppose the pressure distribution was searched for. In order to accomplish this new hypothesis and criteria, a study conducted by Michelin on the contact pressure between tire and rim came to the aid. This study, suggested by manufacturer, concerns an experimental measurements campaign on the contact pressure between tire and rim flange. Tire and rim tested are not the same studied in this thesis, but the flange profile is nearly identical to the GKN rim, so it is reasonable to presume that the experimental results obtained by Michelin have a good validity for our study as well. The pressure measurements have been recorded with a Tekscan sensors matrix composed by 12 x 52 pressure sensors and put between the tire and the internal surface of the rim. The value of the measured contact pressure is the average of 12 sensors. The qualitative disposition of the sensors is shown below (Figure 163):

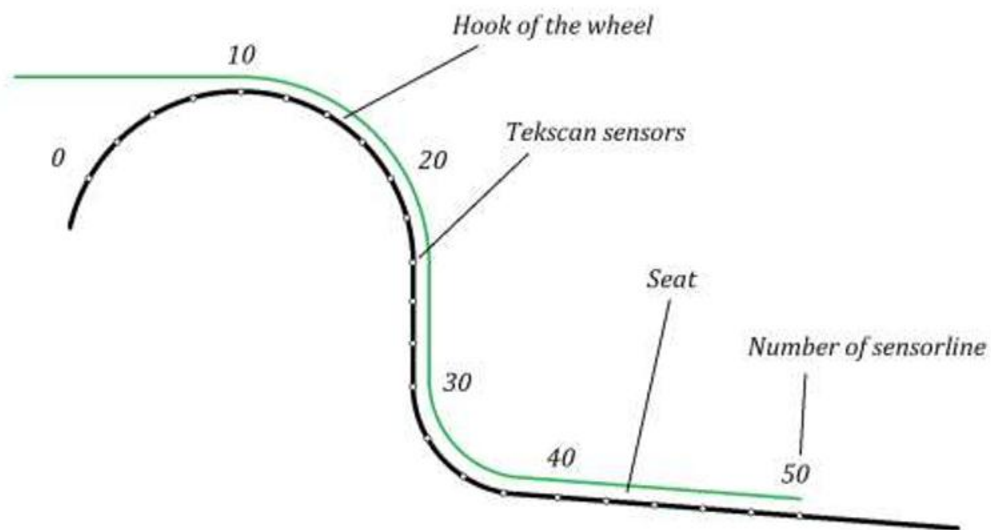


Figure 163 Representation of the Tekscan sensors positioning on the rim flange.

The distance between each of the 52 sensors was about 1,5 mm. The tests carried out by Michelin have been several, with different combination of inflation and radial load parameters. One of the most significant tests produced the results shown below (Figure 164):

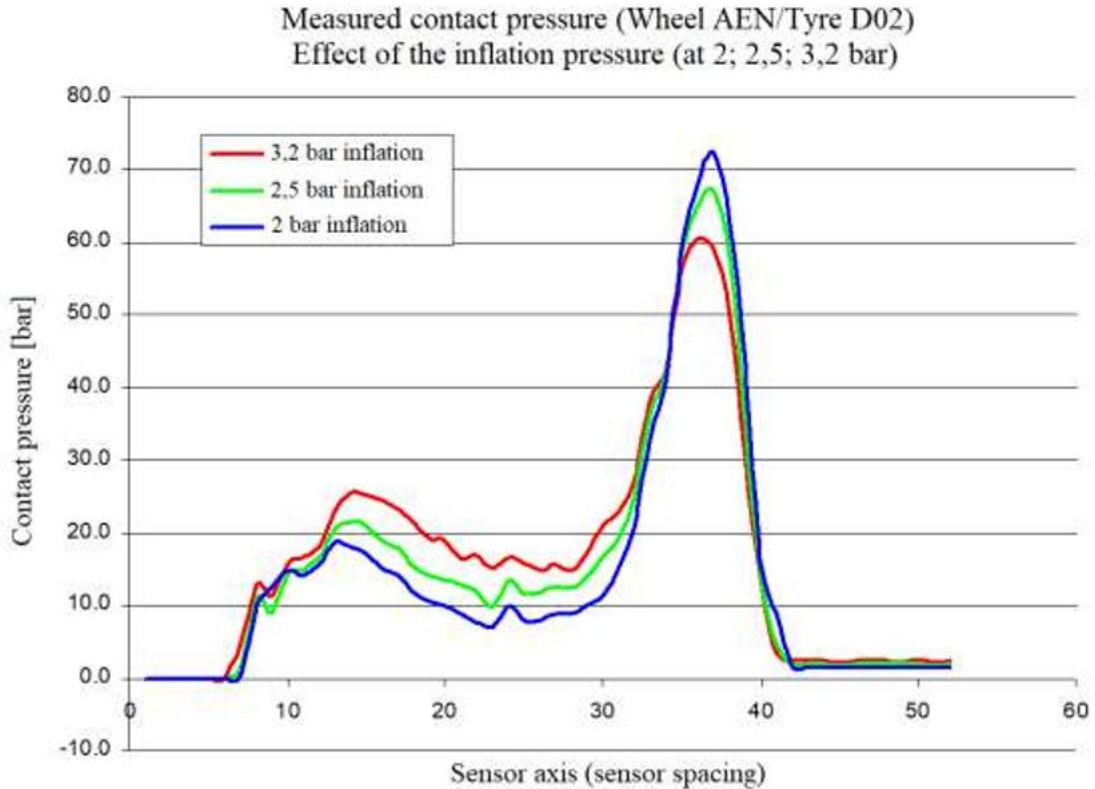


Figure 164 Average measurements given by the Tekscan sensors matrix for different value of inflation pressure.

The study consisted in three different tests, which differed by the inflation pressure value: the aim of the tests was to evaluate the effect of the inflation pressure variations on the contact pressure on the flange area. As can be noticed, the contact pressure distribution measured is more complex than the one supposed for our inflation study. As expected, the whole flange surface is subject to a contact pressure, which value varies along the flange profile. More in detail, two pressure peaks can be detected: the first is set on the hook of the flange, while the second is placed in the seat radius area. In the model previously developed, this pressure peak was not considered. Between the two peaks, a pressure plateau can be detected: graphically, it can be estimated that the values of the contact pressure in this area vary roughly linearly with the inflation pressure, with a ratio of about 4 to 1.

A few other qualitative evaluations can be done; the higher the inflation pressure:

- the lower the contact pressure under the bead wire;
- the higher the contact pressure on the flange hook;
- the higher the contact pressure between seat and hook areas.

All the considerations exposed are purely qualitative, since no sets of numerical data were available but only the resulting graphs and, thus, only a graphical analysis could be carried out. Another significant set of tests carried out by Michelin was about the influence of radial load on the contact pressure. Three different radial load (0, 3.000 and 6.000 daN) were applied to the 3,2 bar inflated tire. The same sensor matrix used for the inflation tests was used for the radial load tests as well; the results are presented below (Figure 165).

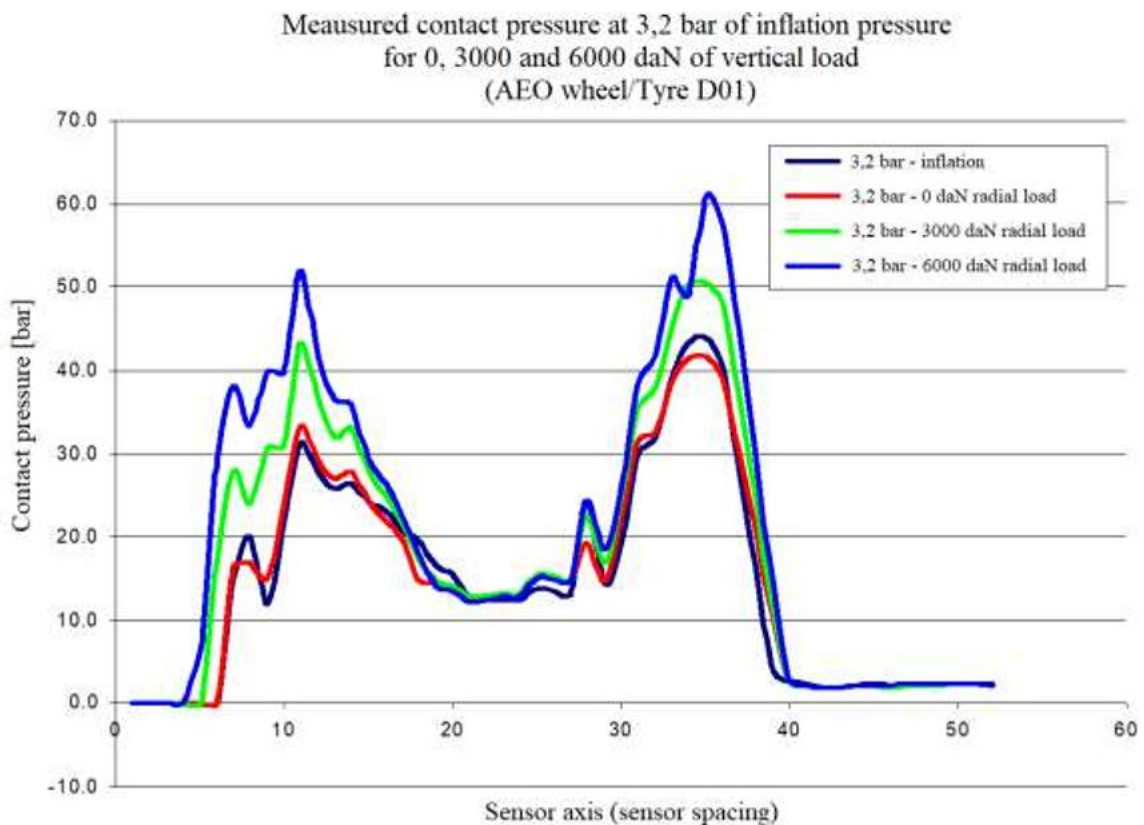


Figure 165 Contact pressure tests results by Michelin. 0, 3000 and 6000 daN radial loads were applied to the wheel.

A few information can be obtained from this graph. In fact, as the radial load applied to the tire rises, the pressure peaks increase as well, while the pressure plateau between the seat radius and the hook does not seem to be affected in any way.

Thus, it is reasonable to state that the radial load produces an increase of the contact pressure on the hook and on the seat radius of the flange, but not on the vertical wall area [26].

Starting from the considerations on the results of Michelin tests, a more complex model was developed. In fact, the contact pressure curve for the 3,2 bar inflation was considered; this curve was chosen because it was the inflation configuration the most similar to the ones studied in this thesis. The graph of the 3,2 bar inflation and no radial load was graphically extrapolated and applied to the geometry of the GKN rim flange; in fact, a good match between the geometrical pattern of the sensors and the discretization of the flange of our model could be found. The result of this transposition is shown below (Figure 166):

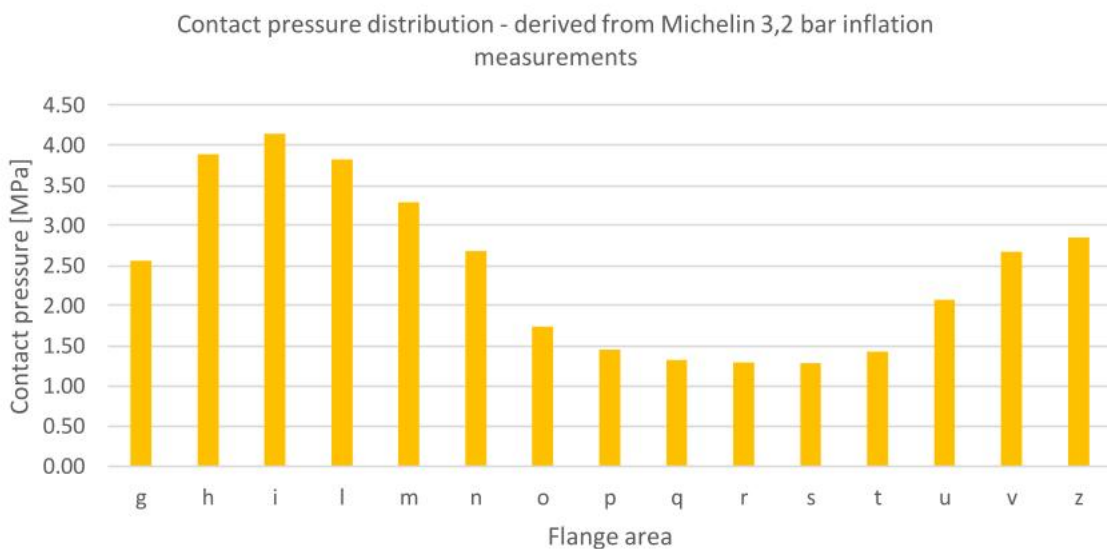


Figure 166 Contact pressure distribution derived from the 3,2 bar inflation measurements results. The Michelin curve was graphically extrapolated and adapted to the GKN rim.

The pressure distribution obtained turned out to be a good base on which the contact model could be built. The criteria applied to it are the following:

- The pressure plateau between seat radius and flange hook is considered fixed and proportional to the inflation pressure, with a ratio of about 4 to 1. Thus, the value of the pressure in this area will not be changed depending on the radial load, since it is considered function of the inflation parameters only.
- The seat radius peak (in the area between “g” and “p”) will be changed in intensity depending on the radial load, but not in position, since it was assumed that the tire heel could not change his loading area once it fit in its seat.
- The hook peak, on the other hand, could be changed in both intensity and position along the flange profile, as the loading area on the upper part of the flange can change depending on the tire design, the inflation pressure and the radial load, as verified in the previous paragraphs.

Starting from this model definition, the 4 and 6 bar load cases have been analysed in order to produce contact pressure diagram for all them. The criteria found analysing Figure 164 and Figure 165 turned out to be very useful in this improved model, as they represented a good starting point on which formulate loading hypotheses. Another essential aspect that distinguishes this model from the previous one, is that no automotive formulas was assumed as a starting point and, hence, no axial force was distributed on the flange surface. Quite the opposite, it was decided that the experimental stress had to be well interpreted both in curve shape and magnitude. In fact, it was reasonable to think that, if a contact pressure distribution was found which could give stress results sufficiently similar to the laboratory ones in terms of both intensity and distribution of the radius stress, that pressure diagram had to be quite similar to the real one. As it will be shown later, corrective k coefficient had to be applied to adjust by only a few percentage points the maximum stress and, therefore, get the best matching between numerical and experimental results. It is good to remember, in fact, that the static results of this set of FE simulations would have been used then as a starting point for the fatigue simulations and the most accurate stress reproduction of the experimental campaign was therefore needed.

The main objective of this model was to evaluate as well as possible the stress values in all the three seat radius areas (F4, F5 and F6). Before presenting the load distributions supposed through this model, a few explanations on the method used to produce them are needed. The curve shape could be modified through three coefficients. The first one, called α , affected the intensity of the seat radius peak, as shown below (Figure 167):

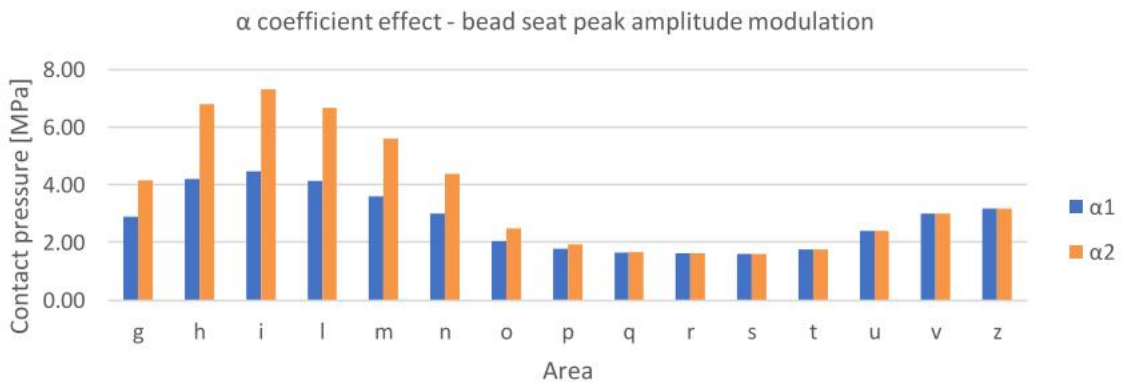


Figure 167 Influence of the α coefficient on the contact pressure diagram.

The second coefficient applied, β , affected the intensity of the hook peak (Figure 168):

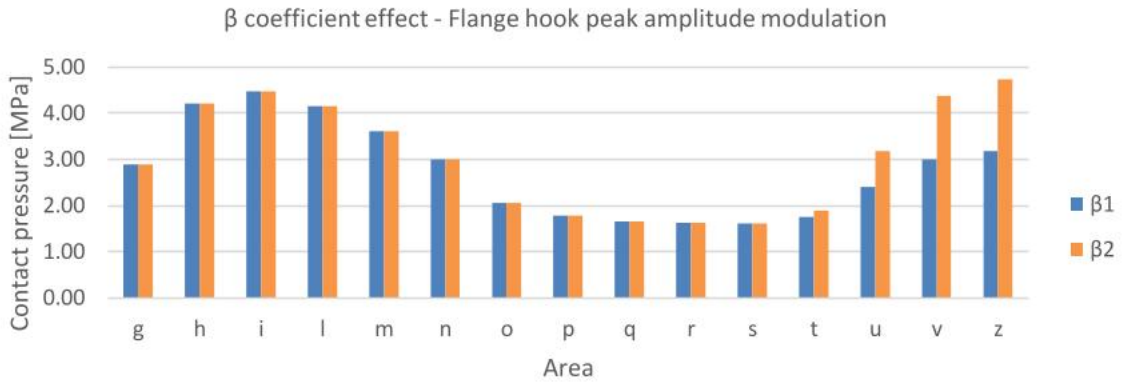


Figure 168 Influence of the β coefficient on the contact pressure diagram.

Finally, the γ coefficient defined the position of the hook peak along the flange profile (Figure 169):

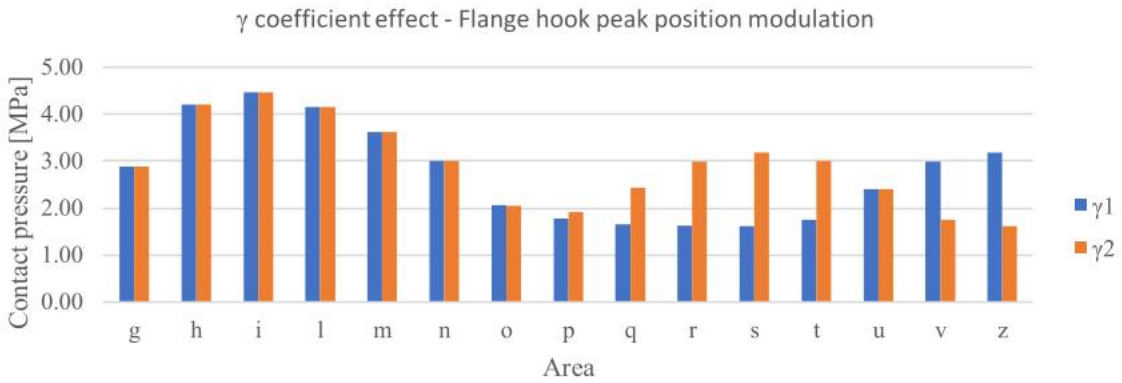


Figure 169 Influence of the γ coefficient on the contact pressure diagram.

On the other hand, the value of the pressure in the plateau area as well as the position of the seat radius peak along the flange profile were considered fixed parameters. The plateau pressure was assumed as a linear function of the inflation pressure only as stated before.

The 3D model of the rim, the mesh sizing and the boundary conditions used for this set of simulations are identical to the ones applied in the inflation analyses described in Paragraph 4.2.5; the only difference consists in the load conditions, which refers to the contact pressure model described above. It is important to remark that the circumferential pressure distribution generated by a vertical radial load should be modelled with a cosine function, which can be compared to the pressure distribution predicted by Hertz for the contact problem. The domain of this function should be centred in the tire-ground mean contact point and should extend in both directions for a semi-amplitude called load angle, whose value varies according to the tire design, the rim design, the inflation pressure and the radial load

applied [25]. However, the aim of this thesis is not to reproduce a faithful distribution of the stress in the rim, but to make the best evaluation of the rim fatigue life possible: for this purpose, modelling the stress distribution along the circumferential direction was completely useless. Thus, in this model any circumferential stress dependency is neglected, as it does not constitute any sort of approximation in terms of evaluation of the fatigue resistance of the component.

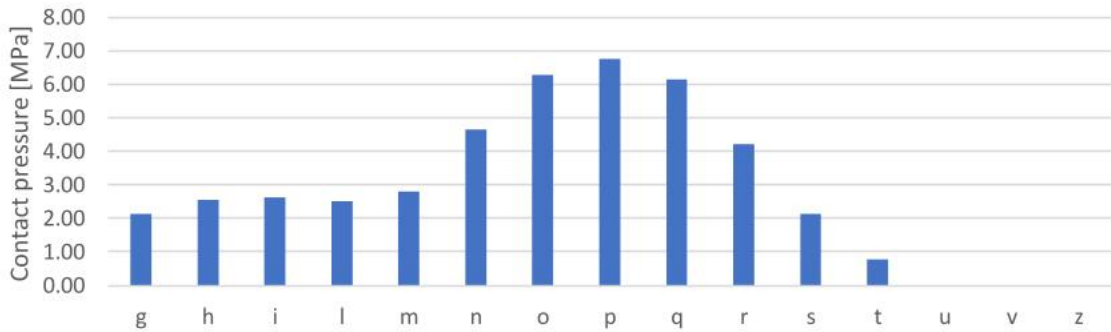
This having been said, the load diagram obtained from the simulations can be presented; it is worth remembering that the criterion on which a pressure diagram could be retained acceptable was a good match between the experimental and numerical results of the F5 and F6 stress (the F4 experimental values were, once, again, very difficult to reproduce in the FE simulations). The contact pressure distributions obtained through this model and the comparison between the experimental and the numerical results are presented in the following figures.

The load diagrams and the results comparisons for the radial tire – 4 bar configurations are shown below (Figure 170; Figure 171; Figure 172; Figure 173; Figure 174):

load diagram - radial - 4 bar – 5.000 kg

AREA	CONTACT PRESSURE [MPa]	AREA	CONTACT PRESSURE [MPa]	AREA	CONTACT PRESSURE [MPa]
g	2,13	n	4,66	s	2,14
h	2,55	o	6,27	t	0,77
i	2,64	p	6,75	u	0,00
l	2,51	q	6,14	v	0,00
m	2,79	r	4,22	z	0,00

Contact pressure diagram - radial - 4 bar - 5.000 kg



Simulation results comparison - radial - 4 bar – 5.000 kg

STRESS RESULTS COMPARISON [MPa]			STRESS RATIOS COMPARISON		
AREA	EXPERIMENTAL	NUMERICAL	AREAS	EXPERIMENTAL	NUMERICAL
F4	130,1	157,2	F4/F5	0,514	0,624
F5	253,0	251,9	F5/F5	1,000	1,000
F6	265,3	265,2	F6/F5	1,049	1,053

Stress results comparison - radial - 4 bar - 5.000 kg

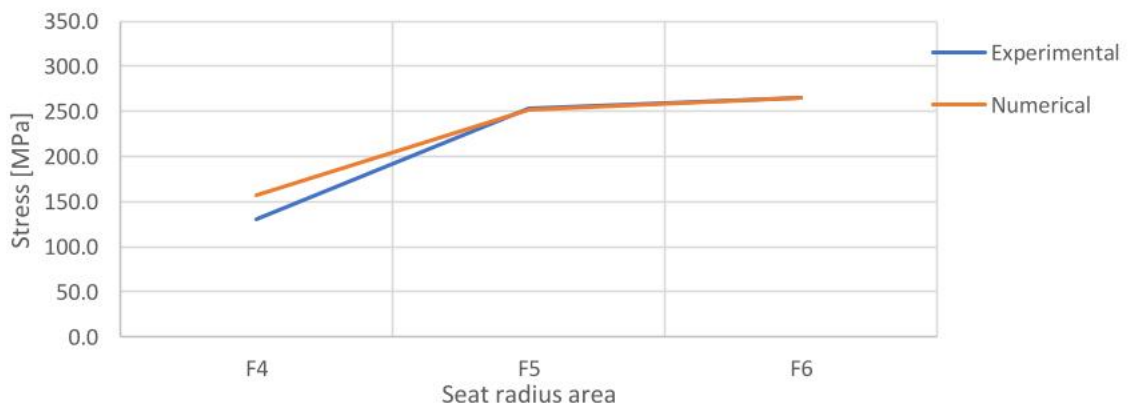
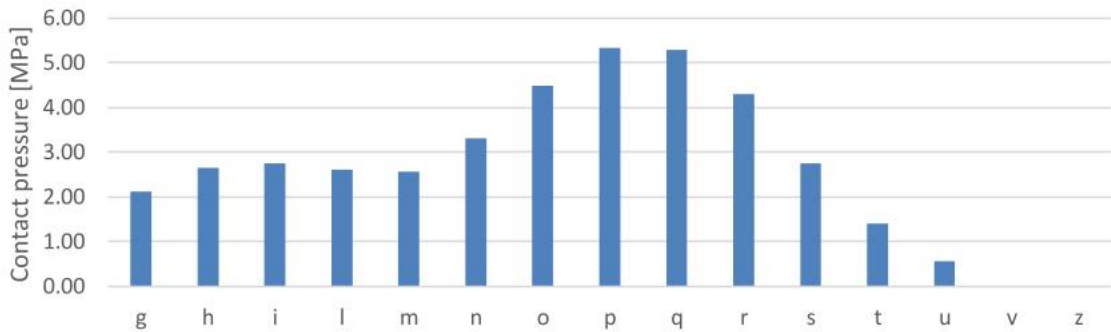


Figure 170 Contact pressure diagram (above) and comparison between experimental and numerical results (below) for the radial tire – 4 bar – 5.000 kg configuration.

Load diagram - radial - 4 bar – 7.500 kg

AREA	CONTACT PRESSURE [MPa]	AREA	CONTACT PRESSURE [MPa]	AREA	CONTACT PRESSURE [MPa]
g	2,12	n	3,30	s	2,74
h	2,64	o	4,47	t	1,40
i	2,75	p	5,32	u	0,55
l	2,61	q	5,28	v	0,00
m	2,56	r	4,30	z	0,00

Contact pressure diagram - radial - 4 bar - 7500 kg



Simulation results comparison - radial - 4 bar – 7.500 kg

STRESS RESULTS COMPARISON [MPa]			STRESS RATIOS COMPARISON		
AREA	EXPERIMENTAL	NUMERICAL	AREAS	EXPERIMENTAL	NUMERICAL
F4	142,60	178,7	F4/F5	0,537	0,673
F5	265,79	265,7	F5/F5	1,000	1,000
F6	272,83	272,5	F6/F5	1,026	1,026

Stress results comparison - radial - 4 bar - 7.500 kg

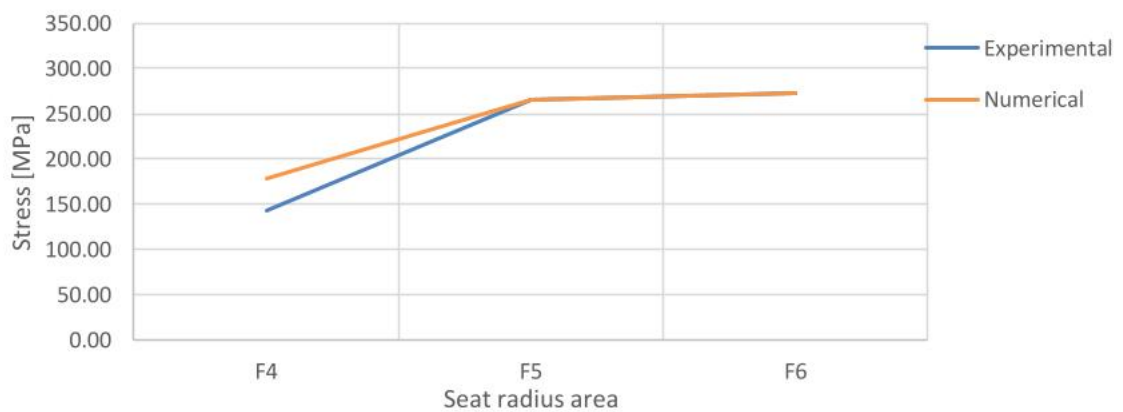
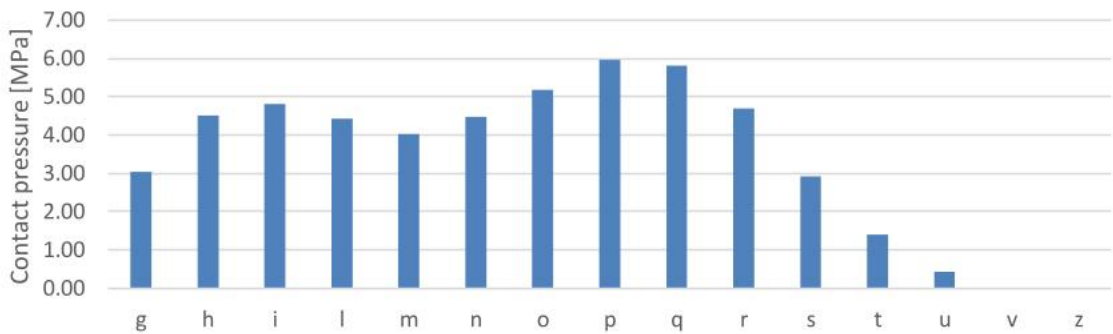


Figure 171 Contact pressure diagram (above) and comparison between experimental and numerical results (below) for the radial tire – 4 bar – 7.500 kg configuration.

Load diagram - radial - 4 bar – 10.000 kg

AREA	CONTACT PRESSURE [MPa]	AREA	CONTACT PRESSURE [MPa]	AREA	CONTACT PRESSURE [MPa]
g	3,04	n	4,46	s	2,92
h	4,51	o	5,17	t	1,39
i	4,80	p	5,95	u	0,43
l	4,43	q	5,82	v	0,00
m	4,03	r	4,69	z	0,00

Contact pressure diagram - radial - 4 bar - 10.000 kg



Simulation results comparison - radial - 4 bar – 10.000 kg

STRESS RESULTS COMPARISON [MPa]			STRESS RATIOS COMPARISON		
AREA	EXPERIMENTAL	NUMERICAL	AREAS	EXPERIMENTAL	NUMERICAL
F4	154,70	183,7	F4/F5	0,556	0,665
F5	278,05	276,1	F5/F5	1,000	1,000
F6	279,65	279,7	F6/F5	1,006	1,013

Stress results comparison - radial - 4 bar - 10.000 kg

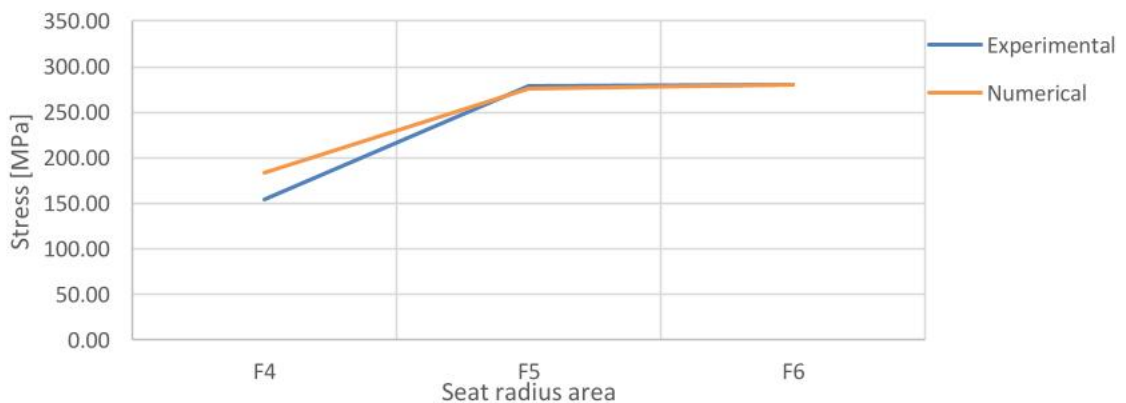
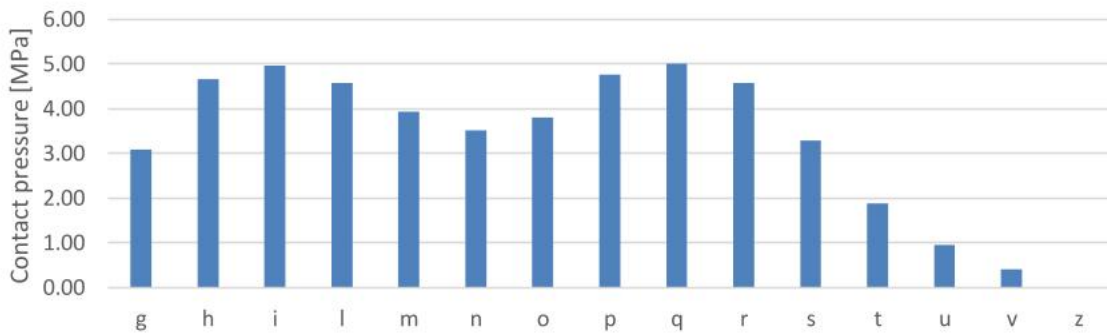


Figure 172 Contact pressure diagram (above) and comparison between experimental and numerical results (below) for the radial tire – 4 bar – 10.000 kg configuration.

Load diagram - radial - 4 bar – 12.500 kg

AREA	CONTACT PRESSURE [MPa]	AREA	CONTACT PRESSURE [MPa]	AREA	CONTACT PRESSURE [MPa]
g	3,09	n	3,52	s	3,28
h	4,66	o	3,81	t	1,88
i	4,96	p	4,76	u	0,94
l	4,58	q	5,00	v	0,40
m	3,93	r	4,58	z	0,00

Contact pressure diagram - radial - 4 bar - 12.500 kg



Simulation results comparison - radial - 4 bar – 12.500 kg

STRESS RESULTS COMPARISON [MPa]			STRESS RATIOS COMPARISON		
AREA	EXPERIMENTAL	NUMERICAL	AREAS	EXPERIMENTAL	NUMERICAL
F4	165,22	202,9	F4/F5	0,573	0,704
F5	288,31	288,4	F5/F5	1,000	1,000
F6	285,47	286,3	F6/F5	0,990	0,993

Stress results comparison - radial - 4 bar - 12.500 kg

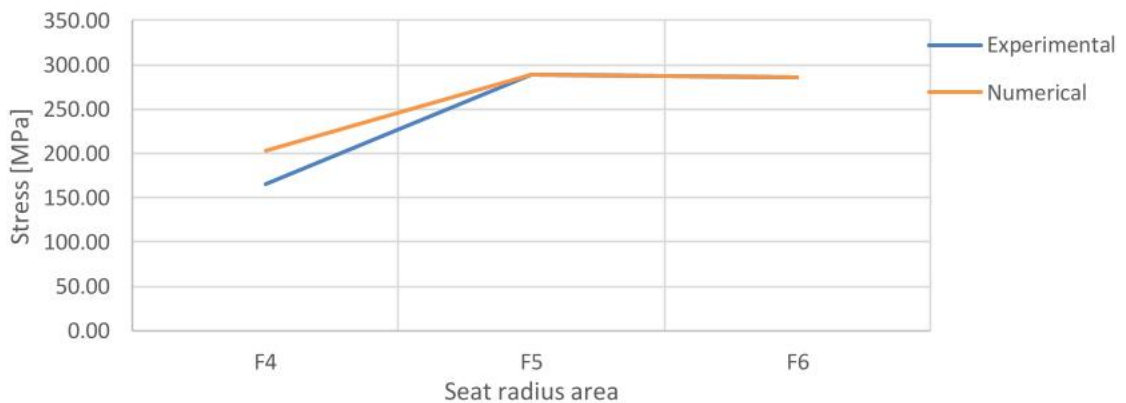
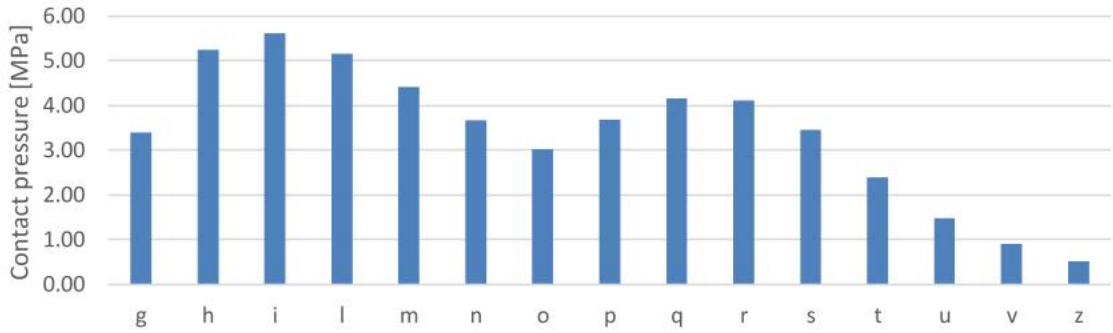


Figure 173 Contact pressure diagram (above) and comparison between experimental and numerical results (below) for the radial tire – 4 bar – 12.500 kg configuration.

Load diagram - radial - 4 bar – 15.100 kg

AREA	CONTACT PRESSURE [MPa]	AREA	CONTACT PRESSURE [MPa]	AREA	CONTACT PRESSURE [MPa]
g	3,39	n	3,66	s	3,45
h	5,25	o	3,01	t	2,39
i	5,61	p	3,67	u	1,47
l	5,16	q	4,15	v	0,90
m	4,40	r	4,11	z	0,51

Contact pressure diagram - radial - 4 bar - 15.100 kg



Simulation results comparison - radial - 4 bar – 15.100 kg

STRESS RESULTS COMPARISON [MPa]			STRESS RATIOS COMPARISON		
AREA	EXPERIMENTAL	NUMERICAL	AREAS	EXPERIMENTAL	NUMERICAL
F4	177,41	221,2	F4/F5	0,589	0,735
F5	301,04	300,8	F5/F5	1,000	1,000
F6	292,10	293,0	F6/F5	0,970	0,974

Stress results comparison - radial - 4 bar - 15.100 kg

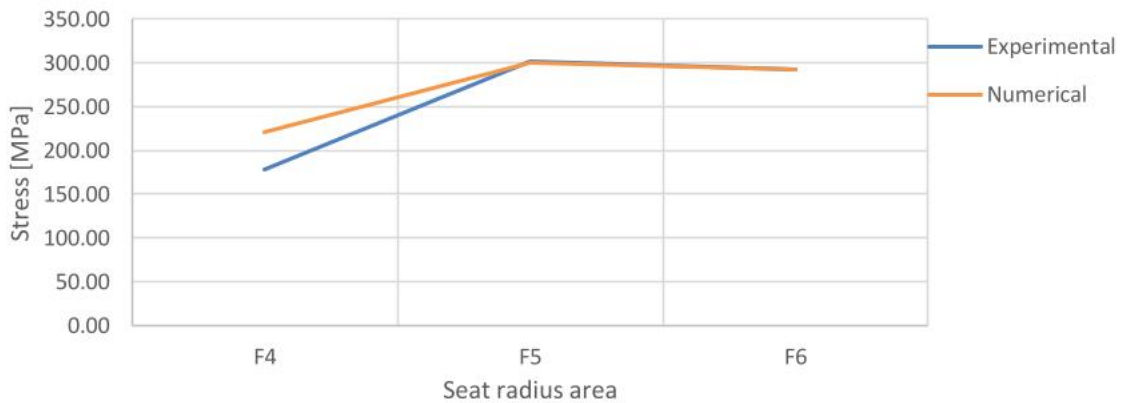
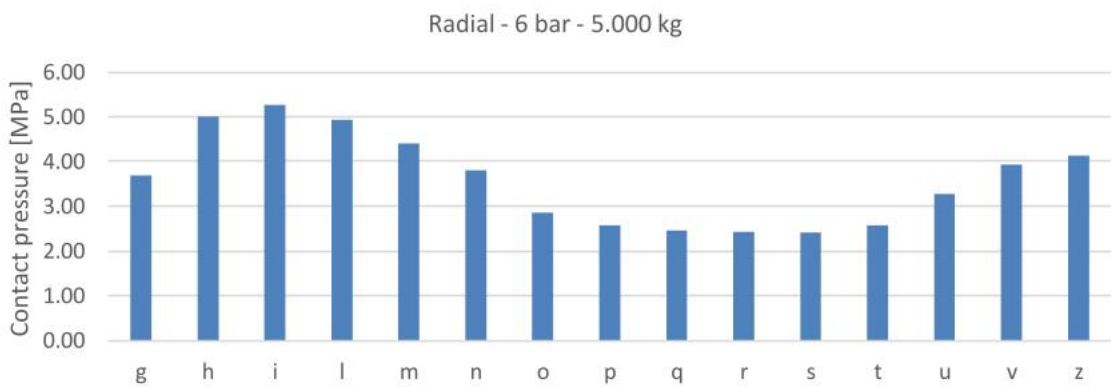


Figure 174 Contact pressure diagram (above) and comparison between experimental and numerical results (below) for the radial tire – 4 bar – 15.100 kg configuration.

The load diagrams and the results comparisons for the radial tire – 6 bar configurations are shown below (Figure 175; Figure 176; Figure 177; Figure 178; Figure 179):

Load diagram - radial - 6 bar – 5.000 kg

AREA	CONTACT PRESSURE [MPa]	AREA	CONTACT PRESSURE [MPa]	AREA	CONTACT PRESSURE [MPa]
g	3,68	n	3,80	s	2,41
h	5,01	o	2,86	t	2,57
i	5,27	p	2,58	u	3,28
l	4,94	q	2,45	v	3,93
m	4,41	r	2,42	z	4,13



Simulation results comparison - radial - 6 bar – 5.000 kg

STRESS RESULTS COMPARISON [MPa]			STRESS RATIOS COMPARISON		
AREA	EXPERIMENTAL	NUMERICAL	AREAS	EXPERIMENTAL	NUMERICAL
F4	191,0	300,4	F4/F5	0,513	0,805
F5	372,3	373,0	F5/F5	1,000	1,000
F6	355,3	355,1	F6/F5	0,954	0,952

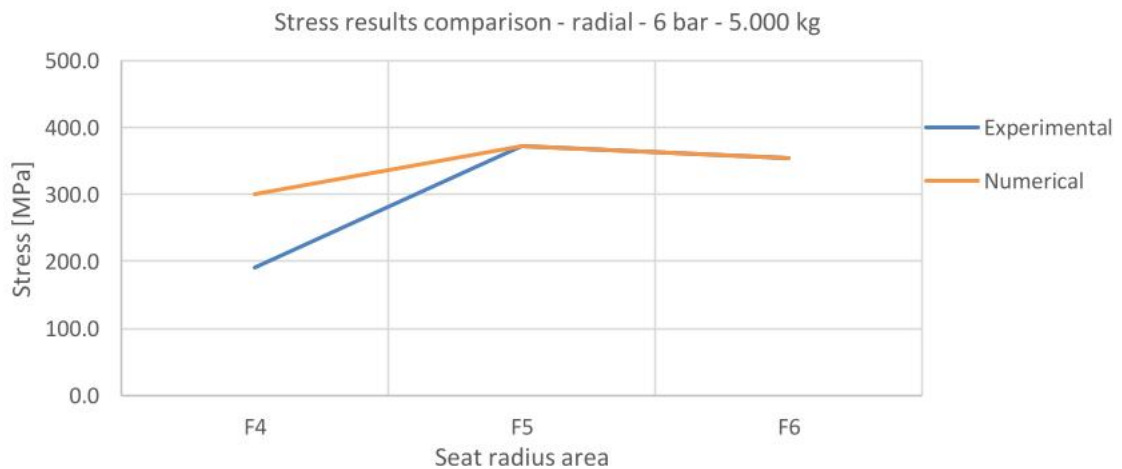
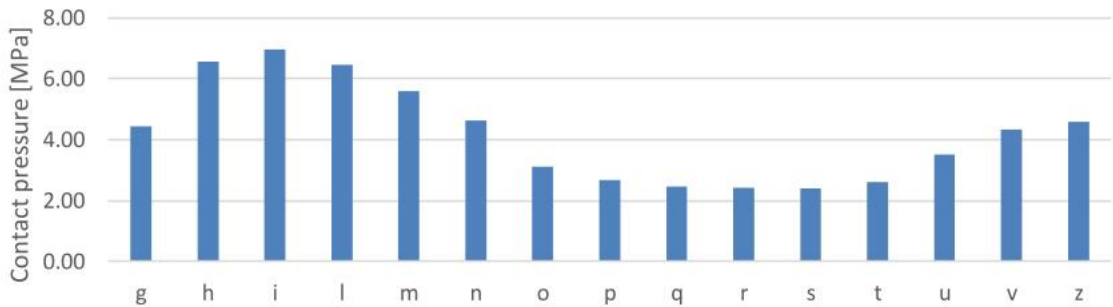


Figure 175 Contact pressure diagram (above) and comparison between experimental and numerical results (below) for the radial tire – 6 bar – 5.000 kg configuration.

Load diagram - radial - 6 bar – 7.500 kg

AREA	CONTACT PRESSURE [MPa]	AREA	CONTACT PRESSURE [MPa]	AREA	CONTACT PRESSURE [MPa]
g	4,44	n	4,63	s	2,41
h	6,56	o	3,12	t	2,61
i	6,97	p	2,67	u	3,51
l	6,45	q	2,47	v	4,35
m	5,60	r	2,42	z	4,59

Radial - 6 bar - 7.500 kg



Simulation results comparison - radial - 6 bar – 7.500 kg

STRESS RESULTS COMPARISON [MPa]			STRESS RATIOS COMPARISON		
AREA	EXPERIMENTAL	NUMERICAL	AREAS	EXPERIMENTAL	NUMERICAL
F4	205,03	313,1	F4/F5	0,531	0,811
F5	386,42	386,2	F5/F5	1,000	1,000
F6	363,62	363,2	F6/F5	0,941	0,940

Stress results comparison - radial - 6 bar - 7.500 kg

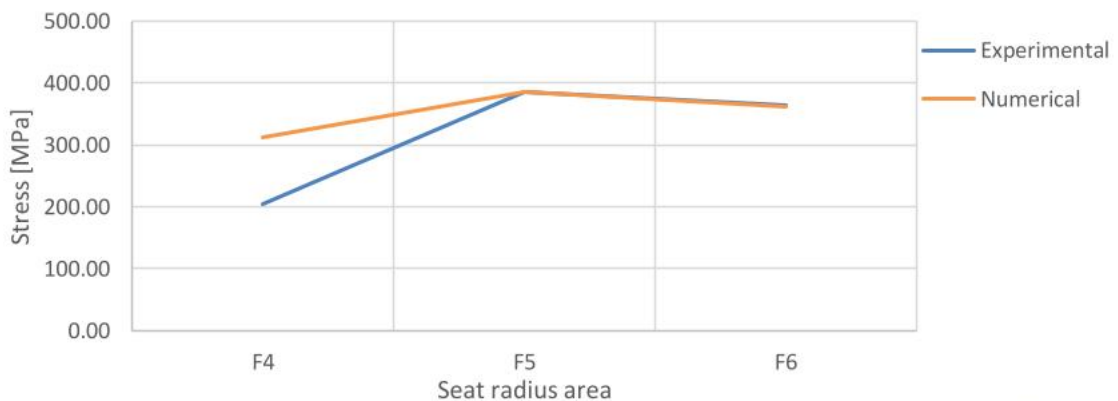
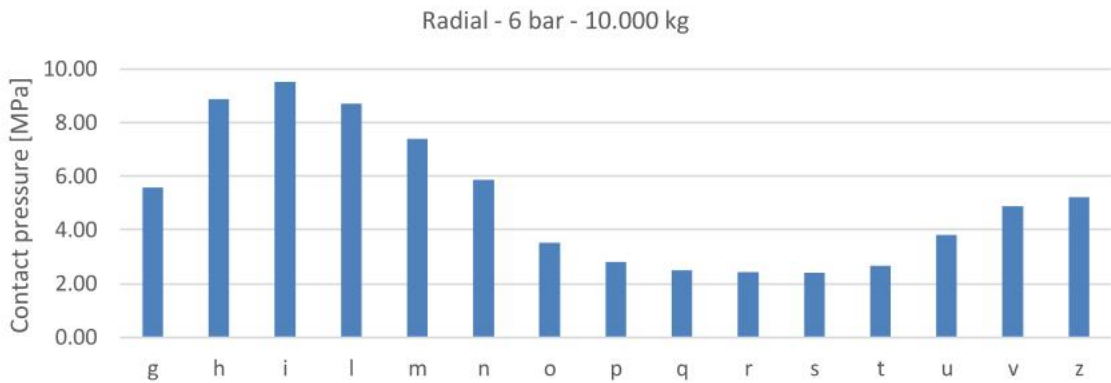


Figure 176 Contact pressure diagram (above) and comparison between experimental and numerical results (below) for the radial tire – 6 bar – 7.500 kg configuration.

Load diagram - radial - 6 bar – 10.000 kg

AREA	CONTACT PRESSURE [MPa]	AREA	CONTACT PRESSURE [MPa]	AREA	CONTACT PRESSURE [MPa]
g	5,57	n	5,86	s	2,40
h	8,87	o	3,51	t	2,66
i	9,51	p	2,80	u	3,82
l	8,71	q	2,49	v	4,89
m	7,38	r	2,42	z	5,21



Simulation results comparison - radial - 6 bar – 10.000 kg

STRESS RESULTS COMPARISON [MPa]			STRESS RATIOS COMPARISON		
AREA	EXPERIMENTAL	NUMERICAL	AREAS	EXPERIMENTAL	NUMERICAL
F4	221,46	329,0	F4/F5	0,550	0,817
F5	402,42	402,6	F5/F5	1,000	1,000
F6	372,04	372,3	F6/F5	0,925	0,925

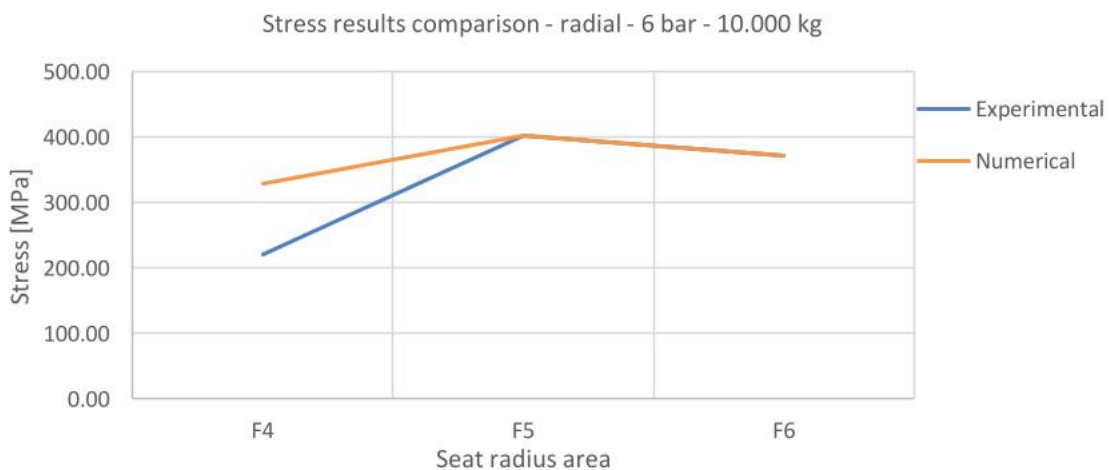
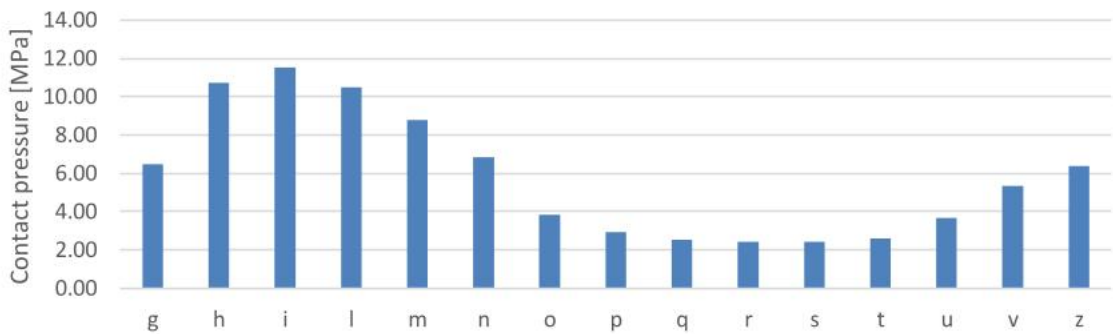


Figure 177 Contact pressure diagram (above) and comparison between experimental and numerical results (below) for the radial tire – 6 bar – 10.000 kg configuration.

Load diagram - radial - 6 bar – 12.500 kg

AREA	CONTACT PRESSURE [MPa]	AREA	CONTACT PRESSURE [MPa]	AREA	CONTACT PRESSURE [MPa]
g	6,47	n	6,84	s	2,41
h	10,70	o	3,83	t	2,59
i	11,53	p	2,92	u	3,66
l	10,49	q	2,52	v	5,33
m	8,79	r	2,42	z	6,38

Radial - 6 bar - 12.500 kg



Simulation results comparison - radial - 6 bar – 12.500 kg

STRESS RESULTS COMPARISON [MPa]			STRESS RATIOS COMPARISON		
AREA	EXPERIMENTAL	NUMERICAL	AREAS	EXPERIMENTAL	NUMERICAL
F4	234,28	341,70	F4/F5	0,565	0,824
F5	414,77	414,60	F5/F5	1,000	1,000
F6	378,26	378,00	F6/F5	0,912	0,912

Stress results comparison - radial - 6 bar - 12.500 kg

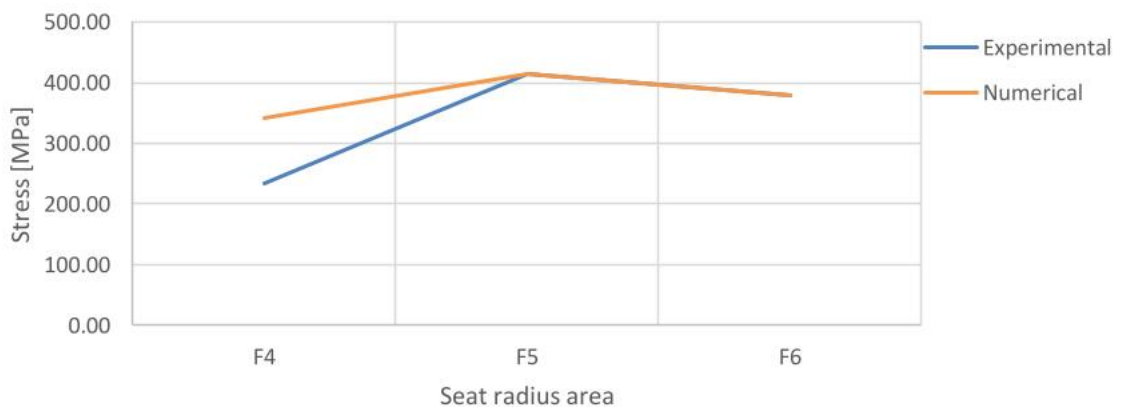
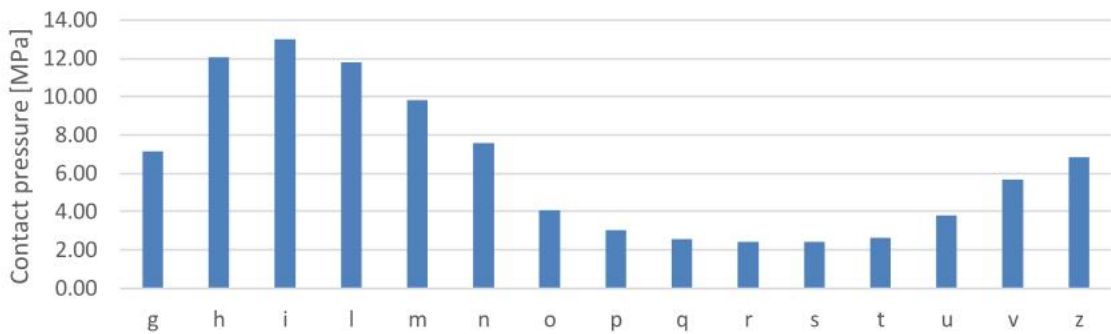


Figure 178 Contact pressure diagram (above) and comparison between experimental and numerical results (below) for the radial tire – 6 bar – 12.500 kg configuration.

Load diagram - radial - 6 bar – 15.100 kg

AREA	CONTACT PRESSURE [MPa]	AREA	CONTACT PRESSURE [MPa]	AREA	CONTACT PRESSURE [MPa]
g	7,12	n	7,56	s	2,42
h	12,04	o	4,07	t	2,62
i	13,00	p	3,01	u	3,81
l	11,80	q	2,54	v	5,68
m	9,82	r	2,43	z	6,84

Radial - 6 bar - 15.100 kg



Simulation results comparison - radial - 6 bar – 15.100 kg

STRESS RESULTS COMPARISON [MPa]			STRESS RATIOS COMPARISON		
AREA	EXPERIMENTAL	NUMERICAL	AREAS	EXPERIMENTAL	NUMERICAL
F4	246,59	352,7	F4/F5	0,578	0,828
F5	426,41	426,2	F5/F5	1,000	1,000
F6	383,62	385,3	F6/F5	0,900	0,904

Stress results comparison - radial - 6 bar - 15.100 kg

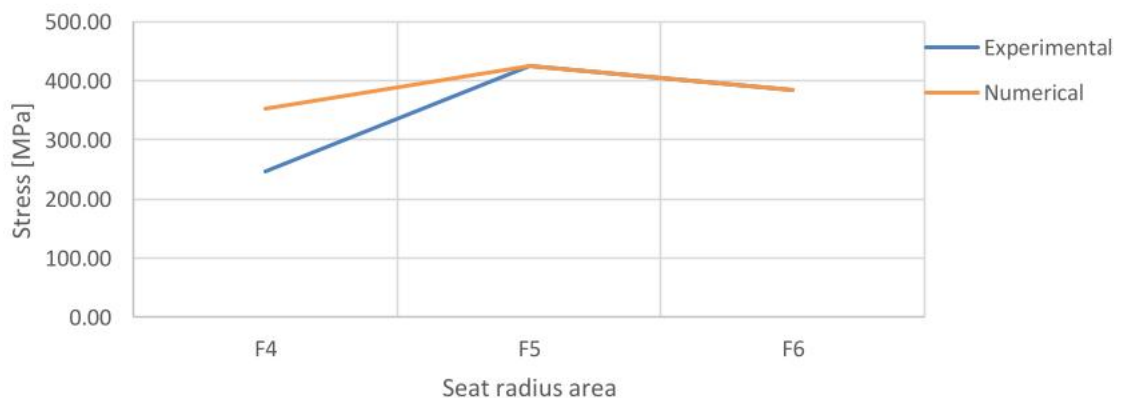
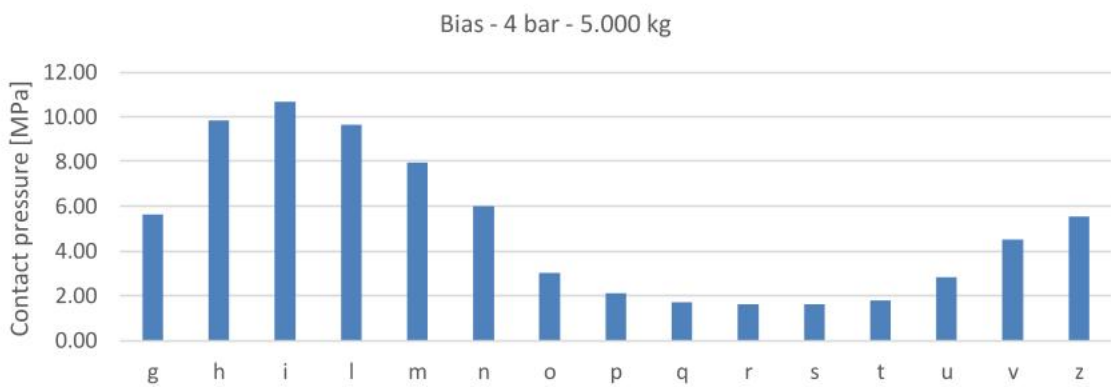


Figure 179 Contact pressure diagram (above) and comparison between experimental and numerical results (below) for the radial tire – 6 bar – 15.100 kg configuration.

The load diagrams and the results comparisons for the bias tire – 4 bar configurations are shown below (Figure 180; Figure 181; Figure 182; Figure 183; Figure 184):

Load diagram - bias - 4 bar – 5.000 kg

AREA	CONTACT PRESSURE [MPa]	AREA	CONTACT PRESSURE [MPa]	AREA	CONTACT PRESSURE [MPa]
g	2,39	n	4,74	s	1,54
h	3,09	o	5,06	t	0,82
i	3,22	p	4,91	u	0,34
l	3,19	q	4,02	v	0,02
m	3,74	r	2,68	z	0,00



Simulation results comparison - bias - 4 bar – 5.000 kg

STRESS RESULTS COMPARISON [MPa]			STRESS RATIOS COMPARISON		
AREA	EXPERIMENTAL	NUMERICAL	AREAS	EXPERIMENTAL	NUMERICAL
F4	145,3	259,6	F4/F5	0,469	0,838
F5	309,7	309,8	F5/F5	1,000	1,000
F6	257,5	275,7	F6/F5	0,831	0,890

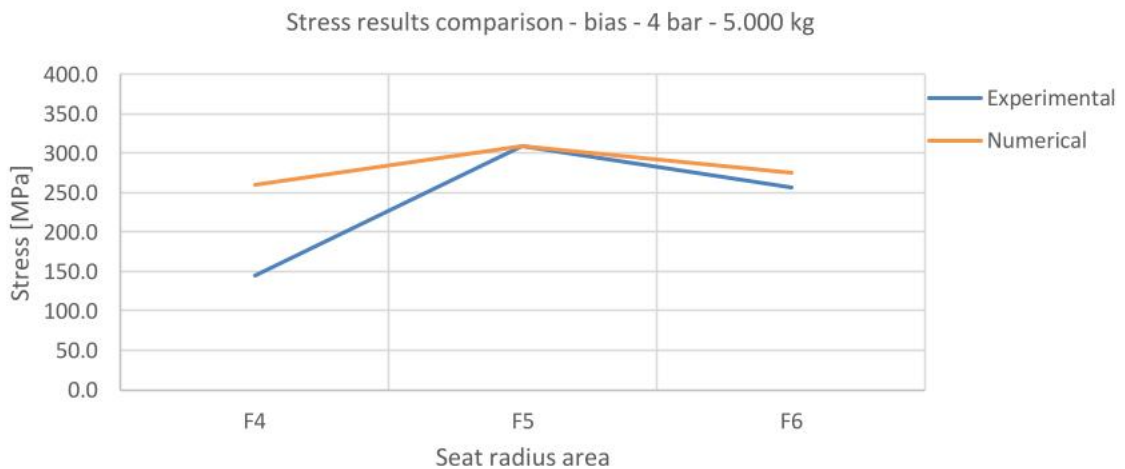
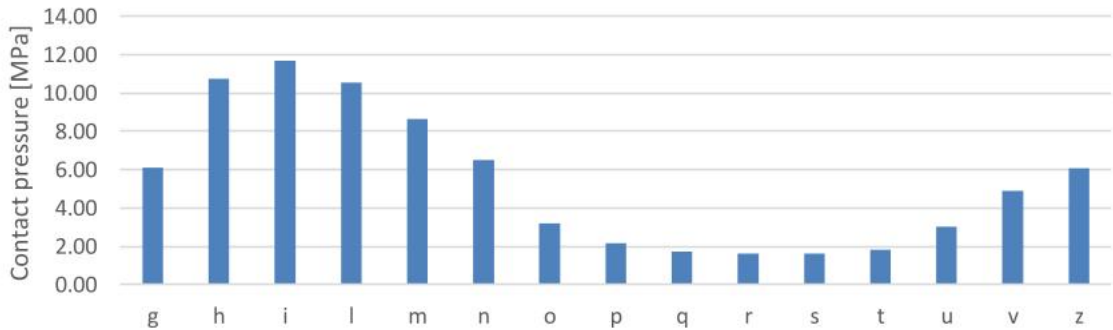


Figure 180 Contact pressure diagram (above) and comparison between experimental and numerical results (below) for the bias tire – 4 bar – 5.000 kg configuration.

Load diagram - bias - 4 bar – 7.500 kg

AREA	CONTACT PRESSURE [MPa]	AREA	CONTACT PRESSURE [MPa]	AREA	CONTACT PRESSURE [MPa]
g	5,64	n	6,01	s	1,61
h	9,85	o	3,01	t	1,78
i	10,68	p	2,10	u	2,84
l	9,65	q	1,71	v	4,51
m	7,95	r	1,61	z	5,55

Bias - 4 bar - 7.500 kg



Simulation results comparison - bias - 4 bar – 7.500 kg

STRESS RESULTS COMPARISON [MPa]			STRESS RATIOS COMPARISON		
AREA	EXPERIMENTAL	NUMERICAL	AREAS	EXPERIMENTAL	NUMERICAL
F4	158,76	274,4	F4/F5	0,487	0,842
F5	326,12	326,0	F5/F5	1,000	1,000
F6	274,53	288,5	F6/F5	0,842	0,885

Stress results comparison - bias - 4 bar - 7.500 kg

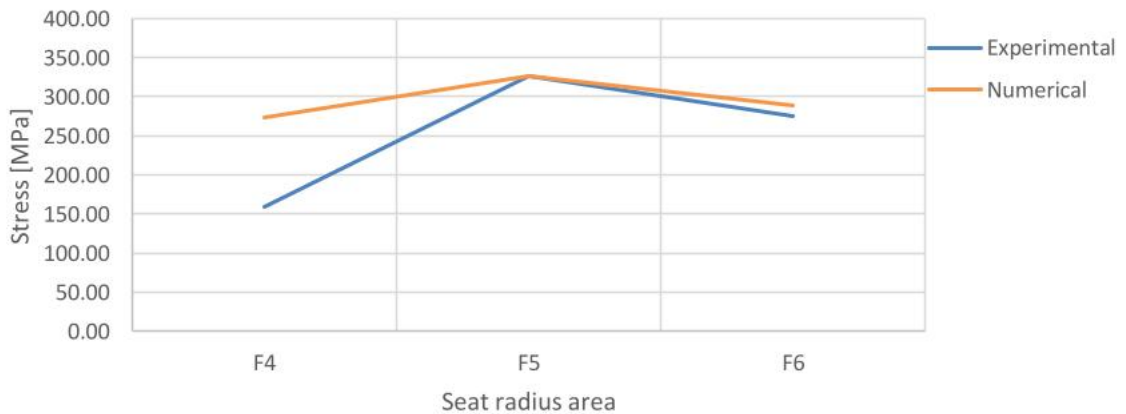
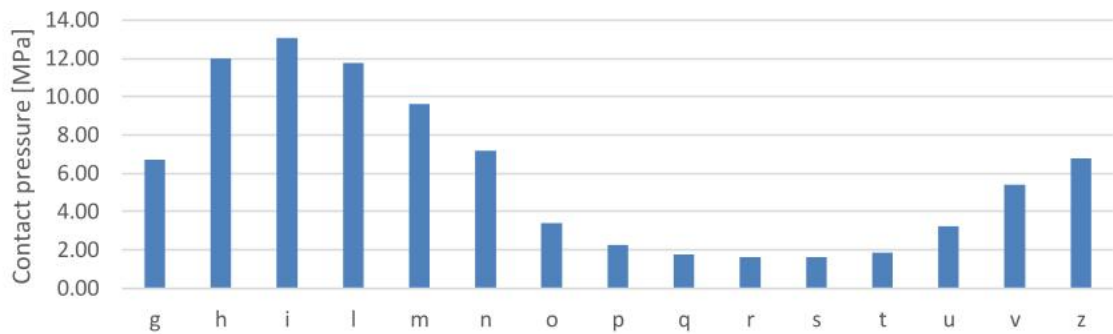


Figure 181 Contact pressure diagram (above) and comparison between experimental and numerical results (below) for the bias tire – 4 bar – 7.500 kg configuration.

Load diagram - bias - 4 bar – 10.000 kg

AREA	CONTACT PRESSURE [MPa]	AREA	CONTACT PRESSURE [MPa]	AREA	CONTACT PRESSURE [MPa]
g	6,10	n	6,51	s	1,63
h	10,77	o	3,19	t	1,82
i	11,69	p	2,18	u	3,02
l	10,55	q	1,74	v	4,90
m	8,66	r	1,63	z	6,07

Bias - 4 bar - 10.000 kg



Simulation results comparison - bias - 4 bar – 10.000 kg

STRESS RESULTS COMPARISON [MPa]			STRESS RATIOS COMPARISON		
AREA	EXPERIMENTAL	NUMERICAL	AREAS	EXPERIMENTAL	NUMERICAL
F4	175,10	291,2	F4/F5	0,509	0,847
F5	343,86	343,6	F5/F5	1,000	1,000
F6	293,70	301,6	F6/F5	0,854	0,878

Stress results comparison - bias - 4 bar - 10.000 kg

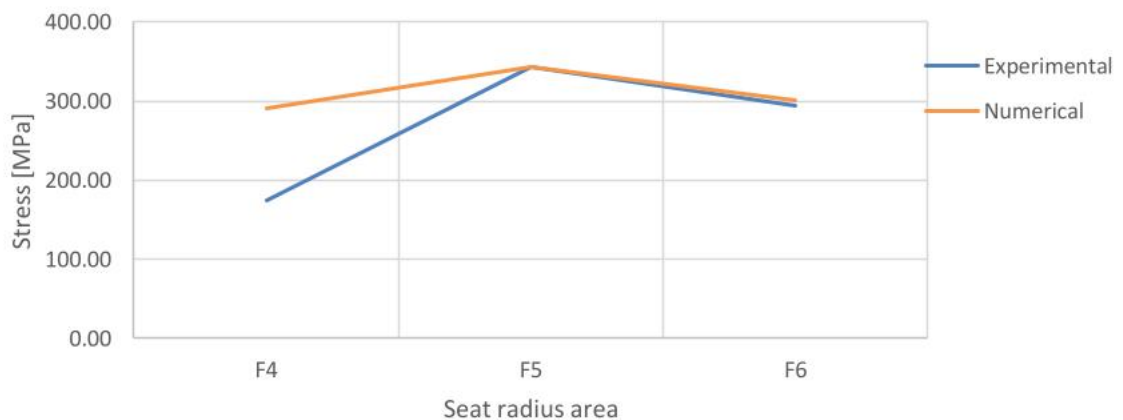
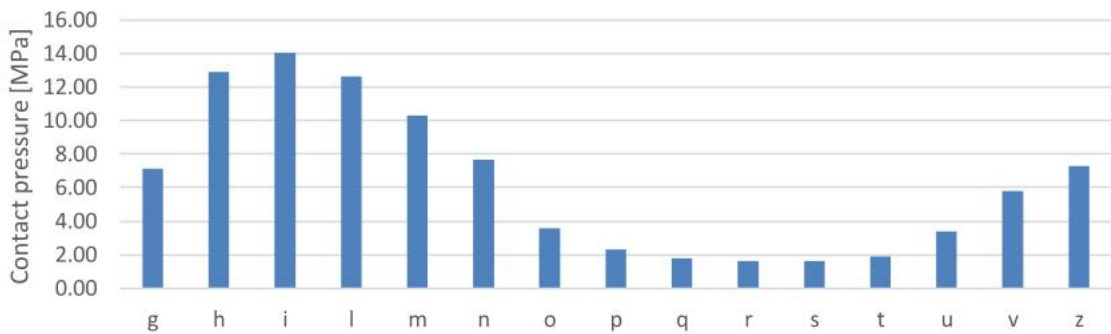


Figure 182 Contact pressure diagram (above) and comparison between experimental and numerical results (below) for the bias tire – 4 bar – 10.000 kg configuration.

Load diagram - bias - 4 bar – 12.500 kg

AREA	CONTACT PRESSURE [MPa]	AREA	CONTACT PRESSURE [MPa]	AREA	CONTACT PRESSURE [MPa]
g	6,69	n	7,16	s	1,62
h	12,00	o	3,39	t	1,84
i	13,04	p	2,24	u	3,23
l	11,74	q	1,74	v	5,40
m	9,60	r	1,62	z	6,76

Bias - 4 bar - 12.500 kg



Simulation results comparison - bias - 4 bar – 12.500 kg

STRESS RESULTS COMPARISON [MPa]			STRESS RATIOS COMPARISON		
AREA	EXPERIMENTAL	NUMERICAL	AREAS	EXPERIMENTAL	NUMERICAL
F4	191,91	305,4	F4/F5	0,534	0,850
F5	359,07	359,1	F5/F5	1,000	1,000
F6	311,71	313,8	F6/F5	0,868	0,874

Stress results comparison - bias - 4 bar - 12.500 kg

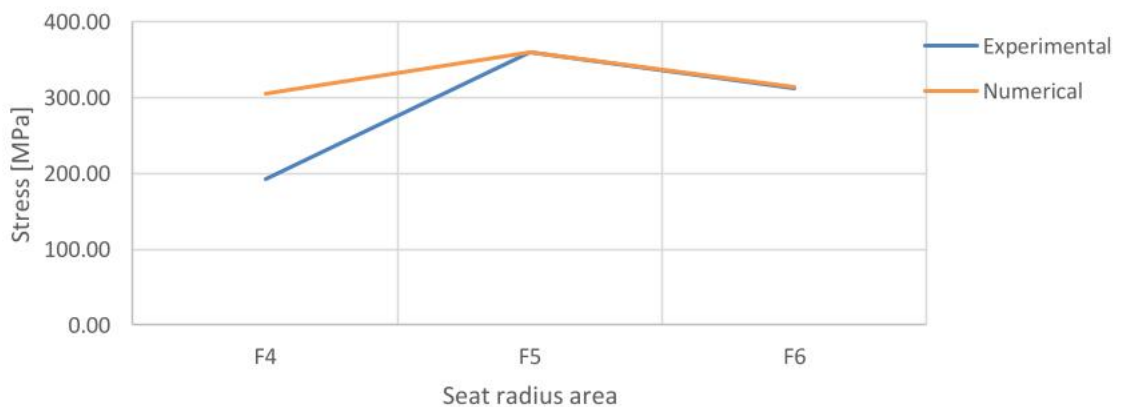
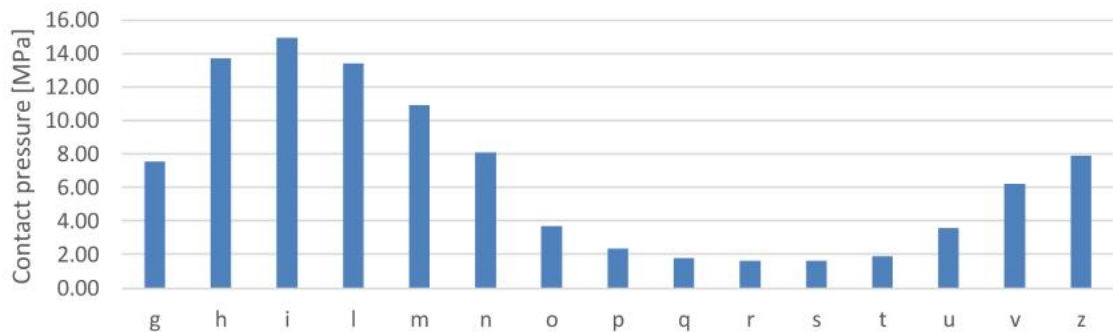


Figure 183 Contact pressure diagram (above) and comparison between experimental and numerical results (below) for the bias tire – 4 bar – 12.500 kg configuration.

Load diagram - bias - 4 bar – 15.100 kg

AREA	CONTACT PRESSURE [MPa]	AREA	CONTACT PRESSURE [MPa]	AREA	CONTACT PRESSURE [MPa]
g	7,14	n	7,65	s	1,64
h	12,90	o	3,55	t	1,88
i	14,02	p	2,31	u	3,39
l	12,62	q	1,77	v	5,78
m	10,30	r	1,64	z	7,27

Bias - 4 bar - 15.100 kg



Simulation results comparison - bias - 4 bar – 15.100 kg

STRESS RESULTS COMPARISON [MPa]			STRESS RATIOS COMPARISON		
AREA	EXPERIMENTAL	NUMERICAL	AREAS	EXPERIMENTAL	NUMERICAL
F4	207,02	322,0	F4/F5	0,549	0,854
F5	377,04	377,0	F5/F5	1,000	1,000
F6	328,27	328,4	F6/F5	0,871	0,871

Stress results comparison - bias - 4 bar - 15.100 kg

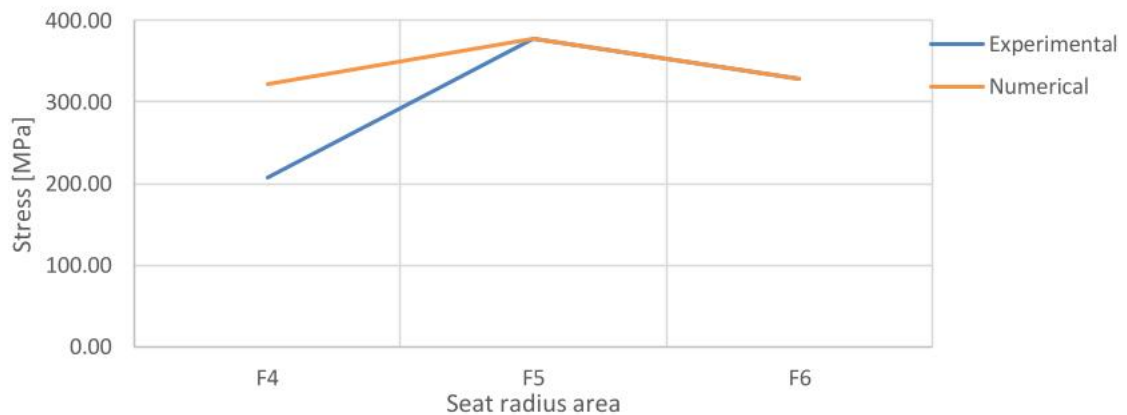
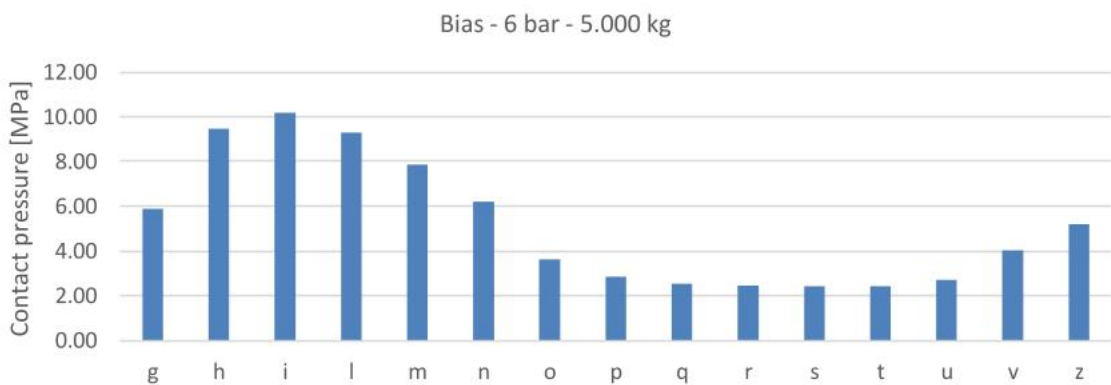


Figure 184 Contact pressure diagram (above) and comparison between experimental and numerical results (below) for the bias tire – 4 bar – 15.100 kg configuration.

The load diagrams and the results comparisons for the bias tire – 6 bar configurations are shown below (Figure 185; Figure 186; Figure 187; Figure 188; Figure 189):

Load diagram - bias - 6 bar – 5.000 kg

AREA	CONTACT PRESSURE [MPa]	AREA	CONTACT PRESSURE [MPa]	AREA	CONTACT PRESSURE [MPa]
g	5,84	n	6,16	s	2,42
h	9,41	o	3,61	t	2,41
i	10,11	p	2,84	u	2,69
l	9,24	q	2,51	v	3,99
m	7,80	r	2,43	z	5,18



Simulation results comparison - bias - 6 bar – 5.000 kg

STRESS RESULTS COMPARISON [MPa]			STRESS RATIOS COMPARISON		
AREA	EXPERIMENTAL	NUMERICAL	AREAS	EXPERIMENTAL	NUMERICAL
F4	188,4	290,7	F4/F5	0,526	0,812
F5	358,1	358,0	F5/F5	1,000	1,000
F6	325,6	327,9	F6/F5	0,909	0,916

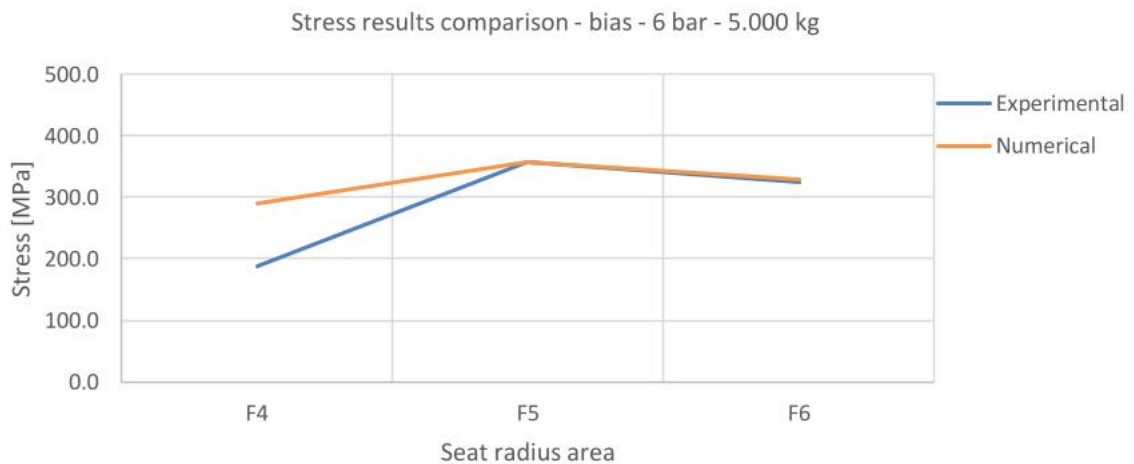
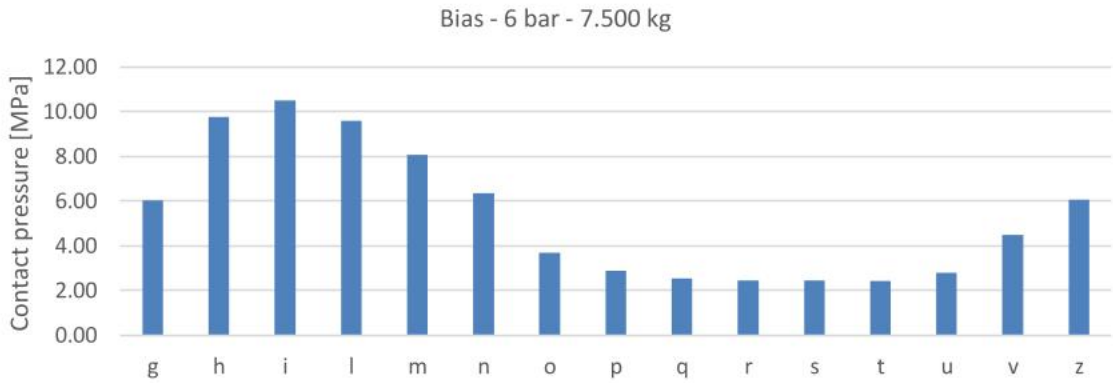


Figure 185 Contact pressure diagram (above) and comparison between experimental and numerical results (below) for the bias tire – 6 bar – 5.000 kg configuration.

Load diagram - bias - 6 bar – 7.500 kg

AREA	CONTACT PRESSURE [MPa]	AREA	CONTACT PRESSURE [MPa]	AREA	CONTACT PRESSURE [MPa]
g	6,02	n	6,35	s	2,44
h	9,76	o	3,69	t	2,43
i	10,49	p	2,89	u	2,80
l	9,58	q	2,53	v	4,49
m	8,07	r	2,45	z	6,06



Simulation results comparison - bias - 6 bar – 7.500 kg

STRESS RESULTS COMPARISON [MPa]			STRESS RATIOS COMPARISON		
AREA	EXPERIMENTAL	NUMERICAL	AREAS	EXPERIMENTAL	NUMERICAL
F4	204,4	310,2	F4/F5	0,539	0,818
F5	379,5	379,0	F5/F5	1,000	1,000
F6	346,9	346,7	F6/F5	0,914	0,915

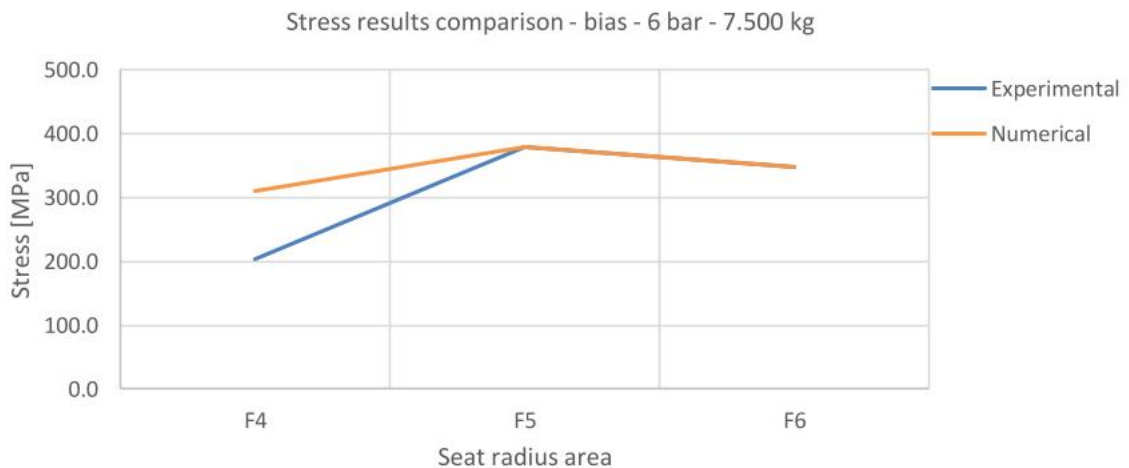
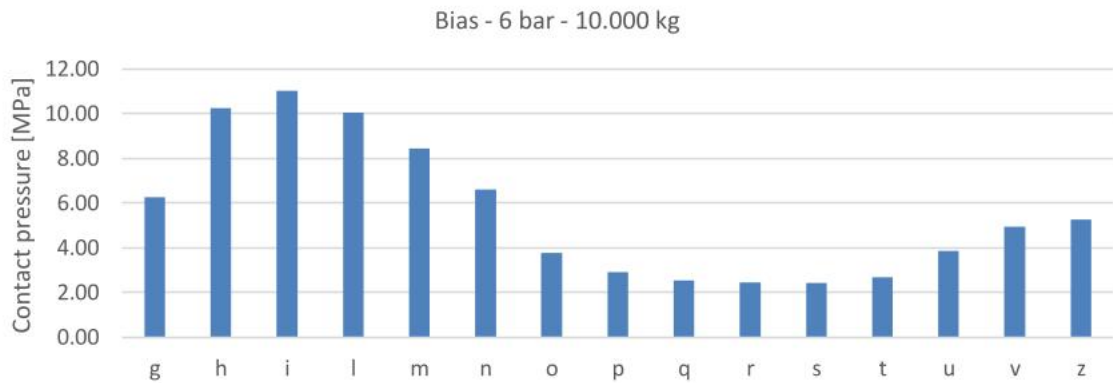


Figure 186 Contact pressure diagram (above) and comparison between experimental and numerical results (below) for the bias tire – 6 bar – 7.500 kg configuration.

Load diagram - bias - 6 bar – 10.000 kg

AREA	CONTACT PRESSURE [MPa]	AREA	CONTACT PRESSURE [MPa]	AREA	CONTACTPRESSURE [MPa]
g	6,25	n	6,61	s	2,42
h	10,24	o	3,77	t	2,68
i	11,02	p	2,91	u	3,85
l	10,05	q	2,53	v	4,93
m	8,44	r	2,44	z	5,25



Simulation results comparison - bias - 6 bar – 10.000 kg

STRESS RESULTS COMPARISON [MPa]			STRESS RATIOS COMPARISON		
AREA	EXPERIMENTAL	NUMERICAL	AREAS	EXPERIMENTAL	NUMERICAL
F4	218,8	327,7	F4/F5	0,546	0,817
F5	400,8	400,9	F5/F5	1,000	1,000
F6	366,1	367,1	F6/F5	0,913	0,916

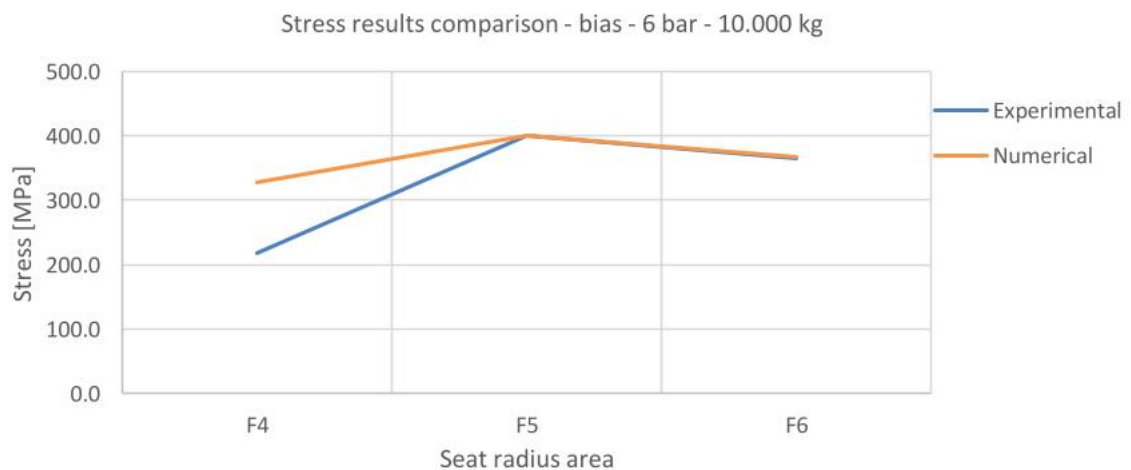
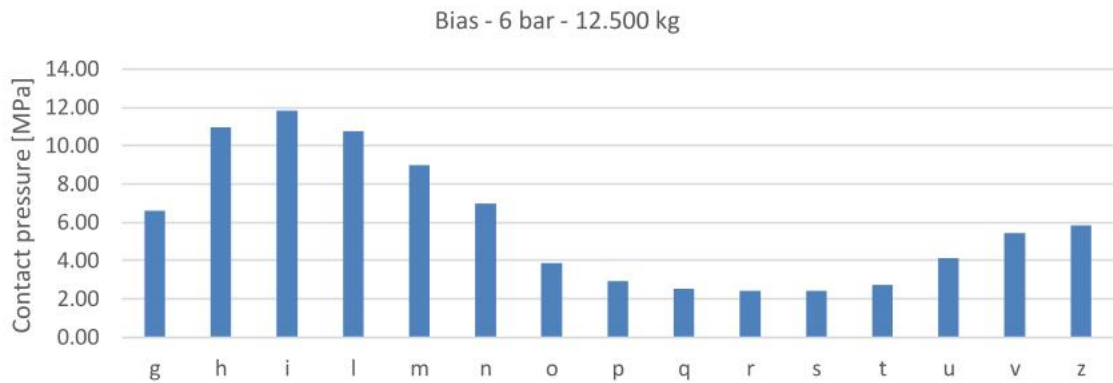


Figure 187 Contact pressure diagram (above) and comparison between experimental and numerical results (below) for the bias tire – 6 bar – 10.000 kg configuration.

Load diagram - bias - 6 bar – 12.500 kg

AREA	CONTACT PRESSURE [MPa]	AREA	CONTACT PRESSURE [MPa]	AREA	CONTACT PRESSURE [MPa]
g	6,59	n	6,98	s	2,41
h	10,95	o	3,87	t	2,72
i	11,81	p	2,93	u	4,14
l	10,74	q	2,52	v	5,45
m	8,99	r	2,42	z	5,84



Simulation results comparison - bias - 6 bar – 12.500 kg

STRESS RESULTS COMPARISON [MPa]			STRESS RATIOS COMPARISON		
AREA	EXPERIMENTAL	NUMERICAL	AREAS	EXPERIMENTAL	NUMERICAL
F4	234,8	346,7	F4/F5	0,557	0,823
F5	421,4	421,3	F5/F5	1,000	1,000
F6	384,6	384,2	F6/F5	0,913	0,912

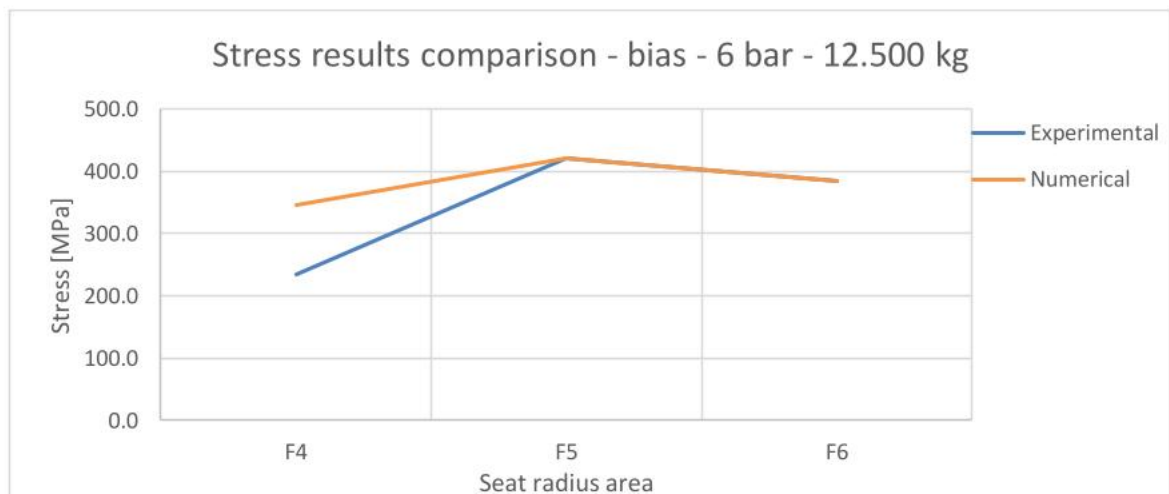
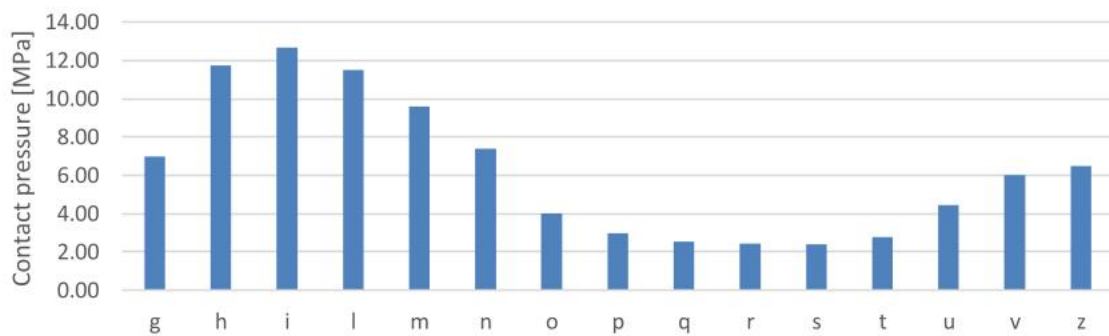


Figure 188 Contact pressure diagram (above) and comparison between experimental and numerical results (below) for the bias tire – 6 bar – 12.500 kg configuration.

Load diagram - bias - 6 bar – 15.100 kg

AREA	CONTACT PRESSURE [MPa]	AREA	CONTACT PRESSURE [MPa]	AREA	CONTACT PRESSURE [MPa]
g	6,98	n	7,40	s	2,41
h	11,74	o	4,01	t	2,78
i	12,68	p	2,98	u	4,45
l	11,51	q	2,53	v	6,00
m	9,59	r	2,43	z	6,47

Bias - 6 bar - 15.100 kg



Simulation results comparison - bias - 6 bar – 15.100 kg

STRESS RESULTS COMPARISON [MPa]			STRESS RATIOS COMPARISON		
AREA	EXPERIMENTAL	NUMERICAL	AREAS	EXPERIMENTAL	NUMERICAL
F4	251,7	367,8	F4/F5	0,566	0,827
F5	444,8	444,5	F5/F5	1,000	1,000
F6	403,7	403,8	F6/F5	0,908	0,908

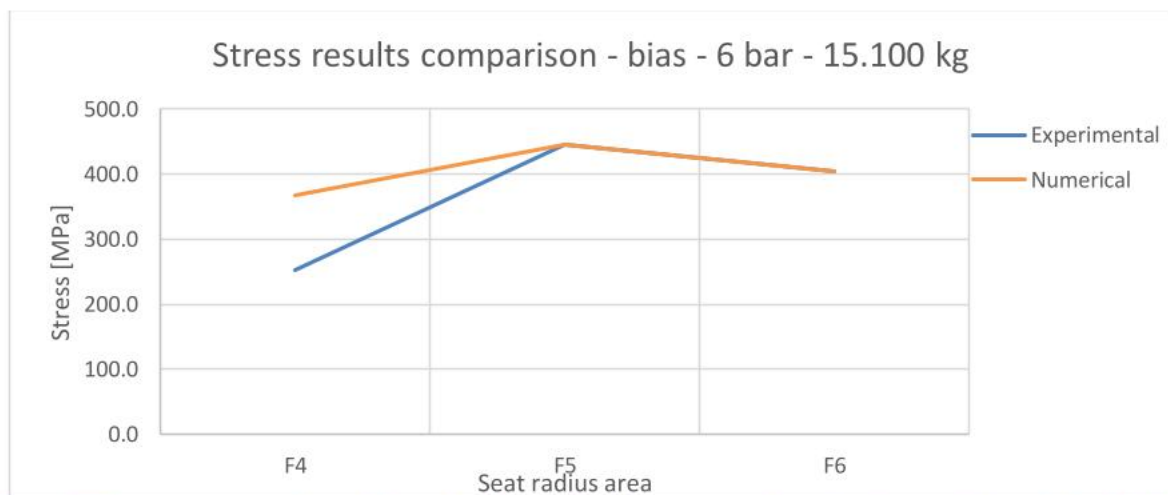


Figure 189 Contact pressure diagram (above) and comparison between experimental and numerical results (below) for the bias tire – 6 bar – 15.100 kg configuration.

Some clarifications about the previous results are needed. As it can be seen, the match between the experimental and the numerical maximum stress is already very good; this is because the k corrective coefficient has already been applied. The intermediate results have not been presented in order to provide a more concise presentation of the work done. Anyway, the gap between the experimental measurements and the FE results obtained by supposing the pressure distributions reached 7% only in the radial tire – 4 bar – 5000 kg configuration, which was the most complex case to study. In all the remaining load configurations, errors below 2% could be obtained. This means that the contact pressure distributions supposed in these simulations can represent a possible solution for the contact problem. It is good to remember that in all the load configurations supposed, the criteria and hypotheses reported above have been respected. Regarding the quality of the results obtained, it must be said that even with this improved model, the F4 experimental results could not be interpreted in any way, since they are systematically and significantly lower than the numerical predictions. The cause of this discrepancy could be many, from inaccuracy of the contact model applied to lack of precision in the application of the strain gauges during the laboratory tests. According to tire manufacturers, two of the major issues that can lead to error in the experimental measurements and, thus, produce discrepancy between the experimental and numerical data are the inaccurate alignment of the strain gauges and the tendency of the gauges to record transversal strains [25]. As said in the previous paragraphs, fortunately the F4 stress is the lower of the stress detected in the seat radius area and, thus, cannot be the most critical on both a static and a fatigue point of view. Regarding the F5 and the F6 results, a good match for both could be reached for almost every load configuration overall. In fact, the most critical load conditions to reproduce were the bias tire – 4 bar – 5000, 7500 and 10000 kg, for which the stress curve shape could not be reproduced precisely. This is due to the stress trend itself: in fact, for these configurations, the F5 values are significantly higher than the F6 ones, so that the curve has a clear stress peak in the middle of the seat radius. This condition could hardly be reproduced in the simulations, since only more gradual curves could be obtained. However, for all the remaining load conditions, a good match for both F5 and F6 stress could be found quite easily. It must be highlighted that finding a good coincidence between the experimental and numerical results for both F5 and F6 values substantially meant to be able to interpret the stress curve in the radius critical area.

Therefore, it can be stated that the load diagrams found might be considered possible solutions of the tire – rim contact problem.

As done in the previous study, a qualitative representation of the contact pressures derived from this model is proposed. Since the pressure distribution is quite similar for all the cases, except for the 4 bar – radial configuration, an exemplificative illustration of all the remaining pressure diagrams is presented (Figure 190):

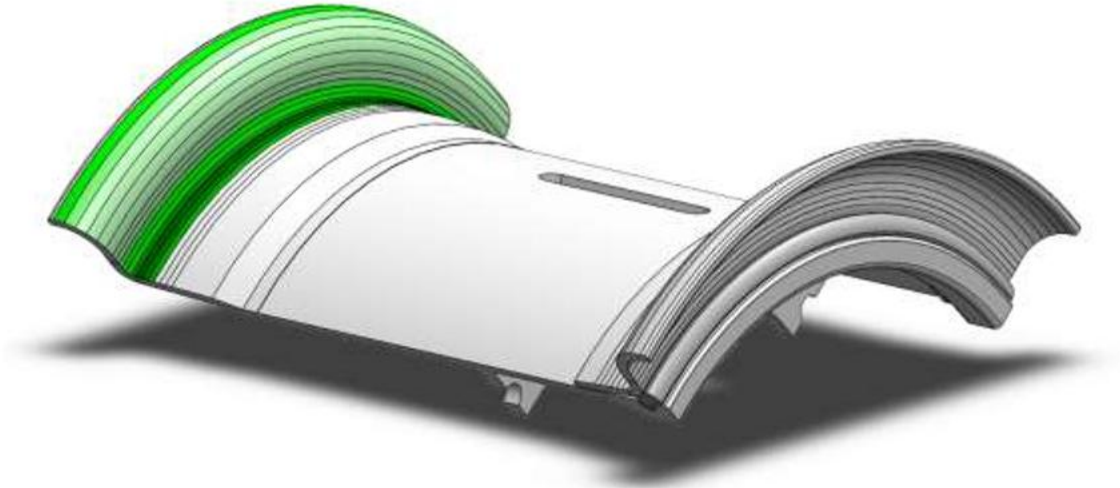


Figure 190 Qualitative representation of the contact pressure distribution found with the empirical model proposed in this paragraph.

An exemplificative graphic representation of the main stress field obtained through the FE simulation with the pressure distribution of the improved contact model is proposed as well (Figure 191):

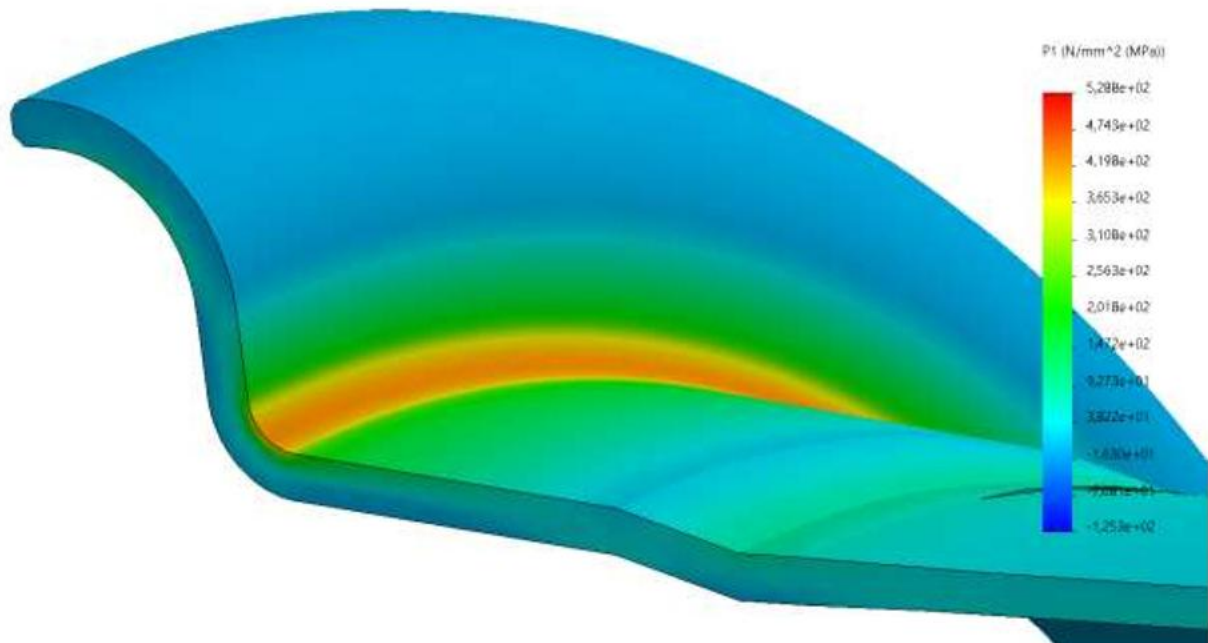


Figure 191 Graphic representation of the main stress field obtained through the FE static simulation for the 6 bar – 15.100 kg – radial tire configuration.

Below, the comparison between the different pressure diagrams referring to all the load configurations are presented (Figure 192; Figure 193; Figure 194; Figure 195):

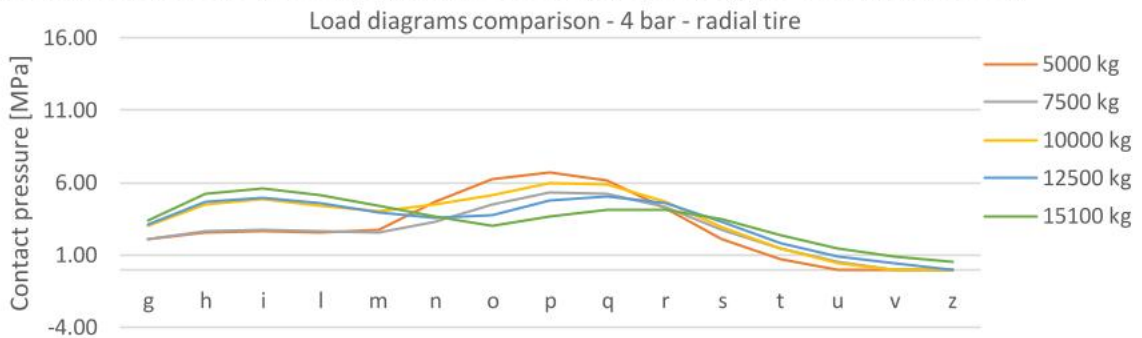


Figure 192 Contact pressure diagrams obtained for the 4 bar – radial tire load configurations.

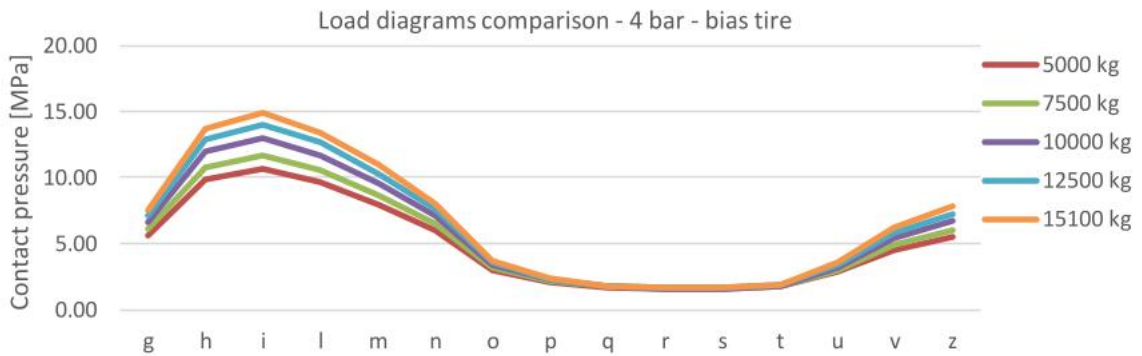


Figure 193 Contact pressure diagrams obtained for the 4 bar – radial tire load configurations.

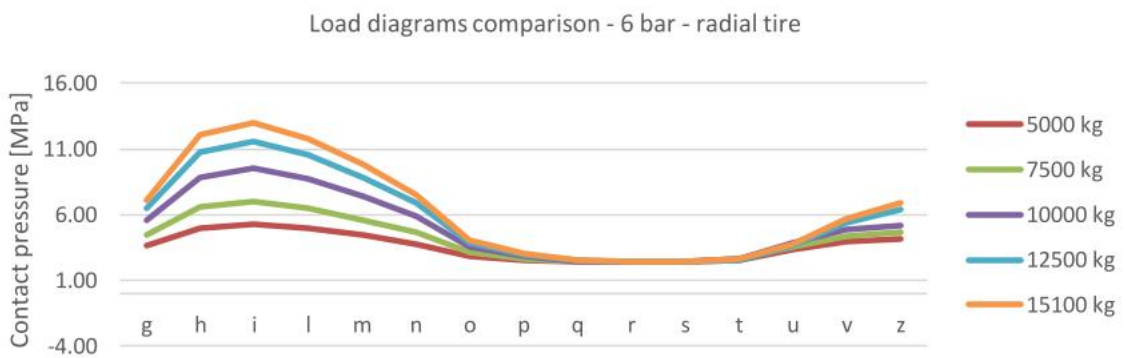


Figure 194 Contact pressure diagrams obtained for the 4 bar – radial tire load configurations.

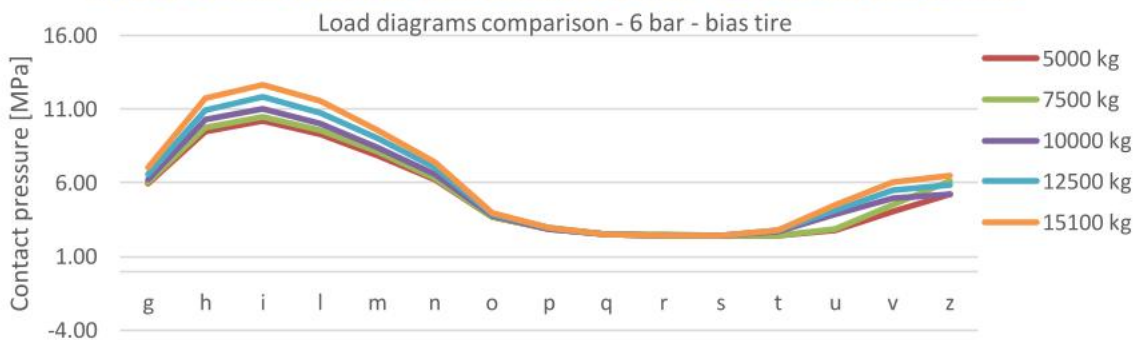


Figure 195 Contact pressure diagrams obtained for the 4 bar – radial tire load configurations.

As can be seen, a good coherence was obtained for the pressure diagrams of all the load configurations, except for the 4 bar – radial tire case, for which a “*Michelin like*” pressure distribution could not be found.

In fact, in order to obtain stress values in the numerical simulation the most similar to the experimental ones, it was necessary to load heavily the area corresponding to the vertical surface of the flange by translating the hook pressure peak. The peak obtained is largely higher than the seat radius peak for the low load cases; as the radial load increases, the hook peak decreases and translates towards the hook area; while the seat radius peak increases and, thus, the pressure diagram tend to a configuration more similar to the *Michelin* one. Assuming that this pressure distribution well overlaps the real one, it could not be explained such an anomalous load diagram. One of the possible reasons could be the particular behaviour of the radial design at low inflation pressures, for which the tire does not load the hook area, but the vertical surface of the flange instead. Regarding the other load configurations, pressure distributions very similar to the *Michelin* one could be easily found, with good results in terms of stress found. It must be highlighted how drastically different the pressure diagrams found for the 4 bar – bias tire is compared to the 4 bar – radial tire. On the other hand, it is interesting how the bias and radial tire can be described by quite similar pressure distributions at the higher inflation pressure of 6 bar; these similarities are weaker for the lower radial loads (5.000 and 7.500 kg). Lastly, it can be noticed that, comparing the 4 bar – radial tire case to the 6 bar cases, an apparently absurd result emerges. In fact, the higher pressures supposed for the 4 bar – radial tire case reach about 15 MPa when a 15.100 kg radial load is applied; while the 6 bar configurations do not exceed 13 MPa in the same conditions. This apparent inconsistency can actually be explained if we consider that the same radial load is applied to a much more rigid tire (the 6 bar inflated one) compared to the 4 bar inflated tire. It becomes clear that in the first case, the same load is applied to a stiff structure and it can be spread more regularly on the flange surface. In the 4 bar case, on the other hand, the tire is much more subject to deformations under the radial load, since it cannot rely on the same stiffness of the 6 bar inflated tire. Thus, the contact pressure distribution can be much less uniform and higher peak can occur.

With these considerations, the static study of the rim can be considered concluded. In fact, the experimental stress values have been reproduced quite accurately in the FE simulations as it was proposed.

As described before, due to the complexity of the contact problem, an empirical model was applied to the study, so that the laboratory results could be used as a starting point. Known contact pressure distributions from other studies have been implemented into our model in order to accelerate the process of recognition of the possible pressure distributions on the GKN rim. Finally, pressure diagrams which granted a good match between experimental and numerical results was identified. These can be considered some possible solutions of the rim – tire contact problem. Other possible solutions are not excluded; however, since the diagrams supposed satisfy the criteria and the condition imposed to the model and grant a good interpretation of the experimental data as well, they were considered acceptable as a base for the fatigue studies that will be presented in the next chapter.

10. FATIGUE STUDY OF THE RIM

10.1. Introduction

In this chapter the fatigue analyses carried out on the rim 3D model will be described. As stated before, the *SolidWorks Simulation* functions do not allow to perform fatigue analyses starting directly from stress data coming from laboratory tests. Instead, the experimental results had to be reproduced in the most accurate way possible within the static simulations presented in *Chapter 9.2*. The *Fatigue analysis* function in *SolidWorks* could then be used to study the cyclic behaviour of the component, by elaborating the static results and making them vary between the cycle extremes deduced by the experimental measurements. In this chapter a study on the material fatigue curve will be dedicated as well; in fact, since precise information on the Wöhler curve of the material were not available, a comparison between different material curves from the dedicated material database *Total Materia* had to be done. The fatigue simulations executed on several materials together with the results from a rolling fatigue test performed by GKN on a tire under the same load conditions allowed us to choose the best approximation of the material fatigue curve. Once the material cyclic properties were estimated, the fatigue analyses could be performed. The results deriving from them could not be compared to any results from a laboratory test campaign, but they represented a good evaluation of the possible fatigue lives of the component under several load conditions. In the next paragraphs, the analysis instruments offered by *SolidWorks Simulation*, the study hypotheses, the study of the fatigue curve of the material, the analysis of the load cycle applied to the rim and the fatigue simulations results will be discussed.

10.1.1. Analysis instruments and functions

The fatigue simulations have been performed within the *Solidworks Simulation* ambient used for the static analyses. The specific type of study applied was the *Fatigue Analysis* function, which allows to make use of the stress results from a static simulation to reproduce cyclic load conditions. In fact, in order to set the fatigue study, the software takes the stress values derived from a static simulation and makes them vary between two extremes, which are the maximum and the minimum stress generated by the cyclic load.

To do so, the static stress result is considered as the maximum stress of the cycle, while the minimum stress is obtained by setting the cycle ratio R , which can be written as:

$$R = \frac{\sigma_{min}}{\sigma_{max}} \quad 10-86$$

More in detail, the fatigue study allows to choose one or several static “events”, which are made to vary between the stress values found in the static simulations, considered as the maximum stress, and the minimum stress found applying the cycle ratio R . The cycle ratio can be set to -1 or 0 if symmetrical alternating cycles or pulsating cycles from zero are needed, but arbitrary values can be assigned as well. The calculation of cycle ratio from the experimental data for each load condition will be exposed in *Paragraph 10.3*. If just one event is set in the simulation, the analysis determines the effect of it on the fatigue life of the component; if several events, even with different cycle ratios, are set, the study evaluates how all the events together affect the fatigue life of the component. In the *Paragraph 10.3* it will be described how it was determined when setting several events was needed, regarding to the stress cycle of one single point on the rim during its rotation. The fatigue simulation needs a few other information and setting adjustments. In fact, the fatigue material properties need to be set by providing the fatigue curve of the material to the software. The curve can be applied by inserting several points. As disclosed previously, the points of the Wöhler curve were taken from the material database *Total Materia*; the criteria that were used to choose the material curve will be described in *Paragraph 10.2*. Finally, a few simulation settings had to be adjusted. In fact, the software allows to choose the stress definition that shall be considered for the fatigue analysis between several options: Von Mises stress, stress intensity P1-P3 and the main absolute stress P1. In these simulations, this last option was considered as reference stress for the fatigue evaluations.

Moreover, *SolidWorks Simulation* allows to choose between many methods of correction of the average stress: Goodman, Gerber or Soderberg. For these studies, it was decided to use the Goodman correction method, so that the term appearing within the $\sigma_{a_{limF}}$ formula is the breaking stress σ_R (Figure 196):

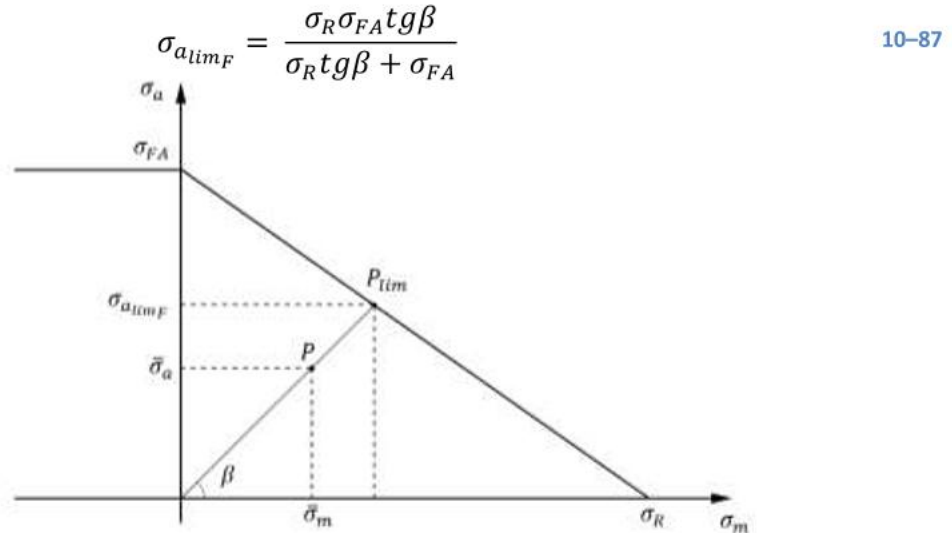


Figure 196 Graphic representation of the Goodman correction method of the average alternated stress.

This choice was motivated by the assumption that in the seat radius area the material had to be highly hardened by the cold deformation process and thus, it could be supposed that the mechanical behaviour of the material in that delimited area was fragile. Starting from this hypothesis, the breaking stress σ_R and yielding stress σ_{sn} had to be considered equal; the value assigned to this stress will be further investigated in *Paragraph 10.2*. As last simulation parameter, the software let the user set the maximum number of cycles that must be simulated in the analysis. In the current study, since the number of cycles to which the rim is subjected can be very high, a maximum number of cycles analysed equal to 10^{10} was set, in order to include any possible result. In the following paragraph the hypotheses on which the fatigue study has been based will be exposed: many of them heavily influenced both the fatigue curve of the material and the simulation parameters.

10.2. Study hypotheses

Before exposing the fatigue, analyses performed on the component, it is necessary to describe the hypotheses on which they are based. In fact, the complexity of the problem was not limited to the non-linearity of the tire mechanical behaviour and of the tire-rim contact phenomenon, but it also regarded the elastic-plastic properties of the rim's processed steel. In fact, the stresses applied to a mechanical component should be classified in three groups. Firstly, manufacturing residual tensions left on the rim during the cold forming process should be considered.

Then pre-stresses due to the assembly of the component should be studied; in this study neglecting the pretension induced by the bolts does not represent an approximation since the coupling holes are placed on the disk far from the critical area of the rim flange. Finally, the static loads caused by the inflation pressure and the static vertical load and the dynamic loads due to the inertia of the vehicle as well as the centrifugal force applied to the rotating masses must be considered. In this thesis, the residual stresses due to the forming process have been neglected since not enough data for a proper study were available [21]. More in detail, the main difficulty of this aspect concerned the lack of information about the entity of both the hardening and the residual stress of the steel in the critical bended portion of the rim, corresponding to the seat radius area which is the main object of this study. Both these properties of the processed material could have been evaluated only through experimental hardness measurements in combination with a model that could link them to the hardening of the steel, or through FE simulations of the plastic deformation process of the seat radius area. Both these methods revealed to be too expensive in terms of time and resources, so two important approximative hypotheses had to be introduced.

- It was supposed that the material elasto-plastic properties were not affected by the cold deformation process involving the rim and, thus, the hardening in the seat radius bended area was considered negligible. It is clearly an approximation of the real mechanical condition of the material after the bending process, but it was necessary as no further studies could be applied to the problem. The complexity of the phenomenon is proved by the measured stress that the steel can sustain. In fact, as visible in Table 18, the stress measurements for the 8 bar inflated tire under a load of 15.100 kg reached a peak of about 600 MPa. This result clearly contradicts the breaking stress data of the material provided by GKN, which declared an ultimate tensile strength for the unprocessed material of about 370 MPa. In fact, the hardening process should increase the yield stress of the material, but not its ultimate tensile strength. Manufacturer confirmed that this experimental evidence occurred in many laboratory campaign performed on several rim models and that it is still not clear how the material can sustain a stress higher than the ultimate tensile strength. For this reason, in this thesis it was opted to consider the steel as fragile hardened material, at least in the radius bended area. As a fragile material, no yield stress was considered, and the ultimate tensile strength was

supposed to be 600 MPa as it was the most downward evaluation justified by the experimental evidence of the rolling tests.

- The second hypothesis is about the residual stress in the seat radius. In this study, the residual stress derived from the cold plastic deformation of the seat radius was ignored, since an evaluation would have been, as stated, too demanding. It is clearly an approximative hypothesis, since residual stresses always occur wherever a plastic deformation is applied. However, as no hardness measurements nor bending process simulations could be performed, it was a necessary approximation. Despite this, it must be determined if it represents an assumption in favour of safety or not. For this purpose, a report on the residual stress measurements carried out for GKN by Università degli Studi di Brescia – Dipartimento di Ingegneria Meccanica e Industriale can be taken into account. In this report, called “Evaluation of the residual stress state in pressed discs by hole drilling method”, two specimens of the seat radius cut from truck rims from GKN have been used. The aim of the experiment was to evaluate the residual stress state of the pressed radius area by hole drilling method. Three holes for each specimen were drilled coinciding with the bending axis. The results do not show great consistency with each other, but considering the most regular results, it can be presumed that the residual stress just below the surface is quite negligible. Some of the results show a positive maximum stress, while other present both maximum and minimum stress as negative tensions. Moreover, it was noticed presence of plasticity during stress relaxation resulting from the introduction of the hole and, therefore, the preliminary hypothesis of linear elastic behaviour was invalidated. Hence, the results of this study should be considered mainly as indicative. In conclusion, the assumption of negligible residual stress next to the rim surface, which can be considered the most probable cracks nucleation area, was applied. As some of the measurements indicate positive maximum residual stresses while other presents negative ones, it could not be ascertained if this approximation was in favour of safety or not [27,28].

The first hypothesis and the supposed ultimate tensile strength of 600 MPa are critical for the Goodman correction of the mean stress component, since the formula applied by the software is:

$$\sigma_{a_{lim_F}} = \frac{\sigma_a}{1 - \left(\frac{\sigma_m}{\sigma_R}\right)} \quad 10-88$$

This means that the assumptions on the ultimate tensile strength of the material are quite crucial on the results of the fatigue analysis.

In conclusion, the following fatigue analyses performed on the component will be based on these fundamental hypotheses; it is important to remark that they represent approximative assumptions, but in the context of this thesis they were needed, as no further studies on the hardening and the residual stress state of the seat radius of the rim could be done.

10.3. Fatigue curve of the material

In order to perform any fatigue analyses on the rim model, information on the cyclic behaviour of the material were needed. More in detail, the main instrument which was necessary was the Wöhler curve, which links the entity of the alternated component of the cyclic stress to the predicted life of the component, according to experimental evidence from tests performed on the material. This curve represents, in other words, the influence parameter of the material in the fatigue problem. Unfortunately, fatigue characterisation tests are extremely expensive to perform, both in terms of time and resources; thus, obtaining specific and significant fatigue properties and curves for a given material is not easy. The Wöhler curve for the rim material was, in fact, not available; GKN could provide us two experimental points of the curve, obtained through cyclic tests on two specimens of the rim steel.

The load applied produced an alternated symmetrical stress. The results of these tests are shown below (Table 19):

Experimental fatigue life results – Material specimens	
σ_a [MPa]	N_f
320	93.000
347	150.000

Table 19 Results of the laboratory tests performed on the specimens of the rim steel.

Of course, two points are not statistically sufficient to build a curve, so they could be used just as an indicative reference. It is clear that even just one alternated stress value should be tested many times to assign a statistical value to the curve point and this would mean a great effort in terms of number of tests. In other words, finding a single curve through laboratory tests would have required testing each one of the alternated stress components σ_a considered and for each of them, many tests would have been necessary to produce a statistical validity. Thus, it was clear that a different approach had to be adopted in order to determine a good approximation of the real material Wöhler curve.

Since performing fatigue tests on the rim steel was too onerous, it had to be found the curve associated to the most similar material from a dedicated database; for this study, the *Total Materia* database was consulted as it contains many mechanical and physical properties for a vast range of materials. Much information about several tests on both static and cyclical characteristics for each material are reported. For example, fatigue curves obtained through different testing methods were available, from axial normal alternated stress to bending normal alternated stress to torsional alternated stress. As the mechanical problem concerning the rim flange is purely flexural, bending alternated stress curves were considered. They would have then been corrected through the Goodman method. Among the *Total Materia* materials, structural steels were searched for, as the steel used for the GKN rim belongs to this category of materials. Considering the data provided by GKN for the ultimate tensile strength, which is equal to about 370 MPa, the most similar material found in the database was the S235JR structural steel, which was assumed as a reference.

However, it was reputed more correct to include into the study other structural steels as well: in fact, it was decided to compare the fatigue curve of many structural steel in order to obtain a wider view of the possible fatigue behaviour of the materials available for the rim production. Some of them were clearly too performing and expensive for a large rim production, but they were investigated even if it constituted a mere speculation. The steels studied are the following: S185, S235JR, S275JR, S355JR, E295, E335 and E360. The flexural alternated fatigue curves found in *Total Materia* for these materials are reported in the table and in the graph below (Figure 197):

Flexural alternated fatigue curve from <i>Total Materia</i>							
N	Stress [MPa]						
	S185	S235JR	S275JR	S355JR	E295	E335	E360
1.000	279	324	387	459	441	531	621
10.000	229	266	318	377	363	434	505
100.000	189	219	262	310	298	355	416
1.000.000	155	180	215	255	245	290	340

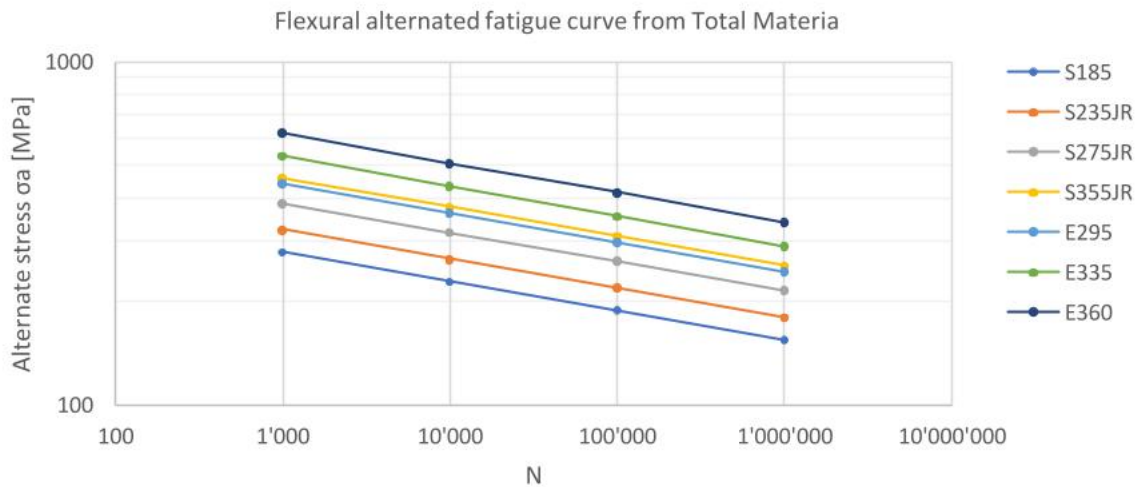


Figure 197 Wöhler experimental curves provided by Total Materia for several structural steels. The curves were obtained under alternated symmetrical flexural load conditions.

As expected, the most performing materials can sustain higher alternated stress components for the same number of cycles. The criterion chosen to select the material that best approximates the real one was based on a laboratory test performed by GKN on the rim. The test was meant to take the rim to failure and give an evaluation of the fatigue life of the rim under the load conditions exposed in the table below. The result of the test is reported as well (Table 20):

ROLLING TEST PARAMETERS AND RESULT

Cold inflation pressure [bar]	6
Radial load [kg]	15.095
Rolling speed [km/h]	12,9
N_f	2.000.194

Table 20 Rolling test parameters and result. The test was protracted until the rim failure, which occurred at 2.000.194 cycles.

This kind of test is extremely expensive in terms of time, since the number of cycles needed to take the rim to failure can be very high. Therefore, having even just one test available was extremely important. In fact, even if it was not statistically significant, it provided an indicative reference that turned out to be extremely useful to understand which fatigue curve best approximated the real material curve. Hence, the following comparison was not meant to find an accurate match between the fatigue life found in laboratory and the numerical predicted one, but it allowed to choose between a set of materials deriving from the database.

Assuming this approach, a fatigue analysis was performed on the 3D model for each material; the fatigue life obtained from the FE simulation would have then been compared with the experimental result in order to choose the material which best approximates the real one [7].

10.3.1. Simulation settings and parameters

The model used for this set of simulations is the same used for the static analyses (Figure 198).



Figure 198 3D model used in the fatigue analyses.

The mesh applied to the 3D model is the same as well (Figure 199). This choice was actually imposed by the software workflow, since a fatigue analysis must be based on a static simulation and the model geometry and mesh parameters cannot be changed.

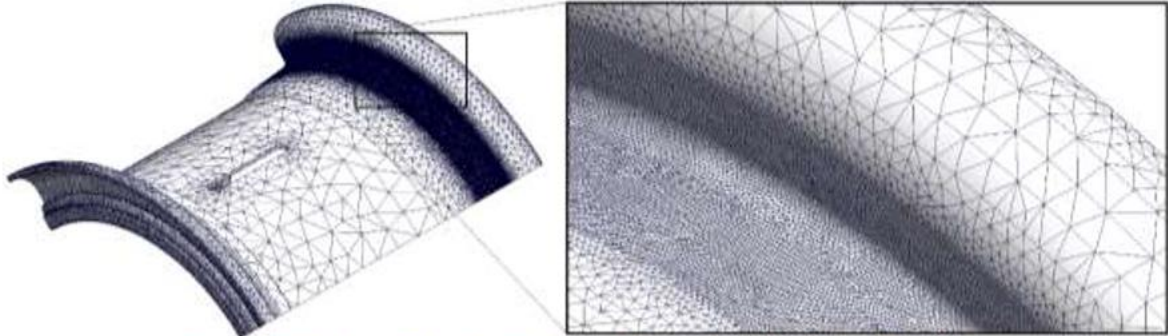


Figure 199 Mesh applied to the 3D rim model to perform the fatigue FE analysis.

It must be said that the dimensions of the mesh elements turned out to be crucial on the predicted life results, as 3 mm elements returned quite different results in terms of life compared to the 1,5 mm ones. For this reason, it was decided to thicken the mesh retroactively in the static simulations as well to obtain the most accurate fatigue results. The mesh in the seat radius area was 1,5 mm, as described previously.

As visible from Table 20, the load and inflation conditions of the rolling test are quite identical to the 6 bar – 15.100 kg – radial tire rolling test presented in *Chapter 9.2*; hence, the associated static simulation was used as base to perform the fatigue analysis. As stated before, the fatigue analysis makes the stress field found in the static simulation to vary between the stress results themselves (the maximum stress) and a lower limit obtained by applying the *R* cycle ratio (the minimum stress).

The stress field associated to the 6 bar – 15.100 kg – radial tire simulation used for this set of fatigue analyses is shown below (Figure 200):

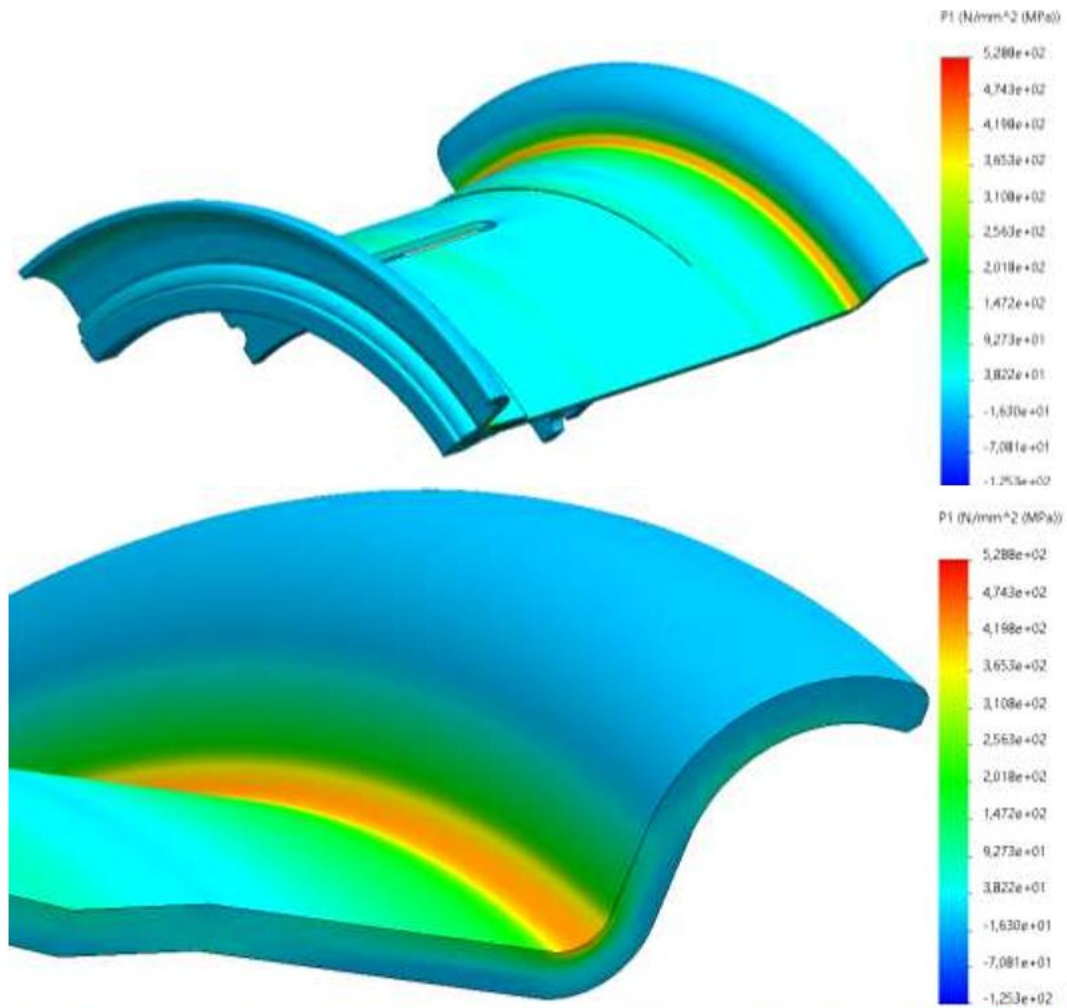


Figure 200 Graphic representation of the main stress field found from the static FE simulation on the 6 bar – 15.100 kg – radial tire configuration.

A fatigue analysis under this stress state was then performed on the model for each material considered.

10.3.2. Analyses results and comparisons

The simulations returned both the predicted life and the cumulated damage for each element of the mesh; in these simulations only the life previsions will be investigated, since they are more immediately comparable with the experimental result.

An example of the graphic representation of the predicted life provided by the software is shown below (Figure 201).

From Figure 201 it is clear how the fatigue solicited part of the rim is actually the flange seat radius; moreover, the higher the mean and the alternated stress components, the wider the area subjected to a limited life (blue area).

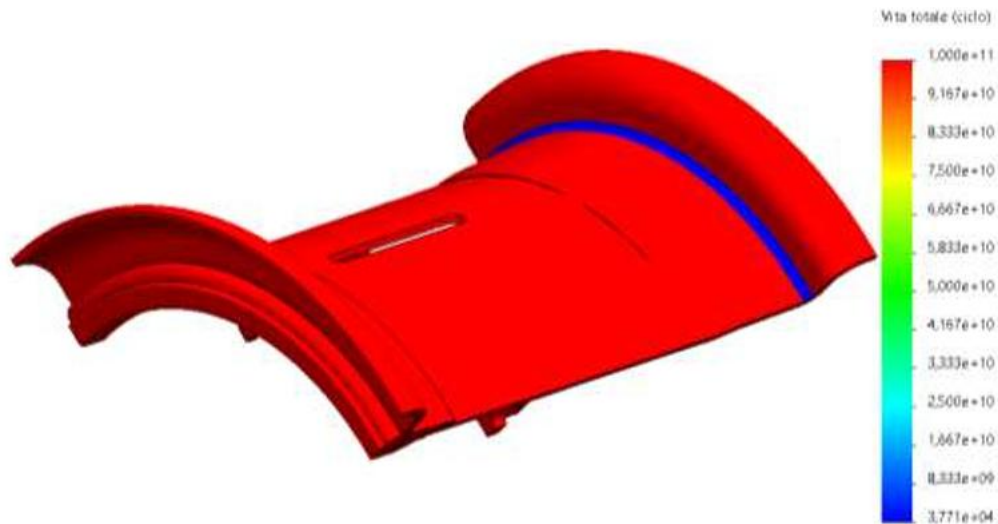


Figure 201 Graphic representation of the life predicted by the SolidWorks Simulation. The red areas are associated to infinite life, while the blue area has a limited predicted life.

In the table below the results for the 6 bar – 15.100 kg – radial tire fatigue simulations on different structural steels from *Total Materia* are reported:

Predicted life for each material considered 6 bar - 15.100 kg - radial tire	
Material	N_f
S185	391.700
S235JR	2.332.000
S275JR	18.230.000
S355JR	134.000.000
E295	83.100.000
E335	516.200.000
E360	Infinite

Table 21 Life predicted by the fatigue simulations on the 6 bar – 15.100 kg – radial tire load configuration for different structural steels from *Total Materia*.

As expected, the structural steel whose numerical life result best approximates the experimental data is the S235JR. The S185 steel widely underestimates the laboratory measurements, while more performing structural steels, starting from the S275JR, overestimate it by at least one order of magnitude.

The E295, E335 and E360 structural steels are high performance materials which have been studied only on a speculative purpose. According to the results shown in Table 21, the S235JR structural steel was assumed as the best approximation of the real material (Table 22):

N_f	
ROLLING TEST RESULT	S235JR
2.000.194	2.332.000

Table 22 Comparison between the laboratory rolling test results and the FE numerical simulations results on the component life; the approximation of the S235JR steel of the real material is indicatively evaluated.

It must be remarked that, since one single rolling test was executed, this comparison must be considered purely indicative, as no statistical considerations can be done. However, given the several orders of magnitude that distinguish the numerical S235JR result from the other structural steels, it can be stated with a good confidence that the S235JR represents the best approximation of the rim steel. Therefore, this material and the associated Wöhler curve were applied in the following fatigue analyses.

Once the material for the 3D model was chosen, the associated fatigue limit σ_{FA} had to be evaluated, as it would be needed for following calculation presented in the next paragraph. The fatigue limit reported by *Total Materia* for the S235JR structural steel is equal to 180 MPa; however, the manufacturer suggested a few corrective coefficients which took in account the forming process applied to the rim. In fact, the following corrective formula was applied:

$$\sigma'_{FA} = k \cdot \sigma_{FA} \quad 10-89$$

Where σ_{FA} is the fatigue limit found in laboratory through tests performed on polished specimens, σ'_{FA} is the corrected fatigue limit and k is the correction factor, which can be written as:

$$k = a \cdot \sigma_R^b \quad 10-90$$

Where σ_R stands for ultimate tensile strength and a and b are coefficients depending on the forming process applied to the material (Table 23):

SURFACE FINISH	a	b
POLISHED	1,58	-0,085
MILLED	4,51	-0,265
HOT ROLLED	57,7	-0,718
RAW FORGED	272	-0,995

Table 23 Corrective coefficients depending on the forming process of the material provided by GKN.

As the steel sheet used for the rim production is hot rolled, corrective coefficients with the following values have been chosen:

$$a = 57,7$$

$$b = -0,718 \quad 10-91$$

By substituting these values in (10-89) and (10-90), the following value for σ'_{FA} was found:

$$\sigma'_{FA} = 57,7 \cdot (370 \text{ MPa})^{-0.718} \cdot 180 = 148,8 \text{ MPa} \quad 10-92$$

This can be considered the corrected fatigue limit for the S235JR, which takes in account the process applied to the steel. This value will be used in the following calculations.

10.4. Analysis of the load cycle applied to the rim

Before presenting the fatigue analyses results, a few considerations about the cyclic load applied to the rim must be done. In fact, the loading cycle to which the rim is subject is not as simple as it could be thought, since the stress curve through the time is not a mere sinusoidal function. The strain gauges measurements analysed through the time axis, in fact, reveal a more complex trend, which is shown in the graph below (Figure 202). In the graph reported below, two full strain cycles are clearly recognisable. A higher strain peak, which correspond to the tire-ground contact, can be detected and it divides one cycle from the other.

Lower peaks can be found between the higher peaks and they are generated by the particular tire-rim contact conditions that occur during the wheel rotation. Between the minor peaks, there is a relative minimum, which shows up when the rim point is in the higher position of the rotation, diametrically opposite to the tire-ground contact point.

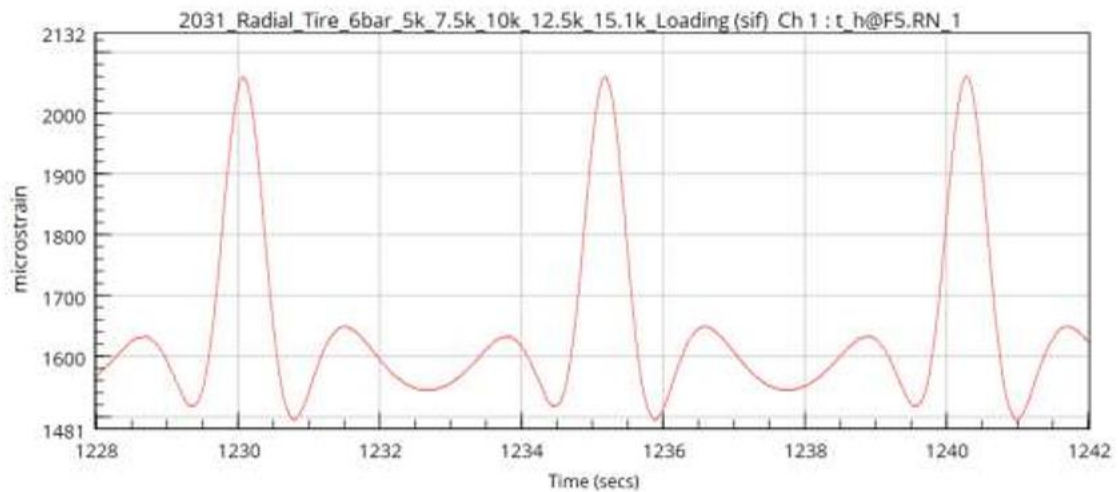


Figure 202 Deformation measured by F6 strain gauge on the 6 bar inflated rim with a radial load of 12.500 kg and radial tire as function of the time.

The cyclic strain measured by F6 strain gauge for the 6 bar – 12.500 kg – radial tire configuration is proposed above as an example since the same patterns occurs in almost all the load configurations, except for some in which the cyclic strain measured is slightly more irregular (Figure 203):

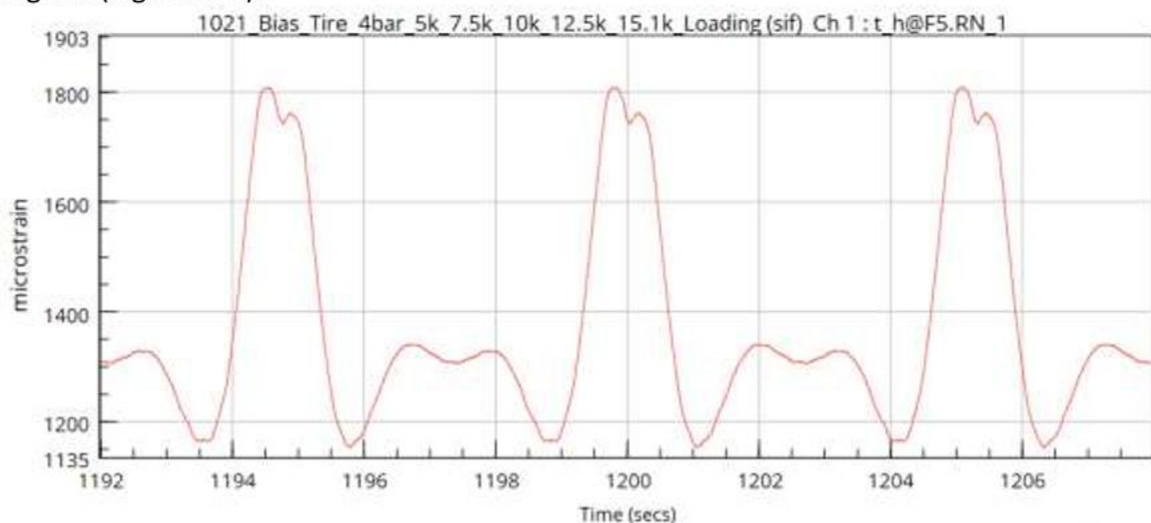


Figure 203 Deformation measured by F6 strain gauge on the 4 bar inflated rim with a load of 12.500 kg and radial tire as function of the time.

As it can be seen, for some load configurations the maximum peak presents some irregularities, whose entity however makes them completely negligible in the scope of the fatigue analyses. The same cannot be stated with the same certainty for the minor peaks that occurs during the upper part of the rotation, opposite to the tire-ground contact point. In fact, in order to determine if the minor peaks affect the cumulative damage of the component, the position of the associated alternated stress point in the Haigh diagram must be verified (Figure 202). As suggested by manufacturer, if the alternated stress point is located under the diagram line, its life influence on the fatigue damaging of the component can be considered negligible with a certain safety factor; if not, the component life should be considered affected, as the $\sigma_{a_{limF}}$ is exceeded. Before this check could be done, the stress values corresponding to the minor peaks must be collected. This operation was done on the *nCode* graphs manually on samples of the cyclic load graph for each load condition. More in detail, the stress values associated to the maximum and the minimum of each cycle peak have been collected. The criterion used to detect the minimum points was based on the tank counting method, according to which the stress-time graph must be imagined like a container filled with some liquid. To detect the maximum and the minimum associated to the same peak, it is sufficient to empty the lowest part of the graph: the maximum and the minimum will be easily graphically found. Some liquid may remain in some cavities, which must be emptied in the same way, allowing to find new associated maximums and minimums. A graphic representation of this technique applied to this study is shown below (Figure 204):

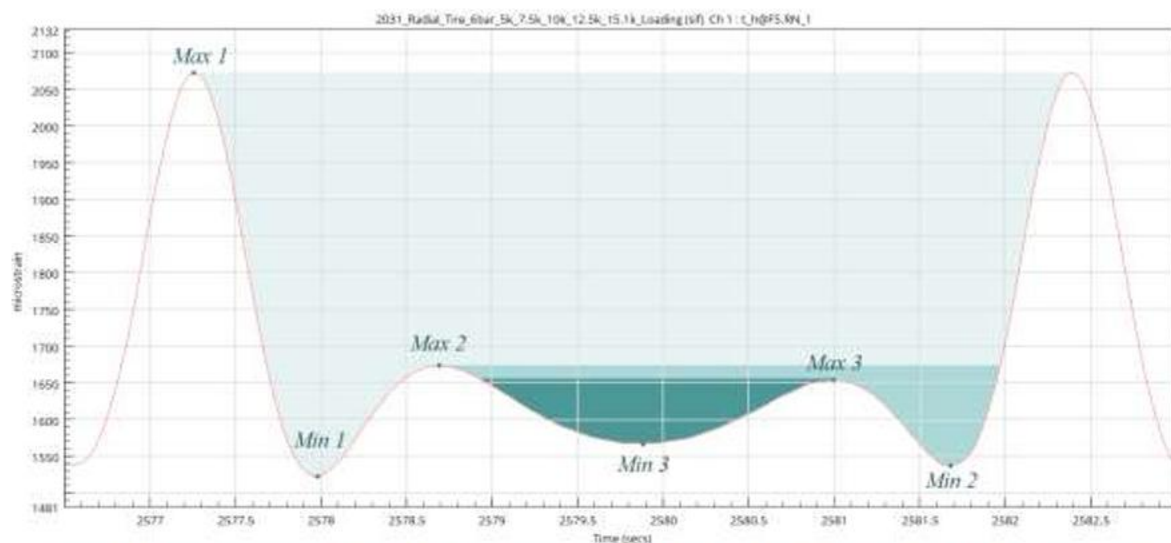


Figure 204 Graphic representation of the tank counting method applied to the cyclic stress of the rim problem.

The results of the sampling on the stress-time graphs from the experimental rolling tests carried out through the tank counting method are shown below (Table 24):

MAIN PEAK															
Stress [MPa] - 4 bar - radial tire															
5000 kg			7500 kg			10000 kg			12500 kg			15100 kg			
F4	F5	F6	F4	F5	F6	F4	F5	F6	F4	F5	F6	F4	F5	F6	
MAX	131,4	253,8	265,6	142,6	265,8	273,0	154,8	278,2	279,6	165,2	288,2	285,4	177,1	300,8	292,2
Min	76,5	195,6	226,0	73,7	193,8	226,6	70,2	190,6	222,6	67,3	188,3	224,2	64,1	186,0	223,3
Stress [MPa] - 6 bar - radial tire															
5000 kg			7500 kg			10000 kg			12500 kg			15100 kg			
F4	F5	F6	F4	F5	F6	F4	F5	F6	F4	F5	F6	F4	F5	F6	
MAX	193,3	374,2	356,6	205,0	386,6	363,8	221,6	402,6	372,2	234,4	414,8	378,4	246,6	426,2	383,6
Min	134,2	312,8	314,8	132,0	311,0	313,4	128,2	307,4	310,6	124,9	304,2	307,6	121,7	301,6	305,2
Stress [MPa] - 4 bar - bias tire															
5000 kg			7500 kg			10000 kg			12500 kg			15100 kg			
F4	F5	F6	F4	F5	F6	F4	F5	F6	F4	F5	F6	F4	F5	F6	
MAX	147,0	311,8	259,4	158,7	326,2	274,6	175,6	344,0	293,8	194,0	359,8	311,8	207,0	377,2	328,2
Min	92,1	241,8	187,0	89,6	238,0	183,4	86,6	234,6	178,9	85,2	230,8	175,9	85,7	227,0	175,6
Stress [MPa] - 6 bar - bias tire															
5000 kg			7500 kg			10000 kg			12500 kg			15100 kg			
F4	F5	F6	F4	F5	F6	F4	F5	F6	F4	F5	F6	F4	F5	F6	
MAX	188,7	378,0	325,6	204,4	398,4	346,8	218,8	418,6	366,2	234,8	439,2	384,6	251,8	459,4	403,8
Min	139,7	314,2	257,4	135,2	309,8	252,2	131,4	306,4	246,6	127,9	305,4	242,2	125,3	304,4	238,2
SECOND PEAK															
Stress [MPa] - 4 bar - radial tire															
5000 kg			7500 kg			10000 kg			12500 kg			15100 kg			
F4	F5	F6	F4	F5	F6	F4	F5	F6	F4	F5	F6	F4	F5	F6	
MAX	89,7	209,6	238,4	90,9	212,0	241,2	92,6	214,6	224,0	94,4	217,6	247,2	96,8	222,4	292,2
Min	76,8	195,9	226,4	73,8	193,9	225,2	70,3	190,6	222,8	67,4	188,3	220,8	64,2	187,8	223,3
Stress [MPa] - 6 bar - radial tire															
5000 kg			7500 kg			10000 kg			12500 kg			15100 kg			
F4	F5	F6	F4	F5	F6	F4	F5	F6	F4	F5	F6	F4	F5	F6	
MAX	148,3	327,4	328	149,7	329,6	330,2	151,6	332,2	333	153,4	334,8	335,8	155,2	337,4	338,6
Min	134,7	312,4	314,8	132,0	311,2	313,6	128,2	307,4	310,6	124,9	304,2	307,6	121,8	301,6	305,2
Stress [MPa] - 4 bar - bias tire															
5000 kg			7500 kg			10000 kg			12500 kg			15100 kg			
F4	F5	F6	F4	F5	F6	F4	F5	F6	F4	F5	F6	F4	F5	F6	
MAX	92,5	266,6	187,9	111,2	267,6	215,2	112,2	268,0	216,8	113,8	266,8	218,6	115,4	266,0	220,8
Min	110,0	245,2	213,2	89,7	240,5	183,6	86,7	235,8	179,0	85,5	231,0	176,3	85,8	228,2	175,7
Stress [MPa] - 6 bar - bias tire															
5000 kg			7500 kg			10000 kg			12500 kg			15100 kg			
F4	F5	F6	F4	F5	F6	F4	F5	F6	F4	F5	F6	F4	F5	F6	
MAX	156,6	337,0	282,2	158,2	340,2	285,2	159,7	343,8	288,0	161,1	347,6	290,4	162,7	351,2	292,8
Min	139,9	317,2	258,8	135,3	312,4	252,4	131,5	308,8	246,8	128,0	307,0	242,2	125,4	304,8	238,4

THIRD PEAK

Stress [MPa] - 4 bar - radial tire															
5000 kg			7500 kg			10000 kg			12500 kg			15100 kg			
	F4	F5	F6	F4	F5	F6	F4	F5	F6	F4	F5	F6	F4	F5	F6
MAX	86,82	206,4	236,4	87,6	208,6	238,6	88,72	210,6	242,0	89,96	213,2	245	91,92	217,6	249,2
Min	81,2	199,3	226,4	80,02	198,8	226,6	78,74	197,8	224,0	77,56	197,3	222,8	77,0	198,3	222,2
Stress [MPa] - 6 bar - radial tire															
5000 kg			7500 kg			10000 kg			12500 kg			15100 kg			
	F4	F5	F6	F4	F5	F6	F4	F5	F6	F4	F5	F6	F4	F5	F6
MAX	145,8	324,6	326,6	146,7	326,4	328,8	148,2	328,6	331,8	149,5	330,8	334,4	150,8	333,2	337,2
Min	139,7	316,0	314,8	138,7	315,8	314,0	137,2	314,4	311,8	136,1	313,4	310,2	135,0	312,6	308,8
Stress [MPa] - 4 bar - bias tire															
5000 kg			7500 kg			10000 kg			12500 kg			15100 kg			
	F4	F5	F6	F4	F5	F6	F4	F5	F6	F4	F5	F6	F4	F5	F6
MAX	108,1	264,6	211,6	109,2	265,6	213,6	109,9	265,6	215,4	111,0	264,0	217,8	112,2	262,8	219,8
Min	106,4	262,3	208,0	106,8	262,4	208,6	106,9	261,6	208,8	107,6	259,6	209,8	108,3	258,2	211,2
Stress [MPa] - 6 bar - bias tire															
5000 kg			7500 kg			10000 kg			12500 kg			15100 kg			
	F4	F5	F6	F4	F5	F6	F4	F5	F6	F4	F5	F6	F4	F5	F6
MAX	154,9	335,3	281,2	156,2	338,3	283,8	157,5	341,6	286,2	158,7	345,2	288,8	159,8	348,4	291,6
Min	153,5	333,6	278,0	153,8	335,2	279,0	154,3	337,4	279,8	154,7	339,8	280,6	155,3	342,4	281,6

Table 24 Stress values extrapolated by the nCode measurements files for the maximum and the minimum of each one of the cycle peaks.

As shown above, the tank counting method produces three different peaks for each cycle. Of course, the highest of the three peaks was already known to be influent on the life of the rim.

Hence, the focus was set on the second and the third peak: it was needed to verify if the corresponding points in the Haigh diagram were placed below the Haigh line; in this case they could have been considered negligible in terms of cumulative damage caused to the rim. If they were placed above the line, on the other hand, they should have been considered indeed influent on the cumulative damage of the component and, thus, should have been included in the fatigue analyses, as ignoring them would have meant overestimating the life of the rim. As an initial evaluation, the most burdensome loading conditions were inspected: in fact, if the highest cyclical stresses had been found to be irrelevant, the lowest would have been too. Thus, the most critical load condition for both the radial and the bias tire were examined, that is 6 bar – 15.100 kg case.

Their representation in the Haigh diagram is presented in Figure 205

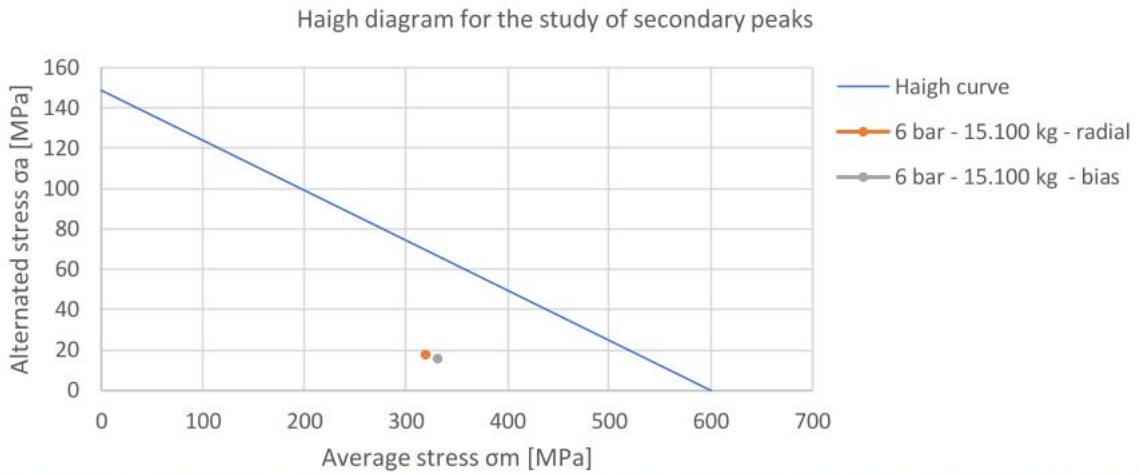


Figure 205 Graphic representation in the Haigh diagram of the points corresponding to the secondary peaks of the load cycle for the 6 bar – 15.100 kg configurations.

As it can be seen from the graph, the points associated to the secondary peaks of the most critical load conditions (6 bar – 15.100 kg – radial tire and 6 bar – 15.100 kg – bias tire), are placed way inside the area delimited by the Haigh curve. This means that they cannot be considered influent on the fatigue life of the component, as the fatigue limit for this point refers to values of about 450 MPa of mean stress and about 30 MPa of alternated stress. It follows that all the lower points associated to the secondary peaks of the remaining load conditions can be automatically considered negligible, as well as the third peaks which are way less critical.

Therefore, the fatigue analyses can be performed referring only to the alternated and mean stress associated to the main load peaks, which are the stress conditions induced by the tire-ground contact. Thus, just one static event was needed to be inserted in each of the fatigue analyses and no counting methods were necessary within the simulations.

10.5. Simulations results

In this paragraph, the fatigue simulations results will be presented, analysed and compared. Once the preliminary hypotheses, the material fatigue curve and the load cycles were investigated, the proper fatigue analyses of the load conditions applied in the Woodridge laboratory tests could finally be performed. The instruments and the setting used have already been described in Paragraph 10.1.1. A fatigue FE simulation was launched for each of the load configurations tested for the 4 and 6 bar inflation cases. It must be highlighted that no experimental data were available for the fatigue life of the component, as performing dynamic

tests till failure for a wide set of load conditions and with statistical value is extremely expensive both in terms of time and resources. Thus, the results of these analyses should be considered mainly indicative. The results obtained by the numerical analyses for the fatigue lives are shown in the table below (Table 24):

INFLATION P [bar]	TIRE DESIGN	RADIAL LOAD [kg]	CRITICAL AREA	R	σ_{max} [MPa]	N_f
4	Radial	5000	F6	0,851	279,0	Infinite
		7500	F6	0,830	290,8	Infinite
		10000	F6	0,796	299,6	Infinite
		12500	F5	0,653	308,7	Infinite
		15100	F5	0,618	318,3	Infinite
	Bias	5000	F5	0,776	318,7	Infinite
		7500	F5	0,730	335,3	Infinite
		10000	F5	0,682	353,4	301.900.000
		12500	F5	0,641	369,3	29.290.000
		15100	F5	0,602	387,2	3.168.000
6	Radial	5000	F5	0,836	388,0	Infinite
		7500	F5	0,804	400,1	Infinite
		10000	F5	0,764	415,7	142.600.000
		12500	F5	0,733	427,3	14.740.000
		15100	F5	0,708	439,3	2.174.000
	Bias	5000	F5	0,831	367,2	Infinite
		7500	F5	0,778	390,6	Infinite
		10000	F5	0,732	412,3	38.270.000
		12500	F5	0,695	434,1	2.763.000
		15100	F5	0,663	457,6	215.500

Table 25 Results for the predicted fatigue lives of the component for each load and inflation condition returned by the FE numerical simulations.

Before commenting the results shown above, it is necessary to specify that the simulated number of cycles has been intentionally set to the high value of 10^{10} . However, it was esteemed that for heavy trucks rims conceived to run relatively low numbers of cycles under heavy loads, an infinite life limit of 10^7 cycles could be considered appropriate. Hence, all the results exceeding this limit should be considered as infinite life results. The predicted life denominated as “infinite” are those whose simulations returned 10^{10} cycles. Following this assumption, some considerations on the predicted lives can be done. First, it must be remarked that, as expected, the 4 bar load cases generally present higher predicted lives: in fact none of the 4 bar – radial tire configurations returned limited lives, while among the 4 bar – bias tire cases, just one provided a limited life for the component, that is the 4 bar – 15.100 kg – bias tire configuration with an estimated life of 3.168.000 cycles.

The 6 bar studies produced more limited life results, which are the 6 bar – 15.100 kg – radial tire, with a predicted 2.174.000 cycles life, and the 6 bar – 12.500 kg bias tire and the 6 bar – 15.100 kg – bias tire, respectively with an estimated life of 2.763.000 and 215.500 cycles. This last result is the most critical one, as it is lesser of one degree of magnitude compared to the other limited predicted lives. It is a prediction that should be further examined, as it could depend whether on some model approximations or on an inaccurate choice of the material fatigue curve. Further studies could possibly deepen the investigation on this result. Secondly, the influence of the maximum stress detected in the static simulation on the predicted life can be discussed as well.

In fact, even if the mean stress values were considered as reference to reproduce the experimental data within the numerical simulations, maximum stresses are actually the responsible for the results in the fatigue analyses. Generally, it can be verified that, the higher the maximum stress detected in the simulation, the lower the predicted life. However, this is not the only variable affecting the fatigue analysis result, as the cycle ratio R plays an equally important role. In fact, the more the cycle ratio is close to the unit value, the more the cyclic load can be associated to a static load and, thus, its impact on the component life reduction decreases. On the other hand, the more the cycle ratio is close to zero, the more the load can be approximated as a cycle pulsing from zero, which is a far heavier condition for the fatigue resistance of the rim. Naturally, this assertion must be weighted taking in account the mean stress component; the higher the mean stress, the heavier the consequences of the same alternated stress, as the Haigh diagram shows. It is immediate to understand how the predicted life, even for a simplified model as the one applied in this study, depends on many parameters. In Chapter 10.6 some considerations and conclusions on the results obtained in this thesis will be discussed. Below, a graphic example of the results of the fatigue FE simulation is proposed (Figure 206):

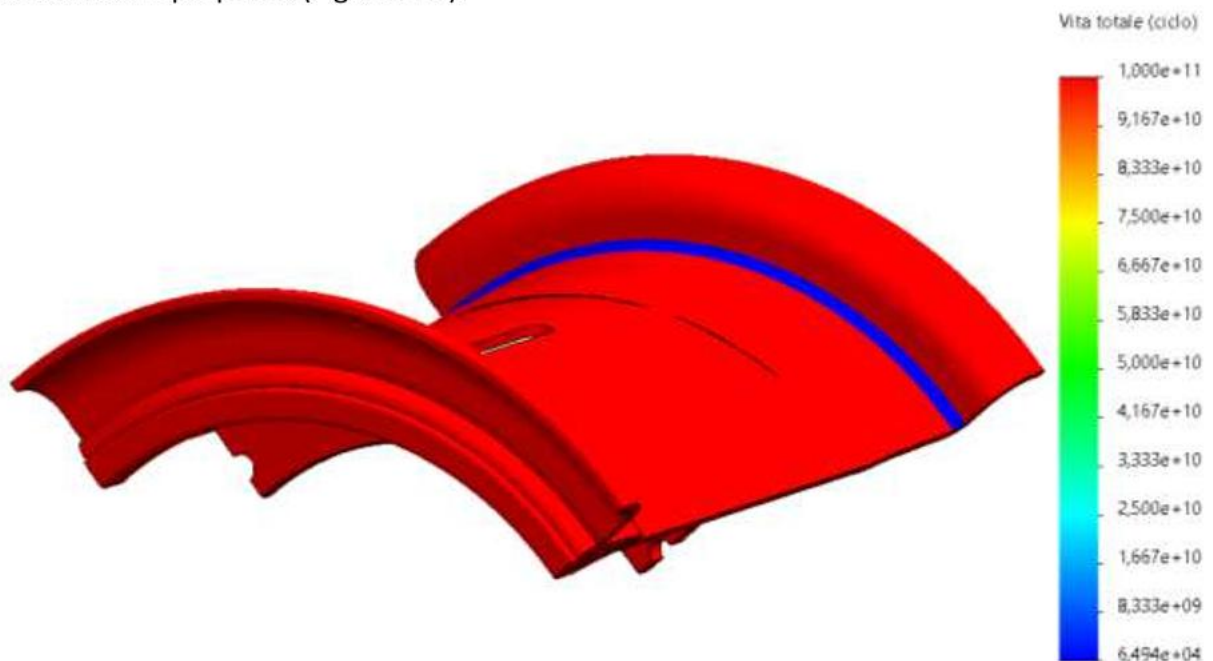


Figure 206 Graphic representation of the FE fatigue simulation for the 6 bar – 12.500 kg – bias tire configuration. The limited life area coinciding with seat radius and indicated in blue can be noticed.

10.6. Conclusions

10.6.1. Results analysis

In this chapter, the conclusions of the study exposed in this thesis are presented. The complexity of the problem in many perspectives made its solution quite challenging, as resolution approaches, which were not initially planned, had to be taken. In fact, the ultimate researching purpose, which was the fatigue analysis and test of the component, implied a series of corollary problems of equally high difficulty and for whose resolution non-conventional study approaches had to be applied.

The first and the toughest problem to be met was the tire-rim contact problem, for which many modelling methods were tried. The complexity of the mechanical non-linear behaviour of the tire and, thus, of the tire-rim contact phenomenon led to a more unconventional approach, in which the experimental data from the laboratory tests would not have been considered as a comparison term for the numerical results, but would have been used as a base for an empirical model instead. In fact, what was applied was substantially a reverse model of interpretation of the experimental results based on the iteration of attempts of solutions for the tire-rim contact pressure. The iteration of the solutions was aided by contact measurements performed in previous studies. Due to the particular study approach employed, in which the experimental data were taken in account at the beginning of the model construction and not at the end as a checking instrument as they usually are intended for, the reverse analysis method applied was defined as "*empirical*". The experimental data, in fact, are the core element of the model construction instead of the comparison term to verify it. The pressure distribution found through it turned out to be quite coherent with the initial expectation. The iteration of the possible solutions for all the loading configurations gave us a much deeper comprehension of the tire-rim contact phenomenon. As a result, what was intended to be a fatigue verification of the component, revealed to carry with it a stimulating study on the mechanical contact between the rim and the tire.

This study context allowed us to better understand the complexity and importance of collecting fatigue data for the materials. In fact, investigating the possible fatigue curves of the rim steel was very interesting and revealing of how small differences in the *Wöhler* curve can produce significant gaps in the predicted life of the component. As described in *Chapter 10*, the real fatigue curve of the rim steel had to be approximated with the *Wöhler* curve from the *Total Materia* database which best interpreted the result from the rolling test. Then it had to be corrected with coefficients, which took in account the forming process influence on the material cyclic behaviour. Of course, it represented an approximation needed due to the lack of a sufficiently wide fatigue data set of the real material.

It must be remarked that this study is based on several approximations and hypotheses exposed during the entire thesis. These assumptions range from the model applied to reproduce the experimental stress results in the FE simulations to the material fatigue curve, but also to the supposed behaviour of the steel in terms of hardening and residual stresses. It follows that the results of the fatigue analyses performed cannot be considered as a precise reference nor a validation of a complex model for the wheel. Instead, these results intend to be mainly an indicative evaluation of the predicted life of the wheel under several load configurations. The main aim of the thesis is remarking the most critical conditions tested on the wheel and giving an estimation of the rim predicted life based on FE numerical calculation performed with a dedicated software.

From the FE fatigue analyses performed, it emerges that the only critical conditions for the life of the rim are the 6 bar – 15.100 kg for the radial tire and the 4 bar – 15.100 kg, the 6 bar – 12.500 kg and the 6 bar – 15.100 kg for the bias tire, with particular emphasis for the last one. In fact, for the 4 bar – 15.100 kg, the 6 bar – 15.100 kg – radial tire and the 6 bar – 12.500 kg – bias tire a predicted life of 3.168.000, 2.174.000 and 2.763.000 respectively has been found. These values are in reasonable accord with the expected life for the kind of rim studied under such heavy load conditions, so these configurations are detected by this study as critical and further detailed analyses can possibly be needed. As far as the 6 bar – 15.100 kg – bias tire configuration is concerned, an extremely low predicted life of 215.000 cycles has been detected from the numerical simulations. This result can be due to many reasons, from some modelling inaccuracies to an excessive simplification introduced through the hypotheses on the material and its mechanical condition after the forming process.

If it is true that the results of this last load configuration cannot be considered accurate, it is also true that this condition is one of the heaviest together with the two exposed above and, therefore, further experimental data collection and analyses may be needed in next studies. Regarding all the remaining load configurations, the FE analyses performed returned a predicted infinite life, as the limit for the limited life has been assumed for 10^7 cycles. A comparison of the component's predicted lives for all the tested load conditions is presented below (Figure 207):

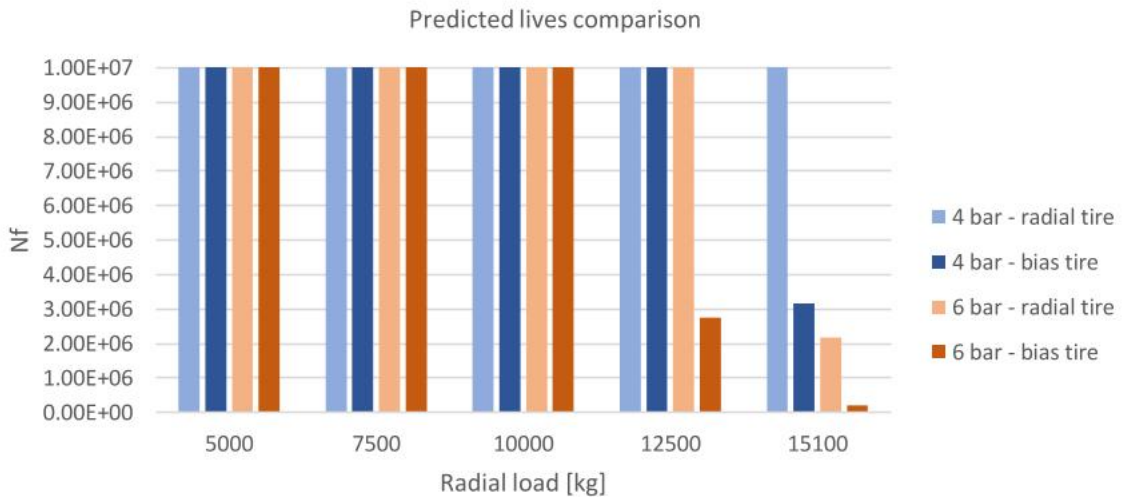


Figure 207 Comparison of the component's predicted lives for all the tested load conditions. The predicted lives are compared on a linear scale.

In the graph shown above, the predicted lives are compared on a linear scale with a maximum life of 10^7 cycles, which have been considered the infinite life limit. The same graph is proposed on a logarithmic scale below (Figure 208):

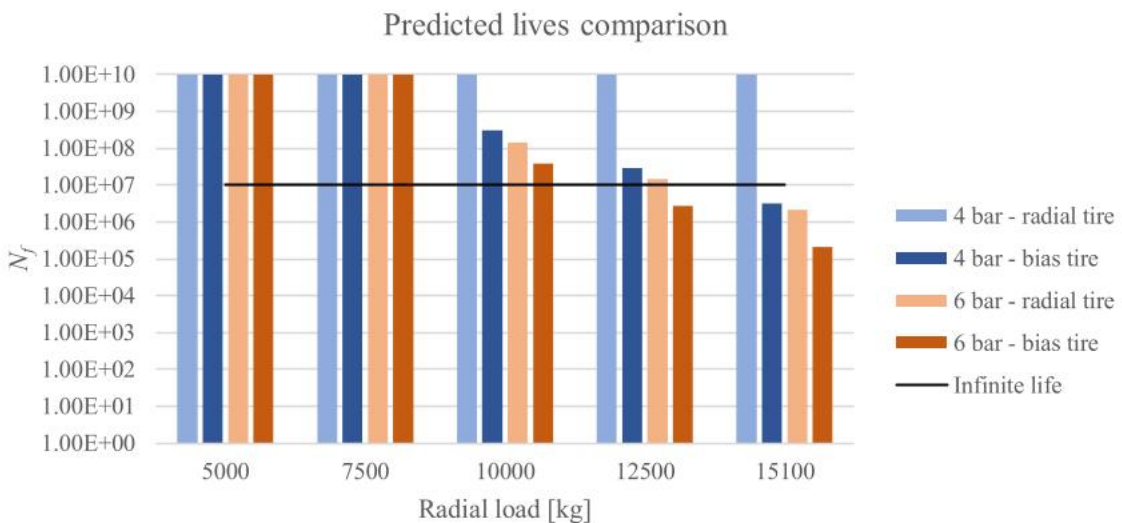


Figure 208 Comparison of the component's predicted lives for all the tested load conditions. The predicted lives are compared on a logarithmic scale.

As it can be noticed, the only tire configuration which never shows limited predicted lives is the 4 bar – radial tire. For all the other tire configurations at least one case of predicted limited life occurs. As disclosed in *Chapter 10*, the simulation result for the predicted life of the component is affected by many parameters; among all, the most influent are surely the entity of the maximum and mean stresses and the cycle ratio R . In fact, the higher the stress values, the highest the damage caused to the material. Moreover, the more the R ratio tends to zero, the more the cyclic stress can be approximated to a cycle pulsating from zero. This load condition can be considered far more critical compared to a cyclic stress with a R ratio which tends to 1, as it is closer to a static stress state.

The influence of the maximum stress and of the cyclic ratio combined is shown in the graph below (Figure 209):

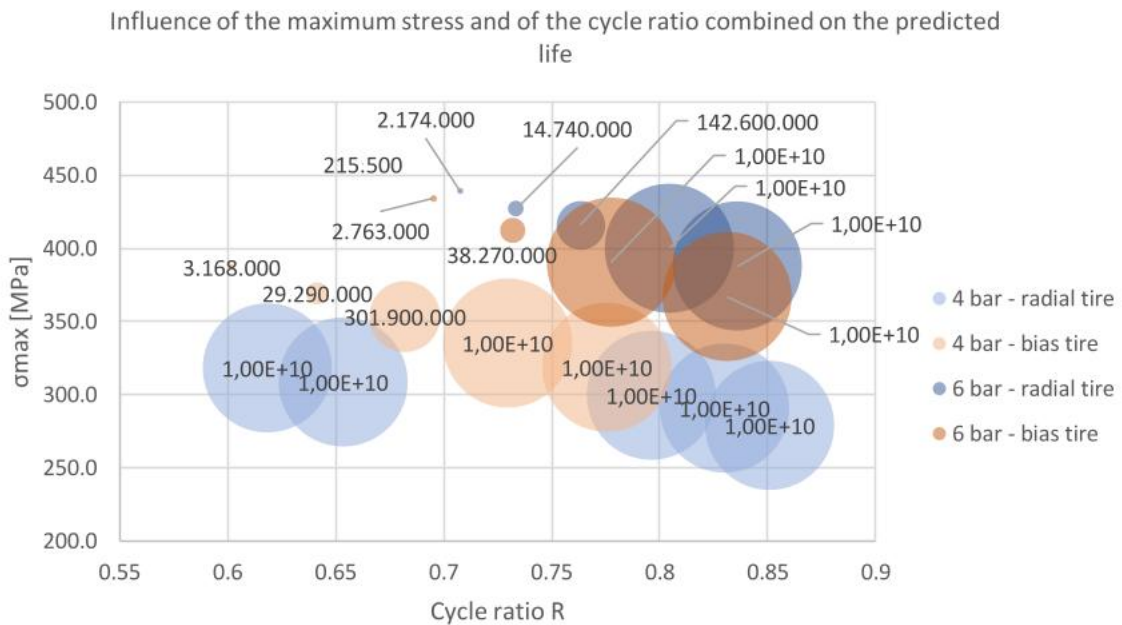


Figure 209 Influence of the maximum stress detected in the simulation model and of the cyclic ratio R recorded in the experimental tests on the numerically predicted life of the component. The bigger the circle, the higher the predicted life.

In the graph reported, the bigger the circle, the higher the numerically predicted life. As clearly shown above, it is the combination of the two parameters which determines the cyclic damaging of the component. In fact, the graph area at the top left is the one which contains the limited life configurations, as it is associated to sufficiently low cycle ratios and enough high maximum stresses.

It is important to remark that the fatigue results obtained refer to inflation pressures that exceed the recommended value proposed by the tire manufacturers, that is 3,2 bar. It was for this reason that the 8 bar tests were excluded from the study, as they represented an inflation configuration that hardly would be used during the exercise of the rim. As a consequence, the evaluation on the fatigue life of the component refer to stress states that exceed the usual ones conceived for the rim. This represents a safety factor for the limited life

results found for some load conditions. The limited predicted lives of the most critical load configurations represent evaluations of conditions that would be rarely applied to the component during the exercise. In fact, inflation pressures of 4 and 6 bar could be possibly used for particular stiffness requirements for the wheels if heavy loads are applied.

Also, as supposed in *Chapter 9.2.2*, increasing the inflation pressure could mean spreading in a more uniform way the load on the rim surface. Finally, under certain load conditions, a low inflation pressure can cause a higher tire displacement and, thus, more critical stress states [25].

The influence of the tire design on the fatigue resistance of the rim can be simplified by stating that the bias tires produces stress states that damage the life of the component more heavily compared to the radial ones. With the same inflation pressure and radial load, in fact, the predicted lives for the bias configurations are lower than the radial ones.

In conclusion, it can be stated that the inflation and loading configurations of 4 bar – 15-100 kg – bias tire, 6 bar – 15.100 kg – radial tire, 6 bar – 12.500 kg – radial tire and 6 bar – 15.100 kg – bias tire are associated to predicted limited lives, with a particularly low life result for the last condition mentioned. For these configurations further studied may be needed.

Ultimately, the results of both the static and the fatigue studies can be summed up as follows:

- Direct modelling of the tire-rim contact pressure through mathematical or FE tire models can hardly produce results which are accurately coherent with the experimental data, especially because the fatigue FE analysis requires to process stress fields from static simulations as similar as possible to the experimental evidence in order to return good life predictions.
- A reverse empirical model based on the iteration of attempts of solution for the contact pressure distribution between rim and tire in the rim flange area has been identified as the most suitable approach for the particular problem faced in this thesis. Following this modelling solution, the experimental results are not used as an empirical comparison term employed to verify the prediction of a direct model, instead they are considered as an experimental basis on which a reverse empirical model can be built. This particular model is not mainly intended to make predictions on the tire-rim interactions (even if many considerations on this phenomenon could be made thanks to it), but to reproduce the experimental results in the FE numerical simulation in the most accurate way possible. Going backwards and analysing the solutions found for the pressure distributions, a deeper understanding of the phenomenon could be reached.
- Previous measurement campaigns and the suggestions of Manufacturer on the contact pressure distribution allowed us to realize that the most loaded areas are the bead seat and the flange hook ones.

-
- The static simulations revealed that the tire design affects the pressure distribution, as it was found that, especially for lower radial loads, bias tires tend to load more the upper areas of the flange hook compared to the radial ones.
 - The inflation pressure affects the load pattern as well, since the simulation results show that the less the tire is inflated, the less its deformed configuration is defined and, thus, the loaded area are not accurately identified as in the high-pressure configurations. Moreover, if the pressure distribution found in this study are considered reliable, it emerges that less inflated configurations can involve higher peaks in the contact pressure, as the deformed states of the tire are probably less rigid than the high inflated ones.
 - Regarding the fatigue analyses, it emerged that small variation in the Wöhler curve can cause high fluctuations in the predicted life results. Therefore, a wide experimental campaign for the cyclic characterization of the material is necessary in order to perform accurate fatigue predictions on the component.
 - Another important step for the material characterization is studying the influence of the forming process on its mechanical properties, as both the residual stresses and the hardening can play an important role in the cyclical behaviour of the cold formed steel.
 - The fatigue FE simulations based on the static numerical results and on the hypotheses of neglecting the residual stresses of the material revealed that the critical load conditions are the high load configurations (12.500 kg and 15.100 kg). These load conditions are quite extreme and reasonably rarely reached by the structure during the exercise. Moreover, these radial loads have been simulated together with inflation pressures that exceed the value recommended by the tire manufacturers, that is 3,2 bar. Thus, these results must be considered as an evaluation of extremely hard load conditions and the limited life predictions must therefore be properly weighted. In any case, the load conditions that eventually need further investigation and study are the ones mentioned above. [29]

11. FEM MODEL FOR PRESSURE PROF. IN IND. RIM (PAPER)

DEVELOPMENT OF A FEM MODEL FOR EVALUATING THE PRESSURE PROFILE IN THE INDUSTRIAL WHEEL AND FATIGUE STRENGTH ANALYSES

M. CIMA(*), L. PIOVANI, L. SCALVINI, L. SOLAZZI, (1)

(1)Brescia University (Università degli Studi di Brescia), Department of Industrial and Mechanical Engineering, via Branze 38, 25123 Brescia, Italy.

ABSTRACT

Industrial wheels are heavily loaded components that undergo severe cyclic stress conditions. Thus, the design of the rims must include a wide fatigue study which articulates in laboratory and field tests, analytical and numerical analyses and comparison of the experimental and computational results. This paper presents the study approach applied in the study of a 25 *m* rim for earth-moving machines manufactured by GKN Wheels. The rim was subject to a design update which provided the reduction of the thickness from 11 *mm* to 9 *mm*. We decided to study the interaction tire-rim because it's a critical zone. The failures affected the area of the seat radius of the fixed flange of the rim, which resulted to be the most stressed part of the rim because of the bending actions of the tire on the flange. In order to deepen the cyclic mechanical behaviour of the component, laboratory inflation and rolling tests were carried out in Woodridge USA considering several combinations of inflation pressure and radial load applied to the wheel. The strain data from the tests were analysed to develop a reverse empirical model for the contact pressure between tire and rim. Once the load diagram applied to the flange for each test was estimated, FEM static simulations could be performed on a 3D model of the rim through SolidWorks Simulation. The stress fields obtained were then used for fatigue FEM numerical analyses which could return an evaluation of the predicted life of the component under several load conditions.

KEYWORDS: fatigue, industrial wheel, FEM analysis, wheel stress profile, material fatigue parameter.

NOMENCLATURE:

φ : coordinate used to determine φ_0 ;

b : the width of the bead seat;

a : tire radius [mm];

W : weight applied on the wheel [N];

UTS: ultimate tensile strength;

sps: sample per second;

FEM: finite element method;

φ_0 : angle that depends on the tire deformation;

r_f : the radius of the load point on the rim flange [mm];

r_b : radius of the bead [mm];

W_r : radial pressure distribution function on the tire [MPa];

W_p : the axial component of the force due to the inflation pressure [N];

W_0 : analytical expression of a pressure due to the weight applied to the wheel [MPa];

T_f : the load per unit of circumferential length of the single rim flange [N/mm];

P_f : uniform pressure due to the axial contribution of the inflation pressure applied over the entire vertical surface of the rim flange [MPa];

P_0 : tire inflation pressure [MPa];

1 INTRODUCTION

The goal of this article is the fatigue study of a rim for earthmoving vehicles. In particular, we want to identify the distribution of loads acting on the fixed flange (Figure 1) see due to rolling, starting from results obtained from laboratory tests. After having highlighted the best distribution of pressures, we proceed with numerous finite element analyses from which it is possible to evaluate the influence of different parameters, such as: the vertical load, the inflation pressure and the type of tire.



Figure 1 Image from cad of the component object of this study.

The wheel under study is produced by GKN Wheels and it is mainly used on wheel loaders. This is defined by the code: 25-19.5/2.5.

Where the first number indicates the rim diameter in inches, the second is the depth of the rim channel (i.e., the maximum width available for housing the tire, measured on the median transverse plane) in inches and the third is the height of the edge of the rim.

This wheel is composed of four elements:

- the base of the rim: made of two components welded together with the submerged arc welding process along the circumferential direction;
- -an elastic ring: with the task of keeping all the components of the wheel assembled;
- two lateral flanges: with the task of containing the tire beads (one fixed and one removable to facilitate the replacement of the tire).

The portion that undergoes the greatest stress due to interaction with the tire is the fixed flange, which can be divided into the zone shown in Figure 2:

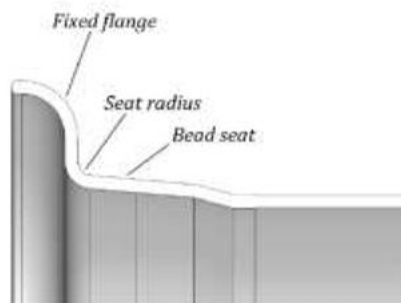


Figure 2 Reference areas of the rim.

bead seat, which is a 5° inclined area where the tire bead rests;

flange radius, which is the radius of connection between the seat of the tire bead and the vertical wall of the edge of the flange;

fixed flange, this area consists of a vertical wall and a subsequent radius of connection with the horizontal end of the flange.

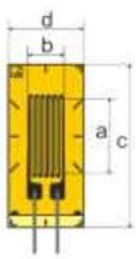
The main loads that the wheel undergoes may be due to:

- the tire inflation pressure;
- the radial load, due to the weight supported by the wheel [1].

The pressure inside the tire supports the weight of the car and pushes the beads inside their seat against the flanges. This generates an additional load on the rim due to the pressurized air. The inflation pressure acts directly on the outer side of the rim and indirectly on the flange, by pushing on the beads. The air, which pushes on the sidewalls of the tire, generates a lateral load, which acts in the axial direction. This force varies according to the type of tire, its proportion of the cross section and its reinforcements [2]. Precisely the complexity of the load conditions on the fixed flange, in particular in the radius area, makes it difficult to estimate the fatigue life of this component.

2 TEST ON FIELD

The laboratory tests were carried out in the Woodridge (United States) laboratory. In this structure, the wheel has been subjected to rolling tests with radial load. The rim has undergone several tests with the use of both radial and bias tires. In order to detect the stresses on the flange, strain gauges of the HBMLY11-3/350 model were applied (Figure 3):



Characteristic		Quantity
Temperature range	[°C]	FROM -200 TO 200
Temperature range (self-compensation)	[°C]	FROM -10 TO 120
Grid length a	[mm]	3
Grid width b [mm]	[mm]	1,6
Stand length c [mm]	[mm]	4,5
Stand width d [mm]	[mm]	4,5
Measuring grid material	/	CONSTANTAN
Grate support material	/	POLYAMIDE

Figure 3 HBMLY11-3/350 strain gauge and table of its technical characteristics.

These were placed on the radius of the flange, which is the most stressed area [3–5]. In particular, the positioning was carried out starting from the centre of the beam (F2, F5) and then the adjacent strain gauges were placed as a continuation based on the size of the grid (Figure 4):

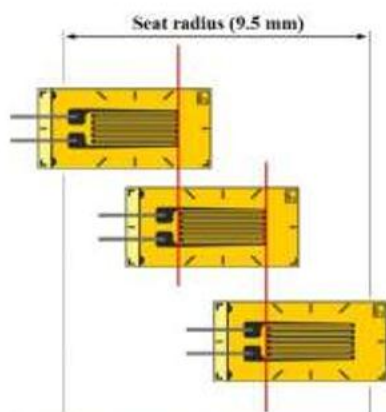


Figure 4 Representation of the methodology for arranging the strain gauges on the radius of the flange being studied.

At the end, the following configuration is obtained (Figure 5):

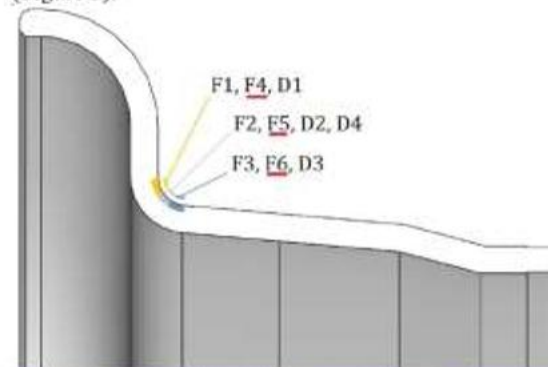


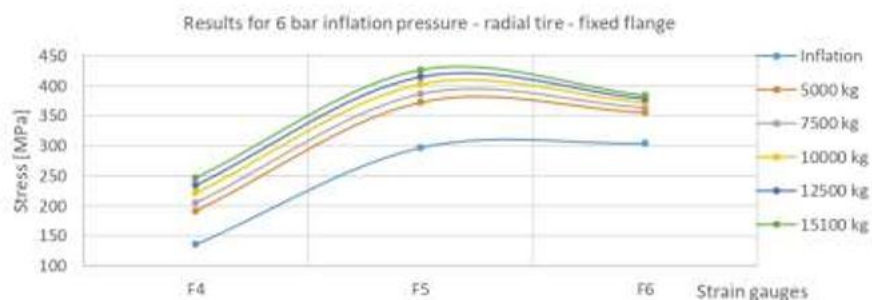
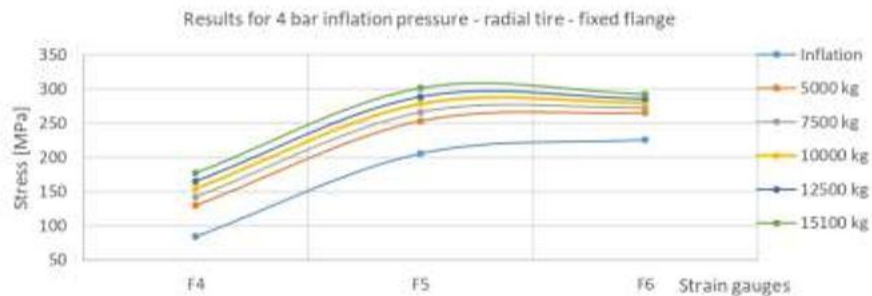
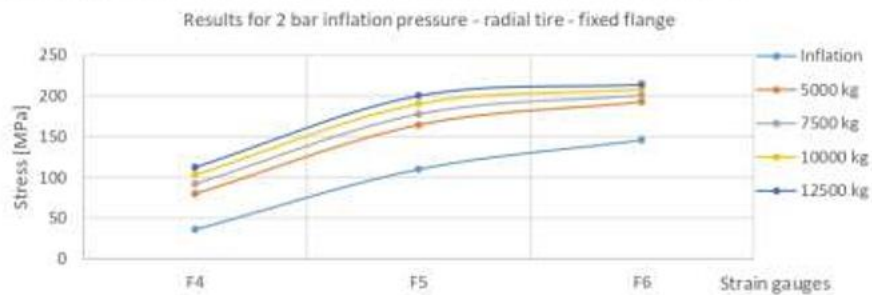
Figure 5 Qualitative representation of the positions of the strain gauges along the radius of the flange.

The points object of this analysis is F4, F5 and F6 strains because are the nearest to the critical zone (see Figure 5).

Where the strain gauges indicated with F refer to the fixed flange. The test sequence was the following for each type of tire:

- application of the strain gauges as shown in Figure 4 on the seat radius surface both on the removable flange side and on the fixed flange one;
- strain gauges connection to the SOMAT E-DAQ Lite acquisition unit, acquired at 1'000 sps;
- inflation of the tire with detection of deformation measurements given by the strain gauges;
- application of stepped loads and detection of strain gauge data;
- deflation of the tire and verification of zero settings of the strain gauges;

This procedure was repeated for four pressure values: 2 bar, 4 bar, 6 bar and 8 bar, in order to detect a possible connection between the breakages that occurred during operation and the tire inflation pressure. The technicians started from the highest-pressure value and applied five different radial loads, respectively of 5.000 kg, 7.500 kg, 10.000 kg, 12.500 kg and 15.100 kg, up to the test with 2 bar where the test was concluded with a maximum applied load of 12.500 kg [6,7].



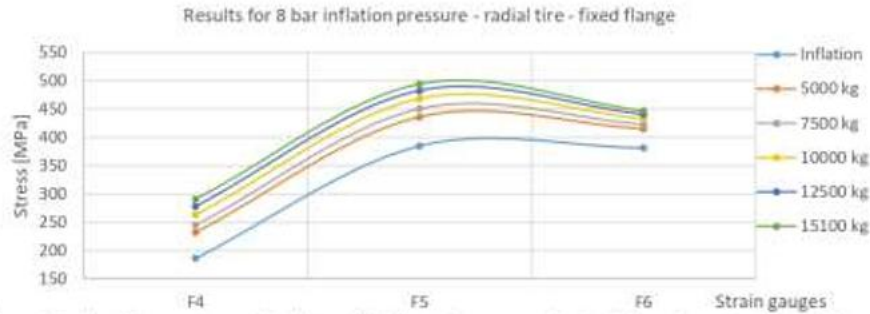


Figure 6 Graphs of the maximum values detected by the strain gauges on the fixed flange when using the radial tire.

The linear decrease does not entail an equal trend in stress, as evidenced by the fact that the spacing between the curves of the graphs does not remain constant. The same behaviour is observed by keeping the inflation pressure constant and by changing the radial load, especially with heavy weights. From Figure 6 we can see that, from the comparison between the uses of a radial and a bias tire, it is possible to notice how the stresses of the strain gauges F5 and F6 are greater in the radial case than in the inflation tests. By keeping the pressure constant and increasing the radial load, it is possible to identify how the bias tire transfers a greater load to the flange. The latter is of particular importance, as it is the area where the breakages were found in operation. It is noted that the radial tire stresses the position F6, while the bias stresses the position F5, demonstrating a different distribution of loads due to the configuration of the tire mounted on the rim. Precisely the positions F5 and F6 have been explored in this article as they are the most critical area of the fixed flange.

3 EXPERIMENTAL MODEL

The equations that correlate the pressure with the load on the rim are 1 and 2:

$$W_p = \pi(a^2 - r_f^2)P_0 \quad [N] \quad (1)$$

$$T_f = \frac{W_p}{2 \cdot 2 \cdot \pi \cdot r_f} = (a^2 - r_f^2) \frac{P_0}{4r_f} \quad [N/mm] \quad (2)$$

These equations (1) and (2) are commonly used in the automotive industry to evaluate the load applied to the rim flange (Figure 7) as a function of the inflation pressure [8,9].

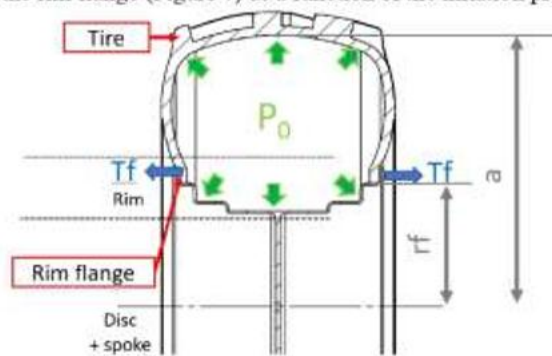


Figure 7 Load condition on the rim due to tire inflation.

They are based on a simple balance of the forces acting on the internal lateral surface of the tire and the ones applied to the external surface of the tire seat by the rim flange. It represents an approximation of the real structure, as, according to the literature and to comparisons between numerical computing and experimental campaigns, the ratio of the flange load to the bead seat one is considered to vary depending on the contact conditions at the tire-rim interface [10].

This is influenced by the type of tire (geometry and material), the inflation pressure, and design of the rim [11,12]. This model was firstly applied to the study of the inflation problem[13] to estimate if it could predict the experimental measurements from laboratory [14]. The axial load provided by the automotive theory was applied to the flange surface of the rim 3D model, as shown in Figure 8.

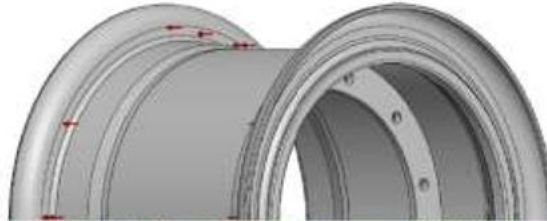


Figure 8 The load predicted by the automotive theory was applied to the flange vertical wall.

A finite elements mesh (see Table 1 and Figure 9) was created on the rim 3D model as shown in Figure 8:

MESH	
Nodes number	513,038
Elements number	321,354
Element type	3D tetrahedral solid elements
Minimum element size – seat radius area	3,7 mm
Maximum element size	35,5 mm

Table 1 Mesh parameters

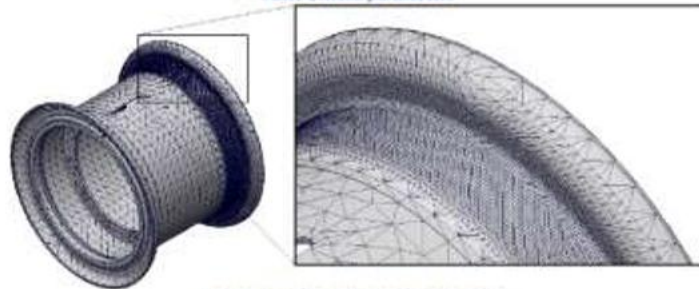


Figure 9 Mesh applied to the 3D model.

A FEM simulation could then be performed on the model; the results expected from the analysis in order to confirm the suitability of the automotive theory formulas should have been in good accordance with the laboratory measurements. However, a good match between the experimental results and the stress field predicted by the automotive theory could not be found. The comparison between numerical and experimental data for the 6 bar inflation case is provided in Figure 10:

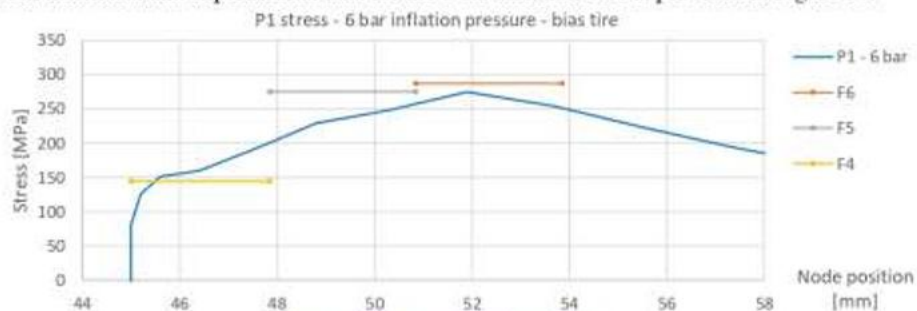


Figure 10 Mesh applied to the 3D model.

As it can be noticed from the Figure 10, good accordance between the experimental measurements and the numerical stress curve could not be found in fact, a deviation of approx. 10-15% on each channel.

Further models based on the automotive theory and calibrated on the laboratory data were attempted, but their predictions for the stress field could not be accepted either. The study based on the automotive theory formulas was therefore abandoned [15,16].



Figure 11 Wheel 3D model.

A second option to develop a direct model of the tire-rim interaction consisted in simulating it through a FEM model of the entire wheel. A 3D model of the wheel was thus created, as shown in Figure 11. FEM analyses can give important information about the contact pressure distribution on the tire-rim interface, which is the main purpose of the current study [17–19]. However, this approach was affected by many limitations, since accurate information on the design of the tire were not available [20,21]. Even nowadays, tire structure modelling and analysis represent a challenging operation as non-linearity occurs in the material properties as well as in the contact boundary conditions. Moreover, the tread pattern, the complex and composite internal tire design and their influence on the load distribution must be considered [22]. In the case of our study, the non-linear and anisotropic mechanical behaviour of a composite component could not be modelled, especially because of the lack of

information on the disposition of the carcass wire and on the tread design. For these reasons, modelling the tire through finite elements was not considered as an option. Generally speaking, developing a direct model of the tire-rim contact phenomenon turned out to be challenging. [22,23] In fact, the complexity of a direct modelling approach not only lies in creating the model, but especially in tuning it on the experimental results from the laboratory tests.

In our case, matching the experimental data in the most accurate way possible was necessary in order to obtain the most reliable evaluations in the fatigue FEM analyses. For these reasons, any direct modelling of the phenomenon was excluded and a reverse approach was adopted instead. Following this method, the experimental data from laboratory tests were not used as a comparison term to validate a direct model, instead they were considered as a starting point of analysis. More in detail, attempts of solutions for the contact pressure distribution were supposed and numerically simulated until a good match between the FEM solutions and the experimental evidence could be found. In order to simplify the process of the hypothesis of the pressure distribution, the surface of the rim 3D model was discretized in the flange area (Figure 12).

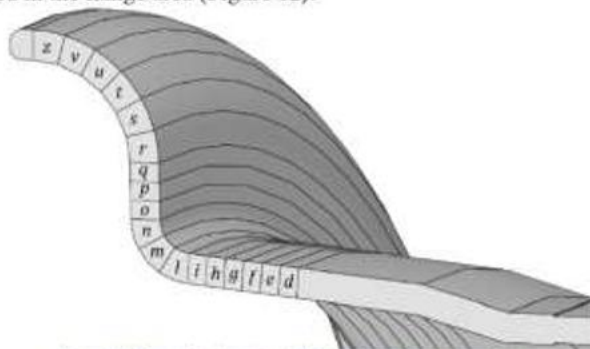


Figure 12 Discretisation adopted for the fixed flange surface.

Dividing the surface into portions on each of which a uniform normal pressure could be applied significantly simplified the formulation of contact pressure solutions. The first step of this process consisted in studying the influence of each loaded area on the shape of the stress curve in the seat radius. To do this, each portion of the flange was loaded singularly like shown in Figure 13 and the stress solution deriving from the FEM simulation was recorded. The graph deriving from this study is reported in Figure 14, which presents the stress curve recorded in the seat radius area for each flange area loaded.

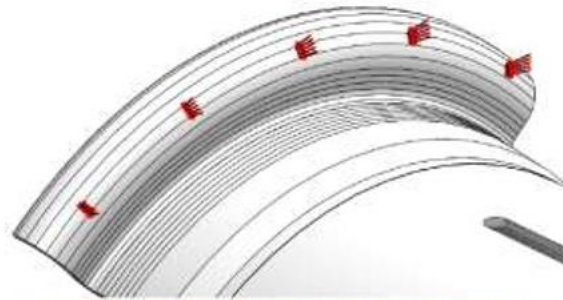


Figure 13 Example of load cond. applied in the FEM performed to study each load area influence on the stress field shape.

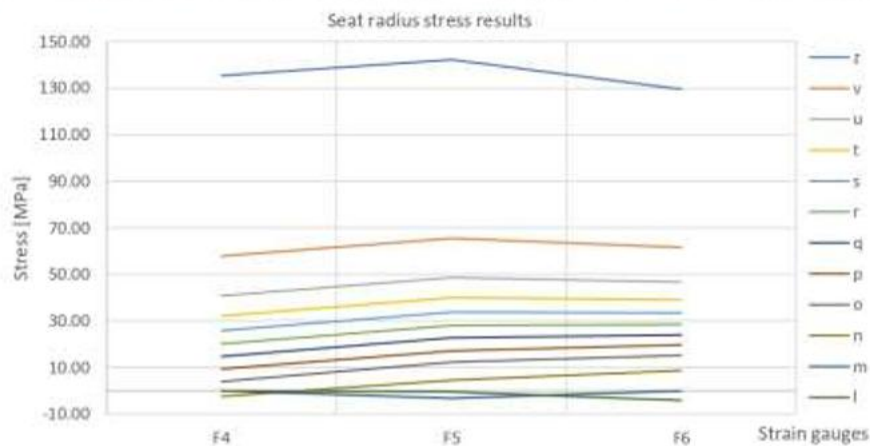


Figure 14 Graphic representation of the simulations results.

As we can see from Figure 14 the stress values obtained in the three areas of the seat radius are reported for each flange zone loaded. The different trends of the stress in the radius in the positions of the sensors. The main significance of this study did not lie in the magnitude of the stress detected, but in the stress curve shape, i.e., the ratios between the stresses recorded on the surfaces corresponding to the F4, F5 and F6 instrumented areas. In this way, reproducing within the FEM simulations the experimental results would have meant finding a linear combination of loaded flange areas. Knowing in which way each area (if loaded) affected the stress curve shape, would have significantly simplified the attempting process. It is important that the application of a linear combination of pressure was possible only thanks to the hypothesis of linear elastic mechanical field in which the material was supposed to be. Only under this condition, in fact, the principle of superposition could be applied. Even if studying the effect of every single flange area was extremely useful to understand how to tune the model, it could not be considered sufficient in order to systematically suppose a great number of solutions for the contact pressure.

As stated before, the experimental data from the theory given from the manufacturer (that comes from a study with the manufacturer of tires) part of its know-how were then adjusted on the GKN rim model discretization. As an example, the pressure distribution measured for the 3,2 bar inflation case and adjusted on the discretized model is presented in Figure 15:

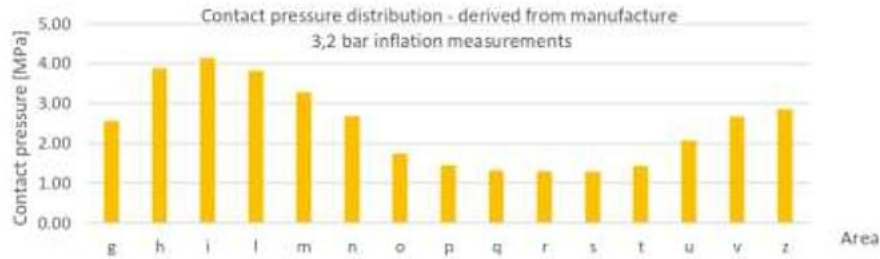


Figure 15 Contact pressure distribution (3,2 bar inflation).

The pressure profile we can see from Figure 15 was graphically extrapolated from manufacturer data and applied to the rim.

The further step of the study would have been adjusting the pressure diagram shown above for each inflation and radial load configuration tested, trying to fit our profile with this performed from the manufacturer just trying to move on X axis our pressure profile. This is done for having a convergence from experimental data numerical simulation by checking the stress in the point where we have placed strain gauge.

4 MODULATION OF THE SIGNALE AND MODEL VALIDATION TUNING

As stated before, a tuning of the pressure distribution obtained by the manufacturer study was needed in order to reproduce the stress state measured during the laboratory tests for each load configuration (see Figure 16).

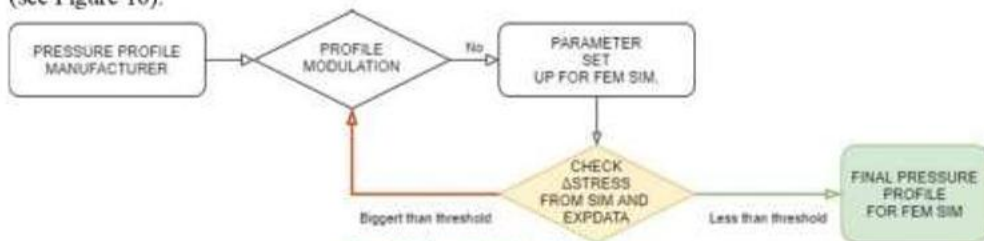


Figure 16 Flow chart of tuning process.

The adjustment of the load diagram consisted in modulating the amplitude of the bead seat peak and both the amplitude and the position of flange hook peak, as shown in Figure 17, Figure 18 and Figure 19:

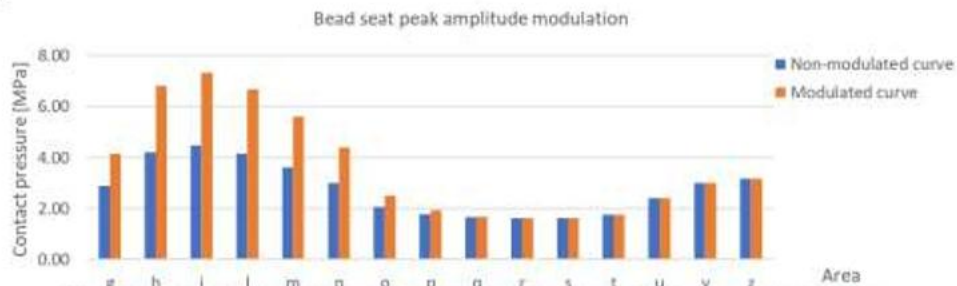


Figure 17 Influence of the modulation of the bead seat peak's amplitude on the contact pressure diagram.

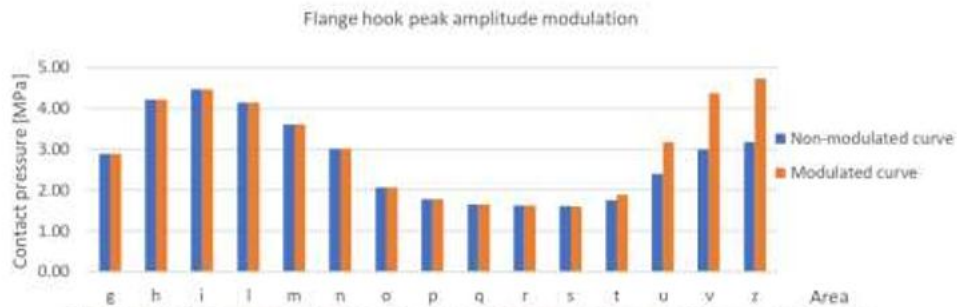


Figure 18 Influence of the modulation of the flange hook peak's amplitude on the contact pressure diagram.

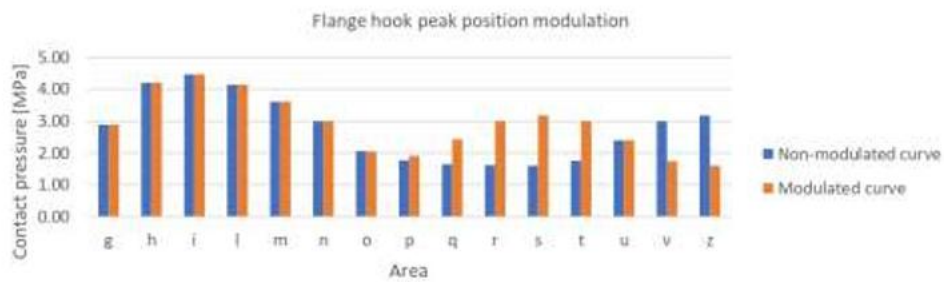


Figure 19 Influence of the modulation of the flange hook peak's position on the contact pressure diagram.

The tuning of the reverse experimental model was done by varying the contact pressure diagram and simulating it through finite elements analyses. The model and the mesh used for these simulations are shown (Figure 20):

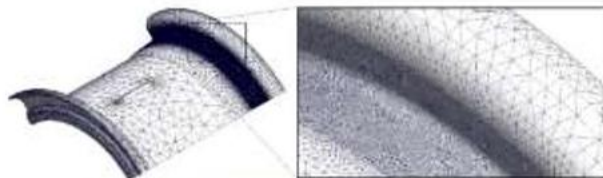


Figure 20 3D model and mesh used for the simulations.

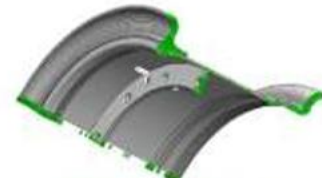


Figure 21 Sliding boundaries.

The thickness of the mesh was highly increased in the critical area to prevent even little inaccuracies in the predicted stress field, as it was ascertained that even small variations in the stress values can produce significant fluctuations in the predicted fatigue life of the component. Moreover, the model was simplified, as it was considered just one sector of the rim thanks to the axial-symmetry of both the component and of the load [24]. To do this, sliding boundaries were applied to the model (Figure 21).

The stress field acquired by the simulations could vary depending on the load conditions, but generally reported a highly stressed area coinciding with the seat radius.

In Figure 22 we show the maximum stress that in the radius zone is in accordance with the values recorded by the strain gauges.

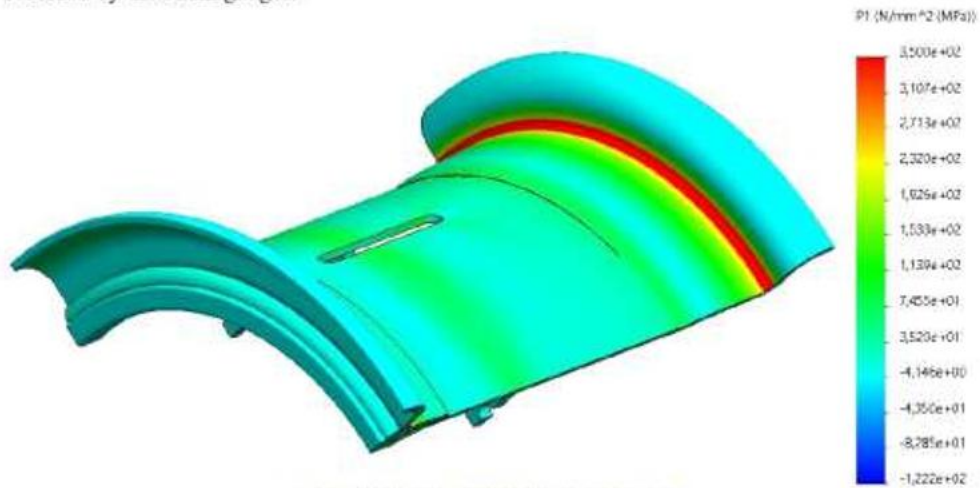


Figure 22 Stress field acquired by FEM simulations.

The tuning of the reverse model was done by comparing the stress field provided by the simulations and the one given by the experimental evidence. An example of the pressure diagram and the comparison between the experimental and numerical data is presented in Figure 23:

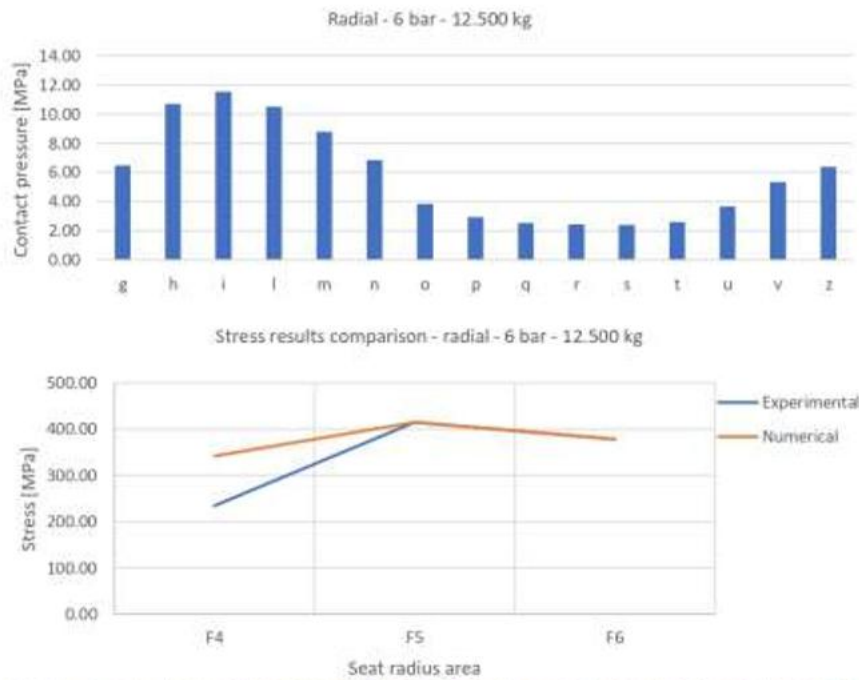


Figure 23 Contact pressure diagram (above) and comparison between experimental and numerical results (Figure 25) for the radial tire – 6 bar – 12.500 kg configuration.

As for the example reported above, a good match between the experimental and numerical results of the F5 and F6 areas could be found. On the other hand, F4 is the only one for that we can't find a correspondence on the model: this was probably due either to inaccuracies in the manual placement and alignment of the strain gauges which could cause the tendency of the gauges to record transversal strains [25] or to excessive approximation of the model. In any case, being the F4 stress the lower of the three recorded, this did not represent a big limitation. A qualitative representation of the mean pressure diagram applied in the simulations is provided in Figure 24; the more intense the pressure applied to the flange area, the darker the colour associated.

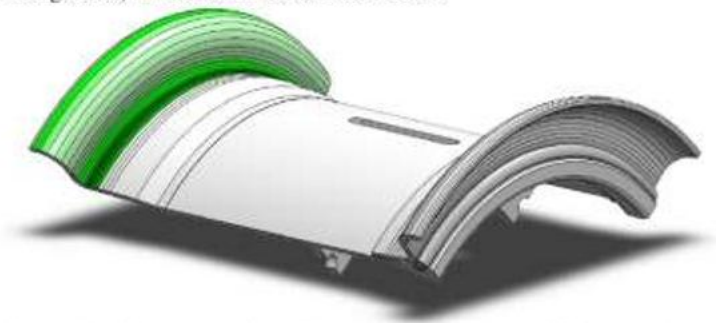
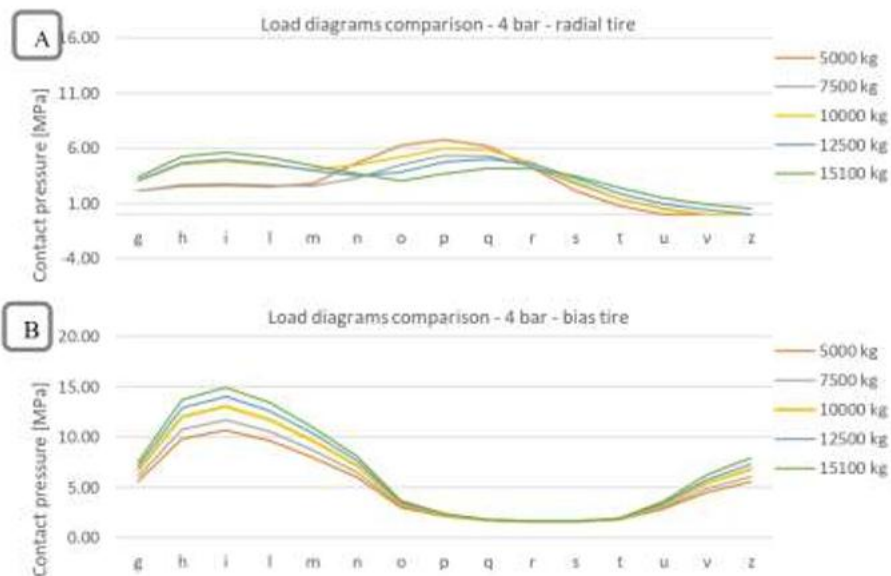


Figure 24 Qualitative representation of the mean pressure diagram applied in the simulations.

The iterative process of hypothesis of the solution was performed for every load configuration until errors above a few percentile points were obtained, leading to the following possible solutions for the contact problem (Figure 25):



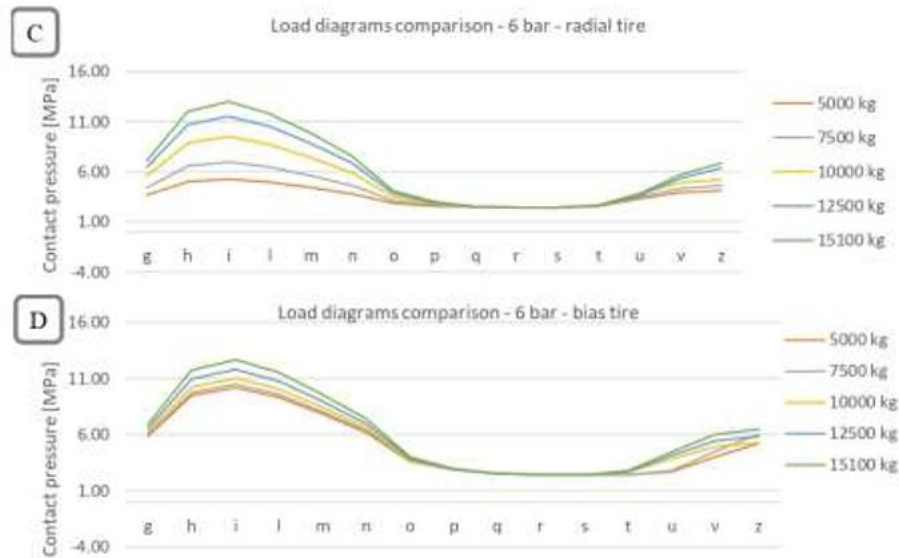


Figure 25 Possible solutions found for the tire-rim contact phenomenon.

5 FATIGUE TESTS RESULTS

The stress fields computed through the FEM static simulations described above were necessary both for a better comprehension of the tire-rim contact phenomenon and for the software's requirements [26,27]. In fact, SolidWorks Simulations needs a stress field from a static analysis in order to perform a fatigue one, as well as many other FEM software [28]. The Solidworks Fatigue Analysis function makes the stress static results to vary between two extremes which, for the nature of our study approach, are identified through the experimental load cycle analysis. More in detail, the maximum and minimum stresses have been identified analytically from the load cycles recorded, which shape can be exemplified by the cycles reported in Figure 26:

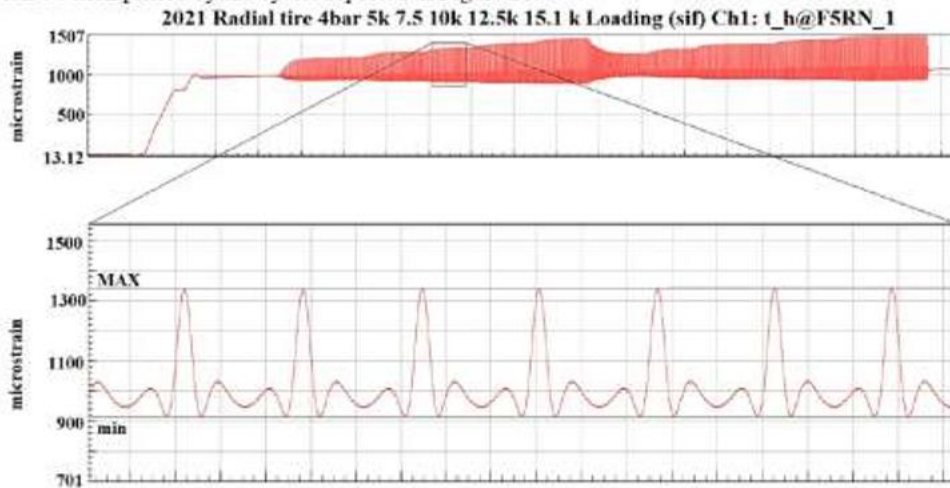


Figure 26 Example of the process of sampling of the cycles from the strain gauges recording (4 bar - 7.500 kg - radial tire).

As visible from the Figure 26 of the strain measured by the gauges, the regularity of the cycle allowed to sample the maximum and minimum values manually for each load configuration. As described previously, the maximum stress value was needed as a reference to be reproduced in the static FEM simulations, while the minimum stress was used to calculate the experimental cycle ratio R (see eq. 3), which is required by the software in order to execute any fatigue analysis and must be given by the user:

$$R = \frac{\sigma_{min}}{\sigma_{max}} \quad (3)$$

This is the reason why *SolidWorks Simulations* requires a stress field deriving from a static analysis and a cycle ratio, obtained in our case from the experimental evidence. A diagram of the workflow applied to this stage of the study is presented in Figure 27.

Once the stress fields were obtained in the static simulations for each of the load configurations, the fatigue FEM analysis could be performed.

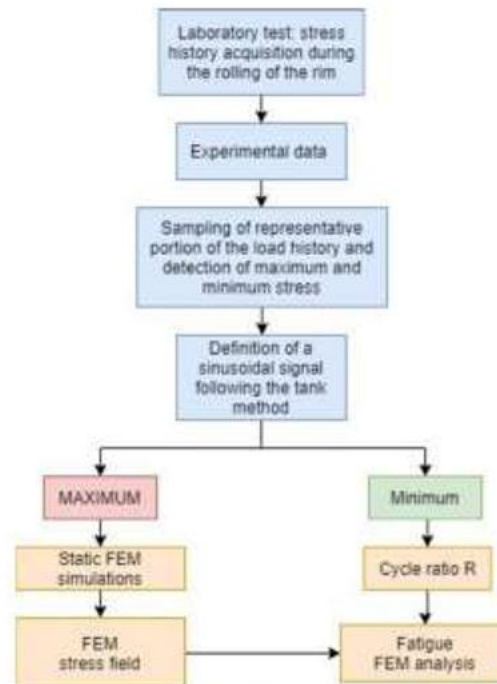


Figure 27 Diagram of the workflow applied to the study. The cycle ratio R has been obtained from the cycle analysis and has been used as input for the fatigue FEM simulations.

The pressure distribution generated by the contact between the tire and the rim makes it possible to have a very reliable model because it is calibrated on the experimental tests of the real load conditions to which the wheel is subjected. Thanks to this distribution, there are certain stresses which were subsequently used for fatigue tests.

In order to perform any fatigue analyses the main instrument necessary was the *Wöhler* curve, obtained by a wide experimental campaign of fatigue experimental tests [29]. In our specific case of study, the *Wöhler* curve had to be found the curve associated to the most similar material from a dedicated database; for this study, the *Total Materia*.

As the mechanical problem concerning the rim flange is purely flexural, the curves related to bending alternated stress tests were considered. Among the *Total Materia* materials, structural steels were searched for, as the steel used for the GKN rim belongs to this category of materials. Considering the data provided by GKN for the ultimate tensile strength, which is equal to about 370 MPa, the most similar material found in the database was the S235JR structural steel, which was assumed as a reference. However, it was reputed more correct to include into the study other structural steels as well: in fact, we compared the fatigue curve of many structural steels in order to obtain a wider view of the possible fatigue behaviour of the materials available. Some types of steel used for this comparison: S185, S235JR, S275JR, S355JR, E295, E335 and E360.

The flexural alternated fatigue curves found in *Total Materia* for this materials are reported in Table 2 [30,31]:

FLEXURAL ALTERNATED FATIGUE CURVE							
N	Stress [MPa]						
	S185	S235JR	S275JR	S355JR	E295	E335	E360
1.000	279	324	387	459	441	531	621
10.000	229	266	318	377	363	434	505
100.000	189	219	262	310	298	355	416
1.000.000	155	180	215	255	245	290	340

Table 2 Wöhler experimental curves provided by Total Materia obtained under alternated symmetrical flexural load.

ROLLING TEST PARAMETERS AND RESULT

Cold inflation pressure [bar]	6
Radial load [kg]	15.095
Rolling speed [km/h]	12,9
N_f	2.000.194

Figure 28 Rolling test parameters and result. The test was protracted until the rim failure, which occurred at 2.000.194 cycles.

Assuming this approach, a fatigue analysis was performed on the 3D model for each material; the fatigue life obtained from the FEM simulation would have then been compared with the experimental result in order to choose the material which best approximates the real one[32,33].

The model used for the study of the material and for the fatigue analyses of the component was the same used for the static analyses.



Figure 29 Example of a wheel during a rolling test.

The final mesh parameters applied to the 3D model wheel are reported in Table 3.

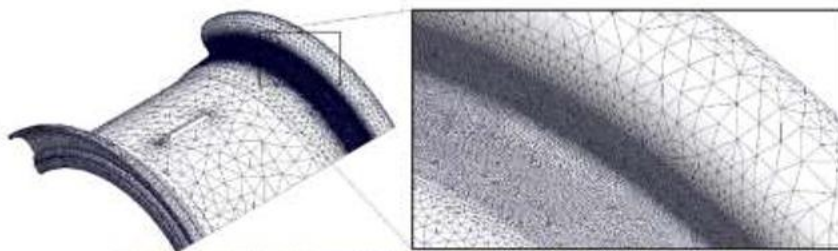


Figure 30 Mesh applied to the 3D rim model to perform the fatigue FEM analysis.

MESH	
Nodes number	1.453.924
Elements number	1.009.933
Element type	Solid CST
Minimum element size – seat radius area	1 mm
Maximum element size	40 mm

Table 3 Mesh parameters applied to the 3D rim model to perform the fatigue FEM analysis.

The dimensions of the mesh elements turned out to be crucial on the predicted life results, as 3 mm elements returned quite different results in terms of life compared to the 1,5 ones. For this reason, it was decided to thicken the mesh retroactively in the static simulations (see Table 1) as well to obtain the most accurate fatigue results. The mesh in the seat radius area was 1 mm, as described in Figure 30 and Table 3.

The tuning of the material applied to the model was performed referring to the 6 bar – 15.100 kg – radial tire configuration, as it was extremely similar to the one applied to the failure test performed by the manufacturer.

The numerically predicted lives for each material considered from *Total Materia* are presented in Table 4:

PREDICTED LIFE FOR EACH MATERIAL considered 6 bar - 15.100 kg - radial tire	
Material	N_f
S185	391.700
S235JR	2.332.000
S275JR	18.230.000
S355JR	134.000.000
E295	83.100.000
E335	516.200.000
E360	Infinite

Table 4 Life predicted by the fatigue simulations 6 bar – 15.100 kg – radial tire load configuration for different steels.

The limited number of cycles reported above refer to the limited life area of the component, i.e., the seat radius area, as clearly visible from the graphical representation of the S235JR simulation. As expected, the structural steel whose numerical life result best approximates the experimental data is the S235JR. The S185 steel widely underestimates the laboratory measurements, while more performing structural steels, starting from the S275JR, overestimate it by at least one order of magnitude.

The E295, E335 and E360 structural steels are high performance materials that have been studied only for a scientific purpose. According to the results shown in Table 4, the S235JR structural steel was assumed as the best approximation (2'000'194 from rolling test vs 2'332'000 from simulation). It must be remarked that, since one single rolling test was executed, this comparison must be considered purely indicative, as no statistical considerations can be done.

However, given the several orders of magnitude that distinguish the numerical S235JR result from the other structural steels, it can be stated with good confidence that the S235JR represents the best approximation of the rim steel. Therefore, this material and the associated *Wöhler* curve were applied in the following fatigue analyses.

Further information needed to perform the fatigue simulations are the fatigue limit σ_{FA} and the method applied for the correction of the mean stress components σ_m of the cycle. As far as the fatigue limit is concerned, Total Materia reported a σ_{FA} equal to 180 MPa for the S235JR.

A few corrective coefficients were applied which took into account the forming process applied to the rim:

$$\sigma'_{FA} = k \cdot \sigma_{FA} \quad (4)$$

The correction factor k can be written as:

$$k = a \cdot \sigma_R^b \quad (5)$$

a and b are coefficients depending on the forming process applied to the material (Table 5):

SURFACE FINISH	a	b
Polished	1,58	-0,085
Milled	4,51	-0,265
Hot rolled	57,7	-0,718
Raw forged	272	-0,995

Table 5 Corrective coefficients depending on the forming process of the material.

As the steel sheet used for the rim production is hot rolled, corrective coefficients with the following values have been chosen:

$$\begin{aligned} a &= 57,7 \\ b &= -0,718 \end{aligned} \quad (6)$$

By substituting these values (6) in (5) and (4), the following value for σ'_{FA} in (7) was found:

$$\sigma'_{FA} = 57,7 \cdot (370 \text{ MPa})^{-0,718} \cdot 180 = 148,8 \text{ MPa} \quad (7)$$

This can be considered the corrected fatigue limit for the S235JR, which takes in account the process applied to the steel; thus, it was used in the following study analyses.

The last assessments needed before performing the fatigue FEM analyses regards the load cycle applied to the rim during its rotation. In fact, the loading cycle to which the rim is subject is not as simple as it could be thought, since the stress curve through the time is not a mere sinusoidal function. The strain gauges measurements analysed through the time axis, in fact, reveal a more complex trend, which is shown in Figure 26. In the graph reported in Figure 26, two full strain cycles are clearly recognisable. A higher strain peak, which corresponds to the tire-ground contact, can be detected and it divides one cycle from the other. Lower peaks can be found between the higher peaks and they are generated by the particular tire-rim contact conditions that occur during the wheel rotation. Between the minor peaks, there is a relative minimum, which shows up when the rim point is in the higher position of the rotation, diametrically opposite to the tire-ground contact point.

What we had to investigate was the influence on the fatigue life of the minor peaks that occurs during the upper part of the rim rotation, opposite to the tire-ground contact point, in order to determine if the minor peaks affect the cumulative damage of the component. If the alternated stress point is located under the Haigh diagram line, its life influence can be considered negligible with a certain safety factor; if not, the component life should be considered affected, as the $\sigma_{altlimF}$ is exceeded. Before this check could be done, the stress values corresponding to the minor peaks must be collected. This operation was done on the *nCode* graphs manually on samples of the cyclic load graph for each load condition. More in detail, the stress values associated to the maximum and the minimum of each cycle peak have been collected. The criterion used to detect the minimum points was based on the tank counting method [34].

From the “tank method” we have three different peaks for each cycle. Of course, the highest of the three peaks was already known to be influent on the life of the rim (highest alternated and average stress) so, the focus was set on the second and the third peak (orange and grey points in Figure 31): We can see from High diagram in Figure 31 the two cycles can be considered negligible in terms of cumulative damage. As an initial evaluation, the most burdensome loading conditions were inspected: in fact, if the highest cyclical stresses had been found to be irrelevant, the lowest would have been too. Thus, the most critical load condition for both the radial and the bias tire were examined, that is 6 bar – 15.100 kg case. Their representation in the High diagram is presented in Figure 31. As it can be seen from the graph, the points associated with the secondary peaks of the most critical load conditions (6 bar – 15.100 kg – radial tire and 6 bar – 15.100 kg – bias tire),

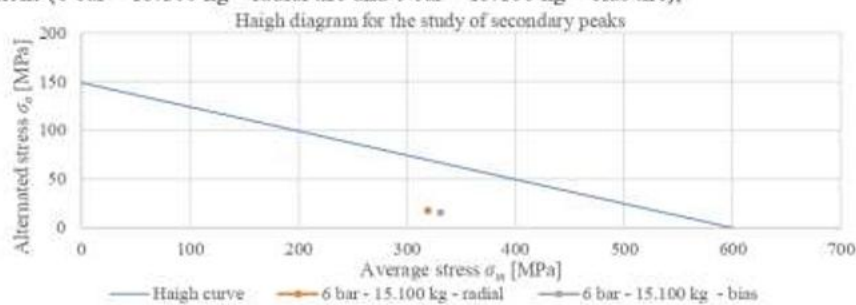


Figure 31 5235 Haigh diagram of the points of the secondary peaks of the load cycle for the 6 bar – 15.100 kg configurations.

Once the load cycle is found, all the fatigue study parameters have been evaluated and, thus, the FEM fatigue simulations can be executed. The software returns both predicted life and cumulative damage outputs, according to the Palmgren-Miner theory [35–39]. The analyses were performed for all the load and tire design configurations available for the 4 and 6 bar inflation pressures. The 3D model and mesh used for this set of simulations are the same presented in Table 3.

The results obtained by the numerical analyses for the fatigue in terms of number of cycles are shown in Table 6:

INFLATION P [bar]	TIRE DESIGN	RADIAL LOAD [kg]	CRITICAL AREA	R	σ_{max} [MPa]	N_f
4	Radial	5000	F6	0,851	279,0	Infinite
		7500	F6	0,830	290,8	Infinite
		10000	F6	0,796	299,6	Infinite
		12500	F5	0,653	308,7	Infinite
		15100	F5	0,618	318,3	Infinite
	Bias	5000	F5	0,776	318,7	Infinite
		7500	F5	0,730	335,3	Infinite
		10000	F5	0,682	353,4	301.900.000
		12500	F5	0,641	369,3	29.290.000
		15100	F5	0,602	387,2	3.168.000
6	Radial	5000	F5	0,836	388,0	Infinite
		7500	F5	0,804	400,1	Infinite
		10000	F5	0,764	415,7	142.600.000
		12500	F5	0,733	427,3	14.740.000
		15100	F5	0,708	439,3	2.174.000
	Bias	5000	F5	0,831	367,2	Infinite
		7500	F5	0,778	390,6	Infinite
		10000	F5	0,732	412,3	38.270.000
		12500	F5	0,695	434,1	2.763.000
		15100	F5	0,663	457,6	215.500

Table 6 Predicted fatigue lives for each load and inflation condition from FEM numerical simulations (S235JR).

A graphic example of the results of the fatigue FEM simulation is proposed (Figure 32):

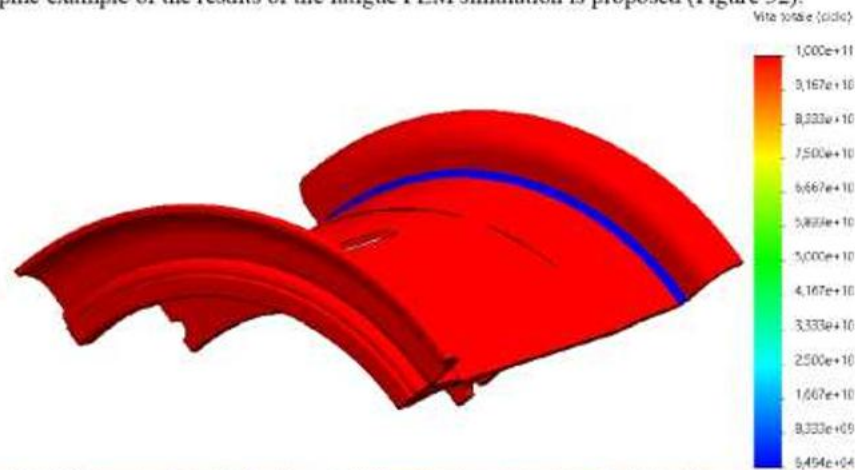


Figure 32 FEM fatigue simulation for the 6 bar – 12.500 kg – bias tire configuration. The limited life area coinciding with seat radius and indicated in blue can be noticed.

6 RESULT

This work can be summarized with the flow chart presented in Figure 33:

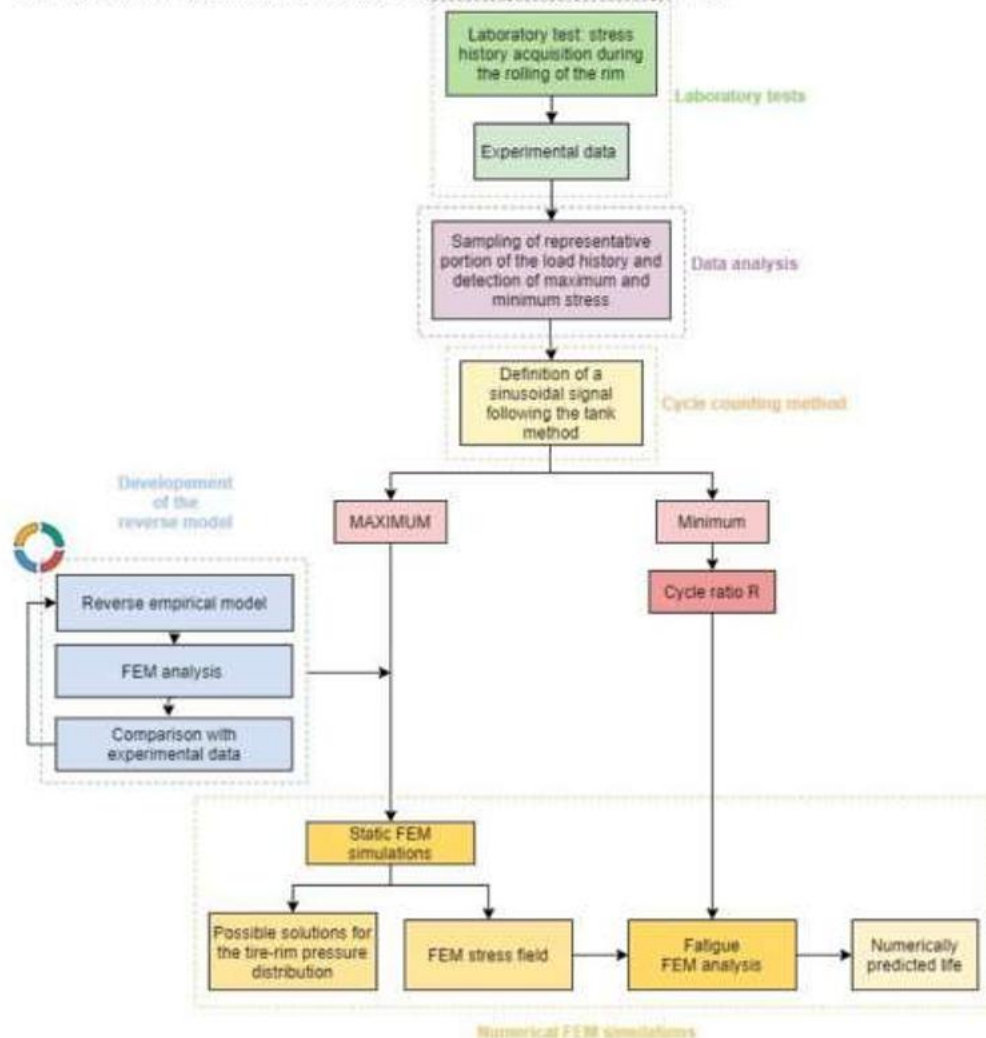


Figure 33 Diagram of the workflow applied to the study.

The Figure 25 shows the trend of the pressure we have on the rim when we change the inflation pressure, the radial load and the tire (radial or bias). The pressure profile is defined by iteration of numerical data obtained from FEM analysis triggered with experimental data acquired with strain gauges by test on field. This iteration is performed until we can reach a convergence in outcomes (Figure 23). The FEM are performed by sizing the rim in different slices (see Figure 12) and by applying to each a defined pressure and at the end checking the strain in the points where we have a certain data, in this way we can validate the FEM model.

This tuning procedure is necessary because what we can predict with different theories, in terms of profile pressure, is a first approximation of the pressure on the rim but every configuration is different (because of the combinations of some variables: geometry, tire, materials). The main deviation we may run into can be the maximum stress on the contact zone between rim and tire.

From the curves we obtained after the tuning process (Figure 25) we can see as the radial load increases, the pressure increases in zone h, i and l unlike on zones near the flange (p,q,r,s,t) the contact pressure is marginally affected by the value of radial load.

We can also observe that the tire type is a key factor on the curve. We find that by fixing the inflation pressure, for example 6 bar, the radial tire is more sensitive to the radial load than the bias one. This is clear from the Figure 25 d where it appears that the curves (mostly in the areas where the pressure is higher: h,i and l) are closer to each other so they are not so affected by a change in radial load applied.

The curves (Figure 25) are used for further numerical analysis to estimate the fatigue life of the component. Table 6 shows the result in the critical zones identified previously with the strain gauges 5 and 6 (F5 and F6 that in our model are on the radius zones that fall in the zone m,i and l). In detail the results show as the pressure of each type of tire and radial load varies the results in terms of maximum stress, cycle ratios and estimations of fatigue life.

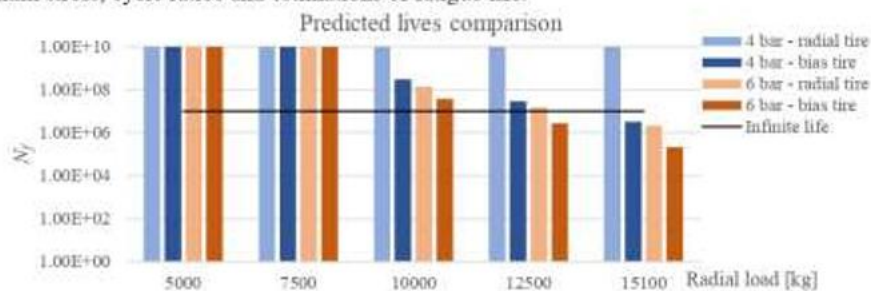


Figure 34 Comparison of the component's predicted lives for all the tested load conditions. The predicted lives are on a log scale. In graph 5.2, the predicted lives are compared on a logarithmic scale with a maximum life of 10^7 cycles, which have been considered the infinite life limit. As it can be noticed, the only tire configuration which never shows limited predicted lives is the 4 bar – radial tire. For all the other tire configurations at least one case of predicted limited life occurs.

Another important parameter is the cycle stress ratio R . In fact, the higher the stress values, the highest the damage caused to the material. Moreover, the more the R ratio tends to zero, the more the cyclic stress can be approximated to a cycle pulsating from zero. This load condition can be considered far more critical compared to a cyclic stress with a R ratio which tends to 1, as it is closer to a static stress state. The influence of the maximum stress and of the cyclic ratio combined is shown in the Figure 35:

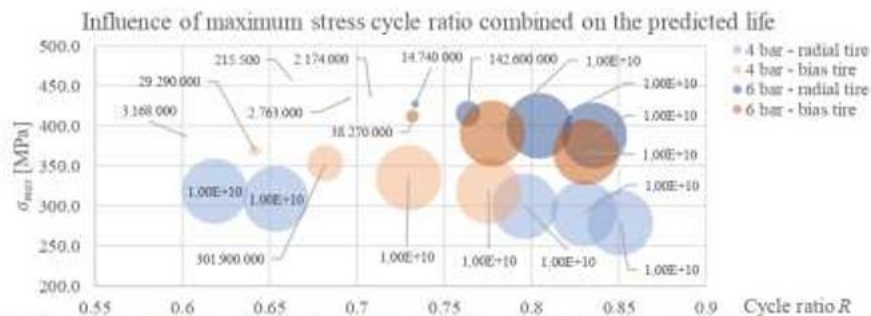


Figure 35 Influence of maximum stress detected in simulation and of the cyclic ratio R the experimental tests on the numerically predicted life of the component. The bigger the circle, the higher the predicted life.

In the graph reported, the bigger the circle, the higher the numerically predicted life. As clearly shown above, it is the combination of the two parameters which determines the cyclic damaging of the component.

7 CONCLUSIONS

Here will be presented the result of this work:

Direct modelling of the tire-rim contact pressure through mathematical or FEM tire models can hardly produce results which are accurately coherent with the experimental data, especially because the fatigue FEM analysis requires to process stress fields from static simulations as similar as possible to the experimental evidence in order to return good life predictions.

A reverse empirical model based on the iteration of attempts of solution for the contact pressure distribution between rim and tire in the rim flange area has been identified as the most suitable approach for the particular problem faced in this study. Following this modelling solution, the experimental results are not used as an empirical comparison term employed to verify the prediction of a direct model, instead they are considered as an experimental basis on which a reverse empirical model can be built. This particular model is not mainly intended to make predictions on the tire-rim interactions (even if many considerations on this phenomenon could be made thanks to it), but to reproduce the experimental results in the FEM numerical simulation in the most accurate way possible. Going backwards and analysing the solutions found for the pressure distributions, a deeper understanding of the phenomenon could be reached.

Previous measurement campaigns on the contact pressure distribution allowed us to realize that the most loaded areas are the bead seat and the flange hook ones.

The static simulations revealed that the tire design affects the pressure distribution, as it was found that, especially for lower radial loads, bias tires tend to load more the upper areas of the flange hook compared to the radial ones, as confirmed by the GKN.

The inflation pressure affects the load pattern as well, since the simulation results show that the less the tire is inflated, the less its deformed configuration is defined and, thus, the loaded area are not accurately identified as in the high-pressure configurations. Moreover, if the pressure distribution found in this study is considered reliable, it emerges that less inflated configurations can involve higher peaks in the contact pressure, as the deformed states of the tire are probably less rigid than the high inflated ones [40,41].

The fatigue FEM simulations based on the static numerical results and on the hypotheses of neglecting the residual stresses of the material revealed that the critical load conditions are the high load configurations (12.500 kg and 15.100 kg). These load conditions are quite extreme and reasonably rarely reached by the structure during the exercise. Moreover, these radial loads have been simulated together with inflation pressures that exceed the value recommended by the tire manufacturers, that is 3,2 bar. Thus, these results must be considered as an evaluation of extremely hard load conditions and the limited life predictions must therefore be properly weighted. In any case, the load conditions that eventually need further investigation and study are the ones mentioned above.

Regarding the fatigue analyses, it emerged that small variation in the *Wöhler* curve can cause high fluctuations in the predicted life results. Therefore, a wide experimental campaign for the cyclic characterization of the material is necessary in order to perform accurate fatigue predictions on the component.

Another important step for the material characterization is studying the influence of the forming process on its mechanical properties, as both the residual stresses and the hardening can play an important role in the cyclical behaviour of the cold formed steel.

BIBLIOGRAPHY:

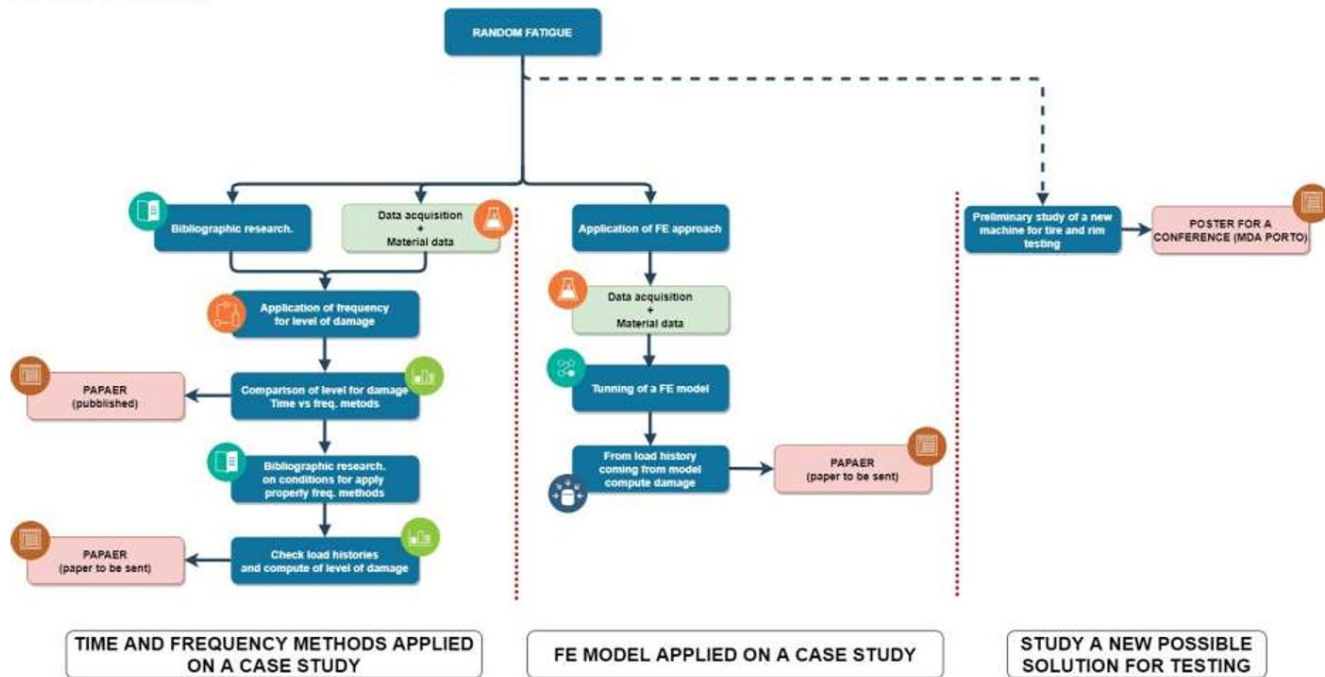
- [1] J.-P. Brüggemann, L. Risse, S. Woodcock, T.D. Joy, J. Neumann, J. Vidner, G. Kullmer, H.A. Richard, Structural optimization of a wheel force transducer component for more realistic acquisition of vehicle load data and fracture mechanical evaluation, *Appl. Eng. Sci.* (2021). <https://doi.org/10.1016/j.apples.2020.100032>.
- [2] J. Stearns, T. Srivatsan, X. Gao, P.C. Lam, Understanding the influence of pressure and radial loads on stress and displacement response of a rotating body: The automobile wheel, *Int. J. Rotating Mach.* (2006). <https://doi.org/10.1155/IJRM/2006/60193>.
- [3] M.S. M. F. Sardella, Studio della fatica random in ruote per macchine movimento terra. Un confronto tra gli approcci classici e quelli nel dominio della frequenza, Università degli studi di Brescia, 2014.
- [4] S.B. P. Davoli, L. Vergani, S. Beretta, M. Guagliano, *Costruzioni di macchine I*, 1st ed., McGraw-Hill Education, 2011.
- [5] M. Cima, L. Solazzi, Experimental and analytical study of random fatigue, in time and frequencies domain, on an industrial wheel, *Eng. Fail. Anal.* (2020). <https://doi.org/10.1016/j.engfailanal.2020.105029>.
- [6] Biaxial Wheel Fatigue Test, 2003. https://saemobilus.sae.org/content/j2562_200308.
- [7] L.D. Nurkala, R.S. Wallace, Development of the SAE biaxial wheel test load file, in: *SAE Tech. Pap.*, 2004. <https://doi.org/10.4271/2004-01-1578>.
- [8] T. Mizoguchi, H. Nishimura, K. Nakata, J. Kawakami, Stress analysis and fatigue strength evaluation of sheet fabricated 2-piece aluminum wheels for passenger cars., *R D RES DEV KOBE STEEL LTD.* V 32 (1982) 8–12.
- [9] P. Reipert, Optimization of an extremely light cast aluminium wheel rim., *Int. J. Veh. Des.* (1985). <https://doi.org/10.1504/IJVD.1985.061385>.
- [10] J.A. Sherwood, B.K. Fussell, W.R. Edwards, T.S. Gross, D.W. Watt, Study of the pressure distribution on an aircraft tire-wheel interface, *J. Aircr.* 32 (1995). <https://doi.org/10.2514/3.46819>.
- [11] G. Machave, P.S. Sambhaji, R. Kathar, Study of Influencer of Pressure and Load on Wheel Rim by Radial Fatigue Test, *Int. J. Eng. Sci. Res. Technol.* 4 (2015) 298–303.
- [12] U. Kocabicak, M. Firat, Numerical analysis of wheel cornering fatigue tests, *Eng. Fail. Anal.* (2001). [https://doi.org/10.1016/S1350-6307\(00\)00031-5](https://doi.org/10.1016/S1350-6307(00)00031-5).
- [13] H. Shiobara, T. Akasaka, S. Kagami, Two-dimensional contact pressure distribution of a radial tire in motion, *Tire Sci. Technol.* (1996). <https://doi.org/10.2346/1.2137524>.
- [14] K. Ishihara, H. Kawashima, Stress Evaluation of Automotive Steel Road Wheel under Radial Load, *Trans. Japan Soc. Mech. Eng. Ser. C.* (1989). <https://doi.org/10.1299/kikaic.55.1254>.
- [15] S. Bošnjak, Z. Petković, N. Zrnčić, M. Pantelić, A. Obradović, Failure analysis and redesign of the bucket wheel excavator two-wheel bogie, *Eng. Fail. Anal.* (2010). <https://doi.org/10.1016/j.engfailanal.2009.09.007>.
- [16] N. Satyanarayana, C. Sambaiah, Fatigue Analysis of Aluminum Alloy Wheel Under Radial Load, *Int. J. Mech. Ind. Eng.* (2012).
- [17] W. Wang, S. Yan, Y. Zhao, Numerical and experimental studies of a radial truck tire with tread pattern, *Simulation.* 91 (2015) 970–979. <https://doi.org/10.1177/0037549715608434>.
- [18] N. Korunović, M. Trajanović, M. Stojković, FEA of tyres subjected to static loading, *J. Serbian Soc. Comput. Mech.* (2007).
- [19] J.A. Guinea Garcia-Alegre, Numerical study of aluminum wheels subjected to biaxial fatigue test, *Politecnico di Milano*, 2017. <https://www.politesi.polimi.it/handle/10589/136225>.
- [20] X. Zhang, S. Rakheja, R. Ganesan, Stress analysis of the multi-layered system of a truck tire, *Tire Sci. Technol.* (2002). <https://doi.org/10.2346/1.2135257>.
- [21] L. Renčín, A. Polcar, F. Bauer, The effect of the tractor tires load on the ground loading pressure, *Acta Univ. Agric. Silv. Mendelianae Brun.* (2017). <https://doi.org/10.11118/actaun201765051607>.

- [22] W. Wang, S. Yan, S. Zhao, Experimental verification and finite element modeling of radial truck tire under static loading, *J. Reinf. Plast. Compos.* (2013). <https://doi.org/10.1177/0731684412474998>.
- [23] J.J. Castillo Aguilar, J.A. Cabrera Carrillo, A.J. Guerra Fernández, S. Postigo Pozo, Optimization of an optical test bench for tire properties measurement and tread defects characterization, *Sensors (Switzerland)*. (2017). <https://doi.org/10.3390/s17040707>.
- [24] P. Sujin, Y. Wansuk, C. Jinrae, K. Beomsoo, Pressure-sensing pad test and computer simulation for the pressure distribution on the contact patch of a tyre, *Proc. Inst. Mech. Eng. Part D J. Automob. Eng.* (2007). <https://doi.org/10.1243/09544070JAUTO382>.
- [25] K. Cosseron, D. Mellé, J.-F. Diebold, F. Hild, S. Roux, Optimized gauging for tire-rim loading identification, *Eur. J. Mech. - A/Solids*. (2020). <https://doi.org/10.1016/j.euromechsol.2020.104192>.
- [26] S. Medvedev, R. Ivanets, U. Ausianka, A. Kasperovich, V. Mozgalev, N. Prokopchuk, Coupled thermomechanical computational solutions for stationary and dynamics rocking of all-metal steel belted tyres, in: *Procedia Eng.*, 2016. <https://doi.org/10.1016/j.proeng.2016.01.166>.
- [27] Y. Deng, Y. Zhao, F. Lin, Z. Xiao, M. Zhu, H. Li, Simulation of steady-state rolling non-pneumatic mechanical elastic wheel using finite element method, *Simul. Model. Pract. Theory*. (2018). <https://doi.org/10.1016/j.simpat.2018.04.001>.
- [28] E. M. Adigio, E. O. Nangi, Computer Aided Design and Simulation of Radial Fatigue Test of Automobile Rim Using ANSYS, *IOSR J. Mech. Civ. Eng.* (2014). <https://doi.org/10.9790/1684-11146873>.
- [29] J. Schijve, *Fatigue of structures and materials*, 2009. <https://doi.org/10.1007/978-1-4020-6808-9>.
- [30] Total Materia, (n.d.). <https://www.totalmateria.com> (accessed 10 February 2020).
- [31] Material fatigue, (n.d.). www.comsol.it/multiphysics/material-fatigue (accessed 10 February 2020).
- [32] F.M. Santiciolli, R. Möller, I. Krause, F.G. Dedini, Simulation of the scenario of the biaxial wheel fatigue test, *Adv. Eng. Softw.* (2017). <https://doi.org/10.1016/j.advengsoft.2017.08.006>.
- [33] G. Wang, H. Sun, J. Li, R. Chai, Study on biaxial fatigue life test and FEA analysis of the steel wheel, in: *ICIC 2010 - 3rd Int. Conf. Inf. Comput.*, 2010. <https://doi.org/10.1109/ICIC.2010.330>.
- [34] C.C. Osgood, Prediction of fatigue life, in: *Fatigue Des.*, Elsevier, 1982: pp. 41–404. <https://doi.org/10.1016/b978-0-08-026167-6.50009-6>.
- [35] Calculating damage with Miner's Rule, (n.d.). <https://community.sw.siemens.com/s/article/calculating-damage-with-miner-s-rule> (accessed 10 February 2020).
- [36] B.L. Barcelos, E.S. Palma, Fatigue analysis of a bucket wheel by using Linear Elastic Fracture Mechanics, *Eng. Fail. Anal.* (2020). <https://doi.org/10.1016/j.engfailanal.2020.104824>.
- [37] Random Load Fatigue, (2013). <https://www.comsol.it/blogs/random-load-fatigue/> (accessed 10 February 2020).
- [38] The Strain Life Approach, (n.d.). <https://community.sw.siemens.com/s/article/The-Strain-Life-Approach>.
- [39] History of Fatigue, (n.d.). <https://community.sw.siemens.com/s/article/history-of-fatigue> (accessed 10 February 2020).
- [40] J. Stearns, T.S. Srivatsan, X. Gao, A. Prahash, P.C. Lam, Analysis of Stress and Strain Distribution in a Vehicle Wheel: Finite Element Analysis Versus the Experimental Method, *J. Strain Anal. Eng. Des.* (2005). <https://doi.org/10.1243/030932405X30786>.
- [41] Y. Morita, H. Kawashima, K. Ishihara, Induced stress evaluation of automotive steel road wheel during endurance tests, *Sumitomo Met.* (1989).

ACKNOWLEDGEMENTS:

The authors of this work are willing to thank Eng. Bramè Giampietro of the company GKN Wheels for the information provided for the development of this research.

12. CONCLUSIONS



Before going into deep, I would like to share the main results and evidence of my research with a flow chart, which shows how we performed the three main activities linked with fatigue and, in particular, applied to industrial wheels. We decided to test industrial wheels because they are safety components of machines and the fatigue has been studied and confronted for years and is still an open topic. Moreover, the University of Brescia is in a good relationship with a manufacturer who supported us during our tests on the field and was open to a critical analysis of our research as well, which we compared with the principles they use every day. The main results our research are listed now below.

After selecting the bibliography about methods on the time and frequency domain and thanks to the availability of load history of industrial wheels, it was possible to compare them to check their reliability and the problems we might face with different models on a real case study.

During this research, we found out that frequency methods are more conservative than the ones in the time domain. They also request some assumptions which are not always easy to achieve with the available data. The key point of this work is the actual comparison of a real case study.

CHANNEL	TIME	NARROW-BAND		WIRSCHING LIGHT		ORTIZ		DIRLIK	
	D	D	η_D	D	η_D	D	η_D	D	η_D
CH 4	7.8E-8	2.9E-8	2.7	1.7E-8	4.57	2.2E-7	3.5E-1	1.5E-7	5.1E-1
CH 6	1.9E-4	1.1E-3	1.7E-1	6.7E-4	2.7E-1	9.2E-3	2E-2	6.5E-4	2.9E-1
	N_f	N_f	ηN_f	N_f	ηN_f	N_f	ηN_f	N_f	ηN_f
CH 4	1.3E7	3.4E7	2.7	5.9E7	0.2	4.5E6	2.8	6.7E6	1.9
CH 6	5.4E3	9.1E2	5.9	1.5E3	3.6	1.1E2	5	1.5E3	3.5

Table 26 Comparison of results of fatigue analysis according to different approaches and theories

It may be interesting to study more into detail the impact of the material data on the results for each different method, and to check the level of the damage with a test on the bench, in order to have a real evaluation of the reliability of the method and to make a full comparison with a certain reference.

Moreover, it would be interesting as well to check how strong an assumption for the application of the frequency methods can be and if they are always correct. Since our focus was on the last point, we decided to examine the assumptions made for the application of the frequency methods (signal: gaussian, ergodic, and not time-dependent).

We analysed the data we had collected from the tests on the field. This was pretty critical since designers usually want to apply their algorithm directly to check the level of the damage that a defined load history can lead. Thanks to this, it would be possible not to waste time checking the assumptions (also because the signal might not fulfil the assumption.)

Checking our case study, we discovered that, for a common component like a wheel, the load history does not respect the hypothesis of Gaussianity; therefore, we used some corrective coefficients found in the bibliography.

These corrections (about a factor of 61,) on our load case on the wheel were without doubt strong, but there were still errors to report: in fact, we noticed that the assumptions force not to consider some cycles with a high level of stress. Subsequently, for our load case, the coefficient λ_{NG} (see chap. 8) is not able to fully correct the non-Gaussian distribution of the input data. In this way, we are able to put a reference on the bibliography of a real case study with a clear procedure to follow; we can also add the information that industrial wheels are critical components for the application of frequency methods.

As well as for the first analysis, we need the material data. This work could be further developed and the algorithm extended to other components with different load cases; the results could be applied to the time domain as well. This work could lead to a corrective factor, tailor-made for different components and different applications. Eventually, a further activity of validation of the model can be performed to check how far, in terms of level of the damage, these methods are, compared to a component that is rolling during a test on the field with the same load history.

After basing this approach on the application of the algorithm, we decided to add the FE analysis. Thanks to the tests we performed on the field, we gathered data of the load history at different inflation pressure. This led to the FE analysis. Following the data we had collected from the strain gauge on the rim, we were able to define the pressure profile on the rim and tune it with the data, through reverse modelling. Our model confirmed us that the

tire design affects the pressure distribution, and, especially for lower radial loads, bias tires tend to load more on the upper areas of the flange hook compared to the radial ones. Obviously, also the inflation pressure affects the load pattern. After a static analysis of the pressure profile, we analysed the fatigue through the software Solidworks, based on the static numerical results.

The analysis led us to define some critical situations and other configurations that are infinite in the fatigue life (see Table 25). In this case, thanks to the data collected, we were able to present a pressure profile on the rim that can be compared and is tuned with experimental data.

This approach is difficult to find in the bibliography but, according to our research, it is very useful because we can skip modelling the tire characteristics, which are not easy to define. Moreover, it is possible to identify the most critical area and apply the FA analysis to it, as well as the FA fatigue analysis. The mechanical data of the materials are difficult to find. For this reason, a study of the production process of the rim (which results hardened in some areas) could be a possible future development of the research.

At the end of the analysis on the material, we were able to perform a statistical validation of the model. This will be later used as a reference for the future models of the rim.

The last step of this research (see some tips on the appendix) was the study of the layout of a testing machine, whose results are close to the ones registered from the tests on the field.

We started from the DOF on the wheel, equal to the one on a real application. Therefore, we used a belt unit to give torque and speed to the wheel on an exapode table, then we connected the wheel through the original suspension to a frame that can slide up and down to simulate the movements of the chassis. To apply pressure on the rim, which is a vertical force, we used a pneumatic cylinder that can be connected to the sliding unit where the junction points of the suspension are directly on the wheel with a special wheel hub.

So far, we have defined the layout and performed a first rough sizing of the structure. After the design of the different groups is ready to be produced, we will be able to analyse the software of the machine, since the table moves according to the force and following the data acquired through the tests on the field or defined for our routine.

12.1. RESERCH ACTIVITY

The papers from our research, which have been published or sent to journals or used during conferences, are listed below:

Here follow the papers, which have been sent or will be sent to Journals:Cima, Michele & Solazzi, Luigi. (2020). EXPERIMENTAL AND ANALYTICAL STUDY OF RANDOM FATIGUE, IN TIME AND FREQUENCIES DOMAIN, ON AN INDUSTRIAL WHEEL. Engineering Failure Analysis. 120. 105029. 10.1016/j.engfailanal.2020.105029.

L. Solazzi, M. Cima (2020) FIRST CONCEPT OF LIFE TEST MACHINE FOR GROUP WHEEL – SUSPENSION; Conference MDA Porto 5-6 Nov 2020; <https://web.fe.up.pt/~mda2020/img/Poster%2035.pdf>

Solazzi, Luigi & Ceresoli, Federico & Cima, Michele. (2019). STRUCTURAL ANALYSIS ON LIGHTWEIGHT EXCAVATOR ARMS. CONFERENCE: 33RD INTERNATIONAL ECMS CONFERENCE ON MODELLING AND SIMULATION 351-357. 10.7148/2019-0351.

Frosini, Lucia & Malinverni, Matteo & Cima, Michele & Anglani, Norma. (2018). THERMAL AND ELECTROMAGNETIC MODELING FOR PROTOTYPING PERMANENT MAGNET DC MOTORS. 1330-1337. 10.1109/ICELMACH.2018.8506965.

Here paper that are sent or have to be sent to Journals:

Cima, Michele & Piovani, Luca & Salvini, Lorenzo & Solazzi, Luigi DEVELOPMENT OF A FEM MODEL FOR EVALUATING THE PRESSURE PROFILE IN THE INDUSTRIAL WHEEL AND FATIGUE STRENGTH ANALYSES

Cima, Michele & Solazzi, Luigi FREQUENCY DOMAIN FATIGUE DAMAGE APPLIED TO A VEHICLE WHEEL

REFERENCES

- [1] C.P. G. Donzella, A. Mazzù, *Costruzione di Macchine – Richiami Teorici e Applicazioni*, Snoopy, 2012.
 - [2] G. F., *Study of tire-rim interaction: finite element models and experimental validation*, Politecnico di Milano, n.d.
 - [3] J. Schijve, *Fatigue of structures and materials*, 2009. <https://doi.org/10.1007/978-1-4020-6808-9>.
 - [4] M.S. M. F. Sardella, *Studio della fatica random in ruote per macchine movimento terra. Un confronto tra gli approcci classici e quelli nel dominio della frequenza*, Università degli studi di Brescia, 2014.
 - [5] ASTM, *ASTM E1049 - Standard Practices for Cycle Counting in Fatigue Analysis*, n.d.
 - [6] *Calculating damage with Miner's Rule*, (n.d.). <https://community.sw.siemens.com/s/article/calculating-damage-with-miner-s-rule> (accessed 10 February 2020).
 - [7] *Total Materia*, (n.d.). <https://www.totalmateria.com> (accessed 10 February 2020).
 - [8] G. Donzella, *Appunti di Costruzioni di Macchine*, (n.d.).
 - [9] *FATIGUE CRACK GROWTH RATE*, (n.d.). <https://www.smtsrl.com/index.php/en/services/mechanical-fracture-test-laboratory/fatigue-crack-growth-rate-da-dn>.
 - [10] *semanticscholar*, (n.d.). <https://www.semanticscholar.org/paper/George-Totten-Totten/73c23233ab3eb0fabe83d0e414ea85664683fb4d#extracted>.
 - [11] *Transgranular corrosion fatigue crack growth in age-hardened Al-Zn-Mg (-Cu) alloys*, (n.d.). <https://www.degruyter.com/view/journals/corrrev/33/6/article-p301.xml>.
 - [12] L. Solazzi, L. Pedrazzani, *Caratterizzazione sperimentale numerica di un cerchione per uso industriale sottoposto a diverse condizioni di carico*, 2004.
 - [13] *No Title*, (n.d.). <https://www.toprovelab.com/en/test/rotating-bending>.
 - [14] X. Wang, X. Zhang, *Simulation of dynamic cornering fatigue test of a steel passenger*
-

-
- car wheel, *Int. J. Fatigue*. (2010). <https://doi.org/10.1016/j.ijfatigue.2009.09.006>.
- [15] No Title, (n.d.). <http://stllabs.com/home/>.
- [16] M.F. Marogna F., *Analisi strutturale di un cerchione per veicoli industriali*, Univertiy of Brescia, 2002.
- [17] F. Liò, *Numerical and experimental analysis of an industrial vehicle's wheel: study of random fatigue in time and frequency domain*, Università degli studi di Brescia, 2018.
- [18] F. Liò, M. Bosio, *Tecnica delle costruzioni meccaniche Project: fatigue in time and frequency domain*, n.d.
- [19] E. M. Adigio, E. O. Nangi, *Computer Aided Design and Simulation of Radial Fatigue Test of Automobile Rim Using ANSYS*, *IOSR J. Mech. Civ. Eng.* (2014). <https://doi.org/10.9790/1684-11146873>.
- [20] N. Korunović, M. Trajanović, M. Stojković, *FEA of tyres subjected to static loading*, *J. Serbian Soc. Comput. Mech.* (2007).
- [21] G. Machave, S. Sambhaji, R. Kathar, *Study of Influence of Pressure and Load on Wheel Rim by Radial Fatigue Test*, (2017). https://www.researchgate.net/publication/320373848_Study_of_Influence_of_Pressure_and_Load_on_Wheel_Rim_by_Radial_Fatigue_Test/citation/download (accessed 5 January 2021).
- [22] W. Wang, S. Yan, S. Zhao, *Experimental verification and finite element modeling of radial truck tire under static loading*, *J. Reinf. Plast. Compos.* (2013). <https://doi.org/10.1177/0731684412474998>.
- [23] W. Wang, S. Yan, Y. Zhao, *Numerical and experimental studies of a radial truck tire with tread pattern*, *Simulation*. 91 (2015) 970–979. <https://doi.org/10.1177/0037549715608434>.
- [24] J.A. Guinea García-Alegre, *Numerical study of aluminum wheels subjected to biaxial fatigue test*, Politecnico di Milano, 2017. <https://www.politesi.polimi.it/handle/10589/136225>.
-

- [25] J. Stearns, T.S. Srivatsan, X. Gao, A. Prahash, P.C. Lam, Analysis of Stress and Strain Distribution in a Vehicle Wheel: Finite Element Analysis Versus the Experimental Method, *J. Strain Anal. Eng. Des.* (2005). <https://doi.org/10.1243/030932405X30786>.
- [26] ARTISMO - Experimental measurements of contact pressure by Michelin (help guide), n.d.
- [27] G. Donzella, R. Gerosa, C. Petrogalli, B. Rivolta, G. Silva, M. Beretta, Evaluation of the residual stresses induced by shot peening on some sintered steels, in: *Procedia Eng.*, 2011. <https://doi.org/10.1016/j.proeng.2011.04.560>.
- [28] N.J. Rendler, I. Vigness, Hole-drilling strain-gage method of measuring residual stresses, *Exp. Mech.* (1966). <https://doi.org/10.1007/bf02326825>.
- [29] L. Piovani, L. Scalvini, Fatigue study of a wheel for earth-moving machines: comparison between experimental and numerical (FEM) analysis, Università degli studi di Brescia, 2020.

NOTE:

Other references are cited at the end of each article (see ch. 7 ch. 8, ch 11).

13. APPENDIX 01: TESTING MACHINE

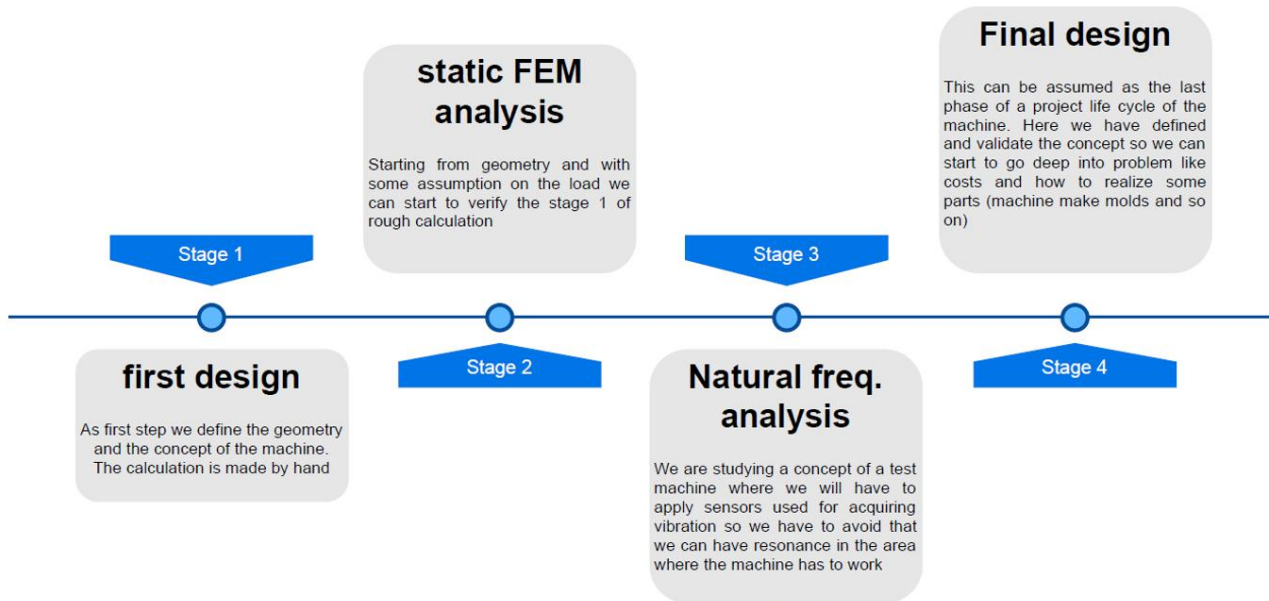


Figure 210 Scheme of work on the concept machine

In this paragraph we will show some step we followed to develop a new concept testing machine for testing all group: tire, rim, wheel hub, suspension arms and force on the junction point.

The aim of this work comes from the idea of have a new tool available. We decided to study a very flexible machine that can perform a very precise study on different load history.

Is clear that we can't think to design a machine from zero in one shot, so we decided to proceed with steps. The first steps we did after defining the concept was a first sizing of the main component, by an estimation of the forces and check of the stress in the different parts. This step gave us the possibility to define roughly the materials of different main parts. We also put attention on another second step on natural frequencies of the machine, because we are studying a testing machine, where will be applied sensor like strain gauge and accelerometer that can be affected in a bad way. At the end we perform also study to reduce the material where is not necessary using the FA software tool, this is done for have a lighter machine and also less material to have a look also on the cost advantage.

This work was presented at MDA 2020 in a conference in Porto (Portugal). Here the link for download the poster: <https://web.fe.up.pt/~mda2020/img/Poster%2035.pdf>

13.1. Machine design

In this chapter we will show the main group of the machine as we thanked it.

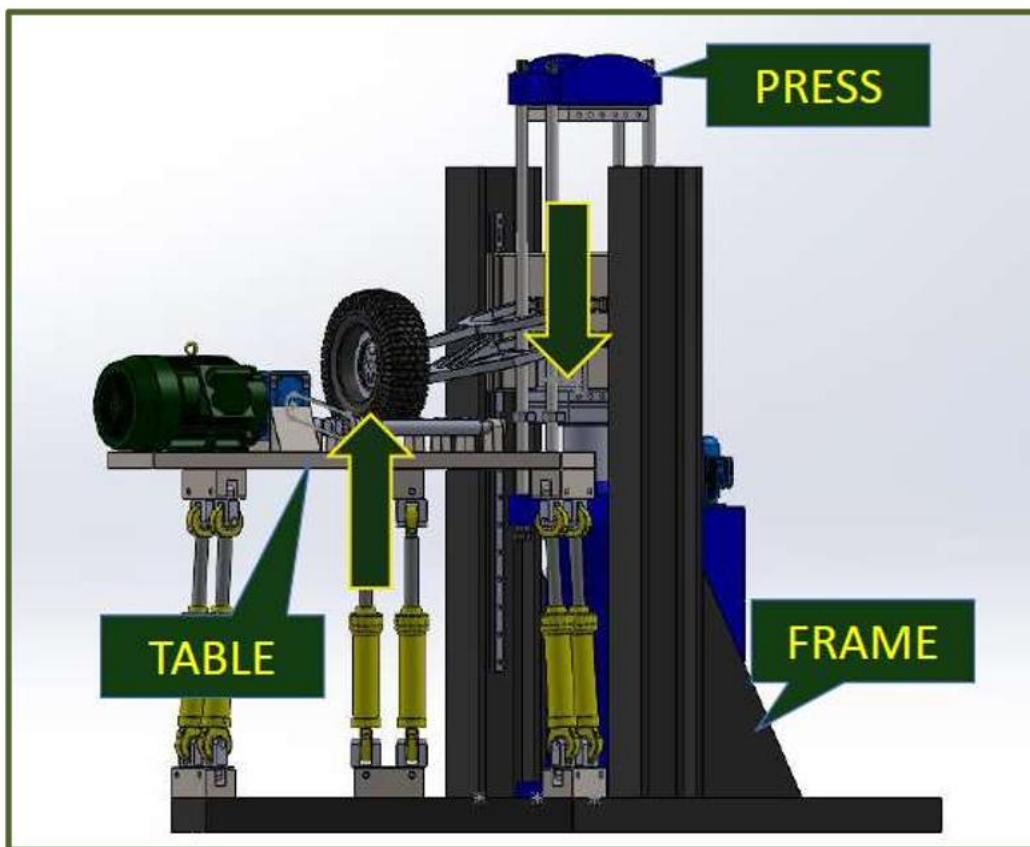


Figure 211 Main groups of the machine

As we can see the machine is multipurpose machine, because we can perform analysis on different component but we have also the possibility to consider all different parts of the suspended mass. In this way we can perform different test that usually is done with different machines. At the end also we can define different set up of the group in study (slip angle, vertical force, torque or speed on wheel).

13.1.1. Gough-Stewart platform (exapode table)

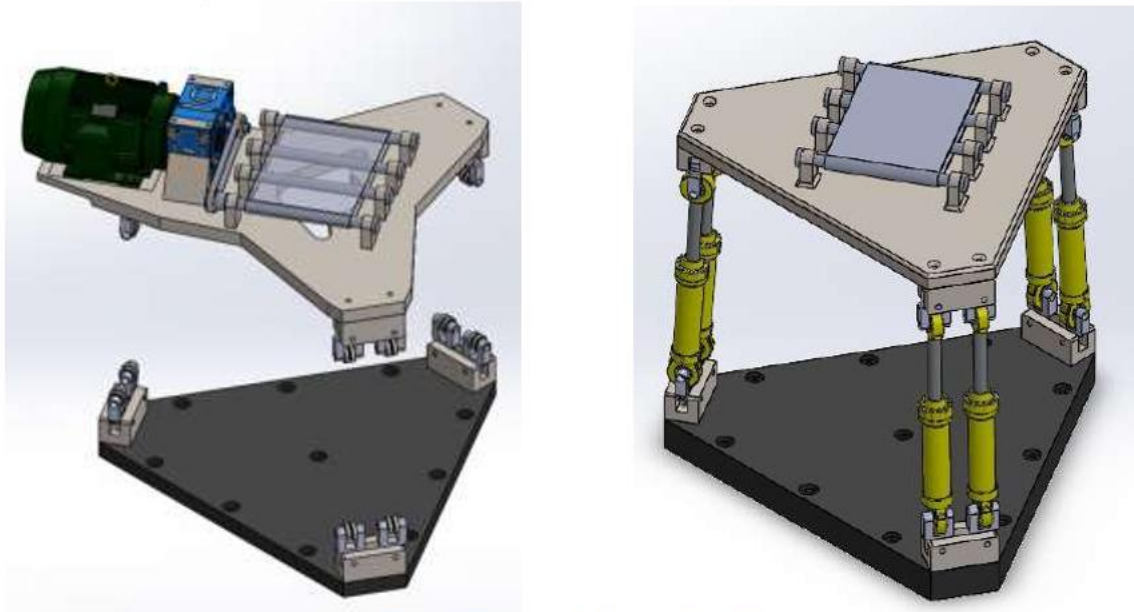


Figure 212 Image of the exapode table

This kind of structure are called parallel robot of Stewart platform. Following moving equation of each six single cylinder the end effect is the movement with different angle of the table. In our case we thinker to place on the centre of the table our belt unit for reduce the inertia moment and give the possibility to have high acceleration. This is one of the most critical part of the machine and is also the core. The problems come to the difficult to have equation of movement (have from the position of the junction point the position in pace of the table), that's way usually the position of the table is find in an experimental way (recursive model). This kind of table can come have high natural frequencies of the structure (we have the possibility to have high load on the legs and this leads to high natural frequencies). Another advantage is that the cylinders works with axial load and very low flexional load.

13.1.2. Belt unit

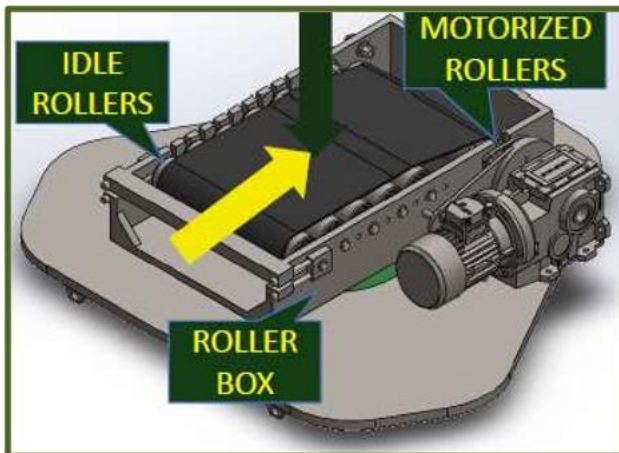


Figure 213 Bel unit

The table as first design is studied in this way:

- Box for rollers;
- Rollers;
- Rollers with motor.

As did for the previous parts we decided to choose as more as we can commercial components. We decided to use reference load to apply on the unit for size the box and rollers. In particular:

- Vertical load 8 kN;
- Lateral load 10 kN.

The length of the table is 800 mm.

13.1.3. Main frame

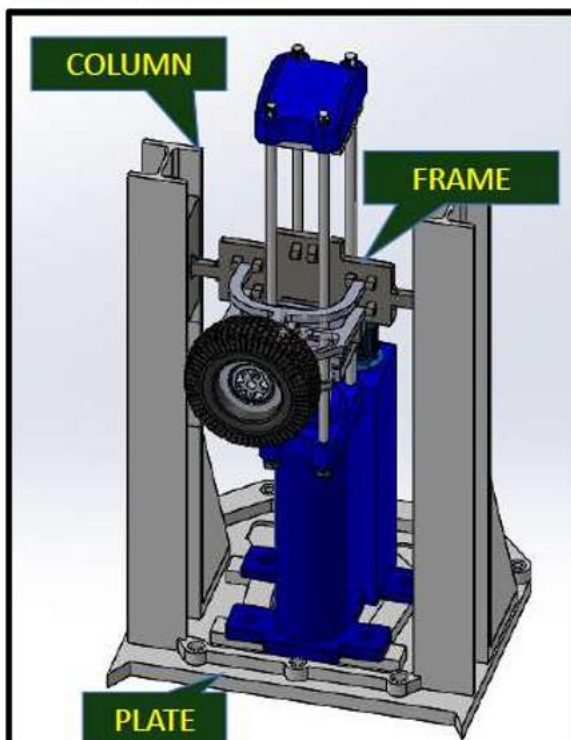


Figure 214 View of the main frame

This part of our application seems not important but is one of the most important group because affect the results of the test on the wheel or pneumatic at first but also give us the possibility to reach frequencies very high on the simulation because of the inertia limit

The main groups of the machine are the frame group. We decided to use a plane guided on two slides fixed on two columns.

The frame is made with a basement of a steel plate machined

On this plate we weld two columns, that have the reference to be inserted in the plan

In this way it's easier to have them parallel.

After weld the basement and have made a treatment of release we can machine the columns because they are so long and need a tolerance at least of 0.1 of parallelism each other to permit to the plate to go up and down on all stroke without too much horizontal stress coming from the tolerance.

For this group some design choose are made

- 1) Use industrial slide at low friction
- 2) Define a plate not connected with the table (cost reduction, easy to move, and hopefully less vibration)
- 3) Be rigid enough to fix the hydraulic press.

13.1.4. Press

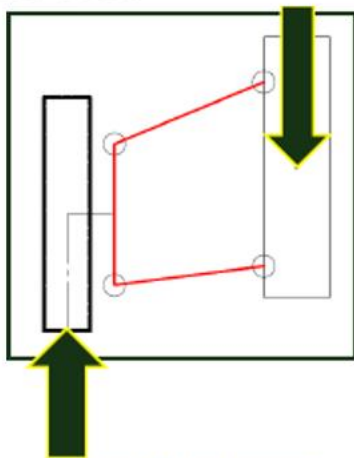


Figure 215 Load concept

For our first design of the machine, we choose a compact form of this with the oil tank and pump inside.

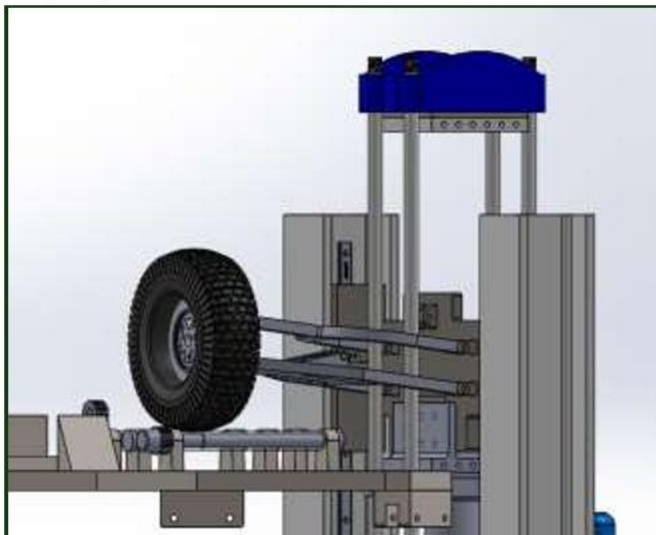


Figure 216 Detail of the press connected to the sliding unit

Before to describe this unit we want to underline that for this first design the force is applied on the sliding table and thanks to the the suspension we can have the reaction on the tire that touch the belt unit. We have also to take in account another step on the developing of this machine by applying load on the wheel hub.

We transmit the movement and the force through this cylinder that is fixed to the plate. So thanks to this movement on vertical axes and thanks of the presence of the shock adsorber mounted on the suspension.

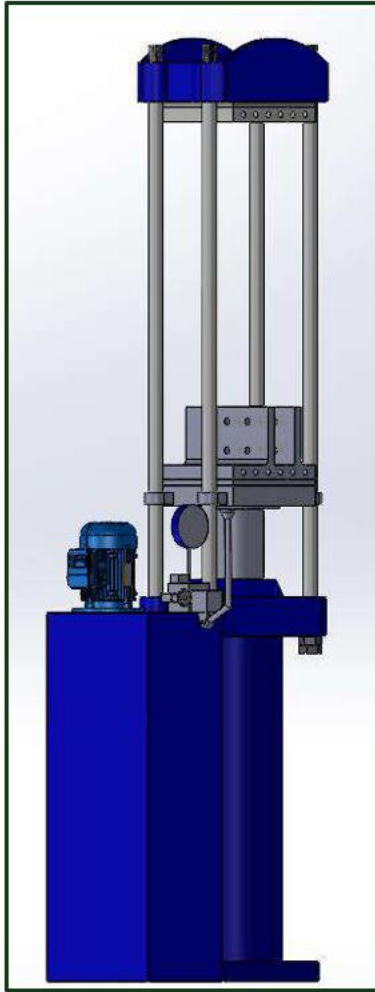


Figure 217 Hydraulic press

13.1.5. FE Analysis

In this chapter we will quickly show some analysis we did. We made a lot of analysis for make a raw sizing of the structures, by adding or removing plates where is necessary.

Have to be clear that this activity has to be accepted as a first design for a concept machine, because to realize a ready to product component require deeper analysis.

We also made a large use (where it was possible) of commercial components (cylinders, motors, roller, exapode table also can be evaluated from Moog see: <https://www.moog.com/content/dam/moog/literature/ICD/Moog-Test-DesignNews-May2011-Article-en.pdf>)

First example are the hydraulic cylinders for the table, where also for them we defined some requirements:

- Axial force: 4.2 kN;
- Stroke: 530 mm
- t for stroke: 1s;
- working pressure: 200 bar.

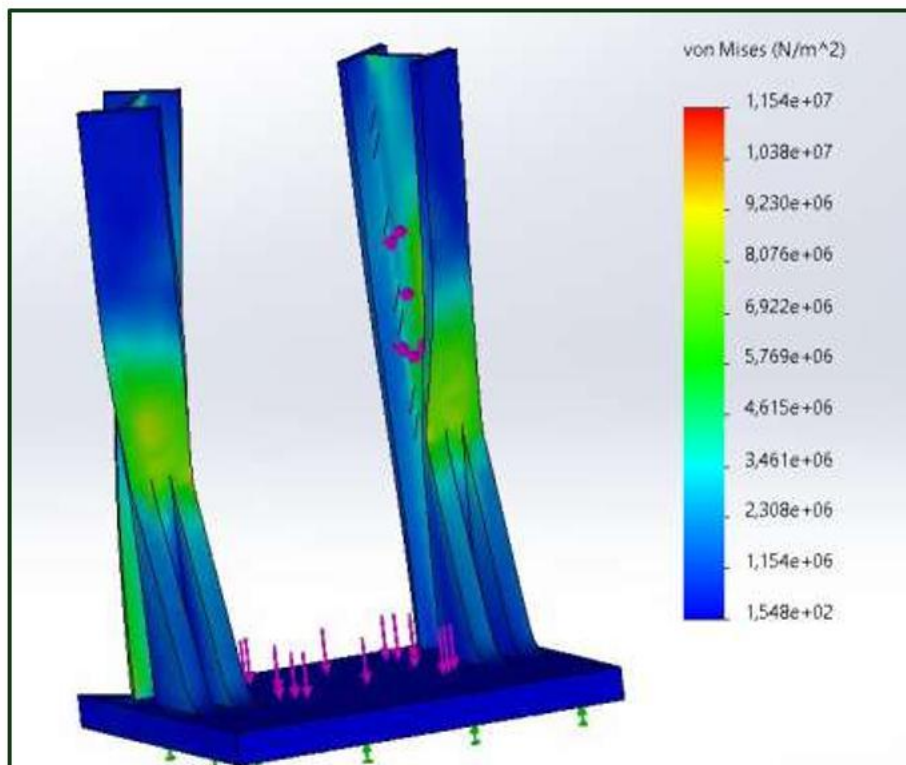
With this data we found and verify some possible options from commercial data sheets.

For the electric motor we made this assumption. We have the tire that can be tested from 50 km/h to 130 km/h and as first attempt we assumed a linear law for the torque, starting from

30 Nm at 0 km/h and a factor of 0.25 Nm/ each rad/s. Starting from this data and matching datasheets of gear box and motor at the end we choose as first attempt a motor (320LP12) of 45 kW and a gearbox with i:2 (manufacturer Rossi ref. code: R I 125 UP2A B3).

Below some example of analysis, we did in the columns of the main frame and basement. We have considered ordinary construction steel for the column (that are commercial components) and laminated plate for the basements (S235JR).

For increase the strength of the structure we add two angular plate that can increase the stiffness of the structure for the horizontal forces. The forces we used for the first sizing are: 10 kN on horizontal direction and 25 kN on vertical direction (this data comes from the data we can find on bibliography on industrial tire).



We also performed a FA analysis on the main plate where we have attachment points for the suspension arms. For this component we applied the forces horizontal and vertical at the same value used for the main frame but considering the presence of the suspension (so by adding an additional torque).

Proprietà	Valore	Unità
Modulo elastico	2.1e+11	N/m ²
Coefficiente di Poisson	0.28	N/A
Modulo di taglio	7.9e+10	N/m ²
Densità di massa	7700	kg/m ³
Resistenza alla trazione	723825600	N/m ²
Resistenza a compressione		N/m ²
Snervamento	620422000	N/m ²
Coefficiente di espansione termica	1.3e-05	/K
Conducibilità termica	50	W/(m·K)
Calore specifico	460	J/(kg·K)
Rapporto di smorzamento del materiale		N/A

Figure 219 Material data used for the plate

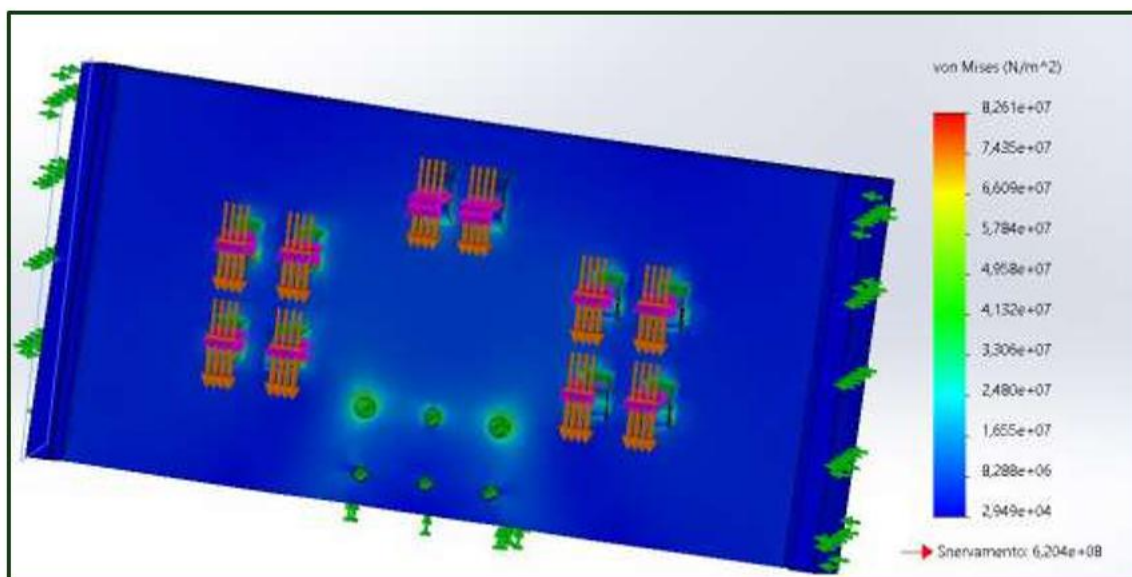


Figure 220 Example of the analysis on the main plate

As we can see the yield stress is one order less that the stress we have found under load.

We finally made the analysis on the plate of the exapode table. We use the same material of the sliding unit.

The load configuration for this component are: 20 kN on vertical direction plus 5kN for the weight of the stuff attacked on the table and 15 kN in orizontal and 25 kN in vertical when the table is at 45°deg.

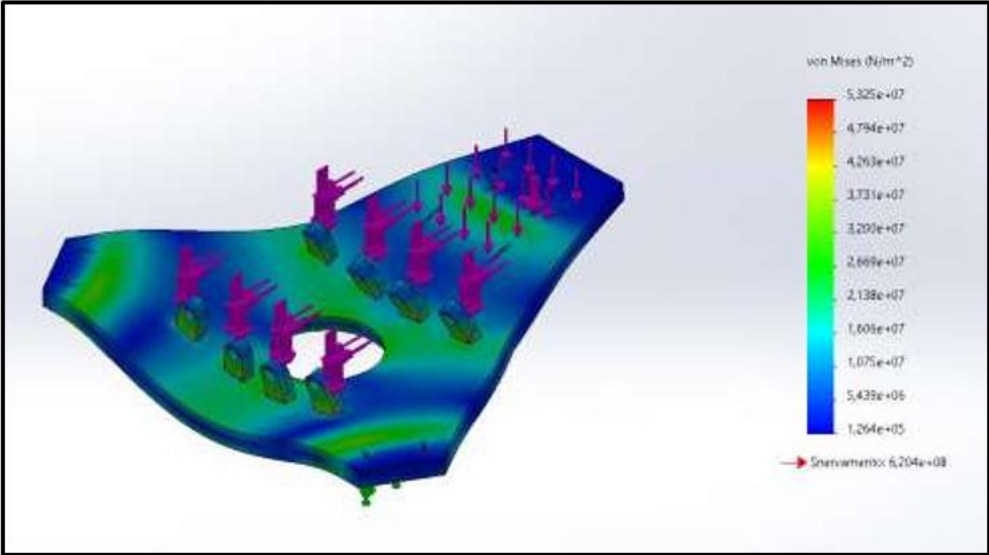


Figure 221 Example of the table plate under second load config.

13.1.6. Natural freq. analysis

Following the work flow presented in Figure 210 we are now ready to check the natural freq. of the testing machine. It’s important to check the machine with all part but for run an analysis of all machine request a lot of time. We decided to consider a few analyses of the different main groups, refine and check them and at the end run with an analysis of all machine.

Before to start we also consider that we have to try to not have natural freq. in the range of freq. where we have to acquire the signal. From papers and the experience of the manufacturer we can say that we have to try to not have natural freq. in the range of 10-30 Hz.

<i>BASEMENT STRUCTURE</i>		<i>BASEMENT STRUCTURE</i>		<i>BASEMENT STRUCTURE</i>		<i>BASEMENT STRUCTURE</i>	
<i>Way of vibration</i>	<i>f [Hz]</i>	<i>Way of vibration</i>	<i>f [Hz]</i>	<i>Way of vibration</i>	<i>f [Hz]</i>	<i>Way of vibration</i>	<i>f [Hz]</i>
1	34.19	1	34.19	1	34.19	1	34.19
2	34.57	2	34.57	2	34.57	2	34.57
3	63.03	3	63.03	3	63.03	3	63.03
4	63.19	4	63.19	4	63.19	4	63.19

Table 27 First four natural freq. of the main group of the machine

As we can see the frequencies of each single part are far enough to avoid resonance problems.

But to assure that we can work safely in a certain range we have to check the frequencies of all structure. After that is mandatory to run with a simulation of the whole structure.

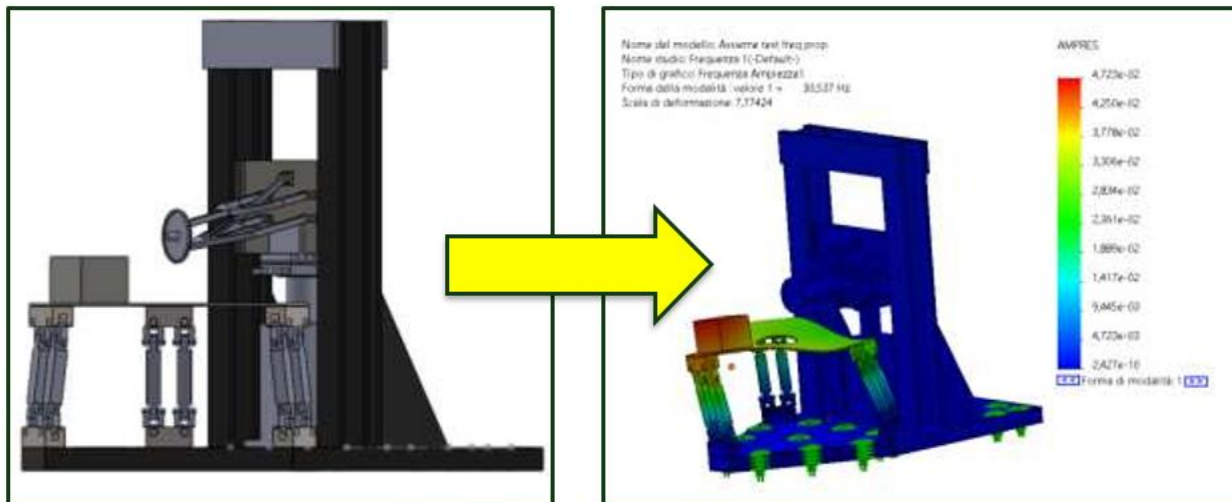


Figure 222 Natural freq. analysis simulation

<i>FULL STRUCTURE</i>	
<i>Way of vibration</i>	<i>f [Hz]</i>
1	30.53
2	32.13
3	38.70
4	41.68

Table 28 Natural freq. of all structure

As we can see, as first design we have a good distribution of natural freq. that are not near 10 Hz to 28.

13.1.7. Optimization and check of natural freq.

In order to reduce weight and off course cost of the machine, for have also a better dynamic response of tha machine we run into a optimization analysis, made group by group.

This process is a cycle where every step need to be checked, in terms of reduction of weight achieved, stress and natural frequency. Below some example:

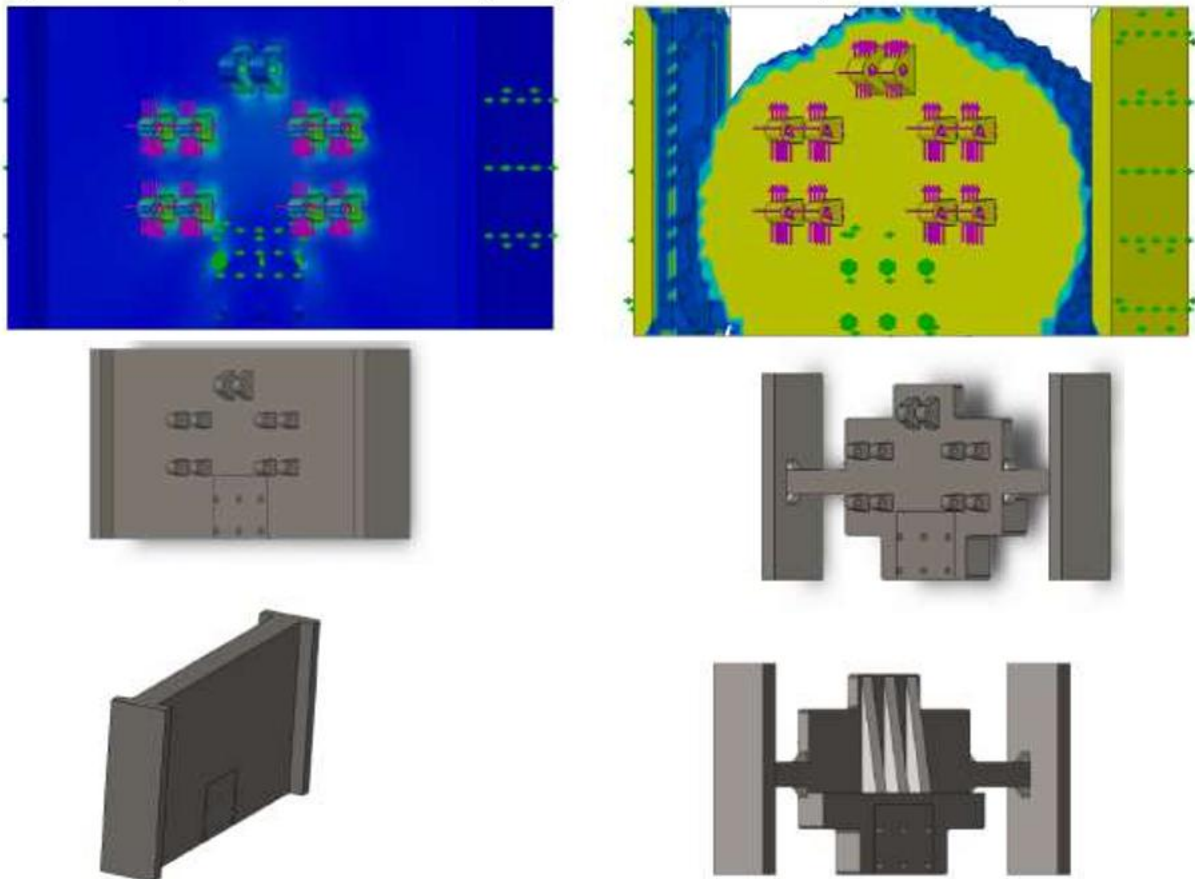


Figure 223 Example of optimization

It's important to clarify that the result form the optimization is not to be followed as it is but we have to compare it with an analysis cost benefits we have also related with the technologic process we follow for the different parts.

13.2. Future developments

For sure to complete the design of the machine we have to consider also to try to simplify it so there are some areas that need to be better investigate for example:

- Change the table with a new one more easy but also less flexible in terms of orientation;
 - Define a new hub for wheel where apply the force and also acquire signal;
 - Modify layout of the machine for change the press and put a motor on the plate so we can adjust the height;
 - Make a cost analysis;
 - Optimize groups and build first concept.
-

